

## Durham E-Theses

---

### *The tectonic evolution of mantle rocks from the lizardophiolite complex, South-West England*

Cook, Charles Andrew

#### How to cite:

---

Cook, Charles Andrew (1999) *The tectonic evolution of mantle rocks from the lizardophiolite complex, South-West England*, Durham theses, Durham University. Available at Durham E-Theses Online:  
<http://etheses.dur.ac.uk/4505/>

#### Use policy

---

The full-text may be used and/or reproduced, and given to third parties in any format or medium, without prior permission or charge, for personal research or study, educational, or not-for-profit purposes provided that:

- a full bibliographic reference is made to the original source
- a [link](#) is made to the metadata record in Durham E-Theses
- the full-text is not changed in any way

The full-text must not be sold in any format or medium without the formal permission of the copyright holders.

Please consult the [full Durham E-Theses policy](#) for further details.

---

Academic Support Office, Durham University, University Office, Old Elvet, Durham DH1 3HP  
e-mail: [e-theses.admin@dur.ac.uk](mailto:e-theses.admin@dur.ac.uk) Tel: +44 0191 334 6107  
<http://etheses.dur.ac.uk>

**The tectonic evolution of mantle rocks from the Lizard  
Ophiolite Complex,  
south-west England**

**by**

**Charles Andrew Cook BSc. (Hons)  
University of St. Andrews.**

The copyright of this thesis rests  
with the author. No quotation from  
it should be published without the  
written consent of the author and  
information derived from it should  
be acknowledged.

**A thesis submitted in partial fulfilment of the requirements for the  
degree of Doctor of Philosophy**

**Department of Geological Sciences,  
University of Durham.**

**April 1999**



**17 JAN 2000**

## DECLARATION

No part of this thesis has been previously submitted for a degree at this or any other university. The work described in this thesis is entirely that of the author, except where reference is made to previously published or unpublished work.

*Charles Cook*

C.A.Cook

University of Durham

Department of Geological Sciences

April 1999

**Copyright © by C.A.Cook**

The copyright of this thesis rests with the author. No quotation or data from it should be published without the authors prior written consent and any information derived from it should be acknowledged.



## ABSTRACT

In SW England, a highly deformed and metamorphosed assemblage of ultramafic, mafic and granitic rocks is interpreted to represent a fragment of upper mantle and lower oceanic crust: the Lizard Ophiolite Complex. Although the processes involved in the tectonic and chemical evolution of mafic rocks and subsequent emplacement of this complex are well documented, the importance of the tectonic evolution of the peridotites is poorly constrained. Structural field mapping of deformed peridotites, ultramafic and mafic cumulates and amphibolites, combined with geochronological (sensitive high mass-resolution ion micro-probe), microstructural (optical microscope and universal stage) and geochemical (X-ray fluorescence, ICP-MS and electron microprobe) analyses undertaken as part of this thesis have identified evidence of four tectono-magmatic events, three of which occurred during the Early to Late Devonian. An earlier episode relates to a fragment of Ordovician basement that became tectonically incorporated within the basal structural unit of the Lizard Ophiolite Complex.

A basement, and structurally lowermost unit, comprising granitic (MOWG) and layered meta-sedimentary and meta-basic (OLHS) rocks of earliest Ordovician age (~499-488Ma) is interpreted as fragments of arc-type crust developed in an active magmatic arc during closure of an ocean basin (Rheic ocean?).

Tectonic exhumation of mantle along extensional lithosphere-scale mantle shear zones in the Early Devonian or earlier (~397 Ma) may be responsible for the early tectonic evolution of the mantle section of the Lizard Ophiolite Complex. It is proposed that this may have occurred during asymmetric extension associated with continental breakup and oceanic rifting. During exhumation, the high-T and high-P mineral assemblage (~1200°C & 15Kb) of the Lizard peridotites progressively re-equilibrated to conditions of lower T and P (~919-1074°C & 5-6Kb). High temperature (~900-1050°C) deformation of ultramafic and mafic Traboe cumulates is consistent with deformation and metamorphism of early formed oceanic crust in the hangingwall of the inferred shear zone, which may have been located at the base of the crustal sequence close to the Moho.

The later evolution of a second generation of oceanic crust sequence shown by gabbro and mafic dyke intrusion in the early to middle Devonian (~ 375 Ma) primarily involved magmatism, but NE-SW directed extension of the oceanic crust may have been predominantly accommodated by low-angle ductile shear zones, suggestive of a magma-starved slow-spreading ridge environment.

Emplacement of the Lizard Ophiolite Complex took place during the Middle to Late Devonian (~390-366Ma). Top-to-the-NW thrusting facilitated decoupling of the mantle and emplacement over deformed and metamorphosed oceanic crust. During emplacement, widespread magmatism involved the intrusion of a mixed suite of felsic and mafic magmas that may well have been focused along the detachment surface. The geochemical characteristics of this suite of intrusive rocks suggests that initial emplacement of the Lizard Ophiolite Complex may have taken place in a subduction zone environment. Extensive, apparently extensional re-activation of thrust contacts involved the development serpentine-filled fault zones.

It is proposed that infiltration of volatile-rich melts during the early mantle deformation and exhumation along extensional shear zones could have led to significant localisation of strain and weakening of the upper mantle. The main evidence supporting this hypothesis being mylonitic peridotites that demonstrate confirmation of chemical enrichment as a result of melt impregnation. Weakening may have occurred by replacement of strong mineral phases e.g. pyroxene by weaker phases e.g. amphibole i.e. reaction softening, characterised by the development of mylonitic amphibole-bearing peridotites. It is concluded that this and other weakening processes may also be responsible for the development and enhancement of mantle shear zones in other ophiolite complexes and present-day oceanic lithosphere during oceanic rifting.

## ACKNOWLEDGEMENTS

- Firstly, I would like to express my gratitude to my three supervisors, Bob Holdsworth, Mike Styles and Julian Pearce, who have provided much appreciated support and encouragement throughout. Mike Styles initially pointed me in the right direction, provided first class supervision in the field and guidance on the microprobe at BGS. This PhD was funded jointly by a British Geological Survey studentship and a Durham University postgraduate research award.
- Special thanks are expressed to David Green, firstly for providing me with the opportunity to spend 6 weeks at the Research School of Earth Sciences at the Australian National University in Canberra. Also, for providing me with tremendous inspiration and many stimulating discussions on the geology of the Lizard, both in the field and at ANU. Allen Nutman and David Green are thanked for providing me SHRIMP data, which has been tremendously invaluable and something I never envisaged receiving. Martin Cmiral, Steve Eggins, Martin Drury (Utrecht) and Airian (Utrecht) for help in the field. Stefan, Vivien, Nick, Paul, Dean, Uli, Bill, Andrew, Romulo, Hugh, Wayne, Eleanor and the rest of the PEP team are thanked for warmly welcoming me to ANU, providing me with assistance on many geological matters, life down-under and excellent coffee breaks.
- George has been tremendously supportive during the last few years. She patiently spent 3 weeks providing me with field assistance and suffered living in a cold caravan. Thank you also for providing me with a home during the last few months, doing my washing, some cooking, cups of tea, whisky, also dragging me out on hairy mountain bike rides to keep me sane.
- Several people are thanked for their academic input. Andy Alexander and Robin Shail for discussions in the field and introducing me to Anne's pasty shop and Porthallow vineyard; Wayne Bailey and Jonny Imber for tons of advice and discussions on structural geology; Nathan Doble and his parents for accommodation whilst in Cornwall and trips to the dodgy night club in Redruth; Jim Andrews for encouragement and discussion on Lizard geology over many pints at TSG conferences; Alfonso Brod and Ercan Aldamaz for help with petrology, XRF analyses and probe data; Danny Donoghue for help with GIS, digitising and allowing me to use the Geography department computer facilities; Graham Pearson for help with geochemical matters and an excellent field trip to Skye; Andrew Rothstein for discussions on the Lizard peridotites; Matt Pritchard for help with various computer problems; Martin Holder (BGS) for advice in the field and in the 'Old Inn'.
- My fellow PhD companions in the department who have made my time in Durham enjoyable. Jonny, Matt, Sarah, Caroline, Ian, Toby, Otter, Loraine, Paul, Janine, Lee, Martyn, Wayne, Alun, Adam, Simon 'Molly', Simon Grant, Gail, Ziad, Jo, Roberto, Ercan, Alfonso, Alwyn and John have all been great company and good friends.

- Ron Hardy has provided me with quality XRF data and discussions on the Highlands. Chris Ottley for ICP-MS analyses, training on sample preparation, combine harvester dust contamination theories, discussions on mountaineering and getting me up the 'In-Pin' on the Cuillin ridge. Dave, Karen, Alan, Julie, Ron Lambert, Carole, Claire, George, Dave and Gerry for great help and advice on many different things.
- George's parents are thanked for giving me somewhere to stay whilst I was working at BGS, keeping me well fed, meals at Lindrick and introducing me to Mansfield bitter.
- My mountain biking companions; Debbie, Nikki, Stuart, Kevin, Martin, Aideen, Hoppy, Doug, Al, Ben, Paul, Jeanette, Gordon, Ian, Claire, Gavin and other Martin for introducing me to some great rides, weekends away and Saw Doctors concerts.
- Finally, to Mum, Dad, Stephen, Richard, Christopher, Colin and Prince (the mutt), who have been extremely supportive during the last 26 years.

# TABLE OF CONTENTS

Declaration	ii
Abstract	iii
Acknowledgements	iv
Contents	vi
 <b>Chapter One: Introduction and terminology</b>	 <b>1</b>
<b>1.1. Introduction.</b>	<b>1</b>
<b>1.2. Peridotite classification, terminology and occurrence</b>	<b>1</b>
1.2.1.a. Composition	2
1.2.1.b. Textures	2
1.2.2. Oceanic ultramafic rocks	7
1.2.3. Continental ultramafic rocks	8
1.2.3.a. Ophiolitic ultramafic rocks	8
<b>1.3. Structural terminology</b>	<b>11</b>
1.3.1. Deformation mechanisms	11
1.3.1.a. Fracture, frictional grain-boundary sliding and cataclastic flow	12
1.3.1.b. Diffusive mass transfer (DMT)	12
1.3.1.c. Crystal plastic flow	13
1.3.2. Grain size effects	16
1.3.3. Aggregate microstructures and rheology	17
1.3.4. Interpretation of peridotite microstructures; olivine petrofabrics	19
1.3.5. Kinematic indicators	21
1.3.5.a. Shear sense indicators – ductile regime	21
<b>1.4. Scientific methods</b>	<b>24</b>
1.4.1. Field methods	24
1.4.2. Laboratory methods (University of Durham)	25
1.4.2.a. Geographical Information System (GIS)	25
1.4.2.b. Olivine petrofabrics	25
1.4.2.c. Whole rock geochemical analyses	25
1.4.3. Data from other sources	25
1.4.3.a. British Geological Survey	26
1.4.3.b. Research School of Earth Sciences (Australian National University)	26
1.4.3.c. Cambridge University (Sedgewick Museum)	26
<b>1.5. Primary objectives and layout of thesis</b>	<b>27</b>
 <b>Chapter Two: Previous Work: The geology of the Lizard Ophiolite Complex.</b>	 <b>29</b>
 <b>2.1. Regional setting of the Lizard Ophiolite Complex</b>	 <b>29</b>
	vi

<b>2.2. Introduction: The geological subdivision of the Lizard Peninsula</b>	31
2.2.1. The Ordovician basement	31
2.2.2. Devonian sediments and volcanic rocks of the Gramscatho Group	34
2.2.3. Devonian rocks of the Lizard ophiolite Complex	36
<b>2.3. The geology of the Lizard ophiolite Complex.</b>	38
2.3.1. Lizard peridotites	40
2.3.2. Ultramafic and Mafic Traboe cumulates	43
2.3.3. Landewednack amphibolites	45
2.3.4. Porthoustock amphibolites	46
2.3.5. Crousa gabbro	47
2.3.6. Mafic dykes	48
2.3.7. Kennack Gneiss	49

## **Chapter Three: Field and geochronological evidence for the structural and magmatic evolution of the Lizard Ophiolite Complex.**

51

<b>3.1. Introduction</b>	51
<b>3.2. Ordovician basement rocks of the Lizard Peninsula</b>	53
3.2.1. The Man of War Gneiss	55
3.2.2. The Old Lizard Head Series and Lizard Head Sill	55
3.2.3. Summary	59
<b>3.3. Early mantle deformation</b>	59
3.3.1. Coarse-grained lherzolites	60
3.3.1.a. Fabric Orientation	65
3.3.2. Mylonitic Peridotites	66
3.3.2.a. Dip-slip fabrics	69
3.3.2.b. Strike-parallel fabrics	69
3.3.3. Kinematics analysis	71
3.3.4. Summary	71
<b>3.4. Oceanic crust construction</b>	72
3.4.1. Ultramafic and mafic Traboe cumulates and gabbroic veins	73
3.4.1.a. Potstone Point – Georges Cove area (GR 670 155; Figure 3.19)	74
3.4.1.b. Parc Bean Cove (GR 666 158; Figure 3.22)	77
3.4.1.c. Nantivet Rock – Kynance Cove area (GR 683 133; Figure 3.23)	79
3.4.1.d. Porthallow Cove – Porthkerris Cove (GR 805 231; Figure 3.28)	81
3.4.1.e. Traboe Boreholes	85
3.4.2. Landewednack Amphibolites	87
3.4.3. Later magmatism and deformation – East coast of Lizard	89
3.4.3.a. Magmatism and deformation associated with the Crousa gabbro	89
3.4.3.b. Porthoustock amphibolites: an extensional shear-zone	89
3.4.4. Summary	96
<b>3.5. Emplacement of the Lizard Ophiolite Complex, and later tectonic/magmatic events</b>	97
3.5.1. Emplacement-related fabrics in the Basement rocks	97
3.5.1.a. Old Lizard Head Series (OLHS)	98
3.5.1.b. Old Lizard Head Thrust (OLHT)	98

3.5.2. Emplacement-related fabrics within the Devonian rocks of the Lizard Ophiolite Complex	100
3.5.2.b. Polbrearn Cove to Kildown Point area (Figure 3.43)	103
3.5.2.c. The Predannack Borehole (GR 6901 1634; Figure 3.55)	110
3.5.3. Emplacement-related fabrics in the Lizard peridotites	114
3.5.4. Magmatism associated with emplacement	115
3.5.5. Later magmatic events	119
3.5.6. High angle brittle extensional faulting	120
3.5.7. Summary	122
<b>3.6. Summary of field and geochronological evidence</b>	<b>123</b>

## **Chapter Four: Microstructures of rocks from the Lizard Ophiolite**

<b>Complex.</b>	<b>125</b>
-----------------	------------

<b>4.1. Introduction</b>	<b>125</b>
<b>4.2. Ordovician basement rocks</b>	<b>125</b>
4.2.1. Old Lizard Head Series (amphibolites)	126
4.2.1.a. Amphibolites interbanded with pelite and psammite	126
4.2.1.b. Porphyritic basic sheets	126
4.2.1.c. Lizard Head Sill	128
4.2.2. Summary	129
<b>4.3. The Lizard peridotites</b>	<b>130</b>
4.3.1. New sub-division of the peridotites	130
4.3.2. Serpentinisation	131
4.3.3. Relict primary microstructures	132
4.3.4. Microstructures of coarse-grained lherzolitic peridotites	133
4.3.4.a. Spinel lherzolite	133
4.3.4.b. Pyroxenite	135
4.3.4.c. Dunite	137
4.3.4.d. Plagioclase lherzolite	138
4.3.5. Microstructures of mylonitic peridotites	139
4.3.5.a. Mylonitic plagioclase-bearing peridotite	140
4.3.5.b. Mylonitic amphibole-bearing peridotite	143
4.3.5.c. Feldspathic bands	144
4.3.6. Petrological variations in the Lizard peridotites: GIS based study	147
4.3.6.a. Lithological map: Primary rock type (Figure 4.17)	147
4.3.6.b. Grain size variations (Figure 4.18)	149
4.3.6.c. Modal volume variations in the constituent mineral	150
4.3.6.d. Clinopyroxene (Figure 4.19)	151
4.3.6.e. Olivine (Figure 4.20)	152
4.3.6.f. Plagioclase (Figure 4.21)	152
4.3.6.g. Serpentinisation (Figure 4.22)	153
4.3.6.h. Secondary amphibole: Colourless-hornblende (Figure 4.23)	155
4.3.7. Olivine petrofabrics and shear sense	158
4.3.7.a. Olivine petrofabrics: Results.	159
4.3.7.b. Olivine slip systems: Deformation temperatures and mechanisms	163
4.3.7.c. Shear-sense implications	167

4.3.8. Hydrous shear zones in the Lizard peridotites	169
4.3.10. Serpentine-filled faults	170
4.3.11. Microstructural evolution of the Lizard peridotites – summary	172
<b>4.4. Petrographic characteristics of the oceanic crust and cumulate rocks</b>	173
4.4.1. Cumulates and amphibolites	173
4.4.1.a. Ultramafic Traboe cumulates	173
4.4.1.b. Mafic Traboe cumulates	175
4.4.1.c. Gabbroic veins	181
4.4.1.d. Landewednack amphibolites	184
4.4.1.e. Porthoustock amphibolites	188
4.4.2. Summary	189
<b>4.5. Summary of microstructural evidence</b>	192

## **Chapter Five: Mineral chemistry of the Lizard peridotites and associated rocks.**

194

<b>5.1. Introduction</b>	194
<b>5.2. Olivine chemistry</b>	195
5.2.1. Olivine chemistry- results	195
5.2.2. Olivine chemistry- interpretation and discussion	196
5.2.3. Olivine chemistry – summary	199
<b>5.3. Orthopyroxene chemistry</b>	199
5.3.1. Orthopyroxene chemistry - results	199
5.3.2. Orthopyroxene chemistry – interpretation and discussion	201
5.3.3. Orthopyroxene chemistry – summary	208
<b>5.4. Clinopyroxene chemistry</b>	208
5.4.1. Clinopyroxene chemistry - results	209
5.4.2. Clinopyroxene chemistry – interpretation and discussion	210
5.4.3. Clinopyroxene chemistry – Landewednack amphibolites	219
5.4.3.a. Results and interpretation	219
5.4.4. Clinopyroxene chemistry – summary	222
<b>5.5. Spinel chemistry</b>	223
5.5.1. Spinel chemistry - results	223
5.5.2. Spinel chemistry – interpretation and discussion	224
5.5.2.a. Partial melting trends	225
5.5.2.b. Metamorphic re-equilibration trends	229
5.5.2.c. Melt-rock interaction trends	231
5.5.2.d. Igneous fractionation trends	235
5.5.2.e. Evidence for the palaeotectonic setting of the Lizard peridotites	237
5.5.3. Spinel chemistry – summary	238
<b>5.6. Amphibole chemistry</b>	239
5.6.1. Amphibole chemistry - results	239
5.6.2. Amphibole chemistry – interpretation and discussion	240
5.6.3. Amphibole chemistry – Landewednack amphibolites	246
5.6.3.a. Results	246
5.6.3.b. Interpretation and discussion	247
5.6.3. Amphibole chemistry – summary	249

<b>5.7. Plagioclase chemistry</b>	250
5.7.1. Plagioclase chemistry – results	250
5.7.2. Plagioclase chemistry – interpretation and discussion	251
5.7.4. Plagioclase chemistry – summary	254
<b>5.8. Temperature and pressure evolution and conditions during deformation</b>	254
5.8.1. Pyroxene thermobarometry	255
5.8.1.a. Results	258
5.8.1.b. Interpretation and discussion	261
5.8.2. Amphibole-plagioclase thermobarometry - Amphibolites	266
5.8.2.a. Results	266
5.8.2.b. Interpretation and discussion	268
5.8.3. Thermobarometry - summary	271
<b>5.9. Mineral chemistry and thermobarometry: summary and discussion</b>	272
5.9.1. Metamorphic re-equilibration	272
5.9.2. Melt-rock interaction	273
5.9.3. Igneous fractionation trends	274
5.9.4. P-T evolution	274

## **Chapter Six: Isotopic, Major, Trace and Rare Earth Element characterisation of the rocks from the Lizard Ophiolite Complex.**

277

<b>6.1. Introduction</b>	277
<b>6.2. Major and trace elements</b>	278
6.2.1. Serpentinisation	278
6.2.2. Lizard peridotites - results	280
6.2.3. Rocks associated with the Lizard peridotites - results	285
6.2.4. Lizard peridotites and associated rocks – Interpretation and discussion	289
6.2.5. Amphibolites and mafic dykes	296
6.2.5.a. Results	297
6.2.5.b. Interpretation and discussion	299
6.2.6. Ordovician basement	299
6.2.6.a. Results	300
6.2.6.b. Interpretation and discussion	300
6.2.7. Summary	300
<b>6.3. Rare Earth Elements</b>	301
6.3.1. Lizard peridotites - results	302
6.3.2. Rocks associated with the Lizard peridotites - results	303
6.3.3. Lizard peridotites and associated rocks – Interpretation and discussion	305
6.3.4. Amphibolites and mafic dykes	310
6.3.4.a. Results	310
6.3.4.b. Interpretation and discussion	314
6.3.5. Ordovician basement	320
6.3.5.a. Results	320
6.3.5.b. Interpretation and discussion	322
6.3.6. Summary	326
<b>6.4. Isotopic evidence – results and interpretation</b>	327
6.4.1. Lizard Ophiolite Complex – results and interpretation	331



6.4.2. Ordovician basement – results and interpretation	331
6.4.3. Summary	332
<b>6.5. Whole rock geochemistry – summary and discussion</b>	332
6.5.1. Lizard peridotites	333
6.5.2. Ultramafic and mafic Traboe cumulates	334
6.5.3. Gabbroic veins	334
6.5.4. Landewednack amphibolites and mafic dykes	334
6.5.5. Porthoustock amphibolites	335
6.5.5. Ordovician basement	335
 <b>Chapter Seven: Synthesis, discussion and conclusions.</b>	 336
 <b>7.1. Introduction</b>	 336
<b>7.2. Summary of the tectonic evolution of the Lizard Ophiolite Complex</b>	336
7.2.1. Early evolution of Ordovician basement	337
7.2.2. Early mantle exhumation and development of oceanic crust	338
7.2.3. Later magmatism and extensional tectonics	346
7.2.4. Emplacement of the Lizard Ophiolite Complex	348
<b>7.3 Regional tectonic implications of evolution of the Lizard Ophiolite Complex</b>	352
7.3.1. Ordovician evolution of NW Europe	352
7.3.2. Devonian tectonic evolution of SW England	353
<b>7.4. Implications for the early evolution of mantle rocks in ophiolite complexes</b>	356
7.4.1. Mantle fabrics in ophiolite complexes	357
7.4.2. Implications of syn-tectonic melt infiltration	359
7.4.3. Rheological implications and strength of the mantle	361
7.4.4. Structural geology of the upper mantle	363
<b>7.5. Final conclusions</b>	364
 <b>References</b>	 366
 <b>Appendices</b>	 389
<b>Appendix A: Analytical techniques</b>	389
A.1 Sample Preparation	389
A.2 X-Ray Fluorescence Analysis	389
A.2.1. XRF Error control	390
A.3. ICP-MS Analysis	392
A.3.1. ICP-MS detection limits	394
A.3.2. ICP-MS precision	395
A.4. Electron Probe Micro-Analysis	401
A.5 Sensitive High Mass-Resolution Ion Micro-Probe (SHRIMP) Analysis	403
A.5.1. Analytical methods and results	403

<b>Appendix B: Geographical Information System (GIS)</b>	409
B.1 INTRODUCTION	409
B.2 OBJECTIVES	410
B.3 METHODOLOGY	410
B.3.1. Thin section selection	411
B.3.2. The pro forma sheet	412
B.3.3. Transferring petrographic data from <i>pro forma</i> sheets onto an Excel database	414
B.3.4. Working with GIS - summary	414
 <b>Appendix C: Thermometry and barometry equations</b>	417
C.1. Wells (1977) pyroxene thermometer	417
C.2. Brey and Kohler (1990) pyroxene thermometer	417
C.3. Brey <i>et al.</i> (1990) pyroxene thermometer	417
C.4. Witt-Eickschen and Seck (1991) pyroxene thermometer	418
C.5. Mercier (1980) pyroxene barometer	418
C.6. Johnson and Rutherford (1989) amphibole barometer	418
C.7. Schmidt (1992)	419
C.8. Spear (1980) amphibole-plagioclase thermometer	419
C.9. Blundy and Holland (1990) amphibole-plagioclase thermobarometer	419
 <b>Appendix D: Geochemical data</b>	420

# **CHAPTER ONE**

## **INTRODUCTION AND TERMINOLOGY**

### **1.1. Introduction.**

It is well established in the literature that ophiolites usually represent fragments of lithosphere, which have become detached from their oceanic substrate and tectonically emplaced (or obducted) onto a continental margin. During the past three decades, a great deal of research has been dedicated to ophiolite complexes. These studies were primarily concerned with comparisons between present-day oceanic rocks and ophiolites. Nowadays, it is recognised that ophiolites provide an ideal opportunity to directly investigate the nature of magmatic and tectonic processes operative in the lowermost crust and upper mantle of oceanic lithosphere. This includes the generation of oceanic crust at mid-ocean or arc spreading centres and also the subsequent closure of ocean basins and emplacement of ophiolite complexes. Peridotites are one of the major rock types of oceanic/ophiolite complexes.

The purpose of this chapter is to outline the nature and occurrence of peridotites and introduce the processes related to the construction and subsequent tectonic emplacement of ophiolite complexes. The objective and layout for the remainder of the thesis is presented at the end of this chapter.

### **1.2. Peridotite classification, terminology and occurrence**

Both composition and texture provide the basis for classification of ultramafic rocks referred to in the text, with textural terms being used as a prefix for classifications based on the composition of ultramafic rocks. In the following sections, the various classification schemes for ultramafic rocks relevant to this thesis are presented. This is followed by a brief outline of the nature and occurrence of peridotites from different tectonic environments.



### 1.2.1.a. Composition

Classification follows IUGS recommendation (Le Maitre *et al.* 1989) and conforms to the BGS Rock Classification Scheme (Gillespie & Styles, 1998). Compositional classification of ultramafic rocks is based on the relative proportions of olivine (OL), orthopyroxene (OPX) and clinopyroxene (CPX) (Figure 1.1). These terms may be qualified by a prefix based on the main accessory phase: plagioclase, spinel, garnet or hornblende.

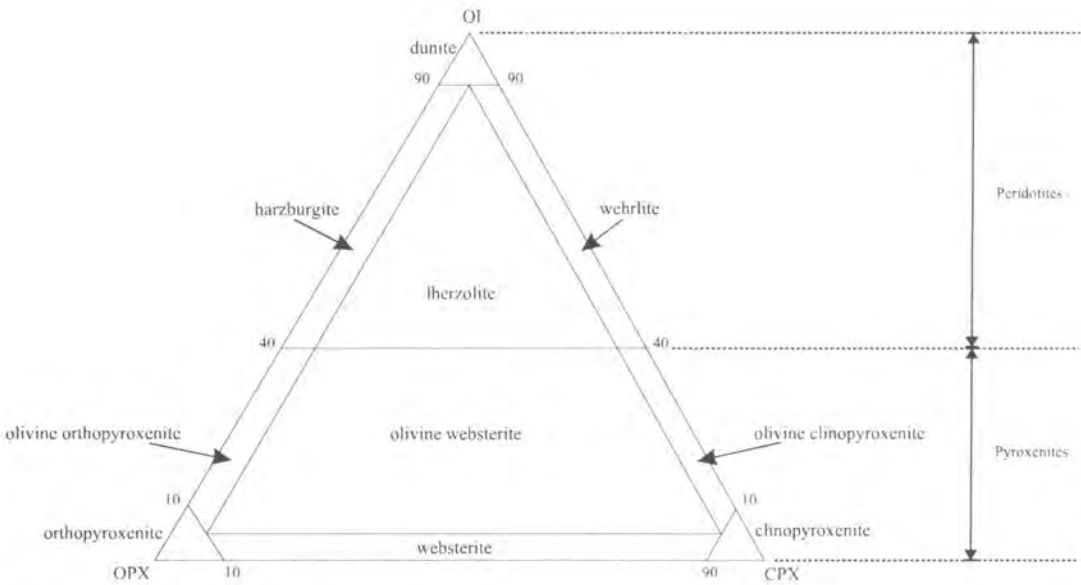


**Figure 1.1.** Classification of ultramafic rocks based on the proportions of primary mineralogies (modified after Le Maitre *et al.*, 1989).

### 1.2.1.b. Textures

The nomenclature ascribed to classification of peridotite textures is extensive. Early classifications of textures of peridotites were mainly concerned with peridotite xenoliths in alkali basalts and kimberlites (Mercier and Nicolas, 1975; Harte, 1977; Pike and Schwarzman, 1977; Mercier, 1985). However, the application of these xenolith-based classifications of peridotite textures to peridotites in ophiolites is difficult (Suhr, 1993). The deformation history suffered by ophiolitic peridotites is very different from peridotites in xenoliths, and hence different textures are present in ophiolitic peridotites. Mercier (1985) has proposed a classification for peridotites from

both ophiolite massifs and xenoliths. Nicolas *et al.* (1980), Nicolas (1986) and Ceuleneer *et al.* (1988) provide textural classifications specifically for peridotites from ophiolitic massifs. A limitation of the classifications of ophiolitic peridotites is that the terms *asthenospheric microstructure* and *lithospheric microstructure* were introduced (Nicolas *et al.*, 1980; Nicolas, 1986; Ceuleneer *et al.*, 1988). The term *asthenospheric microstructure* refers to microstructures that were developed at very high temperature and low stress deformation conditions. These are supposed to be related to the spreading phase in ophiolite development (Suhr, 1993). *Lithospheric microstructures* refer to microstructures which were developed at lower temperature, and higher stress deformation conditions that are supposed to be related to the emplacement of the ophiolites (Suhr, 1993). The use of these terms therefore has direct genetic implications for the geodynamic environment in which the textures were developed and in some examples these implications are difficult or impossible to justify (Suhr, 1993).

None of these classifications are adequate to be used individually to sufficiently describe the textures observed in ophiolitic peridotites. Therefore a classification based on the terminology adopted by Bailey (1997) is utilised in this study. The principal textural types are in order of increasing strain: *coarse granular*, *coarse-grained porphyroclastic*, *fine-grained porphyroclastic*, *mylonitic* and *fluidal*. Following the classification of Bailey (1997) two subtypes, *equidimensional mosaic* and *equidimensional tabular* are used to describe the matrix fabric. For comparison, all of these textural types (except the fine-grained porphyroclastic texture) are shown in Figure 1.2A-F. This scheme incorporates textural terms used in the classifications of Mercier and Nicolas (1975), Mercier (1985) and Girardeau and Mercier (1988). The scheme adopted by Bailey (1997) places an emphasis on descriptive rather than genetic elements and consolidates the various classification schemes, which were produced in parallel by other authors (see above), therefore causing confusion in the literature. The classification presented here differs from that of Bailey (1997), in that his *porphyroclastic* texture has been subdivided to include *coarse-grained porphyroclastic* and *fine-grained porphyroclastic* textures.

***Coarse-granular*** (Figure 1.2A) (Boullier and Nicolas, 1975; *proto-granular* of Mercier and Nicolas, 1975; or *coarse* of Harte, 1977): This term describes a coarse-grained (2-4 mm) rock that lacks porphyroclasts. These textures are the oldest



preserved in xenoliths and hence are considered essentially pre-deformational. The constituent crystals have almost no elongation, and the rocks are devoid of any

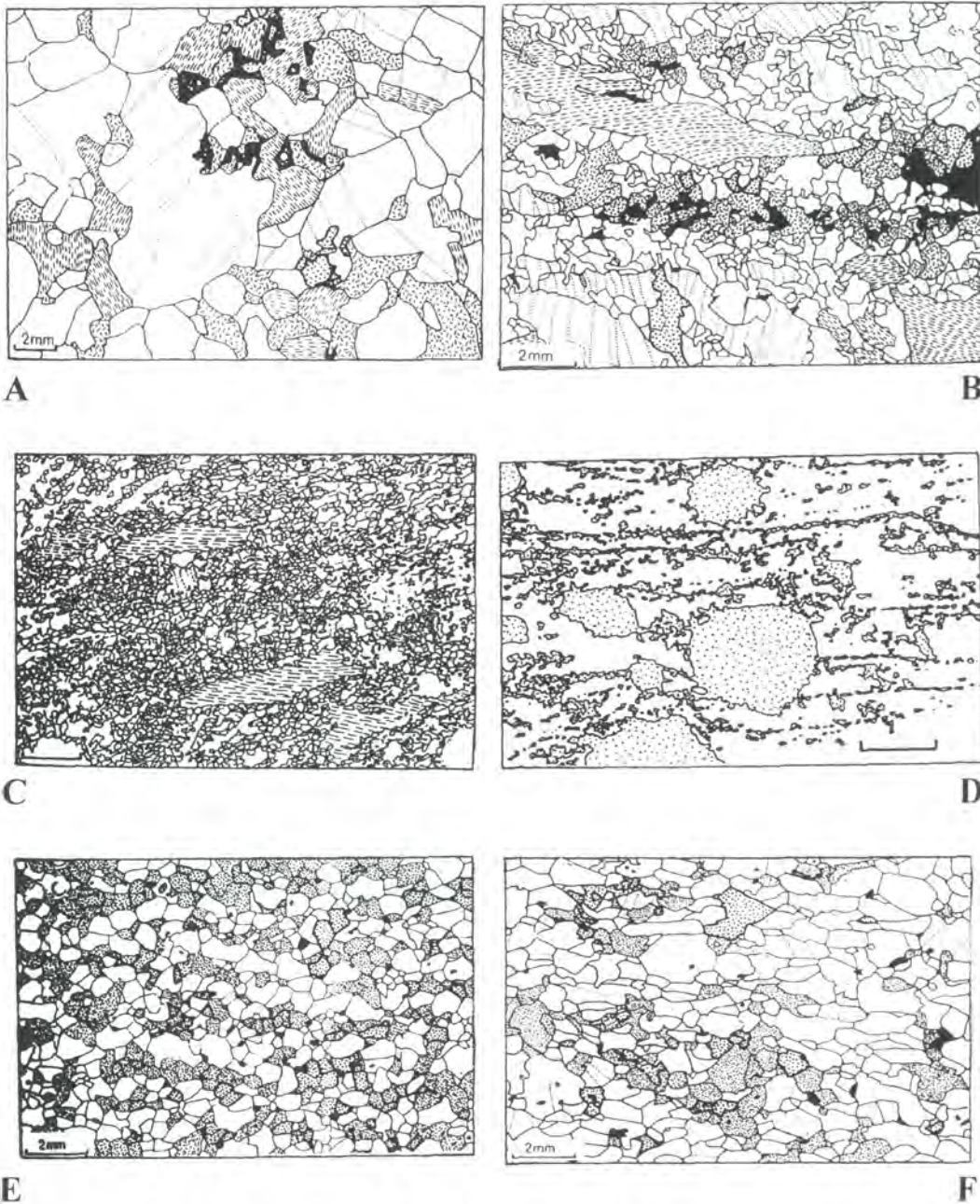


**Figure 1.2.** Classification of peridotite textures. **A.** Coarse granular texture; olivine: blank, except for dotted lines that represent kink-band boundaries. Orthopyroxene: dashes aligned parallel to the (100) plane. Clinopyroxene: random dashes. Spinel: black (from Mercier & Nicolas, 1975). **B.** Coarse-grained porphyroclastic texture. Shading scheme as above (from Mercier & Nicolas, 1975). **C.** Mylonitic texture. (from Bailey, 1997). **D.** Fluidal microstructure. Olivine: blank and completely recrystallised. Orthopyroxene: dotted. (from Bailey, 1997). **E** and **F.** Equigranular mosaic and equigranular tabular respectively. Shading scheme is the same as that used for A and B (from Mercier & Nicolas, 1975).

foliation or lineation. The constituent crystal phases, particularly olivine and orthopyroxene, may show minor recrystallisation along grain boundaries, which may be straight, curvilinear or slightly irregular. Other evidence for minor deformation includes the presence of kink-bands (KB) in olivine crystals. The crystallographic fabrics in olivine and orthopyroxene are weak (Mercier and Nicolas, 1975).

***Coarse-grained porphyroclastic*** (Figure 1.2B) (Boullier and Nicolas, 1975; Mercier and Nicolas, 1977; Pike and Schwarzman, 1977; Harte, 1977; Nicolas *et al.*, 1980; Mercier, 1985): A porphyroclastic texture is transitional from a coarse-granular texture and this transition is identified by the appearance of porphyroclasts (Harte, 1977). Porphyroclasts are coarse (500-5000  $\mu\text{m}$ ), relict strained crystals, which are heavily kinked and often have recrystallised rims. Porphyroclasts are surrounded by a matrix of fine-grained (100-500  $\mu\text{m}$ ), recrystallised strain-free grains (neoblasts). Porphyroclasts, which are predominantly orthopyroxene, are generally flattened and elongate, and therefore define a moderate foliation and lineation within the rock. Spinel displays a characteristic 'holly-leaf' form which is indicative of post-kinematic growth (Mercier and Nicolas, 1975) and are flattened parallel to the porphyroclasts within the foliation plane. Olivine and orthopyroxene display strong crystallographic fabrics.

***Fine-grained porphyroclastic*** (not shown) (Nicolas *et al.*, 1980): The fine-grained porphyroclastic microstructure is transitional from the coarse-grained porphyroclastic microstructure. This transition is characterised by a reduction in the abundance of porphyroclasts and a decrease in the grain size of the porphyroclasts (100-500  $\mu\text{m}$ ) and matrix grains (40-400  $\mu\text{m}$ ). Porphyroclasts are predominantly composed of orthopyroxene and are significantly more flattened and elongate than porphyroclasts present in the coarse-grained porphyroclastic microstructure. These porphyroclasts define a well-developed foliation and lineation within the rock. Spinel also display a 'holly-leaf' form. Olivine and orthopyroxene possess strong crystallographic fabrics.

***Mylonitic*** (Figure 1.2C) (Girardeau & Mercier, 1988): The mylonitic texture is transitional from a fine-grained porphyroclastic microstructure. Mylonitic textures possess a strong foliation and lineation defined by elongate pyroxene porphyroclasts. This texture is characterised by pervasive recrystallisation and a smaller matrix grain

size ( $<100\ \mu\text{m}$ ), which often develops an equigranular mosaic microstructure (see below). Olivine and clinopyroxene are normally completely recrystallised into fine-grained neoblasts, which have a heterogeneous grain size distribution (Nicolas *et al.* 1980). Spinel is commonly drawn out into irregular shaped elongate aggregates with fine-grained tails of spinel adjacent to larger grains. These aggregates define a foliation and lineation within the mylonitic peridotite.

**Fluidal** (Figure 1.2D): Bailey (1997) defines the fluidal texture as follows: “The term ‘fluidal’ is applied to a specific mylonitic texture in which thin ( $<0.03\text{mm}$ ) lamellae of intensely recrystallised, monomineralic material ( $<0.01\text{mm}$ ) define a discontinuous foliation that is connected with porphyroclasts of the same material. The matrix is also very fine-grained ( $<0.01\text{mm}$ ) and predominantly displays an ‘equigranular mosaic’ texture (see below). Fluidal microstructures are interpreted as results of very high strains ( $>1000\%$ ) and are invariably correlated with superplasticity (Boullier and Nicolas, 1975; Boullier and Guegen, 1975; Drury *et al.*, 1990)”.

**Equigranular** (Figure 1.2E-F) (Mercier and Nicolas, 1975; equidimensional mosaic of Pike and Schwarzman, 1976; Harte, 1977; Mercier, 1985): This textural type is divided into two subtypes based on microstructural observations. In the xenolith classification schemes, these textures are considered to be a separate textural type. However, in the present scheme, they are referred to as a sub-type, because they are only ever observed in the matrix of fine-grained porphyroclastic and mylonitic textural types (Bailey, 1997). *Equigranular mosaic* (Figure 1.2F) describes a matrix texture which is fine-grained ( $<0.07\text{mm}$ ), in which olivine, orthopyroxene and clinopyroxene are equidimensional, of relatively constant grain size, and in which crystallographic fabrics are weak. Grain boundaries are commonly straight and converge at triple points defining a polygonal texture (Bailey, 1997). *Equigranular tabular* (Figure 1.2G) textures are also fine-grained, but differ in that they are characterised by parallel, tabular, grains that define a foliation and occasionally weak mineral lineation (Bailey, 1997).



### 1.2.2. Oceanic ultramafic rocks

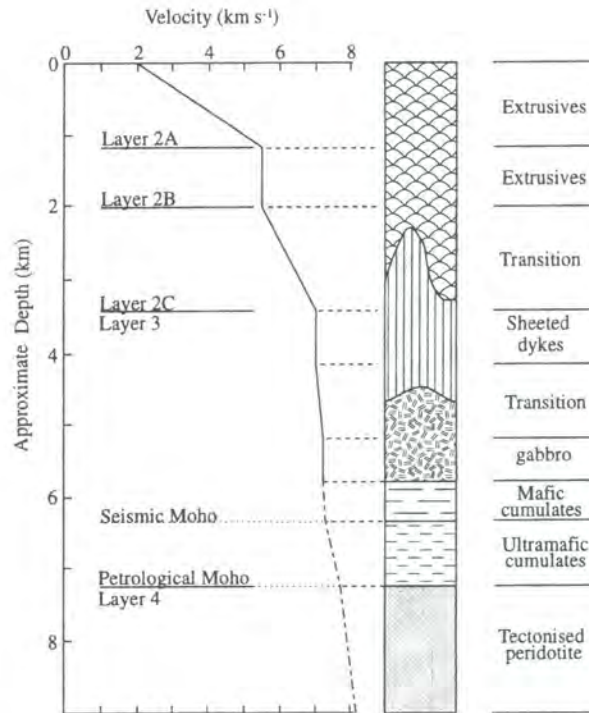


**Figure 1.3.** Idealised velocity-depth profile for the oceanic crust (adapted from Gass (1980) and Fowler (1993) – from Bailey, 1997).

Ultramafic rocks occur in the lower oceanic crust and the upper mantle of generalised oceanic crust. The upper mantle, composed of peridotite, is often termed *Layer 4* in idealised velocity-depth profiles for oceanic crust (Figure 1.3). Ultramafic rocks also occur in *Layer 3*, the oceanic layer, which is predominantly composed of gabbro and ultramafic cumulates. The boundary between layers 3 and 4 may be defined by petrological or seismic criteria (Figure 1.3). The *seismic Moho* is a transition from crustal rocks to ultramafic rocks, based on the changes in seismic velocities. The *petrological Moho* is the boundary between ultramafic cumulates, precipitated from melt, and underlying deformed, residual upper mantle.

Peridotites are exposed on the sea floor in one of four geodynamic environments (Bonatti & Hamlyn, 1981):

- Relatively young crust associated with mid-ocean ridges.
- Crustal sections exposed along transform faults with large offsets (>100km).
- Crustal sections exposed in subduction-related trenches and forearc regions.
- In regions associated with pre-oceanic rifts and continental margins.

Peridotites from these environments are usually strongly serpentinised and are tectonically exposed at the sea floor along faults as serpentinite protrusions. For detailed discussion of the characteristics of peridotites from these different geodynamic environments the reader is referred to the review compiled by Bonatti and Hamlyn (1981).

### **1.2.3. Continental ultramafic rocks**

Two groups of upper mantle rocks are available for direct study and sampling in continental regions. The first group includes xenoliths of subcontinental upper mantle, which have been carried to the surface by basalts or kimberlites. A second group comprises relatively larger fault-bounded units of upper mantle emplaced within the continental crust during orogenesis. Peridotites of this second group exposed in orogenic zones are invariably serpentinised and termed *Alpine*-type (e.g. Thayer, 1960; Coleman, 1971) and may be sub-divided into three groups: (1) ultramafic units within obducted fragments of oceanic lithosphere (e.g. **ophiolites**), (2) peridotites exhumed along mantle shear zones and emplaced into continental crust (e.g. Ronda massif), (3) serpentinites situated along fault zones.

#### **1.2.3.a. Ophiolitic ultramafic rocks**

Better known ophiolite complexes throughout the world include the Oman (Pearce *et al.*, 1981), Bay of Islands, Newfoundland (Williams, 1973), Vourinos Complex, Greece (Moores, 1969) and Troodos Complex, Cyprus (Gass, 1968). Ultramafic rocks are characteristic of the lowest parts of these obducted ophiolite complexes. The stratigraphy observed in ophiolites is broadly similar to that suggested for present-day oceanic crust (Section 1.2.2). Early studies of ophiolites suggested that they were developed at mid-ocean ridges. However, recent studies (e.g. Alabaster *et al.*, 1982; Pearce *et al.*, 1984) have demonstrated that the majority formed in a supra-subduction zone environment. This is a region above a subduction zone where arc, back-arc and fore-arc magmatism occurs (Elthon, 1991). These interpretations are based primarily on the geochemical composition of lavas and cumulates in ophiolites, which are very

different to mid-ocean-ridge basalts (MORB), but comparable to rocks found in supra-subduction zone environments. Interpretation of the origin of an ophiolite body has important implications for regional tectonics and obduction models.

Peridotites occur as layered ultramafic cumulates in the crustal sequence and tectonised spinel or plagioclase-bearing harzburgite or lherzolite in the mantle sequence, which forms the lowermost section of ophiolites. Coleman (1977) proposed that the mantle sequence represents residual upper-mantle after partial melting and that the overlying cumulates formed by fractional crystallisation of magma derived from the mantle section.

Geochemical and petrological studies of peridotites from ophiolites have been primarily concerned with unravelling the complexities of melt segregation processes in the upper mantle (e.g. Ozawa, 1994 *and references therein*). These studies have focused on mantle heterogeneities, which probably reflect differences in the degree of melting, spatial variations in source composition, variations in the efficiency of melt extraction and variations in the amount and composition of melt fluxing through the mantle section (Ozawa, 1994). Mechanisms of melt-rock interaction and metasomatism of peridotites have also been addressed by geochemical and petrological studies (Menzies and Dupuy, 1991 *and references therein*).

Structural studies of peridotites from ophiolites (e.g. Nicolas, 1989; Peters *et al.*, 1991) have dealt with two aspects of the evolution of ophiolites. Earlier processes took place in the upper mantle near to ancient spreading centres while later tectonic processes took place during obduction. Detailed studies of the mantle flow patterns (mantle fabrics) and peridotite textures in ophiolites have demonstrated that these can be related to mantle upwelling beneath spreading centres (e.g. Nicolas *et al.*, 1988; Ceuleneer *et al.*, 1988; Boudier & Nicolas, 1995). This type of study has important implications for the generation of oceanic lithosphere and plate tectonics. Ceuleneer *et al.* (1988) demonstrated that particular mantle flow patterns distinguish between different types of spreading centres, e.g. fast or slow-spreading ridges or transform fault zones. More recently, several authors have proposed that peridotite mylonites and shear-zone structures in a few ophiolites record the uplift of mantle and rifting during continental breakup and the opening of an ocean basin (Drury *et al.*, 1990; Hoogerduijn Strating *et al.*, 1990; Vissers *et al.*, 1991). Other studies (Nicolas *et al.*, 1980; Girardeau & Nicolas, 1981) have shown that basal peridotite mylonites in ophiolite complexes were developed during early thrusting of the oceanic lithosphere during obduction.

These basal mylonites are superimposed over the earlier spreading-related fabrics (Figure 1.4). Basal peridotite mylonites are in structural and kinematic continuity with underlying high-grade metamorphic rocks. These metamorphic rocks have been interpreted as dynamothermal aureoles or metamorphic soles caused by overthrusting of the mantle rocks (Church & Stevens, 1971; Williams & Smyth, 1973; Malpas *et al.*, 1973). It has been shown that dynamothermal aureoles represent oceanic crustal lithologies highly metamorphosed and deformed during thrusting in the oceanic environment (Malpas, 1979; Jamieson, 1980, 1981, 1986; Searle & Malpas, 1980). Metamorphic soles develop from a combination of residual heat in the overlying ophiolite and limited shear heating generated during obduction (Hacker, 1990,1991).

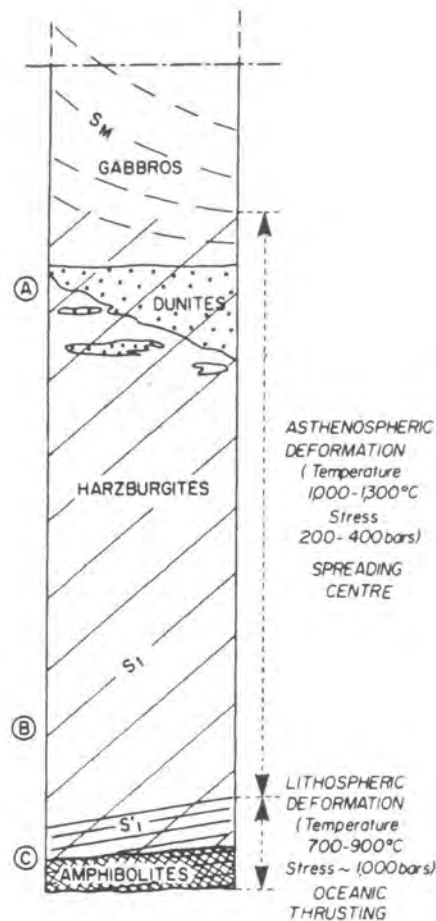


**Figure 1.4.** Schematic cross-section through the lower part of an ophiolite sequence showing obduction related structures ( $S'_1$ ) superimposed on spreading related structures ( $S_1$ ). ( $S_M$ ) is the cumulate layering (from Boudier *et al.*, 1982).

### 1.3. Structural terminology

A key factor in structural analysis is to recognise the conditions responsible for deformation and to establish the mechanisms that facilitate deformation. The purpose of this section is to review natural deformation processes, with particular reference to the mineral olivine, which forms >50% of peridotite. For a more detailed discussion of deformation mechanisms in natural rocks the reader is referred to a detailed review by Knipe (1989) on which the following text is largely based.

#### 1.3.1. Deformation mechanisms

Deformation in rocks is accomplished by a whole host of processes that operate at the scale of individual grains (Passchier & Trouw, 1996). These processes depend on lithological and environmental variables including mineralogy, grain size, temperature, pressure, strain rate, fluid activity, etc (Figure 1.5). Combinations of these factors control which grain-scale material processes are operative and therefore which deformation mechanisms are involved. Three different groups of deformation mechanisms that operate in rocks can be defined (Knipe, 1989):

- Fracture, frictional grain-boundary sliding and cataclastic flow
- Diffusive mass transfer
- Crystal plastic flow

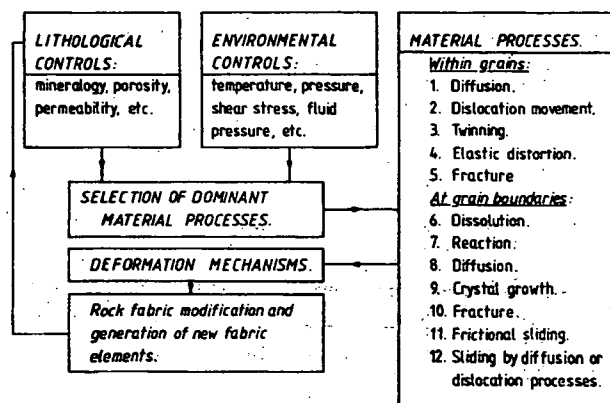


**Figure 1.5.** Flow diagram showing the inter-relationships between lithological and environmental controls and material behaviour during rock deformation (from Knipe, 1989).

In general, no single deformation mechanism operates alone, and in addition to the variables introduced above, activation of one mechanism will influence the operation of others (Williams *et al.*, 1994).

#### **1.3.1.a. Fracture, frictional grain-boundary sliding and cataclastic flow**

Deformation by these methods involves the creation of new surfaces, loss of cohesion due to fracturing, and frictional sliding along grain boundaries and surfaces within the rock (Knipe, 1989).

*Fracture* processes involve the displacement along cracks that have nucleated and propagated during deformation.

*Frictional grain-boundary sliding* involves sliding of grains past each other, where individual grains remain essentially undeformed and act as rigid bodies. Sliding occurs when the cohesion and friction strength between grains is overcome. Frictional grain-boundary sliding is distinguished from high-temperature grain-boundary sliding, where sliding is controlled by diffusion or defect movement along grain boundaries and cohesion is not lost.

*Cataclastic flow* is accomplished by mechanical fragmentation of a rock, due to fine-scale fracturing, movement along fractures and the subsequent sliding and rotation of fragments (Passchier and Trouw, 1996). The conditions responsible for cataclasis depend on the type of mineral involved and on fluid pressures; high fluid pressure promotes cataclasis (Passchier and Trouw, 1996). These processes are also generally favoured by low temperatures and high stresses. Cataclasis of rock is differentiated from deformed and recrystallised rocks by a lack of grain shape-preferred orientation, grains with angular outlines and straight sharp boundaries (Passchier and Trouw, 1996).

#### **1.3.1.b. Diffusive mass transfer (DMT)**

DMT involves the transfer of material away from zones of relatively high intergranular normal stress, or a source, to sites of low normal stress, or a sink (Rutter, 1983; Knipe, 1989). Variations in the chemical potential of a rock aggregate created by internal stress differences (Wheeler, 1987), fluid pressure gradients (Etheridge *et al.*, 1984) or changes in the internal strain energy of grains (Wintsch and Dunning, 1985), are the

mechanism(s) responsible for driving DMT. Several migration processes or *solid-state diffusion creep* processes facilitate diffusion mechanisms. The two basic types are: *Coble creep* which operates by diffusion of vacancies in the crystal lattice along grain boundaries and *Nabarro-Herring creep*, involving diffusion of vacancies throughout the crystal lattice (Passchier and Trouw, 1996). DMT is likely to dominate in fine-grained material, high temperatures for solid-state, in the presence of a fluid and prefers low stresses and strain rates. However, the influence of fluids and grain size on the rate of diffusion mean that deformation mechanisms controlled by DMT can occur at low temperatures in the crust. Characteristic microstructures of DMT include those related to redistribution of material e.g. stylolites, differentiation during crenulation cleavage development where quartz or carbonate migrates. Other microstructures include those which preserve evidence of the mass transfer path involved, e.g., presence of reaction products along selected grain boundaries and the occurrence of overgrowths and pressure shadows (Knipe, 1989 *and references therein*).

#### **1.3.1.c. Crystal plastic flow**

Crystal plasticity involves the accumulation of strain by intracrystalline processes, such as the movement of dislocations (linear lattice defects) and twinning (Barber, 1985). At low temperatures ( $<0.5$  melting temperature), deformation is preferentially accommodated by *dislocation glide*, where dislocation movement is restricted to be along slip planes (Knipe, 1989). During deformation at these temperatures, dislocations become locked and thus dislocation tangles are formed, and this inhibits further dislocation motion. The increase in resistance to straining which results from the resistance to motion is referred to as *work hardening*. At higher temperatures ( $>0.5$  melting temperature), thermally activated *recovery* processes counteract work-hardening by allowing crystal defects to be more mobile in the lattice. Thus tangles are avoided and crystals can lower their internal strain energy and increase the ductility of the material (Knipe, 1989). One of the predominant mechanisms which is involved in recovery is movement of the dislocations by diffusion of atoms to higher or lower slip planes; this basically allows the dislocation to 'climb' over a blocked site, and hence is termed *dislocation climb*. The conditions that facilitate recovery are slow strain rates and/or higher temperatures. The mechanism of dislocation glide with climb of

dislocations is known as *dislocation creep* (Passchier and Trouw, 1996). During these processes of intracrystalline deformation, characteristic sub-structures are developed in olivine crystals:

### ***Olivine sub-structures developed during intracrystalline deformation***

Olivine porphyroclasts, which have suffered intracrystalline deformation, display characteristic *sub-structures*. There is some discrepancy in the literature regarding the terminology used to describe olivine sub-structures and their origin. These substructures include kink-bands and kink-band boundaries (Nicolas *et al.*, 1971), dislocation walls or sub-grain boundaries (sub-boundaries) and sub-grains (Nicolas and Poirier, 1976; Suhr, 1991), and dislocation sub-boundaries (Karato *et al.*, 1986). The reason for the discrepancy in the description of olivine sub-structures is that the different terms often refer to a similar substructure and also to the use of transmitted electron microscopy (TEM) as a method of study in recent publications. TEM studies reveal features of lattice deformation, which cannot be directly viewed using conventional microscopes, hence a new terminology has been developed.

Kink-bands (KB) are a type of planar lattice defect or dislocation within a crystal where the lattice is differently orientated and not curved, which are bounded by kink-band boundaries (KKB) (Nicolas and Poirier, 1976). The development of a kink band results in the overall shortening of a crystal, due to bending and ultimate kinking of a crystal slip plane. Lattice defects geometrically similar to kink bands can develop in a process by which dislocations collect into walls by slip or climb. This results in a slight misorientation between two adjacent regions of crystal or *subgrain*, subgrain boundaries or dislocation walls (Nicolas and Poirier, 1976) that bound these sub-grains. Sub-grains can be distinguished from kink-bands by the magnitude of the change in orientation of the crystal lattice between adjacent subgrains or kink-bands. The angle is usually less than 5° between subgrains (FitzGerald *et al.*, 1983; White and Mawer, 1988) and a mean value of 9° between kink-bands (Nicolas and Poirier, 1976). Different types of subgrain boundary can be classified according to the rotation axis involved during their development. Subgrain boundaries with a rotation axes parallel to the boundary are termed *tiltwalls*, and those normal to the boundary, *twistwalls* (Passchier and Trouw, 1996).



Kink band and subgrains may both develop simultaneously within an olivine porphyroclast. For example in a peridotite from the Lanzo massif, sub-boundaries are related to [100] slip and kink bands to [001] slip. This makes it possible for the porphyroclast to be elongated by [100] slip with associated bending and twisting, and simultaneously shortened by kinking in the [001] direction (Nicolas and Poirier, 1976).

### ***Recrystallisation***

Recrystallisation may occur in a rock during increased mobility of the defects described above. During recrystallisation new relatively strain-free grains (neoblasts) with high-angle grain boundaries may grow from old strained grains (paleoblasts) either after (static) or during (dynamic) deformation. Two mechanisms of dynamic recrystallisation have been recognised (Drury and Urai, 1990):

- **Grain boundary migration recrystallisation**
- **Subgrain rotation recrystallisation**

‘Grain boundary migration recrystallisation’ occurs between adjacent deformed crystals of the same mineral type, when one has high dislocation density (less strained) and the other a low dislocation density (more strained). Migration of grain boundary from the less strained grain into the more highly strained grain occurs, thus reducing overall dislocation density and the strain energy of the system. Local bulging of the grain boundary into the more highly strained crystal may occur and form new independent crystals; this phenomena is known as grain boundary bulging (Passchier and Trouw, 1996). Microstructures indicative of grain boundary migration include highly irregular grain boundaries and abrupt changes in the lattice preferred orientation between paleoblasts and neoblasts.

‘Subgrain rotation recrystallisation’ involves creation of a new grain from a subgrain, due to a gradual increase in the angle between the crystal lattice on both sides of a subgrain boundary. This process develops by progressive misorientation of subgrains due to an increasing number of dislocations accumulating at a subgrain boundary. Subgrain rotation recrystallisation is characterised by gradual changes in the

lattice preferred orientation between paleoblasts and neoblasts, and a gradual transition from aggregates of subgrains to aggregates of new grains (Passchier and Trouw, 1996).

### 1.3.2. Grain size effects

In the upper mantle either dislocation creep or diffusion creep can accommodate plastic deformation (e.g. Karato *et al.*, 1986; Jaroslow *et al.*, 1996):

- *Dislocation creep* regime, in which strain rate is thought to display a power law relationship with stress and flow is facilitated by the movement of defects in the crystal lattice.
- *Diffusion creep* regime, in which strain rate is thought to display a linear relationship to stress and is controlled by diffusive mass transport along either grain boundaries or through grain interiors.

Diffusion creep is strongly dependent on grain size and is therefore termed a *grain size sensitive* deformation mechanism, as opposed to dislocation creep, which is *grain size insensitive*. This is because finer-grained rocks have a greater volume of grain boundaries that accommodate intergranular diffusion, in addition to smaller grain sizes that result in a shorter intracrystalline diffusion paths (Handy, 1989). Experimental work has demonstrated that the activation energy for dislocation creep is higher than that required for diffusion creep (Jaroslow *et al.*, 1996 *and references therein*). Deformation mechanism maps for olivine (Figure 1.6) demonstrate the effects of the variation in grain size on deformation. Strain rate curves in the dislocation creep regime (blank shading) are horizontal, which indicates insignificant dependence on grain size. In the diffusion creep regime (shaded), strain rate curves exhibit a strong dependence on grain size. These two deformation mechanism maps (Figure 1.6) indicate that the diffusion creep field expands with decreasing temperature (800 to 600°) as a result of the smaller activation energy required for diffusion creep relative to dislocation creep. Therefore, a reduction in grain size, accompanied by a decrease in temperature may effect a change in the operative deformation mechanism in the upper mantle (Jaroslow *et al.*, 1996).

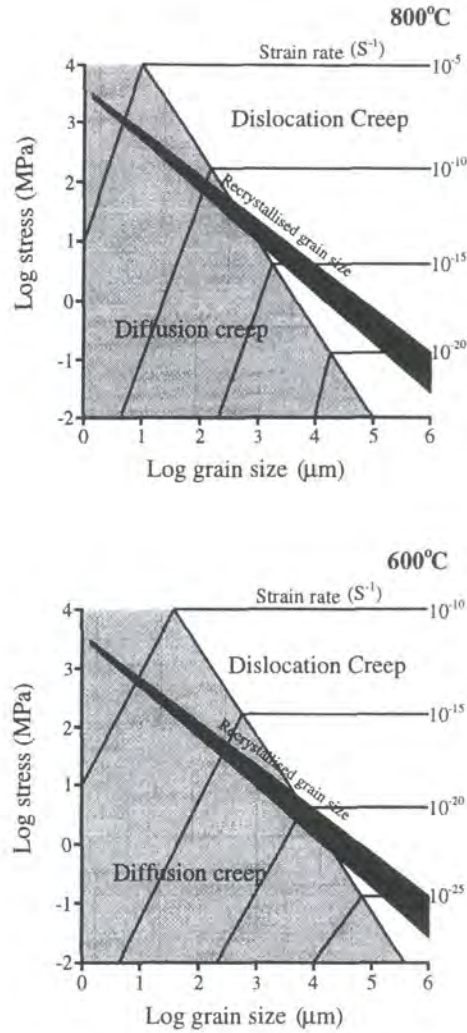


**Figure 1.6.** Deformation mechanism maps for olivine. Parameters and constitutive flow laws are presented in Rutter & Brodie (1988). Estimates for the dynamic recrystallised grain size are derived from the piezometer used by Karato *et al.* (1986). Adapted after Rutter & Brodie (1988).

### 1.3.3. Aggregate microstructures and rheology

The rheology of a polymineralic aggregate is largely controlled by:

- The *relative strength/competence* of the stronger and weaker phases -  $\sigma_{\text{strong mineral}}/\sigma_{\text{weak mineral}}$ , and,
- The *volume proportion* of the weak phase (and degree of interconnectivity) -  $\phi_w$ .

Two basic types of microstructure have been distinguished in naturally and experimentally deformed two-phase aggregates (Figure 1.7) (Handy, 1990; 1994):

- The stronger phase forms a load-bearing framework (LBF microstructure) that contains isolated pockets of the weaker phase;
- The weaker phase forms an interconnected weak matrix or layers (IWL microstructure) separating boudins or clasts of the stronger phase.

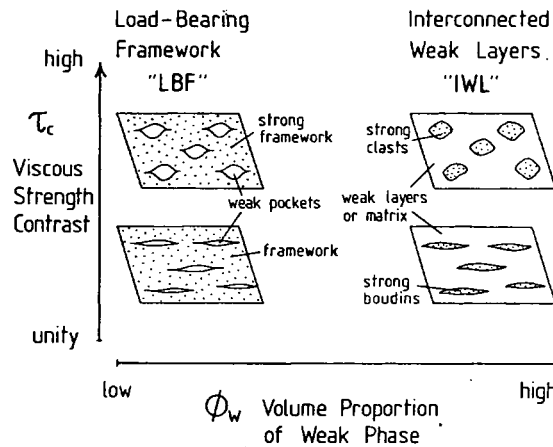


**Figure 1.7.** Microstructures in deformed two-phase viscous materials as a function of the volume proportion of the weaker phase ( $\phi_w$ ) and the relative strength/competence of the stronger and weaker phases -  $\sigma_{\text{strong mineral}}/\sigma_{\text{weak mineral}}$  - ( $\tau_c$ ). LBF and IWL are abbreviations for 'load-bearing framework' and 'interconnected weak layer' microstructures (from Handy, 1994).

In aggregates with the LBF microstructure, strain rate is nearly uniform and stress is concentrated in the load-bearing framework. Handy (1994) demonstrates that aggregates with an IWL microstructure are characterised by strain rate and occasionally also stress higher in the interconnected weak phase than in boudins and clasts of strong phase. The viscous strength contrast and relative amounts of the constituent mineral phases exert a strong control on the degree of stress and strain partitioning (Handy, 1994). The findings of Handy (1994) predict that during steady-state creep, the LBF microstructure is stable only in rocks with low volume proportions of weak phase ( $\phi_w < 0.1$ ) and low to moderate mineral strength contrasts ( $\sigma_{\text{strong mineral}}/\sigma_{\text{weak mineral}} \leq 5$ ), but the IWL microstructure is predicted to be stable over a broad range of two-phase compositions and mineral strength contrasts. Handy (1994) derived flow laws for two-phase aggregates with idealised LBF and IWL microstructures on the basis of microstructural observations in naturally deforming rocks which were used to show how stress and strain partition in rheological and structurally heterogeneous material. Flow laws derived by Handy (1994) predict that rock composition, in addition to

geothermal gradient and regional strain rate have a strong influence on the rheological stratification in the lithosphere, particularly in rocks with low volume proportions of a weak phase and high material contrasts.

#### **1.3.4. Interpretation of peridotite microstructures; olivine petrofabrics**

Measurement of lattice preferred orientation (LPO) is an important technique in understanding the operation of slip systems involved during dislocation creep as a consequence of intracrystalline deformation. Since dislocations may move in specific lattice planes, a rock deforming by movement of dislocations may develop a preferred orientation of the grains that make up the rock (Passchier and Trouw, 1996).

Polarising microscope studies of peridotite samples orientated in the X-Z plane (perpendicular to foliation and parallel to the lineation) reveals that minerals often possess a lattice preferred orientation (LPO) (Nicolas and Poirier 1976, Mercier, 1985). The following discussion will only describe the LPO patterns associated with olivine crystals, although orthopyroxene LPO is commonly utilised (Boudier and Coleman 1981, Mercier, 1985).

The LPO of olivine is revealed by measuring the extinction angles of the [100], [010] and [001] crystallographic axes of the crystals by using a universal stage and plotting the data on stereonet or olivine petrofabric diagrams. The kinematic analysis of LPO is based on the observation that in a peridotite deformed in a non-coaxial flow regime during simple shear, the LPO of olivine is often oblique to the shape fabric (Figure 1.8). As a consequence, asymmetry between the shape fabric and the LPO may be used to determine the sense of shear (Boudier et al., 1982; Bouchez et al., 1983; Smewing et al., 1984). Interpretation of olivine petrofabric diagrams extends beyond simply determining shear sense in a particular sample. They also reveal which of the olivine slip systems were activated during deformation. It is well established from experimental (Carter and Ave Lallemant, 1970) and studies of natural systems (Nicolas et al., 1971; Smewing et al., 1984; Mercier, 1985; Nicolas & Christensen, 1987) that temperature exerts a control on which slip system is activated. In these studies, the temperatures suggested for activation of the different slip systems

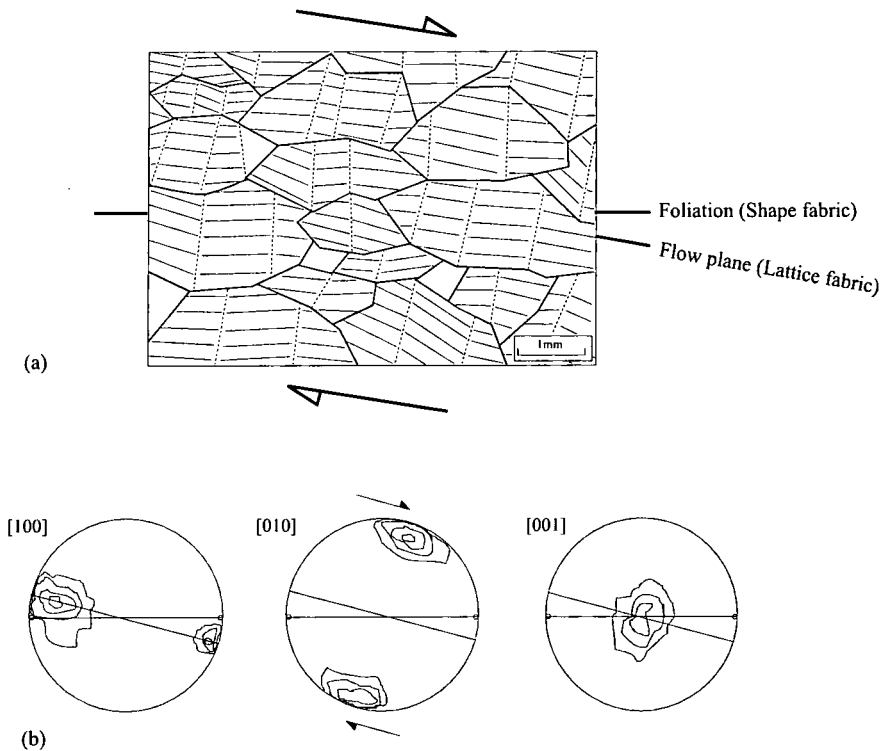


**Figure 1.8.** (a) Schematic section in XZ plane of an olivine aggregate. Dashed lines = trace of sub-grain boundaries, narrow lines = slip planes, thick lines = grain boundaries. (b) Lower hemisphere equal area projection of olivine crystallographic axes. Solid plane = foliation, dot = lineation. Dashed plane = flow plane. The sense of shear is deduced from the orientation of the foliation relative to the average slip plane (equated to the flow plane). Adapted from Boudier *et al.* (1982)

vary, so this investigation refers to the temperatures suggested by Nicolas & Christensen (*op cit.*). At 'low' temperatures (700-1000°C) the slip systems (0kl) [100] or *pencil glide* are operative (where (0kl) refers to the slip plane and [100] the slip direction). Activation of the system (010) [001] (Nicolas & Christensen, 1987) or (110) [001] (Carter & Ave Lallemant, 1970) are also proposed for 'low' temperatures. At 'high' temperatures ( $T > 1000^\circ\text{C}$ ) the system (010) [100] is dominant and at very high temperatures ( $T > 1250^\circ\text{C}$ ) activation of the system (001) [100] is suggested (Nicolas & Christensen, 1987). Petrofabric diagrams enable both the slip direction and the activated slip plane involved in the slip system to be determined.

Other uses of olivine petrofabric diagrams include an average estimate of shear strain by measuring the angle between the foliation and shear plane (LPO) (Bouchez *et al.*, 1983; Ceuleneer *et al.*, 1988).

The type of LPO pattern that is formed in a rock depends on many factors. These include which slip systems are operative and the amount of slip on each slip system, the finite strain, the activity of dynamic recrystallisation and the growth of

grains from solution (Schmid, 1994). The effects of recrystallisation on the LPO pattern are difficult to predict, but they may influence it in several ways. These include weakening of the existing pattern by generation of new, randomly orientated grains or alternatively strengthening a pattern or part of a pattern by removing certain grains with a relatively high dislocation density (Passchier and Trouw, 1996).

### 1.3.5. Kinematic indicators

*Kinematic indicators* are structures that can be used to make reliable inferences about the flow in rocks during progressive deformation (Hanmer & Passchier, 1991). These can occur at the scale of a thin section, outcrop or a geological region. *Shear sense indicators*, which represent a subset of kinematic indicators, are developed during non-coaxial strain and comprise a number of structures, microstructures and fabrics that have an asymmetry reflecting the sense of vorticity (Hanmer & Passchier, 1991). In order to reliably determine the shear sense on a fault/shear-zone, the shear direction must be identified to provide the necessary kinematic framework. The shear direction is defined by linear structures, for example striae, slickenlines and ductile mineral lineations. Once the shear direction has been deduced, shear sense is determined by using the shear sense indicators presented below. Shear sense observations must be made in the XZ plane of the finite strain ellipsoid, which is a plane normal to the shear plane and parallel to the shear direction. No single shear sense indicator may reliably determine the sense of shear; therefore, several different shear sense indicators should be used in conjunction to determine the shear sense along a fault/shear-zone.

#### 1.3.5.a. Shear sense indicators – ductile regime

The following shear sense indicators are discussed in this thesis and the description of these shear sense indicators is based on the comprehensive review of Hanmer & Passchier (1991). The reader is directed to this review for detailed discussion of these shear sense indicators.

- Shape fabrics

- Porphyroclast systems
- Folds

### ***Shape Fabrics***

Shape fabrics include the modification of a generated or pre-existing foliation by rotation or deflection, by shear zones (Ramsay & Graham, 1970) (Figure 1.9); C/S fabrics (Berthé *et al.*, 1979) (Figure 1.10); asymmetrical extensional shear bands (AESBs) (White *et al.*, 1980) (Figure 1.11).

### ***Porphyroclast systems***

Porphyroclast systems most commonly comprise a rigid, monocrystalline core surrounded by a thin, polycrystalline 'tail', that is often derived from the host porphyroclast. However, the tails may also comprise deformed pressure shadows.

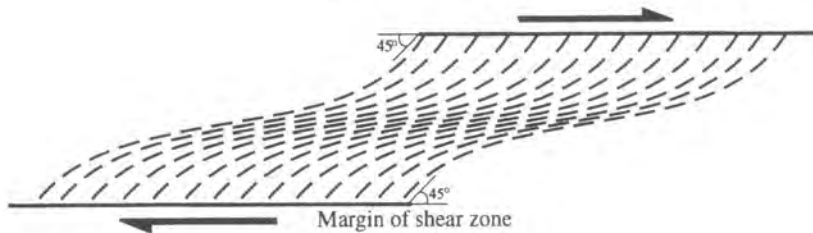


**Figure 1.9.** Shear zone geometry resulting from progressive simple shear. Schistosity originates at  $45^\circ$  to the shear zone boundary and rotates with increasing strain towards parallelism with the shear zone boundary (after Ramsay & Graham, 1970 - from Bailey, 1997).

reaction products or bands of matrix material entrained by the rotation porphyroclast, all of which extend along foliation planes in the direction of shear (Hanmer & Passchier, 1991). Four main types of porphyroclast system:  $\infty$ -type,  $\phi$ -type,  $\sigma$ -type and  $\delta$ -type may be defined on the basis of the geometry of these tails (Passchier & Trouw, 1996).  $\square$ -type objects lack tails and  $\phi$ -type objects have a mantle with orthorhombic symmetry.  $\sigma$ -type and  $\delta$ -type objects have monoclinic shape symmetry. The  $\sigma$ -type objects display stair-stepping, which is defined by tails at different elevations on both sides of a porphyroclast.  $\sigma$ -type and  $\delta$ -type objects can be used as shear sense indicators (Figure 1.12) using their internal asymmetry and the stair- stepping of the tails; the tails step up in the direction of displacement.



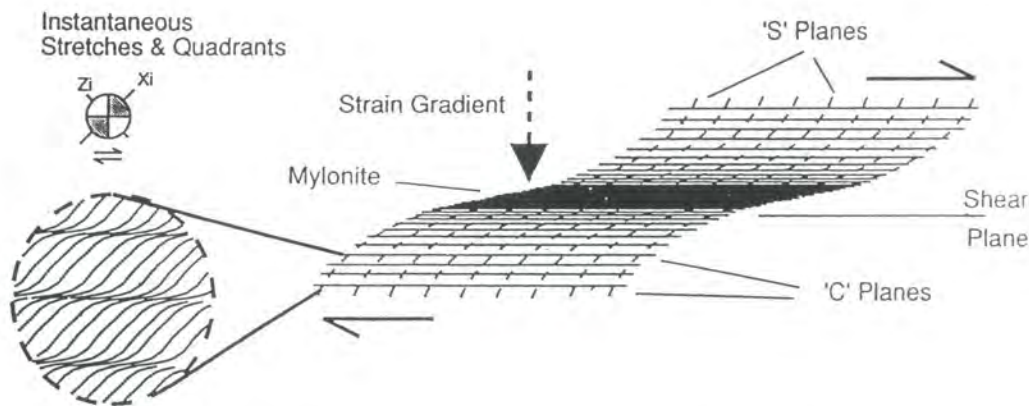


**Figure 1.10.** Idealised C/S fabric in a general non-coaxial flow. C-planes are discrete shear zones that parallel the bulk shear plane and are bound on either side by strain gradients. The rotation of both S- and C-planes into parallelism with the shear plane results from high finite strains (from Hanmer & Passchier, 1991).

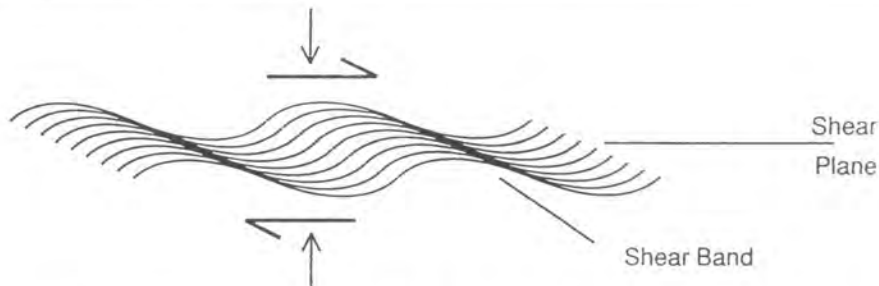


**Figure 1.11.** Asymmetrical extensional shear bands in a general non-coaxial flow. Note the obliquity between shear bands and the bulk shear plane (from Hanmer & Passchier, 1991).

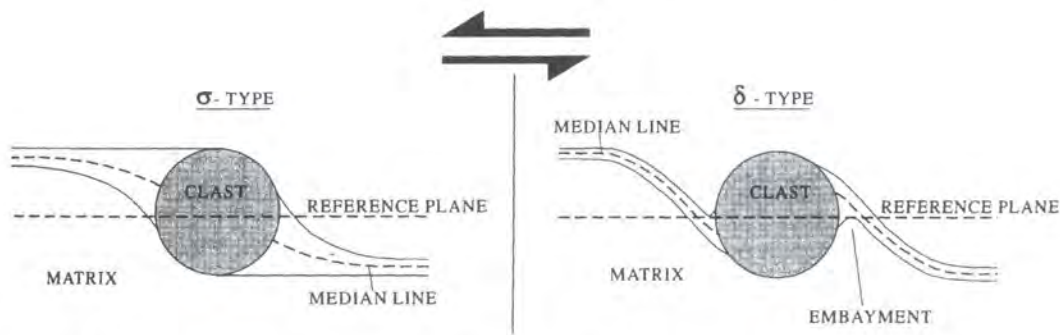


**Figure 1.12.** Geometries of  $\sigma$ - and  $\delta$ -type porphyroclast systems in sinistral shear. Note that tails of both types step up to the left with respect to the trace of the reference plane (after Passchier & Simpson, 1986 - from Bailey, 1997).

**Folds**

Fold asymmetry may result from non-coaxial deformation (Figure 1.13), although folds are generally considered to be the least reliable of shear sense indicators. Fold asymmetry can only be used to infer shear sense where (Hanmer & Passchier, 1991);

(1) a readily identifiable set of contemporaneous folds shows a regionally extensive consistent asymmetry, and/or (2) there is evidence for the progressive development of a fold shape with deformation.

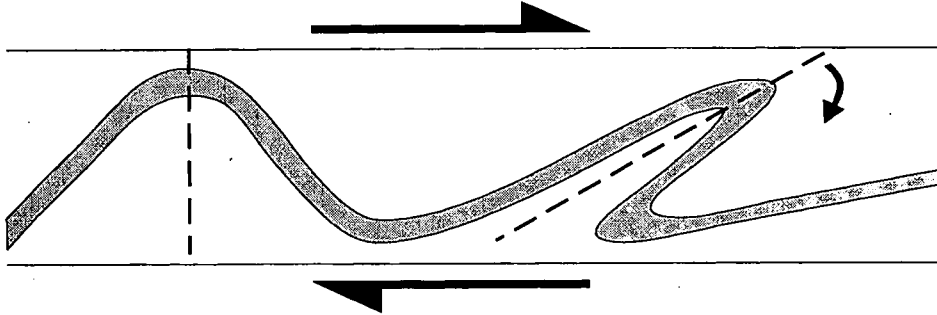


**Figure 1.13.** Asymmetric (*drag*) fold resulting from dextral shear. Planar constituents of the structure orientated at high angles to the shear direction, such as the fold axial plane and fold limbs, rotate with the same sense as the vorticity of the flow during progressive deformation (from Bailey, 1997).

#### 1.4. Scientific methods

A complementary, yet diverse set of scientific methods has been utilised during the course of this study and compilation of this thesis. These include both field and laboratory based methods. The following is a summary of these methods:

##### 1.4.1. Field methods

Field based mapping and structural analysis was conducted individually for 8 weeks and accompanied by M.T.Styles and collaborating parties for 3 weeks. This included detailed mapping of areas of geological importance, identified in the literature and by initial ‘reconnaissance’ mapping of the area. Lithological and structural mapping of inland areas was conducted on 1:10 000 scale topographical base maps, whilst coastal areas were mapped on 1:1500 aerial photograph overlays. Structural logging (Imber, J., *pers comm.* 1998) was utilised in structurally complex areas, for example reactivated fault zones, in order to systematically record observations and structural data. Representative samples of the different ultramafic and mafic rocks were collected for microstructural studies and geochemical analysis.

#### **1.4.2. Laboratory methods (University of Durham)**

A variety of laboratory methods were used for study and analysis of samples collected in the field. In the following text these methods are briefly introduced. A more detailed account of the methods is provided in Appendices A and B.

##### **1.4.2.a. Geographical Information System (GIS)**

Petrological descriptions of the thin sections of peridotite samples from the Lizard ophiolite complex were incorporated in a GIS system (Arcview) in order to produce petrological maps to aid interpretation of petrological variations.

##### **1.4.2.b. Olivine petrofabrics**

Olivine petrofabrics were determined for orientated samples of peridotite using a 5-axis universal stage. This method can provide important kinematic data and constraints regarding the operative deformation mechanisms and conditions during deformation.

##### **1.4.2.c. Whole rock geochemical analyses**

X-Ray Fluorescence (XRF) and Inductively Coupled Plasma Mass Spectrometry (ICP-MS) were used to obtain major, trace and rare earth element data for selected samples collected during the course of fieldwork.

#### **1.4.3. Data from other sources**

The following organisations/people have provided additional data and information that has been incorporated in this thesis.

#### **1.4.3.a. British Geological Survey**

Additional data was obtained from the British Geological Survey (BGS) during a six week visit to the Keyworth offices and subsequent shorter visits (Styles, M.T., *pers comm.* 1996). This data included access to an extensive collection of hand specimens and thin sections of samples collected from the Lizard complex, which included the extensive collection of Flett & Hill (1912). Examination of borehole core, drilled through a variety of lithologies from the Lizard complex was also made available for study and further sampling. Borehole logs, mineral and wholerock geochemical analyses (XRF, ICP-MS and isotopic analyses) were provided for inclusion in this thesis. BGS (Styles, M.T., *pers comm.* 1996) also provided equipment for field work, including base maps, aerial photographs, hammers, etc.

The majority of the electron probe micro-analyses (EPMA) of minerals presented in this thesis were conducted at BGS (Keyworth) by the author. Three visits, each a week long, were required to obtain this data.

#### **1.4.3.b. Research School of Earth Sciences (Australian National University)**

Professor David Green invited the author to spend six weeks at the Research School of Earth Sciences (Australian National University, Canberra) to allow collaboration and integration of new Sensitive High Resolution Ion Micro-Probe (SHRIMP) geochronological data for samples from the Lizard ophiolite Complex into this thesis (Nutman, A., *pers comm.* 1998). During the research visit, major and trace element analyses of rocks from the Lizard complex were made available in addition to thin sections for petrological study. Further electron probe micro-analyses (EPMA) were conducted on the authors own samples and samples provided by Professor Green.

#### **1.4.3.c. Cambridge University (Sedgewick Museum)**

Cambridge University allowed access to the extensive collection of samples collected by D.H.Green (1964a,b,c) and thin sections made from these samples.

---

## **1.5. Primary objectives and layout of thesis**

---

This thesis is principally a structural and geochemical study of the Lizard ophiolite Complex in SW England. The primary objectives of the thesis and the layout of the thesis are presented below:

### ***Primary objectives***

- To produce maps showing variation in peridotites and related rocks in the Lizard Ophiolite Complex.
- To characterise the Lizard peridotites in terms of their structural and geochemical evolution and determine the tectonic environment in which they formed.
- Constrain the emplacement history of the Lizard ophiolite Complex using new geochronological data, with particular attention paid to fabrics developed in peridotites, amphibolites and serpentine-filled faults.
- Present a new model for the tectonothermal evolution of the Lizard ophiolite Complex and its significance regarding the evolution of SW England and the Hercynian belt of northern Europe.
- To suggest what implications this study may have regarding the interpretation of the tectonothermal and geochemical evolution of other ophiolite complexes.

***Layout of thesis***

- Chapter 2: Geology of the Lizard ophiolite Complex and the stratigraphic terminology used with reference to the findings of previous studies.
- Chapter 3: Field observations and structural interpretation of the Lizard ophiolite Complex. Specific reference is made to field relationships, structures and magmatism broadly associated with three tectonothermal events that punctuate the evolution of this ophiolite Complex.
- Chapter 4: Microstructural characteristics of various rocks that comprise the Lizard ophiolite complex. Particular attention is paid to the microstructural evolution of the Lizard peridotites.
- Chapter 5: Geochemical characterisation of the rocks from the Lizard ophiolite Complex using mineral analyses.
- Chapter 6: Geochemistry of rocks from the Lizard ophiolite Complex using XRF, ICP-MS and isotopic analyses.
- Chapter 7: General discussion of the findings and summary of the geological evolution of the Lizard ophiolite Complex and implications for SW England, northern Europe, and ophiolite complexes in general.

## **CHAPTER TWO**

### **PREVIOUS WORK: THE GEOLOGY OF THE LIZARD OPHIOLITE COMPLEX**

#### **2.1. Regional setting of the Lizard Ophiolite Complex**

The Lizard ophiolite Complex is located in south-west Cornwall forming part of the Lizard peninsula, the most southerly point of mainland in the British Isles (Figure 2.1). The Lizard complex forms the highest structural unit exposed in the Variscan nappe stack of south-west England (Holder & Leveridge, 1986a), with the complex of higher-grade metamorphic rocks being separated from the low-grade, Devonian metasediments to the north by faulted contacts.

A plate tectonic reconstruction of western Europe during the Variscan orogenesis is shown in Figure 2.2. The Lizard Ophiolite Complex is inferred to have developed in the Cornwall Basin which was an area of sea bound to the north by the Welsh Massif and London-Brabant Massif landmasses and south by the Normannian High landmasses (Ziegler, 1982).

In models for the tectonic evolution of south Cornwall (Holder & Leveridge, 1986a; Holdsworth, 1989; Leveridge *et al.*, 1990; Clark *et al.*, 1998a,b) generation of oceanic lithosphere, represented by the Lizard ophiolite Complex, is thought to have occurred during the early Devonian. The presence of relict oceanic lithosphere supports the existence of a Rheic ocean (McKerrow & Ziegler, 1972; Burrett & Griffiths, 1977; Cocks & Fortey, 1982) within Rheohercynian zone of northern Europe. Existence of an extensive along-strike basin in the north European Variscides was proposed by Holder & Leveridge (1986b) on the basis of a close similarity of interpreted south Cornish geology to that of the Harz mountains of Germany. More recently Barnes & Andrews (1986) and Holdsworth (1989) suggested that the Gramscatho flysch basin and the Lizard Ophiolite Complex formed in a dextral pull-aparts along a major E-W continental megashear. This model, following Badham (1982) implies that the Lizard Ophiolite Complex represents localised formation of ocean crust rather than extensive ocean crust development as proposed by Holder & Leveridge (1986b). Subsequent closure of this ocean basin occurred during the late

Devonian (Clark *et al.*, 1998a,b) when the Lizard ophiolite complex was obducted and thrust towards the NNW along a major low-angle detachment. During closure, the Lizard ophiolite complex became incorporated within a series of thrust nappes, which included the Normannian High (Figure 2.3). The Normannian High represented a thrust nappe, which was a continental area that was bounded to the north by a deep-water basin (Holder & Leveridge, 1986a). NNW overthrusting of these nappes and consumption of the oceanic basin was possibly accompanied by development of a southward dipping subduction zone (Holder & Leveridge, 1986a). Closure of the ocean basin was followed by continental collision between the Normannian High and the southern part of Laurentia in the Upper Devonian with deformation progressing until the late Carboniferous (Holder & Leveridge, 1986a). Similar tectonic models have been proposed for the Grissen/Selke Nappe, Northern Phyllite Zone and the Mid-German Crystalline Rise of Harz and eastern Rhineland in Germany and support the existence of an extensive along-strike basin in the north European Variscides (Holder & Leveridge, 1986a,b).

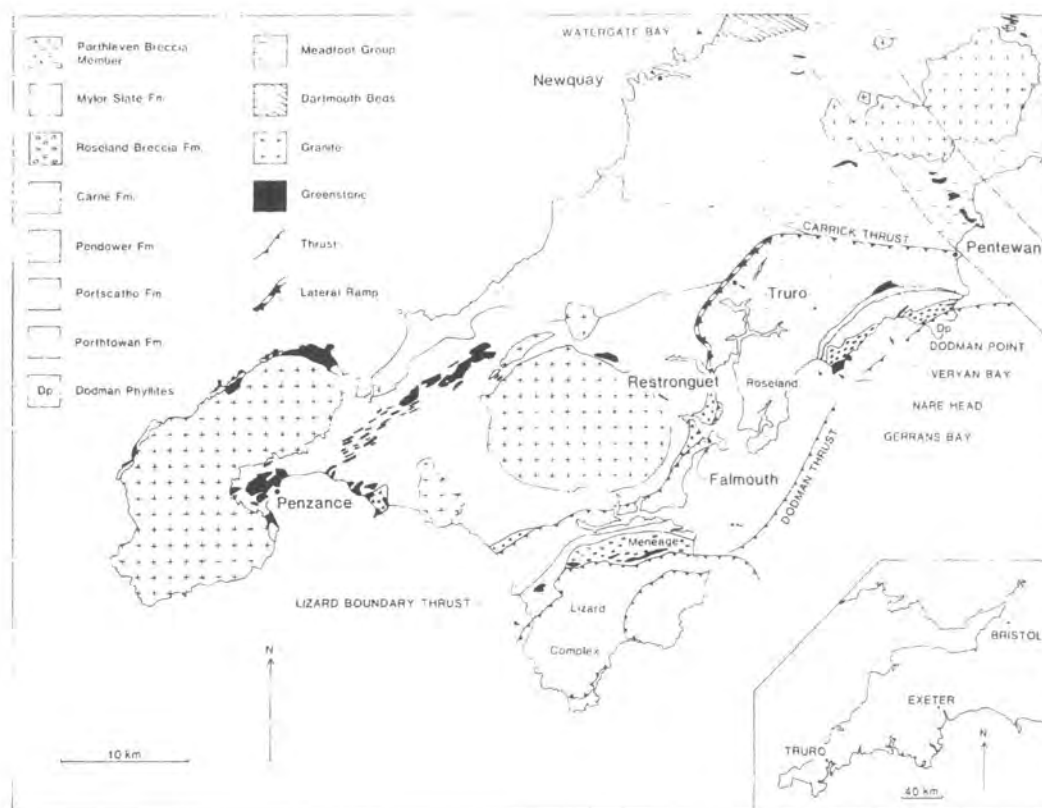


**Figure 2.1.** Present-day location of the Lizard ophiolite Complex in Cornwall (Taken from Holder & Leveridge, 1986a).



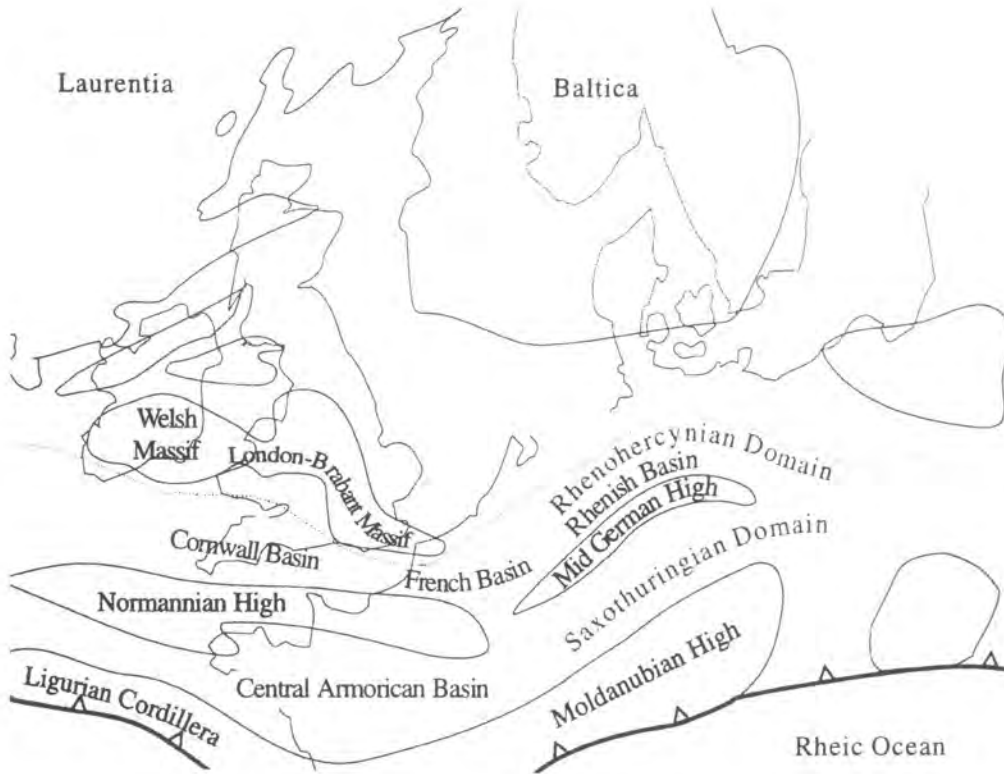


**Figure 2.2.** Structural components of Variscan deposition and deformation in western Europe. Shaded areas represent landmasses emergent during Variscan convergence whilst unshaded areas denote seas. Heavy barbed line represents subduction zone and stippled line follows the trace of the Variscan front (i.e. the northern limit of thrusting). After Ziegler, (1982).

## 2.2. Introduction: The geological subdivision of the Lizard Peninsula

The Lizard Peninsula (Geological Survey 1:50 000 map - Sheet 359) can be divided into three geologically distinct units (Figure 2.4). These are: (1) Ordovician basement; (2) Devonian sediments and volcanic rocks of the Gramscatho Group, and; (3) Devonian rocks of Lizard Ophiolite Complex.

### 2.2.1. The Ordovician basement

Rocks of the Ordovician basement are situated at the south-western extremity of the Lizard Peninsula and occur as limited exposures along the coastal section and rocks

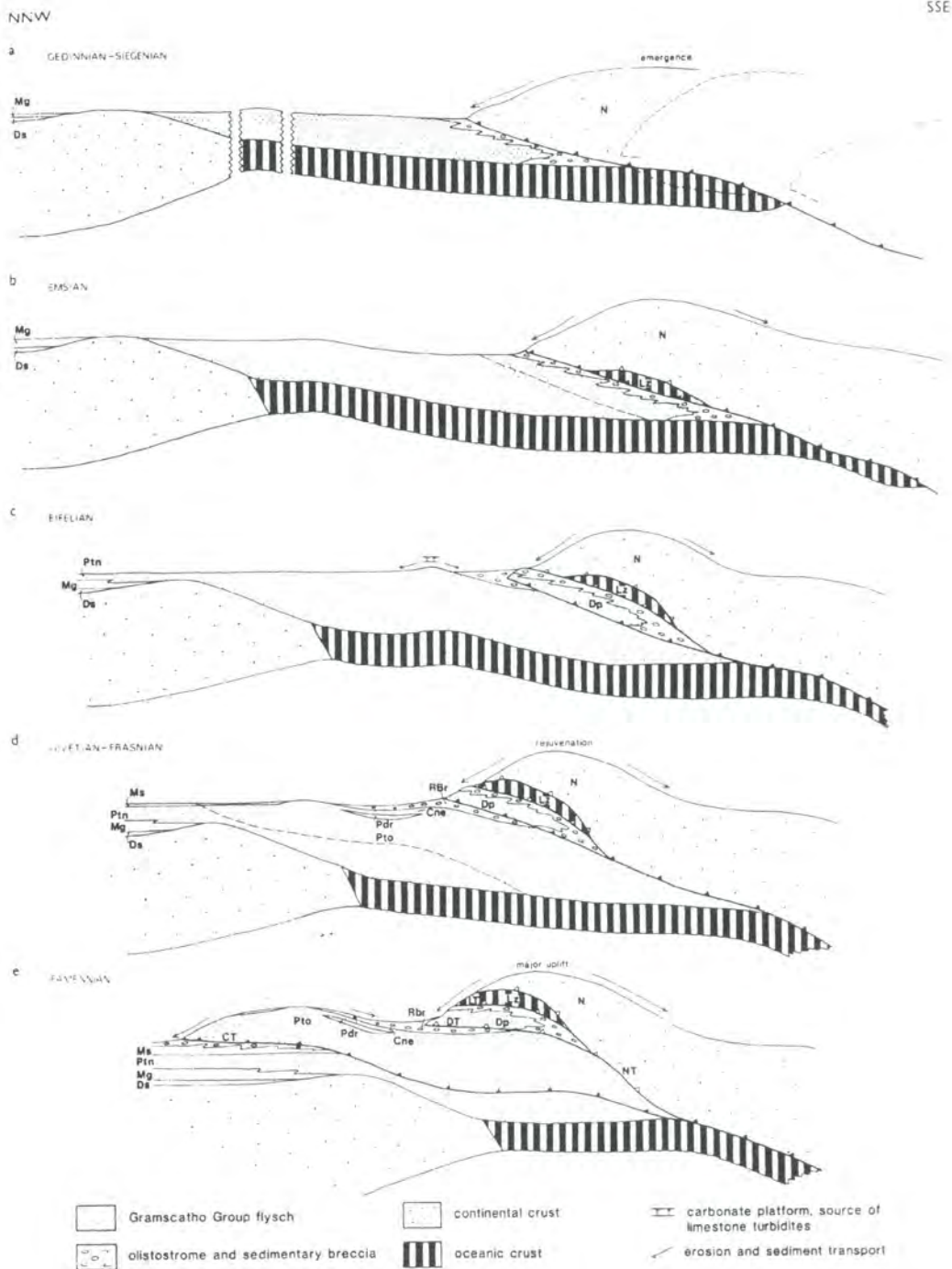


**Figure 2.3.** A model for the Devonian tectonic evolution of south Cornwall.

*Stratigraphic units:* Cne, Carne Formation; Ds, Dartmouth Slates; Mg, Meadfoot Group; Ms, Mylor Slate Formation; Pdr, Pendower Formation; Pto, Portscatho Formation; Ptn, Porthtowan Formation; Rbr, Roseland Breccia Formation.

*Tectonic units:* Ck, Carrick Nappe; CT, Carrick Thrust; Dp, Dodman Nappe; DT, Dodman Thrust; LT, Lizard Thrust; Lz, Lizard Nappe; N, Normannian Nappe; NT, Normannian Thrust. Taken from Holder & Leveridge (1986a).

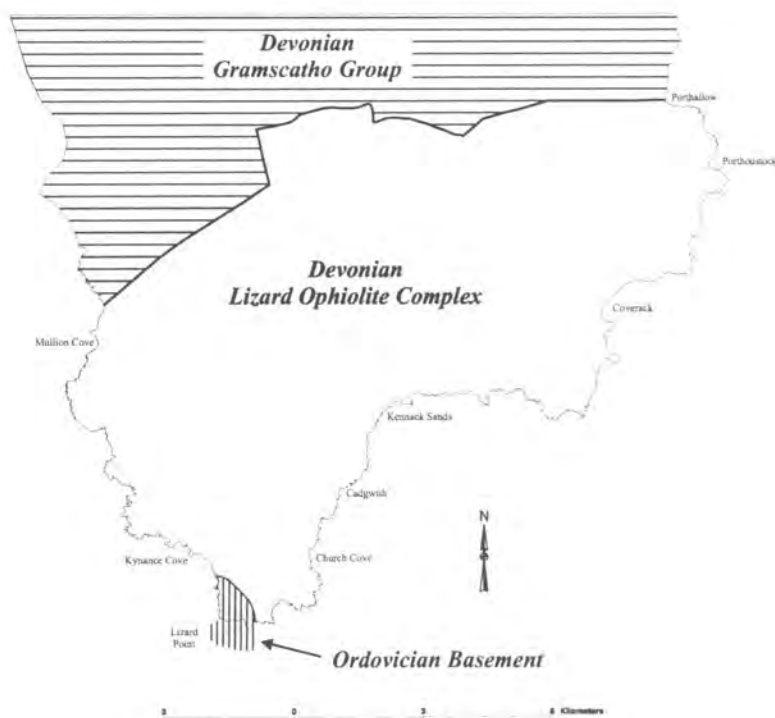


**Figure 2.4.** Geological sub-division of the Lizard peninsula.

and reefs south of Lizard point (Figure 2.4). This basement unit comprises two different suites of rocks: the *Man of War Gneiss* and the *Old Lizard Head Series*. Early studies (Fox, 1888; Flett, 1946) recognised that these rocks are amongst the oldest exposed on the Lizard peninsula and suggested that the Man of War Gneiss represents metamorphosed granites and tonalites that are intrusive into the metasedimentary rocks of the Old Lizard Head Series. A large granitic sill, known as the Lizard Head Sill, which crosscuts the Old Lizard Head Series was interpreted as offshoots of the main body of the Man of War Gneiss (Flett, 1946). The Old Lizard Head Series are composed of pelitic and psammitic rocks interlayered with amphibolites and have long been regarded to represent a series of metamorphosed basaltic lavas, tuffs and quartz-rich and pelitic sediments (Bonney, 1883; Somervail, 1884; Flett, 1946; Floyd *et al.*, 1993). Amphibolite layers in the Old Lizard Head Series were interpreted to be transitional with the Landewednack amphibolites (Green, 1946b,c; Floyd *et al.*, 1993). In recent studies, Jones (1994; 1997) demonstrated the presence of at least four low-angle shear zones that cross cut the Ordovician basement rocks. Jones (1994; 1997) proposed that one of these shear zones, the Old Lizard Head Thrust separate rocks of the Old Lizard Head Series in the hangingwall, from the Man of War Gneiss in the footwall. Sandeman *et al.* (1997) recently established that the Man of War Gneiss is

early Ordovician in age (499 ± 8/-3 Ma). On the basis of this new evidence and the structural relationships founded by Jones (1994), they proposed that the Man of War Gneiss represent a fragment of pre-Hercynian basement incorporated in the Normannian nappe during closure of a Devonian ocean basin. This therefore suggests that the Man of War Gneiss is a distinct geological unit to the Old Lizard Head Series and the Lizard ophiolite Complex. Sandeman *et al.* (1997) emphasise that there are geological and geochronological similarities between the Man of War Gneiss and early Ordovician rocks from Europe and propose that these rocks may represent remnants of Tremadoc arcs that formed oceanward from the northern margin of Gondwana.

Sandeman *et al.* (1997) demonstrated by  $^{40}\text{Ar}$ - $^{39}\text{Ar}$  date for amphiboles that the northern most zone of the Man of War Gneiss was subjected to an amphibolite-grade metamorphic event at ca. 374 Ma (mid Devonian). Clark *et al.* (1998a) demonstrated by laser-probe  $^{40}\text{Ar}$ - $^{39}\text{Ar}$  dating of biotite and muscovite in the Old Lizard Head Series that amphibolite facies metamorphism of this unit began by ca.  $380 \pm 5$  Ma. The authors interpreted this metamorphic event and metamorphism of the Man of War Gneiss to have been related to the development of thrusts and shear-zones, including the Old Lizard Head Thrust, probably associated with the thrust emplacement of the Lizard ophiolite complex.

Rocks interpreted to represent pre-Devonian basement also occur at or near the surface in the Eddystone and Start areas of south Cornwall (Doody & Brooks, 1986). Seismic refraction studies (Doody & Brooks, *op cit.*) suggest that the high grade metamorphic rocks of which this basement is composed are present ca. 3 km beneath the Lizard Ophiolite Complex. These basement rocks may possibly be associated with the Man of War Gneiss and Old Lizard Head Series, but there is insufficient evidence to support this hypothesis.

### **2.2.2. Devonian sediments and volcanic rocks of the Gramscatho Group**

The Gramscatho Group comprises a variable suite of rocks developed in the Gramscatho basin at a similar time to the development of the oceanic lithosphere, represented by the Lizard ophiolite Complex (Barnes & Andrews, 1986). The Gramscatho group structurally underlies the Lizard ophiolite Complex. The contact between these low-grade rocks and the high-grade metamorphic rocks of the Lizard

ophiolite Complex is a normal fault, related to the reactivation of earlier thrust faults (Power *et al.*, 1996). The Gramscatho group is dominated <sup>by</sup> flysch, deposited in submarine fans, which may have had a southerly source (Wilson & Taylor, 1976; Barnes & Andrews, 1986). The rocks immediately in contact with the Lizard ophiolite Complex are termed the Meneage melange and occupy a 3-4 km wide belt of sedimentary and volcanic rocks structurally underlying the Lizard ophiolite Complex (Figure 2.4). These rocks comprise a lower sequence of clasts of wacke, arenite, quartz-arenite and limestone set in a sparse mudstone matrix (Barnes & Andrews, 1986). An upper sequence includes large masses up to several km in size of pillow lava (Mullion Island), brecciated lava, tuff, amphibolite and serpentinite set in a mudstone matrix. Smaller clasts in this mudstone include 'greenstones', basalts, dolerites, and rare gabbros and their metamorphic equivalents, including amphibolites (Barnes, 1984). Relicts of a felsic volcanic suite are also present in the upper sequence of this melange as autochthonous pyroclastic flows and tuffs (Barnes & Andrews, 1986). Leveridge *et al.* (1984) and Holder & Leveridge (1986a) interpret parts of the Meneage melange, including serpentinite, as ophiolitic detritus shed from the advancing Lizard thrust sheet. Floyd *et al.* (1993) concluded that metabasalt clasts within the Meneage melange did not represent the eroded detritus from the Lizard ophiolite complex on the basis of geochemical evidence, but had many chemical similarities.

Folds and development of a penetrative cleavage in these rocks record deformation associated with the closure of the Gramscatho basin (Barnes & Andrews, 1986). Fold vergence and the consistent trend of stretching lineations suggest NNW directed overthrusting (Rattee & Sanderson, 1984). Barnes & Andrews (1984) demonstrated that the Meneage melange sediments and volcanic rocks immediately underlying the Lizard ophiolite complex record a single prograde pumpellyite-actinolite facies metamorphic event. This led the authors to propose a two stage event for the emplacement of the Lizard Complex: an initial hot obduction including decoupling of the mantle sequence and thrusting over oceanic crust, followed by later emplacement over the Meneage melange as a cold thrust sheet. Clark *et al.* (1998a) proposed that  $385 \pm 2$  Ma, whole-rock  $^{40}\text{Ar}$ - $^{39}\text{Ar}$  dates for epizonal metaclasts of the Dodman Formation exposed ca. 15 km NE of the Lizard ophiolite complex record the initial NNW-directed thrusting of the Normannian High over the oldest flysch shed from its leading edge.

### **2.2.3. Devonian rocks of the Lizard ophiolite Complex**

The following lithological units are now recognised within the Lizard Ophiolite Complex (Figure 2.5):

- Variably deformed and serpentinised peridotite (Lizard peridotites)
- Traboe Cumulate Complex (Ultramafic and Mafic Traboe cumulates)
- Metabasalt amphibolites (Landewednack amphibolites)
- Metagabbro and metabasalt amphibolites (Porthoustock amphibolites)
- Massive and weakly layered gabbros (Crousa gabbro)
- Variably metamorphosed mafic dykes
- Banded felsic/mafic intrusive complex (Kennack Gneiss)

The structure and interpretation of the Lizard ophiolite Complex has been the subject of debate for many years. Flett (1946) and Green (1964a,b,c) conducted two of the most complete studies of the Lizard ophiolite Complex. These authors concluded that the Lizard peridotite formed a plug-like or diapiric body and that it was intruded into the Landewednack amphibolites. Flett (1946) suggested that the mafic Traboe cumulates (Traboe hornblende-schists) represent a group of mafic rocks intruded immediately prior to the intrusion of the peridotite. Green (1964b) rejected this hypothesis and alternatively proposed that the mafic Traboe cumulates (Traboe hornblende-schists) represent the high-grade metamorphic equivalent of the Landewednack amphibolites, which developed in a dynamothermal aureole surrounding the Lizard peridotite.

In the 1970s the Lizard ophiolite Complex was re-interpreted by several authors in light of emerging plate tectonic theories that recognised the concept of ophiolites. The recognition that the Lizard ophiolite complex represented a deformed and dismembered ophiolite complex (Figure 2.6) was supported by borehole (Styles & Kirby, 1980) and regional geophysical studies (Doody & Brooks, 1986; Rollin, 1986) evidence that demonstrated that the Lizard had a sheet-like form, supporting the earlier conclusions of Sanders (1955). The tectonic and geochemical relationships between the three areas described above are reviewed in greater detail in Chapter 7 where they are incorporated into a regional tectonic model, which attempts to explain the evolution of the Lizard ophiolite complex and place it in a European context. The units of the Lizard

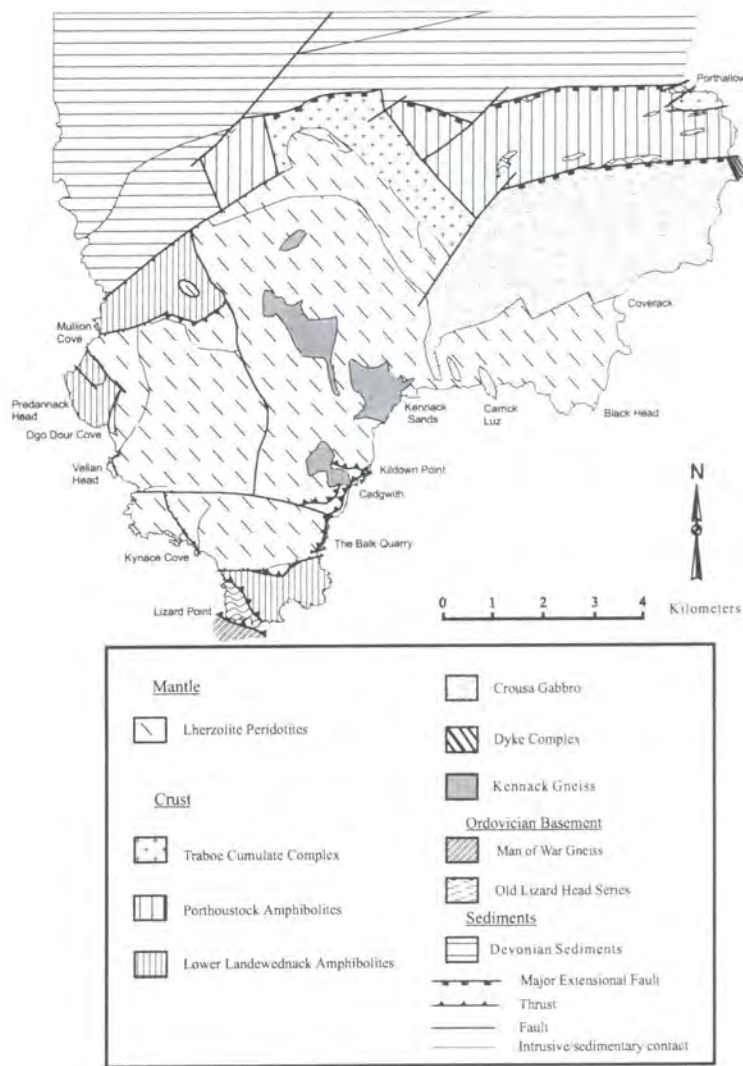


**Figure 2.5.** Simplified geological map of the Lizard ophiolite complex showing the major lithological units: modified after Flett (1946), Green (1964a) and Floyd et al. (1993).

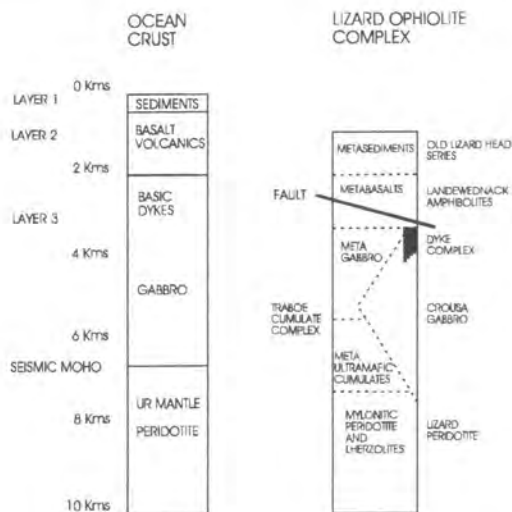


**Figure 2.6.** Geological succession of the Lizard ophiolite complex compared to typical ocean crust. Adapted after Styles (1992).



Ophiolite Complex are discussed in more detail below in section 2.3.

---

### **2.3. The geology of the Lizard ophiolite Complex.**

---

Flett & Hill (1912) and Green (1964a,b,c) produced the first detailed maps of the Lizard Ophiolite Complex and these maps included the first subdivision of the Lizard peridotites. The maps produced by these authors showed that the Lizard peridotite had an almost circular form, with coarser grained peridotites in the central region, surrounded by deformed peridotites. It was this pattern on a map that suggested that the Lizard peridotite was an intrusive diapiric body. Thayer (1969) first proposed that the Lizard Complex represented a deformed ophiolite complex. Bromley (1973; 1975; 1979) supported the ophiolitic origin of the Lizard Ophiolite Complex and conducted several detailed studies on the peridotite-gabbro-sheeted dyke sequence on the eastern part of the Lizard peninsula. Kirby (1979) presented geochemical evidence that demonstrated similarities between the mafic rocks from the Lizard ophiolite Complex and oceanic rocks. Bromley (1979) suggested that the Lizard ophiolite Complex was constructed from a sequence of thrust bounded units (Figure 2.7), that were from top to bottom:

- 1) Crousa Downs Unit – a section on the east coast of the Lizard peninsula where a bottom to top sequence of peridotite-gabbro-sheeted dykes is observed and is comparable with idealised ophiolite stratigraphy.
- 2) Goonhilly Downs Unit – the largest unit, predominantly composed of peridotite and overlain by deformed gabbros, amphibolites and metasediments.
- 3) Basal Unit – this was defined as a narrow belt around the south and the south-east of the Lizard peninsula and includes Landewednack amphibolites, Old Lizard Head Series and the Kennack Gneiss intruded in close proximity to the thrust contact between the Basal Unit and the overlying Goonhilly Downs Unit.



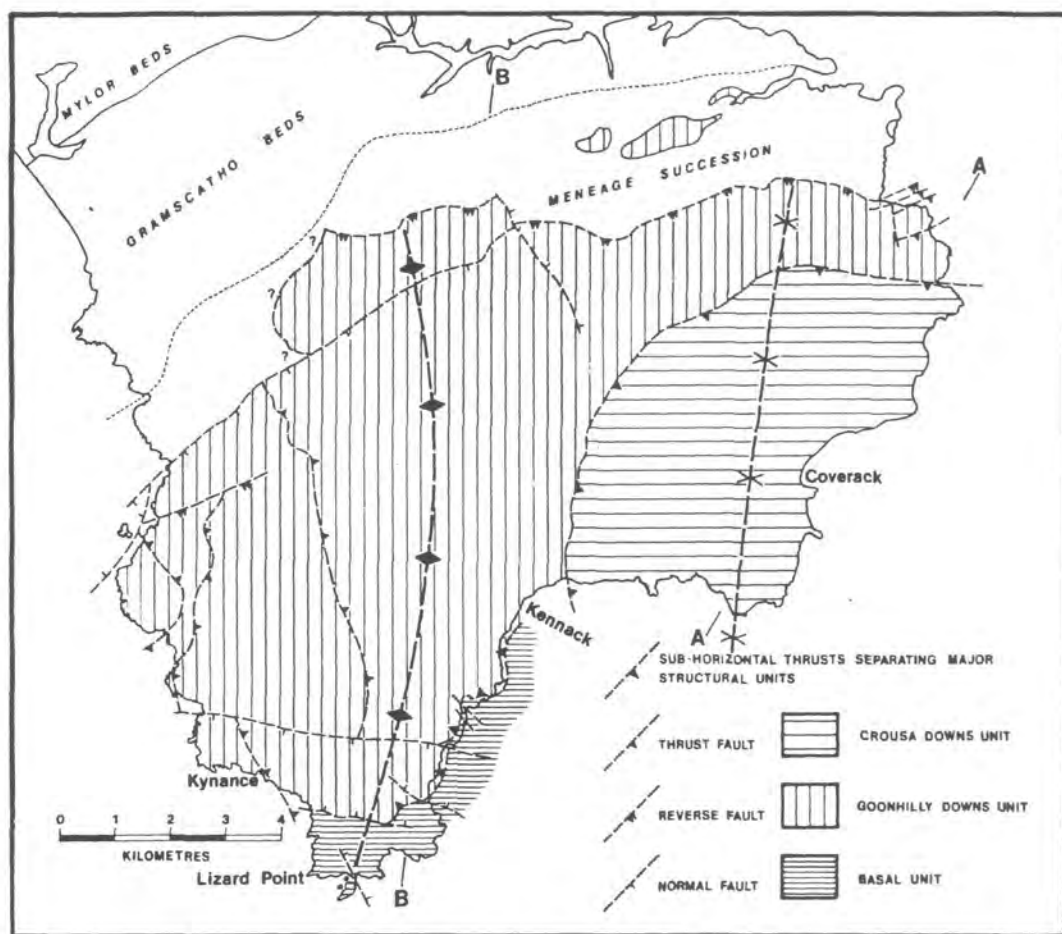


**Figure 2.7.** Structural sub-division of the Lizard ophiolite complex into three tectonic units. Taken from Bromley (1979).

Leake and Styles (1984) questioned the supposed thrust contact between the Crousa Downs Unit and the Goonhilly Downs unit, on the basis of continuity of rock sequences across the contact. Power *et al.* (1996) conducted a detailed structural analysis of the fault architecture of the Lizard ophiolite Complex and proposed a new structural sub-division. The authors proposed that the Crousa Downs Unit of previous workers represents the downfaulted upper level of the Goonhilly Downs Unit, and expanded the Basal Unit to include the Traboe cumulate complex and amphibolites previously included in the Goonhilly Downs Unit. The authors therefore subdivided the Lizard ophiolite Complex into two tectonic units: the Goonhilly Downs Nappe, underlain by the Goonhilly Downs Thrust, and the Basal Nappe, underlain by the Basal Thrust. Jones (1997) conducted a detailed study of the Basal Unit of the Lizard ophiolite Complex and proposed a sub-division of the unit into two allochthonous tectonic units, the Upper Nappe Series and the Lower Nappe Series, each comprising

two Nappes. Jones (1994, 1997) recognised that the Basal Unit was emplaced over the Man of War Gneiss along the Old Lizard Head Thrust.

New geochronological constraints presented in this thesis require a new nomenclature and stratigraphical framework for the units of the Lizard ophiolite Complex and these are presented in the following chapters.

The following section is sub-divided into descriptions of the seven main lithological units that occur in the Lizard ophiolite Complex (see Section 2.2.3).

### **2.3.1. Lizard peridotites**

Flett & Hill (1912) sub-divided the Lizard peridotites into four main types on the basis of detailed mapping and petrological evidence: bastite serpentine, tremolite serpentine, dunite serpentine and chromite serpentine. Serpentine was used as a rock name when the term serpentinite should be used for partially or completely serpentinised ultramafic rock. The authors showed that the bastite serpentine was the least deformed of the Lizard peridotites and occurred in the central and eastern parts of the peridotite body. Tremolite serpentine, which occurred as a belt surrounding the bastite serpentine, was interpreted to represent a highly deformed and recrystallised type that was derived from either metamorphism of the bastite serpentine or an earlier intrusion. Dunite serpentine was thought to have originated as dunite and to have had a significantly different bulk composition. Chromite serpentine was limited to pods and bands in the bastite serpentine and was distinguished by the presence of chromite stringers. Green (1964a) elaborated on the scheme of Flett & Hill (1912) and produced a map showing a similar distribution of peridotite types. On the basis of detailed field observations and a petrographic study and identification of distinct mineral assemblages and textures, Green (1964a) suggested that the different peridotites were related to the intrusion of a single peridotite diapir. Green (1964a) proposed that the different peridotite types were produced at progressively lower temperatures and pressures during several stages of recrystallisation and re-equilibration during intrusion of this diapir, and supported this with mineral and whole rock analyses. A relict *primary assemblage* was similar to the 'bastite serpentine' of Flett & Hill (1912) and consisted of olivine, aluminous orthopyroxene, aluminous clinopyroxene and olive-green spinel. This assemblage had crystallised at high-pressure and high-temperature in the upper mantle. A second type

of peridotite, the *recrystallised anhydrous assemblage*, occurred in a cataclastic, finely foliated and recrystallised marginal shell surrounding a primary core and was similar to the 'tremolite serpentine' of Flett & Hill (1912). This assemblage consisted of olivine, low-alumina orthopyroxene, low-alumina clinopyroxene, plagioclase and brown chromite and crystallised and re-equilibrated at lower pressure and temperature than the primary assemblage. A third assemblage, the *recrystallised hydrous assemblage*, was developed locally in the recrystallised anhydrous assemblage as narrow zones, particularly in the margin of the peridotite body. This assemblage was characterised by the presence of olivine, pargasite amphibole and brown chromium spinel. Green (1964a) proposed that the dunite serpentine of Flett & Hill (1912), was the highly serpentinised equivalent of the recrystallised hydrous assemblage. Green (1964a) demonstrated that all the peridotite assemblages had a similar bulk composition and thus disagreed with the data presented by Flett & Hill (1912), that showed that the 'dunite serpentine' had a different bulk composition to the other peridotite types. The diapir model of Green (1964a) was challenged when borehole evidence (Styles and Kirby, 1980) demonstrated that the peridotite had a sheet-like form and was underlain by amphibolite. This led to models suggesting that the peridotite evolved in the suboceanic mantle and now represents the lowermost stratigraphic slice of an ophiolite complex. Thrusting of a sheet of peridotite over oceanic crust was invoked to explain the amphibolites underlying the Lizard peridotites and comparisons with the Newfoundland and Oman ophiolites were presented in order to support these models (Styles & Kirby, 1980). Although many papers after Green (1964a) discussed the later obduction of an ophiolite slab (Bromley, 1979; Styles & Kirby, 1980; Vearncombe, 1980; Floyd *et al.*, 1993; Jones, 1994, 1997 and Sandeman *et al.*, 1995) none of these publications attempt to adequately explain the earlier tectonic evolution of the Lizard peridotite body. Therefore, although later models dispute the diapiric model of Green (1964a), they can neither provide a satisfactory alternative nor doubt the petrological evidence and mineral assemblages on which the model was in part based, including Styles & Kirby (1980) who agreed with the petrological evidence. Rothstein (1977; 1981; 1988; 1994 and 1998) is one of a minority of authors, since the work of Green (1964a), who has specifically studied the Lizard peridotites. Rothstein (*op cit.*) supported Green's (1964a) sub-division of the Lizard peridotites and presented thermobarometric data to support the high-pressure and high-temperature origin of the primary assemblage peridotite. Rothstein (*op cit.*) also recognised that deformation

fabrics in the peridotites, particularly the recrystallised assemblages, are associated overall with sub-solidus re-equilibration of the pyroxenes at decreasing temperatures. However, Rothstein (*op cit.*) did not suggest any tectonic models to explain the evolution of the Lizard peridotites. Instead, he presented very detailed field and textural evidence for the preservation of earlier, pre-tectonic, textures in the primary assemblage peridotite that developed prior to recrystallisation and re-equilibration. These textures occur in pyroxenite, harzburgite and dunite-rich bands and include a wide range of micro-textures, particularly involving olivine, which are orientated at a steep angle to the mineralogical banding. In a series of publications, Rothstein (*op cit.*) has demonstrated that these textures may be interpreted as relics of cumulates and micro-crescumulates that crystallised from liquids, which are related to one or possibly two early igneous episodes, involving separate pulses of melt or magma within the spinel-lherzolite facies.

Frey (1969) studied the rare earth element (REE) geochemistry of the Lizard peridotites and showed that the primary spinel-lherzolite assemblage had very depleted LREE, typical of residual, mantle-derived Alpine peridotites (Floyd *et al.*, 1993). The recrystallised anhydrous and hydrous assemblages of Green (1964a) were also analysed and showed less depleted REE, the latter close to chondritic abundances with only slight LREE depletion. Davies (1984) also studied the REE geochemistry of the Lizard peridotites in addition to their isotopic composition. Davies (1984) demonstrated that a single sample of plagioclase lherzolite had five times chondrite abundances and slight LREE enrichment. He proposed that the LREE depletion of the primary spinel lherzolite assemblage resulted from a multi-stage melting event, involving the removal of very small increments of melt. This would account for the depleted LREE, whilst retaining a fertile major-element characteristics. The REE geochemistry and Sm-Nd isotopic systematics of the recrystallised anhydrous and hydrous assemblage peridotites were interpreted to probably reflect the infiltration of a LREE-enriched magma.

Most authors have commented on the pervasive serpentinisation that has hampered study of the textural features of the Lizard peridotites. Power *et al.* (1997) conducted a study of the Lizard ophiolite Complex, which was specifically focused on the nature and timing of serpentinisation of the Lizard peridotites. The authors established that there were at least two episodes of serpentinisation, the first resulted in large-scale hydration of the peridotite and was characterised by zones of veins of white serpentine. A second episode was restricted to faults and fractures and occurs as a

pseudo-fibrous mixture of lizardite and chrysotile. Power *et al.* (*op cit.*) proposed a Carboniferous age for the primary episode and a latest Carboniferous to early Permian age for the secondary serpentinisation episode, on the basis of previously published geochronological constraints (Seager *et al.*, 1975; 1978; Halliday & Mitchell, 1976).

### **2.3.2. Ultramafic and Mafic Traboe cumulates**

Flett & Hill (1912) recognised the presence of two distinct types of amphibolite in the Lizard ophiolite complex, which they termed the Landewednack and Traboe types. Flett & Hill (*op cit.*) distinguished the Traboe amphibolites from the Landewednack type (see section 2.3.3) on the basis of a more variable fabric orientation, coarser grain size, compositional differences and the presence of an interlayered and folded association with the Lizard peridotites, in particular the 'dunite serpentine'. The authors concluded that the Traboe amphibolites had been subjected to different metamorphic conditions and were derived from a series of mafic intrusives that immediately preceded the emplacement of the Lizard peridotite body.

On the basis of detailed field and petrographic evidence Green (1964a,b,c) concluded that the Traboe amphibolites, which include a pyroxene granulite assemblage, were the metamorphosed equivalent of the Landewednack amphibolites. In his re-interpretation, Green (*op cit.*) proposed that the Traboe amphibolites were developed within a dynamothermal aureole related to the hot emplacement of the Lizard peridotites as a diapir (Section 2.3.1). Green (*op cit.*) proposed that differences in the stress-field in the margins of the peridotite diapir were responsible for the development of generally steeper and more irregular fabrics in the Traboe amphibolites, compared to the more flat-lying fabrics of the Landewednack amphibolites (Section 2.3.3). Green (*op cit.*) presented a few mineral analyses to support these conclusions, and more specifically, his whole rock analyses suggested that the Traboe and Landewednack amphibolites had a similar composition. Thayer (1969) suggested that the Traboe amphibolites were original gabbros and formed part of the lower crustal sequence of a dismembered ophiolite. Kirby (1979) presented a large number of whole rock geochemical analyses for the Traboe and Landewednack amphibolites and this data clearly showed differences between the Traboe and Landewednack amphibolites, and confirmed that they could not have shared the same pre-metamorphic protolith. On the basis of this data and field relationships, he

concluded that the Traboe amphibolites were derived from cumulate gabbroic rocks. The most convincing evidence that the Traboe amphibolites represented deformed and metamorphosed gabbroic cumulates was presented by Leake & Styles (1984). The authors presented evidence from three borehole sections (IGS Boreholes, 1978) and included a large number whole rock and mineral analyses of the rocks intersected by the boreholes. These boreholes intersected a large variety of rock types, including Traboe amphibolites and layered ultramafic rocks. Ultramafic rocks resembled the 'dunite serpentine' recognised by Flett & Hill (1912) and included dunites and pyroxenites, and on this basis the authors proposed that these ultramafic rocks were deformed and serpentinised layered ultramafic cumulates. Rocks that resembled the Traboe amphibolites included gabbros and anorthosites, leading Leake & Styles (1984) to propose that these rocks were originally mafic cumulates that formed an upper part of a cumulate complex, transitional with the ultramafic cumulates. The authors termed the sequence of rocks the 'Traboe cumulate complex' and suggested that it originated as a layered peridotite-gabbro cumulate complex overlying the Lizard peridotites. Leake & Styles (*op cit.*) also demonstrated that the composition of the mafic rocks was very different from the composition of the Landewednack amphibolites, and that the bulk composition of the ultramafic cumulates was quite different from the lherzolites of the main Lizard peridotite body.

Clark *et al.* (1998b) obtained an age of  $397 \pm 2$  Ma by U-Pb dating of zircons for a plagiogranite that occurred as veins cross-cutting amphibolitised mafic Traboe cumulates. This demonstrates that the cumulates were being deformed and amphibolitised in the Early Devonian and the authors proposed that this occurred during intra-oceanic metamorphism, extensional ductile shearing related to the construction of the oceanic crust section of the Lizard ophiolite complex. This supported the earlier conclusions of Gibbons & Thompson (1991), who suggested that these rocks represent the footwall of a low-angle amphibolite-facies shear zone. Later closure of the ocean basin and emplacement of the Lizard ophiolite complex is recorded by amphibolite facies metamorphism of a leucogabbro associated with the mafic Traboe cumulates. Clark *et al.* (1998a) obtained a amphibole  $^{40}\text{Ar}$ - $^{39}\text{Ar}$  age determination for this rock that suggested that emplacement took place around  $381 \pm 12$  Ma.

Throughout the following chapters of this thesis (Chapters 3-7) the term Traboe amphibolites or Traboe hornblende schist is replaced by 'mafic Traboe cumulates' and the layered ultramafic rocks associated with these mafic rocks are termed the 'ultramafic Traboe cumulates'. It is anticipated that this change of terminology will be better suited to an understanding of the present day interpretation of the geology of the Lizard ophiolite Complex and comparisons with other ophiolite complexes.

### **2.3.3. Landwednack amphibolites**

Flett & Hill (1912) distinguished the Landwednack amphibolites from the mafic Traboe cumulates (Traboe amphibolites) on the basis of a regular, flat-lying foliation, strong mineral lineation, fine-grain size and the presence of epidotic layers. Flett & Hill (*op cit.*) concluded that the Landwednack amphibolites originated as lavas and intrusive sills and were presumably basalts and dolerites. Green (1964a,b,c) proposed that the Landwednack amphibolites were developed during the regional metamorphism of a protolith composed of basaltic lavas and/or sills with minor dykes, tuffs and calcareous sediments.

More recently, authors have proposed that the Landwednack amphibolites consist of metamorphosed basaltic lavas and sills with minor gabbros, which represent a highly deformed and metamorphosed equivalent to oceanic crust (Bromley, 1979; Kirby, 1979; Styles and Kirby, 1980; Floyd *et al.*, 1993; Sandeman *et al.*, 1995; Jones, 1997). Floyd *et al.* (1976) and Kirby (1979) demonstrated that the chemical composition of these rocks is very similar to ocean-floor basalt, therefore supporting the conclusions based on field evidence. Most authors suggested that the metamorphism of these amphibolites and the development of flat-lying fabrics was due to overthrusting of a hot ophiolite slab during obduction. These amphibolites were therefore interpreted to represent a dynamothermal aureole beneath the peridotite. Sandeman *et al.* (1995) presented  $^{40}\text{Ar}$ - $^{39}\text{Ar}$  age determinations for amphiboles from the Landwednack amphibolites, which suggest that the Lizard ophiolite complex was thrust over the Landwednack amphibolites at  $366 \pm 4$  Ma. The authors also presented thermobarometric data and this suggested that the peak P-T conditions during metamorphism of the amphibolites was ca. 600°C and 300-400 Mpa.

Jones (1997) recently proposed that the Basal Unit of the Lizard ophiolite complex, which includes Landewednack amphibolites, preserves evidence of a protracted deformation and accretion history. Jones (*op cit.*) demonstrated evidence for five thrusts and divided the Basal Unit into four nappes on the basis of field evidence. Decoupling of the mantle, emplacement over the Basal Unit and subsequent development of a dynamothermal aureole in the previously accreted Basal Unit was inferred to be a late stage feature. A final stage of syn-emplacement extensional collapse was recognised and was responsible for the reactivation of earlier emplacement-related thrusts.

#### **2.3.4. Porthoustock amphibolites**

When Bromley (1979) sub-divided the Lizard ophiolite complex into separate tectonic units he proposed that the Landewednack amphibolites occur in two different structural units. Bromley (*op cit.*) suggested that the amphibolites in the structurally higher Goonhilly Downs unit represented the deformed equivalent of a gabbro/dyke transition zone, similar to that preserved in the Crousa gabbro. This led Vearncombe (1980) to introduce the terms Upper and Lower Landewednack amphibolites. The Upper Landewednack amphibolites belong to the northern and structurally higher Goonhilly Downs Unit, and Lower Landewednack amphibolites belong to the structurally lower Basal Unit. Vearncombe (*op cit.*) suggested that the Upper Landewednack amphibolites were derived from highly deformed gabbroic rocks and that these rocks do not preserve evidence for the more complex deformational history observed in the Lower Landewednack amphibolites. Gibbons & Thompson (1991) demonstrated that the Upper Landewednack amphibolites resembled mylonitised and amphibolitised metagabbros interleaved with finer-grained mylonitic amphibolites that locally preserved porphyritic dolerite textures. The authors termed this unit the Porthoustock shear zone and noted that rocks were flat-lying and lineations plunged at a low-angle towards the west and south-west. Kinematic indicators suggested a top-to-the-SW sense of shear. These findings contrasted with the top-to-the-NW kinematics observed in the Lower Landewednack amphibolites that were developed during obduction. As a result, Gibbons & Thompson (*op cit.*) proposed that the Porthoustock shear zone (Upper Landewednack amphibolites) represented the deformed equivalent of a gabbro-sheeted



dyke complex and this was generated due to ductile extension at an oceanic spreading centre.

New chemical data for these rocks, presented in this thesis (Chapter 6) supports the findings of Bromley (1979), Vearncombe (1980) and Gibbons & Thompson (1991) and suggests that the Upper Landewednack amphibolites are indeed different from the Lower Landewednack amphibolites. Therefore the term Porthoustock amphibolites is introduced in order to clearly distinguish these rocks, previously known as the Upper Landewednack amphibolites, from the Landewednack amphibolites that occur in the Basal Unit of the Lizard ophiolite complex.

### **2.3.5. Crousa gabbro**

Green (1964c) proposed that the Crousa gabbro represented a part of a large ring intrusion that clearly post-dated the emplacement of the Lizard peridotite body. Green (*op cit.*) also noted the presence of spectacular flaser gabbros and numerous small gabbro dykes associated with the main Crousa gabbro body. Kirby & Badham (1976) suggested an ophiolitic origin for the Crousa gabbro, but showed that the transition from peridotite to the Crousa gabbro was dissimilar to a typical ophiolite succession, as a substantial cumulate succession was missing. They suggested that the gabbro was a later intrusion and possibly related to off-axis magmatism. Kirby (1979) presented chemical analyses of the Crousa gabbro and revealed it became progressively fractionated from south to north, going upwards in the ophiolite sequence. Kirby (*op cit.*) concluded that the chemistry of the Crousa gabbro was consistent with it forming from magma similar to MORB. Styles & Kirby (1980) suggested that a coast section on the eastern side of the Lizard peninsula, which included the Crousa gabbro, was the most convincing evidence for an ophiolitic origin of the Lizard ophiolite complex. They interpreted the transition from peridotite to overlying gabbro to represent the petrological Moho and therefore rejected the finding of Green (1964c), who suggested the gabbro was unrelated to the peridotite. The authors demonstrated that the Crousa gabbro recorded a complex history of intrusive phases and deformation. Floyd (1984) demonstrated that the Crousa gabbros have low incompatible-element contents and LREE depletion and he interpreted this to indicate derivation from a depleted mantle source and consistent with an oceanic origin. Several studies (Gibbons & Thompson,

1991; Roberts *et al.*, 1993 and Hopkinson & Roberts, 1995;1996) have described the presence of low-angle extensional shear zones within the Crousa gabbro. These shear zones have been interpreted by the authors to record ductile extension in the lower oceanic crust in a slow-spreading ridge-axis environment. Davies (1984) obtained a combined mineral and whole rock Sm-Nd isochron for the Crousa gabbro and this yielded an age of  $375 \pm 34$  Ma for the formation of ocean crust. Andrews & Jolly (*in press*) have recently proposed that a large gabbro mylonite body within the Lizard peridotite, the Carrick Luz shear-zone, represents a feeder zone to the overlying Crousa gabbro body. The authors have suggested that the orientations of gabbroic dykes associated with this shear zone are consistent with development of oceanic crust at an oblique spreading centre.

#### **2.3.6. Mafic dykes**

Flett & Hill (1912) and Green (1964c) commented on a suite of NNW-SSE trending basaltic dykes that exhibited chilled contacts against the Lizard peridotite, Crousa gabbro and mafic Traboe cumulates. Green (1964c) suggested that this suite of dykes formed the vertical feeder zones to mafic sills associated with the Kennack Gneiss (Section 2.3.7). Bromley (1973; 1979) sub-divided mafic dykes from the Lizard ophiolite complex into three groups, based on field evidence. He suggested that numerous NW-SE trending subvertical metadolerite dykes, which occupy between 50 and 80% of outcrop in the northern area of the Crousa gabbro body, represented a sheeted dyke complex. Kirby (1984) presented field and chemical evidence to support a sub-division of mafic dykes from the Lizard ophiolite complex into three groups, similar to the groups of Bromley (1979). However, Kirby (1984) suggested a different sequence to Bromley (1979). He suggested that later (olivine) dolerites were the most primitive, with MORB like characteristics, and that an earlier (aphyric) suite were more fractionated with a slightly calc-alkaline composition. Davies (1984) presented REE data for dykes from the Lizard ophiolite complex and proposed that there were two groups, similar to two of the groups of Kirby (1984). An early group was LREE enriched and a later group was MORB-like and LREE depleted. Sandeman (1988) also established the same chemical groups as Kirby (1984) and Davies (1984), but he suggested, in accordance with Bromley (1979) that the LREE enriched, aphyric, suite

were later and not the earliest suite. Roberts et al. (1993) presented the most reliable sub-division of the mafic dykes associated with the Crousa gabbro body from the Lizard ophiolite complex. Identification of the different dyke suites and their relative chronology was based primarily on field observations, including detailed structural analysis, and not chemical data. The authors recognised three dolerite dyke suites, the first two (suites 1 & 2) are restricted<sup>to</sup> the main Crousa gabbro body and are cut by and rotated on a series of extensional faults and shear zones. Later dykes (suite 3) cross-cut the extensional faults and also cross-cut the Lizard peridotites and mafic Traboe cumulates. All the dyke suites show MORB characteristics, although the later dyke (suite 3) are the more primitive, in agreement with the chronology established by Kirby (1984) and Davies (1984). Roberts et al. (*op cit.*) suggested that the sequence of dyke intrusions, their geochemical evolution and inter-relationships with the extensional faults was consistent<sup>with</sup> tectonic and magmatic processes at a slow-spreading ridge.

### **2.3.7. Kennack Gneiss**

The Kennack Gneiss comprises a series of interbanded and mixed felsic and mafic gneissose rocks that occur along the south-east coast of the Lizard peninsula. These rocks are located in proximity to the thrust contact between the underlying Basal Unit and the overlying Goonhilly Downs Unit. Bonney (1887) was one of the earliest workers to study the Kennack Gneiss and he proposed that it was older than the Lizard peridotite and that the peridotite was intrusive into the Gneiss. Flett & Hill (1912) concluded that the Kennack Gneiss was an injection gneiss of mixed felsic and mafic magmas intruded into the Lizard peridotite during a period of deformation and metamorphism.

Sanders (1955) shared Bonney's (*op cit.*) view that the Kennack Gneiss was older than the peridotite, although he proposed tectonic inclusion of Kennack Gneiss in the peridotite rather than intrusion. Sanders (*op cit.*) also proposed that the Kennack Gneiss was the migmatised equivalent of the Landewednack amphibolites and Old Lizard Head Series.

Green (1964c) supported the findings of Flett & Hill (1912) and proposed that the Kennack Gneiss intruded the peridotite as a two-stage event forming composite intrusions. Mafic magmas intruded the peridotite as NNW-SSE trending dykes and as

gently dipping sheets and deformation accompanied their intrusion. Mafic magma was followed by felsic intrusions, which were preferentially intruded along the gently dipping mafic sheets.

Recent interpretations of the Kennack Gneiss are divided into two camps, following the conclusions of previous authors. Kirby (1979), Vearncombe (1980) and Malpas & Langdon (1987) shared the opinion of Sanders (1955) and proposed that the Kennack Gneiss was the migmatised equivalent of the Landewednack amphibolites and Old Lizard Head Series. The authors suggested that the hot overriding ophiolite slab provided the heat necessary for melting. Bromley (1979), Barnes & Andrews (1986), Sandeman (1988) and Sandeman *et al.* (1995) supported the models of Flett & Hill (1912) and Green (1964c). These authors suggested that the Kennack Gneiss was the product of a co-mingled assemblage of mafic and felsic magmas intruded into the base of the Lizard ophiolite complex during obduction. Sandeman (1988) suggested that the mafic portion of the Kennack Gneiss was older than the felsic portion and that both physical and chemical mixing of the two magmas took place. He showed that the mafic portion has chemical characteristics similar to calc-alkaline basalts and that it probably had no close relationships with the felsic magma prior to intrusion.

Sandeman *et al.* (1995) presented estimates of the P-T conditions of dynamothermal metamorphism recorded by the Landewednack amphibolites and mafic portion of the Kennack Gneiss and concluded that they were probably insufficient to cause anatexis of the units underlying the ophiolite.

Styles & Rundle (1984) provided a whole-rock Rb-Sr isochron for a felsic vein in the Kennack Gneiss and this gave an age of  $369 \pm 12$  Ma. The authors interpreted this as a metamorphic age recording the time of emplacement of the Lizard ophiolite complex. A similar age of ca. 366 Ma was obtained by  $^{40}\text{Ar}$ - $^{39}\text{Ar}$  dating of hornblende in the mafic component of the Kennack Gneiss (Sandeman *et al.*, 1995).

## CHAPTER THREE

### FIELD AND GEOCHRONOLOGICAL EVIDENCE FOR THE STRUCTURAL AND MAGMATIC EVOLUTION OF THE LIZARD OPHIOLITE COMPLEX

#### 3.1. Introduction

New geochronological constraints relating to the igneous and metamorphic events that have taken place in the Lizard Ophiolite Complex have been integrated with a tectonic sequence based on detailed field evidence. This new evidence has been used to establish a new chronological order of tectonic and magmatic events that occurred during the evolution of the Lizard Ophiolite Complex.

Geochronological constraints are provided by new U-Pb SHRIMP dating of zircon and monazite obtained from various parts of the Lizard Ophiolite Complex (Figures 3.1 & 3.2) and also existing age constraints provided by previous publications. Isotopic ratios used to obtain primary igneous and metamorphic ages were obtained from separated zircon and monazite crystals by U-Pb SHRIMP analysis at the Research School of Earth Sciences, Australian National University, Canberra (Nutman, A., *pers comm*, 1998). Full details of the sample preparation techniques, methods and results are provided in Appendix A.

The layout of this chapter and subsequent chapters in this thesis is based on the new chronological order of tectonic and magmatic events. This chapter is sub-divided into four main sections. These sections describe the field relationships, structures and magmatism broadly associated with four tectono-magmatic events:

- An early magmatic and tectonic evolution in basement rocks exposed at the SW point of the Lizard peninsula.
- A later sequence of deformation and magmatism in mantle rocks and associated mafic rocks, including the generation of sub-vertical fabrics and peridotite mylonites during construction of early oceanic lithosphere.

- Extensive magmatism resulting in the intrusion of gabbro and basaltic dykes, and associated extensional tectonics, which represent the generation of later oceanic lithosphere.
- Top-to-the-NW thrusting and contemporaneous magmatism, resulting in the emplacement and juxtaposition of the different lithological units that comprise the Lizard Ophiolite Complex as seen today. This includes emplacement of the Lizard Ophiolite Complex structurally over Ordovician basement. Thrust contacts are subsequently reactivated during later deformation events.

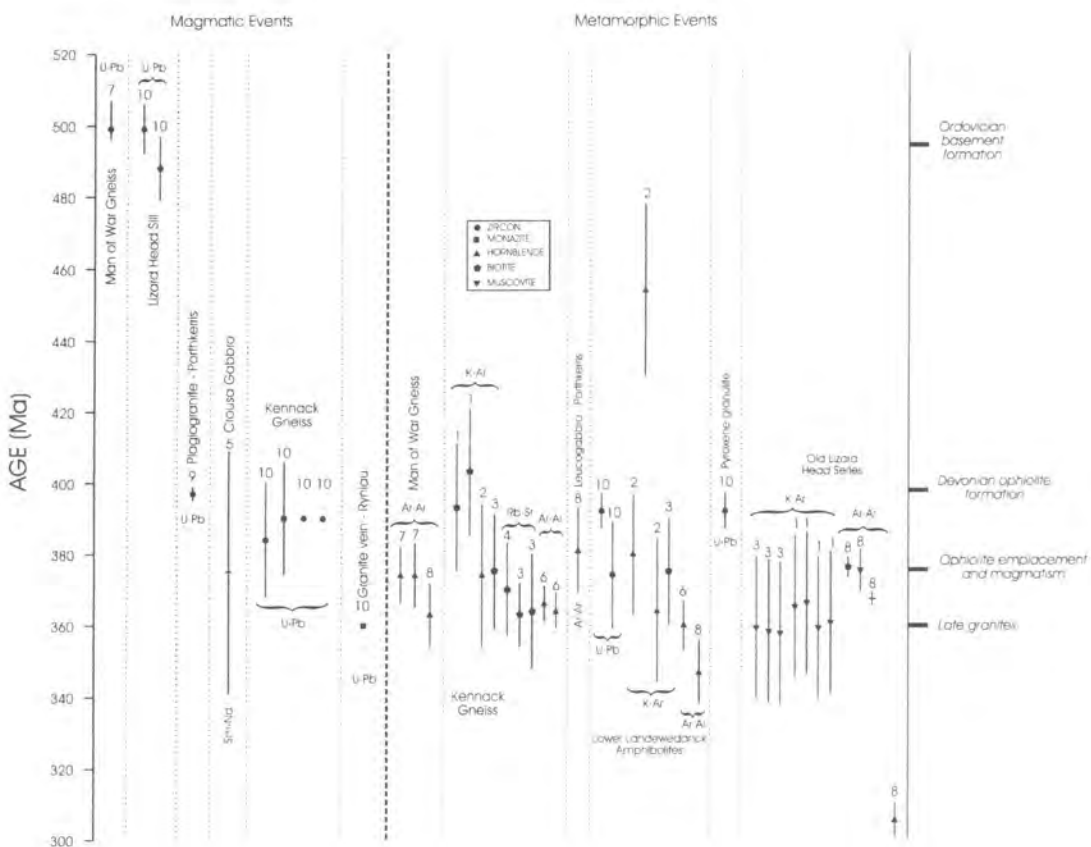


**Figure 3.1.** Summary of chronological data for the Lizard complex showing the interpretation of magmatic and metamorphic events as recorded by geochronological data for rocks of the Lizard complex. Data sources are (1) Miller and Green (1961a); (2) Miller and Green (1961b); (3) Dodson (1961); (4) Styles and Rundle (1984); (5) Davies (1984); (6) Sandeman et al.(1995); (7) Sandeman et al. (1997); (8) Clark et al. (1998a); (9) Clark et al. (1998b); (10) this study.

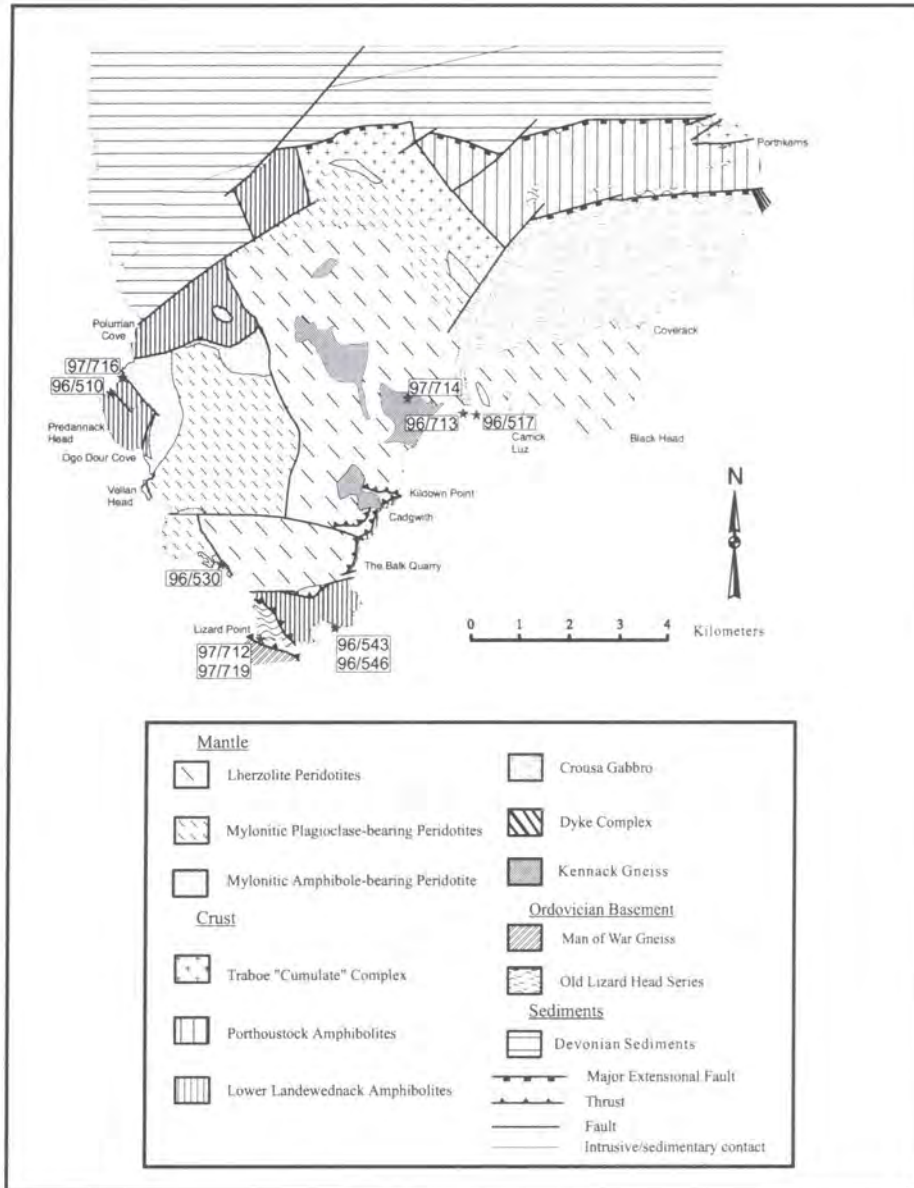


**Figure 3.2.** Simplified geological map of the Lizard complex: modified after Flett (1946), Green (1964a) and Floyd et al. (1993). Location of samples used in geochronological study are shown as stars and labelled accordingly.

### 3.2. Ordovician basement rocks of the Lizard Peninsula

On the SW point of the Lizard peninsula there is an association of supracrustal rocks with oceanic affinity, granitoids and associated intrusives (Figure 3.3). These basement rocks occur in the footwall of thrust contacts with the mafic and ultramafic rocks of the Lizard Ophiolite Complex. New geochronological constraints derived from U-Pb SHRIMP analyses of zircon in these rocks establish that the early steeper fabrics preserved in some of these rocks are at least of early Ordovician age

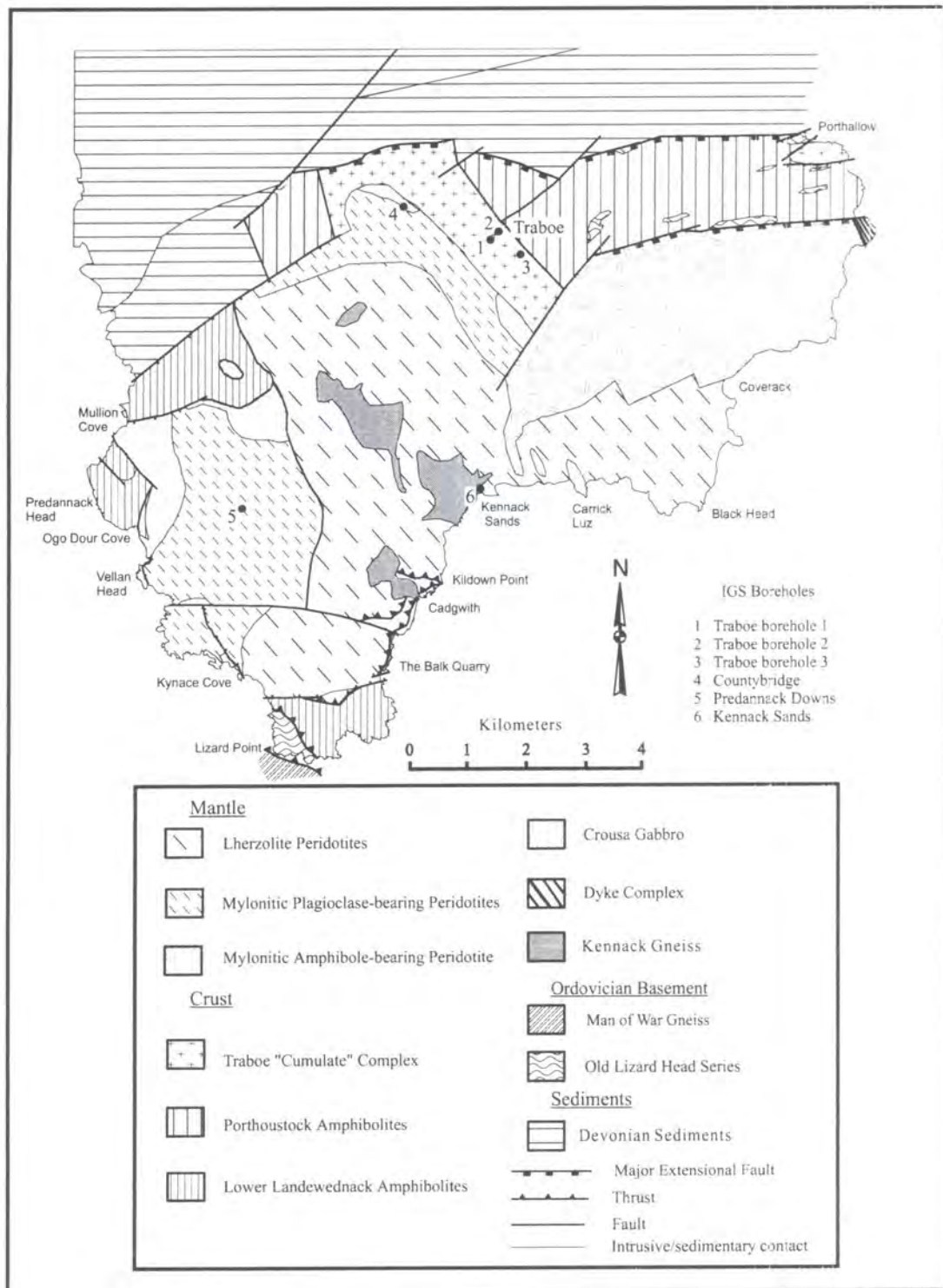


**Figure 3.3.** Simplified geological map of the Lizard complex: modified after Flett (1946), Green (1964a) and Floyd et al. (1993). Including a sub-division of the different peridotite-types and the location of IGS boreholes referred to in the text.



(Appendix A). In all of the rocks discussed below, there is a strong fabric overprint related to the effects of deformation developed during later emplacement of the Lizard Ophiolite Complex (Section 3.5.1.).

### **3.2.1. The Man of War Gneiss**

The Man of War Gneiss (MOWG) outcrops on rocks and reefs south of Lizard Point and these are only accessible at extremely low tide or by boat. In the course of the present study, only the strongly deformed MOWG outcrops on the wave cut platform at Lizard Head (GR 6942 1151) and boulders of the less deformed rock on the shore have been observed (Figure 3.4). Therefore much of the following discussion is based on the detailed observations of previous authors (Chapter 2). In a recent study, Sandeman *et al.* (1997) established by U-Pb dating of zircon that the original magmas that now form the MOWG crystallised in the early Ordovician (499  $\pm$  8/-3 Ma). The outer reefs off the Lizard Head consist of coarse-grained gabbro to tonalite (Sandeman *et al.*, 1997); similar boulders are found on the beach at Polpeor Cove (GR 7000 1150). These rocks are weakly foliated, and the strike of the foliation is variable, although dips are generally steep and lineations have not been reported (Sandeman *et al.* 1997). For further details of the orientation data the reader is directed to the studies of Sandeman *et al.* (1997) and Jones (1994, 1997). The inner reefs and outcrops on the shore at Lizard Head and the southern extremity of Vellan Drang (GR 7000 1127) comprise a strongly deformed variant of the MOWG. These rocks are of fine-grained, mylonitised tonalitic gneiss and foliations dip at a low-angle towards the NE (Sandeman *et al.*, 1997). These mylonites were produced during the re-working of the Man of War Gneiss in the footwall of the Old Lizard Head Thrust (Section 3.5.1.b). Amphibolitised, porphyritic mafic dykes occur in the MOWG, and locally cross-cut the early steeper foliation (Fox, 1888; Flett, 1946; Sandeman *et al.*, 1997).

### **3.2.2. The Old Lizard Head Series and Lizard Head Sill**

The Old Lizard Head Series (OLHS) comprise interleaved pelitic and psammitic schists, hornblende schists and minor amphibolites exposed around the southern area of the Lizard Peninsula between Pentreath Beach (GR 6935 1265) and Polbrean Cove (GR 7023 1150). These rocks have been long regarded as a series of metamorphosed

basaltic lavas, tuffs and quartz-rich and pelitic sediments (Bonney, 1883; Somervail, 1884; Flett and Hill, 1912; Tilley, 1937; Floyd *et al.*, 1991) (Chapter 2). Orientation data for structural features in these rocks are presented in recent papers by Sandeman *et al.* (1997) and Jones (1994, 1997). Pelitic horizons are composed of muscovite, biotite, feldspar, minor quartz and garnet. Pelitic layers alternate with psammites composed of quartz, and minor muscovite, biotite and feldspar (Figure 3.5). Amphibolites comprise abundant, elongate green hornblende and feldspar. These amphibolites are superficially similar to Landwednack amphibolites which are extensively exposed on the east and



**Figure 3.4.** Boulder of Man of War Gneiss on the shore at Polpeor Cove. Note the shear zone (S) that cross-cuts an earlier fabric.

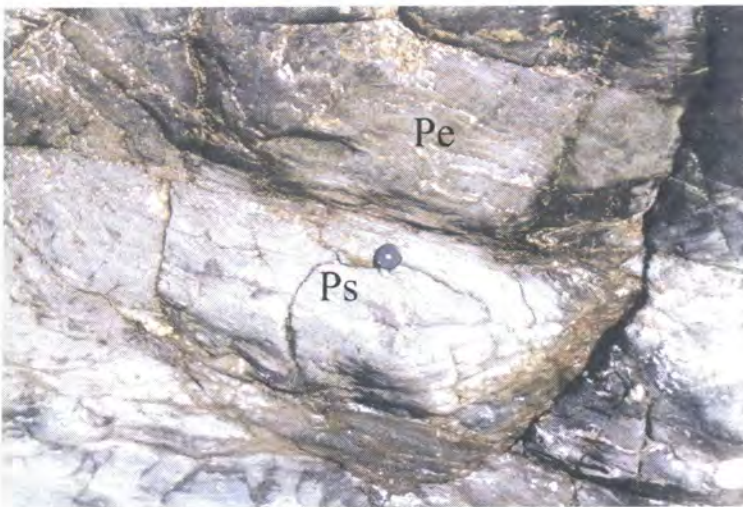


**Figure 3.5.** Typical Old Lizard Head Series metasediments comprising pelitic (Pe) and psammitic (Ps) layers. Note folds and the presence of quartz veins.

west coasts of the Lizard (Section 3.5.2.c), but detailed examination shows that the OLHS amphibolites contain a greater abundance of hornblende and thus can be distinguished from the Landewednack amphibolite. The whole rock geochemistry of the OLHS amphibolites and the other amphibolites is compared in Chapter 6 to provide clues as to the origin of their protoliths. Original textures in these rocks, which include compositional layering, are rarely preserved. In many outcrops, there are later intrusive mafic sheets with relict igneous textures. The textures preserved in these sheets are often coarse-grained, and large plagioclase phenocrysts are observed in hand-specimen (Figure 3.6). The porphyritic, mafic sheets may belong to the same suite of porphyritic mafic rocks, which are observed in the MOWG (Flett, 1946). In a recent paper, Jones (1997) inferred that outcrops of these intrusive mafic rocks all belong to the same intrusion, termed the 'Old Lizard Head Basic Sheet'. This term is rejected in the present study, because it may be confused with the 'Lizard Head Sill' at Lizard Head which is a granitic in composition and is referred to in previous publications (Flett, 1946; Green, 1964c; Sandeman *et al.*, 1997). Two different and unrelated suites of intrusive rock are therefore recognised in the OLHS, a suite of granitic sills and a suite of mafic sheets. The origin of the mafic sheets is unclear. Jones (1997) stated that they are cross-cut by the granitic Lizard Head Sill, but only tectonic contacts between the mafic sheets and granitic rock were observed during the course of the present study. The whole-rock geochemical compositions of porphyritic rocks analysed during this study are very similar to the composition of the Landewednack amphibolites and later dolerite dykes, yet different to the amphibolite layers in the OLHS (Chapter 6). Granitic veins occur in the Polpeor Cove area, 300 m east of the nearest granitic intrusion, but there is no evidence to suggest a relationship between these veins and the Lizard Head Sill.

The granitic Lizard Head Sill (Figure 3.7) is fine-grained, grey coloured and shows granoblastic textures. The Sill has intruded and cross-cut an early fabric developed under upper-amphibolite conditions preserved in the OLHS (Jones, 1997). New U-Pb SHRIMP dating of magmatic zircons (97/712) provide an age of  $488 \pm 8$  Ma (Appendix A), which is interpreted as giving the intrusive age of the granitic sill. U-Pb SHRIMP analyses of zircon from a phacoid of granitic rock (97/719) entrained along the Old Lizard Head Thrust yield an age of  $499 \pm 7$  Ma (Appendix A). The age for the phacoid of granitic rock (97/719) is statistically indistinguishable from that of the



granitic Lizard Head Sill (97/712), and suggests that they belong to the same intrusive suite (Nutman, A., *pers comm* 1998). The early Ordovician age for the intrusion of the Lizard Head Sill is extremely significant in terms of the tectono-stratigraphic evolution



**Figure 3.6.** Coarse-grained mafic sheet containing abundant plagioclase phenocrysts. Compare with OLHS metasediments (Figure 3.5) which lack this porphyritic texture.



**Figure 3.7.** Detail of the Lizard Head Sill (Sill) which has intruded the Old Lizard Head Series (OLHS). Note the sheared margins of the sill.

of the Lizard Ophiolite Complex as this indicates that the OLHS and early fabrics must be early Ordovician or older. The similarity in the age of the MOWG and the Lizard Head Sill suggests that they may be genetically related. This therefore contradicts the previous interpretations of Sandeman *et al.* (1997) and Jones (1997) which suggest that the Lizard Head Sill is unrelated to the MOWG and possibly represents local melting

during Devonian emplacement. The earlier interpretation of Flett (1946) that the Lizard Head Sill represents fractionated offshoots of the MOWG may indeed be justified.

The early fabrics and igneous textures of the OLHS and the Lizard Head Sill are cross-cut by a later pervasive fabrics and several generations of shear-zones related to subsequent emplacement tectonics in the early to late Devonian (Section 3.5.1.a.).

### **3.2.3. Summary**

- Rocks exposed on the SW point of the Lizard peninsula are oldest preserved in the Lizard Ophiolite Complex and hence represent older basement.
- The rocks of the OLHS are at least early Ordovician in age, which has been established by U-Pb SHRIMP dating of magmatic zircon in a granitic sill which cross-cuts original textures and early fabrics.
- In a recent paper, Sandeman *et al.* (1997) established that the MOWG is also early Ordovician in age, and this therefore suggests an association with the OLHS.
- The early evolution of the igneous rocks forming the MOWG and the sedimentary and associated igneous rocks of the OLHS is therefore distinct from the other units of the Lizard Ophiolite Complex.

---

### **3.3. Early mantle deformation**

---

The earliest deformation phase recognised in the Devonian rocks of the Lizard Ophiolite Complex (this excludes the SW basement) is preserved in deformed peridotites. Two main textural types of peridotite can be identified by field observation: coarse-grained lherzolites and mylonitic peridotites. The coarse-grained lherzolites are exposed in the central, southern and eastern parts of the Lizard (Figure 3.3), whilst the mylonitic peridotites are predominant in the northern and western areas. In most areas, the different peridotite types are juxtaposed by later brittle faults, but the similarity in the orientation of fabrics in the different peridotite types, and the presence of gradational contacts in some areas suggests that these fabrics were produced by heterogeneous strain during the same deformation event. In all outcrops of peridotite, there is evidence for the pervasive serpentinisation which has affected the ultramafic rocks of the Lizard Ophiolite Complex. Serpentinisation here involves alteration of olivine and pyroxene in hand-specimen, and the development of cross-cutting veins. As

serpentinisation is ubiquitous it will not be mentioned at every instance the peridotites are discussed. In the northern and western areas of the Lizard, mylonitic peridotites are in contact with highly deformed ultramafic and mafic Traboe cumulates. Flett (1912) regarded the mafic rocks, which he termed the Traboe Hornblende Schists, as being a group of mafic intrusions emplaced into the peridotite. Green (1964a,b,c), however, interpreted the Lizard peridotite as being a diapir intruded into regionally metamorphosed amphibolite, with the mylonitic peridotite forming the highly deformed margin and what he termed 'mafic granulites' as a contact dynamothermal aureole. Evidence from a series of boreholes drilled through the mylonitic peridotite, ultramafic and mafic cumulates in the Traboe area (GR 744 213) of the Lizard Ophiolite Complex led Leake and Styles (1984) to propose that these rocks represent the lowermost crust transitional to the mantle, in what was termed the Traboe cumulate complex (Figure 3.3).

The field characteristics of the different peridotite textural types and associated ultramafic rocks are discussed in the following sections.

### **3.3.1 Coarse-grained lherzolites**

At outcrop, the coarse-grained lherzolites are identified by a moderate to strong foliation, with or without a mineral stretching lineation, defined by stretched bronze coloured orthopyroxene porphyroclasts (1-5mm), usually altered to bastite (the name given to serpentine pseudomorphs after orthopyroxene - Whittaker & Zussman (1965)), and dark brown coloured spinel (Figure 3.8). When fresh, the rock is dark in colour, however weathering results in a pale-brown coloured rock and accentuates the foliation giving the rock a characteristic ribbed appearance. The rock is commonly banded and these bands (1-5cm) are defined by variations in the abundance of pyroxene and olivine. Pyroxene-rich bands between 10-20cm in thickness and metres in length occur, and are here termed pyroxenites (Figure 3.9). Pyroxenite bands are particularly numerous at Carleon Cove (GR 7280 1565), Beagles Point (GR 7660 1655) and Pentreath Beach (GR (GR 6935 1265) where they are commonly orientated parallel to the peridotite fabric. They may be boudinaged and the fabric is also observed to be oblique and cross-cut the pyroxenite bands at some localities. These observations suggest that the pyroxenite bands are a primary layering feature, which predates the



development of the deformation fabric in the coarse-grained lherzolites. Rothstein (1977, 1981, 1988, 1994) proposed that these pyroxenite bands preserve cresscumulate

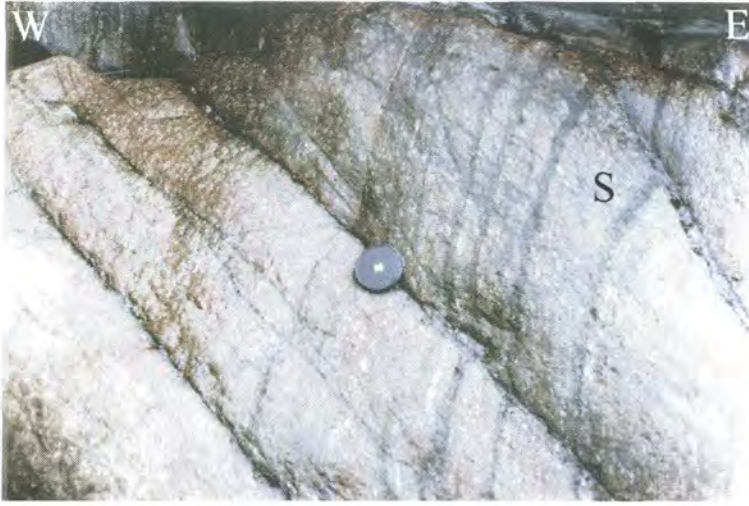


**Figure 3.8.** Coarse-grained lherzolite displaying a strong foliation defined by stretched orthopyroxene porphyroclasts. Cross-cutting black veins (S) are composed of serpentine.

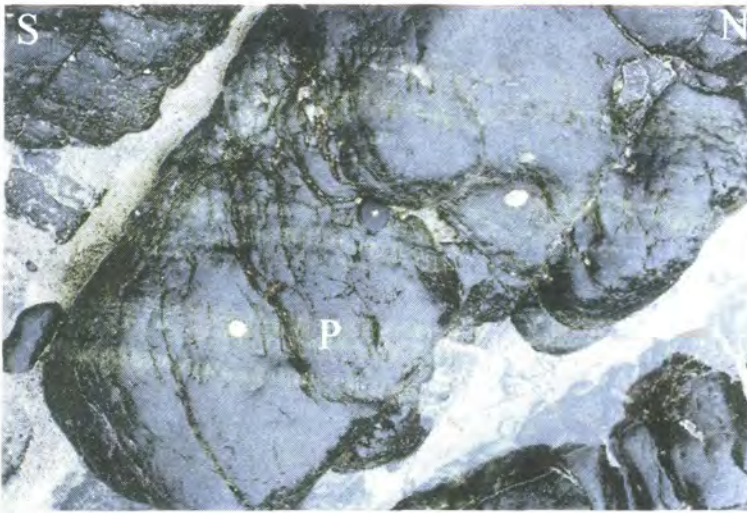


**Figure 3.9.** Plan view looking down at showing pyroxenite bands (P) in coarse-grained lherzolite.

structures. Rothstein (*op cit.*) also described dunite and harzburgite layers and suggested that these preserved similar structures to the pyroxenite bands and these formed during early igneous events prior to deformation of the Lizard peridotites.

Within the areas mapped as coarse-grained lherzolite (Figure 3.3), dunites are numerous. These rocks are a distinctive light-green or brown colour and consist of serpentine after olivine and minor stringers of coarse-grained Cr-spinel (Figure 3.10).

The stringers of Cr-spinel vary in length (10-150cm) and are aligned parallel to the margins of the dunite body and the fabric in the adjacent coarse-grained lherzolite (3.11). Dunites are planar bodies, which generally have a lensoid form and vary in



**Figure 3.10.** Dunite (D) within coarse-grained lherzolite (L). Note the gradational margins to the dunite bodies.

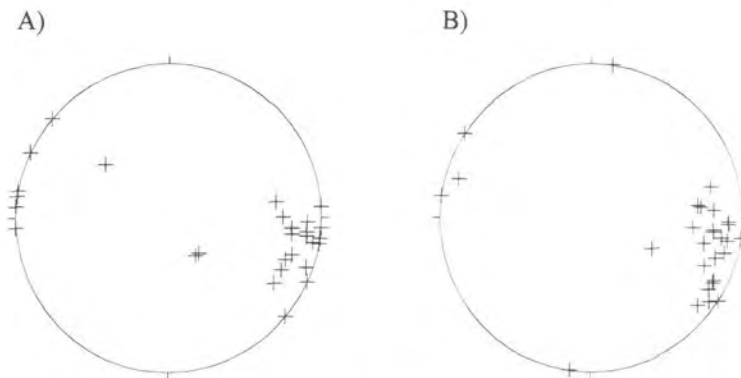


**Figure 3.11.** Stereographic projections showing poles to (A) dunite body margins, and (B) coarse-grained lherzolite foliation along the coastal outcrops between Carrick Luz and Coverack.

width between 10-500cm, extending along strike between tens of centimetres or up to several hundred metres. In the Black Head (GR 7790 1615) to Chynalls Point (GR 7866 1740) coast section dunite, bodies are particularly abundant and detailed mapping (Figure 3.12) has revealed that the dunites coalesce in several zones that are up to 70 metres in width and extend for 350 metres along strike. At Lankidden Cove (GR 7563 1665), on a small rock promontory, an outcrop of dunite 15 metres wide occurs. The dunite body has an anastomosing form and contains screens of lherzolite and



harzburgite, which are between 20cm to 200cm in width. The contacts between the dunite and coarse-grained lherzolite are gradational over 10-30cm. These gradational contacts are characterised by the absence of clinopyroxene, followed <sup>by</sup> orthopyroxene in a traverse from the lherzolite to dunite. The gradational margins between the dunite and

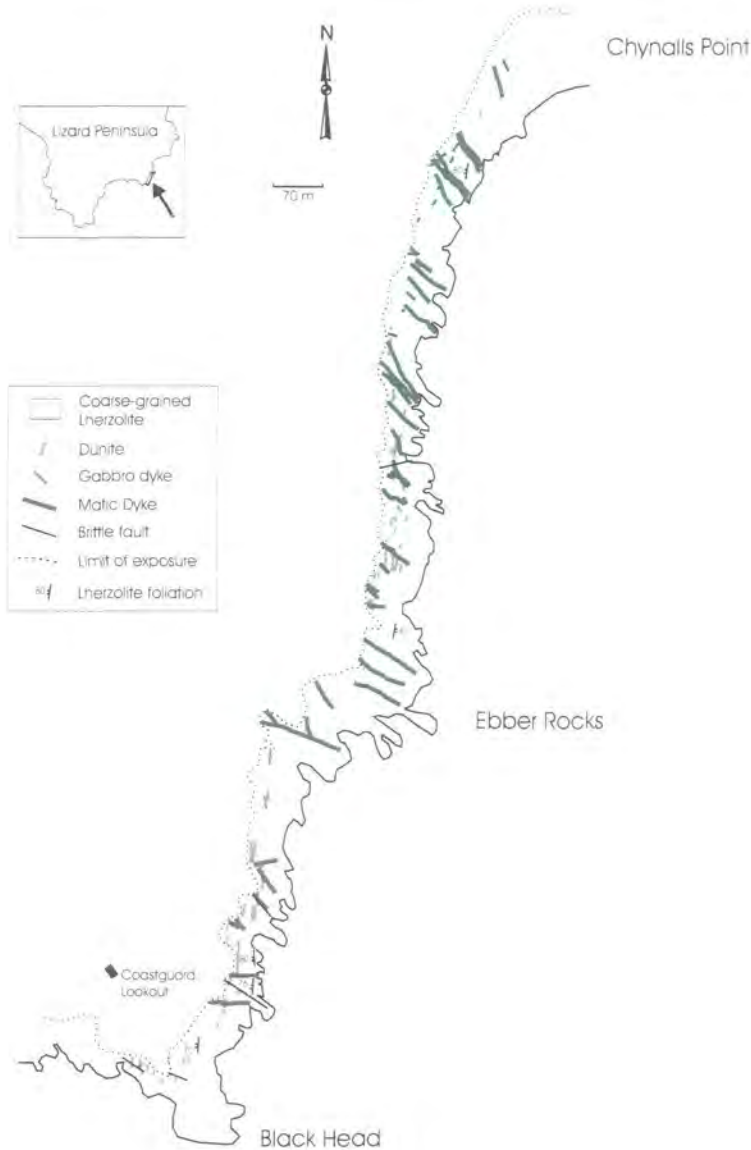


**Figure 3.12.** Geological map of the coastline between Chynalls Point and Black Head showing the distribution of dunite bodies, gabbro dykes and mafic dykes in the coarse-grained lherzolite.

lherzolite are therefore harzburgites. In other outcrops, the harzburgitic margins of dunite bodies are up to 2 metres in width. The form of the dunite bodies and their relationships with the coarse-grained lherzolite suggest that these bodies formed prior to the development of the fabric in the peridotite. These dunites may represent relict

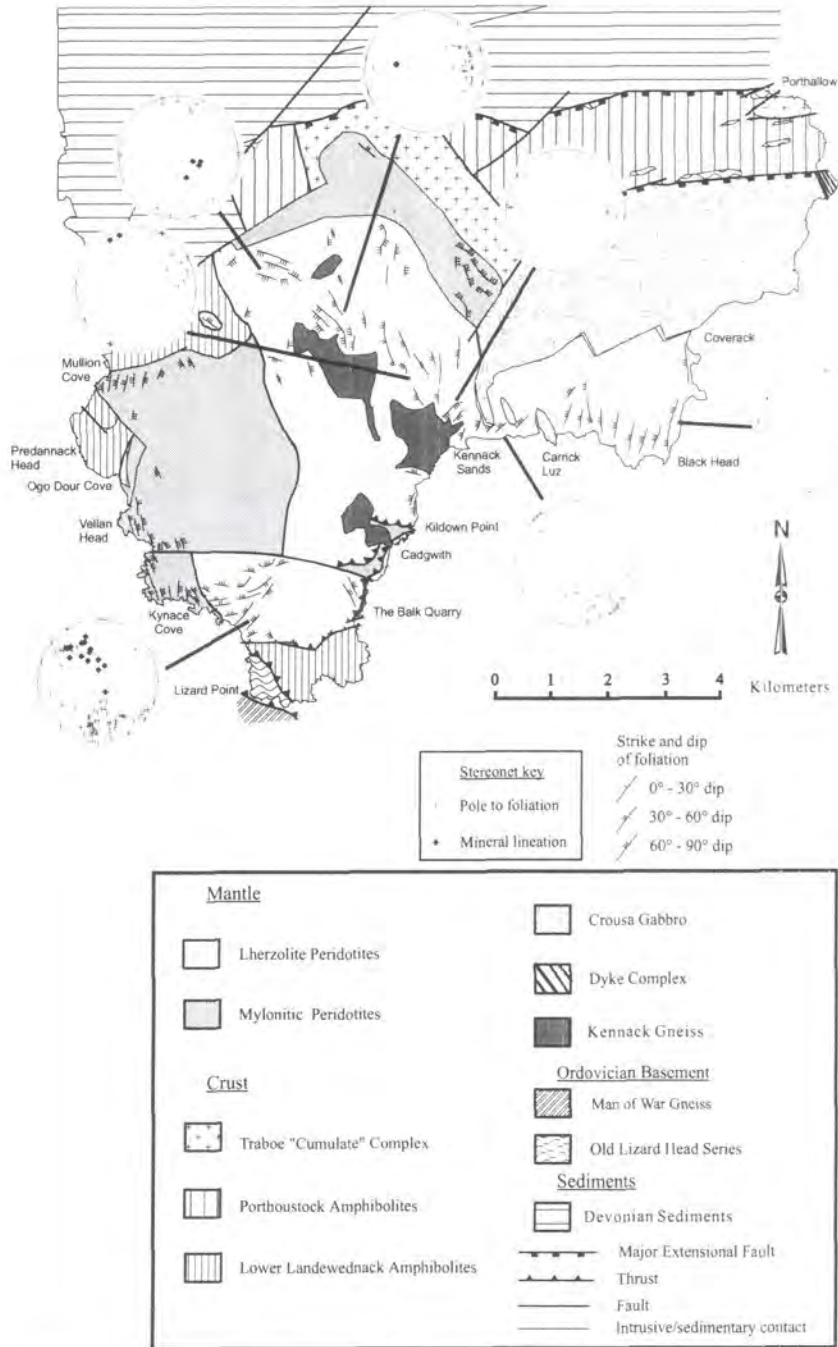


**Figure 3.13.** Geological map of the Lizard Complex. The different fabric domains in the coarse-grained lherzolite are labelled with stereographic projections showing poles to the foliation and plunge of the mineral lineation.

conduits through which melt has percolated and reacted with the host peridotite.

The majority of the coarse-grained lherzolites are a spinel lherzolite assemblage consisting of olivine, orthopyroxene, clinopyroxene and spinel, but in some outcrops, a fine-grained white coloured mineral is observed. This mineral is saussurite, which is derived from the alteration of plagioclase; therefore some of the coarse-grained lherzolites have a plagioclase lherzolite assemblage.

### **3.3.1.a. Fabric Orientation**

The characteristic fabric of the coarse-grained lherzolites is a steep to sub-vertical foliation with mineral stretching lineations plunging down-dip. The fabric shows kilometre-scale variations in orientation throughout the Lizard Ophiolite Complex (Figure 3.13). This may be attributed a heterogeneous strain field or due to the effects of subsequent deformation events. On the east Coast of the Lizard peninsula, between Kennack Sands (GR 7385 1650) and Coverack (GR 7825 1830), the lherzolites show a well-developed sub-vertical foliation whilst mineral lineations are weakly developed or non-existent. This area contains peridotites with a high proportion of relict primary features (Rothstein 1977, 1981, 1988, 1994) and thus appears to represent the least deformed parts of the Lizard peridotites. The foliation between Carrick Luz (GR 7555 1650) and Coverack, is orientated N to NNE and dips steeply W (Figure 3.13). The orientation of the fabric changes in the coastal stretch between Carrick Luz and Kennack Sands, where the foliation trends NE and dips steeply NW and SE. The orientation of the fabric changes abruptly at Chiverton Croft (GR 725 175), one kilometre inland from Kennack Sands. In this area the foliation is orientated NW to N and dips steeply W. This transition in the fabric orientation does not appear to be gradational, and instead it is suggested that a later fault contact separates the two areas with a contrasting fabric orientation. This fault was not observed in the field, but it is suggested that it represents a continuation of the fault that juxtaposes peridotite with gabbro north-east of this area. In the Clahar (GR 6867 2003) to Bochym Hill (GR 6950 2030) area, the foliation is orientated E to ESE, and dips steeply N and S. The transition in the orientation of the fabric between this area, and in the Chiverton Croft to Trenoon area to the south-east appears to be abrupt, and it is suggested that a later fault contact separates these areas.

At Kynance cove (GR 6847 1330), in the south western part of the Lizard peninsula the fabric in the coarse-grained lherzolite is strongly developed and transitional to mylonitic peridotite. The orientation of the fabric is different to the localities described above and also on the south-east coast of the Lizard in the Parn Voose Cove (GR 7150 1304) area. Between Kynance Cove and Pentreath Beach (GR 6935 1270) the foliation is orientated NE to E and dips moderately-steeply to the NW, mineral stretching lineations plunge moderately down-dip towards the NW (Figure 3.13). The transition from coarse-grained lherzolite to mylonitic peridotite occurs over

a distance of two hundred metres, from the south-east to north-west, close to Tor Balk (GR 6849 1342) at Kynance Cove (Figure 3.14). The transition is characterised as a

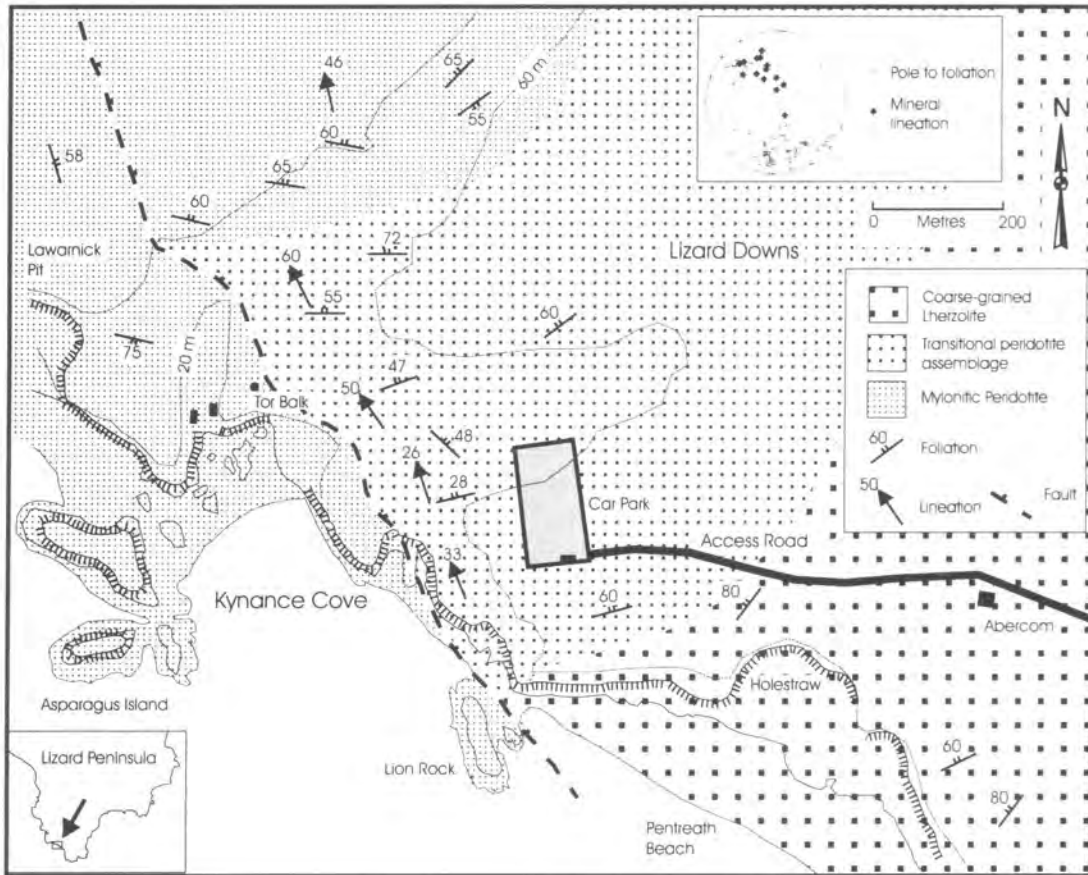


**Figure 3.14.** Geological map of the Kynance Cove to Pentreath Beach area. The distribution of coarse-grained lherzolite, a transitional assemblage and mylonitic peridotite are shown and the orientation of the foliation and mineral lineation in representative outcrops.

decrease in the overall grain-size of the peridotite and the development of a stronger fabric. There is possibly a transition from coarse-grained lherzolite to mylonitic peridotite in the northern area of the Lizard, west of Trelan (GR 7450 1885), although interpretation of the field relationships in this area is hampered by a lack of outcrop.

### 3.3.2. Mylonitic Peridotites

A reduction in the overall grain size, an increase in the degree of elongation of pyroxene porphyroclasts, and the development of a mylonitic fabric with a stronger foliation and mineral stretching lineation distinguish the mylonitic peridotites from the coarse-grained lherzolites. Mylonitic peridotites outcrop on the west coast of the



Lizard, at Mullion Cove (GR 6660 1775) and inland to Penhale (GR 6975 1847) and Mount Careless (GR 7016 1613), and along the coast between Potstone Point (GR 6684 1561) and Kynance Cove (GR 6847 1330). In the northern area of the Lizard, the mylonitic peridotites outcrop in a two kilometre wide zone between Bonython (GR 7000 2105), Trevassick (GR 7103 2243) and Trelan (GR 7450 1885). Limited areas of outcrop occur on the east coast near to Black Rock (GR 7280 1549), Kildown Point (7262 1470), Cadgwith (GR 7220 1450) to Carn Barrow (GR 7190 1384), The Balk (GR 7154 1283), Lizard village (GR 7035 1250) and the south end of Pentreath Beach (GR 6935 1270) (Figure 3.3).

Two different sub-types of mylonitic peridotite are recognised by examination of hand specimens. An assemblage consisting of olivine, orthopyroxene, clinopyroxene and plagioclase (commonly saussuritised) and spinel define a mylonitic plagioclase-bearing peridotite (Figure 3.15). This assemblage is transitional into a mylonitic amphibole-bearing peridotite assemblage, which is characterised by the presence of distinct yellow-green amphibole grains in hand-specimen (Figure 3.16). The two different mylonitic peridotite sub-types are often interbanded on a centimetre scale and kilometre scale domains of the different sub-types also occur. The distribution of the different sub-types of mylonitic peridotite shown in Figure 3.3 has been deduced by detailed mapping and geographic information system (GIS) study of data from thin sections (Chapter 4). Outcrops of mylonitic amphibole-bearing peridotite occur at Henscath (GR 6650 1802), Mullion Cliff (GR 6670 1765), Meaver (GR 6857 1898), and Potstone Point (GR 6684 1561) to Vellan Head (GR 6680 1490), Kynance Farm (GR 6801 1455) and Kynance Cove on the west coast of the Lizard. On the east coast, mylonitic amphibole-bearing peridotite is exposed at The Balk, Carn Barrow, Cadgwith and Kildown Point. In the northern area of the Lizard, outcrops of mylonitic amphibole-bearing peridotite occur between Trevassick, Traboe Cross (GR 7360 2055), Kernewas (GR 7443 2024) and one kilometre north-west of Trelan. Pyroxenite layers and dunite bodies characteristic of the coarse-grained lherzolites are never observed in the mylonitic peridotites; and it is therefore assumed that deformation and recrystallisation has obliterated these primary features. Within both mylonitic peridotite sub-types, feldspathic bands occur and form thin discontinuous bands <2cm wide (Figure 3.17). The bands have sharply defined margins, which are parallel to the foliation in the adjacent peridotite. The bands often occur as several thin layers, interbanded with the host peridotite in zones up to 30cm wide. In the outcrop, no



**Figure 3.15.** Mylonitic plagioclase-bearing peridotite. Note the strong foliation and prominent down-dip plunging mineral lineation on foliation surfaces.



**Figure 3.16.** Plan view looking down at mylonitic amphibole-bearing peridotite. Note the stretched orthopyroxene porphyroclasts aligned parallel to the foliation.

connectivity between adjacent bands is observed. These bands are pale-green or white coloured and in hand specimen are observed to be composed of plagioclase, pyroxene and amphibole.

At several localities in the Lizard Ophiolite Complex, mylonitic amphibole-bearing peridotites are intimately associated with gabbroic veins (petrologically and chemically distinct from the Crousa gabbro) and mafic Traboe cumulates. At these localities the two different lithologies are interbanded and interfolded, and fabrics are parallel. The field relationships, structures within the peridotites, gabbroic veins and



**Figure 3.17.** Foliation parallel feldspathic bands (pale) within mylonitic amphibole-bearing peridotite.

Mafic Traboe cumulates and their significance are described in Section 3.4.

### **3.3.2.a. Dip-slip fabrics**

At the majority of outcrops the mylonitic peridotites show a consistent NW- to NNW-orientated foliation which dips steeply to the ENE, whilst mineral lineations plunge down-dip (Figure 3.18). This contrasts with the more variable fabric orientations observed in the coarse-grained lherzolites.

### **3.3.2.b. Strike-parallel fabrics**

In the area of Mullion Cove (GR 6670 1780), Mullion Cliff (GR 6670 1765) and inland to Isle of Wight (GR 6767 1743) and Tenerife Farms (GR 6724 1670) a fault-bounded unit of mylonitic peridotite occurs with a fabric orientation that contrasts with orientation observed elsewhere in the Lizard peridotites. The mylonitic peridotites in this area are predominantly composed of the mylonitic amphibole-bearing sub-type,



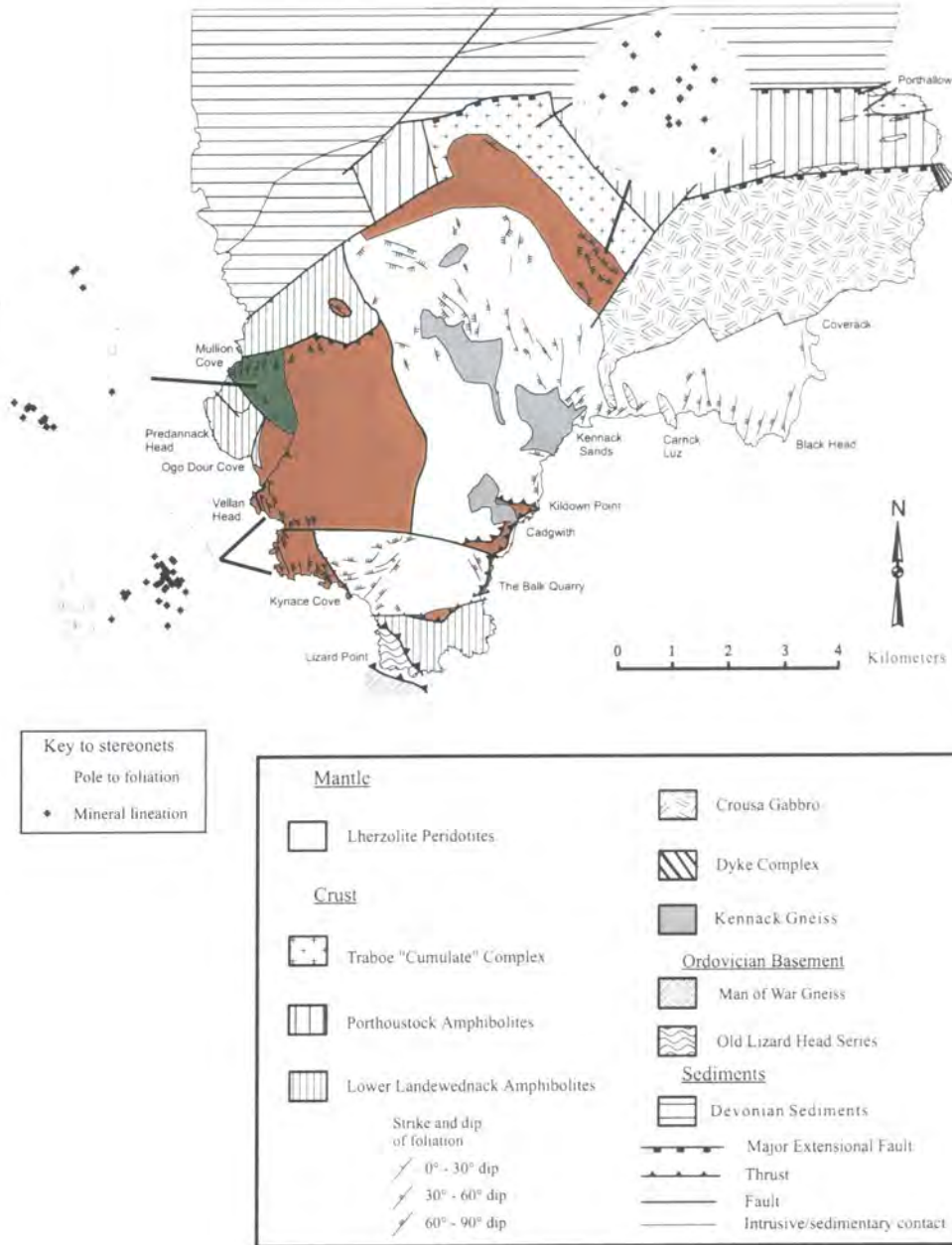


**Figure 3.18.** A geological map of the Lizard Complex, including a sub-division of the mylonitic peridotites into a 'dip-slip' fabric domains (red) and a 'strike-parallel' fabric domain (green). Stereographic projections show poles to the foliation and plunge of mineral stretching lineation in these fabric domains.

with only very minor occurrences of plagioclase-bearing zones. The foliation in this area is consistently orientated N to NNE and dips predominately W (Figure 3.18). Mineral lineations are sub-horizontal, and plunge at a low angle towards the SSW, which contrasts with the 'dip-slip' fabrics observed in peridotites in all other areas of the Lizard. This area of peridotites with a 'strike-parallel' fabric is separated from 'dip-slip' mylonitic peridotites to the east, by a N-S striking fault (Figure 3.18).



### **3.3.3. Kinematics analysis**

In outcrop, determination of the shear-sense using conventional shear-sense indicators (e.g. asymmetric porphyroclasts) is ambiguous and shear bands, folds and other shear-sense indicators are not observed in these rocks. The asymmetry of the pyroxene-rich bands in the peridotite and the cross-cutting fabric may also be used as a potential kinematic indicator. This method, however, is only applicable if the original orientation of the pyroxene-rich bands is established and this is not known in the deformed peridotites of the Lizard. Therefore a different approach has been used to determine the sense of shear in these rocks and has involved collection of orientated specimens of peridotite. Thin sections made from orientated specimens have been used in a study of lattice-preferred orientation or LPO of olivine, which has then been used to determine the sense of shear. The LPO technique and the results of its application on the Lizard peridotites are discussed in Chapter 4.

### **3.3.4. Summary**

- In areas of low-strain the peridotites preserve evidence for an early, coarse-grained spinel lherzolite assemblage, associated with pyroxene-rich bands, and minor harzburgite and dunite bodies. This assemblage is cross-cut by larger anastomosing dunite bodies.
- Early textures and contacts preserved in these rocks are cross-cut by a later pervasive fabric, which is characterised by a subvertical foliation and down-dip mineral lineations.
- Spinel lherzolites possess a coarse-grained porphyroclastic fabric and in many outcrops, the spinel lherzolite assemblage is replaced by a plagioclase lherzolite assemblage.
- Coarse-grained lherzolites show a transition to mylonitic plagioclase-bearing peridotites and transitional mylonitic amphibole-bearing peridotites in areas of high-strain.
- At several localities the mylonitic peridotites are in contact with gabbroic veins and ultramafic and mafic Traboe cumulates.
- The presence of plagioclase-bearing peridotites and association with mafic rocks suggests that this deformation occurred in the upper mantle/lower crust.

### 3.4. Oceanic crust construction

It has been previously recognised that the mafic rocks exposed in the Lizard Ophiolite Complex are highly variable in character, and several controversial interpretations for the origin of these rocks have been proposed (see Chapter 2 for a more comprehensive review). During the course of the present study, it has been established on the basis of field, microstructure (see Chapter 4) and geochemical evidence (see Chapters 5 and 6) that the existing terminology (Chapter 2) for the mafic rocks can be inconsistent and is often misleading. Therefore the terminology which will be referred to in this thesis is presented below (Table 3.1). This includes ultramafic and mafic rocks that are thought to represent relict oceanic crust associated with the peridotites of the Lizard Ophiolite Complex. The ultramafic and mafic rocks are subdivided into five groups on the basis of field, petrological (Chapter 4) and geochemical evidence (Chapters 5 & 6).

- Highly deformed and metamorphosed ultramafic and mafic cumulates (Ultramafic and Mafic Traboe cumulates)
- Gabbroic veins (Petrologically and geochemically distinct from Crousa gabbro)
- Metamorphosed basaltic and gabbroic rocks (Landewednack amphibolites)
- A large gabbro intrusion (Crousa gabbro) with associated gabbro dykes
- Porthoustock amphibolites.

Revised Scheme	Flett & Hill (1912)	Green (1964a,b,c)	Bromley (1979)
<b>Ultramafic Traboe cumulate</b>	Dunite serpentine	Lizard peridotite	Peridotite
<b>Mafic Traboe cumulate</b>	Traboe hornblende schist	Traboe hornblende schist	Traboe schist
<b>Gabbroic vein</b>	Traboe hornblende schist	Hornblende/pyroxene granulite	Granulite
<b>Landewednack amphibolite</b>	Landewednack hornblende schist	Landewednack hornblende schist	Lower Landewednack schist
<b>Crousa Gabbro</b>	Lizard gabbro	Lizard gabbro	Lizard gabbro
<b>Porthoustock amphibolite</b>	Landewednack hornblende schist	Landewednack hornblende schist	Upper Landewednack schist

**Table 3.1.** Comparison of the terminology for the ultramafic and mafic rocks used in the revised scheme with the published terminology for the same rocks developed by Flett & Hill (1912), Green (1964a,b,c) and Bromley (1979).

The ultramafic and mafic Traboe cumulates are exposed along a one kilometre coastal section on the west of the Lizard (Figure 3.3), a ca. 6 km<sup>2</sup> inland area near

Traboe (GR 74 21) and at the north-east part of the Lizard, along one kilometre of coast at Porthkerris (805 230). Outcrops of the Landewednack amphibolites occur along the south east coast of the Lizard peninsula and along the west coast between Parc Bean Cove (GR 666 158) and Polurrian Cove (GR 6675 1865).

The Crousa gabbro and associated gabbro dykes, outcrop on the east coast of the Lizard, between Porthoustock (GR 8064 2185) and Coverack (GR 7820 1837). Gabbro intrusions and dykes, which may be related to the Crousa Gabbro, outcrop between Carleon Cove (GR 7281 1565) and Church Cove (GR 7150 1280). The Porthoustock amphibolites, which represent a distinct geochemical (Chapter 6) and tectonic suite of amphibolites, outcrop on the east coast between Porthkerris Cove and Porthoustock and inland exposures extend to the Traboe area.

The field evidence is discussed in this section in the context of a tectonic chronology established by detailed mapping of fabrics and U-Pb SHRIMP dating of zircon. Field evidence for the Ultramafic and mafic Traboe cumulates and gabbroic veins associated with mylonitic peridotites are described in a separate section to the Landewednack amphibolites, Crousa gabbro and Porthoustock amphibolites, which are not directly associated ultramafic rocks.

#### **3.4.1. Ultramafic and mafic Traboe cumulates and gabbroic veins**

On the west coast of the Lizard, at localities near Potstone Point (GR 6684 1560), Parc Bean Cove (GR 6657 1584), Kynance Cove (GR 6835 1332) and on the east coast at Porthkerris (80502300), ultramafic rocks are in contact with gabbroic veins and ultramafic and mafic Traboe cumulates. At all of these localities mylonitic amphibole-bearing peridotites show complex interbanded and interfolded relationships with gabbroic veins and/or ultramafic and mafic Traboe cumulates. At some localities, the gabbroic veins appear to be intrusive into both the peridotite and ultramafic and mafic Traboe cumulates. The interbanded/interfolded relationship between these gabbroic veins and the mylonitic peridotite can be used to distinguish them from gabbro dykes associated with the Crousa gabbro, which do not show these relationships. Detailed descriptions of the lithological and structural characteristics of these rocks are presented, with reference to the localities mentioned above, in the following subsections.

Similar relationships to those viewed in the field are observed in borehole cores drilled by I.G.S. (BGS) in the Traboe area (GR 74 21) of the Lizard Ophiolite Complex (Leake and Styles, 1984). The borehole logs and observations are discussed in this section following detailed discussions of the field relationships at exposed outcrops.

#### **3.4.1.a. Potstone Point – Georges Cove area (GR 670 155; Figure 3.19)**

Along a approximately 500m stretch of coastline between Potstone Point and Georges Cove (Figure 3.19), located on the western coast of the Lizard peninsula, mylonitic amphibole-bearing peridotites are in contact with gabbroic veins and ultramafic and mafic Traboe cumulates. Interpretations of contact relationships between the peridotite and amphibolite in the outcrop in this area have been the source of much controversy and debate over the last century (Fox and Teall, 1889; Green, 1964b; Bromley, 1979; Jones, 1997). The rocks in this area are juxtaposed with mylonitic plagioclase-bearing peridotites to the east and south by later brittle fault contacts and to the north-east with massive Landewednack amphibolites by a steeply dipping ductile shear zone.

Mylonitic amphibole-bearing peridotites occur at the north-eastern margin of this locality, in the cliffs above Potstone Point. The peridotite has weathered a brown colour, and shows a strong fabric, defined by orthopyroxene porphyroclasts and spinel. The rock has a stronger mylonitic fabric than the mylonitic plagioclase-bearing peridotite which outcrops 400m south-east of Potstone Point. In a 3 metre wide gully on Potstone Point, the mylonitic amphibole-bearing peridotite is in contact with ultramafic and mafic Traboe cumulates (Figure 3.20). The mylonitic peridotite and Traboe cumulates are interbanded at a centimetre scale and folded, and there appears to be a wide range of transitional lithologies, between ultramafic and mafic rock. This banding is very similar to layered mafic and ultramafic cumulate rocks and suggests that these rocks may represent deformed cumulates. Deformation and shearing has obliterated any evidence for any intrusive relationships between the different lithologies. Close to this gully, the mylonitic peridotite, Traboe cumulates and transitional lithologies are cross-cut by two porphyritic basaltic dykes, which are orientated north-west and dip steeply towards the north-east. On the shoreline, on the south-east side of Potstone Point, massive coarse-grained mafic Traboe cumulates occur, and these locally show complex interfolded and interbanded contact relationships with ultramafic rock, similar to those seen in the gully in the cliff above.

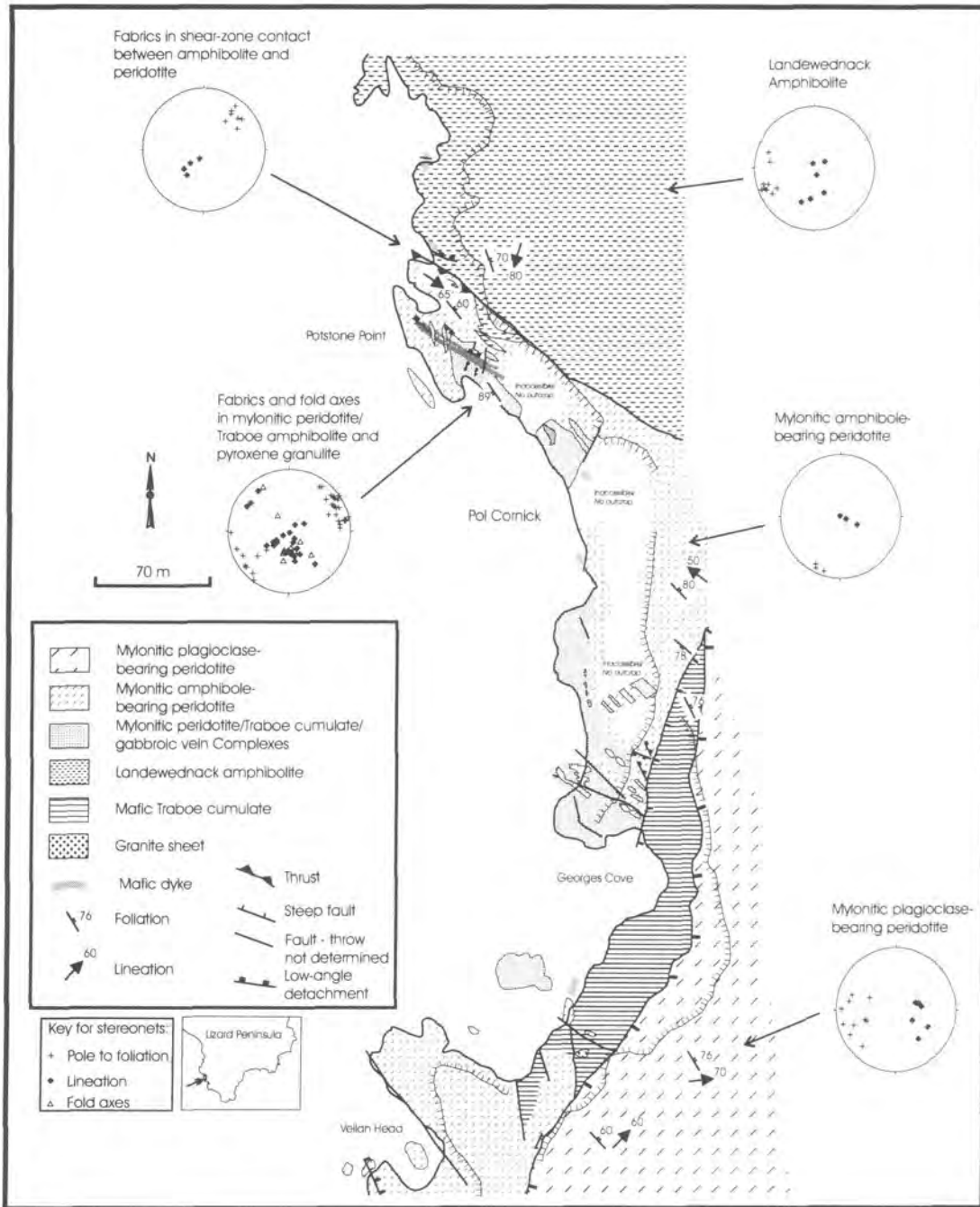


**Figure 3.19.** Geological map of the Potstone Point to Vellan Head area. The distribution of the different mylonitic peridotite-types and amphibolite-types are shown. Stereographic projections show poles to the foliation, plunge of mineral lineation and fold axes in selected lithological units.

Small patches of plagioclase-amphibole bearing veinlets are observed, which cross-cut the fabric in the cumulates, Green (1964b) and M.T.Styles (*Pers Comm*, 1996) describe the occurrence of a similar rock at Ogo Dour Cove. The amphiboles in these veinlets are coarse-grained and a dark brown colour, suggesting that they may be kaersutitic.

These veinlets may represent minor kaersutite gabbro intrusions (M.T.Styles, *Pers Comm* 1996).

Fox and Teall (1889) describe the presence of a 'porphyritic diorite', on the north-western side of Potstone Point, which is only accessible with the aid of a rope. Fox and Teall (1889) show that this rock cross-cuts the fabric in the mylonitic



**Figure 3.20.** Plan view looking down at interbanded and folded mylonitic peridotite and ultramafic and mafic Traboe cumulates.



**Figure 3.21.** Gabbroic vein (G) cross-cutting mylonitic peridotite (P), ultramafic and mafic Traboe cumulates (C).



peridotite, Traboe cumulates and transitional lithologies. This 'porphyritic diorite' is itself cross-cut by later mafic dykes. Similar field relationships are seen at the Georges Cove, where a coarse-grained gabbroic vein is observed to cross-cut the fabric in the mylonitic peridotite, ultramafic and mafic Traboe cumulates (Figure 3.21). These gabbroic veins contain large crystals of pyroxene or amphibole, and plagioclase and the rock locally possesses a fabric, which is parallel to the margins of the contact with adjacent rocks. A K-Ar age determination on hornblende in a gabbroic vein from this area, produced an age of 492 Ma (Green, 1964c). If this age determination is reliable, it could suggest that the gabbroic veins were intruded at ca.492Ma, and therefore the peridotites and associated Traboe cumulates are older.

The foliations in both the mylonitic peridotite and ultramafic and mafic Traboe cumulates at Potstone Point are consistently orientated north-west, and dip steeply towards the south-west or north-east. Mineral lineations plunge steeply down-dip, towards the south-east. Fold axes of isoclinal folds, observed in mylonitic peridotite and ultramafic and mafic Traboe cumulates, also plunge steeply towards the south-east, and hence parallel to the lineation. Unfortunately, no shear sense criteria has been found at the Potstone Point-Georges Cove locality.

#### **3.4.1.b. Parc Bean Cove (GR 666 158; Figure 3.22)**

At the Parc Bean Cove locality, strongly serpentinised mylonitic amphibole-bearing peridotite is interbanded at a metre scale with coarse-grained gabbroic veins and ultramafic and mafic Traboe cumulates (Figure 3.22). The rocks at this locality do not show the fine-scale interbanding and folding observed at Potstone Point. The gabbroic veins at this locality are similar to the cross-cutting gabbroic veins observed at Georges Cove. Mafic dykes cross-cut the ultramafic and mafic rocks at this locality. To the east, the mylonitic peridotites-mafic rocks are in contact with massive coarse-grained Landewednack amphibolites. The contact is a NW-orientated brittle fault, which dips towards the E. Shear-sense criteria within the fault zone suggest a dextral normal displacement.

The curved outcrop pattern and orientation of foliations in ultramafic and mafic rocks at this locality suggests the presence of a NW plunging antiform. Detailed mapping of the fabrics at this locality suggests that the apparent fold form is related to the presence of a series of ductile shear zones which cross-cut and rotate the earlier

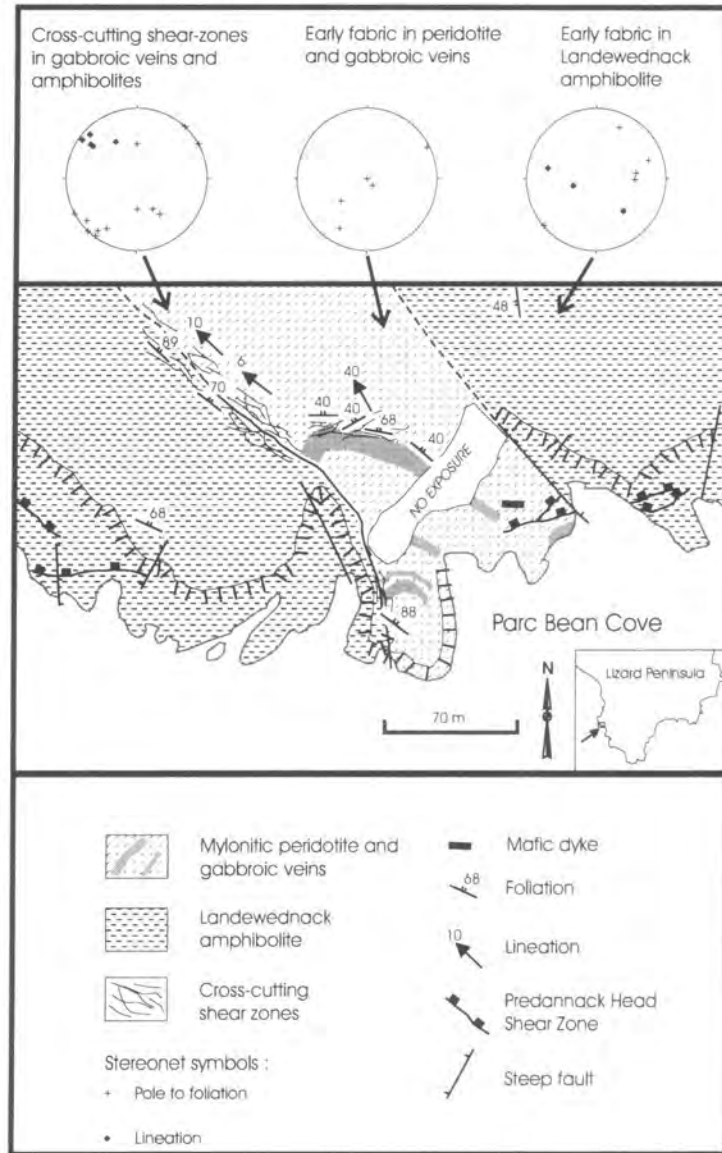


**Figure 3.22.** Geological map of the Parc Bean Cove, showing the distribution of mylonitic peridotite, gabbroic veins, Landewednack amphibolite and cross-cutting shear-zones. Stereographic projections show poles to the foliation and plunge of mineral lineation. Dashed line indicates extrapolation of faults.

fabrics. The early fabric preserved in the mylonitic peridotite, gabbroic vein and Traboe amphibolite is a subvertical NW-orientated foliation, with mineral lineations plunging down-dip. This fabric is truncated by a series of low-angle shear-zones, which dip towards the N, and are related to later emplacement tectonics (Section 3.5.2.b). These later shear-zones juxtapose the mylonitic peridotite-mafic rocks with the more massive Landewednack amphibolites to the west.



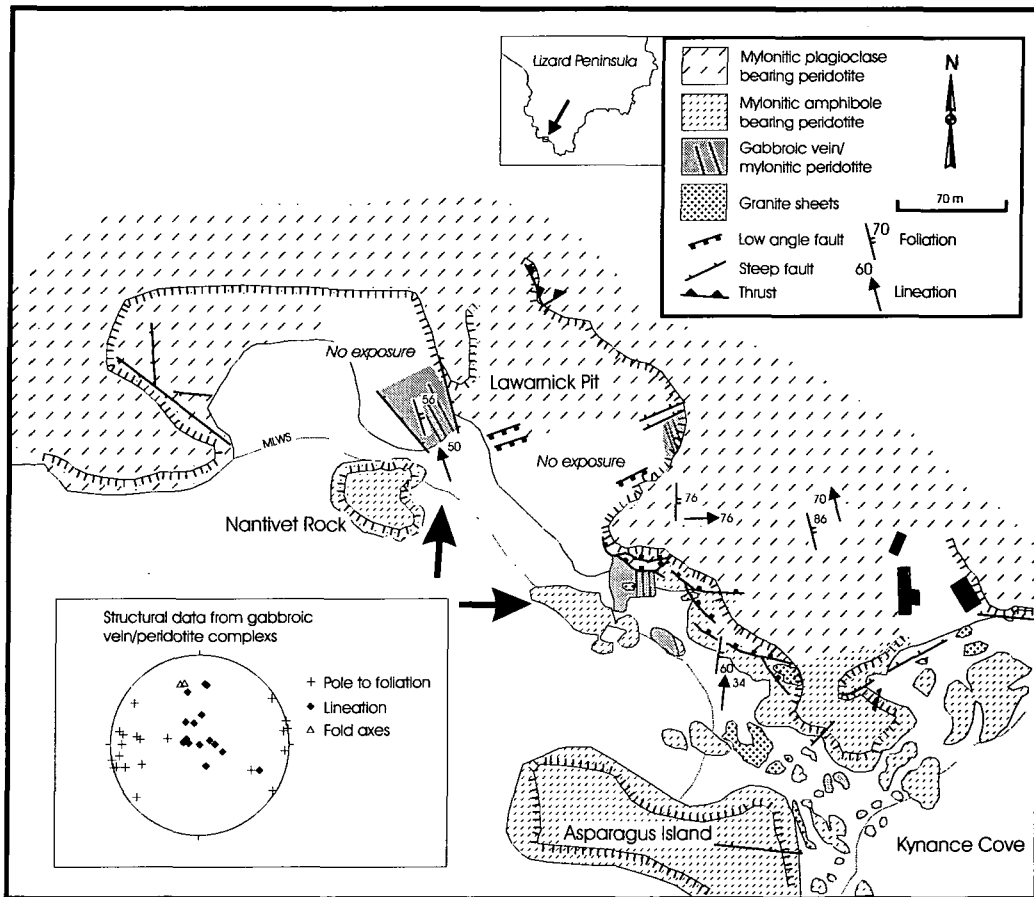


**Figure 3.23.** Geological map of the Nantivet Rock to Kynance Cove region. The distribution of the mylonitic plagioclase-bearing and mylonitic amphibole-bearing peridotites and gabbroic veins is shown. Stereographic projections display poles to the foliation, plunge of mineral lineations and fold axes in selected areas.

#### 3.4.1.c. Nantivet Rock – Kynance Cove area (GR 683 133; Figure 3.23)

Along an approximately 300m coastal section, between Nantivet Rock and Kynance Cove, mylonitic amphibole-bearing peridotites are associated with gabbroic veins (Figure 3.23). The two different rock types are associated in a north-west trending zone, which forms an inlet between Asparagus Island and mainland. Intrusions of granite, that cross-cut the fabric in the peridotite and gabbroic vein, are numerous in the Kynance Cove and the cliffs to the west. Rocks in this area have been subjected to later brittle faulting, and in the largest of these extensional faults, mylonitic plagioclase-bearing peridotites in the hanging-wall overly mylonitic amphibole-bearing peridotite and gabbroic veins in the footwall (Figure 3.24). At Nantivet Rock – Kynance Cove locality, the mylonitic peridotite-gabbroic vein contact relationships are seen at Nantivet Rock, Lawarnick Pit, north of Asparagus Island and Kynance Cove. Contact



**Figure 3.24.** Interbanded and folded mylonitic amphibole-bearing peridotite (MAB) and gabbroic veins (G) in the footwall of a fault (marked by white line) at Lawarnick Pit. Mylonitic plagioclase-bearing peridotite (MPB) is exposed in the hangingwall of the fault.

relationships at Nantivet Rock and north of Asparagus Island have been logged in detail (Figure 3.25) in two traverses and these structural logs reveal the complexities of the relationships between the two lithologies. Mylonitic peridotite and gabbroic vein are folded and interbanded on a centimetre to metre scale (Figure 3.26) and isoclinal fold axes plunge moderately towards the NW. The contacts between the mylonitic peridotite and gabbroic vein are generally sharp, although gradational contacts do occur, which result in the generation of transitional lithologies. The gabbroic veins vary between massive coarse-grained rocks, which resemble gabbro in hand specimen (Figure 3.27) and fine-grained, banded rocks. Within the mylonitic peridotite and fine-grained gabbroic veins, fabrics are parallel and a strong foliation strikes NNW, dips steeply towards the NE and SW and mineral lineations plunge steeply down-dip. Within the coarse-grained gabbroic veins, the fabric is less well developed, but it is parallel with the fabric in the peridotite and fine-grained gabbroic veins. The effects of folding and the development of the fabric in the rock have obliterated any evidence for an intrusive relationship between the mylonitic peridotite and gabbroic vein at this locality. These gabbroic veins could therefore represent either later gabbroic intrusions, which have subsequently been deformed, or deformed mafic cumulate layers. A sample of gabbroic vein (96/530) from this locality was used in the SHRIMP dating study. Metamorphic zircons were analysed by SHRIMP and established that there was a metamorphic event at  $385 \pm 7$  Ma. A single zircon grain showed zircon inheritance with an age of 450-500

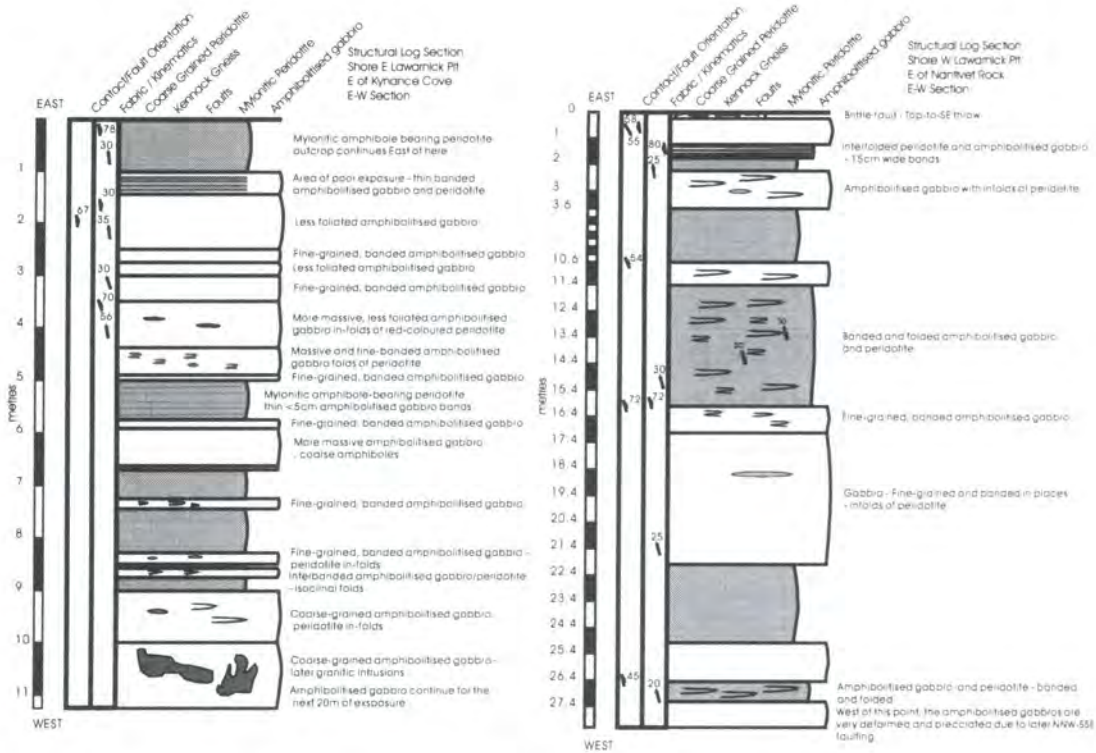


**Figure 3.25.** Structural log sections from the Kynance Cove area. Log sections show the relationships between mylonitic peridotite (dark shade) and gabbroic veins (light shade). Structural data is included and orientations are relative to the vertical axes of the log, which represents N.

Ma, which could either represent an inherited grain of unknown origin or a rare magmatic grain (Nutman, A., *pers comm* 1998). The thermal event at  $385 \pm 7$  Ma could either be associated with metamorphism during the development of the steep fabric, or later deformation events. The mineral chemistry and whole rock composition of these gabbroic veins is used to establish their origin in Chapters 5 and 6.

#### 3.4.1.d. Porthallow Cove – Porthkerris Cove (GR 805 231; Figure 3.28)

Along the 2 Km section of coastline between Porthallow Cove and Porthkerris Cove, a remarkably variable sequence of rocks are observed (Figure 3.28). An ENE trending, southerly dipping extensional fault 200 m east of the Five Pilchards Inn at Porthallow juxtaposes shales and volcanic rocks to the north, with rocks of much higher metamorphic grade to the south. The first lithology encountered south of this extensional fault is fine-grained garnet-mica schists and, although they are very sheared and altered, are very similar to the Old Lizard Head Series schists observed in the Lizard Head area. Another extensional fault contact separates the garnet- micaschists





**Figure 3.26.** Plan view looking down at interbanded and interfolded gabbroic veins (pale) within serpentinised mylonitic amphibole-bearing peridotite (red) at Lawarnick Pit.



**Figure 3.27.** Coarse-grained portion of a gabbroic vein showing large pyroxene porphyroclasts (dark) set in a matrix of finer-grained pyroxene and plagioclase. Note the development of a foliation defined by elongate pyroxene porphyroclasts.

from mylonitic peridotites to the east. In hand specimen, these mylonitic peridotites contain orthopyroxene porphyroclasts and large amphibole grains, which suggests that these are mylonitic amphibole-bearing peridotites. At Pol Gwarra, further east, further outcrops of mylonitic peridotite also appear to resemble the mylonitic amphibole-bearing peridotite characteristic of the west coast of the Lizard. Between Porthallow Cove and Porthkerris Quarry, the peridotite is strongly serpentinised and only pseudomorphs of the original minerals are observed in hand-specimen. The rock is fine-grained, green-black in colour and contains bastite after orthopyroxene and

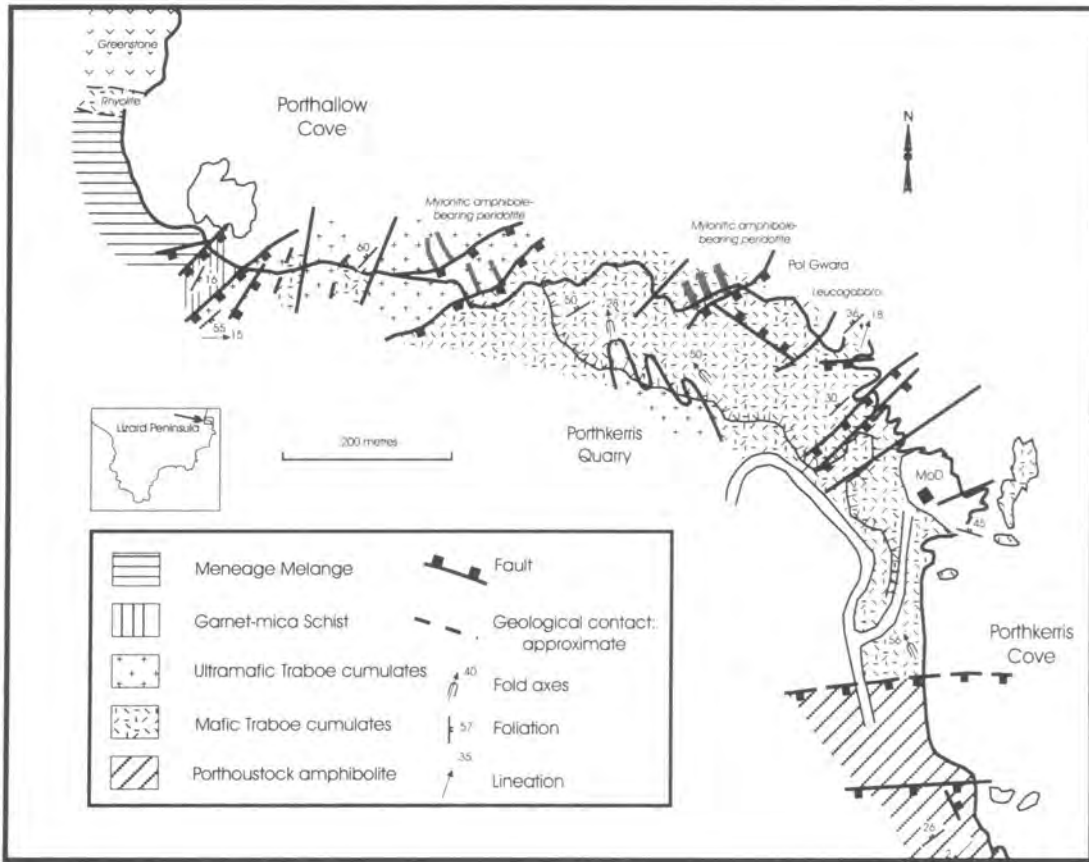


**Figure 3.28.** Geological map of coastal outcrops between Porthallow Cove and Porthkerris Cove showing locations referred to in the text. Modified after Floyd *et al.* (1993).

chlorite pseudomorphs after spinel. Many of these ultramafic rocks i.e. the ultramafic Traboe cumulates, resemble highly serpentinitised dunite. The rock is criss-crossed by a network of chrysotile veinlets (Figure 3.29). The foliation in these rocks strikes ENE and dips moderately towards the N. Serpentinitised ultramafic Traboe cumulates are associated with an extremely variable range of mafic Traboe cumulates. The serpentinitised ultramafic Traboe cumulates are interbanded with mafic Traboe cumulates and this banding is related to repetition by isoclinal folding. In the cliff face of Porthkerris Quarry, the ultramafic Traboe cumulates form the core of a series of antiforms associated with mafic Traboe cumulates, which plunge at a moderate angle towards the NW. The mafic Traboe cumulates at Porthkerris Quarry and Porthkerris Point are highly deformed and disharmonic folding is observed (Figure 3.30). A wider range of rock types is observed in mafic Traboe cumulates at this locality than at the localities described in previous sections. The rocks vary in composition between amphibole- and pyroxene-rich layers to plagioclase-rich layers, and in many places



resemble deformed gabbroic rocks. The association of serpentinised ultramafic Traboe cumulates, including dunites, pyroxene-rich rocks and gabbroic rocks suggests that these outcrops represent a highly deformed and metamorphosed cumulate complex. Geochemical evidence for a cumulate origin for rocks similar to these is presented in Chapter 6. The highly folded nature of these rocks and the presence of ductile shear zones suggest that they have been subjected to several phases of high-temperature deformation. Granitic veinlets (1 – 25cm) at Porthkerris Quarry cross-cut the fabric



**Figure 3.29.** Serpentinised ultramafic Traboe cumulate at Porthallow. This rock resembles dunite and is criss-crossed by a network of chrysotile veinlets.



**Figure 3.30.** Strongly deformed and folded mafic Traboe cumulates at Porthkerris Quarry. Note the large variation in composition, from plagioclase-rich anorthosite layers (white) to amphibolised pyroxenite layers (dark).

within the mafic Traboe cumulates. A few granite veins are parallel to the fabric in the host amphibolite and fabrics within the veins are also concordant with the amphibolite fabric. Later folding has deformed the veinlets. Clark *et al.* (1998b) recently dated a granitic vein from Porthkerris, which they describe as a plagiogranite, by U-Pb analysis of zircon. The plagiogranites described by Clark *et al.* (1998b) are believed to be identical to the granite veins observed during the present study. An age of  $397 \pm 2$  Ma was obtained from the zircons, which is interpreted by Clark *et al.* (1998b) to record the crystallisation of the plagiogranite. This zircon age therefore constrains the deformation in ultramafic and mafic Traboe cumulates at Porthkerris to an age of  $397 \pm 2$  Ma or earlier. At Pol Gwarra, a highly deformed coarse-grained leucogabbro is exposed and is cross-cut by gabbro mylonite shear-zones and gabbro pegmatites.

The fabric orientation and composition of ultramafic and mafic Traboe cumulates contrasts with Porthoustock amphibolites on the south side of Porthkerris Cove. On the south side of the Cove, the Porthoustock amphibolites are massive, with little of the variation seen at Porthkerris Quarry and Point, and the foliation is flat-lying with sub-horizontal mineral lineations plunging predominantly SW. It is postulated that an unexposed fault in Porthkerris Cove forms the contact between these two contrasting lithological units.

#### 3.4.1.e. Traboe Boreholes

In 1978, three near vertical boreholes were drilled to the W and SW of Traboe (1,2 & 3 on Figure 3.3). These boreholes were drilled as part of a geochemical survey by the I.G.S. (BGS). Leake and Styles (1984) published simplified graphical logs presented in this section (Figure 3.31). Leake and Styles (1984) concluded that the ultramafic and mafic rocks preserved in the borehole core represent a deformed and dismembered cumulate complex, termed the Traboe cumulate complex, overlying the Lizard peridotite.

During the course of this study, the borehole core has been studied at the Keyworth offices of the British Geological Survey. The study of this core complements the detailed field observations described in the preceding sections.

A wide range of lithologies is observed in the borehole core and these are very similar to the rocks observed at the Porthkerris coastal section (3.4.2.d.). The lithologies range in composition between serpentinitised mylonitic peridotites to

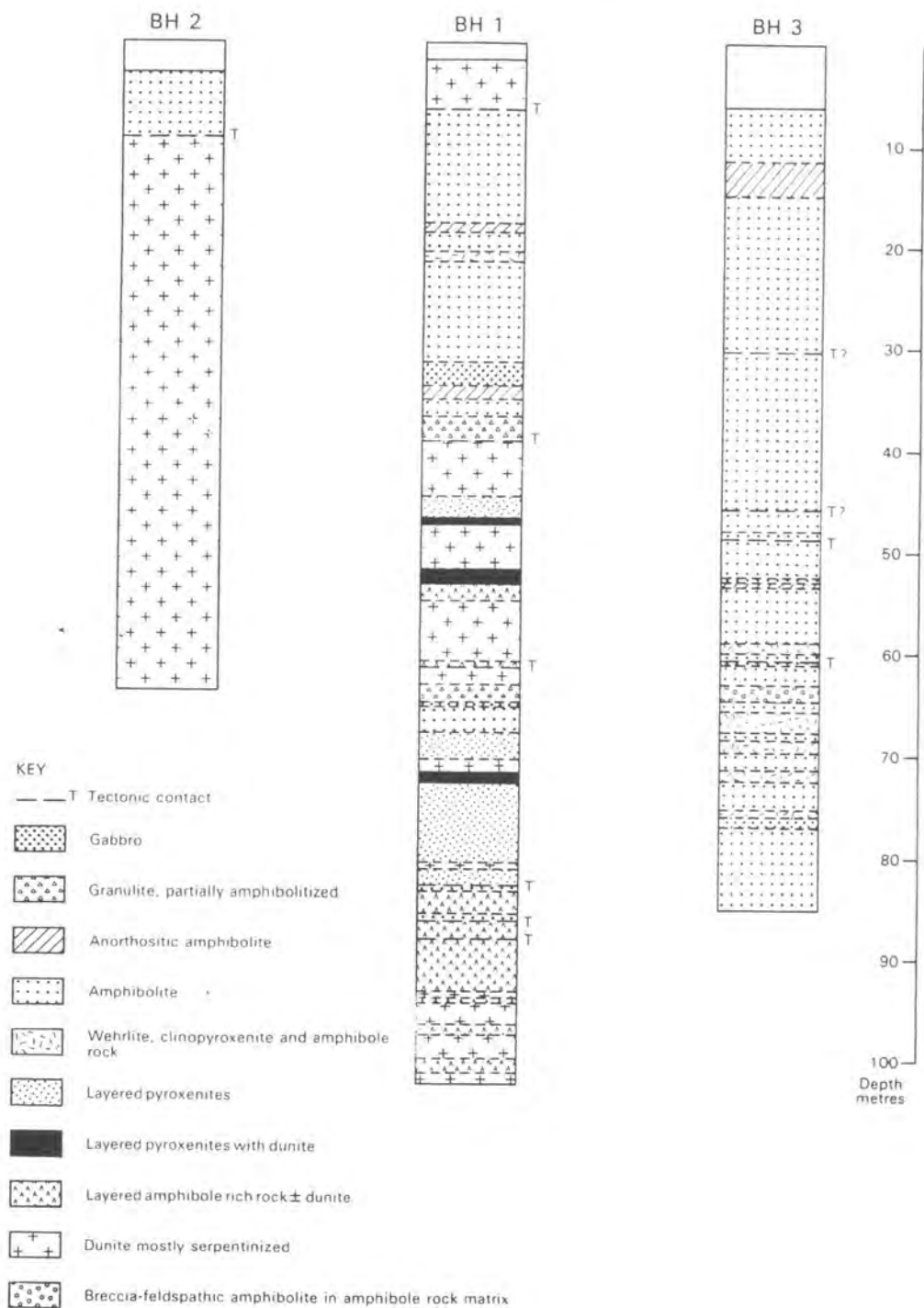


**Figure 3.31.** Simplified graphic logs of the Traboe boreholes (from Leake & Styles, 1984).

anorthosites. All of the rocks are highly deformed, with a well-developed foliation, which is usually folded. Later faulting has disrupted the sequences observed in the core. The core from borehole 1 displays the most variable range of lithologies that includes serpentinised dunites, mylonitic peridotite, layered pyroxenites, amphibolites and granulites. The different lithologies are layered at a cm to m scale and layer boundaries



are often gradational. Borehole 2 consists almost entirely of serpentinitised peridotite; both dunite and mylonitic peridotite are observed. The uppermost section of borehole 2 consists of Traboe amphibolite. Borehole 3 consists predominantly of Traboe amphibolite, with minor pyroxenite and anorthositic layers. There appears therefore to be a stratigraphic sequence from borehole 2 to 1 to 3. Borehole 2, which is predominantly composed of ultramafic rocks represents the upper mantle/lower crust and borehole 3, which is almost entirely mafic rocks, represents the highest stratigraphical unit and is equivalent to oceanic crust. Borehole 1 consists of deformed layered ultramafic and mafic cumulates as a transitional sequence. The boreholes do not represent a complete sequence through the cumulate complex, presumably due to the effects of later faulting. Leake and Styles (1984) concluded that the borehole intersections originated as a layered peridotite-gabbro cumulate complex, with possible cyclic units. The petrography and geochemical compositions of selected borehole samples is discussed in Chapters 4, 5 & 6, and is compared with samples collected from field outcrops to provide a correlation with the borehole evidence.

### **3.4.2. Landewednack Amphibolites**

The Landewednack amphibolites outcrop extensively between Polurrian Cove (GR 6675 1865) and Mullion Cove (GR 6665 1780), Ryniau (GR 6645 1731) to Ogo Dour Cove (GR 6682 1575), and the southern end of Pentreath Beach (GR 6933 1266) on the west coast of the Lizard. On the east coast outcrops occur on the coast and inland between Polbrean Cove (GR 7020 1150) and Kildown Point (GR 7264 1468)(Figure 3.3).

Amphibolites described in this section do not show any complex interbanded and interfolded relationships with ultramafic rocks. The contacts between Landewednack amphibolites and the mafic Traboe cumulates observed in field localities and described in the previous section are generally ductile shear-zone contacts. The following discussion is focused on evidence for early textures/fabrics in the Landewednack amphibolites, which develop prior to later emplacement-related fabrics. At Polurrian Cove there is evidence for preservation of lithological layering, which pre-dates the development of later fabrics in the amphibolite. At Polurrian Cove and Pen Olver (GR 7130 1170), these early textures are cross-cut by a series of medium-grained mafic dykes, which have themselves been deformed by the later

fabrics. These early textures are interpreted to be primary crystallisation textures in a suite of gabbroic and basaltic rocks (Chapter 6), which have been subsequently been deformed and amphibolitised. In several outcrops, particularly at Pen Olver, there are pelitic horizons interbanded with the amphibolite.

The earliest fabric to effect the early textures is related to an amphibolite-grade metamorphism (Chapter 4). These early steep fabrics are preserved in amphibolites on the west coast between Polurrian Cove and Ogo Dour Cove. These early fabrics are cross-cut by later, low-angle fabrics, related to the emplacement of the Lizard Ophiolite Complex. Jones (1997) concludes that these early fabrics are contemporaneous with early fabrics preserved in areas of low-strain within the OLHS, and thus related to the same deformation event. Currently there is insufficient geochronological evidence to link these amphibolites and early fabrics with the early fabrics preserved in the OLHS. The amphibolites and OLHS are juxtaposed by later thrust contacts, related to Devonian emplacement of the Lizard Ophiolite Complex, and it is impossible, therefore, on the basis of field evidence to justify a genetic relationship between the amphibolites and the OLHS. It should be noted, however, that early fabrics preserved in both the OLHS and the amphibolites are relatively steep in comparison to the gently dipping fabrics related to emplacement, which are seen in both the OLHS and amphibolites. Amphibolites, which outcrop on the east coast of the Lizard, between Kildown Point and Polbrean Cove, preserve little evidence for earlier textures and fabrics. The fabrics in these amphibolites are dominantly sub-horizontal and related to later emplacement-related tectonics. At Kilcobben Point (GR 7173 1250), however, outcrops of amphibolite locally preserve evidence for an earlier, steep fabric, which has been subsequently re-worked by sub-horizontal fabrics. In the Predannack Cliff (GR 66 16) to Ogo Dour Cove area foliations strike NW-SE and plunge moderately to steeply SW and NE. Mineral stretching lineations moderately plunge down-dip. The orientation of fabrics in these amphibolites is similar to fabrics in gabbroic veins, ultramafic and mafic Traboe cumulates on the west coast and at Porthkerris (Section 3.2.4), but there is insufficient evidence to determine whether these are contemporaneous. Sub-horizontal fabrics that relate to later emplacement tectonics (Section 3.5) cross-cut these early steep fabrics. At Ogo Dour Cove, these fabrics are cross-cut by a suite of NW-SE striking mafic dykes, which are similar in composition to dykes (Chapter 6) observed on the east coast of the Lizard e.g. Coverack (GR 7830 1835).

### **3.4.3. Later magmatism and deformation – East coast of Lizard**

On the east coast of the Lizard peninsula, between Porthkerris (GR 805 231) and Coverack (GR 7830 1835), there is evidence for extensive magmatism and deformation that appears to post-date the magmatism and tectonism discussed in preceding sections. Evidence for this includes the presence of gabbro dykes cross-cutting the fabrics in the Lizard peridotites and also mafic Traboe cumulates in the Traboe borehole core (Leake & Styles, 1984). This includes a combination of contemporaneous magmatism and structural events associated with the intrusion of the Crousa gabbro (Roberts *et al.*, 1993). North of Porthoustock (GR 8060 2180), massive amphibolites outcrop, which are termed the Porthoustock amphibolites. Field and geochemical (Chapter 6) evidence suggest that fabrics preserved in these amphibolites were developed in a different tectonic environment to fabrics observed in the Landewednack amphibolites. The field evidence for these structural and magmatic events, and available geochronological constraints is discussed below.

#### **3.4.3.a. Magmatism and deformation associated with the Crousa gabbro**

The Crousa gabbro is exposed in a ca. 22 km<sup>2</sup> area between Porthoustock and Coverack on the east coast, and the northern margin of the gabbro has an arcuate contact with the Porthoustock amphibolites, Traboe cumulate complex and Lizard peridotites between Porthoustock and Gwenter (GR 7410 1789). At Carrick Luz (GR 7555 1650), a massive deformed gabbro dyke outcrops in the steep cliffs of this peninsula. At Coverack the contact between the gabbro and coarse-grained lherzolites is observed in outcrops on the beach (Figure 3.32). The contact is a complex zone of interdigitating gabbro intrusions and peridotite, which represents a petrological Moho and dips at a low-angle towards the north. The fabric in the peridotite is cross-cut by gabbro sills and the foliation is sub-vertical striking N-S to NE-SW. Troctolite bodies are the first intrusive phase observed to post-date the peridotite fabric at Coverack. The troctolite forms a series of irregular intrusions, which enclose xenoliths of peridotite, and in hand specimen consist of a wide range of compositions including plagioclase, olivine and clinopyroxene. The olivine is invariably altered to serpentine and the plagioclase to saussurite, which gives the rock a distinctive red and white mottled appearance. Field evidence at Coverack shows that gabbro sills associated with the Crousa gabbro intrude

the troctolite. The intrusion and crystallisation of the main body of the gabbro has been constrained by a combined mineral and whole rock Sm-Nd isochron, which gave an age of  $375 \pm 34\text{Ma}$  (Davies, 1984). At Coverack, and along the coast south to Black Head (GR 7793 1615), the peridotite is intruded by coarse-grained gabbro dykes, which are often gabbro pegmatites. These dykes have variable orientations, the majority dip steeply ( $>45^\circ$ ). In hand specimen, the gabbro and gabbro dykes consist of clinopyroxene and plagioclase, with minor olivine, and these primary minerals are

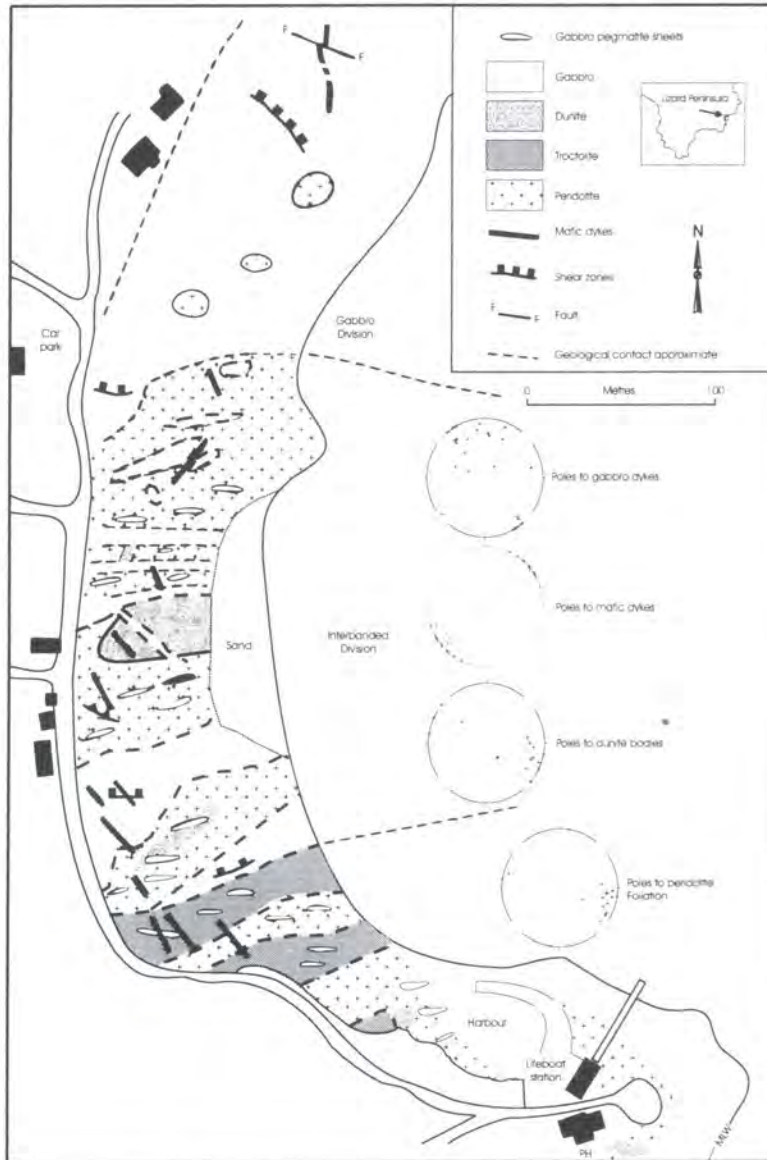


**Figure 3.32.** Geological map of Coverack Bay. Stereonets display poles to peridotite foliation, dunite bodies, gabbro dykes and mafic dykes. Modified after Floyd *et al.* 1993.

commonly altered to amphibole, saussurite and serpentine respectively.

North of the contact zone at Coverack, the gabbro is intruded by a series of flat-lying, irregular dolerite sheets, which lack chilled margins. These dolerite dykes are

cross-cut by a series of steeply-dipping plagioclase-phyric dykes (Roberts *et al.*, 1993), which are particularly abundant at Porthoustock Point (GR 8105 2165) and there comprise a sheeted dyke complex. At Coverack, ductile shear-zones defined by aligned and elongate plagioclase, pyroxene and amphibole crystals cross-cut the gabbro, dolerite sheets and plagioclase-phyric dykes. The shear-zones strike NW-SE and dip moderately towards the NE. The field evidence suggests that these shear-zones are extensional, which is consistent with the detailed investigation by Roberts *et al.* (1993), who demonstrated that these shear-zones are extensional and show a top-to-the-northeast sense of displacement. A later suite of dolerite dykes cross-cut the ductile shear-zones, gabbro, earlier plagioclase-phyric dykes, dolerite sheets, troctolite and peridotite at Coverack. The dykes have chilled margins, and trend NW-SE and dip steeply ( $<50^\circ$ ) to the NE and SW. These dykes are aphyric to plagioclase-phyric in composition, and up to 2 metres in width (Figure 3.33). Mafic dykes with an identical

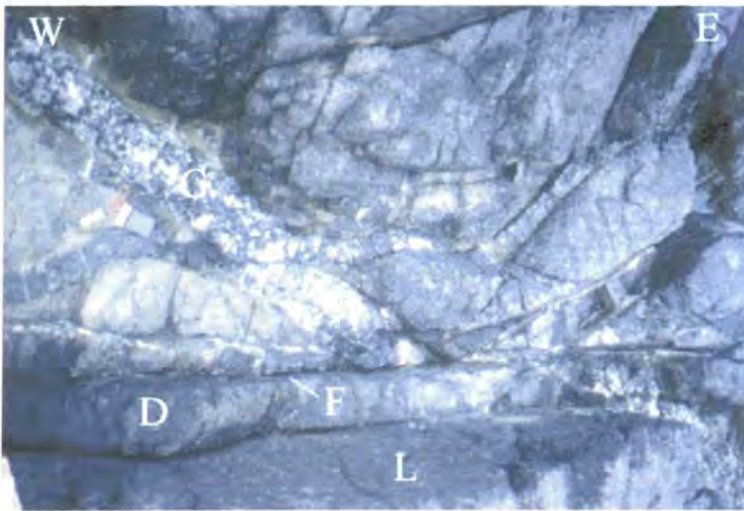


**Figure 3.33.** Mafic dyke (D) cross-cutting coarse-grained lherzolite (L) and a gabbroic dyke (G)(associated with Crousa gabbro). Note that the mafic dyke is itself cross-cut by a later brittle fault (F).

trend (Figure 3.34) and similar composition (Chapter 6) occur throughout the Lizard Ophiolite Complex, for example, cross-cutting peridotite/gabbroic vein and ultramafic and mafic Traboe cumulates at Potstone Point (Section 3.2.4.a) and also between Kennack Sands (GR 7390 1660) and Church Cove (GR 7150 1280). This suggests that this later dyke suite is an extensive intrusive phase, which is not restricted to the gabbro body.

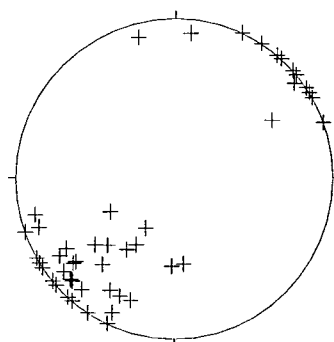


**Figure 3.34.** Lower hemisphere stereographic projection displaying poles to all mafic dykes (late dyke suite).

At Carrick Luz, on the east coast of the Lizard, a large body of spectacular flaser gabbros and gabbro mylonites is exposed and is known<sup>as</sup> the Carrick Luz shear-zone (Andrews and Jolly, *in press*). This shear-zone is approximately 150 metres wide and strikes NW-SE and dips steeply NE (Figure 3.35). The foliation in the flaser-mylonitic gabbros within the shear-zone is similarly orientated NW-SE, and dips steeply NE, and mineral stretching lineations are sub-horizontal, plunging shallowly NW and SE. Shear-sense indicators (shear-bands and asymmetric porphyroclasts) consistently show a dextral shear-sense. The intensity of the fabric is very variable, and varies between coarser-grained flaser gabbros, and intensifies into gabbro mylonites, and is often localised into shear-zones of ultramylonite. The shear-zone is in contact with coarse-grained lherzolite on both its NE and SW margins. On the NE margin, the contact dominantly consists of an irregular contact with many gabbro dykes (Andrews and Jolly, *in press*). On the SW margin, the subvertical N-S to NNE-SSW foliation in the peridotite is re-worked in the margins of the Carrick Luz shear-zone. In a transition zone 5 metres wide, the peridotite fabric is re-orientated into parallelism with the NW-SE trending fabric in the adjacent gabbro mylonites. The peridotites adjacent (<2m) to the contact with gabbro mylonites are 'peridotite mylonites' (Figure 3.36), and have a strongly developed fabric and sub-horizontal mineral lineations. The 'peridotite mylonites' are different from the "mylonitic peridotites", which outcrop on the west coast of the Lizard (Section 3.2.2). In hand specimen the 'peridotite mylonites' are composed of an original spinel lherzolite mineralogy (Section 3.2.1.), which is reworked by shear-zones composed of colourless amphibole and chlorite. These amphibole and chlorite-bearing shear-zones are very similar to hydrous shear-zones observed at thrust contacts between peridotite and Landewednack amphibolite on the east coast (Section 3.5.1).



Shear-sense indicators within the peridotite mylonite show a dextral sense of displacement, consistent with the fabric within the gabbro. In many outcrops along the SW margin of the Carrick Luz shear-zone, elongate, phacoids of 'peridotite mylonite' occur within host gabbro mylonites.

Coarse-grained, deformed, gabbro intrusions and gabbro pegmatite dykes also outcrop extensively in the Carn Barrow (GR 7190 1390) to Parn Voose Cove

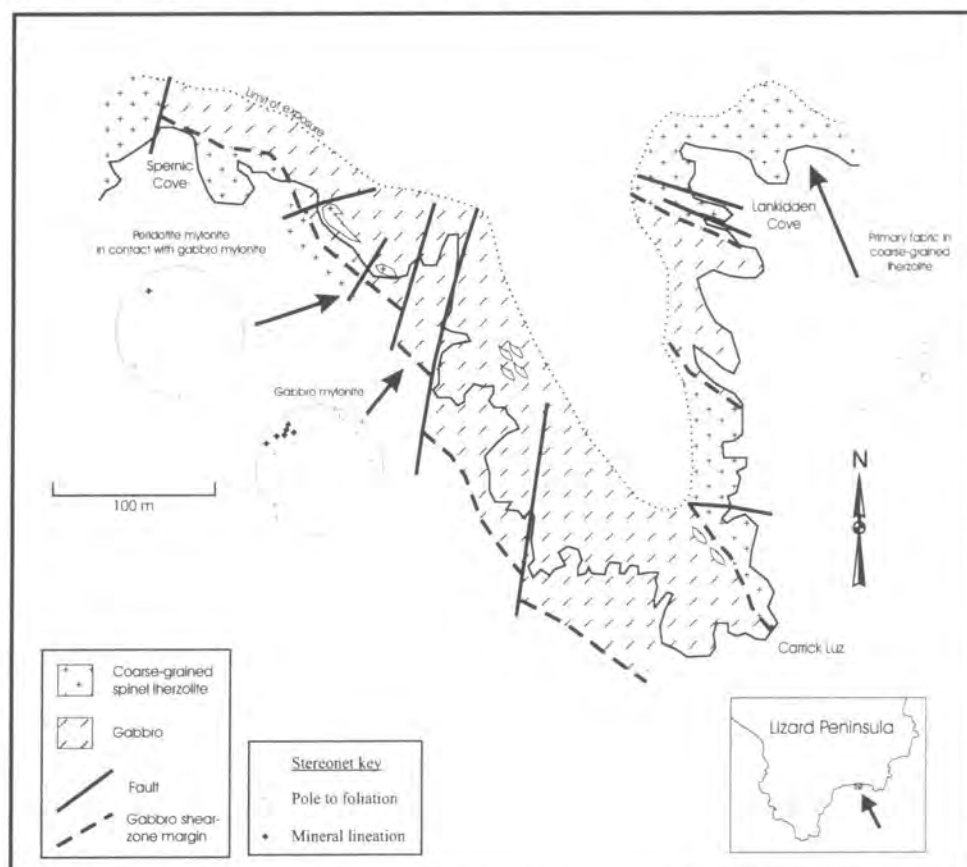


**Figure 3.35.** Geological map of the Carrick Luz peninsula. Stereonets display poles to foliation and lineation plunge in gabbro and 'peridotite mylonites' on the western margin of the peninsula, and coarse-grained herzolites on the eastern margin. Modified after Floyd *et al.* (1993).

(GR 7148 1303) area of the Lizard peninsula. These gabbro intrusions post-date the peridotite fabric in this area, and pre-date the intrusion of mixed felsic and mafic Kennack Gneiss. The relationship between these gabbro intrusions and the Crousa gabbro is unknown, but Sandeman (1988) suggests that they are not directly related, based on contrasting whole rock geochemical compositions. The gabbros are variably deformed, and evidence for localised deformation includes the presence of shear-zones composed of gabbro mylonite.

### 3.4.3.b. Porthoustock amphibolites: an extensional shear-zone

North of the sheeted dyke complex at Porthoustock Point, massive amphibolites are exposed along ca. 1 km of coast between Porthkerris Cove and Porthoustock and inland to Traboe. These have been previously known as the Upper Landewednack amphibolites (Bromley, 1979; Vearncombe, 1980) and are restricted to this area of the Lizard Ophiolite Complex. On the basis of contrasting tectonic fabrics (see below) and different whole rock geochemical compositions (Chapter 6) from the other amphibolites in the Lizard Ophiolite Complex, the amphibolites discussed in this section are termed the *Porthoustock amphibolites*. A late brittle fault is assumed to form the contact between the sheeted dyke complex and these amphibolites at Porthoustock. At Porthkerris Cove, an assumed fault contact separates these amphibolites from ultramafic rocks and Traboe amphibolites to the north.

On coastal outcrops, north of Porthoustock and in old quarry workings (GR 8090 2200), the amphibolites are variable in composition. The amphibolites consist of coarse-grained and fine-grained varieties, which are interbanded on a centimetre to metre scale (Figure 3.37). The coarse-grained amphibolites consist of conspicuous plagioclase phenocrysts set in a matrix of finer grained plagioclase and amphibole, and textures suggest that these may represent deformed gabbros. The fine-grained amphibolites lack plagioclase phenocrysts and are composed of fine-grained plagioclase and amphibole, and these may represent deformed mafic dykes. Further north, near Porthkerris Cove, the fine-grained amphibolite is predominant over the coarse-grained variety. Minor pelitic horizons (~10cm wide) are interbanded with the amphibolites in the Pencra Head area (GR 8095 2239). In all the outcrops of Porthoustock amphibolite there is a strongly developed flat-lying fabric (Figure 3.38), defined by the shape-preferred orientation of plagioclase and amphibole. The foliation strikes NW-SE and dips at a low-angle ( $<15^\circ$ ) towards the NE and SW, with dips towards the SW being predominant. Mineral stretching lineations plunge down-dip, predominantly towards the SW, with minor plunges towards the NE. Asymmetric plagioclase porphyroclasts in the coarse-grained amphibolites and shear-band fabrics show a consistent top-to-the-SW shear-sense in these amphibolites, which is consistent with the observations of Gibbons and Thompson (1991).



The orientation of the fabrics and top-to-the-SW shear-sense, is very different from the top-to-the-NW shear-sense in the Landewednack amphibolites on the SE Coast of the Lizard (Section 3.5). This evidence suggests that the Porthoustock amphibolites were developed in a different tectonic environment, and this was possibly

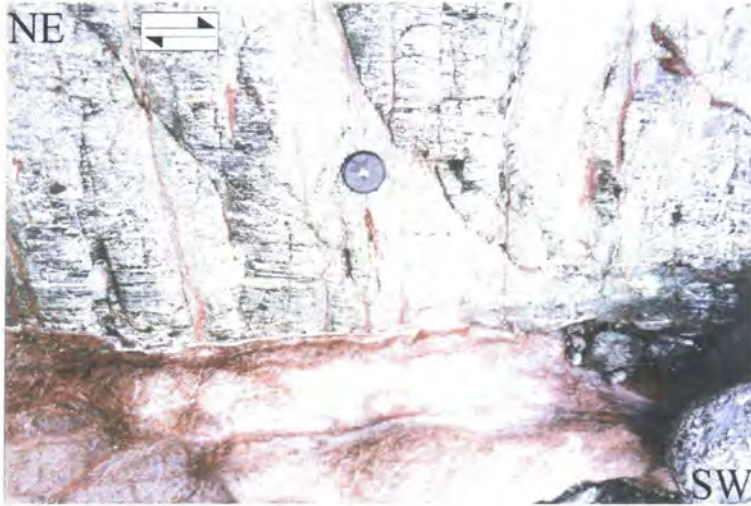


**Figure 3.36.** Plan view looking down at a contact between gabbro mylonite (G) and mylonitised peridotite on the western margin of the Carrick Luz shear-zone. Asymmetric porphyroclast systems developed in amphiboles (dark) in the gabbro mylonite indicate dextral shear.

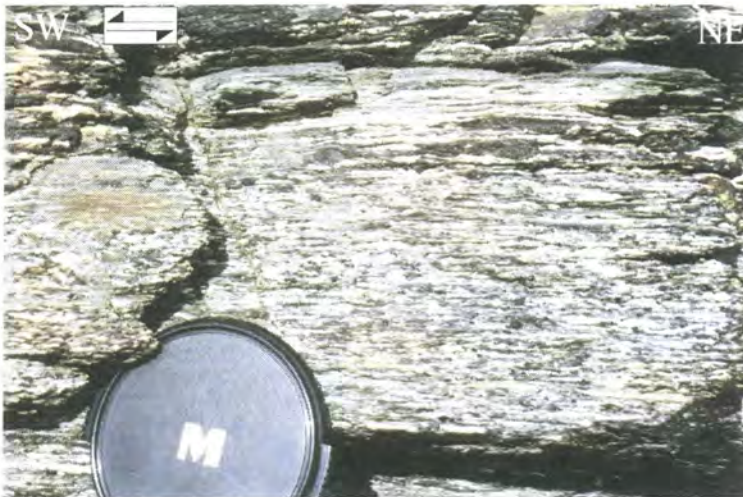


**Figure 3.37.** Coarse-grained (middle and lower part of photograph) and fine-grained (top of photograph) Porthoustock amphibolite. Aligned amphibole porphyroclasts (dark) define a lineation and are set in a matrix of recrystallised plagioclase (white). Asymmetric porphyroclast systems developed in amphiboles indicate top-to-the-SW shear.

during extension related to the construction of oceanic crust, and therefore related to the extensional shear-zones in the Crousa gabbro (see above). The whole rock composition (Chapter 6) of the Porthoustock amphibolites is distinctly different to the Traboe cumulates and Landewednack amphibolites of the Lizard Ophiolite Complex.

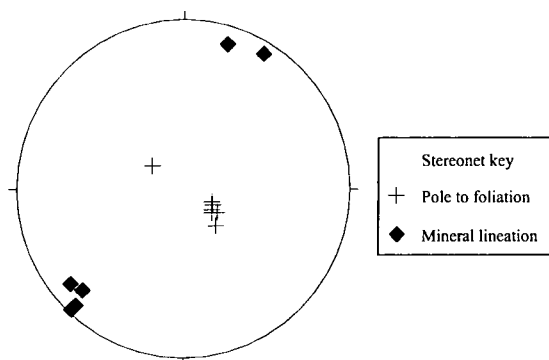


**Figure 3.38.** Lower hemisphere stereographic projection displaying poles to foliation and mineral lineation plunge in Porthoustock amphibolites.

#### 3.4.4. Summary

- The association of gabbroic veins, ultramafic and mafic Traboe cumulates and Landewednack amphibolites, which preserve relict textures and field relationships indicative of gabbro and basaltic dyke protoliths, with ultramafic rocks suggests that these rocks represent deformed upper mantle/lower crust.
- It is proposed that early steep fabrics preserved in these rocks may have developed during deformation that accommodated the extension of oceanic crust and upper mantle rocks during the early stages of ocean rifting.
- The generation of early steep fabrics in mafic Traboe cumulates has been constrained to an age of  $397 \pm 2$  Ma or earlier by dating of a cross-cutting plagiogranite vein (Clark *et al.*, 1998b).
- Later gabbro (Crousa gabbro –  $375 \pm 34$  Ma, Davies 1984), mafic dyke intrusions and contemporaneous extensional tectonics are linked to this phase of ocean lithosphere development, but may represent slightly later off-axis magmatism and deformation.
- The Porthoustock amphibolites preserve low-angle fabrics and shear-sense indicators suggest top-to-the-SW, apparently extensional displacements. The fabrics developed in these amphibolites may be contemporaneous with shear-zones in the Crousa Gabbro.

---

### 3.5. Emplacement of the Lizard Ophiolite Complex, and later tectonic/magmatic events

---

The majority of the rocks exposed in the Lizard peninsula show evidence for later, emplacement-related tectonic events. This includes the development of cross-cutting large-scale and localised sub-horizontal shear-zones, which re-work earlier fabrics in the Ordovician basement rocks (MOWG and OLHS), and the Devonian rocks of the Lizard Ophiolite Complex (peridotites, associated ultramafic<sup>and mafic</sup> rocks, and Landewednack amphibolites). These shear-zones were developed during top-to-the-NW thrusting of the different lithological units of the Lizard Ophiolite Complex. At major shear-zone contacts on the east coast of the Lizard, mantle peridotites overthrust Landewednack amphibolites, which represent the deformed equivalent of oceanic crust. Metamorphic zircons within the Landewednack amphibolite have been dated by U-Pb SHRIMP analysis and constrain the metamorphism associated with thrusting to the early to late Devonian. During this thrusting event there is evidence for extensive magmatism which is identified by numerous intrusions of a mixed suite of felsic and mafic rock known as the Kennack Gneiss. This magmatism is closely associated with the shear-zones.

Later tectonic/magmatic events include re-activation of thrust contacts and intrusion of later post-tectonic granites. Finally, high angle brittle extensional faulting results in dismemberment of the Lizard Ophiolite Complex (Alexander and Shail, 1996; Power *et al.*, 1996).

#### 3.5.1. Emplacement-related fabrics in the Basement rocks

In section 3.2 it was established that the MOWG and OLHS which outcrop on the south-west most extremity of the Lizard peninsula represent Ordovician basement, and preserve early textures and fabrics developed at this time. It was also established that these early fabrics are re-worked by a series of later sub-horizontal shear-zones. The fabrics and structures associated with these later shear-zones have not been studied in detail during the course of the present study, and much of the following discussion (Sections 3.5.1.a & b) of structural relationships is a summary of the detailed work of Jones (1994) and Jones (1997).

### 3.5.1.a. Old Lizard Head Series (OLHS)

In section 3.2, relict, primary igneous textures and early fabrics were described, and the occurrence of a cross-cutting granitic sill (Lizard Head Sill). An igneous protolith age of  $488 \pm 8\text{Ma}$  (Appendix A) was established by U-Pb SHRIMP dating of zircon from the Lizard Head Sill. The primary textures, early fabrics and the granitic sill have been subsequently deformed and re-worked by a series of sub-horizontal shear-zones. The fabric in these later shear-zones strikes NE-SW and dips at a low-angle ( $<20^\circ$ ) towards the SE, and mineral lineations plunge down-dip, towards the SE (Jones, 1994). Jones (*op cit.*) demonstrated that the mylonitic fabric intensifies into four major shear-zones, the Most Southerly Point Shear Zone (MSPSZ), Polbreame Cove Shear Zone (PCSZ), the Polbreame Cove Thrust (PCT) and the Old Lizard Head Thrust (OLHT) (Figure 3.39). Landewednack amphibolites, which are Devonian rocks of the Lizard Ophiolite Complex, are exposed in the hangingwall of the PCT and PCSZ. Mineral lineations and sheath fold axes within OLHS rocks in the footwall of the PCT plunge at shallow angles towards the south (Jones, *op cit.*). Shear-sense indicators suggest top-to-the-

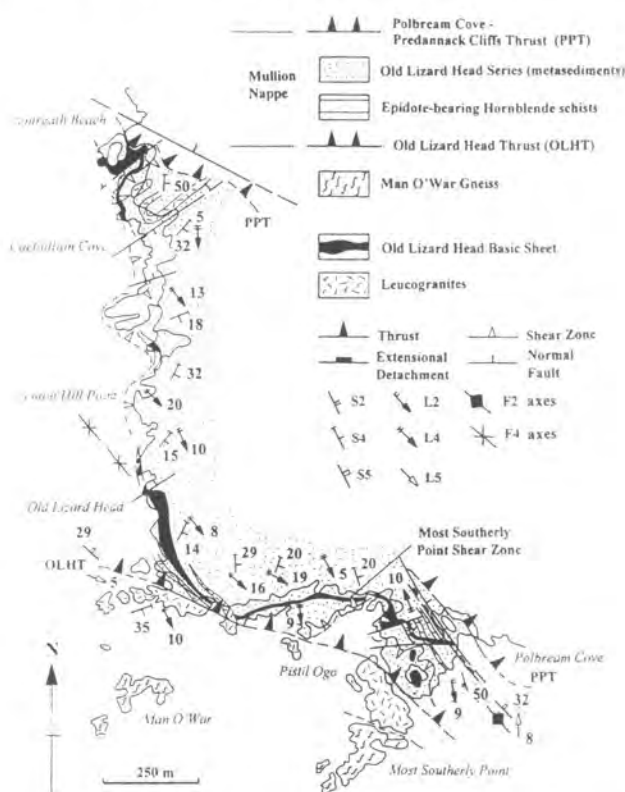


**Figure 3.39.** Geology of the south-west most extremity of the Lizard peninsula showing the Most Southerly Point Shear Zone (MSPSZ), Polbreame Cove Thrust (PCT) and the Old Lizard Head Thrust (OLHT) (from Jones, 1997).



north-directed overthrusting occurred on the PCT (Jones, *op cit.*). This suggests that the PCT and PCSZ are responsible for emplacement and juxtaposition of Landwednack amphibolites (Section 3.4.2) structurally over the OLHS (Jones, *op cit.*). The PCT and PCSZ therefore represent major detachments that facilitated emplacement of Devonian rocks of the Lizard Ophiolite Complex structurally over these Ordovician basement rocks. The fabrics and structures associated with the OLHT are discussed in the following section (Section 3.5.1.b.). Shear-sense indicators in the MSPT suggest a top-to-the-NW thrusting (Jones, 1994). Recent geochronological work (Clark *et al.*, 1998a) constrains the age of amphibolite facies metamorphism in OLHS rocks associated with this thrusting to ca. 354-377 Ma (Figure 3.1). These are similar to metamorphic ages of samples of Landwednack amphibolite in the Lizard Ophiolite Complex obtained during the course of this study by SHRIMP dating (Section 3.5.2.).

### 3.5.1.b. Old Lizard Head Thrust (OLHT)

The OLHT thrust, which outcrops at Lizard Head (GR 6945 1150), is a zone of ductile to brittle faulting up to 50 metres wide that strikes NW-SE and dips at a low angle towards the NE. The hangingwall of this thrust zone consists of strongly sheared rocks of the Old Lizard Head Series. Within the thrust zone, asymmetric phacoids of Old Lizard Head Series rock, Lizard Head Sill and Man of War Gneiss, S-C structures and

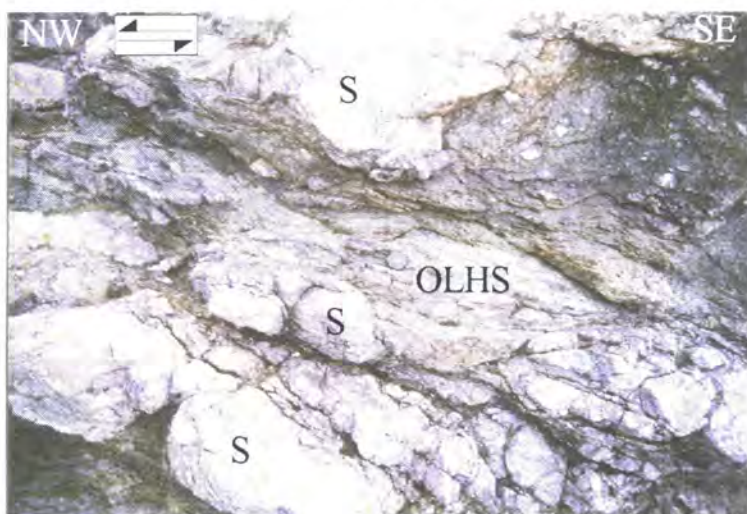


**Figure 3.40.** The Old Lizard Head Thrust (OLHT). Note the phacoids of Lizard Head Sill (S) set in a matrix of sheared Old Lizard Head Series (OLHS) rocks. Shear-sense indicators including asymmetric phacoids indicate a top-to-the-NW displacement along this thrust.

shear-bands indicate top-to-the-NW senses of displacement (Figure 3.40). A  $^{40}\text{Ar}$ - $^{39}\text{Ar}$  step-heating analysis of amphiboles in samples of mylonitised Man of War Gneiss in the footwall of this thrust suggest that they have been subjected to an amphibolite-grade metamorphic event at *ca.* 374 Ma (Sandeman *et al.*, 1997). Recent hornblende-plateau fusion-furnace results are <sup>with</sup> in error, at  $363 \pm 9\text{Ma}$  (Clark *et al.* 1998a). This amphibolite-grade metamorphic event was presumably contemporaneous with reworking and displacement along the Old Lizard Head Thrust.

### **3.5.2. Emplacement-related fabrics within the Devonian rocks of the Lizard Ophiolite Complex**

Sub-horizontal fabrics and shear-zones were developed during top-to-the-NW thrusting within the mafic and ultramafic rocks that comprise the Devonian rocks of Lizard Ophiolite Complex. During this thrusting event, the Devonian rocks of the Lizard Ophiolite Complex were thrust over Ordovician basement (MOWG and OLHS), and mantle peridotites were emplaced over oceanic crust (Landewednack amphibolites). Cross-cutting hydrous shear-zones developed in the mantle peridotites and similar, ductile-thrust contacts between the peridotite and Landewednack amphibolite formed and are preserved on the east coast of the Lizard. On the east coast of the Lizard pervasive emplacement-related mylonite fabrics are developed in the Landewednack amphibolites, but on the west coast there is only localised development of emplacement-related shear-zones which cross-cut earlier, steep fabrics.

#### **3.5.2.a. Mullion Cliff to Ogo-dour Cove (Figure 3.41)**

Earlier steeper fabrics which are preserved in the amphibolites (Section 3.4.2) exposed near Ryniau are re-worked by low-angle shear-zones (Figure 3.41). To the north, the amphibolites are in contact with mylonitic peridotites. The contact between these different lithologies is a later NW-SE striking, steep brittle fault. To the south, the change in orientation, from earlier steep fabrics to flat-lying fabrics of the low-angle shear-zones is transitional over a distance of 5 metres in a contact zone which strikes N-S and dips ( $\sim 45^\circ$ ) to the east. The field evidence suggests that this contact may represent the margin of a large shear-zone, with amphibolites with an original steeper

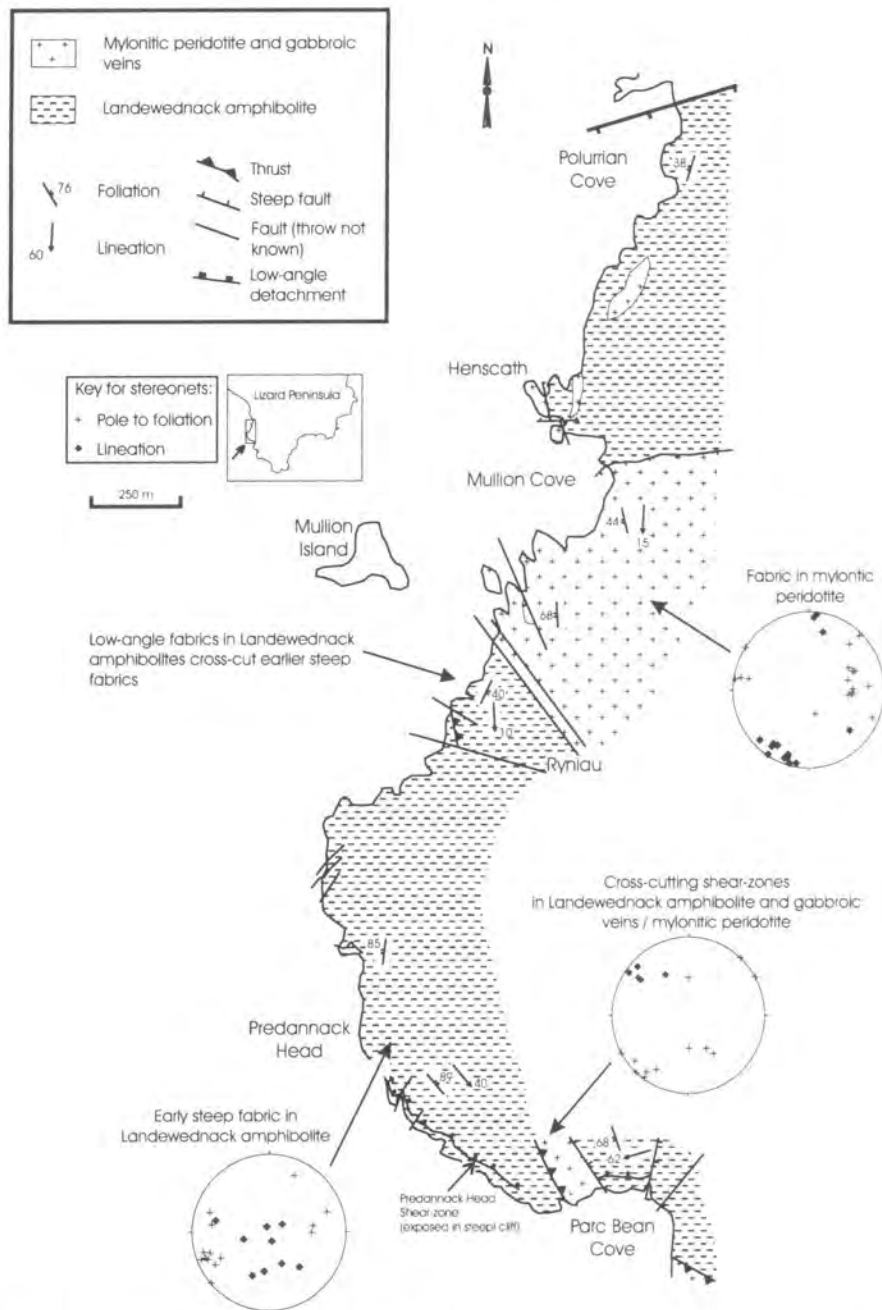


**Figure 3.41.** Geological map of the NW coast of the Lizard complex between Polurrian Cove and Parc Bean Cove. Stereonets display poles to foliation and plunges of mineral lineation in the mylonitic peridotites, Landewednack amphibolites and cross-cutting shear-zones.

fabric in the footwall, and amphibolites with a flat-lying fabric being developed within the shear-zone. Alternatively, this contact may represent a thrust contact, juxtaposing two different units of amphibolite. The transition in fabric in the amphibolites is also marked by change in the character of the amphibolites, from coarser-grained amphibolites in the footwall, to fine-grained, more uniform amphibolites with a mylonitic fabric within the overlying shear-zone. The amphibolites with a flat-lying fabric are characterised by the presence of epidote rich bands, which may represent



later zones of alteration in the amphibolites. The whole-rock geochemistry of the amphibolites both within the shear-zone, and the in the footwall is very similar (Chapter 6) and characteristic of the Landewednack-type, this suggests that this shear-zone is related to emplacement of the Lizard Ophiolite Complex. Within the shear-zone, the amphibolites strike NE-SW and dip at a low angle ( $< 40^\circ$ ) towards the south, mineral lineations consistently plunge down-dip. Asymmetric plagioclase porphyroclasts and shear-band fabrics, determine a top-to-the-NW shear-sense in these amphibolite mylonites.

South of the shear-zone at Ryniau, the Landewednack amphibolites have steep fabrics, and are coarser grained. Metamorphic zircons from a sample of amphibolite (96/510) in this area have been analysed by SHRIMP and a metamorphic age of  $392 \pm 5$  Ma has been obtained. It is not clear if this metamorphic age corresponds to the metamorphism associated with the development of the steep fabric or later sub-horizontal fabrics. Between Predannack Head and Ogo Dour Cove, however, there is evidence for later cross-cutting shear-zones, including the Predannack Head Shear – Zone (PHSZ). The PHSZ is observed in the cliff-section between Predannack Head and Ogo Dour Cove, although in several places it is truncated by later brittle-faults and down-faulted below sea level. The PHSZ consists of an anastomosing network, on narrow ( $< 1$  m) mylonite zones, which have a distinctive white colour and cross-cut the steep fabrics in the amphibolite. The PHSZ strikes NE-SW to E-W and dips at a moderate-angle ( $< 56^\circ$ ) toward the north, mineral lineations plunge down-dip (Figure 3.42). Shear-sense indicators, including the deflection of the steeper fabric of the

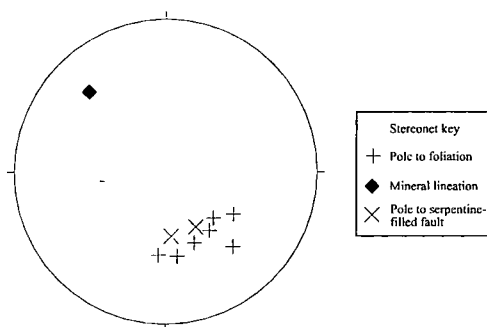


**Figure 3.42.** Lower hemisphere stereographic projection displaying structural data from the Predannack Head shear-zone (PHSZ). Poles to the foliation and plunge of mineral lineation in the shear-zone are shown and poles to serpentine-filled faults which reactivate the shear-zone.

amphibolites into the mylonite zones indicate a top-to-the-north displacement. The development of the PHSZ and the amphibolite mylonite shear-zone near Ryniau may

be contemporaneous, as both show a top-to-the-north displacement, however, there is insufficient field-evidence to determine whether they are directly related. Where the PHSZ outcrops, later serpentine-filled brittle/ductile faults are observed. These faults have re-activated the PHSZ and strike NE-SW, and dip at a moderate-angle ( $<38^\circ$ ) NW. A top-to-the-NW shear-sense within these faults zones is suggested by S-C' fabrics.

At Parc Bean Cove, it has already been demonstrated (Section 3.4.1.b) that in outcrops of mylonitic peridotite and gabbroic veins, earlier steeper fabrics are cross-cut by a series of shear-zones composed of amphibolite mylonite. These shear-zones strike NE-SW, dip at a moderate-angle ( $<40^\circ$ ) towards the NW and mineral lineations plunge down-dip. Shear sense criteria suggest that the shear-zones are extensional, with a top-to-the-north displacement. At the western side of this locality, these low-angle fabrics are rotated into a north-west-orientated foliation, which dips steeply towards the north-east and mineral lineations plunge at a shallow angle towards the north-west. The sense of rotation of the low-angle fabrics into this sub-vertical fabric suggests a sinistral displacement in this strike-slip shear zone, and this strike-slip shear zone is likely to be a transfer zone, developed during displacement on the low-angle top-to-the-NW shear zones. This shear zone juxtaposes the mylonitic peridotite and gabbroic veins with the more massive Landewednack amphibolites, with steep fabrics (see above) to the west. A later, NNW-SSE striking, sub-vertical brittle fault re-activates this sub-vertical, strike-slip shear-zone. These shear-zones are believed to be related to the emplacement of the Lizard Ophiolite Complex, and therefore contemporaneous with the shear-zone at Ryniau, and emplacement-related fabrics in Landewednack amphibolites on the east coast of the Lizard (see below).

### **3.5.2.b. Polbream Cove to Kildown Point area (Figure 3.43)**

In the southern part of this area (Figure 3.43), the rocks are predominantly composed of amphibolite, but in the northern part, mantle peridotites are observed in contact with amphibolite and there are numerous intrusions of Kennack Gneiss (Chapter 2). The amphibolites are predominantly the Landewednack-type, and are generally massive and dark green in colour, although in some outcrops there are layers more

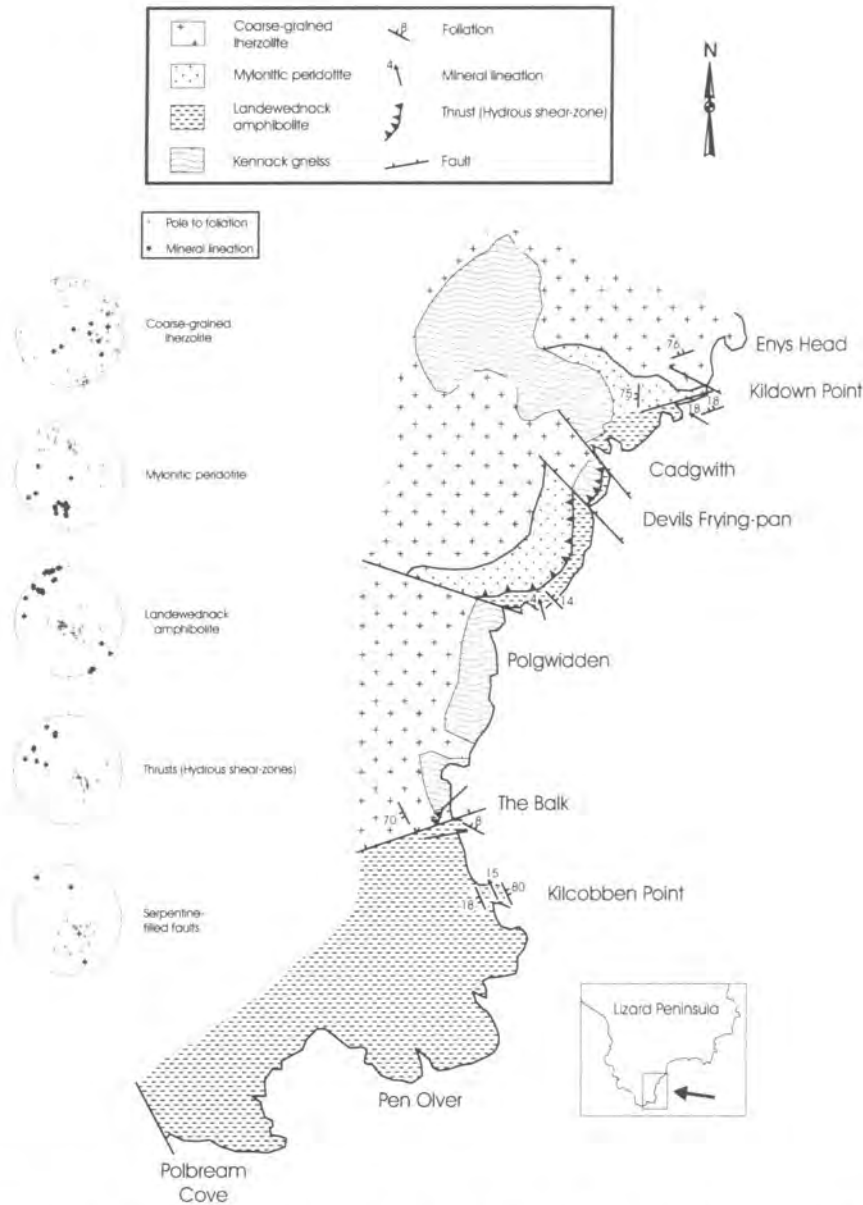


**Figure 3.43.** Geological map of the SE coast of the Lizard complex between Polbream Cove and Enys Head. Stereonets display poles to foliation and plunges of mineral lineations in coarse-grained lherzolites, mylonitic peridotites, Landwednack amphibolites, thrusts (hydrous shear-zones) and serpentine-filled faults related to reactivation of thrusts.

rich in plagioclase or amphibole. Bands rich in epidote (<20cm) are also fairly abundant and characteristic of these amphibolites, and these are very similar to the epidote rich bands observed in mylonitic Landwednack amphibolites at Ryniau (see above). The predominant fabric in the amphibolites is shallow (Figure 3.44) and post-dates earlier steeper fabrics (Section 3.4.2). At Kilcobben Point, the sub-horizontal fabrics are observed to cross-cut and re-work earlier steeper fabrics. Geochronological constraints for the thermal event associated with the metamorphism and development



**Figure 3.44.** Typical exposures of Landewednack amphibolite near The Balk. Note the shallow foliation which dips towards the east.

of the sub-horizontal fabrics are provided by SHRIMP analysis of metamorphic zircon grains within a sample of amphibolite (96/543) from Pen Olver which suggest that a thermal event occurred at  $374 \pm 15$  Ma. Zircons in a pelite (96/546) produced several age populations at ~390 Ma, ~425 Ma, 450-500 Ma, ~750 Ma and >1100 Ma. The youngest age, ~390 Ma, may represent a thermal event related metamorphism and development of the sub-horizontal fabrics. The zircons in the pelite are small and difficult to analyse (Nutman, A., *pers comm*, 1998) and therefore these age populations are difficult to interpret. The presence of older inherited grains suggests that this pelite layer is a sedimentary layer, possibly of volcanic origin, which contains detritus from older basement rocks.

The foliation in the amphibolites strikes NE-SW and dips at a low-angle towards the NE or SW, mineral lineations plunge down-dips towards the NW or SE. Shear-sense indicators, which include asymmetric porphyroclast shapes and shear-band fabrics, consistently suggest a top-to-the-NW displacement. At many localities, isoclinal folds are observed, the fold hinges being parallel to the mineral lineations.

The contact relationships between peridotite and amphibolite are well exposed along the east coast of the Lizard at Kildown Point (Figures 3.45 & 3.46), the Devils Frying-pan (Figures 3.47 & 3.48) and The Balk (Figures 3.49 & 3.50). Detailed structural logging of the contacts at these localities has revealed the presence of shear-zones and faults that were developed during a complex sequence of deformational

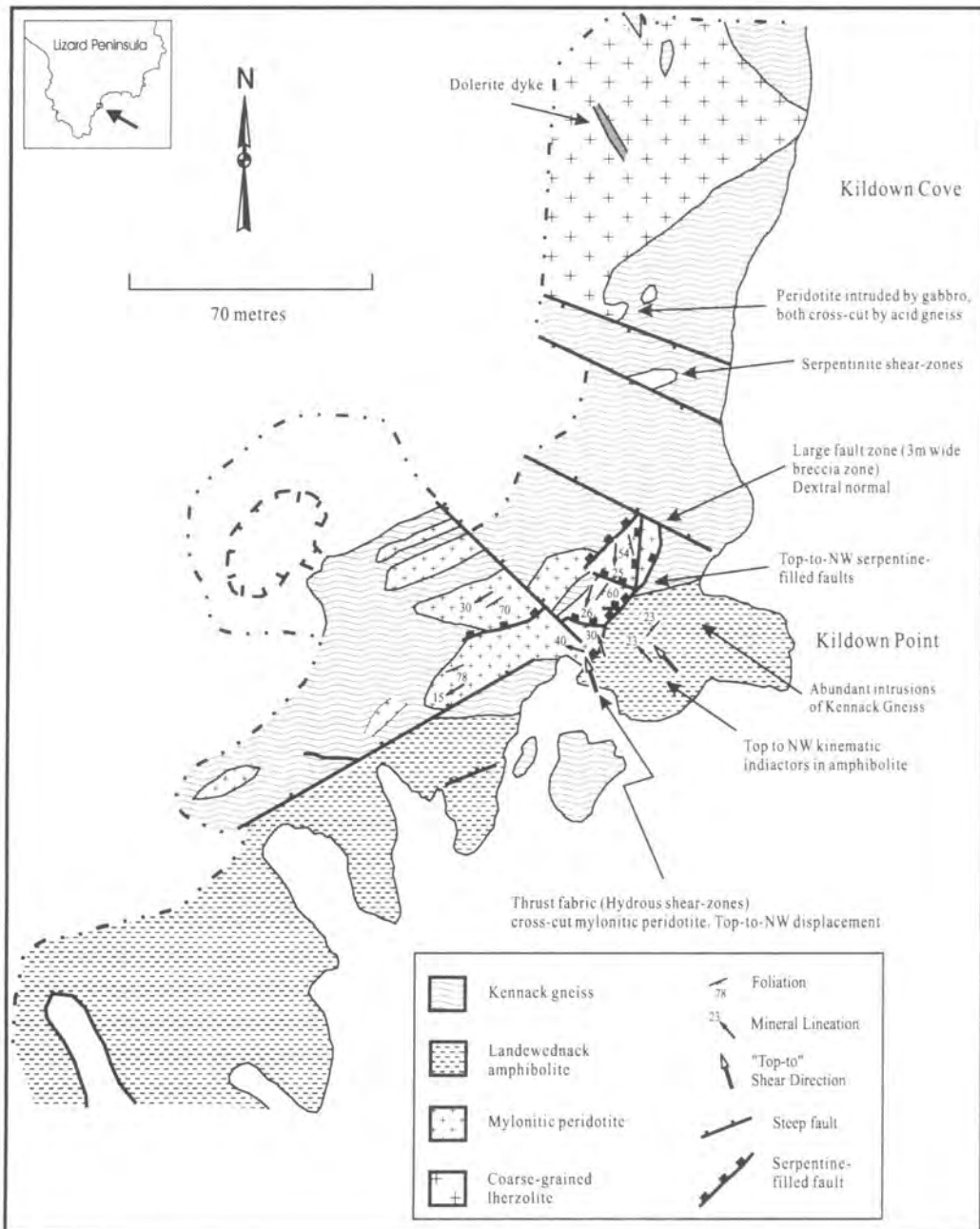


**Figure 3.45.** Geological map of the Kildown Point area, displaying the ductile thrust contact between peridotite and Landwednack amphibolite. Serpentine-filled faults related to reactivation of the thrust contact are also shown.

events associated with the emplacement of the Lizard Ophiolite Complex (Figures 3.46, 3.48 & 3.50). At these contacts coarse-grained lherzolite and mylonitic amphibole-bearing peridotite structurally overlies Landwednack amphibolite. An early phase of ductile deformation is responsible for the generation of hydrous shear-zones (Section 3.53), which cross-cut pre-existing sub-vertical fabrics in peridotites. These shear-

zones strike NE-SW and dip at a low-angle ( $12^{\circ}$  to  $62^{\circ}$ ) towards the NW. Elongate hornblende and relict augen of orthopyroxene define mineral lineations in these shear-

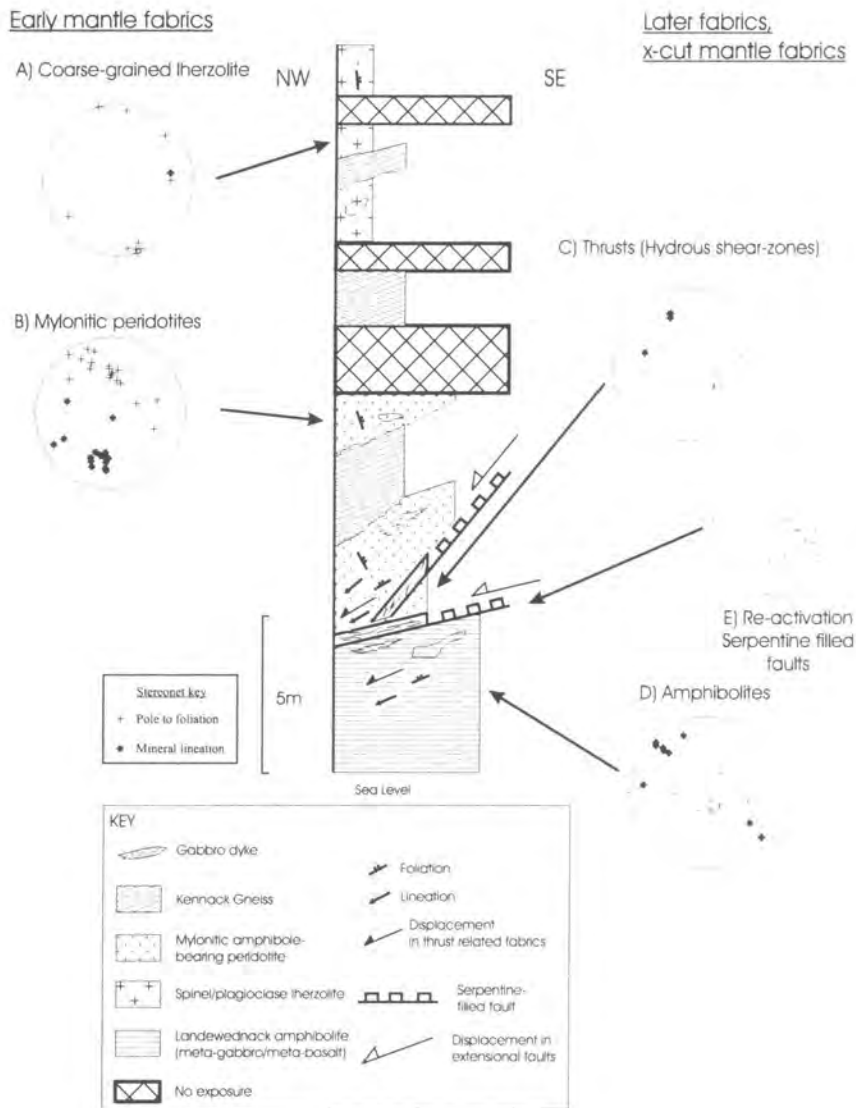


**Figure 3.46.** Structural log across the thrust contact between peridotite and Landwednack amphibolite at Kildown Point. Serpentine-filled faults related to reactivation of the thrust contact are also shown. Stereonets display structural data for the different units and tectonic contacts.

-zones which plunge down-dip. The shear-zones have the appearance of a schistose rock, and are composed of hornblende, chlorite and serpentine (Figure 5.51). At The Balk quarry, an anastomosing network of these shear-zones is exposed. The shear zones have a mylonitic fabric which wraps around phacoids of peridotite and gabbro. Shape fabrics within these shear-zones at all of the localities indicate a top-to-the-NW, apparent extensional sense of displacement.



The shear-zones are gradational into the underlying Landwednack amphibolite. The fabric in the amphibolite is sub-parallel to the shear-zones, with foliations striking NE-SW and dipping at a low-angle ( $8^{\circ}$  to  $50^{\circ}$ ) to the NW, and mineral stretching

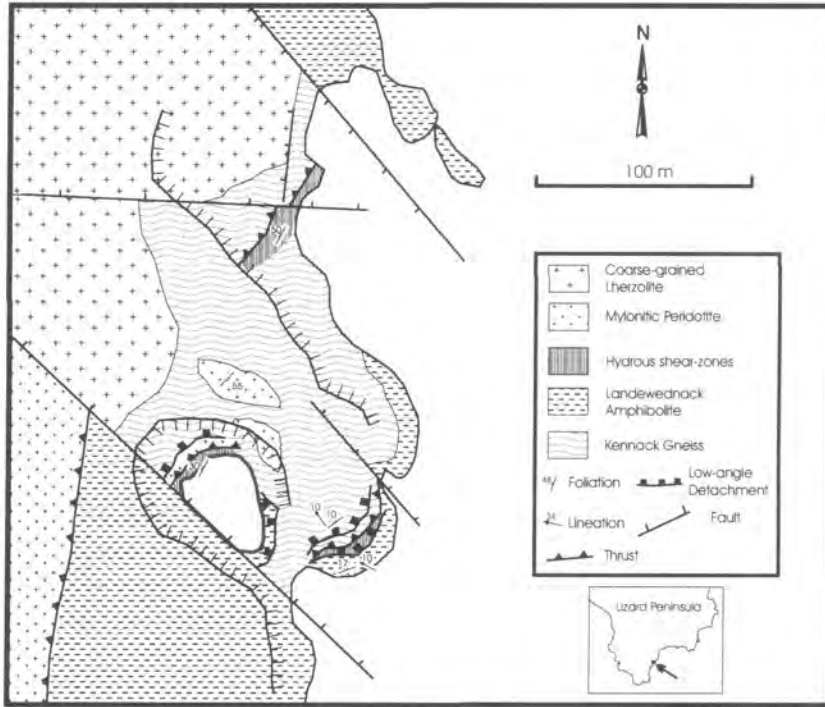


**Figure 3.47.** Geological map of the Devils Frying-pan area, near Cadgwith. Thrust contacts between peridotite and Landwednack amphibolite are shown, and low-angle serpentine-filled faults related to reactivation of thrust contacts.

lineations plunge down-dip. Shear bands and shape fabrics in the amphibolite (Figure 5.52) are consistent with a top-to-the-NW, apparent extensional sense of shear.

Banded felsic and mafic Kennack Gneiss intrusions cross-cut the fabric in the peridotites, hydrous shear-zones and amphibolites. The fabric in the Kennack Gneiss is sub-parallel to the fabric in the amphibolites and contact shear-zone. Foliations strike NE-SW and dip at a low-angle ( $1^{\circ}$  to  $18^{\circ}$ ) towards the NW and mineral lineations plunge down dip. The banded Gneiss is folded, and tight folds have an axes which plunges at a low-angle ( $5^{\circ}$  to  $18^{\circ}$ ) predominantly towards the NW.

Later reactivation of high-temperature ductile contacts by cm-scale, foliated, light-green serpentinite-filled fault-zones is ubiquitous at these contact zones (Figures 3.53 & 3.54). These faults enclose phacoids of mylonitic peridotite, amphibolite and Kennack Gneiss. The faults strike NE-SW and dip at a low-angle ( $13^{\circ}$  to  $52^{\circ}$ ) to the NW, and long axes of the phacoids plunge towards the NW. S-C fabrics and



asymmetric phacoids within the serpentinite-filled fault zones indicate a top-to-the-NW, apparent extensional displacement. At Kildown Point, the largest of the serpentinite-filled faults forms a basal detachment at the contact between amphibolite and peridotite (Figure 5.54). In the outcrops of peridotite above this detachment, smaller

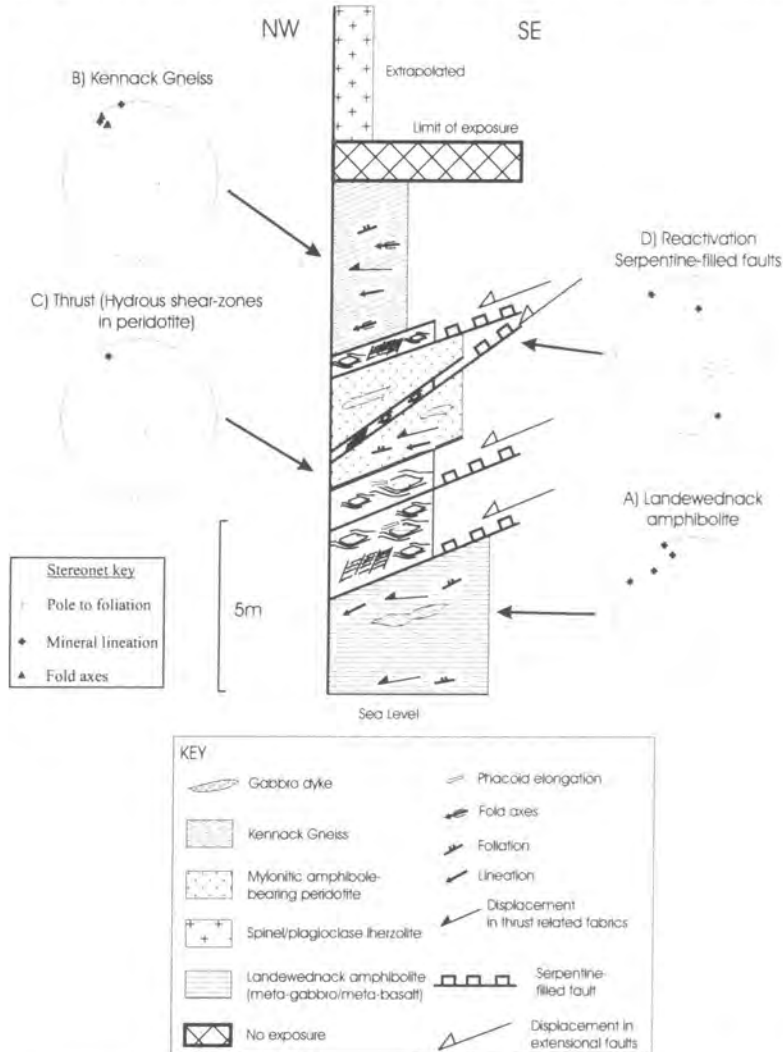


**Figure 3.48.** Structural log across the thrust contact between peridotite and Landwednack amphibolite at the Devils Frying-pan. Serpentine-filled faults related to reactivation of the thrust contact are also shown. Stereonets display structural data for the different units and tectonic contacts.

serpentinite-filled faults which are often steeply dipping are linked to the basal detachment. Reactivation of the thrust contacts was facilitated by displacement along serpentinite-filled faults and probably occurred in response to late stage collapse of the entire nappe pile (Jones, 1997). The apparently extensional nature of these thrust contacts may be explained by fault-block rotations associated with later brittle faults (Section 3.5.6).

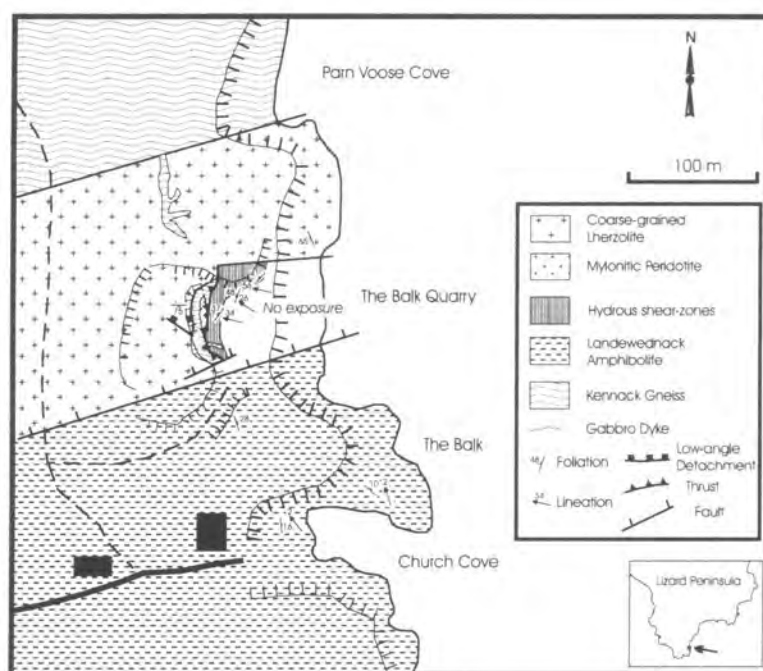


**Figure 3.49.** Geological map of the Balk Quarry area, near Church Cove. The thrust contact between peridotite and Landewednack amphibolite is shown and serpentine-filled faults related to reactivation of the thrust contact.

In summary, at all of these localities between Polbrearn Cove and Kildown Point the tectonic contacts, early and late, between these rocks consistently strike NE-SW and dip to the NW ( $4^{\circ}$  to  $60^{\circ}$ E) and structures indicate NW-directed, apparently extensional displacement. Intrusions of mixed felsic and mafic components of Kennack Gneiss are invariably associated with these contacts.

### 3.5.2.c. The Predannack Borehole (GR 6901 1634; Figure 3.55)

A borehole drilled by the British Geological Survey on Predannack Down (GR 6901 1634) (Institute of Geological Sciences, 1978) (Figure 3.3) encountered a contact between peridotite and amphibolite (Figure 3.55). The borehole was terminated at 326 m, and was predominantly drilled through mylonitic peridotite (plagioclase and amphibole-bearing) with a steeply dipping foliation. At a depth of 300 m a sub-horizontal contact between mylonitic peridotite and underlying amphibolite is seen. The discovery of this contact is highly significant as it shows that the peridotite has a sheet-like form, at least 300m thick, and is not a plug-like intrusion as suggested by previous authors (Flett and Hill, 1912; Green, 1964a). The amphibolites below this contact zone have a character that is very similar to the Landewednack amphibolites

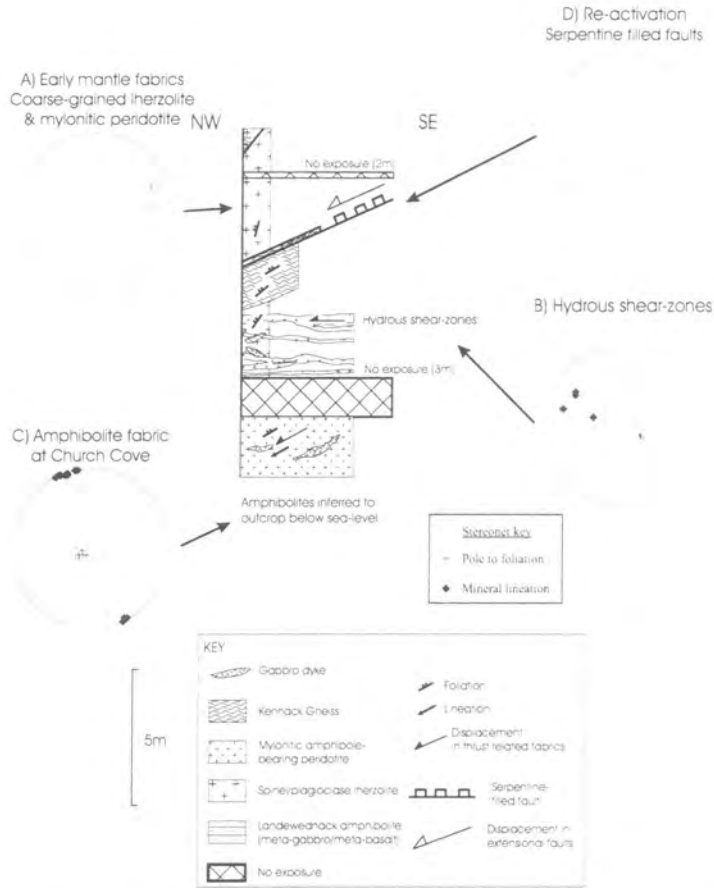


**Figure 3.50.** Structural log across the thrust contact between peridotite and Landwednack amphibolite at the Balk Quarry locality. Serpentine-filled faults related to reactivation of the thrust contact are also shown. Stereonets display structural data for the different units and tectonic contacts.

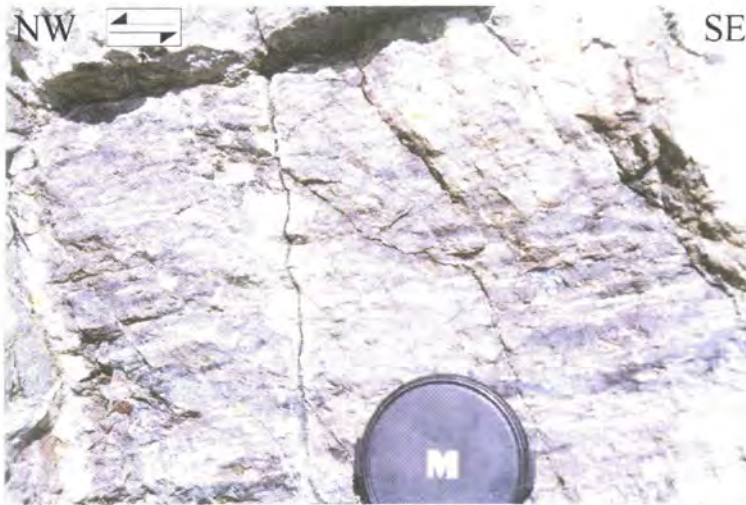


**Figure 3.51.** Hydrous shear-zones (pale) re-working mylonitic peridotite at the thrust contact at The Balk. Orthopyroxene porphyroclasts are stretched-out in these shear-zones. Asymmetric porphyroclast systems developed in pyroxene indicate top-to-the-NW shear.





**Figure 3.52.** Landewednack amphibolites near Cadgwith. Shear-bands cross-cut an earlier steeper fabric and indicate a top-to-the-NW sense of shear.



**Figure 3.53.** Serpentine-filled faults (marked by white line) reactivate the thrust contact between peridotite (P) and amphibolite (A) at the Devils Frying-pan (Figure 3.48). Note the interbanded felsic (pink) and mafic (dark) Kennack Gneiss at the top of the exposure.



**Figure 3.54.** Serpentine-filled fault (marked by white line) forming a basal detachment at the contact between Landwednack amphibolite (A) and mylonitic peridotite (P) at Kildown Point. A steeply dipping serpentine-filled fault is also shown.

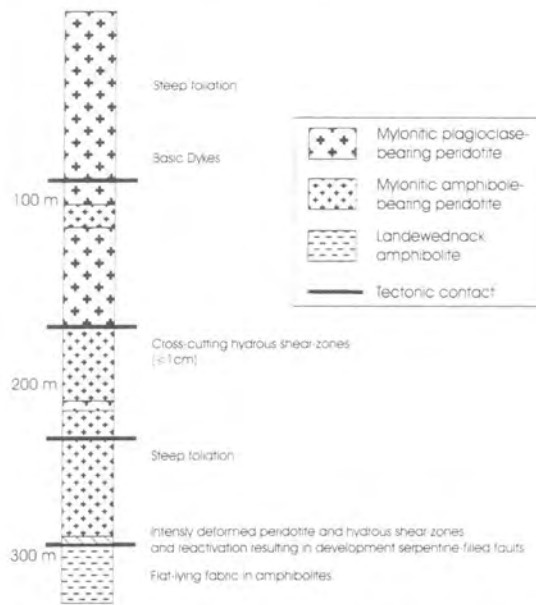


**Figure 3.55.** Borehole log based on core from the Predannack Borehole. The thrust contact between peridotite and Lanwednack amphibolite is shown.

exposed on the east coast of the Lizard, and the localities discussed above. The foliation in the amphibolites is sub-horizontal. The contact between the peridotite and amphibolite is complex and is extensively veined by talc and carbonate. In the mylonitic peridotite above the contact zone, there are several sub-horizontal, cross-cutting, hydrous shear-zones. These shear-zones are several centimetres in width and are composed of pale-coloured hornblende and chlorite. The contact zone itself is a zone of serpentine-filled faults, which have reactivated the hydrous shear-zones that



formed the original contact between the mylonitic peridotite and amphibolite. Phacoids of peridotite within the serpentinite-filled fault zone, contain hydrous shear-zones. Shear-sense indicators (Shear bands and asymmetric porphyroclasts) are preserved in these shear-zones, but they cannot be orientated in this borehole core.

### 3.5.3. Emplacement-related fabrics in the Lizard peridotites

Thin (<30cm) hydrous shear-zones cross-cut the sub-vertical fabric of the peridotite (Figure 3.56) at many outcrops of coarse-grained lherzolite, mylonitic plagioclase-bearing or mylonitic amphibole-bearing peridotite throughout the Lizard Ophiolite

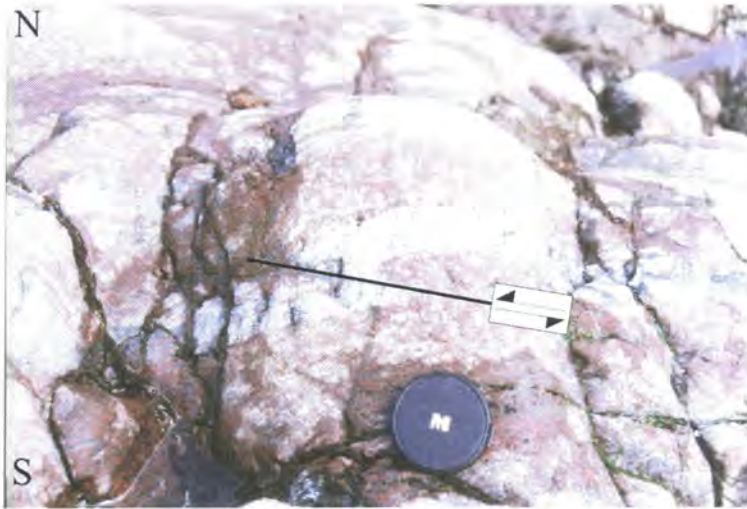


**Figure 3.56.** Plan view looking down on a hydrous shear-zone (marked by black line) cross-cutting coarse-grained lherzolite and pyroxene-rich layers (pale) at Pentreath Beach. The rotation of the pyroxene-rich layer into the shear-zone indicates a top-to-the-NW, apparently extensional displacement.

Complex. These shear-zones have an anastomosing form that wraps around relict phacoids of peridotite. The shear-zones are composed of pale-coloured hornblende and chlorite, which replace the original peridotite mineral assemblage. At Pentreath Beach (GR 6923 1285), spectacular examples of these hydrous shear-zones are observed in steeply foliated coarse-grained lherzolite, which is exposed in the cliff and on the wave cut platform. Pyroxene rich layers in                      rotated into the shear-zone (Figure 3.56) indicating a top-to-the-NW, apparent extensional displacement.



Throughout the Lizard Ophiolite Complex, the later shear-zones are dominantly sub-horizontal, with a foliation which strikes NW-SE to NE-SW, and dips to the NW to NE. Mineral lineations, defined by aligned hornblende prisms, plunge at low angles

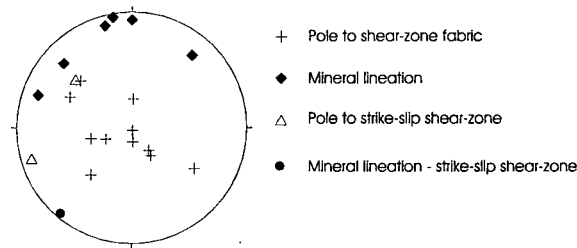


**Figure 3.57.** Lower hemisphere stereographic projections display structural data for the hydrous shear-zones that cross-cut peridotite fabrics. Poles to shear-zone fabric and plunges of mineral lineations for sub-horizontal and strike-slip shear-zones are included.

(4° to 20°) towards the NW to NE, NNW plunges predominantly (Figure 3.57). Drag of the original peridotite fabric or pyroxene-rich layers into these shear-zones and shape fabrics show that top-to-the-NNW and top-to-the-SSE occur, however, top-to-the-NNW and apparently extensional displacements are dominant. More rarely, sub-vertical orientated shear-zones (<30 cm) occur (Carleon Cove (GR 7279 1563); Mullion Cliff (GR 6712 1750)) and sub-horizontal lineations within these shear-zones suggest a strike-slip displacement. In the strike-slip shear-zones examined in the field (Figure 3.58), sinistral displacements were indicated by the drag of the original peridotite fabric into the shear-zones.

The sub-horizontal shear-zones have similar mineral assemblages and are structurally identical to shear-zones that occur in the contact zones between peridotite and amphibolite on the east coast of the Lizard Ophiolite Complex (Section 3.5.2), and are hence interpreted to be contemporaneous.

#### **3.5.4. Magmatism associated with emplacement**

The Kennack Gneiss has been introduced in Chapter 2 and briefly described in the previous section (3.5.2). U-Pb dating by SHRIMP analysis of igneous zircons within the granitic component of the Kennack Gneiss (96/ 517; 97/713 and 97/714) yielded ages of  $384 \pm 16$  Ma (Monazite –  $390 \pm 16$  Ma) and ca. 390 Ma, which are interpreted to represent the crystallisation of the igneous protolith. Inherited zircons yielded ages of 500-600 Ma and >1700 Ma, which suggests that the protolith may be derived from

melting of older basement rocks. In a study by Styles and Rundle (1984), an age of  $369 \pm 12$  was obtained for an felsic vein of the Kennack Gneiss using a whole-rock Rb-Sr isochron, which was interpreted to represent a metamorphic age. In a recent study, Sandeman *et al.* (1995) obtained  $^{40}\text{Ar}/^{39}\text{Ar}$  high-temperature plateau ages of  $366.1 \pm 4.2$ ,  $364.2 \pm 4.8$  and  $359.8 \pm 7.4$  Ma for hornblendes in two samples of mafic Kennack Gneiss and a sample of Landewednack amphibolite respectively. This data is consistent with the geochronology obtained during the present study and the field evidence that suggests that deformation of the Kennack Gneiss is contemporaneous with a phase of deformation in the Landewednack amphibolites.

The Kennack Gneiss is exposed extensively along the east coast of the Lizard, between Green Saddle (GR 7445 1657) and Parn Voose Cove (GR 7150 1305). On the west coast of the Lizard, outcrops of the Kennack Gneiss are limited to the coast section at Pentreath Beach (GR 6920 1290). There are also several large, poorly exposed areas of Kennack Gneiss which occur inland. Inland exposures of significance ( $>0.5 \text{ km}^2$ ) include an area 1.5 km NE of Penhale (GR 705 195), in the valley running south between Trenoon (GR 7072 1852) and Treal (GR 7174 1612), in the valley at Cadgwith (GR 717 149) and a large area between Kennack Sands (GR 7380 1670) and Gwendreath Farm (GR 7306 1696). Core from a borehole drilled by the I.G.S. (I.G.S., 1979) at Kennack Sands (Gr 7325 1647) has been examined during the course of this study and Kennack Gneiss is observed in the core interbanded with coarse-grained lherzolite to a depth of 150 m where drilling terminated. The borehole evidence demonstrates that the Kennack Gneiss is not a simple, localised zone of intrusions, but a more complex zone, at least 150 m thick. In the majority of outcrops of the Kennack Gneiss there are two rock types, a rock of granitic composition and a mafic rock, resembling amphibolite. The two different rocks occur as distinct intrusions, as homogenous bands in composite banded intrusions (Figure 3.59), and as mixed hybrid forms with a composition transitional between the granitic and mafic components. Along the coast, east of Kennack Sands and inland at Gwendreath Farm, there are several large intrusions that are composed entirely of the granitic component. The granitic rock is characteristically pink, medium-grained and often foliated. Hand-specimens of the granitic rock contain quartz, feldspar and minor biotite. The mafic component does not form large intrusions. The mafic rock is dark in colour, fine- to medium-grained and nearly always foliated, and distinct plagioclase xenocrysts are

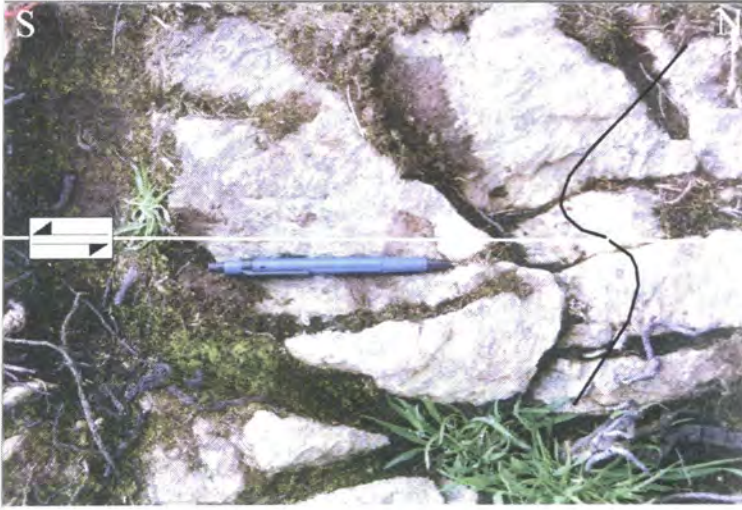


**Figure 5.58.** Plan view looking down on a sub-vertical hydrous shear-zone (marked by white line) cross-cutting the pre-existing fabric (marked by black line) in mylonitic amphibole-bearing peridotite. The sense of rotation of the pre-existing foliation into the shear-zone indicates sinistral displacement.



**Figure 3.59.** Plan view looking down on mixed intrusions of felsic (pale) and mafic (dark) Kennack Gneiss at Pentreath Beach. Note the folding, shearing and boundinage of the felsic component.

often observed. In hand specimen, the rock is composed predominantly of green amphibole, plagioclase and minor biotite, which distinguishes it from the Landewednack amphibolites discussed in previous sections (Section 3.5.2). The field-relationships suggest that the granitic component of the Gneiss intrudes the mafic component, and both rocks have been subsequently deformed, this interpretation is consistent with the detailed work of previous authors (Flett, 1912; Green, 1964c; Styles



and Rundle, 1984; Sandeman, 1988; Floyd *et al.*, 1993). The Kennack Gneiss therefore appears to represent a series of composite intrusions, with an earlier mafic phase and a later granitic component. These two intrusive phases were very close together.

The relationships between the Kennack Gneiss and the peridotite, gabbro, amphibolites can be observed in many localities on the east and west coasts of the Lizard. The gneiss clearly intrudes the peridotite and cross-cuts the steep fabric. It clearly intrudes the gabbro mylonites at Carrick Luz (GR 7546 1655) and gabbro bodies at Parn Voose Cove. Granite veins at Polpeor Cove (GR 7000 1150) cross-cut the OLHS and may be part of the same intrusive suite as the Kennack Gneiss. The gneiss intrudes Landewednack amphibolites, but at Cadgwith (GR 7215 1450) and Kildown Point (GR 7270 1471), both lithologies preserve sub-horizontal fabrics (Section 3.5.2) and thus a phase of deformation appears to post-date the intrusion of the gneiss. This fabric is interpreted to have developed during top-to-the-NW thrusting of mantle over amphibolite, and therefore the field-relationships at Cadgwith and Kildown Point suggest that the Kennack Gneiss was intruded during this tectonic event (Section 3.5.2). This interpretation is consistent with the available geochronological evidence.

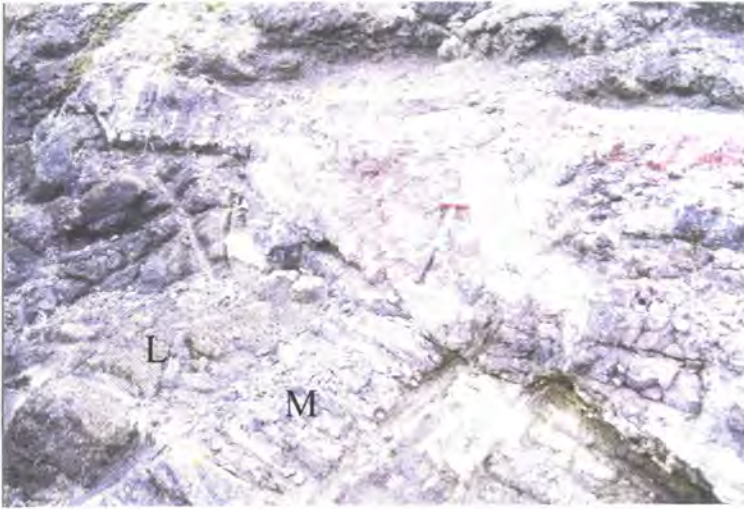


**Figure 3.60.** Vertical mafic dyke (M) cross-cutting coarse-grained lherzolite (L) and itself truncated at the margin of low-angle intrusion of mixed felsic (pink) and mafic (dark) Kennack Gneiss at Enys Head. The field relationships can be interpreted in two ways (see text).

The field-relationships between the Kennack Gneiss and the NW-SE trending mafic dykes (Section 3.4.3) are less clear. In some outcrops, for example near Green Saddle (GR 7446 1660), the dykes have the form of feeders to mafic sills within the Kennack

Gneiss, but in outcrops at Kennack Sands, a mafic dyke is cross-cut by banded Gneiss and mafic dykes later than the Gneiss. An outcrop at Enys Head (GR 7289 1494), which demonstrates a relationship between the Kennack Gneiss and a mafic dyke, has been studied in detail (Figure 3.60). At this outcrop a 75cm wide, NW-SE trending near-vertical mafic dyke intrudes peridotite and is truncated by a body of banded gneiss. The lithological banding in the gneiss and foliation strike NE-SW and dip at a low-angle ( $\sim 6^\circ$ ) towards the NW and mineral lineations plunge down-dip. The mafic dyke is smeared/sheared-out at the base of this banded gneiss intrusion, and forms a lobate protrusion, 1.5 metres long, which stretches towards the west. Thin 1cm veins of granitic gneiss have subsequently intruded this protrusion. The mafic dyke is not observed to continue in outcrops of peridotite above the sub-horizontal banded gneiss body. The field-relationships at this locality can be interpreted in two ways:

- The mafic dyke forms a vertical feeder to the banded gneiss, where it feeds sub-horizontal sills of mafic gneiss intrusions, which have subsequently been sheared.
- Alternatively, the intrusion of the mafic dyke pre-dates the banded gneiss, and was subsequently smeared/sheared-out along the base of this composite intrusion.

The second interpretation would imply that there has been extensive displacement during the intrusion of the gneiss, because the mafic dyke is not observed outcrops above the intrusion.

The serpentine-filled faults related to re-activation of thrust contacts between peridotite and amphibolite (Section 3.5.2) and later steep brittle-faults (Section 3.5.5) clearly cross-cut and therefore post-date the intrusion of the Kennack Gneiss.

### **3.5.5. Later magmatic events**

At many localities throughout the Lizard Ophiolite Complex there are small ( $< 5\text{m}$ ) granite intrusions; e.g. Ryniau (GR 6644 1730), Georges Cove (GR 6695 1511), Pengersick (GR 6694 1480), Gew Graze (GR 6760 1441) and Kynance Cove (GR 6838 1329) and Porthallow Cove (GR 7990 2315). The granites are generally pink, coarse-grained and composed of quartz and feldspar, with minor mica. These granites are rarely foliated and do not show any association with mafic rocks, and are therefore regarded to be distinct from the granitic rocks that comprise in-part the Kennack Gneiss. New U-Pb SHRIMP dating of monazites with an igneous morphology from a

granite at Ryniau yielded an age of ca. 360 Ma. This date clearly reveals that these granites are unrelated to the granitic component of the Kennack Gneiss, which was intruded ca. 384 – 390 Ma (Section 3.5.4). These granites represent the final phase of igneous activity associated with the Lizard Ophiolite Complex. The granites are cross-cut by later high angle brittle extensional faults (see below), which often occur in association with the granites, possibly suggesting that they re-activate the same weakness that the granite sheets have exploited. The geochronological evidence presented above demonstrates that these granites are unrelated to the granites of the Cornubian Batholith, which were emplaced ca. 274 – 293 Ma (Chen *et al.*, 1993).

### 3.5.6. High angle brittle extensional faulting

The tectonic-stratigraphy of the Lizard Ophiolite Complex is strongly influenced by displacements along high angle, brittle extensional faults. The faults post-date all of the tectonic and magmatic events discussed above, and therefore represent one of the youngest deformation events to effect the Lizard Ophiolite Complex. Detailed mapping of faults throughout the Lizard Ophiolite Complex in the course of the present study has revealed that there are two dominant sets of high angle brittle extensional faults (Figure 3.61) in accordance with the findings of Alexander and Shail (1996) and Power

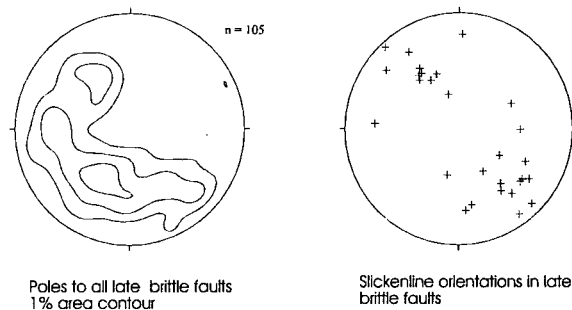


**Figure 3.61.** Lower hemisphere stereographic projections for structural data from brittle faults exposed in the Lizard complex. 1% area contour for the poles to brittle faults and plunges of slickenlines are displayed.

*et al.* (1996). The first set strike NE-SW to NNE-WSW and dip steeply ( $20^\circ$  to  $90^\circ$ ) towards the north and south. Slickenlines on fault planes generally have a high pitch. This set of faults occasionally reactivates the serpentinite-filled fault zones described above. The second set of faults, which usually cross-cut the first set, strike N-S to NNW-SSE and dip steeply east and west. Slickenlines within this second set of fault



predominantly have a low pitch, which suggests strike-slip displacement. The association of these two fault sets therefore suggests that the second set represent transfers (Alexander and Shail, 1996; Power *et al.*, 1996).

The Lizard Boundary Fault, which outcrops at Porthallow (GR 7966 2320) in the north-east of the Lizard, and Polurrian Cove (GR 6692 1884) in the west forms the contact between the high-grade metamorphic rocks of the Lizard Ophiolite Complex and the lower-grade Gramscatho Group metasediments to the north. This fault is an ENE-WSW striking high angle extensional fault, and it is probably related to the reactivation and extensional cut-out of an earlier thrust fault (Flett, 1946; Alexander and Shail, 1996; Power *et al.*, 1996). Other ENE-WSW striking high angle extensional faults also have a strong influence on the tectonic-stratigraphy of the Lizard Ophiolite Complex. An unexposed fault, at Porthoustock (GR 8065 2183), forms the contact between the Porthoustock amphibolites to the north and the Crousa gabbro to the south. Faults at Pentreath Beach (GR 6943 1267) and The Balk (GR 7153 1282), in the south of the Lizard, form the contact between peridotite in the hangingwall, and Landewednack amphibolite in the footwall. Major and stratigraphically significant ENE-WSW striking faults also occur at Georges Cove (GR 6703 1527), Mullion Cove (GR 6672 1778) and Porthkerris Cove (GR 8056 2273). The second set of NNW-SSE striking faults also have a major influence on the stratigraphy of the Lizard Ophiolite Complex, important faults occur at Ryniau (GR 6640 1745), Georges Cove (GR 6703 1527) and Kynance Cove (GR 6864 1325).

A further fault set, which<sup>is</sup> relatively rare, strikes E-W to WNW-ESE and often show strike-slip displacements. A major fault belonging to this set outcrops at Gew Graze (GR 6760 1439) on the west coast of the Lizard, and a fault at Polbarrow (GR 7180 1377) on the east coast of the Lizard is believed to be the same fault. The fault at Gew Graze strikes E-W and dips steeply (50°) towards the south. Slickenlines in this fault zone have a both a high and low pitch, which suggests that there has been reactivation. The displacement is therefore both dip-slip normal and strike-slip, both sinistral and dextral shear-sense is observed.

Fault block rotations produced by displacement along these different fault sets may explain the apparently extensional nature of the top-to-the-NW emplacement-related thrusts on the east coast of the Lizard (Section 3.5.2).

### **3.5.7. Summary**

- The basement rocks, ultramafic rocks and associated gabbroic veins/Traboe cumulates and Landewednack amphibolites, which represent different lithological units are all cross-cut by pervasive sub-horizontal shear-zones that show top-to-the-NW displacements.
- The different units are also juxtaposed along sub-horizontal thrust contacts, which also show top-to-the-NW displacements and are therefore contemporaneous with the shear-zones.
- The basement rocks comprise the lowermost structural unit, Landewednack amphibolites are thrust over these, and mantle rock is emplaced over the amphibolite.
- Magmatism contemporaneous with emplacement of the mantle rocks resulted in the intrusion of mixed suite granitic and mafic magmas (Kennack Gneiss), in close association with thrust contacts.
- The metamorphism of the amphibolites (ca 374 – 392 Ma), associated with thrusting and the intrusion of the granitic component of the Kennack Gneiss (ca 384 – 390 Ma) are contemporaneous having occurred in the mid-early Devonian.
- These thrust contacts always show evidence for extensive re-activation, involving the development of apparently extensional serpentine-filled fault zones, possibly related to late stage collapse of the entire nappe pile
- Fault-block rotation associated with displacement along later high-angle brittle faulting may be responsible for the present-day, apparent extensional geometry of emplacement-related thrusts.

### 3.6. Summary of field and geochronological evidence

In the previous sections, field and geochronological evidence has been presented that establishes a tectono-magmatic evolution for the different units of the Lizard Ophiolite Complex. A summary of these events is presented below:

- An early association of supracrustal rocks and granitic rocks, which includes the Man of War Gneiss and Old Lizard Head Series and associated intrusions, represent basement associated with the Lizard Ophiolite Complex. Metasedimentary and metavolcanic rocks known as the Old Lizard Head Series preserve evidence for an early fabric in areas of low-strain (Jones, 1997), which pre-dates emplacement related fabrics (see below). A granitic sill cross-cuts this early fabric and a primary igneous age of ca.490 Ma for this rock has been obtained by U-Pb SHRIMP analysis of zircon (Appendix A). An igneous protolith crystallisation age of  $499 \pm 8/-3$  Ma has also been obtained by U-Pb dating of zircon (Sandeman *et al.*, 1997) of a series of deformed gabbro to tonalite rocks, known as the Man of War Gneiss which outcrop on rocks and reefs south of Lizard Point.
- Early (middle Devonian?), deformation of a coarse-grained lherzolite protolith in upper mantle produced coarse-grained porphyroclastic lherzolites and mylonitic peridotites.
- Gabbroic veins and ultramafic and mafic Traboe cumulates associated with the peridotites represent the deformed equivalent of mafic/ultramafic cumulate rocks and oceanic crust associated with the mantle peridotites. The development of fabrics in the peridotite, and ultramafic and mafic rocks, occurred prior to the intrusion of the Crousa gabbro, but the available field, geochemical (Chapter 6) and geochronological evidence suggest that they are broadly associated and related by a contemporaneous phase of oceanic lithosphere construction. The development of the fabric in mafic Traboe cumulates at Porthkerris has been constrained to an age of  $397 \pm 2$  Ma by U-Pb dating of zircon in a syn-tectonic granite vein (Clark *et al.*, 1998b).

Construction of a second generation oceanic crust in the early to middle Devonian has been constrained by the intrusion of the Crousa gabbro. The gabbro is

believed to have crystallised during the formation of ocean crust and an Sm-Nd combined mineral and whole-rock isochron has yielded an age of  $375 \pm 34$  Ma (Davies, 1984). The Crousa gabbro and Porthoustock amphibolites have been deformed by a series of ridge-parallel ductile shear-zones during ductile extension of the lower oceanic crust in a slow-spreading ridge-axis environment (Gibbons & Thompson, 1991; Roberts *et al.*, 1993; Hopkinson & Roberts, 1995).

- Later deformation and emplacement of the Ordovician basement rocks and Devonian rocks of the Lizard Ophiolite Complex has been constrained to occur during the middle to late Devonian by U-Pb SHRIMP dating of metamorphic zircons within amphibolites. This prolonged tectonic episode was accompanied by the development of low-angle shear-zones and top-to-the-NW thrusting within the ocean lithosphere rocks (Landwednack amphibolites) and, finally, mantle decoupling and emplacement over the previously accreted units (Jones, 1997). Magmatism contemporaneous with emplacement includes the intrusion of a complex interbanded suite of felsic and mafic rocks, known as the Kennack Gneiss, in close association with thrust contacts. U-Pb SHRIMP dating of zircons within the granitic component of the Kennack Gneiss yielded ages of  $384 \pm 16$  Ma and ca. 390 Ma, which are interpreted to represent the crystallisation of the igneous protolith. Later reactivation of thrust contacts is identified by the presence of serpentinite-filled fault zones. The apparently extensional nature of the emplacement-related thrust contacts may be explained by fault block rotation associated with later high-angle brittle faulting.

A late phase of magmatism involved the intrusion of minor granites, and U-Pb SHRIMP dating of monazites with an igneous morphology within one of the granites yielded an age of ca. 360 Ma.

Finally, high angle brittle extensional faulting, results in the reactivation of the Lizard Boundary Fault (Alexander and Shail, 1996; Power *et al.*, 1996) and dismemberment of the Lizard Ophiolite Complex.

---

## CHAPTER FOUR

### MICROSTRUCTURES OF ROCKS FROM THE LIZARD OPHIOLITE COMPLEX

---

---

#### 4.1. Introduction

---

In the previous chapter (Chapter 3) a structural and magmatic evolution of the Lizard Ophiolite Complex was proposed based on field evidence, in addition to new and existing geochronological constraints. The aim of this chapter is to: (a) characterise the different lithologies on the basis of microstructure, (b) correlate the microstructural characteristics and mineralogical chronology with the field evidence and geochronological constraints, (c) constrain the conditions during deformation accompanying the evolution of the Lizard peridotites, and (d) use the field, geochronological and microstructural constraints as a basis for the investigation of the geochemical properties of the different lithologies (Chapters 5 & 6).

This chapter is sub-divided into descriptions of microstructures in three main lithological associations, namely: the *Ordovician basement rocks*, the *Lizard peridotites*, and finally the *Lizard oceanic crust and cumulate rocks*. Discussions of the microstructural characteristics of each lithological unit are sub-divided into a mineralogical chronology, including primary relict and later metamorphic assemblages.

---

#### 4.2. Ordovician basement rocks

---

In the previous chapter (Chapter 3) it was established that the metamorphic and igneous rocks which are exposed around the southerly peninsula of the Lizard are Ordovician in age and are thus older and unrelated to the younger Devonian rock of the Lizard Ophiolite Complex. In many previous publications (e.g. Green, 1964c; Floyd *et al.*, 1993; Jones, 1997), the Old Lizard Head Series (OLHS) rocks, which are included here in the Ordovician basement, were interpreted to be a transitional assemblage with the Landewednack amphibolites. This interpretation was based partly on the presence of amphibolites in the OLHS similar in composition and appearance to the Landewednack amphibolites. This interpretation is inconsistent with the new geochronological data and therefore the petrology of the OLHS amphibolites is described separately. A

petrological description of the samples of the Lizard Head Sill analysed in the geochronological dating program is also included.

#### **4.2.1. Old Lizard Head Series (amphibolites)**

Specimens of OLHS amphibolite that have been examined are described below; specimens of OLHS pelite and psammite have not been examined and are therefore not discussed. The purpose of examining the OLHS amphibolites is to compare and contrast petrographic characteristics with the Landewednack amphibolites. Two different types of amphibolite have been identified in the OLHS based on detailed field observation (Section 3.2.2): amphibolites interbanded pelite and psammite and, amphibolitised porphyritic basic sheets. The petrographic features of these rocks are discussed separately below.

##### **4.2.1.a. Amphibolites interbanded with pelite and psammite**

These rocks are fine-grained amphibolites with nematoblastic textures composed of green amphibole, plagioclase and opaque accessory minerals (Figure 4.1). Specimens of amphibolite commonly exhibit a foliation defined by aligned amphibole prisms and tight crenulation folding of this foliation on thin section scale. Green amphiboles are subhedral and have a characteristic elongate, acicular form, which contrasts with the form of amphiboles in the porphyritic basic sheets (see below) and the Landewednack amphibolite (Section 4.4.1.d). Anhedral plagioclase is always recrystallised to fine-grained aggregates, which define a foliation in the rock. The plagioclase usually shows breakdown to a secondary assemblage of saussurite. Opaque minerals often occur in elongate clusters, parallel to the fabric defined by the amphibole and plagioclase. Relict primary minerals or textures were not observed in the specimens of OLHS amphibolite examined.

##### **4.2.1.b. Porphyritic basic sheets**

These rocks can be distinguished from the OLHS amphibolites discussed above and the Landewednack amphibolites by the presence of conspicuous relict plagioclase phenocrysts. The form of the amphibole in these rocks is also different from the OLHS



amphibolites. The rocks are medium- to fine-grained and display porphyroclastic to nematoblastic textures (Figure 4.2). Subhedral, prismatic green amphiboles occur in aligned clusters that define a planar fabric in the rock. These clusters wrap around coarser-grained porphyroclasts of amphibole and relict plagioclase phenocrysts.

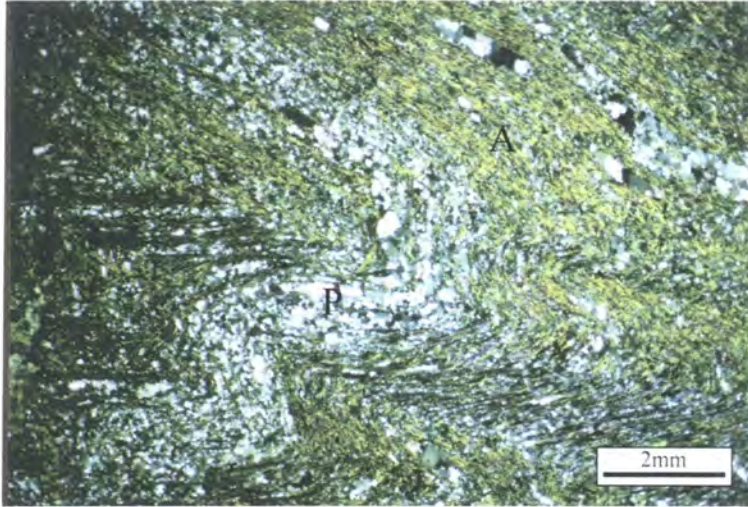


**Figure 4.1.** Folded foliation in OLHS amphibolite defined by aligned amphibole (A) and plagioclase (P) (Sample CAC184). *CPZ*

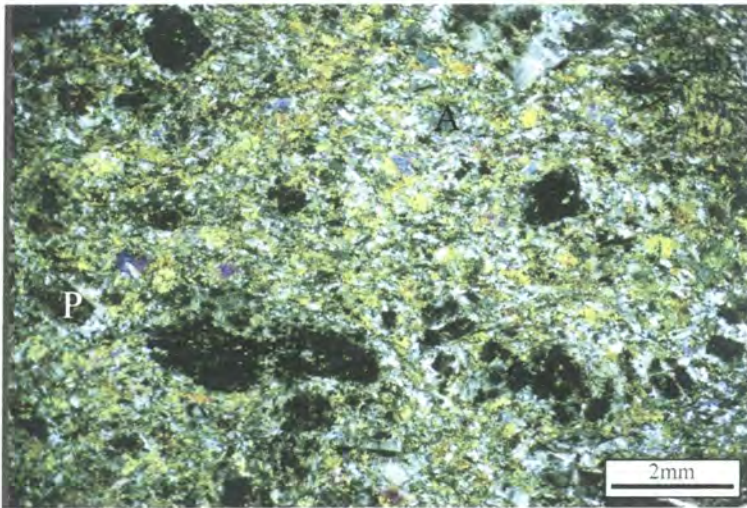


**Figure 4.2.** Relict porphyroclasts of plagioclase (P) and amphibole (A) enclosed by a matrix of aligned clusters of amphibole and plagioclase. (Sample CAC186). *CPZ*

Inclusions of opaque minerals are common in the green amphibole. Plagioclase occurs as coarse-grained, subhedral to euhedral phenocrysts and fine-grained, anhedral recrystallised grains, which occur as mantles around relict, coarse-grained plagioclase

cores. In more retrogressed samples, plagioclase phenocrysts are rare or not present and the rock is composed entirely of fine-grained green amphibole and plagioclase, with nematoblastic textures. In thin section these rocks resemble samples of retrogressed dolerite dykes.

#### 4.2.1.c. Lizard Head Sill

The Lizard Head Sill is a fine-grained trondhjemitic rock (Sandeman *et al.*, 1997) and is composed predominantly of anhedral grains of quartz and plagioclase, which have a granoblastic texture. The plagioclase is extensively altered to saussurite. The rock is foliated and this fabric is defined by aligned chlorite which pseudomorphs biotite (Figure 4.3). Subhedral titanite occurs as a common accessory mineral in addition to euhedral opaque minerals. The Lizard Head Sill rocks are therefore represented by a

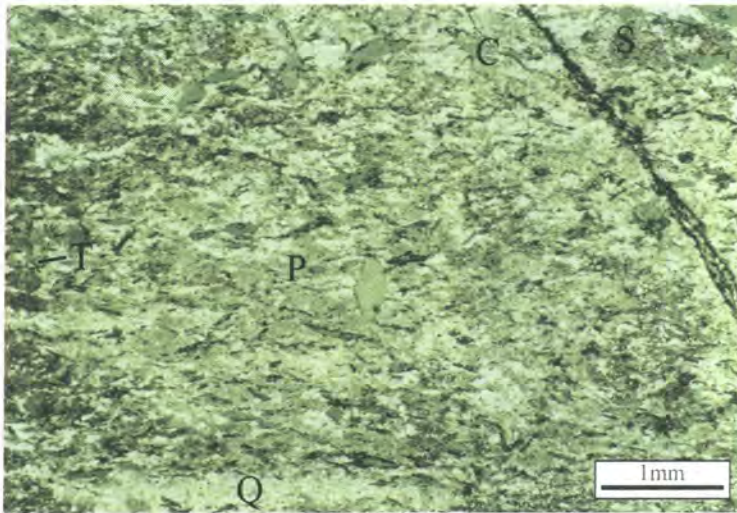


**Figure 4.3.** Aligned chlorite (C) pseudomorphs after biotite define a fabric, the matrix is composed of quartz (Q) and plagioclase (P). Plagioclase is altered to saussurite (S) and titanite is also present (T). (Sample MS1668). PPZ

deformed and retrogressed mineral assemblage and primary igneous textures are not preserved.

#### 4.2.2. Summary

- Two types of amphibolite are recognised in the OLHS and these have been distinguished in the field on the basis of macroscopic characteristics.
- The amphibolites that are interbanded with the OLHS psammities are distinguished from the amphibolitised porphyritic basic sheets by differences in the form of the amphibole and the presence of relict plagioclase phenocrysts in latter units.
- The form of the amphibole in the OLHS amphibolites and the relict plagioclase phenocrysts in these rocks also distinguishes them from the Landwednack amphibolites (Section 4.4.1.d).
- The Lizard Head Sill is trondhjemitic in composition (Sandeman *et al.*, 1997) and is therefore different to the rocks of the Man of War Gneiss, which are predominantly tonalitic or quartz dioritic in composition (Sandeman *et al.*, 1997).

---

#### 4.3. The Lizard peridotites

---

In the following sections the microstructure of the different peridotite types, associated ultramafic rocks and later cross-cutting shear zone structures are described. This discussion includes the introduction of a revised sub-division of the Lizard peridotites based in part on microstructural characteristics. Geographical information system (GIS) based map production is utilised to clarify the distribution of petrological variations in the peridotites. A study of the lattice preferred orientation (LPO) of olivine is applied to constrain the deformation mechanisms that operated during the microstructural evolution of the peridotites.

Field (Section 3.3) evidence suggested that the *spinel lherzolite* is the least deformed of the lizard peridotites and preserves evidence of a relict pre-deformation mineral assemblage. The *plagioclase lherzolite*, *mylonitic plagioclase-bearing peridotite* and *mylonitic amphibole-bearing peridotite* are transitional with the *spinel lherzolite* through a process of increasing strain, which is recognised in the field by a fabric evolution from coarse-grained peridotites with a moderately developed fabric to finer-grained mylonitic peridotites with a well developed fabric.

Other ultramafic rocks, which are associated with the peridotites, include dunite and websterite. The microstructure of these rocks and of feldspathic bands within the

mylonitic peridotite are discussed in the context of their relationships to the host peridotite assemblage.

Hydrous shear zones cross-cut the peridotite fabrics, websterite and feldspathic bands, and these shear zones are in turn re-worked by serpentine-filled faults. The microstructure of these shear zone structures is reviewed at the end of this section.

#### 4.3.1. New sub-division of the peridotites

The terminology classifying the Lizard peridotites has been revised (Table 4.1) to incorporate the results of new field, microstructural, geochemical work and the results of previous studies (Flett and Hill, 1912; Green, 1964a; Davies, 1984).

Revised Scheme	Flett and Hill (1912)	Green (1964a)	Davies (1984)
<b>Spinel lherzolite</b>	Bastite serpentine	Primary peridotite	Spinel Lherzolite
<b>Plagioclase lherzolite</b>	Bastite serpentine	Primary peridotite	Plagioclase Lherzolite (Undeformed)
<b>Mylonitic plagioclase-bearing peridotite</b>	Tremolite serpentine	Anhydrous recrystallised peridotite	Plagioclase Lherzolite (Deformed)
<b>Mylonitic Amphibole-bearing peridotite</b>	Tremolite serpentine	Hydrous recrystallised peridotite	Pargasite Harzburgite
<b>Feldspathic bands</b>	N/A	Mafic bands	Pargasite Lherzolite
<b>Dunite</b>	Chromite serpentine	Chromite serpentine	N/A

**Table 4.1.** Comparison of the terminology for the Lizard peridotites used in the revised scheme with the published terminology for the same rocks developed by previous workers.

The coarse-grained peridotites (spinel and plagioclase lherzolites and dunites) have been classified based on the modal abundance of olivine, clinopyroxene and orthopyroxene (Figure 4.4). This classification shows that the rocks (with the exception of the dunites) are predominantly lherzolitic in composition, although there is overlap into the harzburgite field. For the sake of convenience, the rocks will still be termed 'lherzolites', because the harzburgitic-types are of minor abundance and are often specific to particular circumstances (Section 4.3.4.c). Mylonitic peridotites are not included in this classification diagram because the fine-grained nature of these rocks makes it difficult to distinguish between olivine and pyroxenes.



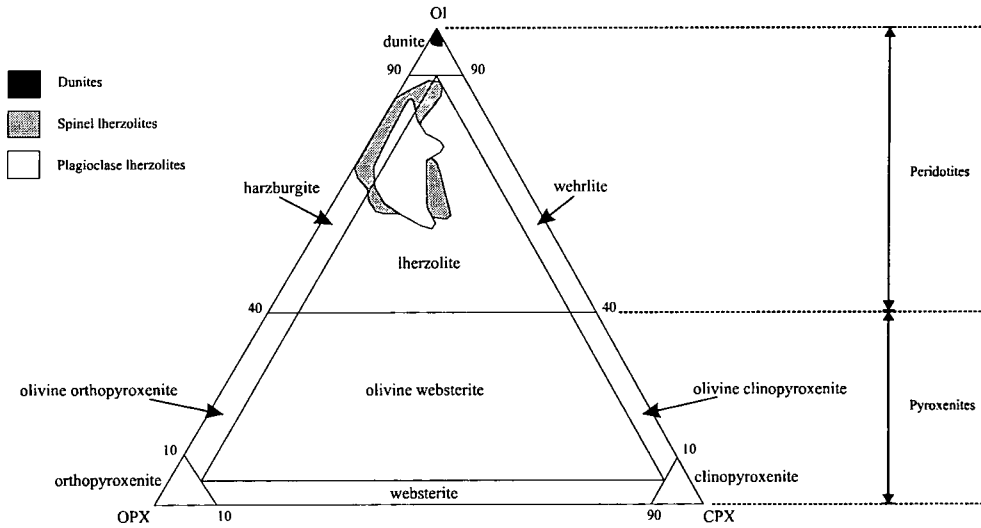


**Figure 4.4.** Terminology of ultramafic rocks based on the proportions of primary minerals (after Le Maitre *et al.*, 1989). The range of compositions for the coarse-grained peridotites is displayed.

#### 4.3.2. Serpentinisation

The effects of serpentinisation are widely preserved in the peridotites of the Lizard Ophiolite Complex and involve the heterogeneous alteration of the peridotites to lizardite, chrysotile and magnetite (Power *et al.*, 1997). Power *et al.* (1997) document a second phase of serpentinisation which is volumetrically minor, and represented by laterally persistent veins comprising lizardite and chrysotile (vein serpentine).

The variability and extent of the first, pervasive serpentinisation phase, is demonstrated by GIS analysis of the lizard peridotites (see section 4.3.6.g). The present study is primarily concerned with mineral assemblages and microstructures, which precede serpentinisation, but the form of the serpentine minerals provides an indication of the mineral they have replaced and its original abundance. Olivine is replaced by *mesh* textured serpentine dominated by a lizardite+/-chrysotile and/or antigorite assemblage (Selfridge, 1935) and *bladed-mat* textured serpentine consisting of an assemblage of antigorite+/-lizardite+/-chrysotile (Maltman, 1978). Orthopyroxene is pseudomorphed by the serpentine mineral *bastite*, which is composed of lizardite and chrysotile (Whittaker and Zussman, 1956). Spinel alters to *magnetite* and also *ferritic chromite*, which has a composition which is intermediate between relict chromite and magnetite (Bailey, 1997). Plagioclase is altered to a saussuritic assemblage of fine-grained masses of epidote and mica.

#### 4.3.3. Relict primary microstructures

Field evidence (Section 3.3) has revealed that the least deformed of the Lizard peridotites occur in the eastern part of the Lizard, between Kennack Sands (GR 7390 1665) and Coverack (GR 7824 1845). Rothstein (1977, 1981, 1988, 1994) shows that in several peridotite samples from this area, a high proportion of relict primary textures are preserved, particularly in a kilometre stretch of coastline between Downas Cove (GR 7640 1676) and Pedn Boar (GR 7715 1619). These relict textures occur within cm scale layers of dunitic, harzburgitic and lherzolitic varieties of the peridotite and include olivine micro-textures orientated at a steep angle to the layering, which developed at a high pressure and high temperature within the spinel lherzolite facies (Rothstein, 1994).

Although pristine, undeformed, 'primary' assemblage peridotite is never observed in the Lizard, relict, pre-deformation microstructures have been observed within deformed spinel lherzolites. The relict assemblage consists of olivine, orthopyroxene, clinopyroxene and spinel. Coarse-granular textures, if they were ever present, are not preserved. Orthopyroxene porphyroclasts often display relict microstructures by enclosing olivine crystals and, in many examples, the porphyroclasts are embayed by olivine (Figure 4.5). Similar textures in the Josephine peridotites described by Dick (1977) are related to the breakdown of orthopyroxene producing olivine and melt during partial melting. Clusters of orthopyroxene-clinopyroxene-spinel are not observed in even the least deformed peridotite samples. These microstructures are often characteristic of undeformed, coarse-granular peridotites, and are interpreted as being derived from garnet (Nicolas, 1986; Fabries *et al.*, 1991). Therefore, microstructural evidence alone suggests that the relict assemblage was developed within the spinel facies and not the garnet facies. However, it cannot be ruled out that later deformation may have obliterated the former presence of orthopyroxene-clinopyroxene-spinel clusters.

The microstructure of primary pyroxene-rich layers within the spinel lherzolite and dunite bodies associated with the spinel lherzolite has been studied in detail, but, no relict primary microstructure is present. Hence the microstructure of these rocks will be discussed in the following sections.



#### 4.3.4. Microstructures of coarse-grained lherzolitic peridotites

Spinel lherzolite is the least deformed of the Lizard peridotites and contains a high proportion of primary relict textures (see above). Plagioclase lherzolites are a metamorphic assemblage, transitional from the spinel lherzolite, in response to a decrease in pressure, and are distinguished by the appearance of plagioclase.

##### 4.3.4.a. Spinel lherzolite

The spinel lherzolite is composed of olivine, orthopyroxene, clinopyroxene and spinel in varying proportions (Section 4.3.6) and is generally medium-grained (500 - 1500  $\mu\text{m}$ ). The texture of the spinel lherzolite varies between fine- to coarse-grained porphyroclastic (Figure 4.6), which overprint the relict, primary microstructures (Rothstein, 1977; 1981; 1988; 1994) described in the preceding section.

The microstructure is characterised by the presence of a varied olivine grain size, which includes large crystals (average 500 - 2250  $\mu\text{m}$ ) and fine-grained (100 - 500  $\mu\text{m}$ ) recrystallised neoblasts. The large olivine crystals are often tabular and undulose extinction is observed. Occasionally a kink-like subgrain structure (Drury et al. 1990) is observed in large olivine crystals. The modal proportion of olivine in the spinel lherzolite varies between 50 - 80%.

Orthopyroxene is generally the coarsest mineral phase in the spinel lherzolite, forming medium- to coarse-grained anhedral porphyroclasts (500 - 4200  $\mu\text{m}$ ) which often have a tabular form. Clinopyroxene exsolution, either as fine lamellae or irregular, anhedral, blebs are nearly always present. Undulatory extinction, kinked clinopyroxene exsolution lamellae and curved kink bands, are observed in the orthopyroxene porphyroclasts, and these textural features show that the porphyroclasts are deformed. The margins of the porphyroclasts usually lack the exsolution lamellae typical of the cores, Davies (1983) suggests that this is related to significant re-equilibration of the porphyroclast rims. Porphyroclasts have fractured margins which are associated with rims or mantles of recrystallised orthopyroxene, and orthopyroxenes in the matrix also occur as fine-grained recrystallised grains (90 - 500  $\mu\text{m}$ ). The modal volume of orthopyroxene in the spinel lherzolite varies between 10 - 25 %.

Clinopyroxene rarely occurs as large porphyroclasts, usually it forms smaller

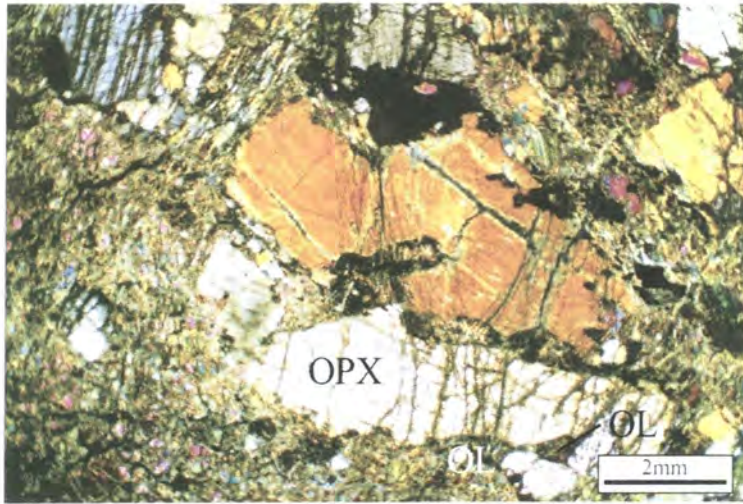


**Figure 4.5.** Relict orthopyroxene porphyroblast (OPX) is embayed by olivine (OL) and also encloses olivine. (Sample E57879). *CPZ*

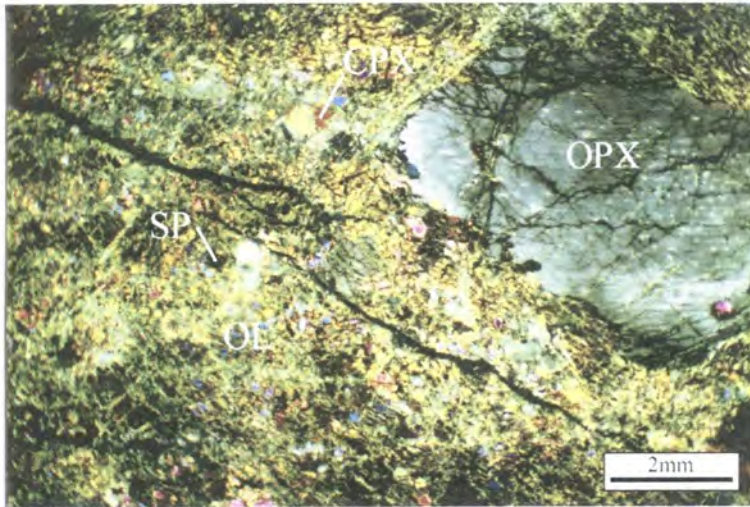


**Figure 4.6.** Relict, coarse-grained porphyroblast of orthopyroxene (OPX) surrounded by a matrix of recrystallised clinopyroxene (CPX), olivine (OL) and spinel (SP). (Sample CAC65). *CPZ*

anhedral grains (500 - 1000  $\mu\text{m}$ ). However, these are usually recrystallised clusters of smaller equidimensional grains (50 - 500  $\mu\text{m}$ ) which are aligned in the foliation plane. These clusters occur as interstitial grains at the triple junctions of olivine crystals. Davies (1983) notes that the clinopyroxenes at olivine triple junctions may extend as narrow septa along grain boundaries, and he interprets this as suggesting interstitial crystallisation of a trapped liquid remaining after inefficient melt extraction. Clinopyroxene modal volumes vary between 5 - 15%.

Spinel is commonly brown coloured, and more rarely olive-green coloured. The coarse spinel grains (500 – 1500  $\mu\text{m}$ ) usually have a holly-leaf form (Figure 4.7), which is indicative of post-kinematic growth (Mercier and Nicolas, 1975). Spinel is also present as small (<500  $\mu\text{m}$ ) anhedral grains.

Several textural features can be related to greater deformation in some lherzolites (fine-grained, porphyroclastic) compared to less-deformed examples (medium- to coarse-grained, porphyroclastic). In lherzolites subjected to greater deformation the degree of re-crystallisation of olivine and clinopyroxene is more pronounced and the olivine grains have a tabular form. Orthopyroxene, the least readily deforming mineral phase, develops porphyroclasts with a tabular form, and displays recrystallisation of the margins of porphyroclasts to fine grains. Spinel also develops a tabular form and is often present as diffuse aligned aggregates defining a well-developed mineral lineation.

#### 4.3.4.b. Pyroxenite

The modal analyses of two representative pyroxenite samples are presented below:

*CAC 44* - 75% clinopyroxene, 20% orthopyroxene, 5% olivine, <1% spinel.

*CAC 99* - 70% clinopyroxene, 15% orthopyroxene, 10% plagioclase, 5% olivine, <1% spinel.

The modal analyses of the two pyroxenites show that they are primarily websterites, although they are clinopyroxene-rich. The constituent mineral phases within the pyroxenites are extensively recrystallised (Figure 4.8) and therefore the pyroxenites were developed prior to deformation of the coarse-grained lherzolite host rock. Plagioclase, which is a secondary metamorphic phase, is completely altered to saussurite, although the original textural relationships of the plagioclase are still preserved. It occurs as fine interstitial grains with respect to clinopyroxene, orthopyroxene, and olivine and as rims around skeletal spinels. It occurs predominantly at the triple-junctions of recrystallised clinopyroxenes and also extends as septa along the clinopyroxene grain boundaries. Examination of the clinopyroxenes reveals the presence of plagioclase exsolution within the larger porphyroclasts.

Clinopyroxene occurs as both coarse-grained porphyroclasts and recrystallised grains with a varied grain size, although predominantly fine-grained. The



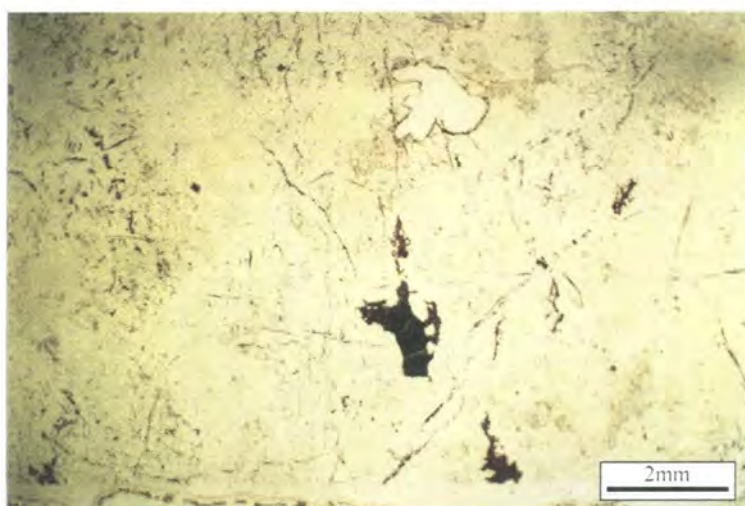


**Figure 4.7.** Brown spinels with a holly-leaf form in a matrix of serpentinite after olivine. (Sample CAC1). *PPZ*

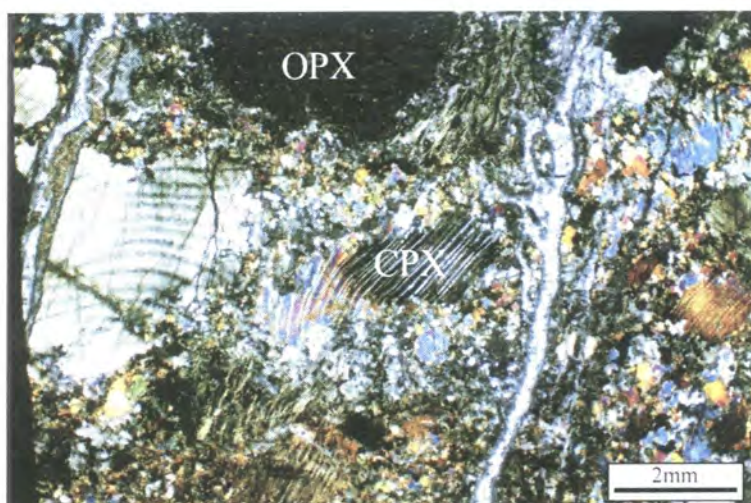


**Figure 4.8.** Clinopyroxene porphyroclasts (CPX) with bent exsolution lamellae mantled by finer-grained recrystallised clinopyroxene. Bastite pseudomorphs orthopyroxene porphyroclasts (OPX). (Sample CAC44). *CPL*

porphyroclasts possess rims and mantles of fine-grained recrystallised grains. The porphyroclasts show other evidence of deformation, including bent exsolution lamellae, curved kink-bands and undulose extinction. Generally, the recrystallised clinopyroxenes are less deformed and do not have exsolution lamellae, although some grains do exhibit undulose extinction. The recrystallised grain boundaries meet adjacent boundaries at  $120^\circ$  triple junctions.

Descriptions of the pyroxenite bands by Green (1964a) reveal that the petrology of the pyroxenites is more variable. Green (1964a) describes pyroxenites from Pedn

Boar (GR 76401676) which are olivine websterites, containing - 15% olivine, 39% orthopyroxene, 31% clinopyroxene, 15% recrystallised, olivine, clinopyroxene, orthopyroxene and altered plagioclase.

Rothstein (1977,1981,1988,1994) has conducted a detailed examination of the microstructure of the pyroxenites and concludes that they originated as a primary layering feature. The microstructure of pyroxenites examined in the present study shows that the pyroxenites were developed prior to deformation, and this is consistent with interpretation of Rothstein (1977,1981,1988,1994).

#### **4.3.4.c. Dunite**

The microstructures described in this section refer to the large dunite bodies described in Section 3.3.1, and not the smaller scale primary dunite layers discussed by Rothstein (1977,1981,1988,1994).

In all of the samples of dunite examined, the olivine is completely altered to serpentine. The original microstructure of the olivine can be recognised by the presence of a 'ghost texture'; olivine has a medium to coarse grain size, an anhedral form and meets at 120° triple junctions. Olivine (serpentine) comprises 80-95% of most samples. Spinels comprise between 5-20% volume in the thin-sections studied, and form elongate trails in thin-section (Figure 4.9). Microstructures suggests that the spinels are the disaggregated remnants of larger spinel grains, and suggests that a fabric formed in the rock in response to later deformation. Spinel also shows internal fracturing, which is evidence of internal deformation associated with the disaggregation. Spinels are medium- to coarse-grained and have an anhedral interstitial form. They vary from a deep brown to a black colour, depending on the degree of secondary alteration and commonly have secondary chlorite rims. They usually have concave crystal margins against adjacent olivine and often poikilitically enclose fine-grained olivine. These features suggest that the spinel crystallised later than the olivine.

In some sections, microstructures suggest the former presence of pyroxene. It is not known if this reflects secondary alteration or whether there was original clinopyroxene or orthopyroxene. Pyroxenes are fine-grained, anhedral and have an interstitial form with concave margins against adjacent olivine and usually comprises <2% of the sections.

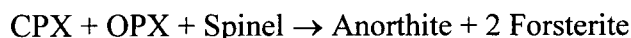
The microstructures of harzburgites, which occur as gradational margins

between the dunite and spinel lherzolite, have been examined in order to deduce the relationship between dunite and spinel lherzolite. In all the samples examined, however, pervasive serpentinisation has severely hampered identification of the original microstructure. Large bastite pseudomorphs occur after orthopyroxene porphyroclasts and the microstructure and abundance appears to be similar to orthopyroxene in the spinel lherzolite. Spinel is red-brown in colour and has an anhedral form, with the holly-leaf form observed in spinel lherzolite. Spinel may have a rim of saussurite, and alteration product after plagioclase.

#### 4.3.4.d. Plagioclase lherzolite

Plagioclase lherzolites possess a similar microstructure to the spinel lherzolites, and represent a transitional assemblage between the spinel lherzolite and mylonitic plagioclase-bearing peridotite described in the next section. Plagioclase lherzolite is distinguished from spinel lherzolite by the presence of 5 - 15 % modal volume saussurite, a secondary replacement mineral after plagioclase (Figure 4.10). Plagioclase is fine- to medium-grained (150-1500  $\mu\text{m}$ ) and often forms rims around spinel grain, as interstitial grains to olivine and orthopyroxene, and within the clinopyroxene clusters. The interstitial grains have an elongate form and have the appearance of stringers, which may enclose small crystals of olivine and orthopyroxene.

The transformation from a spinel lherzolite to plagioclase lherzolite assemblage is a sub-solidus transition that occurs in response to a progressive decrease in P and is described by a univariant reaction (Rampone *et al.*, 1993):-



The reaction is mainly dependent on P at high T, and has been determined at ~8 kbar for  $T > 900^\circ\text{C}$  from experimental work (Rampone *et al.*, 1993 and references therein).

The plagioclase lherzolites described here are chemically different (see Chapter 6) from the plagioclase lherzolites with plagioclase-rich veinlets related to melt-impregnation described by Davies (1983) from exposures near Coverack and are therefore not directly analogous.



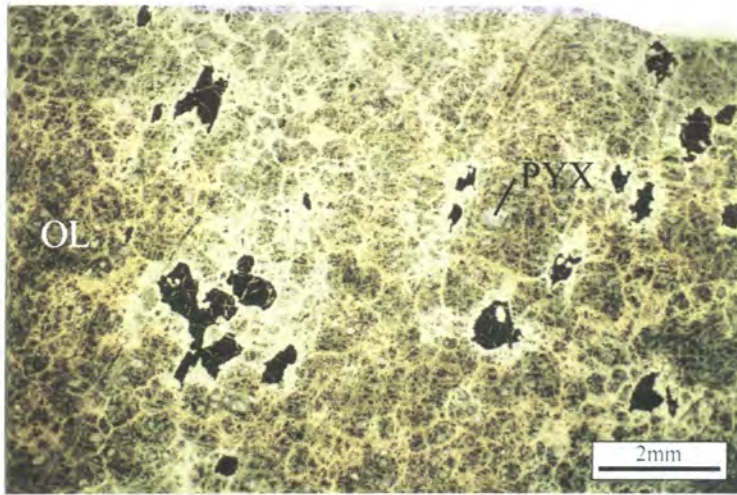


**Figure 4.9.** Anhedronal spinel grains (black) surrounded by serpentinised olivine (OL) grains and minor, altered pyroxene (PYX). (Sample CAC 37). PPL

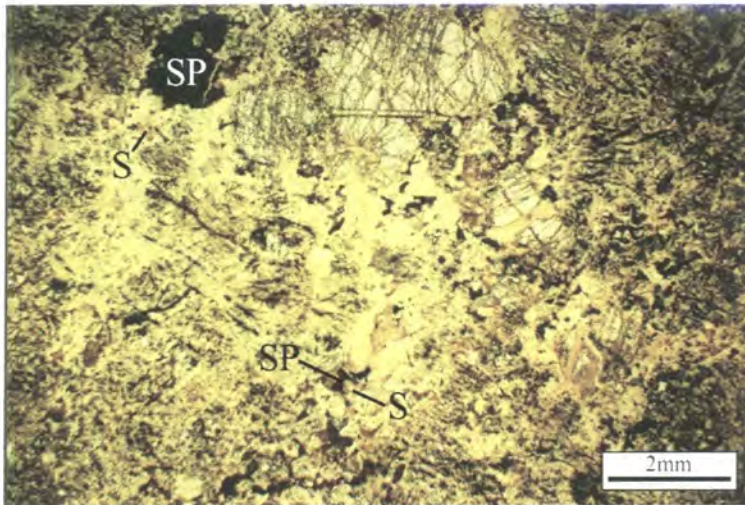


**Figure 4.10.** Plagioclase is altered to saussurite (S) that forms rims around spinel grains (SP) and aligned clusters within the peridotite. (Sample CAC61). PPL

#### 4.3.5. Microstructures of mylonitic peridotites

A decrease in overall grain-size, increase in the degree of recrystallisation, development of fine-grained porphyroclastic microstructures and the presence of Ti-pargasite amphibole, characterises a transition from plagioclase lherzolite (see above) to mylonitic peridotite. Plagioclase lherzolite is also distinguished from mylonitic peridotite on the basis of whole-rock geochemical composition (see Chapter 6). Two sub-types of mylonitic peridotite are recognised: *mylonitic plagioclase-bearing peridotite* and *mylonitic amphibole-bearing peridotite*. The mylonitic amphibole-

bearing peridotite is transitional with the mylonitic plagioclase-bearing peridotite and both sub-types are often interbanded at a cm scale.

#### 4.3.5.a. Mylonitic plagioclase-bearing peridotite

Mylonitic plagioclase-bearing peridotites are typically fine- to medium-grained and possess fine-grained porphyroclastic to mylonitic textures. These textures are similar to the equigranular/ tabular-equigranular textures described by Mercier and Nicolas (1975).

In specimens orientated parallel to the X-Z plane (i.e. parallel to the mineral stretching lineation and perpendicular to the foliation), the peridotite displays a weak mineral banding parallel to the foliation plane. This banding is produced by variations in the modal volume of olivine and pyroxene.

The mylonitic plagioclase-bearing peridotites are characterised by plagioclase and, in many samples, brown amphibole (Figure 4.11). Plagioclase is present in abundances up to 15% modal volume and is usually altered to a brown secondary alteration product, saussurite. Plagioclase is always found in two textural associations, firstly as fine-grained aggregates forming rims around spinel, and secondly, as fine-grained crystals interstitial with respect to olivine and pyroxene. Plagioclases often display undulose extinction, which suggests that they have been subjected to stress during deformation.

Olivine commonly occurs in two forms. 1) Tabular grains with a strong shaped preferred orientation, a medium- to fine-grain size (200 - 500  $\mu\text{m}$ ), straight to curved grain boundaries; these grains may show a kink-like subgrain structure (Drury et al. 1990). 2) Fine, recrystallised anhedral grains (40 - 150  $\mu\text{m}$ ) which usually have curved grain boundaries. These grains commonly occur with orthopyroxene, plagioclase and clinopyroxene as polycrystalline aggregate porphyroclasts, or granoblastic domains with an equidimensional mosaic microstructure (Figure 4.12). Anhedral, brown-coloured, very fine-grained spinel (5-10  $\mu\text{m}$ ) is often associated with these granoblastic domains. Olivine, with an amoeboid form and curved grain boundaries, also occurs as reaction rims associated with fine-grained recrystallised orthopyroxene, at the margin of orthopyroxene porphyroclasts. Green (1964a) noted this recrystallisation microstructure and describes "ball-like aggregates" and suggested that they represent



recrystallised pyroxene porphyroclasts. However, this ball-like aggregate appearance is a phenomena related to selective serpentinisation of the surrounding area. This has been

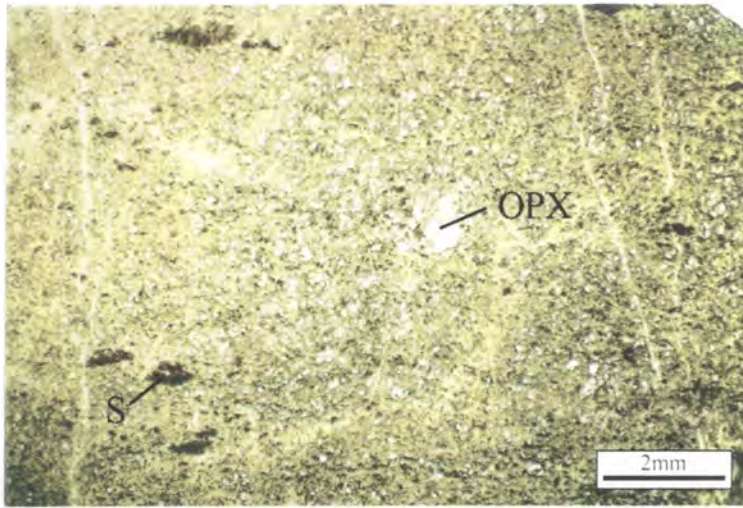


**Figure 4.11.** Fine-grained mylonitic plagioclase-bearing peridotite with relict orthopyroxene (OPX) porphyroclasts and brown patches of saussurite (S) after plagioclase. (Sample CAC13). *PPL*

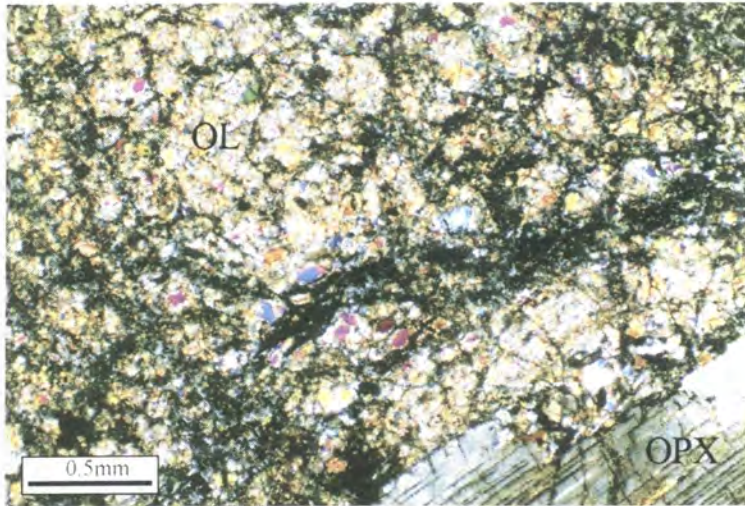
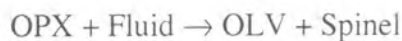


**Figure 4.12.** Fine-grained matrix comprising a granoblastic domain of olivine grains (OL) with an equidimensional mosaic microstructure. A relict orthopyroxene (OPX) porphyroclast is preserved. (Sample E7457). *CPL*

recognised, as in less serpentinised samples, the entire matrix has this aggregate appearance. In situ mineral analyses confirm that the microstructure is composed of olivine and orthopyroxene (Chapter 5). Disequilibrium textures similar to those described above are suggestive of the fluid-induced incongruent breakdown of orthopyroxene to olivine and spinel (Edwards and Malpas, 1995):-



Recrystallised olivine often displays a mineral preferred orientation, although it is not as strong as that displayed by the coarser grains, which lies parallel to the lineation defined by stretched orthopyroxene porphyroclasts and spinels.

Orthopyroxene crystals generally form fine-grained recrystallised grains (40 - 400  $\mu\text{m}$ ), although many samples contain relict coarser grained orthopyroxene porphyroclasts. The porphyroclasts have fractured margins associated with recrystallised fine-grained orthopyroxene. Occasionally, flattened porphyroclasts are observed and are inferred to have developed due to slip on the (100) planes (Drury et al., 1990).

Clinopyroxene is usually present as fine-grained interstitial recrystallised grains (40 - 500  $\mu\text{m}$ ) in the matrix and relict porphyroclasts of clinopyroxene are rarely preserved.

Spinel crystals vary in size from fine- to medium-grained (50 - 750  $\mu\text{m}$ ), although spinels with the fine grain size are usually more abundant. The larger spinels usually have a skeletal form with concave margins against the adjacent plagioclase rims. The spinels are commonly drawn out into irregular shaped elongate aggregates with fine tails of spinel adjacent to larger grains. These aggregates define a foliation plane within the mylonitic peridotite.

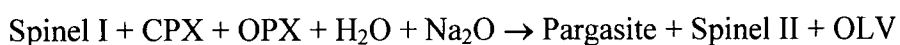
In rare samples, large green spinel crystals are present; these spinels have thin plagioclase rims and appear to have a syn- or post-kinematic origin. Larger spinel crystals usually display a holly-leaf form (Mercier and Nicolas, 1975). Green (1964a) notes that the large green-coloured spinels do not exhibit any evidence of strain and a lack of deflection of the peridotite foliation around the spinels. He therefore proposed that the larger green spinels represent porphyroblasts, and not porphyroclasts. They are, therefore, not augen of earlier large crystals as proposed for the pyroxene porphyroclasts. These large green spinels are often associated with plagioclase-rich regions, and in some circumstances, coarse-grained clinopyroxene and Ti-rich pargasitic-hornblende/tschermakite/pargasite amphibole.

Interstitial brown-coloured amphiboles are commonly present, but not ubiquitous in the mylonitic plagioclase-bearing peridotite. These are Ti-pargasite to kaersutite according to the IMA classification scheme of Leake (1978) (Chapter 5). Amphiboles are a minor phase in samples of the mylonitic plagioclase-bearing peridotite, rarely exceeding 3% modal volume. They form rims on clinopyroxene

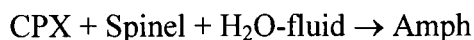
grains and this suggests that their development is related to the breakdown of clinopyroxene. Possible reactions responsible for amphibole being produced are discussed in the following section. An absence of brown amphibole in the coarse-grained spinel and plagioclase lherzolites suggests that the amphibole was created during the mylonitisation of the Lizard peridotites.

#### 4.3.5.b. Mylonitic amphibole-bearing peridotite

Mylonitic amphibole-bearing peridotites are characterised by the assemblage olivine + orthopyroxene + amphibole + spinel +/- clinopyroxene +/- plagioclase. The amphibole, pargasitic hornblende and edenitic hornblende according to the IMA classification of Leake (1978)(Chapter 5), commonly has abundances between 15-25 % modal volume and rarely exceeds 30% modal volume. Pale green-coloured amphibole (Figure 4.13) displays a strong mineral preferred orientation which defines a strong foliation and mineral stretching lineation, parallel with tabular olivine crystals. Amphibole is assumed to be transitional with the brown-coloured amphibole in the mylonitic plagioclase-bearing peridotite. This transition is accompanied by a change in colour of the amphibole from brown to pale-green in response to an increase in its modal abundance. Amphibole is observed to form rims and intergrowths in association with clinopyroxene (when present), suggesting that clinopyroxene is being consumed during amphibole formation. A relative lack of clinopyroxene in the mylonitic amphibole-bearing peridotite in comparison to the mylonitic plagioclase-bearing peridotite supports this hypothesis. Spinel is a rare phase in the mylonitic amphibole-bearing peridotite and is usually present as fine-grained Cr-spinel crystals (30 - 300  $\mu\text{m}$ ) enclosed within amphiboles. These spinels appear to be secondary, in comparison to the coarser-grained spinels in the mylonitic plagioclase-bearing peridotite and their textural association with amphibole suggests that they are related to the amphibole-producing reactions. Orthopyroxene does not show the textural relationships observed between amphibole and clinopyroxene, and is therefore probably not a significant reactant in the amphibole-producing reactions. However, similar textural associations have been described in amphibole peridotites by Agrinier *et al.* (1993) and involve both clinopyroxene and orthopyroxene in a amphibole-producing reaction:-



A second reaction, which does not involve orthopyroxene is proposed by Bonatti *et al.* (1986):-



The above reactions suggests the involvement of a hydrous metasomatic fluids and further evidence for metasomatism is presented on the basis of geochemical evidence in Chapters 5 & 6. The origin of these metasomatic fluids and their influence on the tectonic and geochemical evolution of the Lizard peridotites is discussed in Chapter 7.

Mylonitic amphibole-bearing peridotite has an overall grain size within the fine- to medium-grain size range. Pargasitic-hornblende crystals are usually slightly coarser than the olivine (20 - 625  $\mu\text{m}$ ) and pyroxene grains and usually form fine to medium-grained euhedral crystals (60 - 1250  $\mu\text{m}$ ). The overall texture of the mylonitic amphibole-bearing peridotite is fine-grained porphyroclastic to mylonitic.

In sections orientated in the X-Z plane, amphibole defines a weak banding (Figure 4.14) composed entirely of pargasitic-hornblende that appears to grade into bands containing olivine +/- orthopyroxene +/- amphibole.

The Lizard mylonitic amphibole-bearing peridotites are similar to amphibole peridotites described in the Voltri Massif (Hoogerduijn Strating *et al.*, 1993) and at Zarbargad Island (Red Sea) (Piccardo *et al.*, 1988, Dupuy *et al.*, 1991, Agrinier *et al.*, 1993, Kurat *et al.*, 1993).

#### 4.3.5.c. Feldspathic bands

Feldspathic bands occur in both the mylonitic plagioclase-bearing peridotite and mylonitic amphibole-bearing peridotite.

Feldspathic bands are plagioclase-, amphibole- and clinopyroxene-rich in comparison with the mylonitic peridotite in which they occur, but there is a great variability in the constituent phases between different bands. The modal volumes of the constituent phases in the three representative bands are shown below, to demonstrate the variability in modal composition:

*CAC 180* – 25% clinopyroxene, 25% colourless amphibole (after clinopyroxene), 50% saussurite (after plagioclase), <1% spinel.



CAC 73 - 50% pargasitic hornblende, 20% plagioclase, 20% orthopyroxene, 10% clinopyroxene, <1% spinel.

E 50308 - 55% plagioclase, 25% pargasitic hornblende, 20% clinopyroxene, <1% spinel and orthopyroxene.

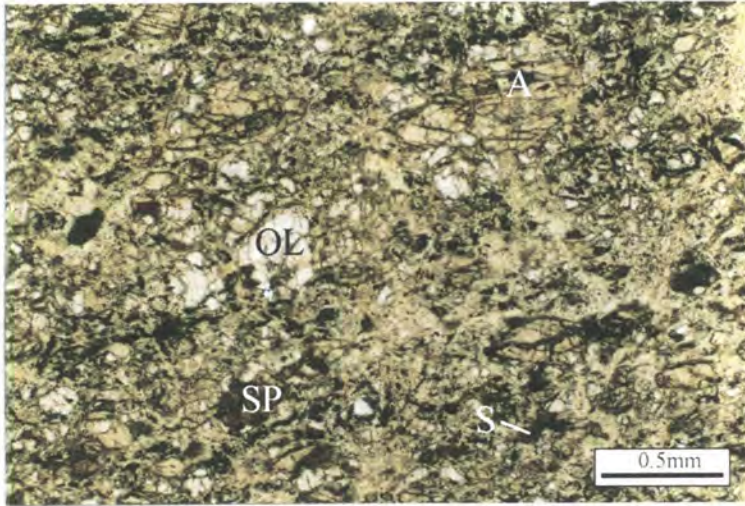


**Figure 4.13.** Aligned pale-brown amphibole (A) and olivine (OL) grains define a strong fabric. Spinel (SP) and saussurite (S) after plagioclase are also present. (Sample CAC32). *PPC*

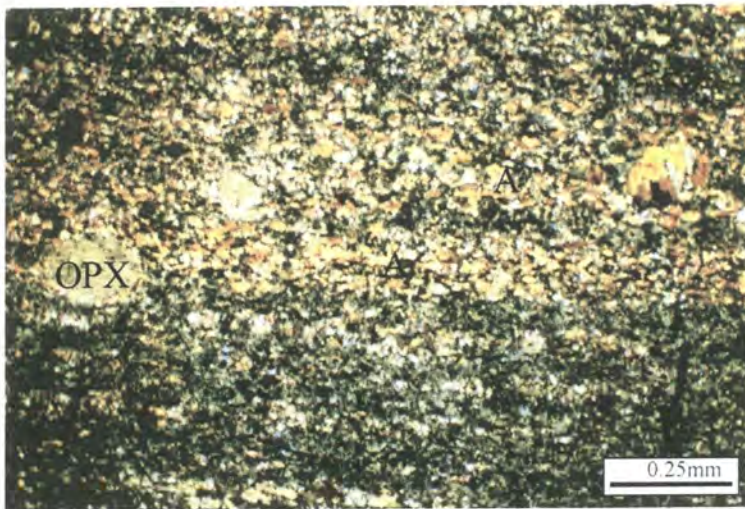


**Figure 4.14.** Amphibole (A) rich bands within mylonitic amphibole-bearing peridotite, relict porphyroclasts of orthopyroxene (OPX) are also present. (Sample CAC81). *CPCL*

The grain size of the bands is distinctly coarser (average 1-2 mm) than the adjacent mylonitic peridotite host rocks (average 0.1-0.3 mm) and this may be a *grain boundary area reduction* phenomenon (Passchier & Trouw, 1996). The grains within

the feldspathic bands are oriented parallel to the margins on the bands which is concordant with foliation in the adjacent peridotite (Figure 4.15). The grains have curved boundaries and the band has a granoblastic texture. Generally, the grains in the

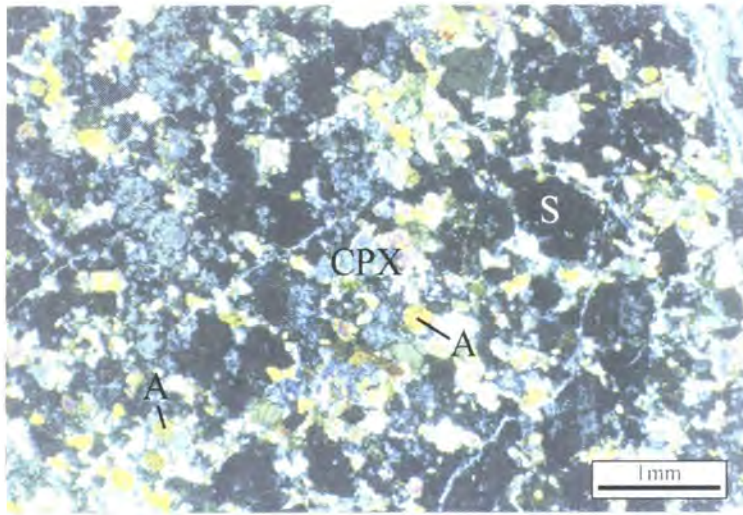


**Figure 4.15.** Feldspathic band composed of clinopyroxene (CPX), saussurite (S) after plagioclase and secondary amphibole (A) after clinopyroxene. (Sample E50308). *CPL*

bands appear to be less deformed than grains in adjacent mylonitic peridotite. These bands are up to 10 mm wide and have margins that are amphibole-rich and contain no clinopyroxene or plagioclase, and grade into the adjacent mylonitic peridotite. Amphibole is usually brown-coloured and it often rims clinopyroxene or occurs along cleavage planes, which suggests that it replaces clinopyroxene. In some bands, brown amphibole is not present, and a colourless, fibrous amphibole is present instead. This also rims clinopyroxene, and represents a reaction product derived from the breakdown of the pyroxene. Colourless amphibole also replaces brown amphiboles as rim growths and within pull-apart fractures. Spinel has a ‘holly-leaf’ form, and is usually red-brown in colour, but in some samples it is olive green, whilst spinel in the adjacent mylonitic peridotite is a red-brown colour. The spinel is rimmed by plagioclase.

Several unusual samples do not show banding, preserving instead small (<1 cm) veinlets/pods, elongate parallel to the peridotite foliation. The veinlets consist of 70% plagioclase, 25% clinopyroxene and 5% Ti-rich pargasite. The grains in the segregation are coarser (2–5 mm) than the adjacent peridotite (0.25–2 mm) and have sharp contacts with the adjacent peridotite. Both the plagioclase and the clinopyroxene have an anhedral form with straight to curved grain boundaries. Clinopyroxenes in the veinlets exhibit a notable feature not observed in band: they contain small (0.1–0.25 mm)



exsolution patches (up to 10%) of brown amphibole (Ti-pargasite), which has a similar composition to the amphibole in the veinlet (Chapter 5). These clinopyroxenes also contain fine-grained exsolutions of spinel. The clinopyroxenes within the peridotite adjacent to the veinlets do not show the amphibole exsolution. These veinlets are assumed to be analogous to the bands, but they contain less amphibole and more plagioclase, they probably represent the initial form of a band, i.e. a series of interconnected veinlets.

#### **4.3.6. Petrological variations in the Lizard peridotites: GIS based study**

In this section, the results of a GIS (Geographical Information System) based study on petrological variations in the Lizard peridotites are reviewed and the implications for petrogenesis and deformation are discussed. This method is based on detailed examination of petrographic features observed in thin-sections of the Lizard peridotites. Figure 4.16a shows an introductory map, which includes the digitised coastline, major lithological boundaries, and 1km-grid lines. The map also includes labels for place names in the Lizard which will be referred to in the following discussions and a subdivision of the Lizard into several fault-bounded 'areas', these being the northern, eastern, southern, western, and central areas. These 'areas' are referred to in the following sections. Figure 4.16b displays the location of all the samples used in this study. Full details of the objectives and methodology used in this GIS study are provided in Appendix B.

##### **4.3.6.a. Lithological map: Primary rock type (Figure 4.17)**

The distribution of the peridotite types on Figure 4.17 is very similar to Figure 3.3, although the distribution of plagioclase lherzolite is included on Figure 4.17. The GIS-based map also supports the field evidence (Figure 3.3) for the distribution of mylonitic peridotite in the Trevassick (GR 71002250) to Trelan area (GR 74501870) around the northern margin. This data is consistent with the textural evolution discussed in the previous section. Several of the previous publications that describe the Lizard peridotites have proposed that the coarse-grained peridotites are both lherzolitic and harzburgitic in composition (Bromley, 1979; Kirby, 1979, Leake & Styles, 1984). The petrographic examination for the GIS-based study reveals that the coarse-grained lherzolites are predominantly spinel lherzolites and that harzburgites are rare in the



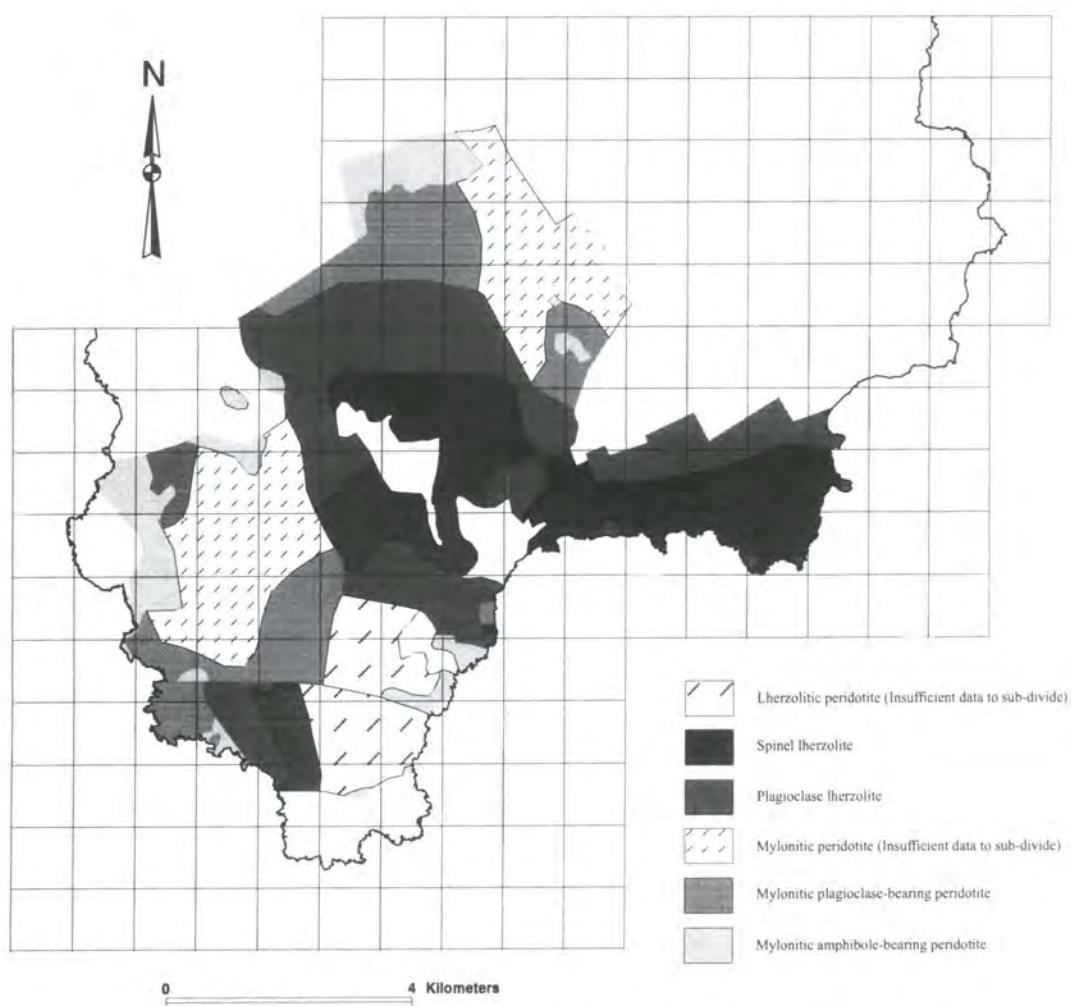


**Figure 4.17.** Summary map displaying the distribution of the different peridotite types, interpreted from GIS data plots.

Lizard Ophiolite Complex, usually being restricted to the margins of dunite bodies (Section 4.3.4.c.). It appears that in the previous work (Kirby, 1979; Leake & Styles, 1984) the classification of the peridotites as harzburgite or lherzolite was based largely on whole-rock composition and not petrography.

#### 4.3.6.b. Grain size variations (Figure 4.18)

The summary map showing the grain size of the Lizard peridotites establishes that there are significant variations in the study area. These variations occur in coarse-grained lherzolites and mylonitic peridotites. The lherzolites in the southern area in general have a 'finer' grain size (medium grained) than lherzolites in the central and eastern areas (coarse/medium & medium grained), which suggests that they are more

deformed. This observation has been confirmed by fieldwork (Section 3.3.), which reveals that the peridotites in the southern area have a strong foliation and a mineral stretching lineation. Lherzolites in the central and eastern areas vary between coarse/medium to medium grained. In the central area there appear to be variations in the grain size across the strike of the peridotite fabric (Figure 3.13.); this is also observed in the eastern area. The grain size of the peridotites between Kennack Sands (GR 7390 1665) and Black Head (GR 7780 1615) is predominantly coarse/medium. However, there are 'zones' where the peridotite is medium-grained and these may represent zones of higher strain formed during deformation of the peridotite. In the Coverack (GR 7824 1845) to Trelan (GR 7455 1889) section and in the southern unit there appears to be a correlation between grain size and the peridotite type, the spinel lherzolites being 'coarser'-grained than plagioclase lherzolites.

In the northern area, shown in Figure 4.17 to comprise mylonitic peridotite, there are significant variations in the grain size of the peridotite. The grain size decreases from the S to N, and these variations in grain size correspond to the different 'zones' of mylonitic peridotite type: mylonitic plagioclase-bearing and mylonitic amphibole-bearing peridotite (Figure 4.17). The mylonitic plagioclase-bearing peridotites are generally medium/fine-grained and the mylonitic amphibole-bearing peridotites are predominantly fine-grained. In the western area, at Vellan Head (GR 6682 1485), there is a contrast in the grain size of the mylonitic peridotite, also related to the composition of the peridotite. On the W side of a fault at Vellan Head mylonitic amphibole-bearing peridotites are predominantly fine-grained, and on the E side of the fault mylonitic plagioclase-bearing peridotites are medium/fine-grained.

#### **4.3.6.c. Modal volume variations in the constituent mineral**

In this section only minerals showing significant variation in modal abundance are included, these being clinopyroxene, olivine, plagioclase and colourless hornblende. In the following discussions of modal volume of constituent phases, variations in clinopyroxene and olivine in mylonitic peridotites are not included due to the fine grain size of these rocks hampering the distinction between pyroxene and olivine and therefore rendering estimates of modal volumes unreliable.



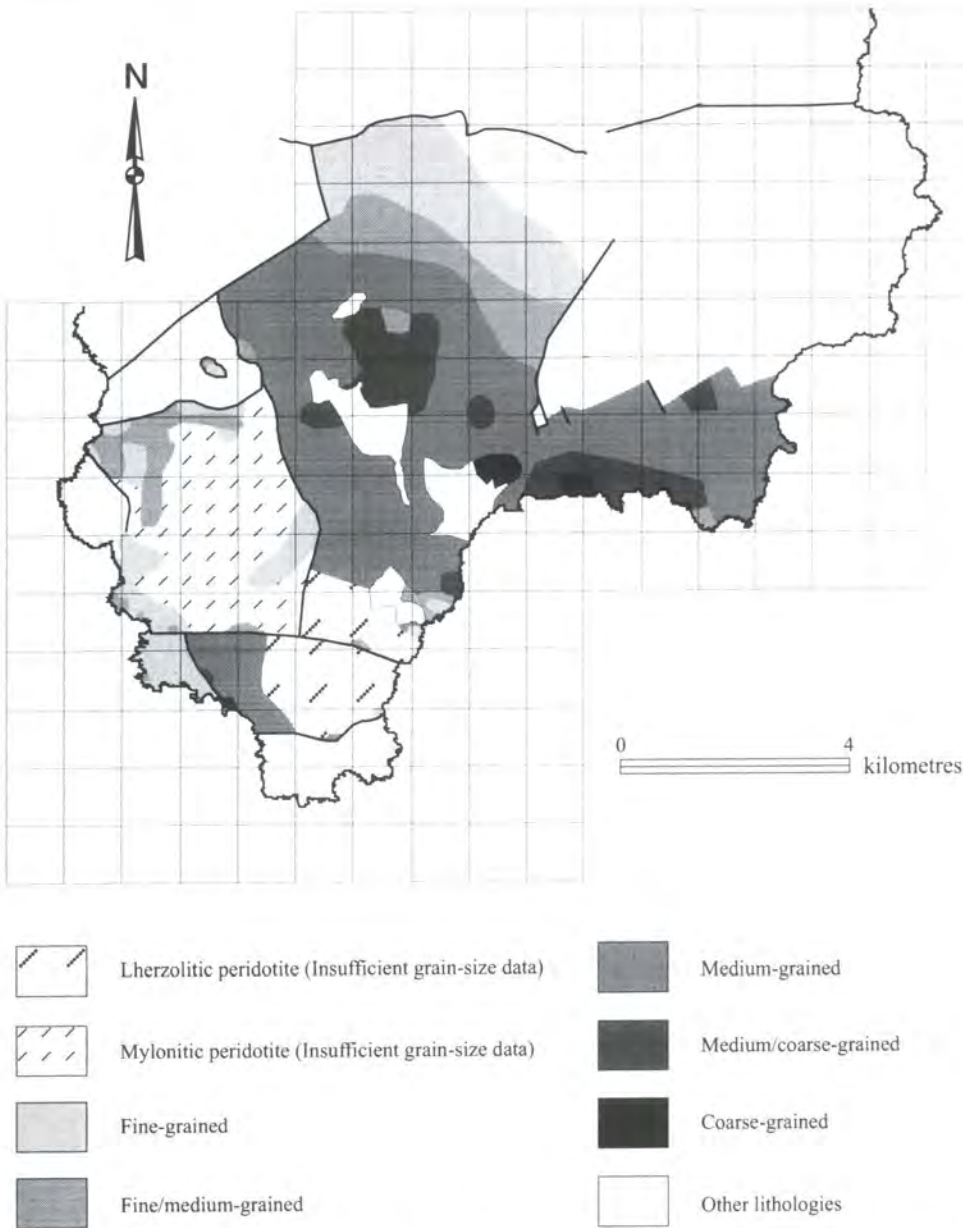


**Figure 4.18.** Geological map of the Lizard Ophiolite Complex displaying variations in the grain size of peridotite based on GIS data. Major faults and lithological contacts after Floyd et al. (1993).

#### 4.3.6.d. Clinopyroxene (Figure 4.19)

An estimate of the modal volume of clinopyroxene in the Lizard peridotites is important, particularly because the modal volume in a peridotite provides an indication of the degree of depletion of the peridotite with respect to partial melting processes. A harzburgite, which by definition has <5% clinopyroxene, has suffered a greater degree of melt extraction due to partial melting processes than a lherzolite with >5% clinopyroxene. Figure 4.19 shows that there are variations in the modal volume of clinopyroxene in coarse-grained lherzolites. In the southern area, all the lherzolites

show >5% clinopyroxene, and in places 9 – 17%. In the central area the modal volume of clinopyroxene in the lherzolites falls within the 5-8% range, although, some areas have up to 15% clinopyroxene. In the eastern area, many lherzolites display a relatively high abundance of clinopyroxene, up to 17% modal volume. Between Coverack and Trelan, near the contact with the Crousa gabbro, lherzolites show higher clinopyroxene contents than those on the coast between Kennack Sands and Black Head. This observation is inconsistent with idealised ophiolite stratigraphy (Roberts & Neary, 1993), where the peridotites close to the contacts with gabbros of the lower oceanic crust are often depleted in clinopyroxene relative to those lower in the mantle section. However, this observation is consistent with the Crousa gabbro representing a later off-axis intrusion and the clinopyroxene abundances in the peridotite being a primary feature unrelated to the intrusion of the gabbro. Microstructures in the lherzolites from the Coverack to Trelan area do not show any evidence for melt-impregnation (Suhr & Robinson, 1994), and the relatively high clinopyroxene content is therefore believed to be a primary feature.

#### **4.3.6.e. Olivine (Figure 4.20)**

There appear to be several variations in the olivine content, which are related to the geographic distribution of the peridotite. Within the central area of the Lizard, lherzolites in the northern part (GR 7217 & 7317) have a lower olivine content than lherzolites in the south. Within the eastern area, lherzolites at Gwenter (GR 74001800), Poldowrian (GR 75001690) and Lankidden Cove (GR 75601665) show the olivine contents within the 70-90% range. This compares to the other lherzolites within the eastern area, in which the olivine contents are within the 50-69% range.

#### **4.3.6.f. Plagioclase (Figure 4.21)**

Figure 4.21 reveals that the mylonitic plagioclase-bearing peridotites have higher plagioclase contents than the plagioclase lherzolites. The mylonitic plagioclase-bearing peridotites contain up to 9-12% plagioclase. There appears to be a variation in the plagioclase content of the peridotites between the central and northern areas of the Lizard. Plagioclase lherzolites in the northern part of the central area show the highest modal volume of plagioclase, in comparison with elsewhere in the central area. This

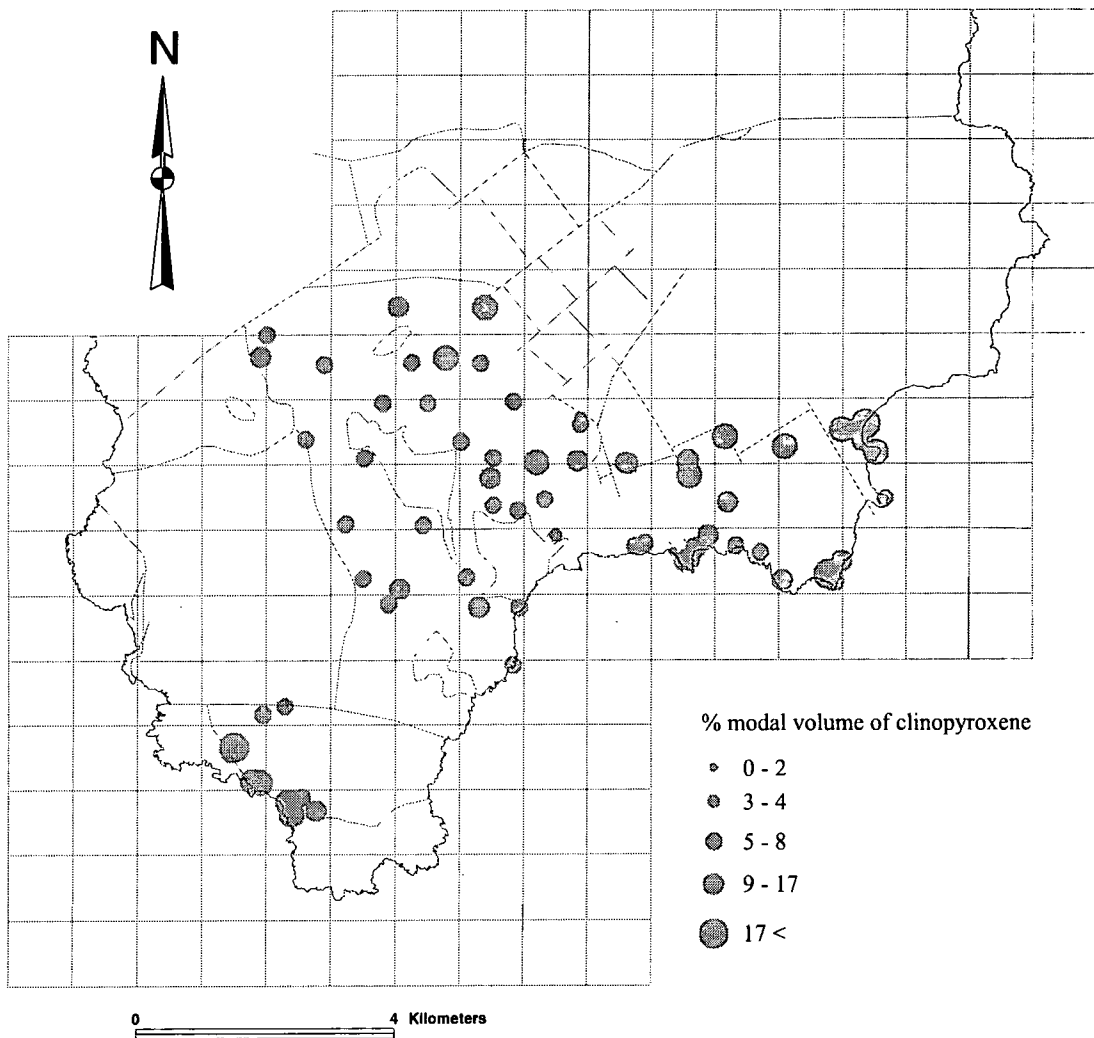


**Figure 4.19.** Geological map of the Lizard Ophiolite Complex which displays the results of GIS data for the 'theme' Clinopyroxene in coarse-grained lherzolites. Area proportional circles represent the % modal volume of clinopyroxene in the lherzolites. Intervals are chosen to include value ranges <5% and >5%, which allows distinction between harzburgite and lherzolite peridotite-types.

increase in plagioclase in this area may be related to a transition into mylonitic plagioclase-bearing peridotites to the north (Figure 4.17.), which is consistent with the variations in grain size (Figure 4.18.).

#### 4.3.6.g. Serpentinisation (Figure 4.22)

In this example serpentine, refers to the modal volume of lizardite and chrysotile (after olivine) and bastite (after pyroxene). The Lizard peridotites have suffered pervasive serpentinisation. The degree of alteration falls into the range of 20-80% in the majority

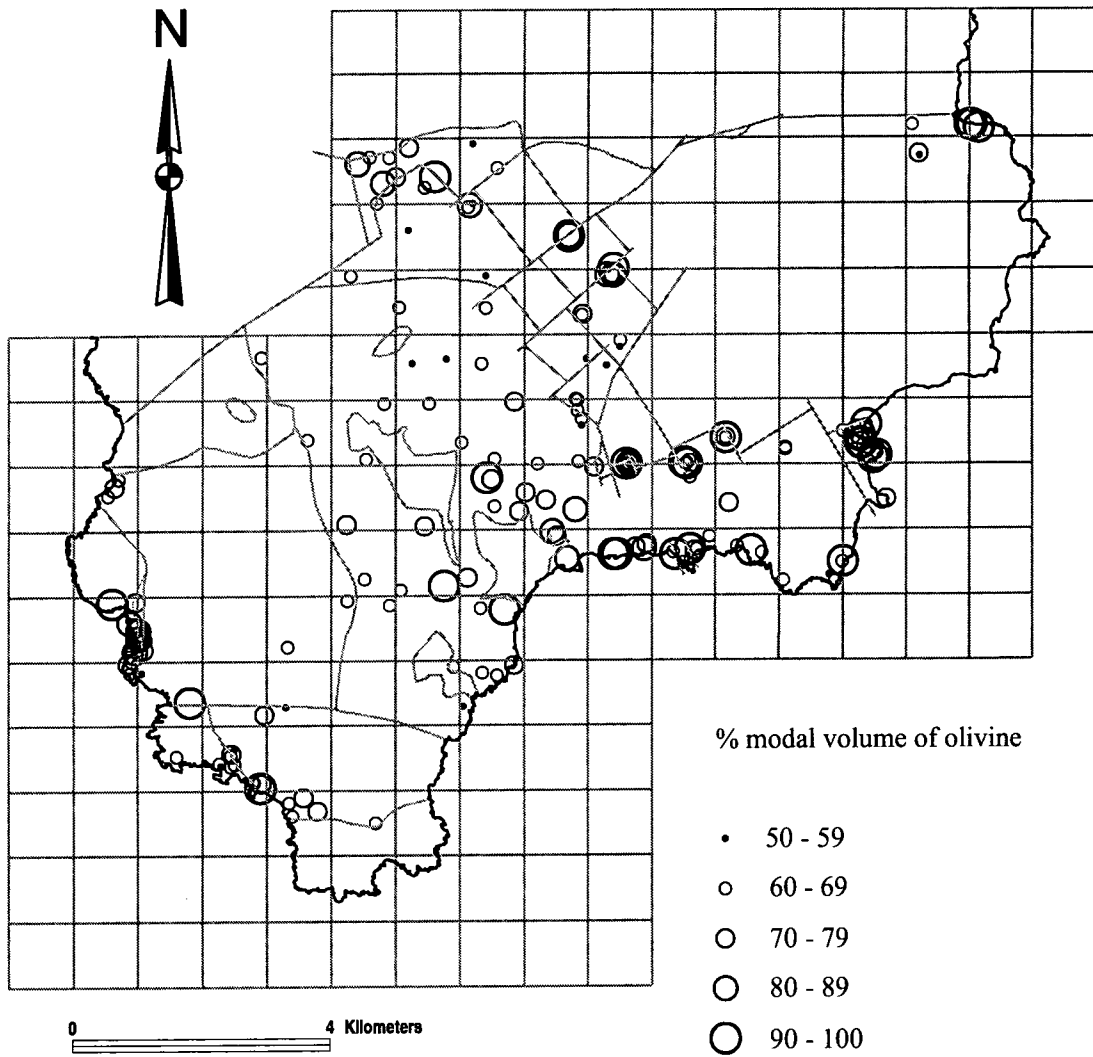


**Figure 4.20.** Geological map of the Lizard Ophiolite Complex displaying the results of GIS data for the 'theme' olivine in the coarse-grained lherzolites. Area proportional circles represent the % modal volume of olivine.

of peridotites, and only a minority, <5% are within the 1-20% serpentinisation range i.e. relatively fresh. In summary, the most serpentinised peridotites are located between Vellan Head and Ogo Dour Cove (GR 6683 1577) in the Western area, between Trevassick Quarry (GR 7116 2212) and Trelan in the northern area, and at Poldowrian (GR 7497 1671), Carrick Luz (GR 7554 1651) and Coverack in the eastern area. Peridotites in the Porthkerris (GR 805 231) area are extremely serpentinised, most sections showing 100% serpentinisation. The geographic distribution of the serpentinisation appears to be related to several geological controls, including both lithology and tectonics. Dunite is the most serpentinised peridotite type, because it is predominantly composed of olivine, one of the most susceptible mineral phases to serpentinisation (Floyd et al., 1993). Serpentinisation is also influenced by the presence

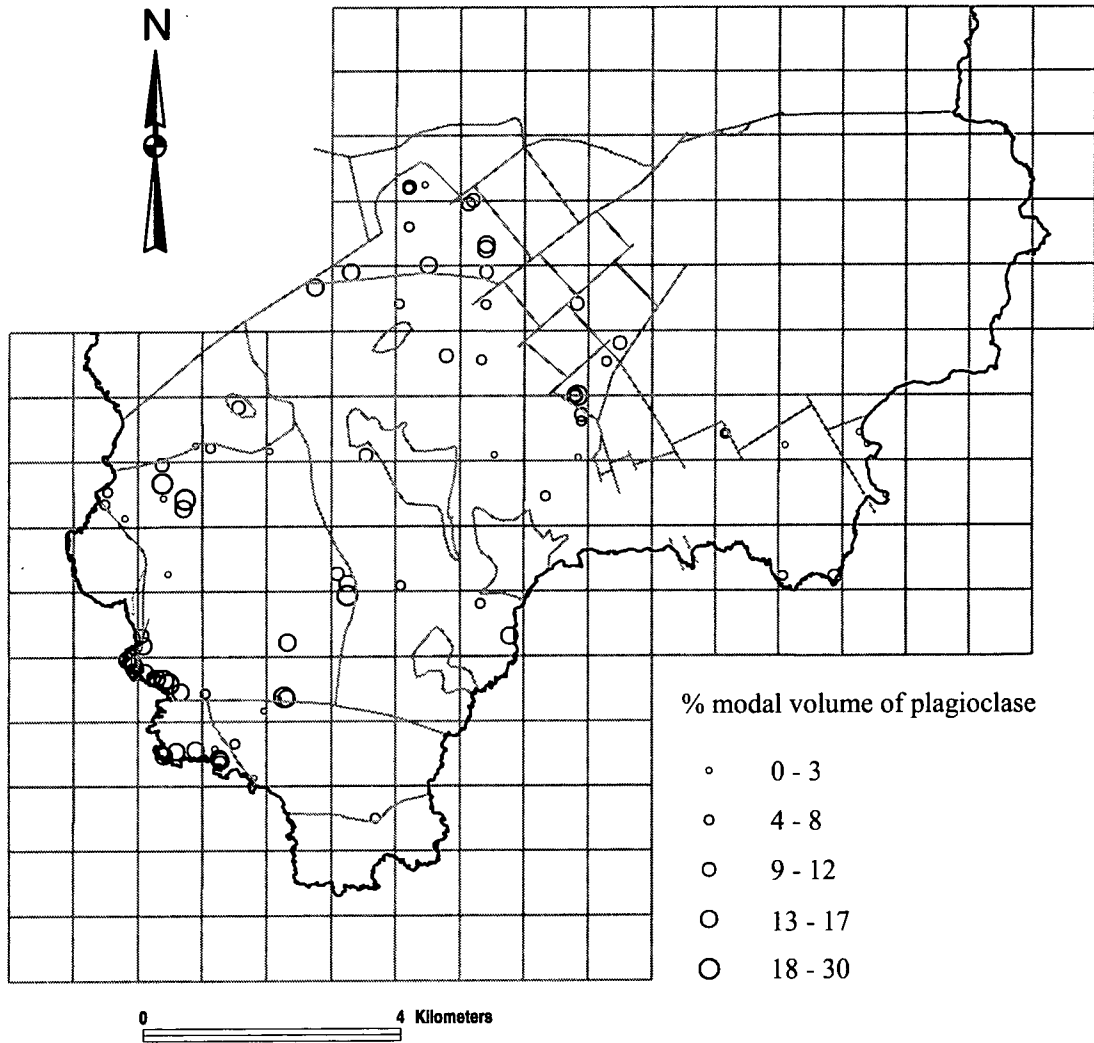


**Figure 4.21.** Geological map of the Lizard Ophiolite Complex displaying the results of GIS data for the 'theme' plagioclase the peridotites. Area proportional circles represent the % modal volume of plagioclase. Samples with >10% plagioclase are not ultramafic rocks and represent plagioclase-rich bands within the peridotite.

of faults. In areas of the Lizard where faults are prevalent, e.g. Vellan Head, the peridotites show a higher degree of serpentinisation than areas where there are fewer faults.

#### 4.3.6.h. Secondary amphibole: Colourless-hornblende (Figure 4.23)

In the central area of the Lizard, mylonitic peridotites and pyroxenites south of Carleon cove at GR 728154 contain the highest content of colourless-hornblende, in the 21-33% range. Mylonitic amphibole-bearing peridotites associated with the tectonic contacts at Kildown point (GR 72651470) and in Cadgwith (GR 71961486) contain colourless-

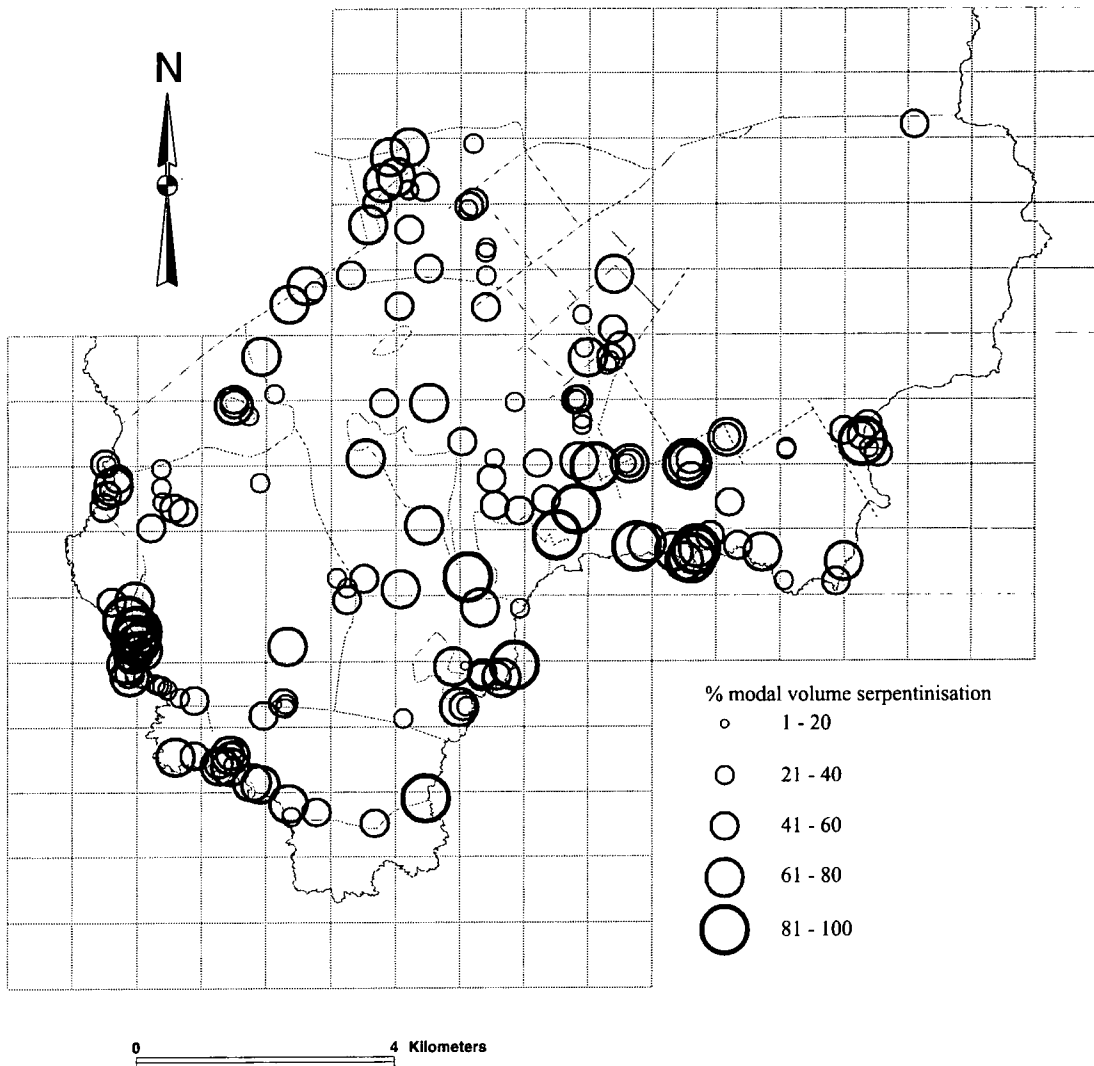


**Figure 4.22.** Geological map of the Lizard Ophiolite Complex displaying the results of GIS data for the 'theme' serpentinisation in all the peridotites. Area proportional circles represent the % modal volume of serpentinisation.

hornblende in the 3-20% range. Other localities where the peridotites in the central area contain colourless-hornblende as a conspicuous secondary phase include a locality (GR 69041906) near Penhale and GR 73781893 west of Trelan. In the eastern area of the Lizard, coarse-grained lherzolites at Carrick Luz contain colourless -hornblende in the 3-14% range, whilst at Downas cove (GR 76341675) colourless-hornblende contents are in the 3-7% range. At Coverack, a few lherzolites contain colourless-hornblende in the 3-7% range. Other localities in the eastern area where lherzolites contain colourless-hornblende include GR 753179 and GR 74681800 west of Ponsongath, and GR 75881687 at Arrowan farm.



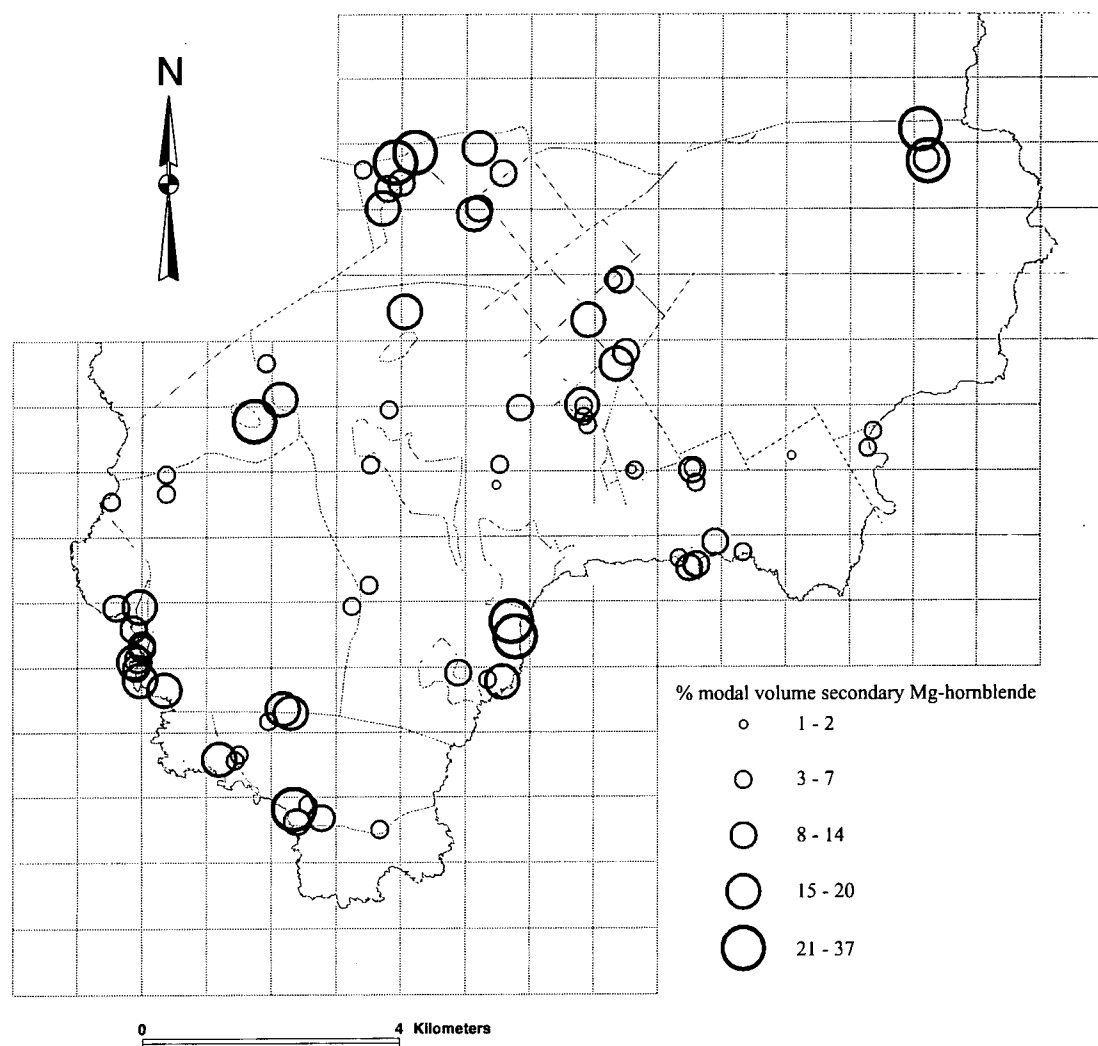


**Figure 4.23.** Geological map of the Lizard Ophiolite Complex displaying the results of GIS data for the 'theme' colourless hornblende in the peridotites. Area proportional circles represent the % modal volume of colourless hornblende.

In the southern area of the Lizard, colourless-hornblende is seen in the 3-33% range in peridotites from four localities –

- 1) Near GR 691142, which is close to an E-W fault, colourless-hornblende occurs in both mylonitic peridotites and coarse-grained peridotites at this locality.
- 2) Close to the NW striking fault at Kynance Cove (GR 684136).
- 3) At the SE end of Pentreath beach (GR 693127).
- 4) Mylonitic amphibole-bearing peridotite at Lizard village (GR 70751249).

In the western area of the Lizard, mylonitic peridotite from the Lawarnick area (GR 682136) contains colourless-hornblende in the 15-20% modal volume range. Field

evidence shows that there are hydrous shear zones in peridotites from this area, and many later faults. Between Gew Graze (GR 6760 1438) and Parc Bean Cove (GR 6667 1583), mylonitic peridotites contain colourless-hornblende within the 15-33% modal volume range, field evidence again reveals the presence of hydrous shear zones and also later sub-vertical fault zones in this area. South-east of Meaver, at GR 68741870, mylonitic peridotite contains colourless-hornblende in the 21-33% range, and mylonitic peridotites at Mullion Cliff (GR 665 175) and SE of the Predannack airfield (GR 6765 1555) have between 6-14% colourless-hornblende. The colourless-hornblende in these peridotites may also be associated with hydrous shear zones.

#### 4.3.7. Olivine petrofabrics and shear sense

Olivine petrofabric diagrams are used to determine which slip systems were activated during deformation in the different peridotite types. These diagrams can also be used to determine the sense of shear in orientated specimens. The principles relevant to this technique have been outlined in Chapter 1. A universal stage (U-stage) was used to determine and measure the olivine lattice preferred orientation (LPO) in selected samples. Petrofabric diagrams, which are equal-area projections on a lower hemisphere were constructed using this data. The foliation or lineation defined by spinel and pyroxene in hand-specimen is used as a reference frame. For a detailed review of the technique of using the universal stage the reader is referred to *Turner & Weiss (1963)*.

Olivine petrofabric diagrams are presented for one coarse-grained spinel lherzolite, one coarse-grained plagioclase lherzolite and one transitional-assemblage peridotite (plagioclase lherzolite to mylonitic plagioclase-bearing peridotite), all of which have coarse-grained porphyroclastic textures. Olivine petrofabrics presented for the mylonitic peridotites include three mylonitic plagioclase-bearing peridotites and two mylonitic amphibole-bearing peridotites with fine-grained porphyroclastic textures. It is immediately evident upon examination of the petrofabric diagrams that the coarse-grained lherzolites and transitional-assemblage peridotite have stronger point maxima of the [100], [010] and [001] crystallographic axes (i.e. stronger LPO) than the mylonitic peridotites. Separate summaries of the olivine petrofabric diagrams for the different samples are presented below.

#### 4.3.7.a. Olivine petrofabrics: Results.

##### *Sample CAC 64 – coarse-grained spinel lherzolite (Figure 4.24a)*

CAC 64 has a strong olivine lattice fabric with (100) concentrated close to the lineation (21/344), however (010) and (001) define partial girdles with maximum concentrations (010) - (33/253) and (001) – (51/092) oblique to the foliation plane. The results suggest that the dominant slip system was (0kl) [100] and there was possibly activation and interchange with (010) and (001) slip planes.

##### *Sample CAC 158 – coarse-grained plagioclase lherzolite (Figure 4.24b)*

Petrofabric data indicates a moderate olivine lattice fabric for CAC 158, including a concentration of (100) close to the lineation (6/345). The (010) direction has a maximum perpendicular to the foliation plane (3/261) and (001) defines a maximum within the foliation plane and perpendicular to the lineation (72/200). This data suggest activation of the (010) [100] slip system, however a spread of (001) suggests that contribution by (0kl) [100] cannot be excluded.

##### *Sample CAC 159 –transitional assemblage (Plagioclase lherzolite to mylonitic plagioclase-bearing peridotite) (Figure 4.24c)*

The petrofabric diagram for the CAC 159 shows a strong maximum concentration of (100) close to the lineation (12/175), and maximums of (010) perpendicular to the foliation plane (6/246) and (001) within the foliation plane and perpendicular to the lineation (81/020). This lattice fabric suggests that the activated slip system was (010) [100], although there may have been contribution of {0kl} [100].

##### *Sample CAC 113 – mylonitic plagioclase-bearing peridotite (Figure 4.25a)*

The olivine petrofabric diagram for this sample, and those below, is weak in comparison to the previous samples. The (100) direction defines a weak maximum close to the lineation (3/019), however there are also three other weak concentrations close to the lineation and symmetrical about this point. A weak maximum (3/120) is also defined by (010), which is perpendicular to the foliation plane and there are also three diffuse concentrations within symmetrical about this point and another within the

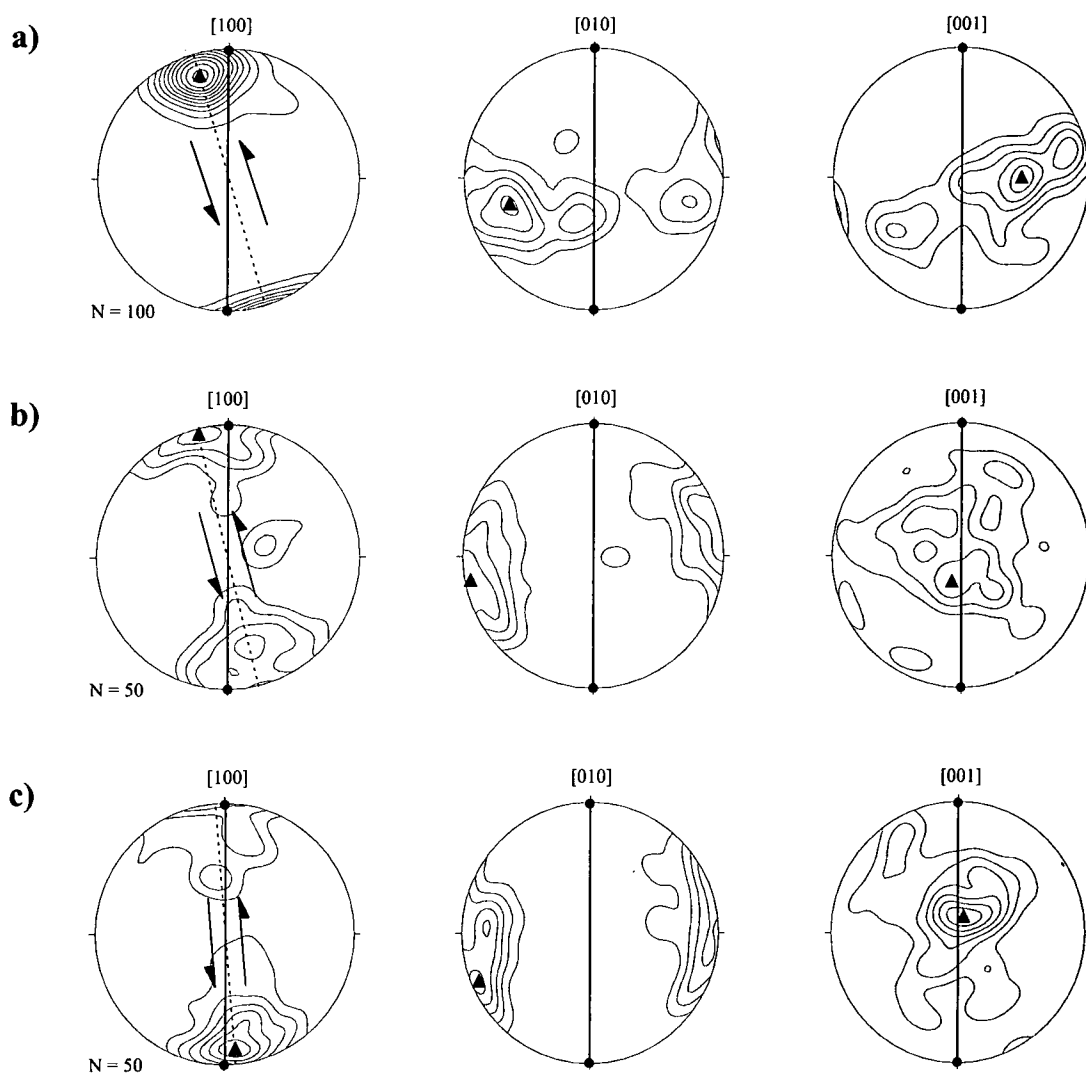


**Figure 4.24.** Stereographic projections display 1% area contours of poles to olivine lattice orientations (Olivine petrofabric diagrams) for coarse-grained herzolite and transitional peridotite assemblages. (a) CAC 64 - spinel herzolite. (b) CAC 158 - plagioclase herzolite. (c) CAC 159 - transitional peridotite. Solid line = trace of foliation, dashed line = trace of shear-plane, arrows show shear-sense, dot = lineation, triangle = point maximum.

foliation plane. The (001) direction defines weak maximum perpendicular to the lineation and within the foliation plane (54/230) and there are several other weak concentrations. The lattice pattern of this sample is difficult to interpret and activation of several different slip systems is proposed.

***Sample CAC 157 - mylonitic plagioclase-bearing peridotite (Figure 4.25b)***

The lattice pattern of this sample is weak and similar to CAC 113. Again (100) defines four concentrations close to and symmetrical about the lineation with a point maximum

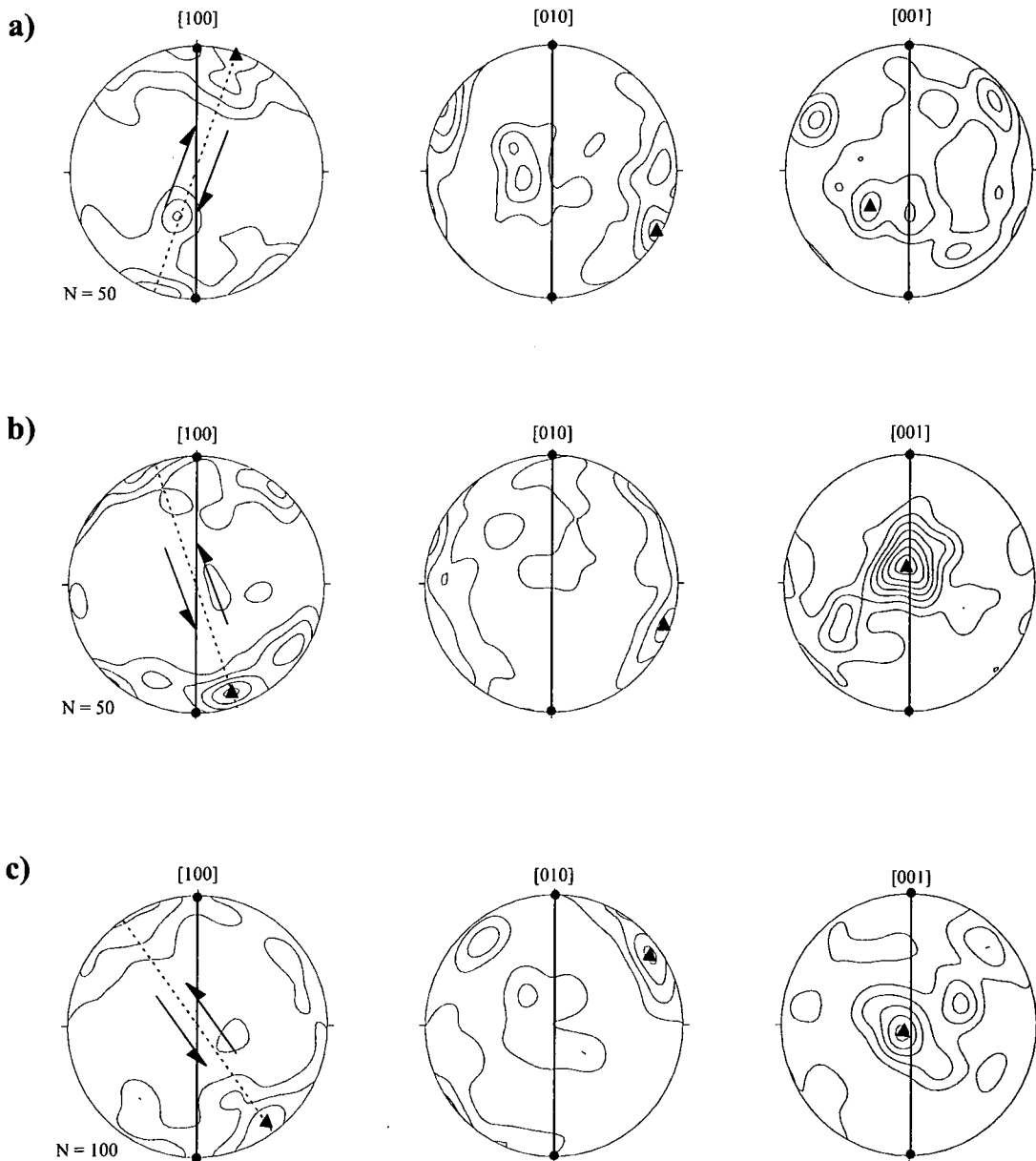


**Figure 4.25.** Stereographic projections display 1% area contours of poles to olivine lattice orientations (Olivine petrofabric diagrams) for mylonitic plagioclase-bearing peridotites. (a) CAC 113. (b) CAC 157. (c) CAC 67. Solid line = trace of foliation, dashed line = trace of shear-plane, arrows show shear-sense, dot = lineation, triangle = point maximum.

at (12/162). The (010) direction defines four weak concentrations perpendicular to the foliation and symmetrical with respect to each other, with a maximum at (3/110). A strong point maximum (78/345) is defined by (001) perpendicular to the lineation and within the foliation plane, and there are several other weak concentrations. The lattice pattern is difficult to interpret, and in common with CAC 113, activation of several different slip systems is proposed.

***Sample CAC 67 - mylonitic plagioclase-bearing peridotite (Figure 4.25c)***

This sample has the stronger olivine LPO than all the other mylonitic peridotites. This may be due in part to the larger number of measurements, 100 in contrast to 50 in the other samples. The lattice fabric shows a moderate maximum concentration of (100) oblique to the lineation (8/144), and weak concentrations also occur. The (010) direction forms concentrations perpendicular to the foliation plane with a maximum at (8/053) and a weak concentration within the foliation plane and perpendicular to the lineation. A maximum concentration of (001) occurs within the foliation plane and perpendicular to the lineation (81/220), and there are several weak concentrations that define a partial girdle. In common with the other mylonitic peridotites this lattice pattern is difficult to interpret, although the stronger lattice pattern facilitates interpretation. The lattice patterns suggest that the activated slip system was (0kl) [100] and the weak concentrations suggest that contribution by several other slip systems cannot be excluded.

***Sample CAC 110 - mylonitic amphibole-bearing peridotite (Figure 4.26a)***

A moderate LPO is shown by this sample. The (100) direction defines several concentrations oblique and symmetrical about the lineation, with a moderate maximum at (12/342). Two concentrations are defined by (010) with the stronger maximum at (72/070) within the foliation plane and perpendicular to the lineation and the weaker concentration perpendicular to the foliation plane. The (001) direction defines a maximum concentration (87/180) within the foliation plane and perpendicular to the lineation, and several weaker concentrations oblique to and symmetrical about the lineation. This lattice pattern, which is difficult to interpret, suggests the involvement of several different slip systems.

***Sample CAC 131 - mylonitic amphibole-bearing peridotite (Figure 4.26b)***

CAC 131 shows a moderate LPO. The (100) direction defines several concentrations oblique to and symmetrical about the lineation with a maximum concentration at (12/203). Several concentrations are also defined by (010), which has a maximum concentration perpendicular to the foliation plane and slightly oblique to the lineation (24/330). There are several (010) concentrations perpendicular to the foliation plane



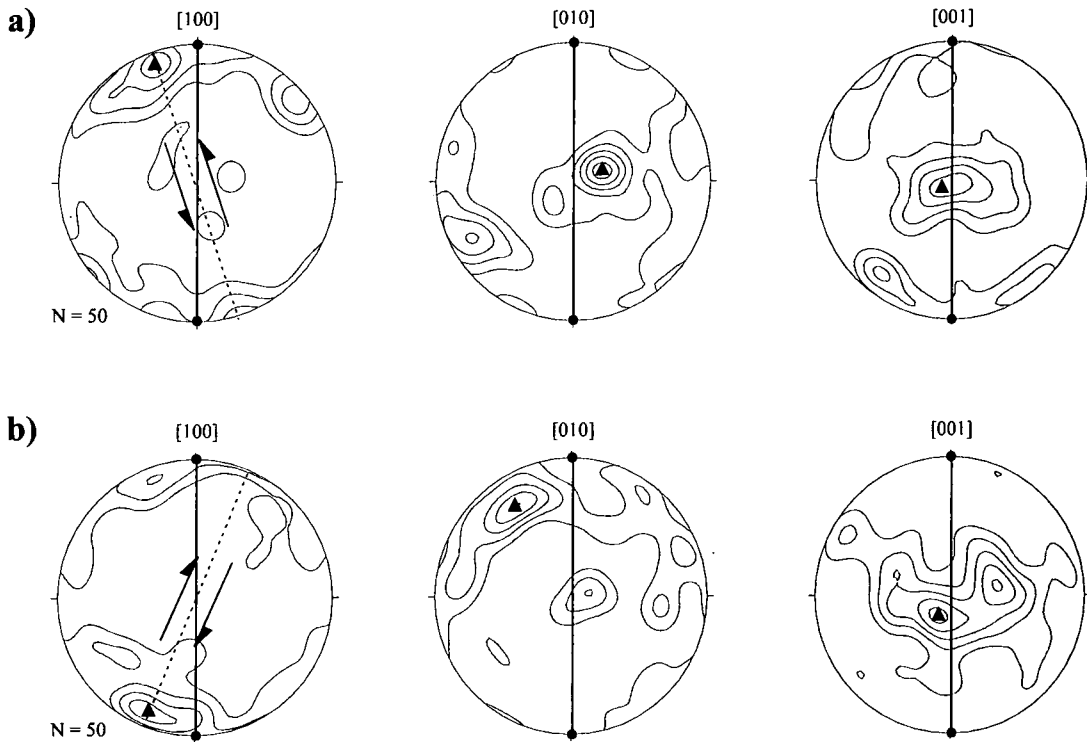


**Figure 4.26.** Stereographic projections display 1% area contours of poles to olivine lattice orientations (Olivine petrofabric diagrams) for mylonitic amphibole-bearing peridotites. (a) CAC 110. (b) CAC 131. Solid line = trace of foliation, dashed line = trace of shear-plane, arrows show shear-sense, dot = lineation, triangle = point maximum.

and a concentration within the foliation plane. The (001) direction defines two concentrations within the foliation plane and perpendicular to the lineation with a maximum concentration at (75/216). The activation of several different slip systems is proposed for this sample.

#### 4.3.7.b. Olivine slip systems: Deformation temperatures and mechanisms

##### *Deformation temperatures*

The results presented above suggest that in the coarse-grained lherzolites to transitional assemblage peridotites, the dominant slip system activated during deformation was (010) [100] and there is contribution by (0kl) [100] in one sample (CAC 64). In the mylonitic peridotites, the lattice fabrics are difficult to interpret and it is proposed that the simultaneous activation of several slip systems is responsible; in one sample (CAC 67), the activation of the (0kl) [100] is identified. In Chapter 1 it was established from a review of the literature, including both experimental work and studies on natural

systems, that temperature exerts a control on which slip system is activated. The (010) [100] slip system is dominant at 'high' temperatures ( $T > 1000^{\circ}\text{C}$ ) (Nicolas & Christensen, 1987). The (0kl) [100] slip system identified in one of the coarse-grained lherzolites and a mylonitic peridotite (see above) has been referred to as *pencil glide* by Nicolas & Christensen (1987) and it was proposed that this slip system is operative at 'low' temperatures ( $700\text{--}1000^{\circ}\text{C}$ ). The temperature conditions at which the simultaneous slip systems were activated in the majority of the mylonitic peridotites is more difficult to establish. Similar olivine lattice fabrics are observed in the basal ultramylonites from peridotites in the Table Mountain massif (Bay of Islands ophiolite, Newfoundland) and lower temperatures ( $< 1000^{\circ}\text{C}$ ) are proposed in this example (Suhr, 1993). Comparable olivine lattice fabrics to the Lizard mylonitic peridotites are also observed in peridotites from Baldissero (Ivera Zone, western Alps) where activation of the (010) [100] and {0kl} [100] slip systems has been proposed (Nicolas *et al.*, 1971; Nicolas and Poirier, 1976). The results for the Lizard rocks suggest, therefore, that deformation of the coarse-grained lherzolites occurred at relatively high temperatures ( $T > 1000^{\circ}\text{C}$ ) whilst the mylonitic peridotites were deformed at lower temperatures ( $700\text{--}1000^{\circ}\text{C}$ ). The temperature of deformation may be further constrained in the mylonitic peridotites by the presence of calcic-amphibole to an inferred upper temperature limit of  $1100^{\circ}\text{C}$ . Calcic-amphibole has an upper stability limit of between  $825^{\circ}\text{C}$  (Jaroslow *et al.*, 1996) to  $1100^{\circ}\text{C}$  (Nicolas, 1986). The presence of pargasitic amphibole (IMA classification of Leake, 1978) in the mylonitic plagioclase-bearing peridotite allows further temperature constraints. Recent experimental work (*pers comm.* Niidua and Green, 1997) establishes that between 18-25Kb, the maximum temperature stability limit of pargasite is  $1075^{\circ}\text{C}$ . Further temperature constraints are provided by geothermometric techniques in Chapter 5.

### ***Deformation mechanisms***

A common feature of the lattice fabrics in all the Lizard peridotites is the occurrence of [100] direction maximum concentration close to the lineation. This establishes that the slip direction in these peridotites always coincides with [100] and this lies close to the bulk shear direction defined by the lineation. In the Lizard samples, the consistent asymmetry between the foliation/lineation and the olivine lattice fabric suggests that a significant component of rotational strain occurred during deformation (Bouchez *et al.*,

1983) and this can therefore be used to determine a sense of shear (see below). It has already been established that the (010) [100] slip system was dominant and that this is characteristic of high temperatures and low differential stress. In the coarse-grained lherzolites, the lattice fabric is measured using both fine- and coarse-grained olivines, and the strong LPO suggests that they have a similar lattice fabric. It is therefore proposed that the fine-grained olivines were developed from the coarse ones through subgrain rotation (Jin *et al.*, 1998 and references therein), and that the new, fine grains inherit the lattice orientation of the coarser parent grains (Jin *et al.*, 1998). In order to inherit a similar LPO from coarser parent grains, the degree of subgrain rotation must be limited, as during continued subgrain rotation there should be a progressive weakening of the lattice fabric (Lloyd, G.E., *pers comm.* 1998). The relatively coarse grain size of these lherzolites and the strong LPO suggest dislocation creep-dominated flow during which only one slip system is usually involved. When only a single slip system operates the crystal must deform heterogeneously on the grain scale and other deformation mechanisms must be operative (Paterson, 1969; Bouchez *et al.*, 1983). Alternative mechanisms include diffusion, flexure of the crystal lattice, twisting and parting (Bouchez *et al.*, 1983).

The comparative weakness of the lattice fabrics of the mylonitic peridotites in comparison with the lherzolites may reflect several different processes. These may indicate the activation of several different slip systems that contribute equally to the LPO to produce a diffuse lattice fabric (Nicolas and Christensen, 1987). The degree of subgrain rotation in the olivine neoblasts in the mylonitic peridotite is likely to be more extensive than in the coarse-grained lherzolites. Hence, the progressive misorientation of the lattice fabric of the olivine neoblasts in the mylonitic peridotites could weaken the overall lattice fabric of the rock. An alternative explanation is that a significant contribution of grain-boundary sliding in the mylonitic peridotites may cause diffuse LPO (Jin *et al.*, 1998). Jaroslow *et al.* (1996) demonstrate that the crystallographic fabric of olivines decreases in intensity with a decrease in grain size. These phenomena may be related to the partial activation of grain size sensitive diffusion creep at lower temperatures (~600°C) and higher strain rates, although the dominant deformation mechanism is grain size insensitive dislocation creep. The microstructural evidence in mylonitic peridotites from the Lizard suggests that diffusion creep processes have not had a strong influence. This evidence includes the presence of weak-moderate LPO and

the minimum grain size for recrystallised olivine observed in the mylonitic plagioclase-bearing peridotite is  $\sim 40\ \mu\text{m}$  and in the mylonitic amphibole-bearing peridotite  $\sim 20\ \mu\text{m}$ . If olivine were to deform by grain size sensitive diffusion creep alone there would be little or no LPO and a recrystallised olivine grain size  $\leq 10\ \mu\text{m}$  would be observed (Jaroslow *et al.*, (1996). It is possible that both deformation mechanisms were operative if deformation lay close to the boundary between diffusion and dislocation creep in stress-grain size space (Figure 1.7)(Jin *et al.*, 1998). In the previous section, the LPO of the mylonitic peridotites was compared with the LPO of peridotites from Baldissero (Ivera Zone, western Alps). A feature that both the Lizard mylonitic peridotites and the Baldissero share is the presence of several concentrations of the lattice directions, symmetrical about the foliation plane. Nicolas *et al.* (1971) suggested that the Baldissero peridotite fabric could be attributed to the presence of two olivine lattice planes, which are symmetrical to the foliation plane and  $20^\circ$  oblique to it (Figure 4.27). A similar interpretation is proposed for the Lizard mylonitic peridotites. In the Baldissero example, the two lattice planes are explained by the presence of two shear planes S1 and S2 that are symmetrically inclined to the maximum principle stress direction and these determine, by rotation, the symmetrical orientations of the olivine glide system to the foliation (Nicolas *et al.*, 1971). The mylonitic peridotites from the Lizard do not display small olivine grains forming the boundaries between surrounding larger grains, which is observed in the Baldissero peridotites (Nicolas *et al.*, 1971). These boundaries are interpreted by Nicolas *et al.* (1971) to represent the active surfaces along which the crystals undergo relative displacements. In summary, several

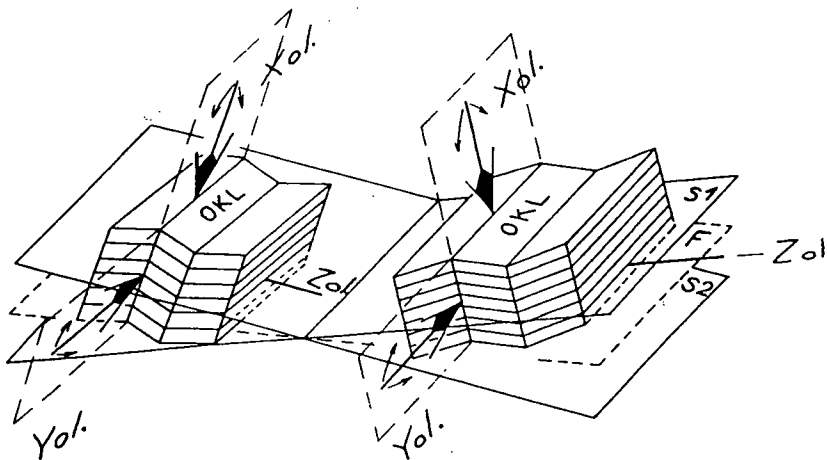


**Figure 4.27.** Theoretical sketch illustrating the orientation of olivine relative to kinematic elements. Example from the Baldissero Massif showing the relationship between orientations of olivine and two shear planes S1 and S2 (from Nicolas *et al.*, 1971).

different mechanisms may account for the unusual LPO displayed by the mylonitic peridotites. It is not possible, however, to determine, with the current data, which of these mechanisms or combination of mechanisms is responsible.<sup>1</sup>

In both the coarse-grained lherzolites and the mylonitic peridotites, microstructural evidence shows that grain-size reducing processes have operated. There are two main grain-size reducing processes proposed in the literature; dynamic recrystallisation (e.g. Drury *et al.*, 1990; Girardeau and Mercier, 1988; Jin *et al.*, 1998) and high-temperature cataclasis (Vissers *et al.*, 1995; Jaroslow *et al.*, 1996). Evidence in the coarse-grained lherzolites shows that neoblasts have a similar LPO to palaeoblasts; this suggests operation of subgrain rotation recrystallisation. The presence of fractured orthopyroxene porphyroclasts in the coarse-grained lherzolites is suggestive of high-temperatures cataclasis mechanisms. Flattened orthopyroxene porphyroclasts are observed in the mylonitic peridotites and these are inferred to develop due to slip on the (100) planes (Drury *et al.*, 1990).

#### 4.3.7.c. Shear-sense implications

The use of LPO in a kinematic study in order to determine the kinematics of flow in peridotites from the Lizard Ophiolite Complex has been inhibited for three reasons:

- 1) Over 50% of the orientated sections collected proved to be too serpentinitised to allow determination of the LPO of olivine.
- 2) It cannot be determined by how much the fabrics have been re-oriented by later thrusting and faulting.

A total of 15 lherzolite and mylonitic peridotites with a dip-slip fabric have been included, based on detailed LPO analysis by U-stage and assessment of obliquity of extinction of olivine in XZ sections. These show both reverse and extensional kinematics with respect to the orientation of the fabric in the field, but as the fabric is steeply dipping this makes interpretation ambiguous. Therefore the kinematics have

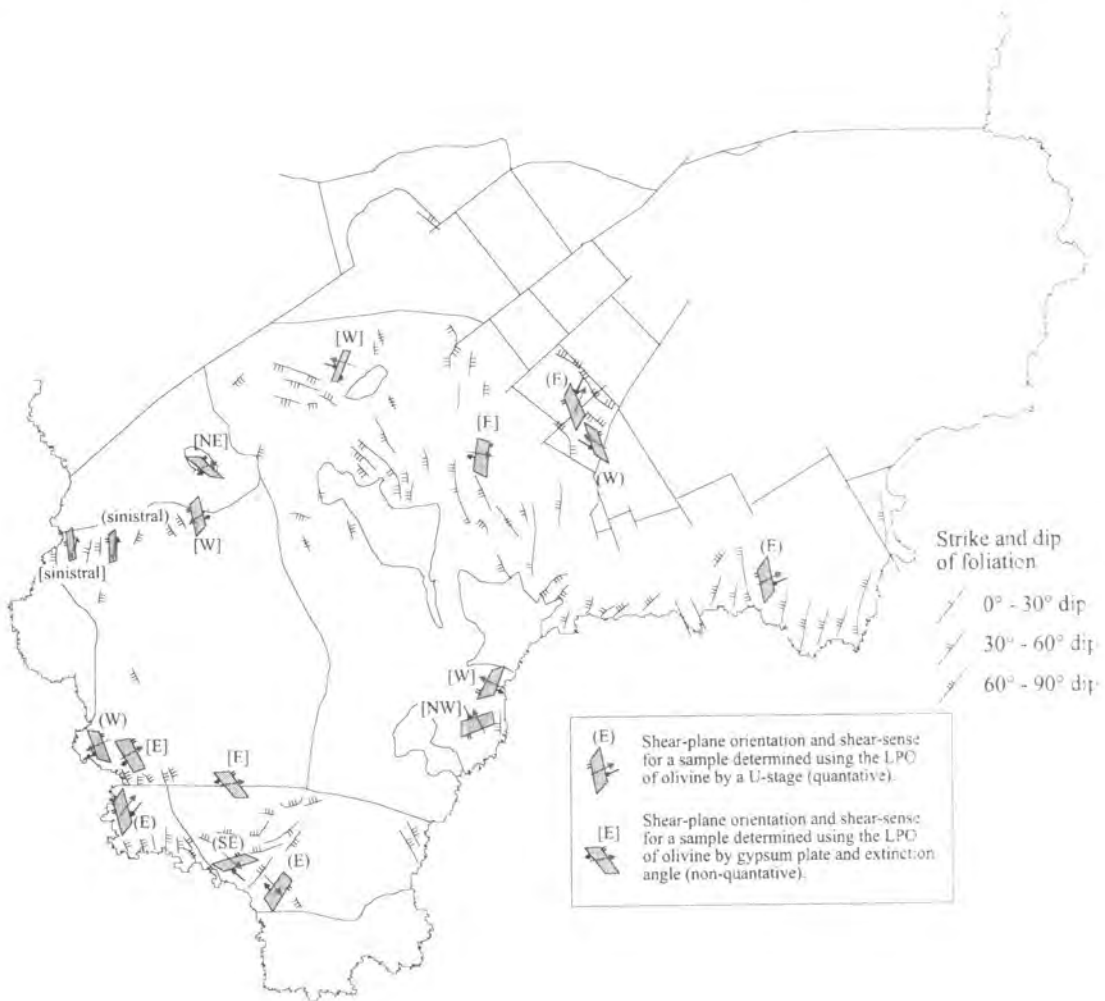


**Figure 4.28.** Geological map of the Lizard Ophiolite Complex displaying the shear-sense in the peridotites, represented by shear-planes orientated and with dip-direction. Arrows indicate the shear-sense, with the larger arrow representing the 'hangingwall' of the shear-plane. The letters in brackets represent the displacement in terms of a 'top-to-the-' present-day geographic direction.

been examined in terms of their "downthrow" direction relative to present-day orientation. This is either to the east or west as the fabrics dominantly strike NW-SE. Of the 15 peridotites studied, 9 show a E-side down and 6 show a W-side down shear-sense (Figure 4.28). It is suggested, therefore, that dip-slip fabrics in the lherzolite and mylonitic peridotites are related to deformation with dominantly E-side down shear sense. The high-strain zones (mylonitic peridotite) dip predominantly towards the E, suggesting that the dip-slip movements were extensional. This extension event may be responsible for the exhumation of the Lizard peridotites. The mylonitic amphibole-bearing peridotites in the Mullion area show a strike-parallel fabric. Olivine LPO patterns reveal a sinistral shear sense and the asymmetry of amphibole extinction with



respect to the shape fabric is also consistent with a sinistral shear sense. The tectonic implications of the peridotite fabric orientations and shear-sense are discussed in Chapter 7.

#### **4.3.8. Hydrous shear zones in the Lizard peridotites**

Hydrous shear zones possess a mylonitic fabric and cross-cut fabrics in the spinel lherzolite, plagioclase lherzolite, mylonitic plagioclase-bearing peridotite and mylonitic amphibole-bearing peridotite, which are rotated into these later shear zones. These shear zones are dominated by narrow (~0.5mm wide) anastomosing hornblende and chlorite-bearing shear bands (Figure 4.29) that extend across the length of a thin section. The shear bands wrap around relict orthopyroxene and olivine porphyroclasts forming tails defining asymmetric porphyroclast systems. The shear band also wrap around asymmetric lenticular domains of olivine. Orthopyroxene porphyroclasts are usually altered to bastite and stretched by displacement along brittle fractures with length:width ratios of up to 10:1, which defines a lineation parallel to the strike of the amphibole and chlorite-bearing shear zones. Porphyroclasts display evidence of internal deformation including undulose extinction, kink-banding and bent clinopyroxene exsolution lamellae. Pull-apart fractures and clinopyroxene exsolution lamellae within the orthopyroxene porphyroclasts are infilled with amphibole, and brittle fractured clasts at margins of porphyroclasts are also enveloped in amphibole fibre growths. Amphibole also develops as fibre growth reaction rims around orthopyroxene, and has the same composition of the amphibole in the shear bands (Chapter 5). Clinopyroxene grains are never present within these shear zones, which is attributed to its replacement by amphibole.

Olivine grains, within the matrix of shear zones cross-cutting peridotite mylonites, display a similar grain-size (range 100-2000  $\mu\text{m}$ ) to olivine grains within the adjacent peridotite mylonite. The coarser-grained olivine grains are often elongate, with long dimensions parallel to the stretching lineation. However, the majority of the olivine grains are equant, with curved grain-boundaries and little evidence for internal deformation. Olivine within shear zones which cross-cut the coarse-grained spinel and plagioclase lherzolite are finer-grained in comparison to the adjacent lherzolite.

The hornblende- and chlorite-bearing shear bands consist of fine-grained, elongate amphiboles (50-100  $\mu\text{m}$ ), which usually possess a well defined crystallographic- and

shape-preferred orientation parallel to the margins of the shear band. The development of amphibole is therefore inferred to be syn-kinematic and indicates the infiltration of a hydrous fluid and its interaction with the peridotite mineral assemblage (Drury *et al.* 1990; Bailey, 1997). Fine-grained chlorite (50-150  $\mu\text{m}$ ) usually occupies the central portion of these shear bands and develops a fabric which often cross-cuts the amphibole fabric, and also shows asymmetric fabrics which wrap-around amphibole porphyroclasts (Figure 4.30). The chlorite within these shear bands usually possesses a strong crystallographic- and shape-preferred orientation. However, randomly orientated grains also occur, often developed as rims surrounding relict Cr-bearing spinel. Spinel porphyroclasts are fractured and show fine-grained tails of Cr-spinel, or magnetite, in a matrix of fine-grained amphibole and chlorite.

In many samples of coarse-grained spinel and plagioclase lherzolite and mylonitic peridotite, amphibole and chlorite occur as randomly orientated mineral growths, often forming replacement rims around spinel and pyroxene, and within internal fractures within pyroxene and the matrix. In these samples, the development of a shear band fabric is limited. The similarity in the form and composition (Chapter 5) of the amphibole and chlorite, and associations with spinel and pyroxene, suggests that these textures were developed simultaneously with the development of shear bands observed in more deformed rocks. The less-deformed, amphibole- and chlorite-bearing rocks are likely to be one of the assemblages which Flett and Hill (1912) classified as 'tremolite serpentine'. The presence of amphibole constrains the deformation temperature of these shear zones to between 825°C and 1100°C (Section 4.3.7.b) and the development of a amphibole+chlorite+olivine assemblage suggests temperatures between 500-800°C (Hoogerduijn Strating *et al.*, 1993).

Lizardite serpentine veins, which may exhibit 'extensional jogs', cross-cut the original peridotite fabric, hydrous shear zones and are therefore considered to be one of the youngest deformation phases to have affected the peridotites.

#### **4.3.10. Serpentine-filled faults**

Samples collected from shear zones, which form the contacts between peridotite and amphibolite (e.g. Kildown Point (GR 7265 1470), Balk Quarry (GR 714 129) and the Predannack borehole (GR 6901 1634)), contain evidence for several deformation phases, each characterised by a particular mineral assemblage.

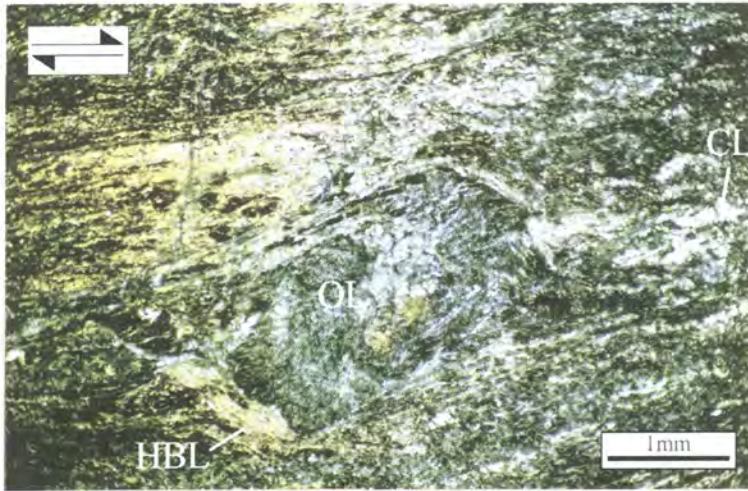


**Figure 4.29.** Hornblende (HBL) and chlorite-bearing (CL) hydrous shear zones wrap around a relict asymmetric olivine (OL) porphyroblast. (Sample CAC149). *CPZ*

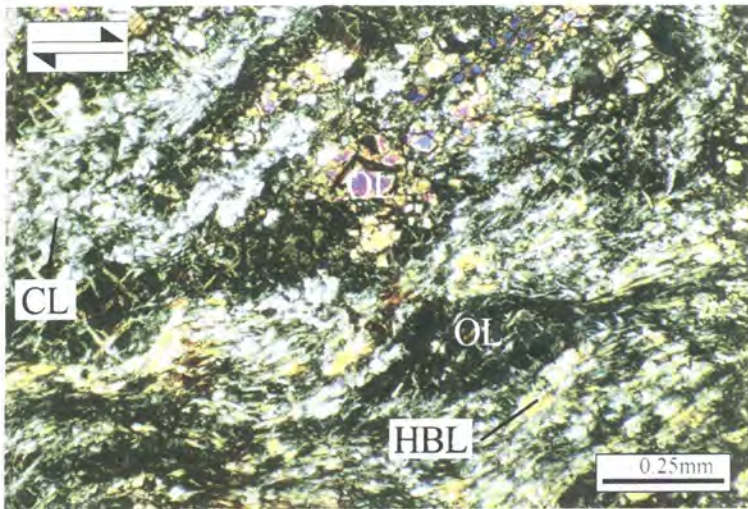


**Figure 4.30.** Anastomosing hydrous shear zones, showing both aligned and randomly orientated chlorite grains (CL) and aligned hornblende grains (HBL) that wrap around asymmetric lenticular domains of olivine (OL). (Sample CAC115). *CPZ*

An early peridotite fabric is cross-cut by hydrous shear zones that are reworked in turn by a later fabric defined by the shape-preferred orientation of serpentine minerals (antigorite?)+/- talc, and brucite as a minor phase. These mineral phases are fine-grained (50-150 $\mu$ m), and form elongate grains, and their development appears to be related to the replacement of olivine, amphibole and chlorite. The presence of serpentine minerals, possibly antigorite, indicates temperatures between 300 and 500°C for these serpentine-bearing shear zones (Hoogerduijn Strating *et al.*, 1993).

#### 4.3.11. Microstructural evolution of the Lizard peridotites – summary

The microstructural evidence presented in the preceding sections supports the field evidence for a tectonic evolution of the peridotites from a coarse-grained lherzolite protolith to mylonitic peridotites. Relict primary textures are preserved in a small proportion of samples of spinel lherzolite. The spinel lherzolite assemblage is transitional to mylonitic peridotite via an intermediate plagioclase lherzolite assemblage that has a similar microstructure to the spinel lherzolite but is distinguished by the presence of plagioclase, or its alteration product, saussurite. Microstructures suggest that a process of increasing deformation, dynamic recrystallisation, grain size reduction and metamorphic re-equilibration is responsible for the transition from coarse-grained lherzolite to mylonitic peridotite. Two types of mylonitic peridotite are recognised: mylonitic plagioclase-bearing peridotite and mylonitic amphibole-bearing peridotite. The mylonitic amphibole-bearing peridotite is transitional from the mylonitic plagioclase-bearing peridotite and this transition is identified by the breakdown of clinopyroxene to pargasitic hornblende, a metamorphic change probably related to a metasomatic interaction with hydrous fluids.

The microstructural chronology presented above is consistent with the main findings of a detailed study of the peridotites by Green (1964a) who suggested that there is evidence for chemical re-equilibration of lherzolitic peridotite under conditions of decreasing temperature and pressure. Although there are differences in detail, Green (1964a) proposed a nearly identical microstructural evolution responsible for the preservation of several different peridotite mineral assemblages.

A study of the LPO of olivine in the peridotites has suggested that deformation of the coarse-grained lherzolites occurred at relatively high temperature ( $T > 1000^{\circ}\text{C}$ ) and in the mylonitic peridotites the deformation progressed to lower temperatures ( $700\text{--}1000^{\circ}\text{C}$ ). The presence of plagioclase co-existing with olivine in the plagioclase lherzolite and the mylonitic peridotites establishes that deformation also progressed to conditions of lower pressure, because this mineral assemblage is only stable below 8 kbar (Rampone *et al.*, 1993 and references therein).

The microstructure of cross-cutting hydrous shear zones shows that they are later structures and developed in response to deformation at conditions of lower temperature than the mylonitic peridotites.

The microstructural evolution of the Lizard peridotites is further constrained in Chapters 5 & 6 by an investigation into the geochemical properties of these rocks and their minerals.

---

#### **4.4. Petrographic characteristics of the oceanic crust and cumulate rocks**

---

In this section the petrographic characteristics of rocks directly and indirectly associated with the mantle peridotites (Section 4.3) are described. These rocks include ultramafic and mafic cumulates and amphibolites that are related to the construction and evolution of oceanic lithosphere during the formation of the Lizard ophiolite complex. Some of these rocks, for instance the ultramafic Traboe cumulates, are genetically related to the Lizard peridotites, whilst others, including the Crousa gabbro are not.

##### **4.4.1. Cumulates and amphibolites**

Field evidence (Chapter 3) revealed that the amphibolites and associated could be sub-divided into several groups; this sub-division is confirmed by differences in mineral chemistry (Chapter 5) and whole rock chemistry (Chapter 6). In this section, the petrographic features of these groups, including ultramafic Traboe cumulates, mafic Traboe cumulates, gabbroic veins, Landewednack amphibolites and Porthoustock amphibolites are described. The descriptions are sub-divided into *relict primary assemblages* and *later metamorphic assemblages* where possible.

##### **4.4.1.a. Ultramafic Traboe cumulates**

The microstructure of these rocks, which resemble ultramafic cumulates from other ophiolites (Hebert *et al.*, 1989; Harris, 1995), is described with reference to samples collected from the Potstone Point (GR 6683 1565) on the west coast of the Lizard, Porthkerris Quarry (GR 805 231) on the north-east coast of the Lizard and from the Traboe borehole core (BGS collection).

The samples collected from the field outcrops occur in close proximity to mylonitic peridotite (Section 4.3.5) and mafic Traboe cumulate. The microstructure of these samples is very variable and all of the rocks have been subjected to secondary

alteration. They are predominantly medium to fine-grained and preserve granular or mylonitic textures. The samples comprise variable proportions of olivine, clinopyroxene, orthopyroxene, plagioclase and brown amphibole as primary mineral phases. Spinel occurs as a minor mineral phase. Brown amphibole also occurs as a secondary mineral phase, replacing pyroxene. Colourless hornblende forms a secondary retrogressive phase after pyroxene, and saussurite after plagioclase. Talc, chlorite and serpentine minerals are also common, related to the breakdown of olivine and pyroxene. Colourless hornblende and chlorite also occur as the host-mineral phase in cross-cutting hydrous shear zones, identical to the shear zones observed in the coarse-grained and mylonitic peridotites (Section 4.3.8).

In all examples, the primary mineral phases show evidence for extensive recrystallisation and relict porphyroclasts are rarely preserved. Primary textures are rarely preserved, as they are overprinted by secondary metamorphic textures. Relict primary textures include modal layering, with olivine-, pyroxene- and plagioclase-rich layers (<0.5 cm)(Figure 4.31). This modal layering distinguishes these rocks from the feldspathic bands and gabbroic veins discussed in Sections 4.3.5.c. and 4.4.1.c., which do not exhibit modal layering. However, a few samples have a microstructure that strongly resembles the gabbroic veins described in Section 4.4.1.c. It is difficult to determine whether these rocks represent gabbroic veins or pyroxene-rich cumulate layers, because later shearing, recrystallisation and folding has obliterated original textures. The individual layers show both sharp and gradational contacts with adjacent horizons. The olivine, pyroxene and plagioclase generally have an anhedral form and display curved grain boundaries. Spinel occurs as medium grained porphyroclasts and as fine-grained recrystallised grains. It is predominantly associated with olivine or pyroxene-rich layers. Plagioclase or saussurite invariably rims spinel. The spinel is generally a red-brown colour, although, in several samples, the spinel is an olive green colour, very different from spinels in the mylonitic peridotites.

A more variable of range microstructures has been observed in samples obtained from the Traboe borehole core (cf. Leake and Styles, 1984). The microstructure in many of these rocks is difficult to interpret because of the effects of later alteration, including pervasive serpentinisation. A large proportion of the ultramafic rocks in the borehole samples, particularly borehole 2, are mylonitic peridotites. However, several samples appear to be dunitic in composition and superficially resemble serpentinised mylonitic peridotite. They are distinguished by the



abundance of spinel (5-10% modal volume) which is far higher than in the mylonitic peridotites (< 2% modal volume). The spinel in the dunitic rocks is also generally medium-grained, in comparison to fine-grained spinels in the mylonitic peridotites (Figure 4.32). The spinels in the dunitic rocks often show a sub-euhedral form, which is never observed in the mylonitic peridotites, where the spinels are anhedral. The dunitic rocks are commonly interlayered at a mm to cm scale with pyroxene or plagioclase rich layers, and show either sharp or gradational margins. These layers are often highly folded, in response to later deformation. In the pyroxene-rich rocks, both orthopyroxene and clinopyroxene are observed in variable proportions. Relict porphyroclasts of medium-grained orthopyroxene and clinopyroxene are observed in these rocks, surrounded by a matrix of fine-grained, recrystallised pyroxene in a granoblastic matrix. This textural evidence suggests that these rocks have been extensively recrystallised, which explains the lack of preservation of primary igneous textures.

The microstructure of the ultramafic rocks discussed above suggests that these represent deformed and recrystallised, originally layered ultramafic cumulate rocks. These rocks are intimately associated with the mylonitic peridotites of the Lizard Ophiolite Complex and also mafic Traboe cumulate rocks (Section 4.4.1.b.). The mineral and whole rock geochemistry of these cumulates is discussed in Chapters 5 and 6.

#### **4.4.1.b. Mafic Traboe cumulates**

The rocks described in this section were sampled from areas mapped as the Traboe cumulate complex (Leake and Styles, 1984) (Chapter 3). Due to the effects of later amphibolite facies metamorphism, the microstructure of the mafic Traboe cumulates is very similar to the Landwednack amphibolites. Therefore, in addition to microstructural methods, whole rock geochemistry has also been used to distinguish between the different rock types (Chapter 6). The samples were collected from outcrops, where they are inter-layered with ultramafic Traboe cumulates (see above) and from outcrops where there are no associated ultramafic rocks. Samples collected from the I.G.S. Traboe borehole (Leake and Styles, 1984) have also been examined, and in many cases the amphibolitised mafic Traboe cumulates were interlayered with ultramafic rock. These rocks are therefore layered cumulates and represent the upper

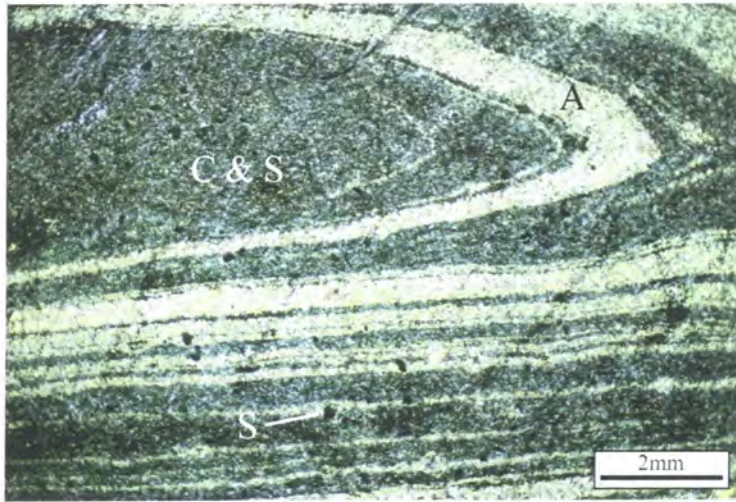


**Figure 4.31.** Folded and altered relict modal layering in ultramafic Traboe cumulates. Layers are composed of chlorite (C) and serpentine minerals (S) after olivine and, colourless hornblende (A) after pyroxene (Sample E52180). *CP*

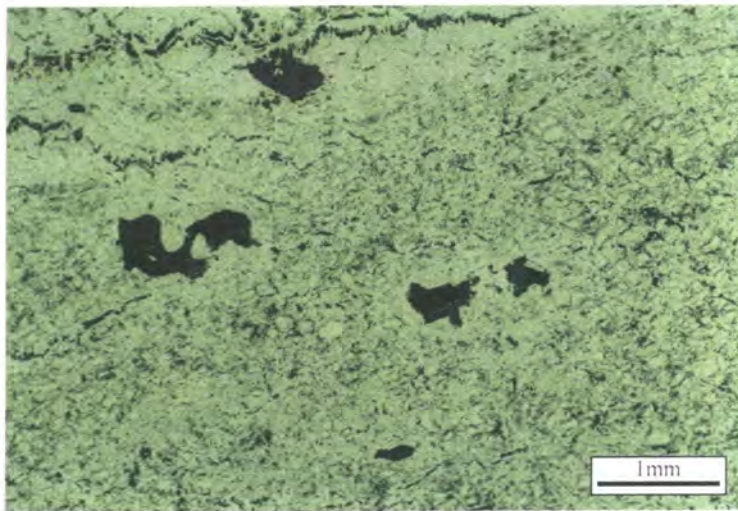


**Figure 4.32.** Sub-euhedral spinel grains (black) in a dunitic layer (serpentinised olivine) of ultramafic Traboe cumulate. (Sample E52167) *PP*

levels of the cumulate stratigraphy, transitional with the ultramafic rocks described above (Leake and Styles, 1984).

### *Relict primary assemblage*

The original primary minerals and textures are very rarely preserved in samples of mafic Traboe cumulate and therefore much of the following discussion refers to later metamorphic assemblages and associated textures. Primary mineral phases include

clinopyroxene, orthopyroxene and plagioclase, which usually occur as relict, coarser-grained porphyroclasts mantled by a recrystallised matrix of fine-grained pyroxene, plagioclase or amphibole. Relict primary igneous textures preserved in these mafic Traboe cumulates include the presence<sup>of</sup> mineral layering (Figure 4.33). The layering is defined by variations in the modal abundance of pyroxene and plagioclase, and when altered, amphibole and plagioclase or saussurite. The petrological features and composition of these layers suggests that, prior to deformation and amphibolite facies metamorphism, the original protoliths were layered gabbroic cumulates. The layering generally shows gradational boundaries, although sharp contacts between individual layers are observed. The scale of the layering is on the mm to cm scale. In some samples, layers may be composed of monomineralic plagioclase or pyroxene/amphibole, and this suggests the development of anorthosite and pyroxenite layers. The layering, characteristic in the mafic Traboe cumulates, is never observed in samples of Landwednack-type amphibolites and can therefore be used to distinguish the different rocks. The layering is thought to have originated by primary igneous cumulate processes in the upper levels of the Traboe cumulate complex.

The mafic Traboe cumulates usually show a weak foliation and lineation defined by the alignment of amphibole, plagioclase and rare relict primary phases. The rocks are generally fine- to medium-grained, although the grain size may show a large variation even at the scale of a single thin-section. The majority of samples have porphyroclastic or granoblastic textures consistent with widespread recrystallisation of these rocks.

### ***Later metamorphic assemblages***

The majority of samples of mafic Traboe cumulate preserve several distinct metamorphic assemblages, which may be related to different tectono-thermal events or phases during an essentially continuous deformation phase.

The earliest metamorphic assemblage recognised comprises relict orthopyroxene or clinopyroxene, brown amphibole and plagioclase (Figure 4.34). This assemblage is rarely preserved, but it is observed in samples collected from the Georges Cove area. In samples where it can be recognised there is evidence for extensive retrogression to later metamorphic assemblages. The rock is fine- to medium-grained and show a wide range textures, including porphyroclastic, granoblastic and

nematoblastic types. Relict pyroxene occurs as either porphyroclasts or recrystallised aggregates with a polygonal granoblastic texture. The pyroxene is invariably rimmed by brown amphibole, suggesting that the amphibole is the product of retrogression of the pyroxene. The brown amphibole typically has a euhedral, elongate prismatic form, which defines the foliation and lineation in the rock. The brown amphibole often contains inclusions of opaque minerals. AnhedraI plagioclase is recrystallised to fine-grained aggregates and is extensively altered to a saussurite.

A second metamorphic assemblage comprises green amphibole, plagioclase and rare relict orthopyroxene or clinopyroxene (Figure 4.35). It is this assemblage that is most similar to the Landewednack amphibolites. It is characteristic of rocks with a fine- to medium grain size with nematoblastic textures. Green amphiboles have a euhedral, elongate prismatic form and are generally fine-grained. They occur as distinct grains or nematoblastic aggregates that pseudomorph former brown amphiboles or pyroxenes. When preserved, relict porphyroclasts of brown amphibole or pyroxene are mantled by an aggregate of green amphibole, which produces well-developed asymmetric porphyroclast shape fabrics. The green amphiboles commonly host inclusions of opaque minerals. Plagioclase is fine-grained, has an anhedraI form and is extensively recrystallised. Secondary alteration of the plagioclase to saussurite often obscures its original texture.

A third and relatively minor metamorphic assemblage is characterised by the presence of a fibrous, fine-grained colourless hornblende (Figure 4.36). The colourless hornblende commonly hosts discrete ( $<0.25\text{mm}$ ) anastomosing shear zones, which crosscut pre-existing fabrics and relict porphyroclasts of brown or green amphibole. Within these shear zones the colourless hornblende displays a marked shape-preferred orientation parallel to the shear zone margins. The colourless hornblende also occurs as randomly orientated, fibrous grains, which rim relict porphyroclasts of green or brown amphibole and plagioclase, and forms the host phase within fractured amphiboles. The colourless hornblende therefore represents a retrograde metamorphic phase, related to the breakdown of pre-existing metamorphic minerals.

Other later low temperature retrograde phases include chlorite after hornblende, saussurite replacing plagioclase and epidote-rich veins that crosscut the shear zones discussed above.



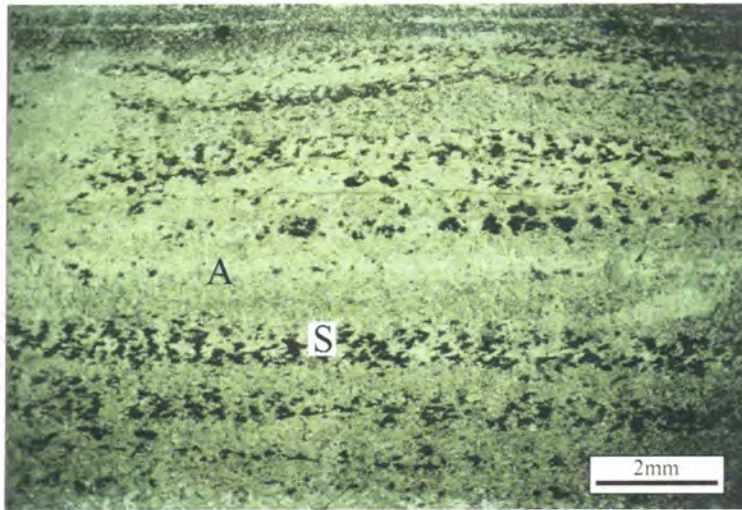


**Figure 4.33.** Mineral layering in mafic Traboe cumulates, individual layers are composed of saussurite (S) after plagioclase and amphibole (A) after pyroxene (Sample E52184). PP $\angle$

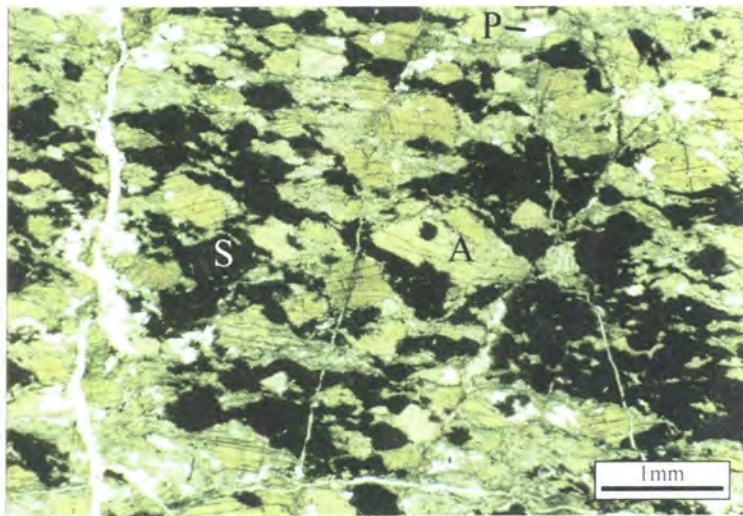


**Figure 4.34.** Brown amphibole-bearing assemblage of the mafic Traboe cumulates, note brown amphibole (A) after pyroxene and most of the plagioclase (P) is now altered to saussurite (S)(Sample CAC143). PP $\angle$

### *Correlation with field evidence*

The different metamorphic assemblages observed in the mafic Traboe cumulates can be correlated with different fabric and/or shear zone orientations. The earliest metamorphic assemblage (relict orthopyroxene or clinopyroxene, brown amphibole and plagioclase) is characteristic of cumulates with a steep fabric, for example in the Porthkerris and Georges Cove areas. Where this assemblage is observed in areas with flat-lying to moderately dipping fabrics (e.g. south-east coast of the Lizard), the assemblage is

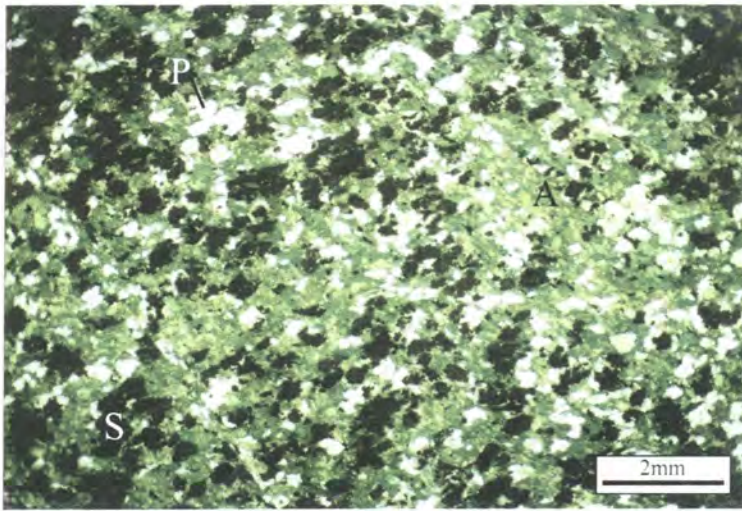


**Figure 4.35.** Green amphibole-bearing assemblage of the mafic Traboe cumulates, note green amphibole (A) after pyroxene and brown amphibole, and the majority of plagioclase grains (P) are altered to saussurite (S)(Sample CAC162). *PPL*

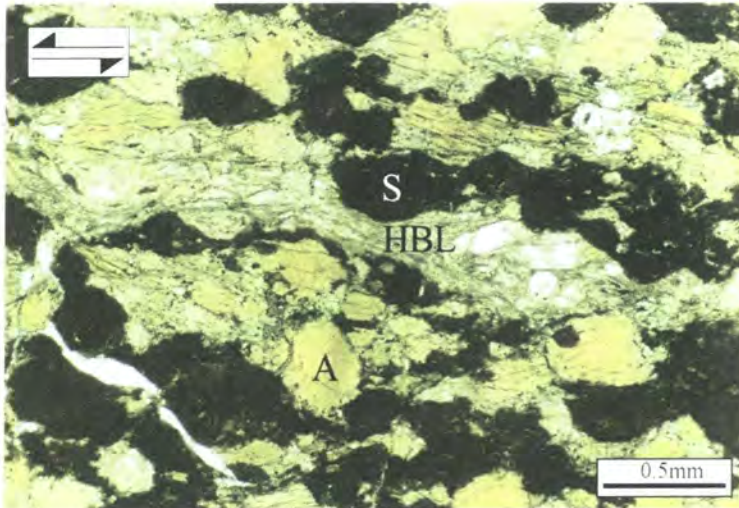


**Figure 4.36.** Brown amphibole-bearing assemblage of the Mafic traboe cumulates with cross-cutting colourless hornblende-bearing shear zones (HBL), which wrap around relict brown amphibole grains (A). Plagioclase grains are completely altered to saussurite (S) (Sample CAC143). *PPL*

always retrogressed to the second metamorphic assemblage characterised by the presence of green amphibole. The green amphibole-bearing assemblage is also observed in samples collected from outcrops with a steep fabric. The third metamorphic and retrograde assemblage, defined by the presence of fibrous, colourless hornblende occurs in proximity to narrow, sub-horizontal shear zones, for example below the peridotite at Kildown Point.

Evidence for later low temperature retrograde alteration is observed in all samples, and includes chlorite, saussurite and epidote. The alteration is often related to



brittle fractures.

#### 4.4.1.c. Gabbroic veins

The microstructure of the gabbroic veins is similar to the microstructure of the smaller feldspathic bands in the mylonitic peridotite (Section 4.3.5.c.). However, the gabbroic veins form much larger and more extensive bodies. Representative modal volumes of the constituent phases in what are regarded as the least altered gabbroic veins are presented below.

**CAC 151** – 45% cpx, 35% saussurite (plagioclase), 10% opx, 5% brown amphibole, 5% opaques.

**CAC 147** – 50% saussurite (plagioclase), 40% cpx, 5% opx, 4% opaques, 1% brown amphibole.

#### *Relict primary assemblage*

The modal volumes of the representative gabbroic veins shows that plagioclase and clinopyroxene are major phases and orthopyroxene, brown amphibole and opaque minerals are minor phases. The rocks are medium to fine-grained (Figure 4.37), and often show a weak foliation defined by the shape-preferred orientation of pyroxene and plagioclase. The texture of the rock is granoblastic, although in some specimens, later alteration and deformation has modified the original textures. Clinopyroxene forms anhedral, medium- to fine-grained crystals, but relict porphyroclasts are preserved in some samples. Where preserved, they are coarse-grained and mantled by medium- to fine-grained, anhedral clinopyroxenes. The presence of porphyroclasts with bent cleavage is further evidence for deformation and this results in recrystallisation to finer-grained clinopyroxenes. Orthopyroxene shows similar textures to the clinopyroxene, and also evidence for extensive recrystallisation.

Plagioclase occurs as medium- to fine-grained crystals with an anhedral form with well developed multiple twinning. In all samples examined, plagioclase occurs as recrystallised grains, associated with pyroxene in a granoblastic texture.

In the majority of specimens, brown amphibole occurs (1-15% modal volume) as a minor phase. The amphibole has an anhedral form and is medium to fine-grained.

The textural relationship between the brown amphibole and pyroxene are complex and may be difficult to interpret. The amphibole often occurs as fine-grained rims to pyroxene and more rarely as a replacement phase along cleavage or exsolution lamellae. In a few specimens, the brown amphibole is a dominant phase (>50 % modal volume) and occurs as large porphyroclasts, whilst pyroxene is relatively scarce and extensively rimmed by amphibole. In most examples, brown amphibole occurs as interlocking grains with the pyroxene. These textural relationships suggest that in the majority of samples, brown amphibole is close to textural equilibrium with the two-pyroxene and plagioclase assemblage. In a minority of examples, however, the amphibole shows evidence for either incipient or extensive replacement of pyroxene.

### ***Secondary alteration of gabbroic veins***

In all samples of gabbroic veins, there is evidence for secondary alteration of the primary mineral assemblage. Plagioclase is commonly entirely replaced by an amorphous, brown-coloured mass of saussurite. Most samples preserve evidence for the breakdown and replacement of pyroxene and, when present, brown amphibole, by pale-green or colourless, fine-grained hornblende (Figure 4.38). The colourless hornblende occurs as randomly orientated, fine-grained laths, which often completely replace an original pyroxene or brown amphibole crystal. The colourless hornblende also occurs as extensive replacement rims or occupies pull-apart fractures associated with pyroxene or brown amphibole. These textures suggest that the colourless hornblende is a later replacement phase related to later retrograde metamorphism of the two-pyroxene or two-pyroxene + brown amphibole assemblage. Titanite occurs as euhedral grains in a few samples. Titanite only occurs where there is extensive development of green amphibole or colourless hornblende and this suggests that it is a metamorphic phase. In a few samples, the colourless hornblende is associated with shear zones, which cross-cut the two-pyroxene + brown amphibole assemblage. Where these samples have been collected, there is usually evidence in the field for cross-cutting shear zones, e.g. Parc Bean Cove (Section 3.4.2.b.). In thin-section, the shear zones are composed of fine-grained colourless hornblende, which shows a mineral preferred orientation parallel to the shear zone margins. Colourless hornblende wraps around relict asymmetric porphyroclasts of pyroxene, plagioclase and brown amphibole. It also occupies pull-apart fractures within these porphyroclasts and

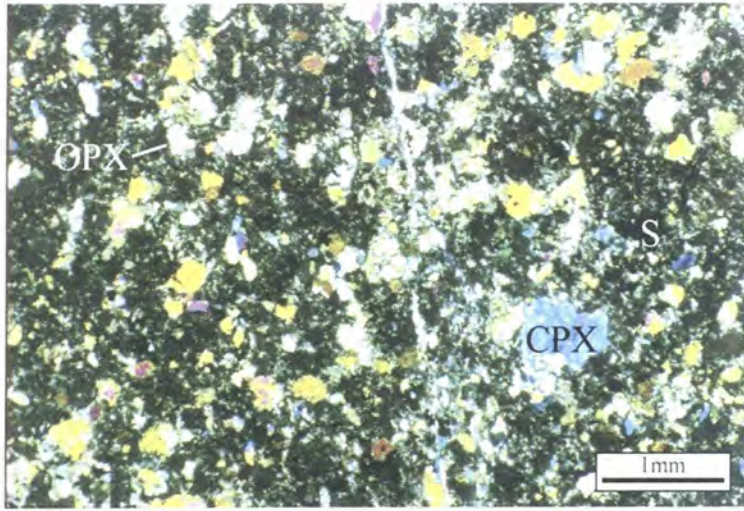


**Figure 4.37.** Gabbroic vein comprising recrystallised clinopyroxene (CPX) and orthopyroxene (OPX) grains. Plagioclase is completely altered to saussurite (S). (Sample CAC151). *CPX*

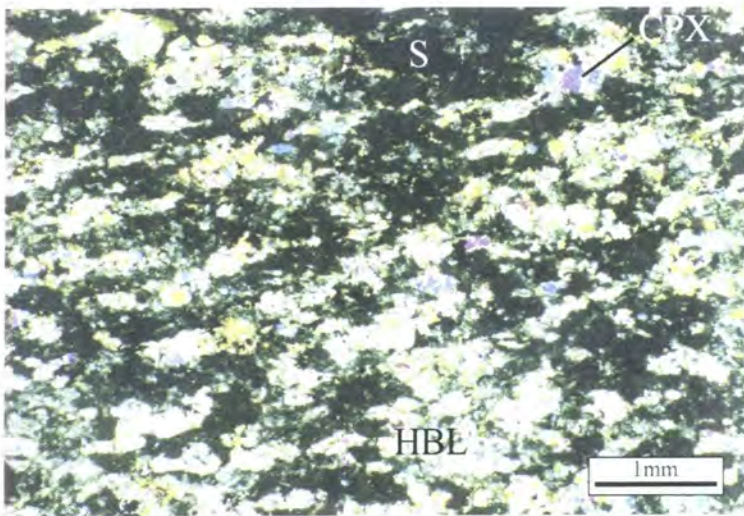


**Figure 4.38.** Secondary alteration of a gabbroic vein. Note that colourless hornblende (HBL) replaces clinopyroxene (CPX), and plagioclase is altered to saussurite (S)(Sample CAC28). *CPX*

develops in fine-grained, recrystallised tails associated with these relict porphyroclasts. Textural features suggest that not only is the hornblende a later retrogressive phases, but that it is also product of the later development of shear zones which cross-cut the fabric defined by the earlier two-pyroxene and two-pyroxene + brown amphibole assemblage. These colourless hornblende-bearing shear zones are texturally identical to the hydrous shear zones identified in the Lizard peridotites (Section 4.3.8.).

#### 4.4.1.d. Landewednack amphibolites

Landewednack amphibolites are distinguished from the amphibolitised mafic Traboe cumulates (Section 4.4.1.b) on the basis of geochemistry (Chapters 5 & 6) and microstructure. The Landewednack amphibolites exhibit a wide range of mineral assemblages and textures that correspond to relict primary and several metamorphic assemblages.

##### *Relict primary assemblage*

In all samples of Landewednack amphibolite examined there is little preservation of the original primary mineral assemblage, which is inferred to be igneous. The original primary assemblage is inferred to have consisted of clinopyroxene and plagioclase. A weak layering of the metamorphic minerals may represent a relict primary igneous layering or be an artefact of tectonic transposition of the metamorphic mineral assemblages.

##### *Later metamorphic assemblages*

The earliest metamorphic mineral assemblage preserved in the Landewednack amphibolites is identified by the presence of brown amphibole. The amphibole occurs in association with relict clinopyroxene and plagioclase (Figure 4.39). Samples preserving this assemblage are fine- to medium-grained and show a weak foliation and lineation defined by aligned amphibole and plagioclase grains. Textures vary between nematoblastic and granoblastic. The brown amphibole is typically euhedral and elongate prismatic. The amphibole often hosts inclusions of opaque minerals. Plagioclase is anhedral and often occurs in granular clusters, although secondary alteration to saussurite commonly obscures the original textures. The plagioclase commonly hosts small, prismatic apatite grains. Relict clinopyroxene occurs as 'corroded' anhedral porphyroclasts and minor brown amphiboles are common as a secondary replacement mineral assemblage along cleavage planes. Further evidence for the breakdown of clinopyroxene to brown amphibole includes the presence of brown amphibole rims around clinopyroxene. The brown amphiboles often wrap-around the clinopyroxene and develop distinctive asymmetric porphyroclast shapes.



A second metamorphic mineral assemblage is distinguished, from the brown amphibole-bearing assemblage by the appearance of green amphibole and titanite (Figure 4.40). The presence of titanite distinguishes this assemblage from the green amphibole-bearing assemblage observed in amphibolitised mafic Traboe cumulates (Section 4.4.1.b.). The lack of titanite in the latter units is attributed to the low abundance of Ti in these meta-gabbroic rocks in contrast to the higher Ti in the meta-basaltic Landwednack amphibolites (Chapter 6). The green amphibole + titanite bearing assemblage may partially or wholly replace the brown amphibole-bearing

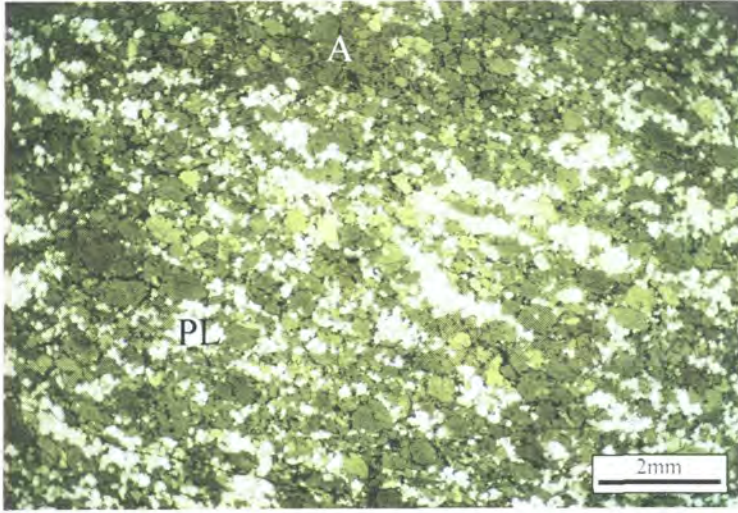


**Figure 4.39.** Typical brown amphibole-bearing assemblage of the Landwednack amphibolites. Note aligned clusters of recrystallised plagioclase (PL) and brown amphibole (A). Opaque minerals are also observed. (Sample CAC152). *PPL*

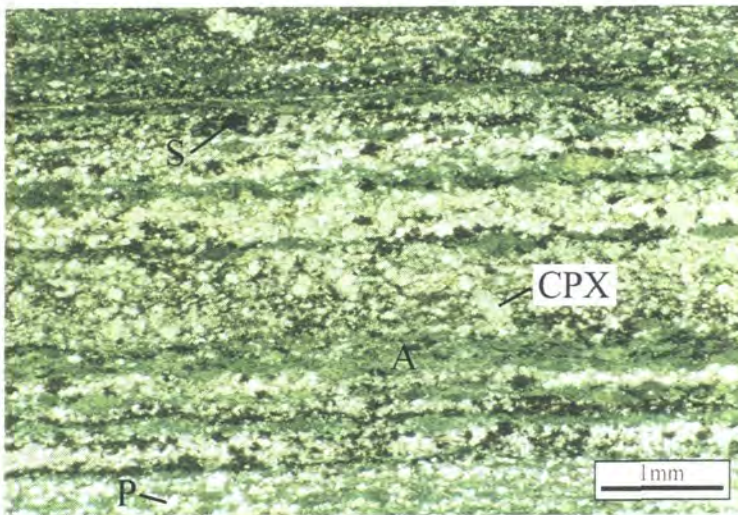


**Figure 4.40.** Green amphibole-bearing assemblage of the Landwednack amphibolite. Note layers composed of clinopyroxene (CPX) and green amphibole (A) after clinopyroxene and brown amphibole. Plagioclase (P) is altered to saussurite (S) (Sample CAC153). *PPL*

assemblage. Evidence for incipient retrogression of the brown amphibole-bearing assemblage is seen where fine-grained green amphibole grains surround porphyroclasts of brown amphibole or brown amphiboles with green rims (Figure 4.41). In many samples, the only evidence for an earlier assemblage is the presence of green amphiboles with relict brown cores. Relict clinopyroxene porphyroclasts are common and are always rimmed by green amphibole, which may define asymmetric porphyroclast shapes. The green amphibole also occurs as small crystals along cleavage planes within the relict clinopyroxene. The clinopyroxene grains may define a layering in the rock, alternating with amphibole-rich layers; this presumably reflects local variations in the degree of retrogression of clinopyroxene. The green amphibole + titanite-bearing rocks are fine- to medium-grained and predominantly have nematoblastic textures. They are generally finer-grained than rocks characterised by an earlier brown amphibole-bearing assemblage, and this undoubtedly reflects a greater degree of recrystallisation in the later assemblage, possibly related to higher-strain. The foliation and lineation are better developed in the green amphibole + titanite-bearing assemblage. Two crystal forms of green amphibole are identified, coarser-grained amphiboles with a euhedral and prismatic form, and fine-grained, subhedral to anhedral amphiboles. The fine-grained amphiboles occur as fibrous grains that form elongate clusters that wrap around and rim the coarser-grained amphiboles. The coarser-grained amphiboles occasionally preserve brown cores and it is suggested, therefore, that these are relict porphyroclasts. Anhedral plagioclase occurs in recrystallised clusters that commonly host small acicular apatites. Titanite, typically euhedral to anhedral, often occurs in elongate clusters that define a foliation in the rock. Minor minerals that occur in this metamorphic assemblage include rare biotite and opaque minerals.

A third metamorphic mineral assemblage can be identified in rocks with either a brown amphibole or a green amphibole + titanite-bearing assemblage. This metamorphic assemblage is characterised by the presence of colourless hornblende (Figure 4.42). Hornblende occurs as randomly orientated fibrous laths that rim earlier clinopyroxenes, brown amphiboles or green amphiboles. The hornblende also hosts narrow cross-cutting shear zones that may wrap around relict porphyroclasts of the pre-existing mineral assemblage.

Epidote hosts veinlets cross-cut all mineral assemblages and other later, retrograde, assemblages include chlorite and prehnite.



### *Distribution of the different metamorphic assemblages*

The different metamorphic mineral assemblages can be correlated with different fabric orientations and shear zones in the field. Amphibolites characterised by a brown amphibole-bearing assemblage are correlated with steep fabrics in the amphibolites on the west coast of the Lizard, e.g. Polurrian Cove, Predannack Head and Ogo Dour Cove

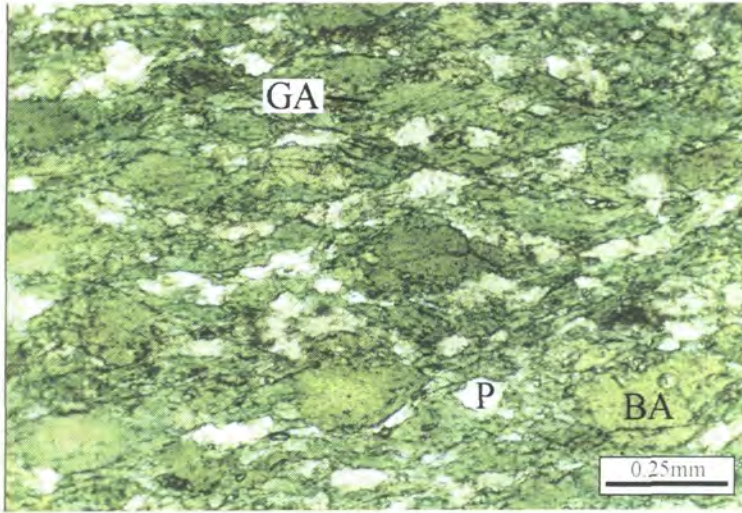


**Figure 4.41.** Relict brown amphiboles (BA) rimmed by green amphibole (GA) – Green amphibole-bearing assemblage of the Landewednack amphibolite. Plagioclase (P) is also present (Sample CAC153). *PPL*

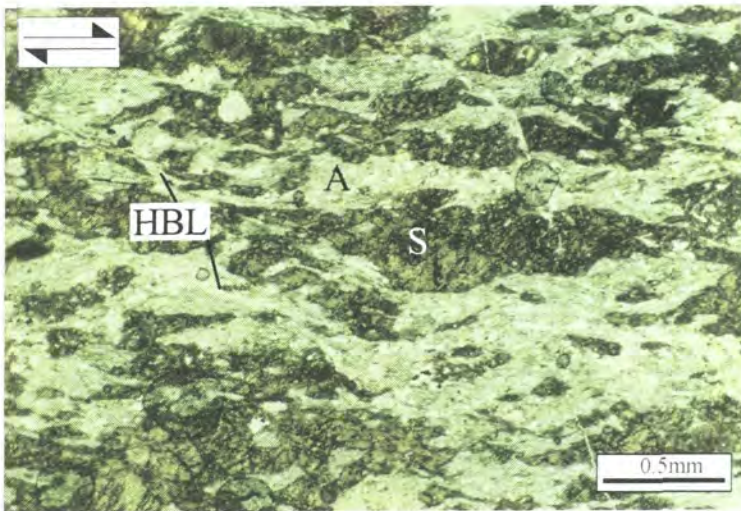


**Figure 4.42.** Sheared green amphibole-bearing assemblage of the Landewednack amphibolite. Note that colourless hornblende (HBL) wraps around relict green amphibole (A) and also hosts narrow anastomosing shear zones. Plagioclase is completely replaced by saussurite (S) (Sample CAC116). *PPL*

(Section 3.4.3). Amphibolites with relatively flat-lying fabrics exposed at Ryniau (Section 3.5.2.b), on the south-east coast of the Lizard between Kildown Point and Polbream Cove (Section 3.5.2.c) and also in the Predannack borehole core, predominantly consist of a green amphibole + titanite-bearing assemblage. In some areas on the south-east coast of the Lizard, amphibolites with a steeper fabric are preserved, for example Kilcobben Point (Section 3.5.2.c), and are characterised by a brown amphibole-bearing assemblage. The colourless hornblende-bearing assemblage is generally more localised in its occurrence. This assemblage fills cross-cutting shear zones within amphibolites in the contact zone with peridotites in the Predannack borehole core and also at similar contact zones at Kildown Point.

Microstructural evidence therefore suggests that the Landewednack amphibolites underwent an initial high-temperature metamorphism of an igneous protolith, resulting in the development of a characteristic by the brown amphibole-bearing assemblage; fabrics are steeply dipping. Two subsequent retrograde metamorphic events are identified by the development green amphibole and colourless hornblende-bearing amphibolites. These different mineral assemblages are correlated with different, low-angle, fabric orientations and shear zone structures preserved in field-outcrop.

#### **4.4.1.e. Porthoustock amphibolites**

Porthoustock amphibolite samples are almost indistinguishable from the green amphibole + titanite-bearing assemblage of the Landewednack amphibolites. Both rock types consist of green amphibole, plagioclase and titanite. The Porthoustock units are distinguished by the presence of relict porphyroclasts of plagioclase, which have an igneous form (Figure 4.43). They also exhibit a greater range of grain size variation, ranging between coarse- and fine-grained varieties, often at the scale of a single thin-section. This grain size variation is attributed to varying protolith lithologies, including meta-gabbros and meta-basaltic dykes, and also to the presence of cross-cutting shear-band fabrics. Other than plagioclase, no relict igneous minerals are observed. The rocks have a nematoblastic to mylonitic textures and a fabric defined by the preferred orientation of amphibole and plagioclase. Subhedral amphibole occurs in clusters that wrap around larger amphibole or plagioclase porphyroclasts, and develop asymmetric porphyroclast shape fabrics. Anhedral plagioclase in the matrix is usually recrystallised

and defines elongate clusters in the rock. Rare, small apatite needles are enclosed by the plagioclase. Minor accessory minerals include subhedral titanite and opaque minerals.

The microstructural evidence suggests that the Porthoustock amphibolites are a retrograde metamorphic assemblage, similar to the Landwednack amphibolites. Whole rock geochemical compositions are different (Chapter 6) and show that the

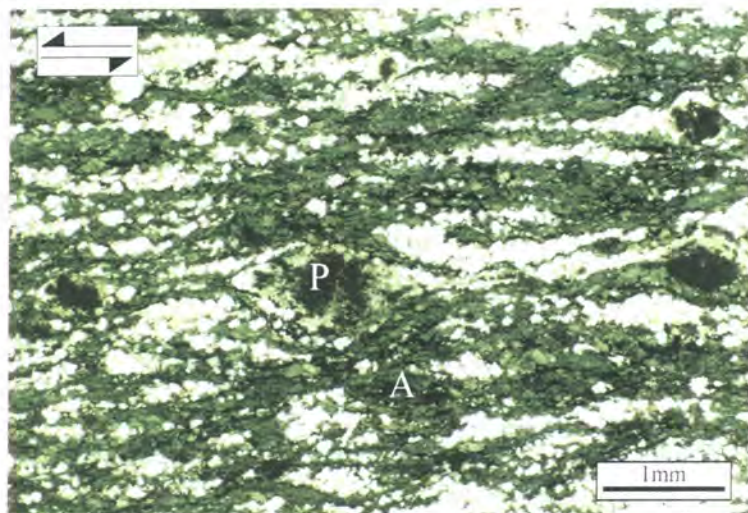


**Figure 4.43.** Porthoustock amphibolite - Asymmetric porphyroclasts of green amphibole (A) and plagioclase (P) (partially altered to saussurite) set in a matrix of aligned clusters of recrystallised amphibole and plagioclase (Sample CAC160). PPL

Landwednack and Porthoustock amphibolites are derived from different igneous protoliths.

#### 4.4.2. Summary

In this section petrographic and microstructural descriptions of a large variety of different lithologies have been presented. In the majority of examples, relict primary mineral assemblages and textures are rarely preserved and later metamorphic mineral assemblages and textures are predominant. In most of the lithologies, regardless of protolith composition and textures, similar metamorphic assemblages and textures are observed. A mineralogical chronology establishes that in some lithological units up to three metamorphic mineral assemblages are present. The three different mineral assemblages are mainly characterised by the colour of amphibole, which reflects its composition (Chapter 5) and these include (a) a brown amphibole + plagioclase high-



temperature metamorphic assemblage, (b) a green amphibole + plagioclase retrograde assemblage, and (c) a second retrograde assemblage characterised by the presence of colourless hornblende. The different metamorphic mineral assemblages are interpreted to be the product of early high-temperature metamorphism, followed by later retrograde tectonothermal events. A correlation between different fabric orientations and shear zones observed in the field (Chapter 3) and the different metamorphic assemblages has been established. The brown amphibole + plagioclase metamorphic assemblage is characteristic of the rocks with steep foliations, which are the earliest fabric preserved in the Lizard rocks. The green amphibole + plagioclase metamorphic assemblage is correlated with flat-lying to moderately dipping fabrics, for example amphibolites on the SE coast of the Lizard. The colourless hornblende-bearing metamorphic assemblage has a more restricted distribution and is typical of the shear zone contacts between peridotite and amphibolite on the SE coast of the Lizard. These correlations are only general and it should be noted that there are exceptions, for example, the occurrence of the green amphibole + plagioclase assemblage in amphibolites with a steep foliation in the Predannack Cliff area.

Green (1964b) recognised the presence of several different metamorphic mineral assemblages in the Lizard amphibolites and proposed that these were developed during a period of regional metamorphism and contemporaneous metamorphism in the aureole of an intrusive peridotite body. Although the same metamorphic mineral assemblages are recognised in the present study, a different sequence of tectonic and metamorphic events is proposed to account for the microstructural evolution. This microstructural evolution is based on presence of different fabric and shear zone structures in the amphibolites and the recognition of both an early high-temperature and later retrograde metamorphic mineral assemblages. This contrasts with the interpretation of Green (1964b), who maintained that the different metamorphic mineral assemblages relate to an entirely prograde metamorphic evolution of an initial blue-green hornblende amphibolite assemblage (with a basaltic composition) in the aureole of the Lizard peridotite. Thus, the brown-green hornblende, brown hornblende with orthopyroxene and clinopyroxene, and orthopyroxene and clinopyroxene pyroxene granulites were viewed as higher-grade equivalents of the blue-green hornblende amphibolite. The present study further demonstrates that rocks characterised by a different metamorphic mineral assemblage do not necessarily have

the same bulk composition, e.g. the gabbroic veins (Chapter 6), suggesting that they are not the metamorphic equivalent of the blue-green hornblende amphibolites.

It should also be noted that there is no petrological evidence for presence of an inverted metamorphic zonation in amphibolites immediately beneath the peridotites (e.g. Kildown Point, Devils Frying-pan, Balk Quarry and Predannack borehole core). Inverted metamorphic zonation has been described in several of the best documented ophiolite complexes, including the Bay of Islands complex (Malpas *et al.*, 1973; Williams and Smyth, 1973; Malpas, 1979; McCaig, 1983; Fergusson and Cawood, 1995) and White Hills ophiolite (Jamieson, 1977, 1979; Girardeau, 1982) in Newfoundland and the Semail ophiolite (Searle *et al.*, 1980; Searle and Malpas, 1980; Searle and Malpas, 1982) in Oman. These sub-ophiolitic metamorphic 'dynamothermal aureoles' are characterised by decreasing metamorphic grade with depth beneath the peridotite (e.g. high-grade amphibolites to unmetamorphosed rocks via greenschist facies rocks) and parallel orientations of the fabrics in basal ultramafic rocks and underlying metamorphic rocks. Although the Lizard Ophiolite Complex does not preserve a dynamothermal aureole directly comparable to the examples documented above, metamorphic rocks of oceanic crust character (Chapter 6) are observed underlying ultramafic rocks at the localities mentioned above (Chapter 3). Field evidence reveals that the fabrics in these metamorphic rocks (Landewednack amphibolites) are parallel to local shear zone fabrics that crosscut the ultramafic rocks at these localities (Chapter 3). Mineral assemblages in shear-zones in the Landewednack amphibolites are also similar to the shear-zones in the ultramafic rocks. The evidence suggests, therefore, that although there is no evidence preserved for a decreasing metamorphic grade with depth, metamorphism in rocks underlying the ultramafic rocks maybe related to a tectonothermal event accompanying tectonic emplacement or obduction of the Lizard Ophiolite Complex. The structural and metamorphic relationships between the ultramafic (peridotites) and metamorphic rocks (Landewednack amphibolites) of the Lizard Ophiolite Complex and the tectonic implications are discussed in more detail, with additional geochemical constraints (Chapters 5 & 6) and compared with other ophiolite complexes in Chapter 7.

---

#### **4.5. Summary of microstructural evidence**

---

Peridotites preserve evidence in the least deformed samples of a relict primary mineral assemblage and textures, which were developed in the spinel lherzolite stability field. Subsequent deformation and a metamorphic evolution of the peridotites was initiated in the spinel lherzolite stability field and produced coarse-grained porphyroclastic textures. A pressure decrease during deformation resulted in the peridotites passing into the plagioclase stability field, and coarse-grained plagioclase lherzolites record this transition. In areas of high-strain, mylonitic plagioclase-bearing peridotite and mylonitic amphibole-bearing peridotite were developed in response to grain-size reduction and recrystallisation. Olivine petrofabrics indicate that the transition from coarse-grained lherzolites to the mylonitic peridotites was also accompanied by a decrease in temperature. The occurrence of amphibole grains in the mylonitic peridotites indicates that fluids or hydrous melts were present during deformation. Later hydrous, low-angle, shear-zones that cross-cut the steeper peridotite fabrics on the east coast of the Lizard, were developed during retrogression of the peridotite. They are composed of colourless hornblende and chlorite that replace pyroxene and earlier amphibole grains.

The microstructure preserved in the ultramafic and mafic Traboe cumulates, Landewednack amphibolites and other rocks related to the generation of oceanic crust, also include relict primary mineral assemblages and textures. These rocks, like the peridotites, also show evidence for a metamorphic evolution and this includes three mineral assemblages and associated textures that correspond to three metamorphic events. The three mineral assemblages, in a mineralogical chronological order are: (a) a brown amphibole + plagioclase high-temperature metamorphic assemblage, (b) a green amphibole + plagioclase retrograde assemblage, and (c) a colourless hornblende-bearing retrograde assemblage. The thermal events that were responsible for the early high-temperature and later retrograde metamorphism are correlated with the different fabric orientations and shear zones observed in the field. The colourless hornblende-bearing assemblage observed in these 'crustal' rocks, is likely to be the metamorphic equivalent to the hydrous shear zones that occur in the peridotites, since both are observed at contacts between peridotite and amphibolite on the SE coast of the Lizard.

The interpretation presented here suggests a history of progressive retrogression during exhumation of an initially high grade metamorphic assemblage. This contrasts



with the entirely prograde metamorphic evolution of the Lizard amphibolites proposed by Green (1964b). In the following chapters (Chapters 5 & 6) geochemical evidence is utilised to further constrain the microstructural and mineralogical evolution of the rocks of the Lizard Ophiolite Complex.

## CHAPTER 5

### MINERAL CHEMISTRY OF THE LIZARD PERIDOTITES AND ASSOCIATED ROCKS

#### 5.1. Introduction

In the previous chapter (Chapter 4), detailed petrological descriptions provided the basis for a study of the composition, and particularly variations in composition, with changes in microstructure of the constituent mineral phases in the rocks of the Lizard peninsula. It has already been established that the Lizard peridotites show a transition in microstructure from coarse-grained lherzolites to mylonitic peridotites. Thus, one of the aims of this chapter is to determine whether there is any variation in the composition of the constituent phases allied to this microstructural transition. A variety of different mafic and ultramafic rocks including dunite, pyroxenite, feldspathic bands, mafic cumulate rocks and troctolite are associated with the Lizard peridotites. The composition of minerals in these rocks is thus examined to allow comparison with the coarse-grained lherzolites and mylonitic peridotites. In this chapter the rocks of the Traboe cumulate complex are subdivided into two types: *mafic Traboe cumulates* and *ultramafic Traboe cumulates* on the basis of petrological characteristics (Chapter 4). Analyses of minerals for Traboe cumulates from the Traboe borehole core are included in this chapter (Leake and Styles, 1984).

Variations in microstructure are also observed in the Landewednack amphibolites and this includes a variation in the colour of amphiboles (Chapter 4) in amphibolites with different fabric orientations and/or associated with different shear-zone structures (Chapter 3). The compositions of the different amphibole types are examined to determine the nature of the correlation between amphibole colour and composition, and the metamorphic significance of the amphibole compositions.

Thermobarometric constraints are provided for the evolution of the peridotites and amphibolites of the Lizard Ophiolite Complex. These constraints are based on the application to these rocks of published thermobarometers using the composition of the constituent mineral phases, specifically mineral pairs.

The overall aim of this chapter is to use mineral compositions to further constrain the microstructural evolution of the rocks of the Lizard Ophiolite Complex

and allow comparison with similar microstructural and mineral compositional variations in other ophiolite complexes documented in the literature. The results presented in this chapter and comparisons with other ophiolites will further constrain the tectonothermal and magmatic evolution of the Lizard Ophiolite Complex.

## 5.2. Olivine chemistry

Olivine compositions in all the different peridotite-types defined by field (Chapter 3) and microstructural (Chapter 4) evidence are presented in this section. The compositions of olivines in feldspathic bands associated with the mylonitic peridotites, and also of olivines in the Traboe cumulate complex rocks, including examples from the Traboe borehole core (Leake and Styles, 1984) and a sample of Coverack troctolite, are included for comparison. The composition of olivines in the Lizard Ophiolite Complex is compared with those in rocks from ophiolites and oceanic environments documented in the literature. The composition of olivines in ultramafic rocks is a sensitive petrogenetic indicator and provides important clues to the degree of melting, fractionation and also interaction with melts during the evolution of these rocks.

### 5.2.1. Olivine chemistry- results

The main compositional variations in olivine in the Lizard peridotites and associated ultramafic/mafic rocks are outlined below. Representative mineral analyses are given in Table 5.1. The full electron probe data set is presented in Appendix D.

	%Fo (range)	%Fo (average)	Wt% NiO
Spinel lherzolite	90.0-91.1	90.6	0.33-0.43
Plagioclase lherzolite	89.7-90.7	90.2	0.43
Transitional assemblage	89.2-89.3	89.3	0.36
Mylonitic plagioclase-bearing peridotite	89.0-90.9	89.7	0.23-0.40
Mylonitic amphibole-bearing peridotite	88.7-90.7	89.7	0.37-0.39
Feldspathic bands	89.3	-	-
Troctolite	80.8	-	-
Ultramafic Traboe cumulates	78.1-91.0	87.9	0.13-0.46

**Table 5.1.** Summary of the compositions of olivines in the Lizard peridotites and the rocks associated with the Lizard peridotites.

Overall, Fo in olivines in the Lizard peridotites and the associated ultramafic/mafic rocks ranges from 78.1 to 91.1 (Figure 5.1; Table 5.1). Spinel lherzolites (90.6) and plagioclase lherzolites (90.2) have the highest average Fo, and ultramafic Traboe cumulates (87.9) the lowest. The ultramafic Traboe cumulates also display the greatest range of Fo (78.1-91.0). The highest and lowest Nickel contents, and the greatest range of Nickel contents are displayed by the ultramafic Traboe cumulates, which vary from 0.13 to 0.46 wt% NiO. The CaO content (Appendix D) of the olivines is invariably low (i.e. <0.09 wt%) and there is no significant variation in composition allied to the different microstructures (Chapter 4).

### 5.2.2. Olivine chemistry- interpretation and discussion

Figure 5.1 displays the range of olivine forsterite (Fo) values obtained from the Lizard peridotites and associated ultramafic/mafic rocks and illustrates that they overlap the compositional range of olivines from various ultramafic rocks in different tectonic

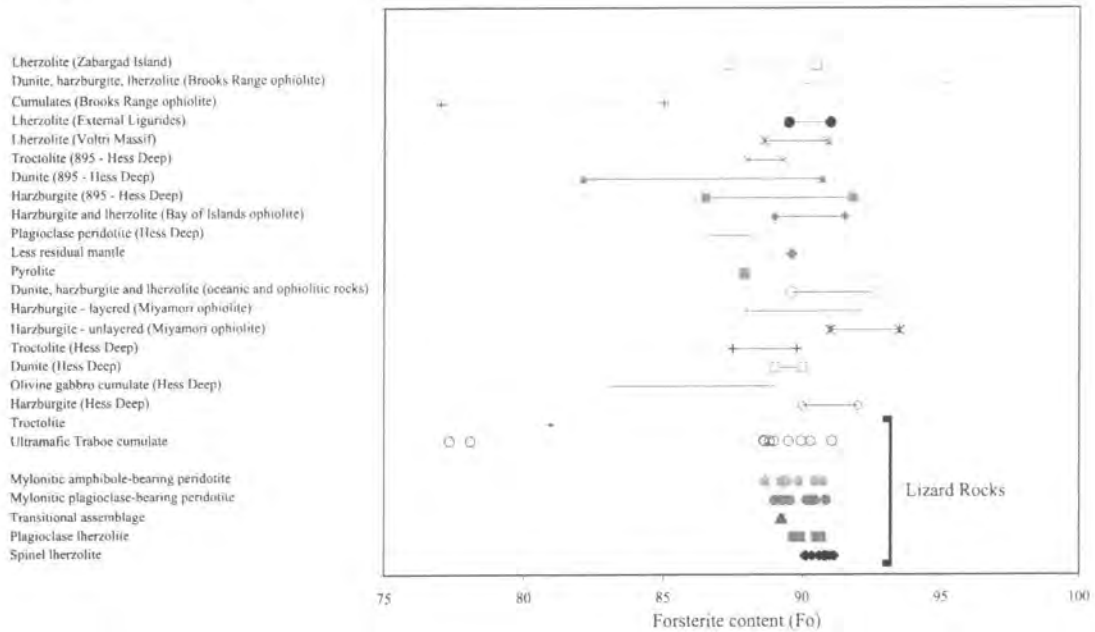


**Figure 5.1.** Forsterite contents of olivines for the Lizard peridotites and associated rocks compared with forsterite contents of olivines for ultramafic rocks from oceanic and ophiolitic environments. Data taken from the literature includes: Hess Deep samples (Hekinian *et al.*, 1993), Miyamori ophiolite, Japan (Ozawa, 1994), oceanic and ophiolitic rocks (Girardeau and Francheteau, 1993), Pyrolite (Ringwood, 1966), Less residual mantle (Mercier *et al.*, 1993), Hess Deep plagioclase peridotite (Girardeau and Francheteau, 1993), Bay of Islands ophiolite (Varfalvy *et al.*, 1996), ODP 895 Hess Deep (Edwards and Malpas, 1996), Voltri Massif Hoogerduijn Strating *et al.* 1993), (External Ligurides (Rampone *et al.*, 1995), Brooks Range ophiolite (Harris, 1995), Zabargad Island (Bonatti *et al.*, 1986).

settings. Four main physical and/or chemical processes may be responsible for the variations in the compositions of olivines in the mafic and ultramafic rocks from the Lizard, and these are: (1) partial melting, (2) spinel- to plagioclase-facies re-equilibration, (3) melt-rock interaction, (4) fractional crystallisation. In the following discussions the variations in the compositions of olivines are discussed in order to evaluate which of these processes are responsible for the compositional variations displayed by olivines in the ultramafic rocks from the Lizard complex.

Figure 5.2 displays wt% NiO versus Fo composition of the olivines in the Lizard peridotites and associated rocks and demonstrates that they overlap the range defined by olivines in oceanic and ophiolitic peridotites. The olivines in the Lizard spinel lherzolites have a composition that lies on a partial melting trend based on an estimate of primitive mantle composition (Less Residual Mantle)(Mercier *et al.*, 1993). This suggests that the composition of the olivine in the spinel lherzolites may be related to partial melting prior to the later deformation and development of the mylonitic peridotites. Olivines in the mylonitic peridotites do not lie on this partial melting trend:

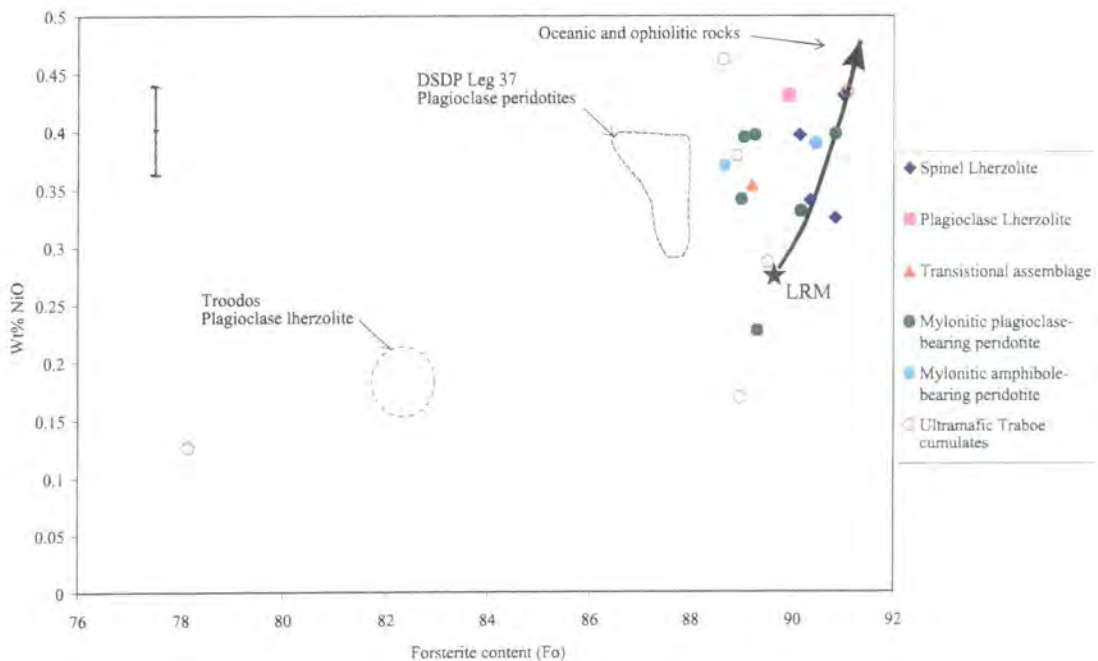


**Figure 5.2.** Plot of wt% NiO versus forsterite content of olivine for peridotites and ultramafic Troaboe cumulates from the Lizard Ophiolite Complex compared with olivines from Troodos plagioclase lherzolite (Benn and Laurent, 1987), oceanic environments (DSDP Leg 45,82 and 107) and ophiolites (Table Mountain and Oman)(Girardeau and Francheteau, 1993), DSDP Leg 37 'metasomatised' plagioclase lherzolites (Girardeau and Francheteau, 1993). Star is for less residual mantle (LRM) defined by Mercier *et al.*, (1993) and the arrow shows the partial melting trend.

therefore it is proposed that the compositional variations in these olivines are not related to partial melting. Olivines in the ultramafic Traboe cumulates from the Lizard have the lowest Fo and NiO composition, which are related to fractionation processes rather than partial melting.

Fo contents (Figure 5.1) in olivines from the Lizard peridotites shows a systematic decrease from the coarse-grained spinel lherzolites to the mylonitic peridotites i.e. there is a progressive Fe enrichment, and this is directly correlated with a decrease in the grain-size of the olivine in response to re-crystallisation (Chapter 4). Evidence presented in the literature (e.g. Hoogerduijn Strating *et al.*, 1993; Rampone *et al.*, 1995) suggests that decreasing Fo values (i.e. Fe-enrichment) in olivine are not related to spinel- to plagioclase-facies re-equilibration of peridotites. Therefore, it is suggested that the decreasing Fo values (i.e. Fe-enrichment), that accompany a decrease in grain-size of olivine from spinel lherzolite to mylonitic peridotite in the Lizard rocks (Chapter 4) are not related to closed-system re-equilibration of olivine at conditions of lower P and T during syn-tectonic recrystallisation.

The compositional trends displayed by the Lizard olivines do not correspond either to melting or to resultant melt segregation of the spinel lherzolite protolith, which would be characterised by an increase in Mg# and NiO in olivine (Ozawa, 1993). Instead, the compositional trends displayed by Lizard olivines may be interpreted to reflect re-equilibration of olivine in response to interaction with a melt. Melt-rock interactions and accompanying mineral compositional changes, including those seen in olivine are well documented in the literature (Edwards and Malpas, 1996; Ozawa, 1994). Melt-impregnated harzburgites from ODP Site 895 (Hess Deep) show a decrease in olivine Fo values and NiO contents in contrast to harzburgites that have not been impregnated by melt (Edwards and Malpas, 1996). Similarly, olivines in peridotites from the Miyamori ophiolite complex (Japan) show a trend of decreasing Fo values and NiO contents and are interpreted by Ozawa (1994) to result from interaction between residual harzburgites and slightly evolved melts. These examples from the literature demonstrate that decreasing Fo values and NiO contents in olivine occur in response to melt-rock interaction. Therefore, it is proposed that similar compositional trends in olivines from the Lizard peridotites are also related to melt-rock interaction. Further evidence for melt-rock interactions on the basis on mineral composition changes are discussed in the following sections and in Chapter 6 the whole rock composition of the Lizard peridotites provides further evidence for melt interaction.



### 5.2.3. Olivine chemistry – summary

- The analyses of olivine compositions in the Lizard peridotites demonstrates that there is a ~~suggestion of~~ trend of decreasing Fo values in olivine from spinel lherzolite to mylonitic amphibole-bearing peridotite. This is also accompanied by a slight decrease in NiO contents.
- It is suggested that the variation in olivine composition from spinel lherzolite to mylonitic peridotite is not related to spinel- to plagioclase-facies re-equilibration or to related partial melting.
- It is proposed that the compositional variations are related to melt-rock interaction.
- The more variable range of olivine compositions defined by the ultramafic Traboe cumulates is probably related to igneous fractionation in contrast to the melt-rock interaction trends defined by the peridotites.

---

### 5.3. Orthopyroxene chemistry

---

Electron microprobe analyses of orthopyroxene in the Lizard peridotites are examined and discussed to determine if there is any correlation between microstructure and orthopyroxene composition. The results are compared with examples from the literature of peridotites from oceanic environments and ophiolites, in order to interpret any tectonic and/or magmatic processes that may have caused the trends observed in orthopyroxene in the Lizard peridotites. The compositions of orthopyroxenes in feldspathic bands and the gabbroic veins interbanded/veining with the mylonitic peridotites, and also in ultramafic Traboe cumulates, including examples from the Traboe borehole core (Leake and Styles, 1984) are compared with the orthopyroxene in the Lizard peridotites.

#### 5.3.1. Orthopyroxene chemistry - results

The main compositional variations in orthopyroxene are outlined below. Representative mineral analyses are given in Table 5.2. The full electron probe data set is presented in Appendix D.

	Fs-En-Wo	Wt% CaO	Wt% Al <sub>2</sub> O <sub>3</sub>	Wt% Cr <sub>2</sub> O <sub>3</sub>	Mg#	Wt% TiO <sub>2</sub>
Spinel lherzolite (PC)	Fs <sub>9.6</sub> En <sub>86.8</sub> Wo <sub>3.5</sub>	1.39-2.29	3.46-5.84	0.47-0.95	89.7-91.0	0.062-0.17
Spinel lherzolite (PR)	-	1.55-2.14	4.07-5.21	0.53-0.96	-	-
Spinel lherzolite (N)	-	1.04-2.31	4.27-4.7	0.48-0.54	90.0-90.4	0.02-0.11
Plagioclase lherzolite (PC)	Fs <sub>10</sub> En <sub>87.3</sub> Wo <sub>2.7</sub>	0.83-1.93	3.11-4.92	0.79-0.84	89.4-90.4	0.1-0.14
Plagioclase lherzolite (PR)	-	0.83-1.28	2.37-3.51	0.73-0.8	-	-
Plagioclase lherzolite (N)	-	1.05-1.39	2.4-2.59	0.58-0.69	89.5-89.9	0.2-0.23
Transitional assemblage (PC)	Fs <sub>10.7</sub> En <sub>86.4</sub> Wo <sub>2.9</sub>	1.32-1.63	3.97-4.07	0.68-0.78	89.0	0.14-0.17
Transitional assemblage (PR)	-	1.09	2.66	0.64-0.68	-	-
Transitional assemblage (N)	-	0.68-0.79	2.11-2.57	0.45	89.3	0.19
Mylonitic plagioclase-Bearing peridotite (PC)	-	0.58-1.6	1.88-4.72	0.33-0.64	88.8-90.0	0.15-0.28
Mylonitic plagioclase-Bearing peridotite (PR)	-	0.51-0.9	2.37-4.72	0.34-0.7	-	-
Mylonitic plagioclase-Bearing peridotite (N)	Fs <sub>10.6</sub> En <sub>88</sub> Wo <sub>1.4</sub>	0.55-1.11	1.19-1.96	0.17-0.49	88.8-90.2	0.14-0.30
Mylonitic amphibole-Bearing peridotite (N)	Fs <sub>10.5</sub> En <sub>88.3</sub> Wo <sub>1.2</sub>	0.55-0.7	1.51-2	0.24-0.37	88.9-90.0	0.06-0.12
Pyroxenite (N)	Fs <sub>11.8</sub> En <sub>85.6</sub> Wo <sub>2.5</sub>	1.3	2.3	0.5	87.9	0.23
Feldspathic bands (P)	-	0.6	3.97	0.36	88.6	0.11
Feldspathic bands (N)	Fs <sub>11.16-11.2</sub> En <sub>87.6-87.7</sub> Wo <sub>1.1-1.2</sub>	0.580.63	1.39-1.67	0.15-0.30	88.9-89.0	0.085-0.2
Ultramafic Traboe cumulates (P)	-	0.4-0.9	2.4-3.5	0.07-0.36	74.1-89.7	0.08-0.14
Ultramafic Traboe cumulates (N)	Fs <sub>9.64-33.0</sub> En <sub>65.7-90.0</sub> Wo <sub>0.3-1.8</sub>	0.13-0.7	0.63-1.8	0.1-0.22	67.0-90.5	0.014-0.14
Mafic Traboe cumulates	Fs <sub>36.4-51.2</sub> En <sub>46.9-61.4</sub> Wo <sub>1.2-2.6</sub>	0.66-1.26	0.63-1.1	0.014-0.19	48.5-89.6	0.008-0.32
Gabbroic veins	Fs <sub>34.0-45.6</sub> En <sub>52.1-63.6</sub> Wo <sub>2.2-6.1</sub>	1.1-1.2	0.86-1.34	0.07-0.14	53.7-65.6	0.15-0.33

**Table 5.2.** Summary of the compositions of orthopyroxenes in the Lizard peridotites and associated ultramafic/mafic rocks. Data for porphyroclasts cores (PC), porphyroclasts rims (PR) and neoblasts (N) are also included.

The orthopyroxenes from the Lizard peridotites and associated ultramafic/mafic rocks plot in the enstatite, bronzite or hypersthene fields with Mg# ranging from 48.5 to 91.0. CaO contents vary from 0.13 to 2.31 wt% and Al<sub>2</sub>O<sub>3</sub> contents from 0.63 to 5.84 wt%. The highest CaO and Al<sub>2</sub>O<sub>3</sub> concentrations are found in the spinel lherzolites and plagioclase lherzolites, whereas the mylonitic plagioclase-bearing peridotites and mylonitic amphibole-bearing peridotites show low CaO and low Al<sub>2</sub>O<sub>3</sub> contents. The ultramafic Traboe cumulates, mafic Traboe cumulates and gabbroic veins show the lowest CaO and Al<sub>2</sub>O<sub>3</sub> values. Cr<sub>2</sub>O<sub>3</sub> contents range from 0.14 to 0.96 wt % with the

highest values being found in the spinel lherzolites and plagioclase lherzolites and the lowest values in the ultramafic Traboe cumulates, mafic Traboe cumulates and gabbroic veins (Table 5.2). Orthopyroxenes in the gabbroic veins and mylonitic plagioclase-bearing peridotites have the highest  $\text{TiO}_2$  concentrations, with values ranging between 0.15 to 0.33 wt%, and 0.14 to 0.30 wt% respectively.

### 5.3.2. Orthopyroxene chemistry – interpretation and discussion

The quadrilateral Fs-En-Wo diagram (Figure 5.3) shows that the compositions of orthopyroxenes in the Lizard peridotites and associated ultramafic/mafic rocks overlaps the range of compositions shown by orthopyroxenes in ultramafic and mafic rocks from ophiolites and oceanic environments. The trend defined by the ultramafic and mafic Traboe cumulates lies close to the 700-900°C isotherms defined by Lindsley (1983)(Figure 5.3b), which suggests these compositions may reflect temperature controlled re-equilibration.

The CaO content of the orthopyroxenes in the Lizard peridotites decreases from cores of porphyroclasts in spinel lherzolite to neoblasts in the mylonitic plagioclase-bearing peridotite and mylonitic amphibole-bearing peridotite and this is accompanied by a decrease in the  $\text{Al}_2\text{O}_3$  concentration (Figure 5.4; Table 5.2). Significantly, the compositional field defined by relict orthopyroxene porphyroclasts in the mylonitic plagioclase-bearing peridotites overlaps the field of porphyroclasts in the spinel and plagioclase lherzolites and transitional assemblage peridotites. This supports the hypothesis that the mylonitic plagioclase-bearing peridotites are the deformed equivalent of the spinel lherzolites and plagioclase lherzolites (Chapter 4). In general there is a decrease in  $\text{Al}_2\text{O}_3$  and CaO content from porphyroclast cores to rims to neoblasts in orthopyroxene in the different peridotite types. However, in some spinel lherzolites, the CaO contents increase in porphyroclast rims (Figure 5.4; Table 5.2). This phenomenon may be attributed in part to the resorption of clinopyroxene-rich exsolution lamellae in the rims of these porphyroclasts (Section 4.3.4.a). Thus, the resultant homogenised composition of the rims is therefore slightly more CaO-rich in than the cores. With one exception, the  $\text{Al}_2\text{O}_3$  and CaO contents of orthopyroxene neoblasts in the spinel lherzolite are lower than porphyroclast core and rim

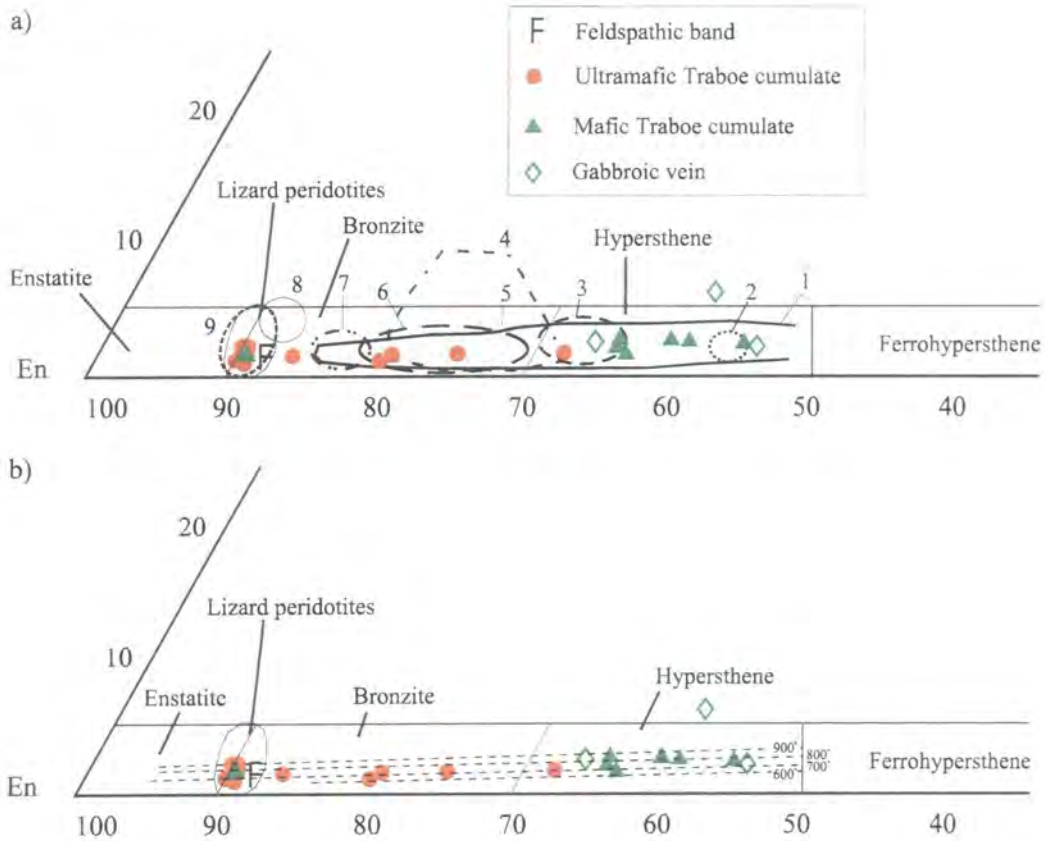


**Figure 5.3.** Fs-En-Wo triangular diagrams of orthopyroxene for ultramafic and mafic rocks associated with the peridotites from the Lizard Ophiolite Complex. (a) Including the compositional fields defined for ultramafic and mafic rocks from the ophiolites and oceanic environments: (1) Oceanic gabbro, 'major oceanic basins' (Hebert *et al.*, 1989 and references therein), (2) Fe-Ti gabbro norite, Garret transform fault (Hebert *et al.*, 1983), (3) Olivine gabbro, Hess Deep (Hekinian *et al.*, 1993), (4) Gabbro, Leg 37, (Hebert *et al.*, 1989 and references therein), (5) Gabbro, Northern Apennine ophiolites (Hebert *et al.*, 1989), (6) Cumulate gabbro and mylonitised gabbro, Hess Deep (Hekinian *et al.*, 1993), (7) Olivine gabbro, Garret transform (Hebert *et al.*, 1983) and ultramafic cumulate, Northern Apennine ophiolites (Hebert *et al.*, 1989), (8) Oceanic ultramafic cumulates (Hebert *et al.*, 1989), (9) Harzburgite and lherzolite, 'major ocean basins' and Northern Apennine ophiolites (Hebert *et al.*, 1989 and references therein), harzburgite, Hess Deep (Hekinian *et al.*, 1993) and Garret transform fault (Hebert *et al.*, 1983), lherzolite, Zabargad Island (Bonatti *et al.*, 1986). (b) Including 600-900°C isotherms from Lindsley (1983).

compositions. In the plagioclase lherzolites, neoblast compositions were analysed in two samples and these have higher CaO contents than porphyroclast rims in the same samples. This phenomenon might be related to equilibrium crystallisation with plagioclase or secondary amphibole.

It is significant that the trend of decreasing  $\text{Al}_2\text{O}_3$  and CaO contents of orthopyroxenes from porphyroclasts to neoblasts, as shown by the Lizard peridotites (Figure 5.4; Table 5.2), is also observed in peridotites described in the literature (Figure

5.5). In comparison to the Lizard peridotites, an overall grain-size reduction of the peridotite and the appearance of plagioclase also accompany the compositional trends shown by orthopyroxenes found in peridotites discussed in the literature. Hoogerduijn Strating *et al.* (1993) interpret the compositional trends in orthopyroxenes in peridotites from the Voltri Massif e.g. decreasing  $\text{Al}_2\text{O}_3$  and CaO contents, to reflect changing conditions of T (and P) during syn-tectonic recrystallisation. More precisely, these compositional changes are a consequence of subsolidus reactions that accompany the spinel- to plagioclase-facies transition in these mantle peridotites. It is suggested that spinel- to plagioclase-facies re-equilibration and the related subsolidus reactions are also responsible for the compositional trends shown by orthopyroxenes found in the Lizard peridotites. This suggestion is based on similarities with trends shown by peridotites discussed in the literature i.e. decreasing  $\text{Al}_2\text{O}_3$  and CaO contents accompanied by decreasing grain size and the development of mylonitic fabrics. In addition, thermobarometric constraints presented in Section 5.8 demonstrate that the mylonitic peridotites from the Lizard re-equilibrated at lower conditions of T and P than the spinel lherzolites. Further evidence for re-equilibration of mineral

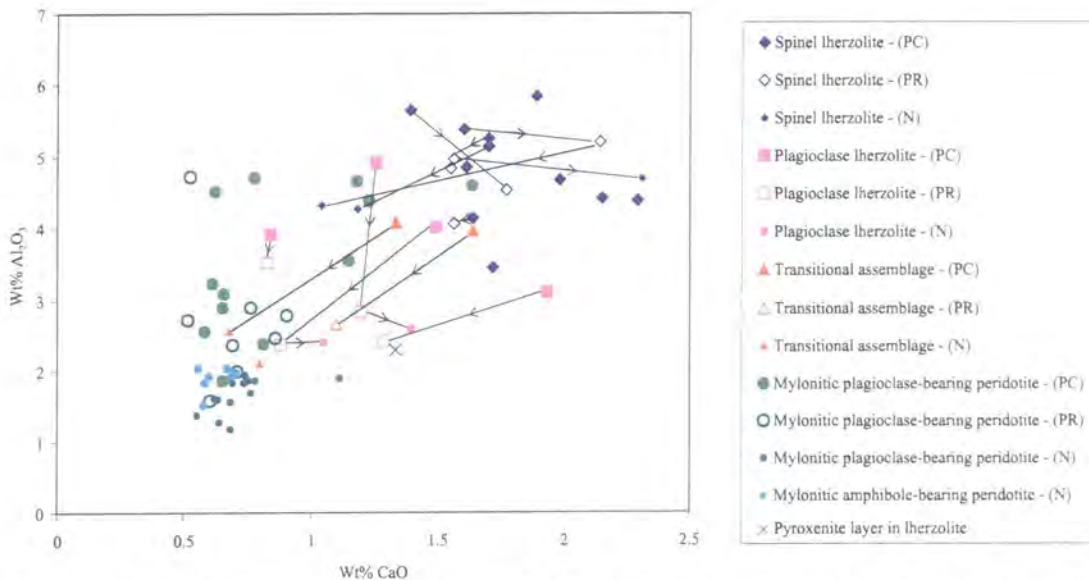


**Figure 5.4.** Plot of wt%  $\text{Al}_2\text{O}_3$  versus wt% CaO of orthopyroxene for peridotites from the Lizard Ophiolite Complex. Tie lines link porphyroclast core (PC), porphyroclast rim (PR), and neoblast (N) compositions of the same sample for the lherzolites and transitional assemblage peridotite.



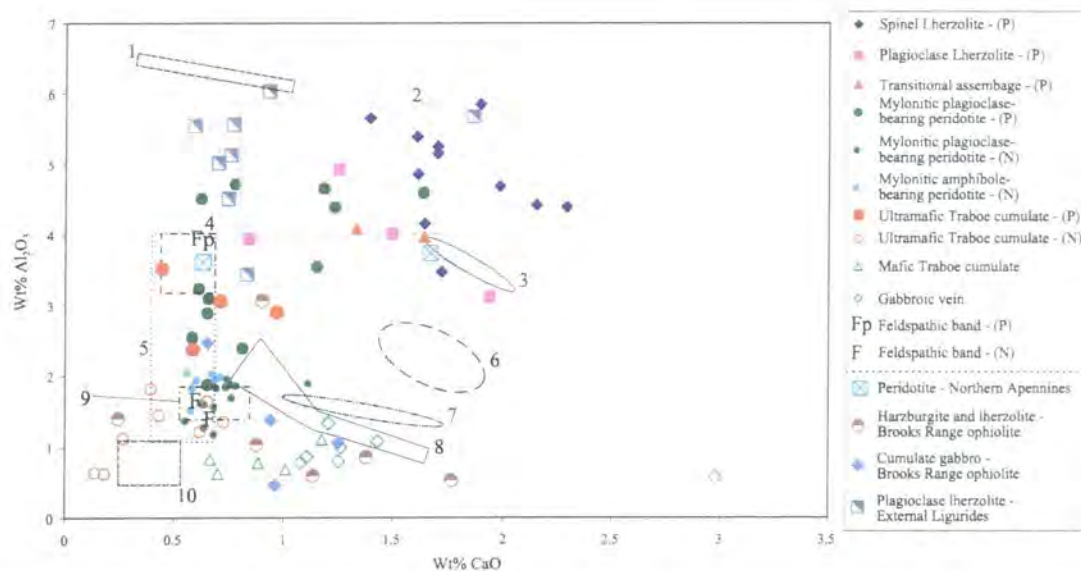


**Figure 5.5.** Plot of wt%  $\text{Al}_2\text{O}_3$  versus wt%  $\text{CaO}$  of orthopyroxene for peridotites, ultramafic and mafic rocks from the Lizard compared with compositional fields defined for ultramafic and mafic rocks from the ophiolites and oceanic environments: (1) Spinel lherzolite, External Ligurides (Rampone *et al.*, 1995), (2) Spinel lherzolite, Voltri Massif (Hoogerduijn Strating *et al.*, 1993), (3) Peridotite, 'major ocean basins' (Hebert *et al.*, 1989 and references therein), (4) Spinel lherzolite, Zabargad Island (Bonatti *et al.*, 1986), (5) Plagioclase lherzolite, Zabargad Island (Bonatti *et al.*, 1986), (6) Harzburgite, Hess Deep (Edwards and Malpas, 1996), (7) Gabbro, Northern Apennine ophiolites (Hebert *et al.*, 1989), (8) Oceanic gabbro, 'major ocean basins' (Hebert *et al.*, 1989 and references therein), (9) Plagioclase-bearing peridotite mylonites, Voltri Massif (Hoogerduijn Strating *et al.*, 1993), (10) Hornblende-bearing peridotite mylonites, Voltri Massif (Hoogerduijn Strating *et al.*, 1993). Also included (see key) are peridotite from Northern Apennine ophiolites (Hebert *et al.*, 1989), harzburgite, lherzolite and cumulates from the Brooks Range ophiolite (Harris, 1995) and plagioclase lherzolite from the External Ligurides (Rampone *et al.*, 1995).

compositions, particularly clinopyroxene and spinel, in response to this spinel- to plagioclase-facies transition will be discussed in later sections.

The  $\text{Al}_2\text{O}_3$  and  $\text{CaO}$  contents of the ultramafic Traboe cumulates, mafic Traboe cumulates and gabbroic veins are distinctly lower than primary orthopyroxenes in ultramafic cumulates and gabbros presented in the literature. This suggests that the orthopyroxenes in cumulates and gabbros from the Lizard are not primary in origin. These compositions are likely to reflect re-equilibration to conditions of lower  $T$  and  $P$  during metamorphism, which is confirmed by estimates of  $T$  and  $P$  presented in Section 5.8.

In Figure 5.6, tie lines link the composition of porphyroclast cores, rims and neoblasts of orthopyroxene in the peridotites and this demonstrates that the  $\text{Cr}_2\text{O}_3$  values generally show a systematic decrease from core to rim to neoblast in the different peridotite assemblages. It is also evident that  $\text{Cr}_2\text{O}_3$  contents decrease from the



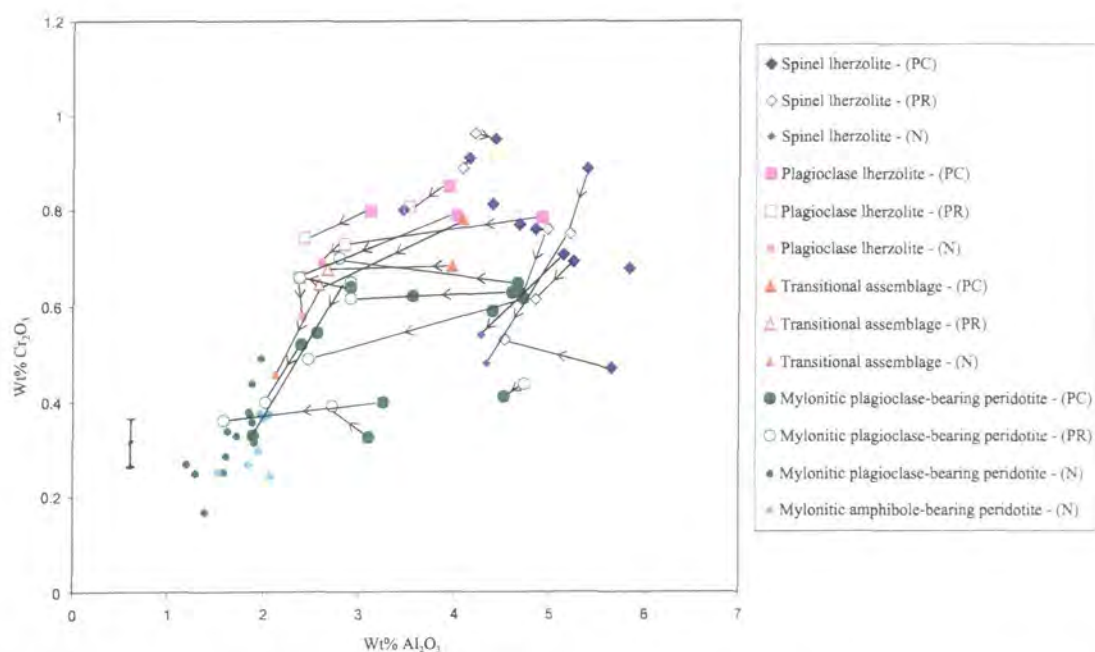


**Figure 5.6.** Plot of wt%  $\text{Cr}_2\text{O}_3$  versus wt%  $\text{Al}_2\text{O}_3$  of orthopyroxene for peridotites from the Lizard Ophiolite Complex. Tie lines link porphyroclast core (PC), porphyroclast rim (PR), and neoblast (N) compositions of the same sample for the lherzolites and transitional assemblage peridotite, and porphyroclast cores (PC) and rims (PR) for the mylonitic plagioclase-bearing peridotite.

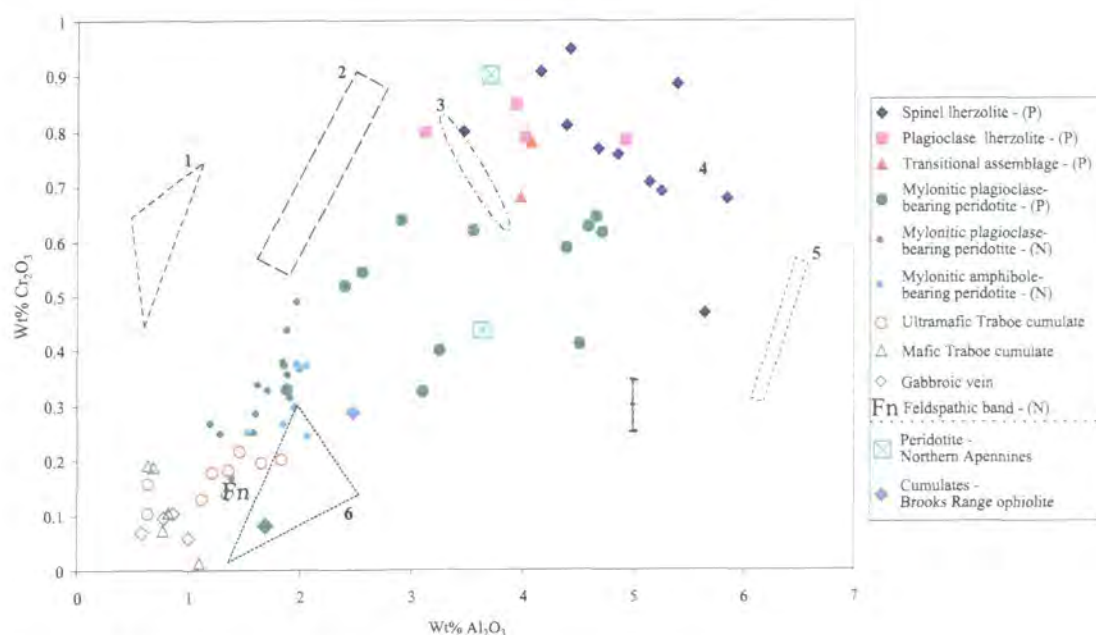


**Figure 5.7.** Plot of wt%  $\text{Cr}_2\text{O}_3$  versus wt%  $\text{Al}_2\text{O}_3$  of orthopyroxene for peridotites, ultramafic and mafic rocks from the Lizard compared with compositional fields defined for ultramafic and mafic rocks from the ophiolites and oceanic environments: (1) Peridotite, the Brooks Range ophiolite (Harris, 1995), (2) Harzburgite, Hess Deep (Edwards and Malpas, 1996), (3) Peridotite, 'major ocean basins' (Hebert *et al.*, 1989 and references therein), (4) Plagioclase lherzolite, External Ligurides (Rampone *et al.*, 1995), (5) Spinel lherzolite, External Ligurides (Rampone *et al.*, 1995), (6) Oceanic gabbro, 'major ocean basins' (Hebert *et al.*, 1989 and references therein). Also included (see key) are peridotite from Northern Apennine ophiolites (Hebert *et al.*, 1989) and cumulates from the Brooks Range ophiolite (Harris, 1995).

spinel lherzolites to the mylonitic peridotites. A decrease of  $\text{Cr}_2\text{O}_3$  in orthopyroxene from coarse-grained porphyroclasts to fine-grain neoblasts is also reported in recrystallised plagioclase-bearing peridotites from the Voltri Massif (Hoogerduijn Strating *et al.*, 1993). This suggests that a decrease in the  $\text{Cr}_2\text{O}_3$  content of orthopyroxenes may be related to spinel- to plagioclase-facies re-equilibration, with  $\text{Cr}_2\text{O}_3$  being re-distributed into spinel, which shows an increase in  $\text{Cr}_2\text{O}_3$  (Section 5.5).

The  $\text{TiO}_2$  contents and  $\text{Mg\#}$  ( $100\text{Mg}/(\text{Mg}+\text{Fe}_{\text{total}})$ ) of orthopyroxene in the different peridotite types also changes with microstructure (Figure 5.8; Table 5.2). The  $\text{TiO}_2$  content of the orthopyroxene is low and therefore close to the detection limit of the microprobe used. However, there are variations that are correlated with changes in peridotite microstructure and consequently these are probably analytically significant. The  $\text{TiO}_2$  contents increase in orthopyroxene from porphyroclast cores in the spinel lherzolites to mylonitic plagioclase-bearing peridotites (Figure 5.8; Table 5.2).

Data presented by Hoogerduijn Strating *et al.* (1993) for peridotites from the Voltri Massif shows that  $\text{TiO}_2$  contents decrease from orthopyroxene porphyroclasts in spinel lherzolites to neoblasts in recrystallised plagioclase-bearing peridotites. The trend of decreasing  $\text{TiO}_2$  with  $\text{Mg\#}$  is possibly related to spinel- to plagioclase-facies re-equilibration, because  $\text{TiO}_2$  may be redistributed into spinel because it cannot be hosted by plagioclase (Rampone *et al.*, 1993). This is the opposite of the trend observed in the Lizard peridotites. This suggests that the trend of increasing  $\text{TiO}_2$  with decreasing  $\text{Mg\#}$  from spinel lherzolite to mylonitic plagioclase-bearing peridotite is not related to spinel- to plagioclase-facies re-equilibration. The increase in  $\text{TiO}_2$  is also inconsistent with different degrees of melting, because the lack of evidence for melting based on microstructural observations (Chapter 4) and bulk compositions (Chapter 6). An alternative process that may modify the  $\text{TiO}_2$  content of orthopyroxene in peridotites is melt impregnation, therefore trend of increasing  $\text{TiO}_2$  in the mylonitic plagioclase-bearing peridotite observed in the Lizard peridotites may be attributed to melt-rock interactions, as suggested by olivine compositions e.g. decreasing Fo values (Section 5.2.2). Orthopyroxenes in the mylonitic amphibole-bearing peridotites show significantly lower  $\text{TiO}_2$  contents than mylonitic plagioclase-bearing peridotites. This  $\text{TiO}_2$  decrease is attributed to the extensive development of pargasitic hornblende in the mylonitic amphibole-bearing peridotite, which results partly from the breakdown of the pyroxene and melt- or fluid-rock interactions (see Section 4.3.5.b).

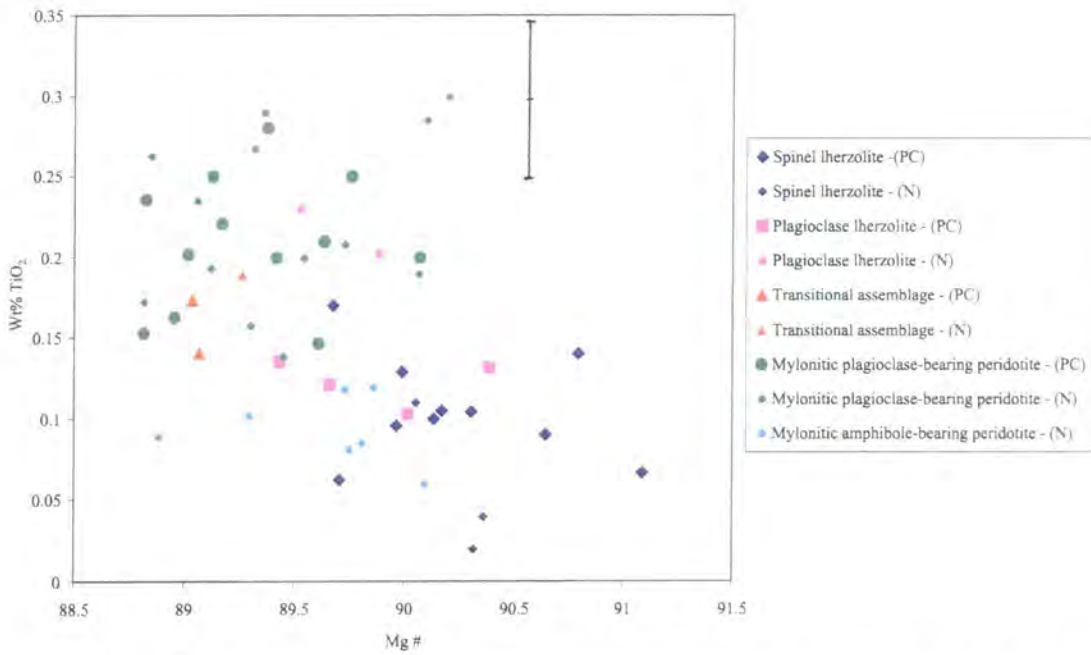


**Figure 5.8.** Plot of wt% TiO<sub>2</sub> versus Mg# (100Mg/(Mg+Fe)) of orthopyroxene for peridotites from the Lizard Ophiolite Complex. The plot includes both porphyroclast core (PC) and neoblast (N) compositions for the lherzolites, transitional assemblage and mylonitic plagioclase-bearing peridotites.

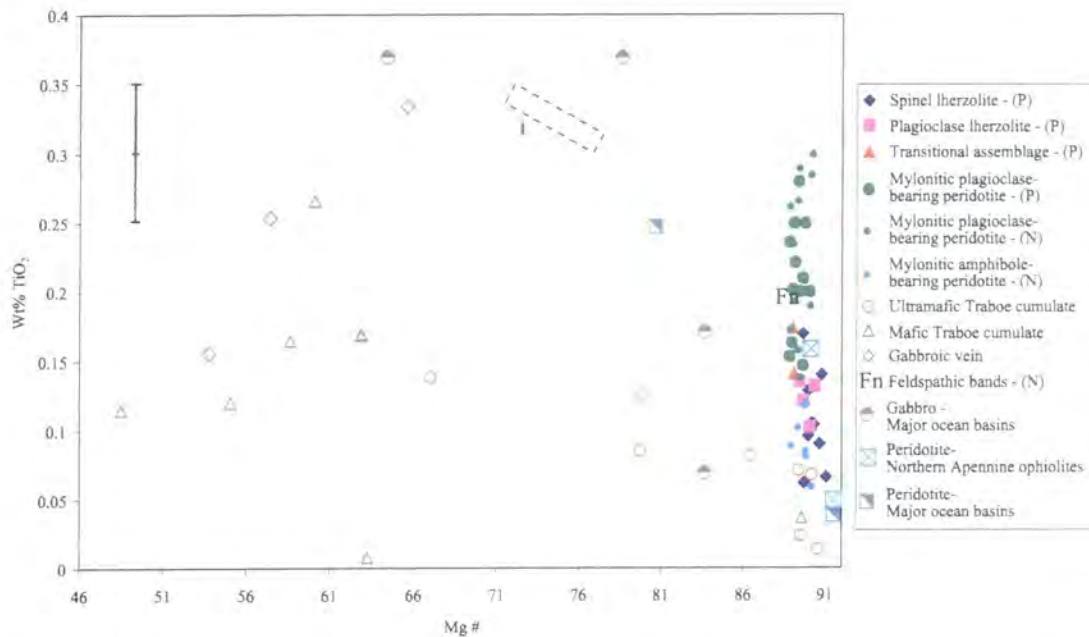


**Figure 5.9.** Plot of wt% TiO<sub>2</sub> versus Mg# (100Mg/(Mg+Fe)) of orthopyroxene for peridotite, ultramafic and mafic rocks from the Lizard Ophiolite Complex compared with compositional fields defined for ultramafic and mafic rocks from the ophiolites and oceanic environments: (I) Gabbro, Northern Apennine ophiolites (Hebert *et al.*, 1989). Also included (see key) are Oceanic gabbro and peridotite from 'major ocean basins' (Hebert *et al.*, 1989 and references therein) and peridotite from Northern Apennine ophiolites (Hebert *et al.*, 1989).

The range of compositions of the major elements in the orthopyroxenes of the ultramafic Traboe cumulates, mafic Traboe cumulates and gabbroic veins may be

attributed to a variety of magmatic processes. The large range of Mg# suggests different degrees of fractionation related to melt segregation during formation. The possibility that some of the compositional variations e.g. decreasing CaO with Al<sub>2</sub>O<sub>3</sub> contents in orthopyroxene in the ultramafic Traboe cumulates, mafic Traboe cumulates and gabbroic veins are related to metamorphic re-equilibration and/or melt-rock interactions cannot be excluded on the basis of the evidence presented here. In particular, it should be noted that these processes have modified the composition of orthopyroxene and olivine in the mylonitic peridotites of the Lizard.

### **5.3.3. Orthopyroxene chemistry – summary**

- The compositional trends in orthopyroxene (e.g. decreasing Al<sub>2</sub>O<sub>3</sub> and CaO) in peridotites from the Lizard Ophiolite Complex are interpreted to reflect re-equilibration following changing conditions of T (and P) during syn-tectonic recrystallisation and more specifically subsolidus reactions that accompany the spinel- to plagioclase-facies transition in these mantle peridotites.
- The trend of increasing TiO<sub>2</sub> in the mylonitic plagioclase-bearing peridotite is not consistent with spinel- to plagioclase-facies re-equilibration or different degrees of melting. Alternatively it is proposed that the TiO<sub>2</sub> increase may be attributed to melt-rock interactions, as suggested by variations in the Fo content of olivines (Section 5.2).
- It is therefore proposed that the compositional variations in orthopyroxene in the Lizard peridotites may be a consequence of both spinel- to plagioclase-facies re-equilibration and melt-rock interactions.
- The large range of Mg# for orthopyroxene in the ultramafic and mafic Traboe cumulates and gabbroic veins suggests different degrees fractionation related to melt segregation during formation.

---

### **5.4. Clinopyroxene chemistry**

---

The results of a electron microprobe study of clinopyroxene composition in the Lizard peridotites and associated ultramafic and mafic rocks are presented in this Section and, in accordance with the previous two Sections, these results are compared with

examples from the literature. The results for the Lizard clinopyroxenes are also interpreted in terms of the metamorphic and/or magmatic processes responsible for the compositions and compositional trends observed. The composition of clinopyroxenes in particular, serves as a sensitive petrogenetic indicator and should therefore provide important clues to the magmatic processes that have occurred during the origin and evolution of the ultramafic and mafic rocks of the Lizard Ophiolite Complex. In a final sub-Section, the analyses of clinopyroxene taken from the Landewednack amphibolites are presented and interpreted in terms of the geological processes responsible for the compositions observed. These analyses are also compared with examples taken from the literature.

#### 5.4.1. Clinopyroxene chemistry - results

	Fs-En-Wo	Wt% CaO	Wt% Al <sub>2</sub> O <sub>3</sub>	Wt% Cr <sub>2</sub> O <sub>3</sub>	Mg#	Wt% TiO <sub>2</sub>
Spinel lherzolite (PC)	Fs <sub>4.3-5.8</sub> En <sub>46.8-52.9</sub> Wo <sub>41.8-49.6</sub>	19.7-23.1	4.2-7.0	1.0-1.4	89.6-91.8	0.18-0.46
Spinel lherzolite (PR)		20.8-21.6	3.12-6.98	1.1-1.4	90.2-91.8	0.26-0.42
Spinel lherzolite (N)		21.4-23.4	3.15-6.11	1.0-1.2	90.9-93.2	0.21-0.37
Plagioclase lherzolite (PC)	Fs <sub>4.8-6.3</sub> En <sub>48.8-50.8</sub> Wo <sub>42.9-46.4</sub>	20.3-22.2	4.5-6.7	1.0-1.3	89.2-91.2	0.21-0.38
Plagioclase lherzolite (N)	-	22.4	4.84	1.24	90.0	0.46
Transitional assemblage (PC)	Fs <sub>5.9-6.2</sub> En <sub>48.5-51.4</sub> Wo <sub>42.4-45.5</sub>	19.9-21.5	5.0-7.0	1.0-1.1	89.1-89.2	0.45-0.47
Transitional assemblage (PR)	-	23.3	6.24	1.15	88.9	0.76
Transitional assemblage (N)	-	22.5	3.6	1.2	90.0	0.62
Mylonitic plagioclase-Bearing peridotite (N)	Fs <sub>4.7-6.6</sub> En <sub>46.3-55.1</sub> Wo <sub>38.3-48.5</sub>	18.5-23.3	2.8-4.75	0.68-1.1	89.3-93.1	0.55-0.93
Mylonitic amphibole-Bearing peridotite (N)	Fs <sub>4.2-4.9</sub> En <sub>47.8-48.7</sub> Wo <sub>46.4-47.9</sub>	22.5-23.9	2.0-2.74	0.61-0.68	91.1-92.3	0.05-0.23
Pyroxenite (N)	Fs <sub>5.5-6.8</sub> En <sub>45.1-50.7</sub> Wo <sub>42.5-49.1</sub>	20.3-22.8	4.8-7.0	0.82-1.2	88.2-89.8	0.2-0.5
Feldspathic bands (N)	Fs <sub>4.1</sub> En <sub>48.4</sub> Wo <sub>47.4</sub>	24.1	1.8	0.31	92.4	0.29
Ultramafic Traboe cumulates (N)	Fs <sub>2.8-8.3</sub> En <sub>43.1-48.6</sub> Wo <sub>46.0-48.6</sub>	22.8-24.2	1.36-4.8	0.26-0.49	84.2-94.5	0.12-0.48
Mafic Traboe cumulates	Fs <sub>4.9-21.0</sub> En <sub>36.5-47.3</sub> Wo <sub>43.3-44.7</sub>	18.9-25.6	0.9-5.4	0.06-0.22	62.0-90.4	0.11-0.83
Gabbroic veins	Fs <sub>14.8-19.1</sub> En <sub>36.2-41.7</sub> Wo <sub>43.3-44.7</sub>	20.6-21.9	1.2-2.4	0.12-0.17	65.6-74.3	0.35-0.61
Mafic dyke	Fs <sub>11.2</sub> En <sub>44.1</sub> Wo <sub>44.6</sub>	21.2	4.4	0.35	79.8	1.2
Troctolite	Fs <sub>9.4</sub> En <sub>45.3</sub> Wo <sub>45.4</sub>	22.0	3.5	0.67	82.8	1.1

**Table 5.3.** Summary of the compositions of clinopyroxenes in the Lizard peridotites and associated ultramafic/mafic rocks. Data for porphyroclasts cores (PC), porphyroclasts rims (PR) and neoblasts (N) are also included.

The main compositional variations in clinopyroxene are outlined below. Representative mineral analyses are given in Table 5.3. The full electron probe data set is presented in Appendix D.

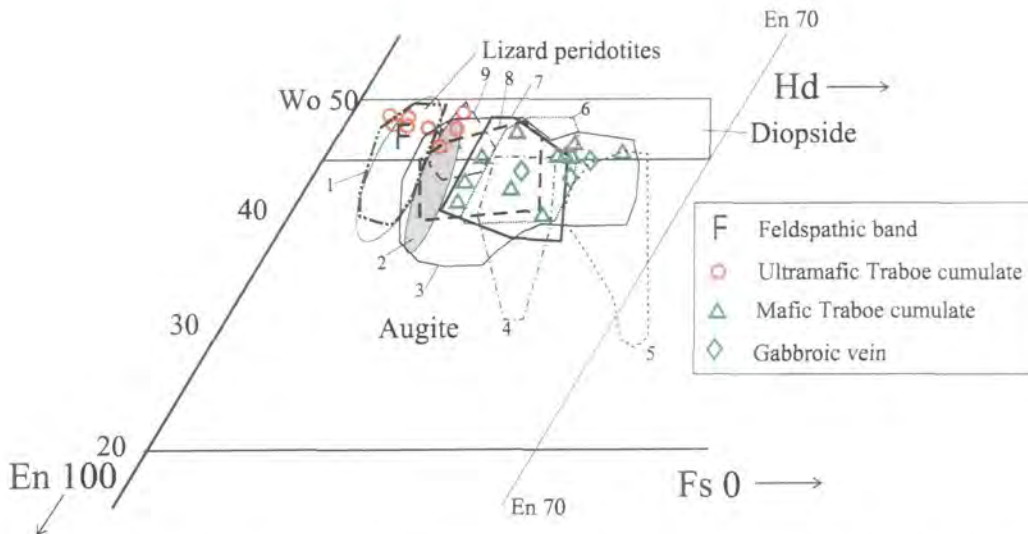
Clinopyroxene compositions range between diopside and augite with wollastonite contents ranging from 42.4 to 49.6 (Table 5.3). CaO contents range from 18.5 to 25.6 wt% with the largest range being found in the mafic Traboe cumulates (18.9-25.6 wt%).  $\text{Al}_2\text{O}_3$  contents vary from 0.9 to 7.0 wt% with the highest concentrations being found in the spinel lherzolites, plagioclase lherzolites and transitional assemblage peridotites, and the lowest values in the mafic Traboe cumulates and gabbroic veins (Table 5.3).  $\text{Cr}_2\text{O}_3$  contents are highest in the peridotites (0.61-1.4 wt%) and lowest in the ultramafic and mafic Traboe cumulates and gabbroic veins (0.06-0.49 wt%). The peridotites display a limited range of Mg# contents (88.2-93.1), whereas the mafic Traboe cumulates show the largest range from 62.0 to 90.4.  $\text{TiO}_2$  contents range from 0.05 to 1.2 wt% with the highest values being found in a mafic dyke.

#### 5.4.2. Clinopyroxene chemistry – interpretation and discussion

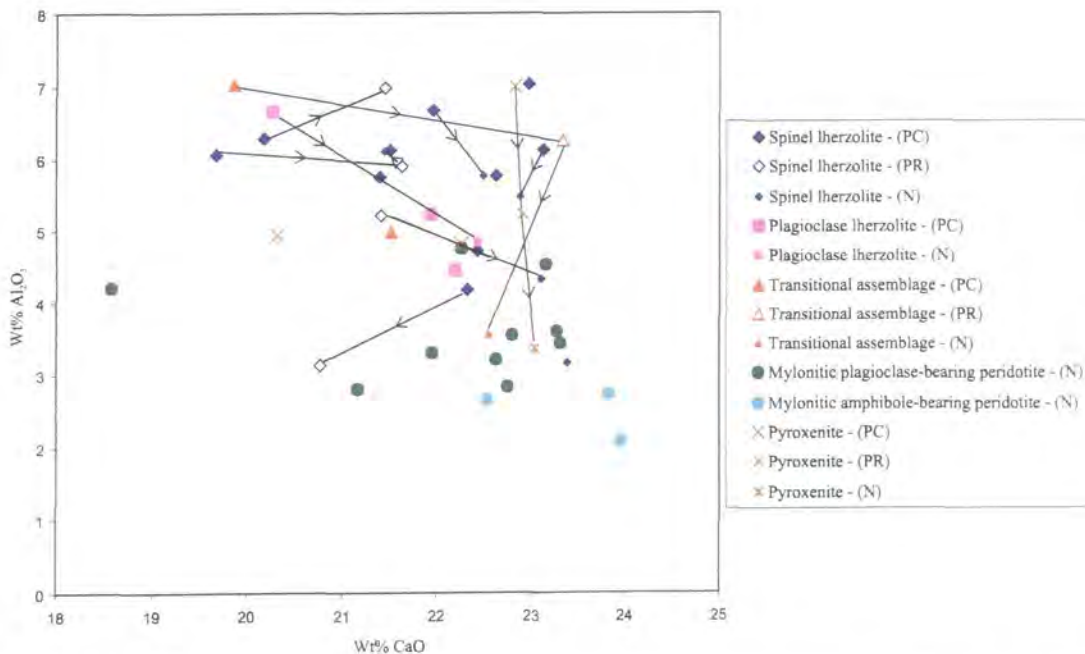
A quadrilateral Fs-En-Wo diagram (Figure 5.10) illustrates that the Lizard peridotites fall within the range defined by ultramafic rocks from ophiolites and oceanic environments and that the ultramafic Traboe cumulates overlap this range. More significantly the mafic Traboe cumulates and gabbroic veins fall within the compositional ranges defined by mafic cumulates and gabbroic rocks, confirming the cumulate origin of these rocks.

Figure 5.11 demonstrates that there is a systematic decrease in  $\text{Al}_2\text{O}_3$  contents, which is correlated with increasing CaO concentrations in clinopyroxenes from the spinel lherzolites to the mylonitic amphibole-bearing peridotites. But, the variations in composition between clinopyroxene porphyroclasts cores, rims and neoblasts in the spinel lherzolite, plagioclase lherzolite and transitional assemblage peridotites are inconsistent, although porphyroclast rims and neoblasts generally show lower  $\text{Al}_2\text{O}_3$  and higher CaO contents than porphyroclast cores (Figure 5.11). In one particular pyroxenite sample (CAC 44); the  $\text{Al}_2\text{O}_3$  contents decrease systematically from porphyroclast core (7 wt%) and rim (5.23 wt%) to the neoblasts (3.34 wt%),





**Figure 5.10.** A Fs-En-Wo triangular diagram of clinopyroxene for peridotites, ultramafic and mafic rocks from the Lizard Ophiolite Complex compared with compositional fields defined for ultramafic and mafic rocks from the ophiolites and oceanic environments: (1) Includes harzburgite, lherzolite and ultramafic cumulates from 'major oceanic basins' (Hebert *et al.*, 1989 and references therein), harzburgite and lherzolite from Northern Apennine ophiolites (Hebert *et al.*, 1989), lherzolite from Zabargad Island (Bonatti *et al.*, 1986), harzburgite from Hess Deep (Hekinian *et al.*, 1993) and harzburgite, Garret transform fault (Hebert *et al.*, 1983), (2) Olivine gabbro, Garret transform (Hebert *et al.*, 1983), (3) Oceanic gabbro, 'major oceanic basins' (Hebert *et al.*, 1989 and references therein), (4) Isotropic gabbro, Hess Deep (Hekinian *et al.*, 1993), (5) Fe-Ti gabbro norite, Garret transform fault (Hebert *et al.*, 1983), (6) Metagabbro and gabbroic mylonites, Hess Deep (Hekinian *et al.*, 1993), (7) Cumulate gabbro, Hess Deep (Hekinian *et al.*, 1993), (8) Gabbro, Northern Apennine ophiolites (Hebert *et al.*, 1989), (9) Olivine gabbro, Hess Deep (Hekinian *et al.*, 1993).



**Figure 5.11.** Plot of wt%  $\text{Al}_2\text{O}_3$  versus wt%  $\text{CaO}$  of clinopyroxene peridotites from the Lizard. Tie lines link porphyroclast core (PC), porphyroclast rim (PR), and neoblast (N) compositions of the same sample for the lherzolites and transitional assemblage peridotite.

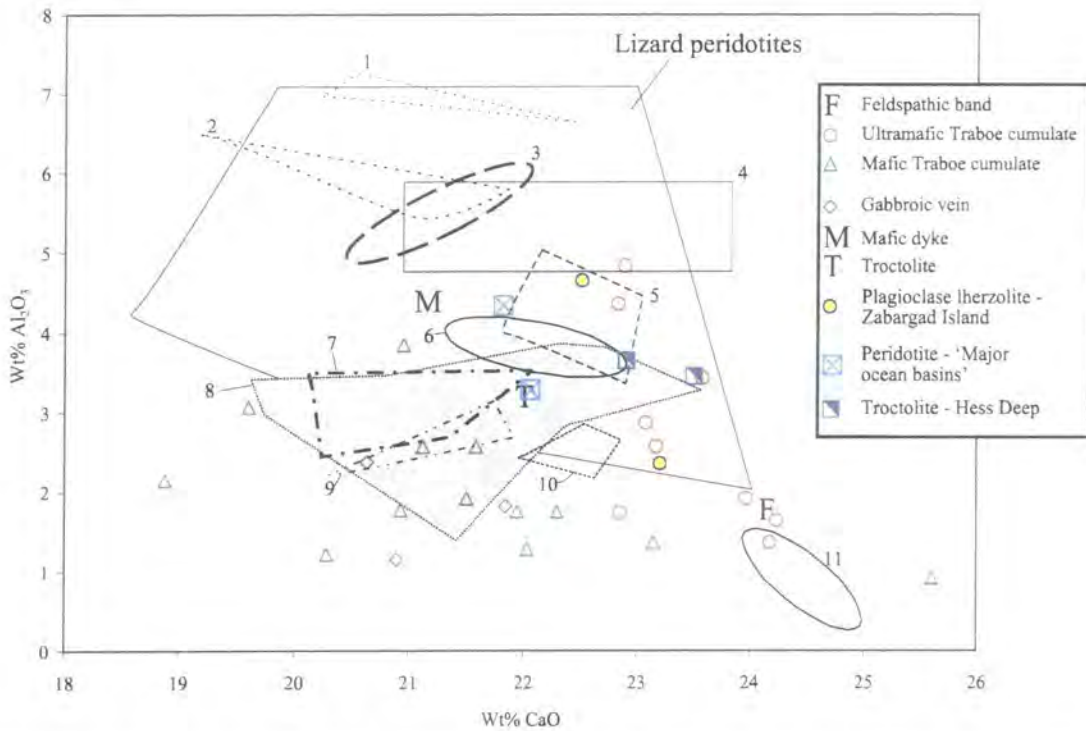


**Figure 5.12.** Plot of wt%  $\text{Al}_2\text{O}_3$  versus wt%  $\text{CaO}$  of clinopyroxene for peridotites, ultramafic and mafic rocks from the Lizard compared with compositional fields defined for ultramafic and mafic rocks from the ophiolites and oceanic environments: (1) Spinel lherzolite, External Ligurides (Rampone *et al.*, 1995), (2) Spinel lherzolite, Zabargad Island (Bonatti *et al.*, 1986), (3) Peridotite, Northern Apennine ophiolites (Hebert *et al.*, 1989), (4) Spinel lherzolite, Voltri Massif (Hoogerduijn Strating *et al.*, 1993), (5) Plagioclase lherzolite, External Ligurides (Rampone *et al.*, 1995), (6) Plagioclase-bearing peridotite mylonites, Voltri Massif (Hoogerduijn Strating *et al.*, 1993), (7) Gabbro, Northern Apennine ophiolites (Hebert *et al.*, 1989), (8) Gabbro cumulates, Brooks Range ophiolite (Harris, 1995), (9) Oceanic gabbro, 'major ocean basins' (Hebert *et al.*, 1989 and references therein), (10) Harzburgite, Hess Deep (Edwards and Malpas, 1996), (11) Hornblende-bearing peridotite mylonites, Voltri Massif (Hoogerduijn Strating *et al.*, 1993). Also included (see key) are: plagioclase lherzolite, Zabargad Island (Bonatti *et al.*, 1986), peridotite, 'major ocean basins' (Hebert *et al.*, 1989 and references therein), troctolite, Hess Deep (Hekinian *et al.*, 1993).

whereas the  $\text{CaO}$  contents show only a slight increase (22.8; 22.9; 23 wt% respectively).

Figure (5.12) demonstrates that the compositional range of  $\text{CaO}$  and  $\text{Al}_2\text{O}_3$  contents in clinopyroxenes in the Lizard peridotites and associated ultramafic/mafic rocks are similar to the range of clinopyroxene compositions defined by ultramafic and mafic rocks from ophiolitic and oceanic environments. In particular this comparison demonstrates that the systematic change of decreasing  $\text{Al}_2\text{O}_3$  and increasing  $\text{CaO}$  in clinopyroxenes from porphyroclasts in spinel lherzolite via neoblasts in mylonitic plagioclase-bearing peridotites to neoblasts mylonitic amphibole-bearing peridotites, is

also observed in peridotites with similar mineral assemblages and microstructural characteristics in various peridotite massifs (e.g. Hoogerduijn Strating *et al.*, 1993). In both the Lizard peridotites and examples discussed in the literature (e.g. Hoogerduijn Strating *et al.*, 1993; Rampone *et al.*, 1993, 1995), the trend of decreasing  $\text{Al}_2\text{O}_3$  and increasing CaO in clinopyroxenes is shown to accompany recrystallisation and an overall grain size reduction in the host peridotites and the appearance of plagioclase as a constituent mineral phase. Such compositional changes in clinopyroxene can be interpreted to reflect a tectono-metamorphic evolution of the peridotites in response to changing conditions of T and P during the subsolidus transition from spinel-facies to plagioclase-facies conditions, particularly when there are no parallel changes in the bulk composition (Piccardo *et al.*, 1990; Hoogerduijn Strating *et al.*, 1993; Rampone *et al.*, 1993, 1995). The compositional changes in the clinopyroxenes are related to equilibrium crystallisation with plagioclase and with orthopyroxene partitioning for CaO. Plagioclase is produced during reactions accompanying this subsolidus transition (Rampone *et al.*, 1993). However, a decrease in  $\text{Al}_2\text{O}_3$  contents and an increase in CaO contents of clinopyroxene can also be related to magmatic processes e.g. melt-rock interaction (Rampone, 1997).

Thus, the compositional trends defined by clinopyroxenes of the Lizard peridotites may be either metamorphic or magmatic in origin. Changes in the bulk composition of these peridotites (Chapter 6) demonstrate that melt-rock interactions have probably modified clinopyroxene compositions. However, on the basis of geothermometric constraints (Section 5.8) and the clear microstructural evolution of the peridotites (Chapter 4) i.e. recrystallisation, overall grainsize reduction and the development of mylonitic fabrics, the compositional changes in the clinopyroxenes are interpreted to predominantly reflect metamorphic re-equilibration. In comparison with the examples discussed in the literature (see above), metamorphic re-equilibration of the Lizard peridotites is interpreted to have occurred in response to changing conditions of T and P during the subsolidus transition from spinel-facies to plagioclase-facies conditions.

The ultramafic Traboe cumulates, mafic Traboe cumulates and gabbroic veins define similar compositional trends (Figure 5.12) i.e. decreasing  $\text{Al}_2\text{O}_3$  concentrations are accompanied by an increase in CaO contents. In addition, the  $\text{Al}_2\text{O}_3$  contents of clinopyroxenes from mafic Traboe cumulates and gabbroic veins in the Lizard extend to lower  $\text{Al}_2\text{O}_3$  concentrations than magmatic clinopyroxenes of troctolite, gabbro and

gabbro cumulates from oceanic environments and ophiolites (Figure 5.12), and this may reflect differences in the conditions of T and P during crystallisation or more extreme re-equilibration.

The  $\text{Cr}_2\text{O}_3$  content of clinopyroxene decreases systematically with decreasing  $\text{Al}_2\text{O}_3$  contents from porphyroclast cores in spinel lherzolites through to neoblasts in mylonitic plagioclase-bearing peridotites and to mylonitic amphibole-bearing peridotites (Figure 5.13). There is a positive correlation between decreasing  $\text{Al}_2\text{O}_3$  and decreasing  $\text{Cr}_2\text{O}_3$  contents in clinopyroxene neoblasts in the mylonitic plagioclase-

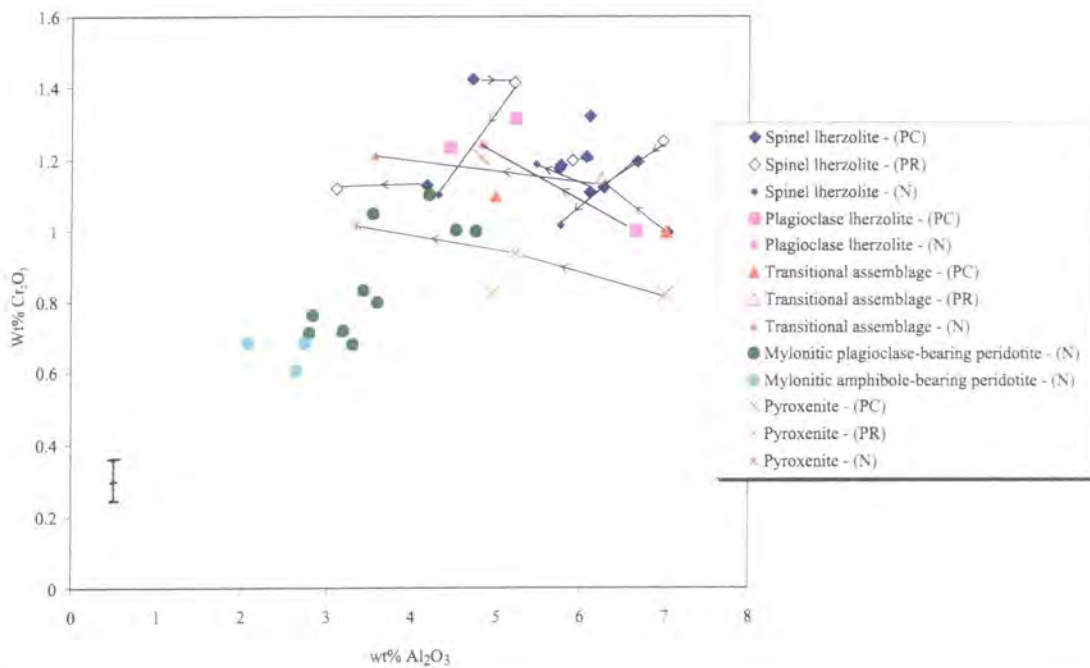


**Figure 5.13.** Plot of wt%  $\text{Cr}_2\text{O}_3$  versus wt%  $\text{Al}_2\text{O}_3$  of clinopyroxene for peridotites from the Lizard Ophiolite Complex. Tie lines link porphyroclast core (PC), porphyroclast rim (PR), and neoblast (N) compositions of the same sample for the lherzolite, transitional assemblage peridotite and pyroxenite.

bearing peridotites. The compositional trends for  $\text{Cr}_2\text{O}_3$  between porphyroclast cores, rims and neoblasts in the same sample are inconsistent, with  $\text{Cr}_2\text{O}_3$  increasing from core-rim-neoblast in some samples and decreasing in others (Figure 5.13). In a single pyroxenite sample (CAC 44),  $\text{Cr}_2\text{O}_3$  increases slightly from porphyroclast cores (0.82 wt%) and rims (0.94 wt%) to neoblasts (1 wt%), which may be due to local equilibration with adjacent  $\text{Cr}_2\text{O}_3$ -rich minerals e.g. spinel. Data presented by Rampone *et al.* (1997) demonstrates that  $\text{Cr}_2\text{O}_3$  concentrations of clinopyroxene may increase in response to melt-rock interactions. The fact that the  $\text{Cr}_2\text{O}_3$  contents of clinopyroxenes found in the Lizard peridotites decreases suggests that the compositional trends are



related to another process. Decreasing  $\text{Cr}_2\text{O}_3$  contents of clinopyroxenes are found in deformed peridotites from the Voltri Massif, N.W. Italy (Hoogerduijn Strating *et al.*, 1993) and are interpreted to be related to metamorphic re-equilibration in response to changing conditions of T and P during the subsolidus transition from spinel-facies to plagioclase-facies conditions. It is suggested that the trend of decreasing  $\text{Cr}_2\text{O}_3$  contents

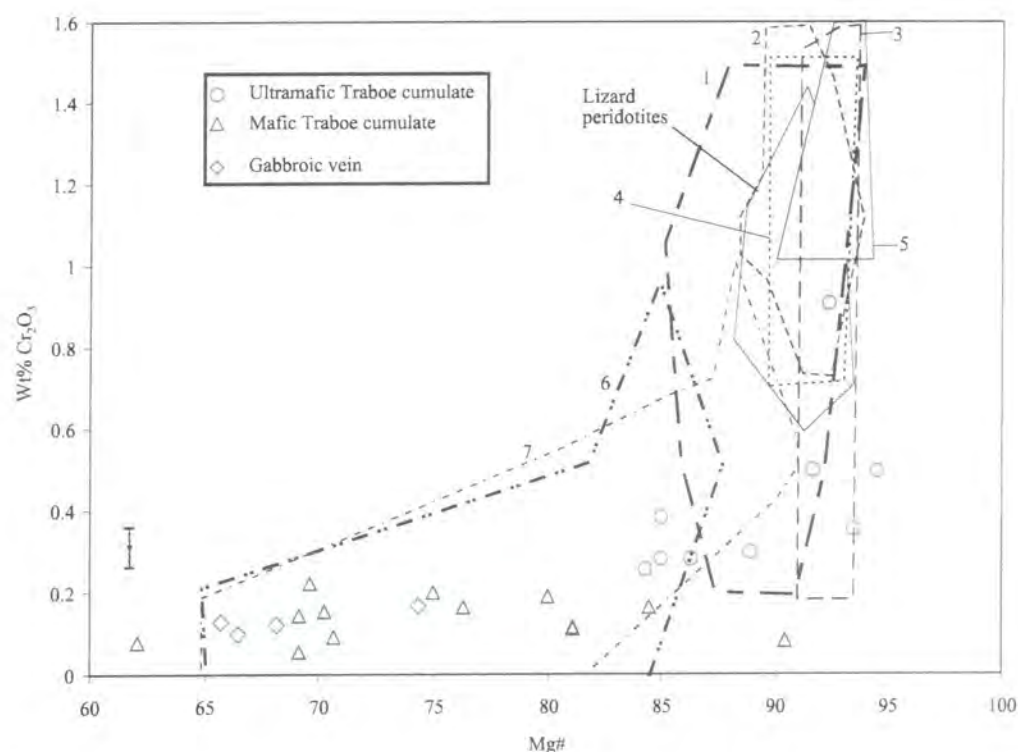


**Figure 5.14.** Plot of wt%  $\text{Cr}_2\text{O}_3$  versus Mg# of clinopyroxene for peridotites, ultramafic and mafic rocks from the Lizard compared with compositional fields defined for ultramafic and mafic rocks from the ophiolites and oceanic environments: (1) ultramafic cumulates, Northern Apennine ophiolites (Hebert *et al.*, 1989), (2) oceanic ultramafic tectonites (Hebert and Laurent, 1989), (3) oceanic harzburgites and lherzolites (Hebert *et al.*, 1989 and references therein), (4) peridotites, Northern Apennine ophiolites (Hebert *et al.*, 1989), (5) oceanic ultramafic cumulates (Hebert and Laurent, 1989), (6) cumulate gabbro, Northern Apennine ophiolites (Hebert *et al.*, 1989), (7) oceanic gabbro (Hebert and Laurent, 1989).

with decreasing  $\text{Al}_2\text{O}_3$  contents as shown by clinopyroxene of the Lizard peridotites is also related to metamorphic re-equilibration, on the basis of geothermometric constraints (Section 5.8) and the interpretation of variations in CaO concentrations (see above).

Figure 5.14 demonstrates that the clinopyroxenes of the ultramafic Traboe cumulates and mafic Traboe cumulates define a trend of decreasing Mg# with decreasing  $\text{Cr}_2\text{O}_3$  contents. This trend, including a large range of Mg#, is also shown by cumulate gabbros from Northern Apennine ophiolites and oceanic gabbros (Figure

5.14). The wide range of Mg# in the ultramafic Traboe cumulates and mafic Traboe cumulates suggests crystal fractionation (Hekinian *et al.*, 1993).

Interestingly, the  $\text{TiO}_2$  contents in clinopyroxene neoblasts in the mylonitic plagioclase-bearing peridotite peridotites are higher than the compositional ranges defined of the other peridotite-types (Figure 5.15). This may be related to local equilibration with  $\text{TiO}_2$ -rich amphibole, which is only present in the mylonitic plagioclase-bearing peridotite. It is also notable that the  $\text{TiO}_2$  contents in clinopyroxenes from the mylonitic amphibole-bearing peridotites are lower than those in the other peridotite-types and the significance of this is discussed below. In general, there are no consistent variations in  $\text{TiO}_2$  content with Mg# between porphyroclast cores, rims or neoblasts in the peridotites.

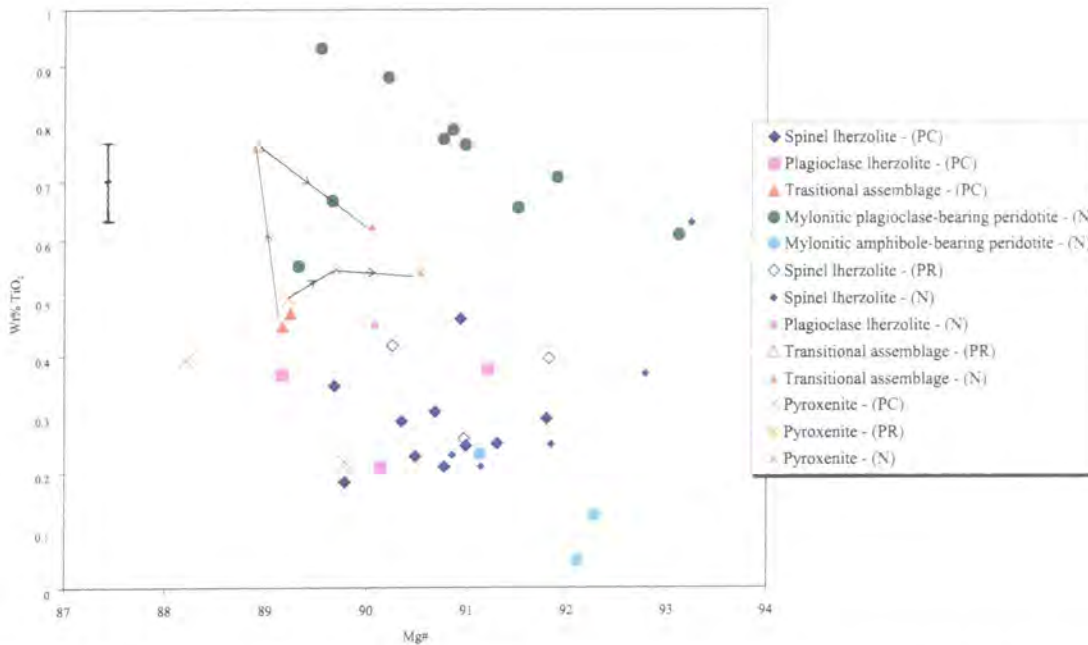


**Figure 5.15.** Plot of wt%  $\text{TiO}_2$  versus Mg# ( $100\text{Mg}/(\text{Mg}+\text{Fe})$ ) of clinopyroxene for peridotites from the Lizard Ophiolite Complex. Tie lines link porphyroclast core (PC), porphyroclast rim (PR), and neoblast (N) compositions of the same sample for the transitional assemblage peridotite and pyroxenite.

The Ti content of clinopyroxenes in the Lizard peridotites and associated ultramafic/mafic rocks is plotted against their Cr content in Figure 5.16 and demonstrates that they overlap the range of compositions found in clinopyroxene in ultramafic and mafic rocks in ophiolitic and oceanic environments. The trend of increasing Ti accompanied by decreasing Cr content in the ultramafic Traboe



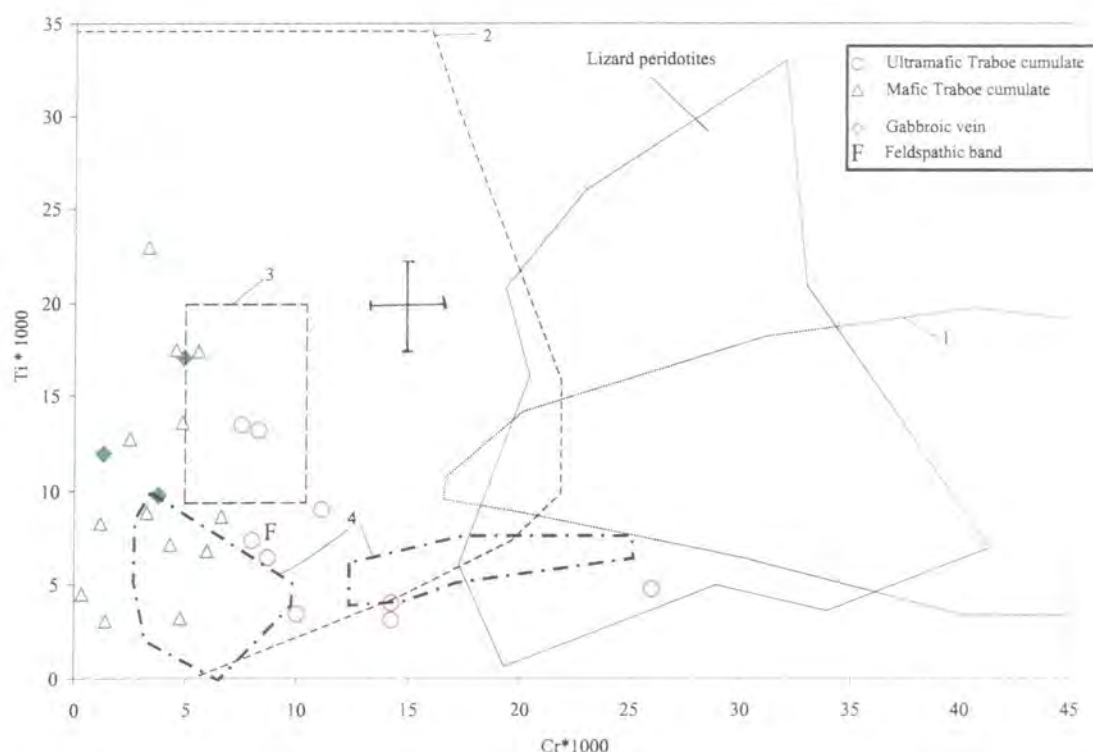
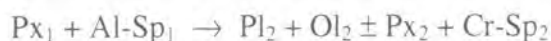


**Figure 5.16.** Plot of Ti versus Cr (number of cations per 6 oxygens) of clinopyroxene for peridotites, ultramafic and mafic rocks from the Lizard compared with compositional fields defined for ultramafic and mafic rocks from the ophiolites and oceanic environments: (1) oceanic ultramafic cumulates (Hebert *et al.*, 1989 and references therein), (2) oceanic gabbro (Hebert *et al.*, 1989 and references therein), (3) Bralorne gabbro suite, Bridge River accretionary complex (Church *et al.*, 1995), (4) Shulaps gabbro suite, Bridge River accretionary complex (Church *et al.*, 1995).

cumulates of the Lizard could be explained by fractional crystallisation (Mercier, 1976). The high Ti contents of clinopyroxene in the mylonitic plagioclase-bearing peridotite could be a signature of melt-rock interaction (Figure 5.15). This effect is documented in melt-impregnated peridotites of the Miyamori ophiolite complex (Ozawa, 1993), the Table Mountain Massif (Bay of Islands Ophiolite) (Suhr and Robinson, 1994) and Hess Deep (Girardeau and Francheteau, 1993; Edwards and Malpas, 1996). An increase in Ti of clinopyroxene can also occur in response to closed-system subsolidus re-equilibration and the following reaction describes the spinel-facies to plagioclase-facies transition of peridotite (Rampone *et al.*, 1993):



The increase of Ti in clinopyroxene found in the mylonitic plagioclase-bearing peridotite is due to the fact that plagioclase and olivine, two of the reaction products, cannot host any Ti released during spinel breakdown.

The microstructures of the mylonitic amphibole-bearing peridotites are very similar to the microstructures of the mylonitic plagioclase-bearing peridotites, yet the Ti contents of clinopyroxene in the former peridotite type are a lot lower. These low values can be explained by the presence of up to 30% modal volume pargasitic hornblende in the mylonitic amphibole-bearing peridotite, which replaces clinopyroxene. The formation of amphibole may be related to melt/fluid-rock interaction and as a consequence clinopyroxene compositions are modified e.g. Ti decreases, due to re-equilibration with the amphibole. The major element compositions of amphiboles in the mylonitic peridotites are discussed in Section 5.6 to provide further evidence to support this hypothesis.

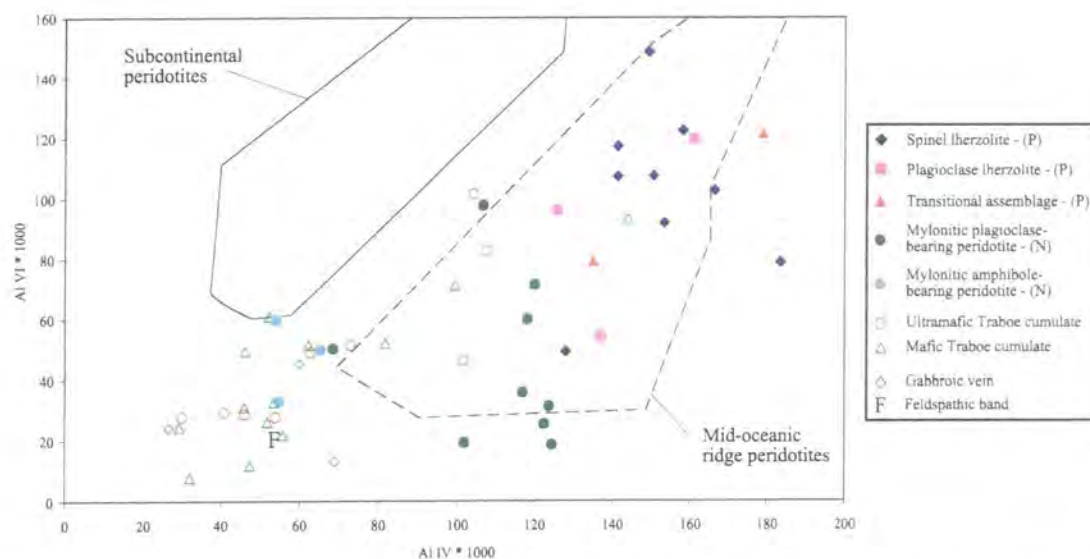


**Figure 5.17.** Plot of cationic proportions of  $\text{Al}^{\text{VI}}$  versus  $\text{Al}^{\text{IV}}$  of clinopyroxene for peridotites, ultramafic and mafic rocks from the Lizard compared with compositional fields defined for subcontinental peridotites and mid-oceanic ridge peridotites (Seyler *et al.*, 1994). Porphyroclast (P) and neoblast (N) compositions are shown.

A plot of the cationic proportions of  $\text{Al}^{\text{VI}}$  versus  $\text{Al}^{\text{IV}}$  in clinopyroxene from the Lizard peridotites has been compared with examples from subcontinental peridotites and mid-oceanic ridge peridotites (Seyler *et al.*, 1994) (Figure 5.17). This plot demonstrates that the compositional trend in the Lizard peridotites is similar to the trend in mid-oceanic ridge peridotites (Seyler *et al.*, 1994) and suggests that the Lizard peridotites may be mid-oceanic in origin. However, Rivalenti *et al.* (1996) demonstrate that differences in clinopyroxene chemistry may reflect mantle processes rather than continental versus oceanic setting. Thus caution should be applied when comparing the

Lizard data with the data of Seyler *et al.* (1994) especially when interpreting the results simply in terms of the tectonic setting of the Lizard peridotites.

### 5.4.3. Clinopyroxene chemistry – Landewednack amphibolites

In a few samples of Landewednack amphibolites, fine-grained clinopyroxenes are preserved and these often form layers (Chapter 4). In the majority of samples, however, all clinopyroxenes have been replaced by amphibole. Analyses of clinopyroxenes taken from the Landewednack amphibolites are presented in the following sub-Section and these results are interpreted and discussed with reference to equivalent data in the literature. Representative analyses of clinopyroxenes for all the amphibolites are presented in Appendix D.

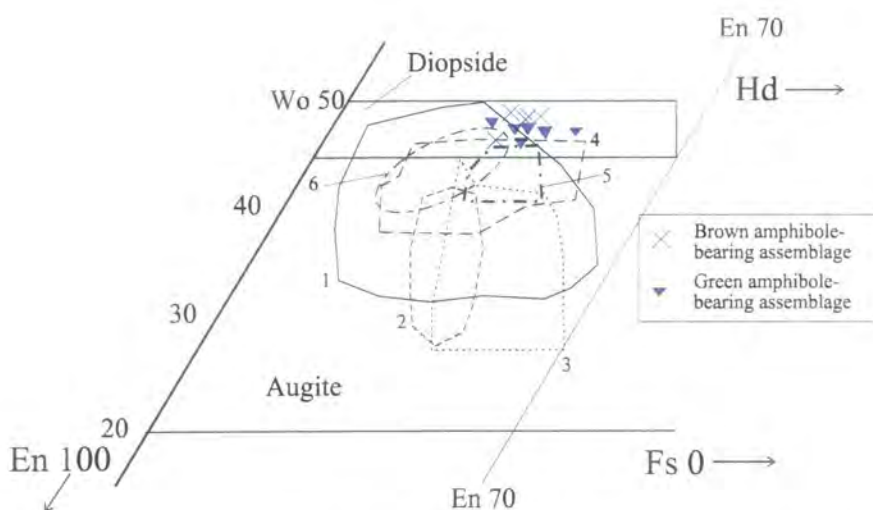
#### 5.4.3.a. Results and interpretation

The main compositional variations in clinopyroxene in the Landewednack amphibolites are discussed below. Representative mineral analyses are given in Table 5.4.

Amphibolites	Fs-En-Wo	Wt% CaO	Wt% Al <sub>2</sub> O <sub>3</sub>	Mg#	Wt% TiO <sub>2</sub>
Brown amphibole-bearing assemblage	Fs <sub>12.7-12.7</sub> En <sub>35.7-40.3</sub> Wo <sub>46.7-49.4</sub>	24-23	0.49-1.46	64-77	0.1-0.27
Green amphibole-bearing assemblage	Fs <sub>11.8-18.7</sub> En <sub>33.4-39.7</sub> Wo <sub>46.7-48.5</sub>	24.6-23.3	0.4-1.67	71-76	0-0.19

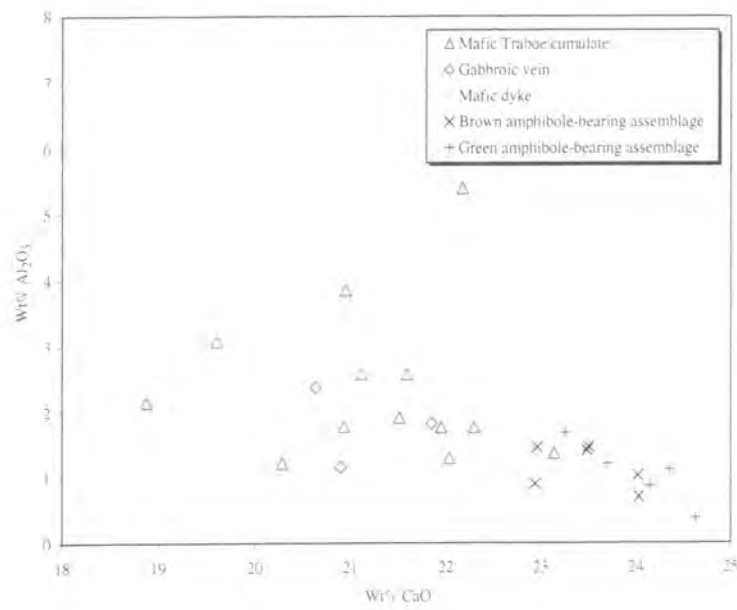
**Table 5.4.** Summary of the compositions of clinopyroxenes for the Landewednack amphibolites from the Lizard Ophiolite Complex. The data from the brown amphibole-bearing assemblage is distinguished from the green amphibole-bearing assemblage.

The clinopyroxenes from both subtypes of amphibolite plot in the diopside compositional field of a Wo-En-Fs diagram (Figure 5.18). This diagram shows that the compositions of the Landewednack amphibolites are generally more calcic than mafic rocks from ophiolites and oceanic environments, but the compositional field of clinopyroxenes from the Landewednack amphibolites does overlap the range of MORB clinopyroxenes defined by the Basaltic Volcanism Study Project (1981). The Landewednack amphibolites are also compositionally distinct from the mafic Traboe cumulates and gabbroic veins from the Lizard (compare with Figure 5.10).



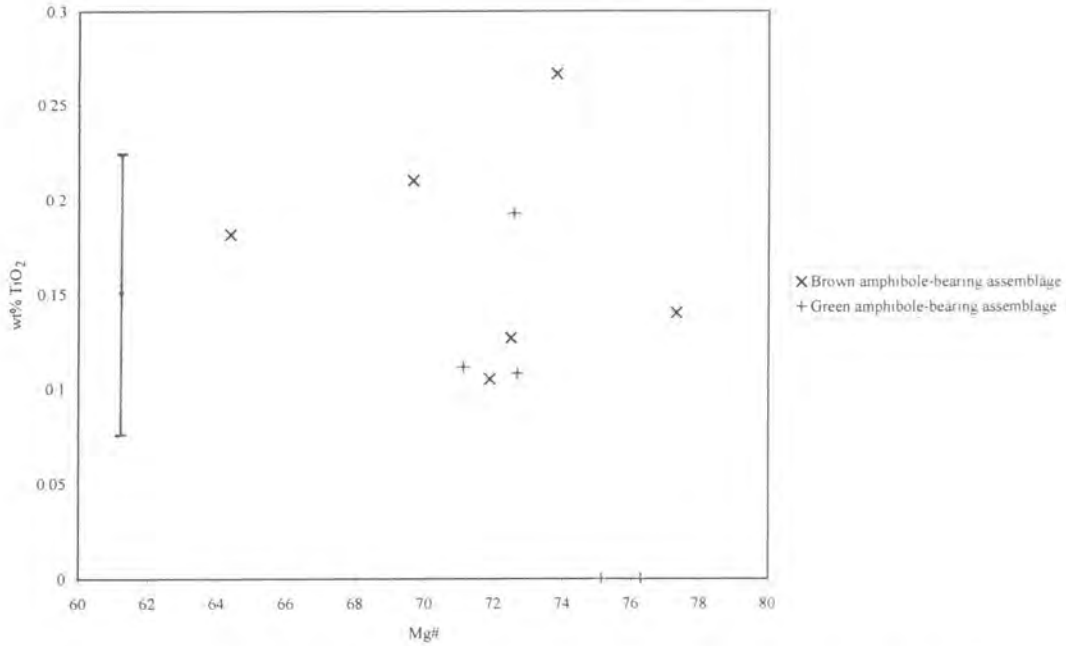
**Figure 5.18.** A Fs-En-Wo triangular diagram of clinopyroxene for Landwednack amphibolites from the Lizard Ophiolite Complex compared with compositional fields defined for mafic rocks from the ophiolites and oceanic environments: (1) Mid-ocean ridge basalt (MORB), (Basaltic Volcanism Study Project, 1981), basalt, Hess Deep (Hekinian *et al.*, 1993), (2) (3) dolerite, Hess Deep (Hekinian *et al.*, 1993), (4) gabbro, 'major ocean basins' (Hebert *et al.*, 1989 and references therein), (5) metagabbro and amphibolites, Hess Deep (Hekinian *et al.*, 1993), (6) gabbro, Northern Apennine ophiolites (Hebert *et al.*, 1989).

Figure 5.19 demonstrates that the CaO contents of the Landwednack amphibolites are higher than those in defined by other mafic rocks from the Lizard, although Al<sub>2</sub>O<sub>3</sub> contents are similar. The high CaO contents (i.e. Wo > 45) suggest that



**Figure 5.19.** Plot of wt% Al<sub>2</sub>O<sub>3</sub> versus wt% CaO of clinopyroxene for Landwednack amphibolites from the Lizard Ophiolite Complex compared with the composition of mafic Traboe cumulates, gabbroic vein and a mafic dyke from the Lizard.





**Figure 5.20.** Plot of wt% TiO<sub>2</sub> versus Mg# of clinopyroxene for Landwednack amphibolites from the Lizard Ophiolite Complex. The data from the brown amphibole-bearing assemblage is distinguished from the green amphibole-bearing assemblage.

these are re-equilibrated metamorphic compositions. The clinopyroxene compositions in both amphibolite types define a trend of decreasing Al<sub>2</sub>O<sub>3</sub> content with increasing CaO.

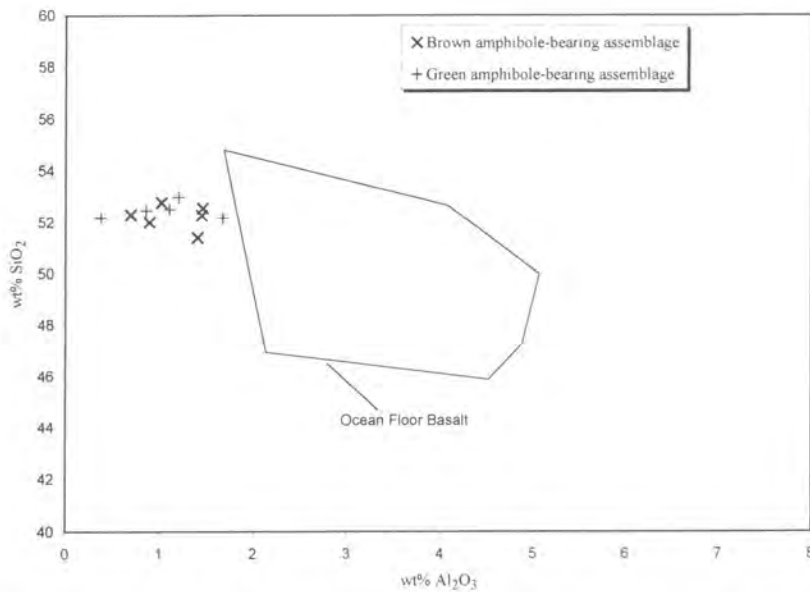


**Figure 5.21.** Plot of wt% SiO<sub>2</sub> versus wt% Al<sub>2</sub>O<sub>3</sub> of clinopyroxene for the Landwednack amphibolites from the Lizard Ophiolite Complex compared with the compositional field defined by ocean floor basalt (Searle *et al.*, 1980).

The  $\text{TiO}_2$  contents of the clinopyroxenes are slightly higher in the brown amphibole-bearing assemblage than in the green amphibole-bearing assemblage (Figure 5.20). This is probably related to the equilibration of the clinopyroxenes with the  $\text{TiO}_2$ -rich brown amphiboles characteristic of the former amphibolite assemblage.

The  $\text{Cr}_2\text{O}_3$  contents of the clinopyroxenes in the Landewednack amphibolites are extremely low and therefore the results are not presented.

A plot of wt%  $\text{SiO}_2$  versus wt%  $\text{Al}_2\text{O}_3$  (Figure 5.21) shows that the compositional range defined by clinopyroxenes in the Landewednack amphibolites is distinct from the compositional field of ocean floor basalt (Searle *et al.*, 1980).

The results show that the clinopyroxene from the Landewednack amphibolites are different in composition to MORB clinopyroxenes. In particular, the Landewednack clinopyroxene are generally richer in CaO and depleted in  $\text{Al}_2\text{O}_3$  relative to igneous clinopyroxene from basaltic rocks. It is suggested that the compositions of the Landewednack amphibolite clinopyroxenes have been modified during metamorphism i.e. the clinopyroxenes have re-equilibrated to lower conditions of T and P. The compositions of the clinopyroxenes are consistent with amphibolite facies metamorphism in the region of 500-600°C (Green, 1964b; Lindsley, 1983)(Section 5.8).

#### 5.4.4. Clinopyroxene chemistry – summary

- A systematic compositional trend of decreasing  $\text{Al}_2\text{O}_3$  and increasing CaO is defined by clinopyroxene from porphyroclasts in spinel lherzolites via neoblasts in mylonitic plagioclase-bearing peridotites to neoblasts mylonitic amphibole-bearing peridotites. This trend is interpreted to reflect a tectono-metamorphic evolution of the peridotites in response to decreasing conditions of T and P during the subsolidus transition from spinel-facies to plagioclase-facies conditions.
- Higher Ti contents are observed in clinopyroxene in the mylonitic plagioclase-bearing peridotites than in the spinel and plagioclase lherzolites. It is suggested that this variation in composition could be a signature of melt-rock interaction or it may have occurred in response to closed-system re-equilibration during the subsolidus transition from spinel-facies to plagioclase-facies conditions. With the data



currently available, it is not possible to distinguish which of these two processes may be responsible for the trends in Ti.

- Thus, it is proposed that compositional variation in clinopyroxenes in the Lizard peridotites may be related to both spinel-facies to plagioclase-facies re-equilibration and melt-rock interaction.
- The low Cr contents and lower range of Mg# in the ultramafic Traboe cumulates and mafic Traboe cumulates in the Lizard suggest crystal fractionation. The trend of increasing Ti accompanied by decreasing Cr content in the ultramafic Traboe cumulates of the Lizard are indicative of a fractional crystallisation effect.
- The compositions of clinopyroxene in the Landwednack amphibolites are also interpreted to reflect to metamorphic re-equilibration.

---

## 5.5. Spinel chemistry

---

It is well established in the literature that the composition of spinel in ultramafic rocks serves as a powerful tool in determining the petrogenetic history of the host rock. For example, Dick and Bullen (1984) have demonstrated that changes in the composition of spinel reflect changes in the degree of partial melting in the mantle source region. With this type of petrogenetic information, it can even be established whether the host rock formed at an island arc or mid-ocean ridge setting. However, changes in spinel chemistry are also the signature of several other geological processes, including metamorphic re-equilibration, melt-rock interaction and igneous fractionation. Therefore, in the following sections analyses of spinel from the rocks of the Lizard Ophiolite Complex are presented and subsequently interpreted and discussed with references to examples taken from the literature. The aim of this investigation is, firstly to determine whether there is any variation in spinel composition in the rocks of the Lizard Ophiolite Complex and then interpret any variations in terms of a plausible process or processes.

### 5.5.1. Spinel chemistry - results

The main compositional variations in spinel are outlined below. Representative mineral analyses are given in Table 5.5. Both core and rim analyses are presented for spinels in

the Lizard peridotites. The full electron probe data set is presented in Appendix D.

Cr# ranges from 3.3 to 55, with the largest range been found in the ultramafic Traboe cumulates (Table 5.5). The ultramafic Traboe cumulates also show the largest range of Mg# from 39.2 to 72.3, when the overall range in the ultramafic rocks of Lizard ranges from 39.2 to 81.8. Mg# is negatively correlated with Cr# and decreases from the spinel lherzolites to mylonitic plagioclase-bearing peridotites. TiO<sub>2</sub> contents are higher in the mylonitic plagioclase-bearing peridotites and transitional assemblage peridotites and the lowest values are found in the spinel lherzolites. V<sub>2</sub>O<sub>3</sub> contents range from 0.07 to 0.42 wt%.

	Cr#	Mg#	Wt% TiO <sub>2</sub>	Wt% V <sub>2</sub> O <sub>3</sub>
Spinel lherzolite (PC)	17-47	51-79	0.08-0.53	0.07-0.35
Spinel lherzolite (PR)	17-45	73-50	-	-
Plagioclase lherzolite (PC)	41-48	52-62	0.25-0.59	0.2
Plagioclase lherzolite (PR)	41	57	-	-
Transitional assemblage (PC)	44-45	52-54	0.74	0.28
Mylonitic plagioclase-Bearing peridotite (N)	31-49	40-67	0.17-0.9	0.24-0.42
Mylonitic amphibole-Bearing peridotite (N)	31-44	53-65	0.1-0.25	0.19
Dunite	28-40	56-76	0.14-0.33	0.13-0.19
Feldspathic bands (Br)	28.2	65.6	0.1	-
Feldspathic bands (Gr)	3.3	81.8	0.055	-
Green spinels in peridotite	13.2-22.7	64.2-73.5	0.054-0.22	0.13-0.19
Ultramafic Traboe cumulates (N)	7.7-55	39.2-72.3	0.012-0.24	0.07-0.34

**Table 5.5.** Summary of the compositions of spinels in the Lizard peridotites and associated ultramafic/mafic rocks. Data for porphyroclasts cores (PC), porphyroclasts rims (PR), brown (Br) and green (Gr) spinels are included.

### 5.5.2. Spinel chemistry – interpretation and discussion

Variations in spinel chemistry in mantle rocks may be attributed to a variety of processes and these include:

- Partial melting,
- Metamorphic re-equilibration,
- Melt-rock interaction,
- Igneous fractionation.

In order to determine which of these processes may be responsible for variations in the composition of spinels of ultramafic rocks from the Lizard complex, this Section is split into four different sub-Sections according to the processes listed above.

### 5.5.2.a. Partial melting trends

A plot of Cr# versus Mg# (Figure 5.22) is utilised to compare the compositions of spinels from the Lizard peridotites with examples from oceanic environments and ophiolites. Nb.  $\text{Cr\#} = 100\text{Cr}/(\text{Cr}+\text{Al})$ ;  $\text{Mg\#} = 100\text{Mg}/(\text{Mg}+\text{Fe}^{2+})$ .

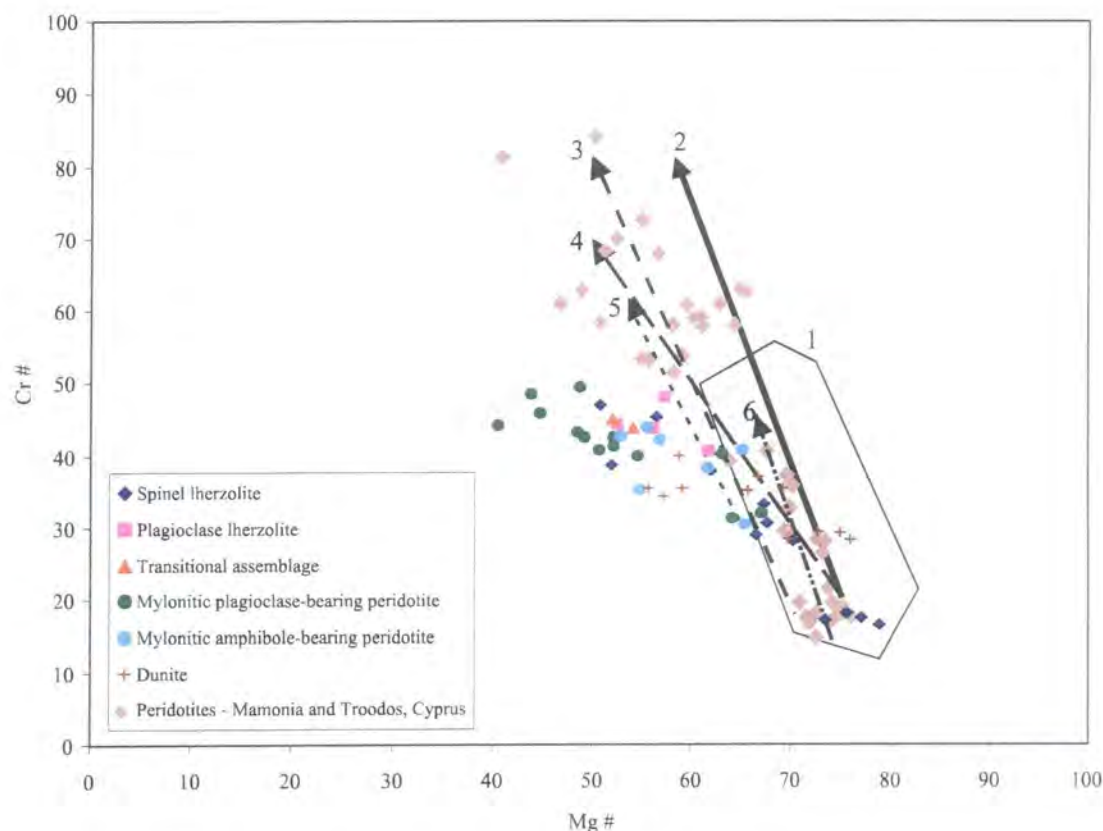


**Figure 5.22.** Plot of Cr# versus Mg# showing the field of spinels for peridotites from the Lizard Ophiolite Complex compared with the composition of spinels from the Mamonia and Troodos peridotites (Wayne Bailey *pers comm*, 1998). The field of abyssal peridotites (1) is also included for comparison (Dick and Bullen, 1984). Arrows indicate the trends defined for spinels for peridotites from ophiolites and oceanic environments, including (2) alpine-type and abyssal peridotites (Dick and Bullen, 1984), (3) peridotite, Bay of Islands ophiolite, Newfoundland (Casey *et al.*, 1985), (4) harzburgite and dunite, Luobusa ophiolite, Tibet (Zhou *et al.*, 1996), (5) harzburgite and dunite, Oman ophiolite (Kelemen *et al.*, 1995), (6) peridotites, Northern Apennine ophiolites (Hebert *et al.*, 1989).

The range for the Lizard peridotites excludes green spinels in spinel lherzolites and mylonitic plagioclase-bearing peridotites and spinels from the ultramafic Traboe cumulates. Figure 5.22 demonstrates that the trend of increasing Cr# with decreasing Mg# is similar to trends shown by peridotites from ophiolites and oceanic environments. However, it is immediately evident that the trend in the Lizard peridotites diverges slightly from the trends defined for peridotites from ophiolites and

oceanic environments presented on Figure 5.22. The compositional trend for spinels in the examples listed above is interpreted to be the result of progressive partial melting, because Cr and Mg are strongly partitioned into the solid and Al strongly partitioned into the melt with increasing degrees of depletion of peridotites (Dick and Bullen, 1984).

Dick and Bullen (1984) defined three sub-types of alpine peridotite based on an extensive study of spinel composition: Type I =  $\text{Cr\#} < 60$ , Type III =  $\text{Cr\#} > 60$ , and Type II have intermediate  $\text{Cr\#}$ . The spinel lherzolites from the Lizard Ophiolite Complex, which are believed to represent the least deformed assemblage and least chemically modified after later melt-rock interaction, plot in low  $\text{Cr\#}$  area of the Type I field of alpine peridotites and the field of abyssal peridotites (Dick and Bullen, 1984). The spinel lherzolites are therefore the residues from only small degrees of melting, in contrast to peridotites with higher  $\text{Cr\#}$  for spinel. Higher  $\text{Cr\#}$  of spinels (e.g. Type III of Dick and Bullen, 1984) are probably related to the presence of a significant amount of

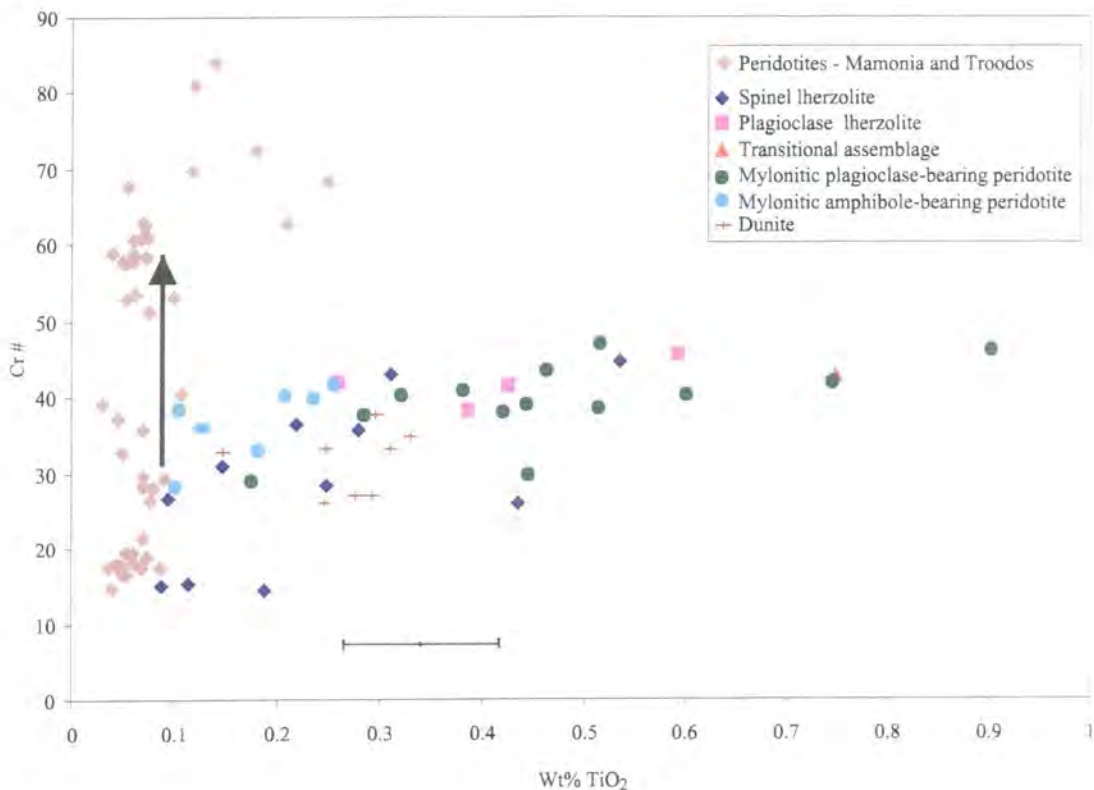


**Figure 5.23.** Plot of  $\text{Cr\#}$  versus  $\text{wt\% TiO}_2$  of spinel for peridotites from the Lizard Ophiolite Complex compared with compositional fields defined for the Mamonia and Troodos peridotites (Wayne Bailey *pers comm*, 1998). The arrow indicates the partial melting trend defined by the composition of spinel for peridotites (Girardeau and Francheteau, 1993; Ozawa, 1993; Edwards and Malpas, 1996).

water during melting i.e. hydrous melt or anomalously low pressure melting (Dick and Bullen, 1984). These requirements and conditions often exist in a subduction zone environment (Bonatti and Hamlyn, 1989) where water is introduced into the mantle wedge above a subducting slab in the form of hydrous melts.

Further evidence for the compositional trends in spinel from the Lizard peridotites not being related to progressive partial melting is provided by changes in the  $\text{TiO}_2$  content of spinel (Figure 5.23). It has already been demonstrated that the  $\text{TiO}_2$  contents increase with Cr# in the spinel lherzolites, and in particular the plagioclase lherzolites, transitional assemblage peridotites and mylonitic plagioclase-bearing peridotites. The trend of increasing  $\text{TiO}_2$  contents with Cr# departs strongly from the partial melting trend in peridotites (Girardeau and Francheteau, 1993; Ozawa, 1993; Edwards and Malpas, 1996), which shows no change in  $\text{TiO}_2$  contents associated with an increase in Cr# (Figure 5.23). This partial melting trend is also demonstrated by spinel compositions taken from the Mamonia and Troodos peridotites, Cyprus (Wayne Bailey *pers comm*, 1998).

An increase in  $\text{V}_2\text{O}_3$  contents is correlated with increasing Cr# in the Lizard

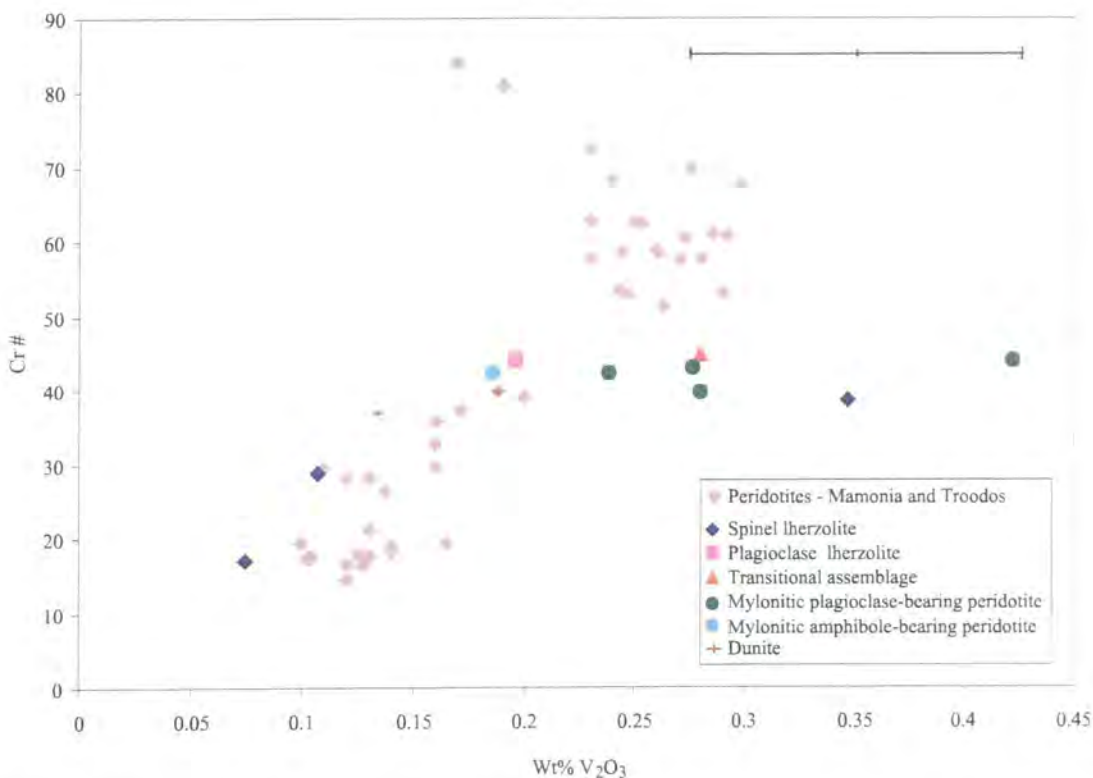


**Figure 5.24.** Plot of Cr# versus wt%  $\text{V}_2\text{O}_3$  of spinel for peridotites from the Lizard Ophiolite Complex compared with compositional fields defined for peridotites from Mamonia and Troodos ophiolites (Wayne Bailey *pers comm*, 1998).



peridotites, from spinel lherzolite to mylonitic plagioclase-bearing peridotite. Spinel from lherzolites and harzburgites from the Mamonia and Troodos ophiolites, SW Cyprus (Wayne Bailey *pers comm*, 1998), are presented in Figure 5.24, and these also show an increase in V contents, which parallels an increase in Cr#. The variations in these rocks are attributed to partial melting processes. However, it may also be possible that the increase in  $V_2O_5$  content is related to plagioclase-facies re-equilibration (Section 5.5.2.b) or a manifest of melt-rock interaction (Section 5.5.2.c). However, there is insufficient evidence in the literature to determine whether this is plausible.

A correlation between Cr# in spinel and olivine Fo% (Figure 5.25) shows that the spinel lherzolite plots within the melting trend defined for Tinaquillo lherzolite at 10 kbar (Jacques and Green, 1980) and falls on the partial melting trend defined by Ozawa (1993). The trend of decreasing olivine Fo% number with increasing Cr# in spinel defined by the plagioclase lherzolites, transitional assemblage peridotites and mylonitic peridotites of the Lizard departs from these melting trends. Changes in

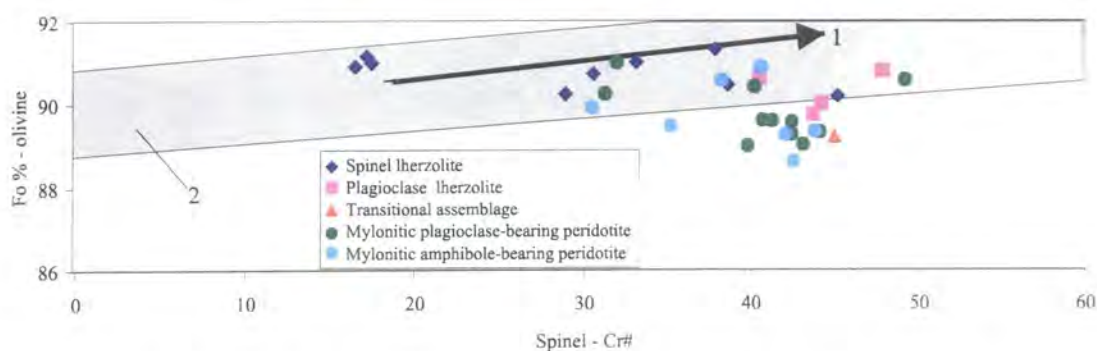


**Figure 5.25.** Plot of olivine Fo% number versus spinel Cr# for peridotites from the Lizard Ophiolite Complex compared with (1) the partial melting trend of peridotites from the Miyamori ophiolite complex (Ozawa, 1993) and (2) the melting trend of Tinaquillo lherzolite (Jacques and Green, 1980).

olivine Fo% are not observed during plagioclase-facies re-equilibration (Hoogerduijn Strating *et al.*, 1993). Thus, the changes in the olivine Fo% combined with increasing Cr# in spinel in the Lizard peridotites are interpreted to be the result of melt-rock interaction (Section 5.2.2.c). Ozawa (1993) shows that olivine Fo% decreases in peridotites that have equilibrated with melt, which supports the interpretation proposed for the Lizard peridotites.



### 5.5.2.b. Metamorphic re-equilibration trends

Figure 5.26 demonstrates that although Cr# increases and Mg# decreases from spinel lherzolites to mylonitic plagioclase-bearing peridotites there are no consistent trends between spinel cores and rims.

The trend for the Lizard peridotites shows a greater decrease in Mg# at a lower Cr# than the examples listed above, and therefore a process other than progressive partial melting must be invoked to account for the compositional trend. The trend for the Lizard peridotites is very similar to the trends observed in peridotites from the Voltri Massif (Hoogerduijn Strating *et al.*, 1993) and External Ligurides (Rampone *et al.*, 1995)(Figure 5.27). In these examples, the trend of increasing Cr# and decreasing Mg# in spinel accompanies a change in the peridotite mineral assemblage and

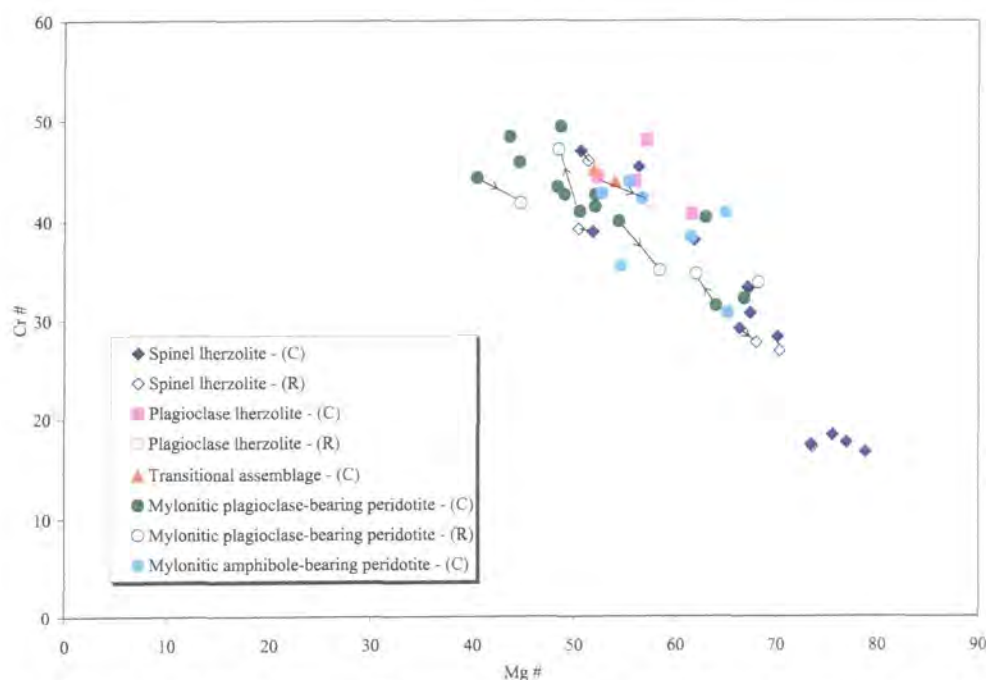


**Figure 5.26.** Plot of Cr# versus Mg# of spinel for peridotites from the Lizard Ophiolite Complex. Tie-lines link core (C) and rim (R) compositions of the spinel.

microstructure, from coarse-grained spinel lherzolites (low Cr#, high Mg#) to deformed-mylonitic plagioclase lherzolites (high Cr#, low Mg#). The trend of increasing Cr# and decreasing Mg# in the Lizard peridotites is also accompanied by a decrease in the overall grain-size, appearance of plagioclase and the development of mylonitic peridotites. These compositional changes could occur in a closed system during the subsolidus reactions that accompany the spinel- to plagioclase-facies

transition in the peridotites in response to re-equilibration of the mineral assemblage to conditions of lower P and T (Rampone *et al.*, 1993). Similar compositional trends can also be produced by melt-rock interaction in peridotites, and thus caution should be applied as these may be indistinguishable from those produced by plagioclase-facies re-equilibration (Section 5.5.2.c).

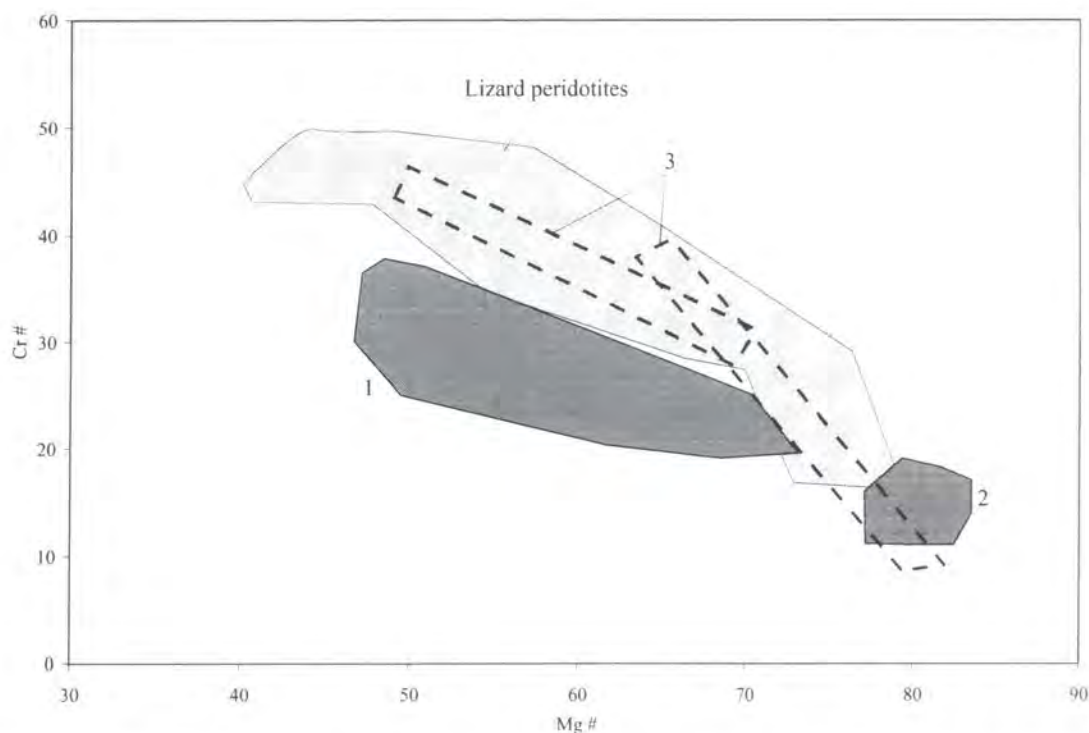
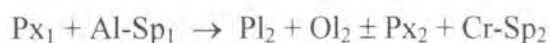


**Figure 5.27.** Plot of Cr# versus Mg# of spinel for peridotites from the Lizard Ophiolite Complex compared with compositional fields defined for peridotites from ophiolites, including: (1) deformed-mylonitic plagioclase lherzolites, Voltri Massif (Hoogerduijn Strating *et al.*, 1993), (2) spinel lherzolites, Voltri Massif (Hoogerduijn Strating *et al.*, 1993), (3) plagioclase and spinel lherzolites, External Ligurides (Rampone *et al.*, 1995).

An increase in TiO<sub>2</sub> contents with Cr# is reported for peridotites from the External Ligurides (Figure 5.28), with TiO<sub>2</sub> increasing progressively from a suite of partially plagioclase-recrystallised samples to strong plagioclase-recrystallised samples (Rampone *et al.*, 1993). Similar compositional correlations have been observed in spinels from the Galicia Bank peridotites (Kornprobst and Tabit, 1988). Rampone *et al.* (1993) propose that an increase in Ti and Cr and a decrease in Al in plagioclase-bearing peridotites from the External Ligurides is due to equilibrium crystallisation of spinel with plagioclase, in response to the transition from spinel- to plagioclase-facies stability field which may be described by the reaction:



The increase in Ti and Cr in spinel in the plagioclase-bearing peridotites is due to the fact that these elements cannot be hosted by plagioclase and olivine, both the products of the above reaction (Rampone *et al.*, 1993). The correlation with the spinel compositional change in the Lizard peridotites with peridotites from the External Ligurides (Rampone *et al.*, 1993) suggests that the processes and reactions described above were responsible for changes observed in the Lizard peridotites. However, this comparison should be treated with caution, because an increase in Ti and Cr, and a decrease in Al in spinel can also occur in response to melt-rock interaction (Section 5.5.2.c).

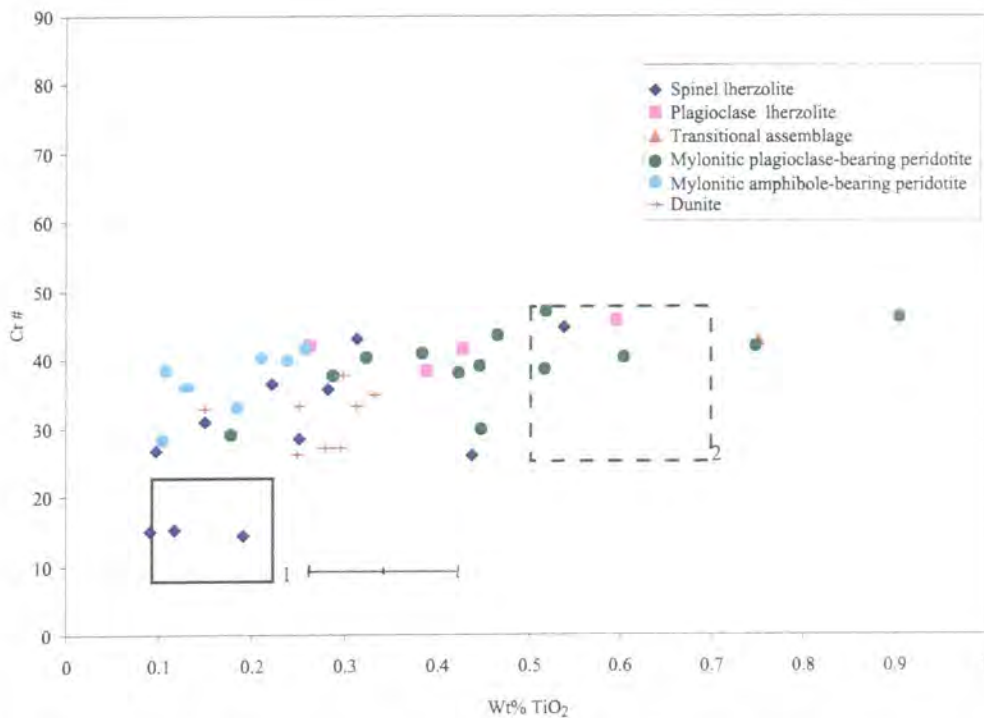


**Figure 5.28.** Plot of Cr# versus wt%  $\text{TiO}_2$  of spinel for peridotites from the Lizard Ophiolite Complex compared with compositional fields defined for: (1) type A, least plagioclase-recrystallised peridotites and (2) type B, strong plagioclase-recrystallised peridotites from External Ligurides (Rampone *et al.*, 1993).

### 5.5.2.c. Melt-rock interaction trends

Edwards and Malpas (1996) show that the composition of spinels in harzburgites that have been modified by melt-rock interaction define a trend similar to the Lizard peridotites (Figure 5.29) and different to progressive partial melting trends (Figure 5.22). A similar compositional trend to the Lizard peridotites is described by Hekinian *et al.* (1993) for spinels in harzburgites impregnated by wehrlite from the Hess Deep; this trend also departs from the partial melting trend.



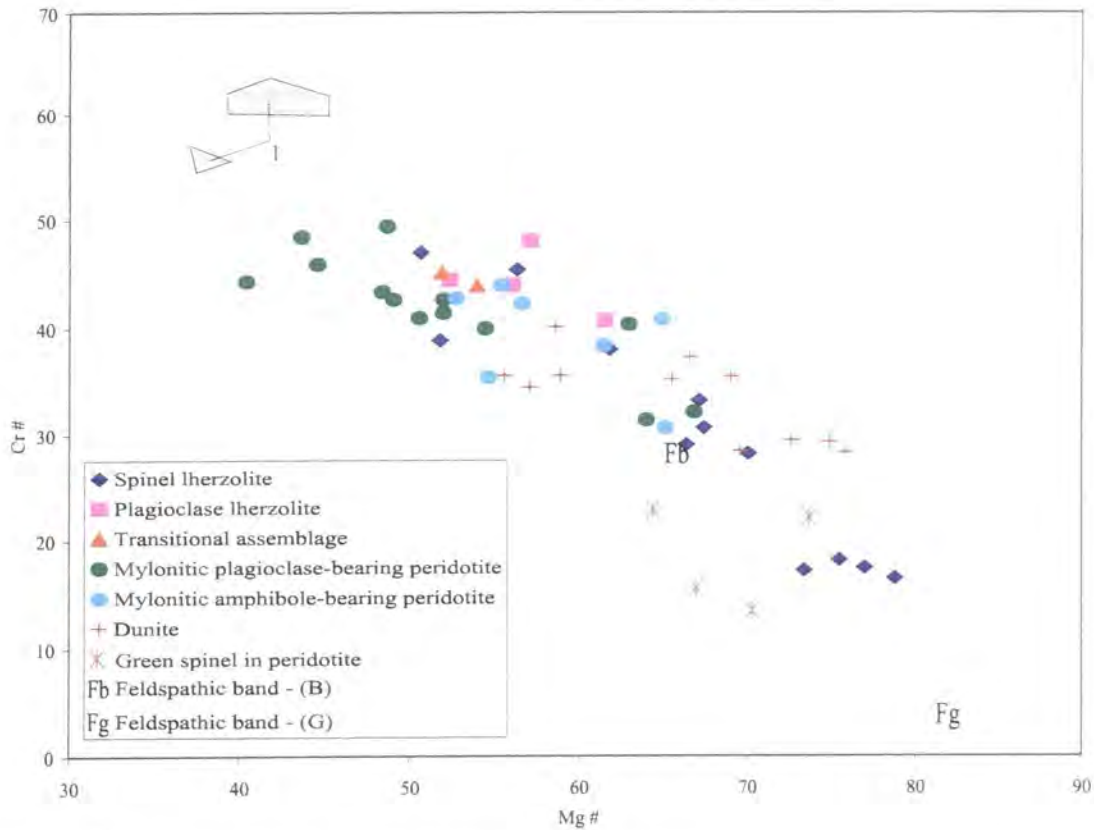


**Figure 5.29.** Plot of Cr# versus Mg# of spinel for peridotites from the Lizard Ophiolite Complex compared with compositional fields defined for melt-impregnated peridotites (**1**) from Hess Deep (Edwards and Malpas, 1996).

Figure 5.30 demonstrates that increasing  $\text{TiO}_2$  contents in the Lizard peridotites define a positive trend with Cr#. Changes in the  $\text{TiO}_2$  concentration of spinel can occur in response to equilibration between the host lherzolite and a migrating melt. Kelemen *et al.* (1995) present evidence for a  $\text{TiO}_2$  increase in spinel from dunites that are believed to represent conduits of focused melt flow and the  $\text{TiO}_2$  increase is therefore in response to open-system melt-rock interaction. An increase of  $\text{TiO}_2$  in spinel is also described in melt-impregnated peridotites and harzburgites that have been modified by melt-rock interaction, in samples from the Hess Deep (Girardeau and Francheteau, 1993; Hekinian *et al.*, 1993; Edwards and Malpas, 1996), melt-impregnated peridotites of the Miyamori ophiolite complex (Northeastern Japan) (Ozawa, 1993), plagioclase-lherzolites of the Bay of Islands ophiolite that are interpreted to be the products of melt-rock interaction (Suhr and Robinson, 1994; Edwards and Malpas, 1995), and dunites of the Luobusa ophiolite (Southern Tibet) that result from melt-rock interaction (Zhou *et al.*, 1996). Whole rock compositional trends of the mylonitic peridotites from the Lizard Ophiolite Complex indicate major and trace element enrichment (Chapter 6.),

which is suggestive of melt-infiltration; therefore the changes in spinel composition are probably a result of both melt-rock interaction and plagioclase-facies re-equilibration. However, whole rock compositions of the spinel lherzolites do not show any evidence for major and trace element enrichment (Chapter 6). It is therefore proposed that the  $\text{TiO}_2$  and Cr# increase in spinel in the spinel lherzolites is related to incipient

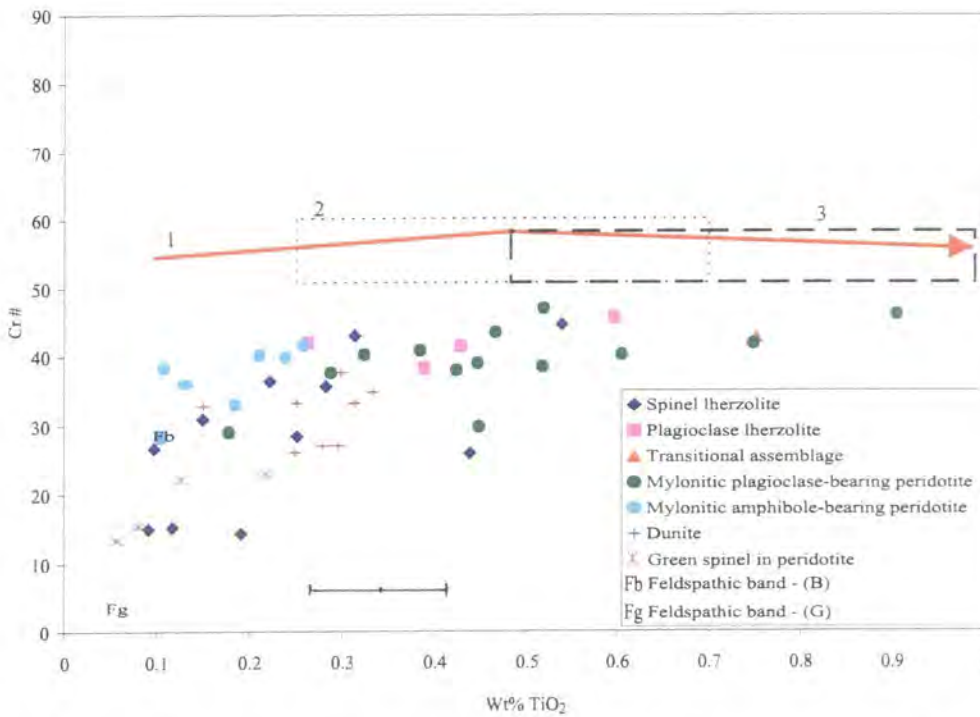


**Figure 5.30.** Plot of Cr# versus wt%  $\text{TiO}_2$  of spinel for peridotites from the Lizard Ophiolite Complex compared with compositional trends and fields defined for melt-impregnated peridotites: (1) arrow shows trend of peridotites from Miyamori ophiolite complex (Ozawa, 1993), (2) dunites from the Oman ophiolite (Kelemen *et al.*, 1995) and (3) plagioclase lherzolites from the Bay of Islands ophiolite (Edwards and Malpas, 1995).

plagioclase-facies re-equilibration (Section 5.2.2.b) and not melt-rock interaction. However, the compositions of spinels found in dunite bodies within the spinel lherzolite are consistent with an origin related to melt-rock interaction, which is suggested by the form of these bodies and the interpretation that they represent the sites of melt flow.

The  $\text{MgO}$  and  $\text{Al}_2\text{O}_3$ -rich and low  $\text{TiO}_2$  green spinels (Figure 5.29 and 5.30) found in the Lizard peridotites, including examples associated with clinopyroxene, plagioclase and pargasitic hornblende veinlets and feldspathic bands (Section 4.3.5.c) are commonly observed in samples which also contain  $\text{Fe}^{2+}$ -,  $\text{Cr}_2\text{O}_3$ - and  $\text{TiO}_2$ -rich brown spinels. The green spinels commonly occur as porphyroblasts and it is suggested

that the spinels may have precipitated from percolating melts. Al-spinel porphyroblasts are described in peridotites from Zabargad Island (Red Sea) and an origin involving precipitation from a melt is similarly proposed (Kurat *et al.*, 1993). However, the green spinels found in the Lizard peridotites show low Cr# and high Mg#. This is not a usual feature of melt precipitation, which usually involves the precipitation of spinels with higher Cr# and lower Mg#. The form of the green spinels, i.e., porphyroblasts, illustrates that these cannot represent relict spinels that have not re-equilibrated to conditions of lower P and T. If the spinels were relicts, one would expect to see deflection of the foliation around the grains. This is not observed and the spinel grains show no evidence

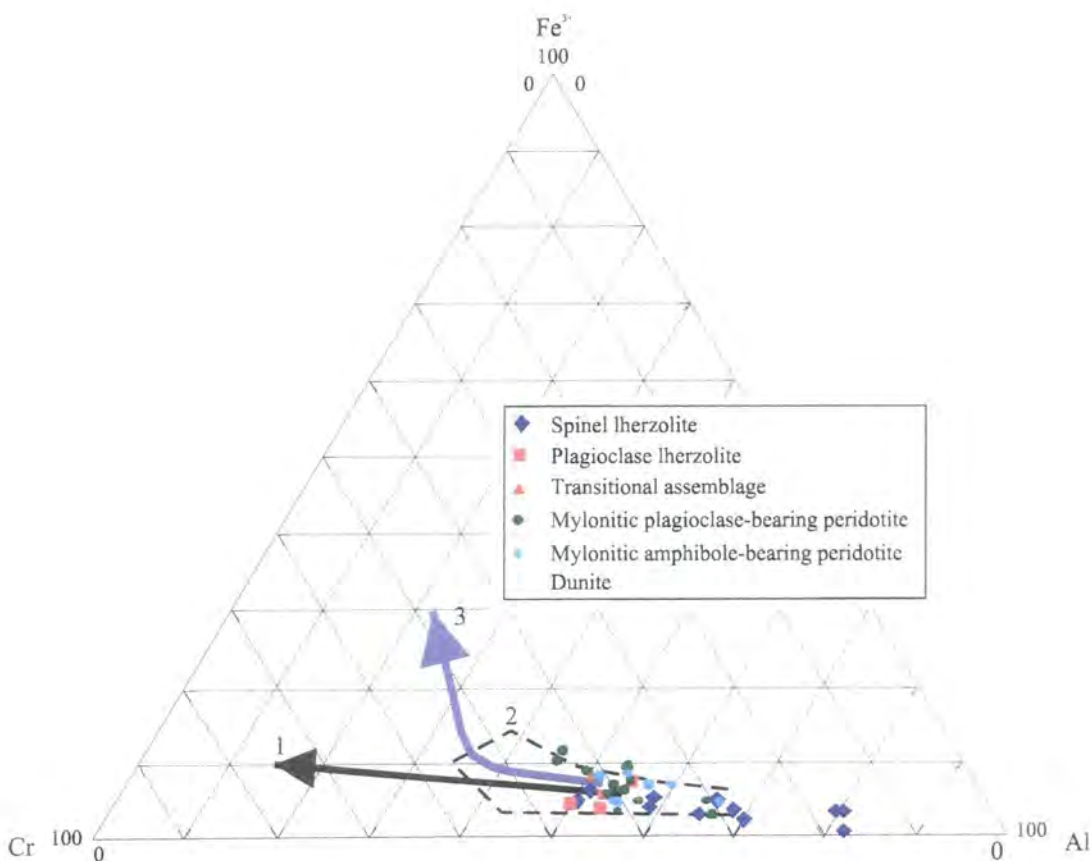


**Figure 5.31.** Triangular plot of  $\text{Fe}^{3+}$ , Cr and Al proportions of spinel for peridotites from the Lizard Ophiolite Complex compared with the (1) partial melting trend of peridotite (Ozawa, 1993), (2) compositional field of abyssal peridotite (Dick and Bullen, 1984) and (3) melt-rock interaction trend of peridotites from the Miyamori ophiolite complex, Japan (Ozawa, 1993).

for internal strain. Green (1964) suggested that these green spinels grew as porphyroblasts whilst the olivine and primary pyroxenes ( $\text{Al}_2\text{O}_3$ -rich) were recrystallising as the rock was deformed. This would require the early stages of deformation of the mylonitic plagioclase-bearing peridotites (in which the green spinels



are found) to occur in the spinel-facies stability field, thus the green Al-rich spinels would be stable. Following the model of Green (*op. cit.*), it is suggested that the plagioclase-rims surrounding these spinel porphyroblasts were developed during the later re-equilibration reactions that accompanied the spinel- to plagioclase-facies transition (Section 5.2.2.b).

A triangular plot of  $\text{Fe}^{3+}$ , Cr and Al contents of spinel (Figure 5.31) shows that the trend defined by the Lizard peridotites lies on the partial melting trend (Ozawa, 1993). But the  $\text{Fe}^{3+}$  increase of the mylonitic plagioclase-bearing peridotites and transitional assemblage peridotites deviates slightly from the partial melting trend and is consistent with melt-rock interaction trends presented by Ozawa (1993).

#### 5.5.2.d. Igneous fractionation trends

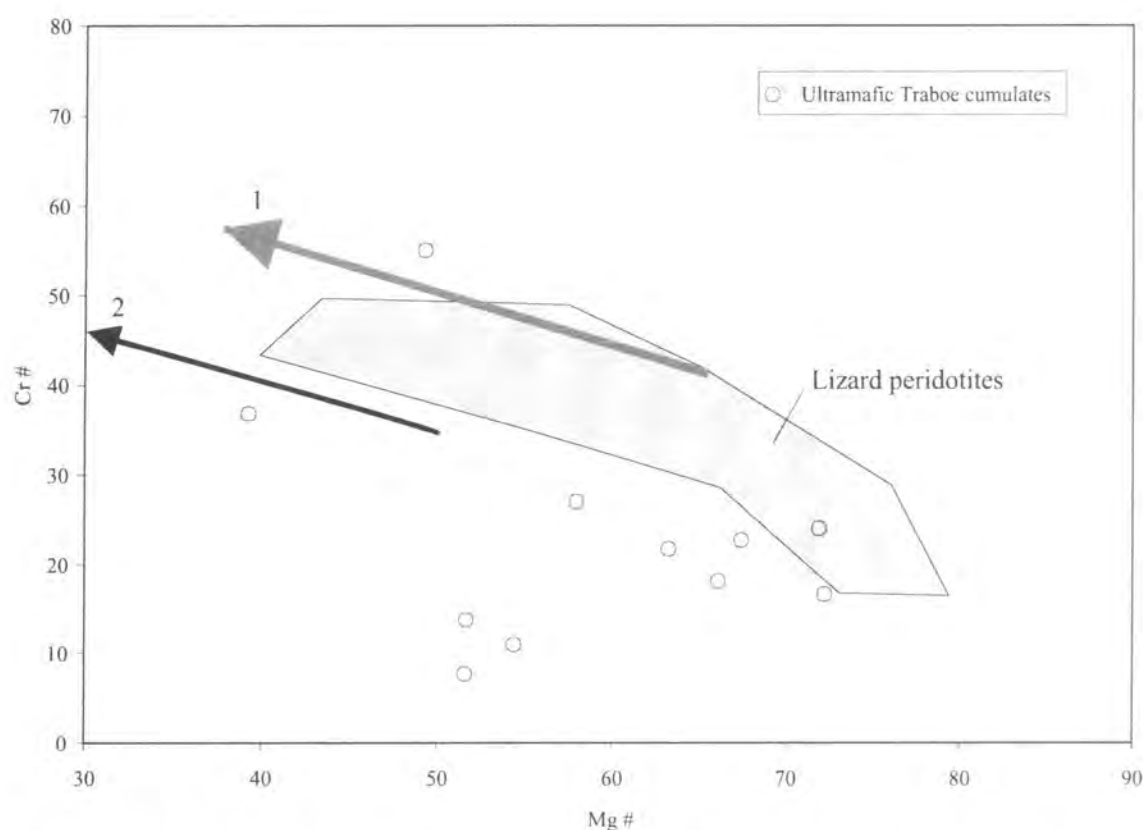


**Figure 5.32.** Plot of Cr# versus Mg# of spinel for ultramafic Traboe cumulates from the Lizard Ophiolite Complex compared with compositional trends defined for (1) ultramafic cumulates from Northern Apennine ophiolites (Hebert *et al.*, 1989) and (2) cumulates from the Brooks Range ophiolite, Alaska (Harris, 1995). The compositional field defined by the peridotites from the Lizard Ophiolite Complex is included for comparison.

The compositional trends defined by Cr# and Mg# for spinels from ultramafic Traboe cumulates of the Lizard deviates from the trends defined for the peridotites (Figure 5.32). The trends in the ultramafic Traboe cumulates are interpreted to represent fractional crystallisation processes. The Fe enrichment (low Mg#) at low Cr# in these ultramafic Traboe cumulates is different to trends in cumulates from the Brooks Range ophiolite (Harris, 1995) and cumulates from the Northern Apennine ophiolites (Hebert *et al.*, 1989)(Figure 5.32).

The  $\text{Fe}^{3+}$  increase, correlated with Cr decrease in the ultramafic Traboe cumulates, although not showing the same range of compositions, is similar to a trend seen in the olivine cumulate peridotites from the Marum ophiolite (Dick and Bullen, 1984 *and references therein*), which is interpreted to be a result of low pressure fractional crystallisation (Figure 5.33). The slight  $\text{Fe}^{3+}$  enrichment of spinels in ultramafic Traboe cumulates, which positively correlates with the low Cr values also suggests fractional crystallisation in the Lizard cumulates.

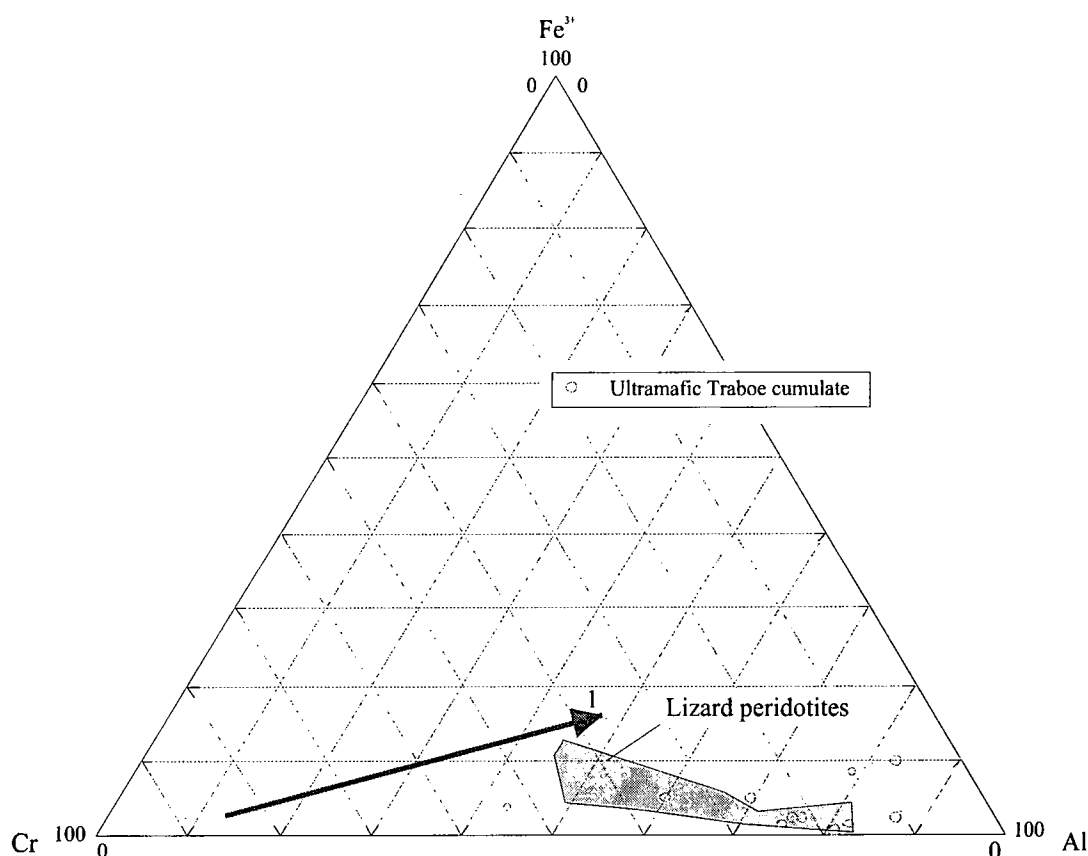


**Figure 5.33.** Triangular plot of  $\text{Fe}^{3+}$ , Cr and Al proportions of spinel for ultramafic Traboe cumulates associated with peridotites from the Lizard Ophiolite Complex compared with (1) fractionation trend of cumulate peridotites from the Marum ophiolite (Dick and Bullen, 1984). The compositional field defined by the peridotites from the Lizard Ophiolite Complex is included for comparison.

### 5.5.2.e. Evidence for the palaeotectonic setting of the Lizard peridotites

Bonatti and Michael (1989) characterised peridotites from a variety of geodynamic environments, from continental, pre-oceanic rifts, to passive ocean margins, to 'mature' mid-ocean ridges and to subduction zones, by compiling mineral

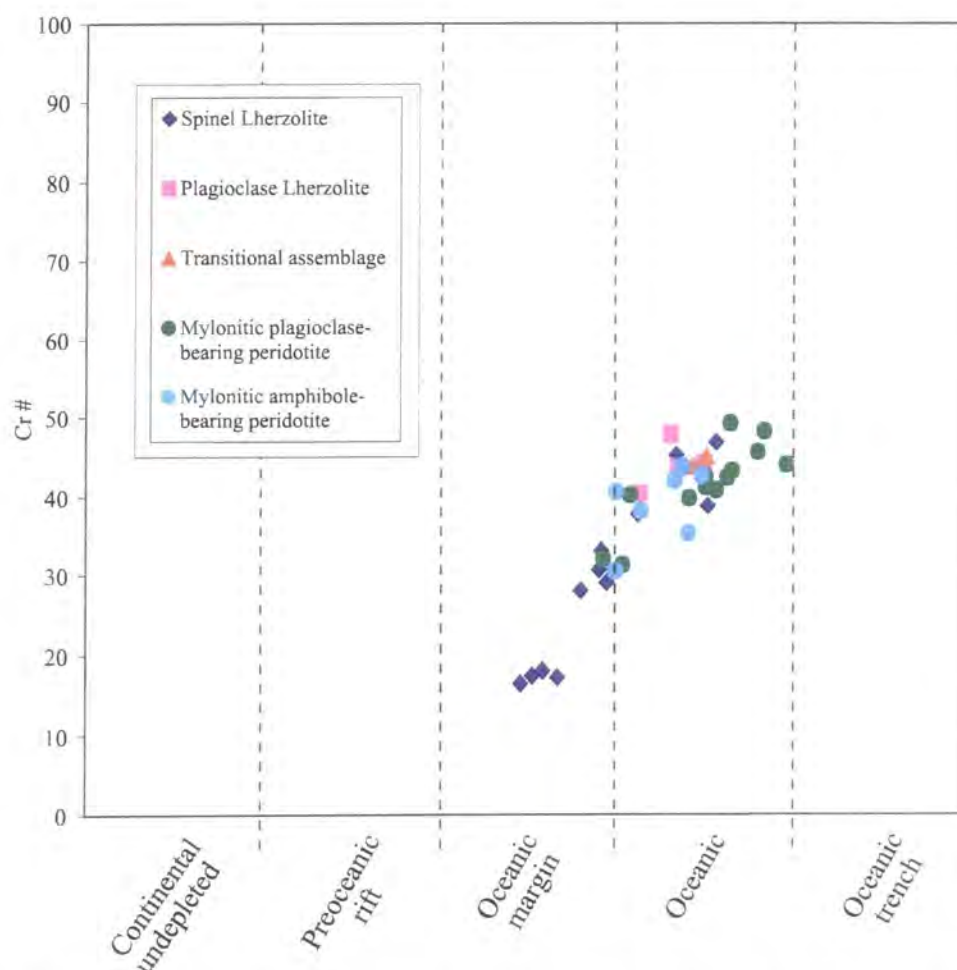


**Figure 5.34.** Spinel Cr# data of Lizard peridotites plotted against inferred tectonic setting. Shaded regions are the ranges of data presented by Bonatti and Michael (1989).

and whole rock geochemical data for peridotites. One of the parameters utilised in the study of Bonatti and Michael (1989) is the Cr# value of spinel, and it is shown that this increases in peridotites going from continental to pre-oceanic rifts to passive ocean margins to 'mature' mid-ocean ridges to subduction zones and reflects an increase in the degree of depletion of the peridotites. In Figure 5.34, the range of Cr# from the Lizard peridotites are plotted against inferred tectonic environment and are compared with the data compiled by Bonatti and Michael (1989). The spinel lherzolites with

primary spinel compositions e.g. low Cr# and high Mg#, plot in the 'ocean margin' field. The spinels with 're-equilibrated' compositions e.g. higher Cr# and lower Mg#, (see Section 5.5.2.b), which include a second group of spinel lherzolites, and plagioclase lherzolites, transitional assemblage peridotites and mylonitic peridotites, plot in the 'oceanic' field. However, the compositions in the 're-equilibrated' spinels cannot be interpreted in terms of a geodynamic setting, because the compositions of these spinels reflect re-equilibration processes and not the degree of depletion due to partial melting processes, which the data of Bonatti and Michael (1989) represents. In summary, the range of data for the spinel lherzolites along the tectonic setting axis illustrates the possibility that they represent mantle derived from an 'oceanic margin' geodynamic setting.

### 5.5.3. Spinel chemistry – summary

- The variations in the Mg#, Cr# and Ti content of spinel in the Lizard peridotites depart from partial melting trends described in the literature. It is therefore suggested that compositional variations are not related to partial melting processes alone, but later chemical and physical processes have modified them.
- The compositional trends defined by spinel in the Lizard peridotites are consistent with spinel- to plagioclase-facies re-equilibration of the peridotites during tectonic exhumation i.e. related to subsolidus reactions that accompany changing conditions of T (and P) during syn-tectonic recrystallisation.
- The same compositional trends are also consistent with melt-rock interaction, which is indicated by whole rock compositions of the mylonitic peridotites (Chapter 6).
- It is therefore concluded that plagioclase-facies re-equilibration and/or melt-rock interaction could have modified the composition of spinels in the Lizard peridotites.
- Spinel compositions in the spinel lherzolites suggest the possibility that prior to the later tectonic and chemical evolution these were derived from an 'oceanic margin' geodynamic setting.
- In contrast to the peridotites it is suggested that the compositional variation in spinels from the ultramafic Traboe cumulates are related to fractional crystallisation processes.

---

## 5.6. Amphibole chemistry

---

Microstructural evidence has shown (Chapter 4) that amphiboles are a common mineral phase in the mylonitic peridotites and also in the ultramafic and mafic Traboe cumulates and other rocks associated with the peridotites. Several populations of amphibole, defined by colour, are also characteristic of the Landwednack amphibolites. The majority of the amphiboles present are secondary in origin, having replaced the primary minerals of the host rocks. However, in some rocks, microstructures suggest that brown amphiboles may be primary in origin (Chapter 4).

### 5.6.1. Amphibole chemistry - results

The main compositional variations in amphibole are outline below. Representative mineral analyses are given in Table 5.6. The full electron probe data set is presented in Appendix D.

The results includes analyses taken of brown-coloured amphiboles, which are the earliest amphibole-type recognised in these rocks and in some examples, may be primary in origin. According to the IMA amphibole classification of Leake (1978), brown amphiboles in the mylonitic plagioclase-bearing peridotite range from kaersutite to Ti-rich pargasite, and tschermakite types. Pale-brown coloured amphiboles in the mylonitic amphibole-bearing peridotite have a different composition and range from edenitic to pargasitic hornblende. Brown amphiboles in the ultramafic Traboe cumulates and the mafic Traboe cumulates also range from edenitic to pargasitic hornblende and ferroan pargasitic hornblende. Amphiboles in a feldspathic band and gabbroic veins are pargasitic hornblende.

Analyses taken from green to colourless amphiboles of secondary origin are also presented. These amphiboles are frequently observed to develop as rims around the earlier brown amphiboles and other primary minerals. These amphiboles also host (in addition to chlorite) cross-cutting shear-zones in the peridotites (Chapter 4). Compositions range from tremolite and tremolitic hornblende to magnesio-hornblende types. Colourless hornblende, which replaces pyroxene in the ultramafic Traboe cumulates ranges between tremolitic hornblende, actinolitic hornblende and magnesio-hornblende types, and are therefore similar in composition to the secondary hornblende

in the Lizard peridotites. Secondary green to colourless-hornblende in the mafic Traboe cumulates, which replaces primary pyroxene and brown amphiboles, ranges from actinolitic hornblende, magnesio-hornblende and ferro-hornblende types. K contents range from 0.0016 to 0.48 (apfu) and Ti contents range from 0.008 to 0.51 (apfu). The highest Cr<sub>2</sub>O<sub>3</sub> contents are shown by brown and pale brown amphiboles found in the mylonitic plagioclase-bearing peridotites and mylonitic amphibole-bearing peridotites and the lowest in colourless hornblendes found in the mafic Traboe cumulates (Table 5.6).

	K (apfu)	Ti (apfu)	Wt% Cr <sub>2</sub> O <sub>3</sub>
Mylonitic plagioclase-Bearing peridotite (B)	0.008-0.07	0.37-0.51	1.56-1.96
Mylonitic amphibole-Bearing peridotite (B-G)	0.005-0.046	0.05-0.2	1.17-2.02
All peridotites (C)	0.0016-0.007	0.008-0.045	0.07-0.62
Feldspathic bands (B-G)	0.009	0.16	1.15
Ultramafic Traboe cumulates (B)	0.028-0.11	0.023-0.28	1.3-1.8
Ultramafic Traboe cumulates (C)	0.009-0.48	0.033-0.1	0.24-0.67
Mafic Traboe cumulates (B-G)	0.02-0.17	0.2-0.3	0.19-0.65
Mafic Traboe cumulates (C)	0.006-0.07	0.022-0.12	0.03-0.4
Gabbroic veins (B)	0.07-0.44	0.31-0.41	0.49-0.61

**Table 5.6.** Summary of the compositions of amphiboles in the Lizard peridotites and associated ultramafic/mafic rocks. (B) = brown amphiboles, (B-G) = brown-green amphiboles, (C) = colourless/secondary amphiboles.

### 5.6.2. Amphibole chemistry – interpretation and discussion

In Figure 5.35, the compositions of amphiboles from the Lizard rocks are compared with examples from the literature using the IMA amphibole classification of Leake (1978). This diagram demonstrates that three different amphibole compositional groups are defined for the amphiboles in the Lizard peridotites and correspond to amphiboles from mylonitic plagioclase-bearing peridotites (kaersutite to Ti-rich pargasite, and tschermakite types), mylonitic amphibole-bearing peridotites (edenitic to pargasitic hornblende) and hydrous shear-zones (tremolite and tremolitic hornblende to magnesio- hornblende types). These different compositional groups within the Lizard



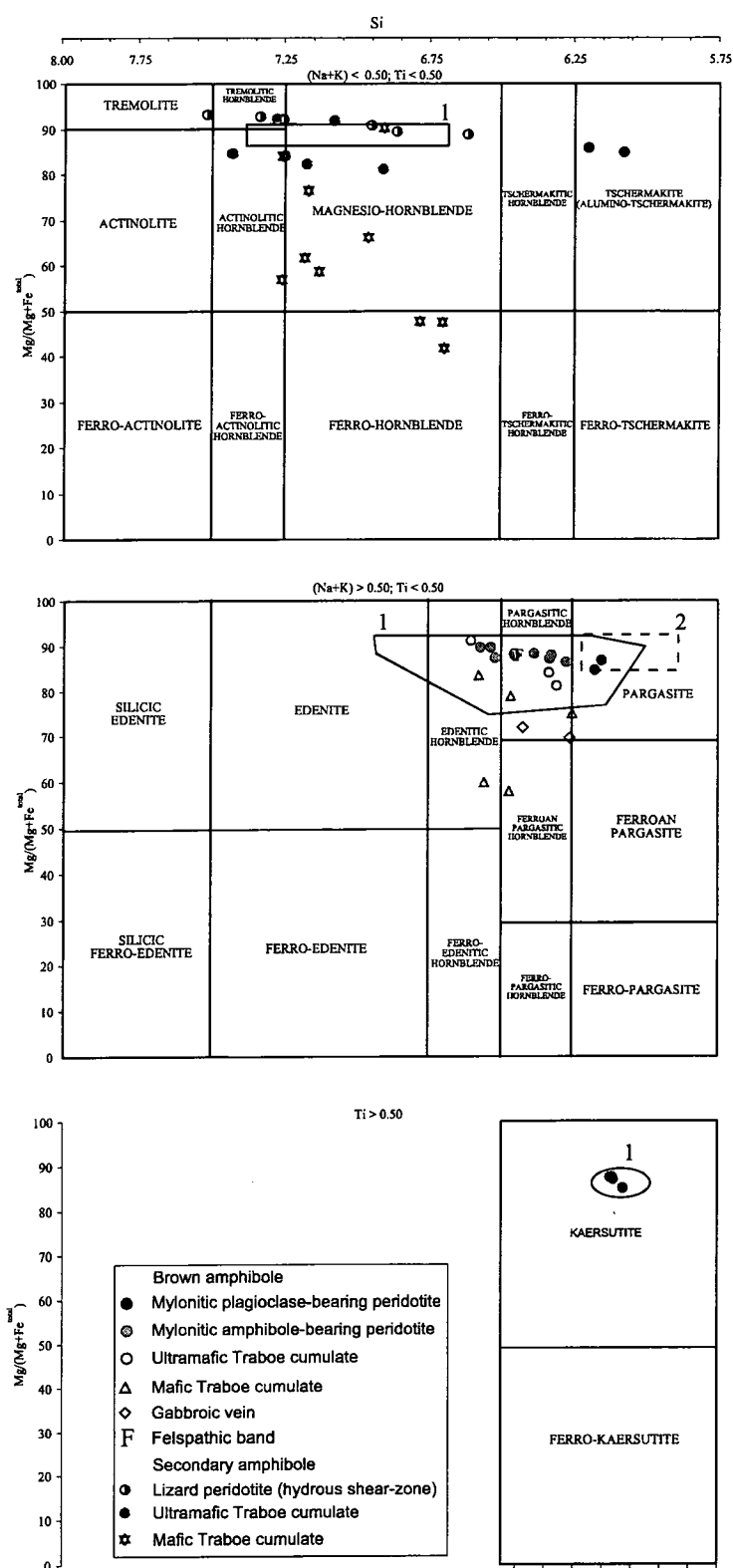


**Figure 5.35.** Classification of calcic amphiboles according to the IMA scheme (Leake, 1978). Amphiboles from the Lizard Ophiolite Complex are compared with examples from the Zabargad Island peridotites, including data from (1) Piccardo *et al.*, (1988) and (2) Bonatti *et al.*, (1986).  $\text{Fe} = \text{Fe}^{\text{total}}$ .

peridotites are similar to compositional groups identified for deformed peridotites from Zabargad Island, Red Sea (Bonatti *et al.*, 1986, Piccardo *et al.*, 1988, Dupuy *et al.*, 1991, Agrinier *et al.*, 1993).

The three compositional groups for the Zabargad Island are summarised by Agrinier *et al.* (1993). These include 'type 1' amphiboles which occur as minor interstitial brown coloured crystals in spinel peridotites, and 'type 2' amphiboles, which are abundant (~30 % modal volume), pale green in colour and characteristic of amphibole peridotites. 'Type 3' amphiboles are green to colourless and are associated with late shear-zones and veins.

'Type 1' amphiboles are predominantly titanian pargasite and, rarely, kaersutite in composition, and 'type 2' amphiboles overlap the pargasite and pargasitic hornblende fields. However, the 'type 3' amphiboles are more variable in composition and range between pargasitic hornblende to tremolitic (where amphibole names are based on the IMA classification of Leake, 1978). The different amphibole groups identified in the Lizard peridotites, in addition to being compositionally very similar to the amphibole groups identified in the Zabargad peridotites (see above), are also texturally similar (Chapter 4). Brown to pale coloured amphibole of feldspathic bands, ultramafic Traboe cumulates, mafic Traboe cumulates and gabbroic veins also overlap the compositional ranges of the 'type 1' and 'type 2' amphiboles from Zabargad Island peridotites. Secondary green to colourless amphiboles in the ultramafic Traboe cumulates are compositionally identical to the 'type 3' amphiboles hosting shear-zones and veins in the Zabargad peridotites (Agrinier *et al.*, 1993). Secondary amphiboles of mafic Traboe cumulates from the Lizard are more Fe-rich than the 'type 3' amphiboles from Zabargad. However, the compositional ranges defined for these rocks do overlap slightly. Interstitial brown amphiboles of Ti-pargasitic to kaersutitic composition (Leake, 1978) are also documented in numerous other peridotite complexes in the literature, including amphibole-bearing peridotites from the Lherz massif (Bodinier *et al.*, 1990; Woodland *et al.*, 1996), Northern Apennine peridotites (Rampone *et al.*, 1993; Rampone *et al.*, 1995), mantle xenoliths (Menzies and Hawkesworth, 1987 and references therein) and peridotite mylonites of basal thrust contacts from the White Hills peridotite (Jamieson, 1980) and the Bay of Islands ophiolite complex (McCaig, 1983) of Newfoundland.

A K versus Ti diagram (Figure 5.36) demonstrates that the brown amphiboles in the mylonitic plagioclase-bearing peridotite (A) have Ti/K ratios similar to brown

amphiboles ('type 1' amphibole) from Zabargad Island spinel peridotites (Dupuy *et al.*, 1991; Agrinier *et al.*, 1993). Brown amphiboles of the Lizard also possess Ti/K ratios that fall within the range defined by amphibole-bearing harzburgite from the Lherz

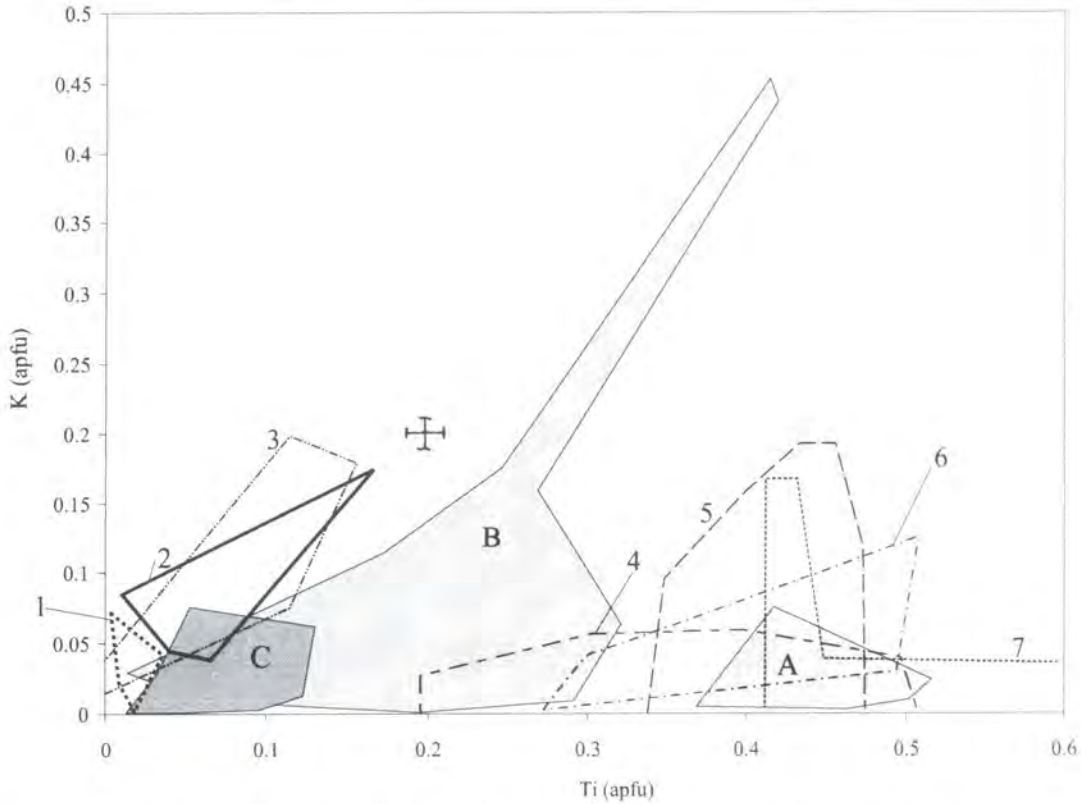


**Figure 5.36.** Plot of K versus Ti (apfu, atoms per formula unit) of amphiboles from rocks of the Lizard Ophiolite Complex, including - (A) brown amphiboles in mylonitic plagioclase-bearing peridotite, (B) pale brown-green coloured amphiboles in mylonitic amphibole-bearing peridotite, cumulate rocks, gabbroic veins and feldspathic band and (C) secondary colourless amphiboles peridotite and cumulate rocks. The amphiboles from the Lizard Ophiolite Complex are compared with compositional fields defined for amphiboles from various ophiolites, including - (1) 'type 3' amphibole, Zabargad Island (Agrinier *et al.*, 1993), (2) 'type 2' amphibole, Zabargad Island (Agrinier *et al.*, 1993), (3) green porphyroclastic amphibole, Zabargad Island (Dupuy *et al.*, 1991), (4) brown amphibole, Zabargad Island (Dupuy *et al.*, 1991), (5) amphibole rich peridotites, Caussou ophiolite (Fabries *et al.*, 1989), (6) 'type 1' amphibole, Zabargad Island (Agrinier *et al.*, 1993), (7) brown amphibole bearing-peridotite, Zabargad Island (Bonatti *et al.*, 1986).

massif (Bodinier *et al.*, 1990) and amphibole-rich peridotites from Caussou peridotites (Fabries *et al.*, 1989). The Ti/K ratio of pale coloured amphiboles in the mylonitic amphibole-bearing peridotite, feldspathic band, ultramafic Traboe cumulates, mafic Traboe cumulates and gabbroic vein from the Lizard (B) overlap the compositional range of both green porphyroclastic ('type 2') amphibole of amphibole peridotites and brown amphibole ('type 1') of spinel peridotites from Zabargad Island (Dupuy *et al.*,

1991; Agrinier *et al.*, 1993). The 'type 3' amphiboles that host shear-zones in the Zabargad peridotites have Ti/K ratios which are very similar to the range of Ti/K ratios observed in colourless hornblende-bearing shear-zones in the Lizard peridotites and in secondary green to colourless amphiboles in the ultramafic Traboe cumulates and mafic Traboe cumulates (C).

A plot of wt% Cr<sub>2</sub>O<sub>3</sub> versus TiO<sub>2</sub> (Figure 5.37) shows that the compositional ranges defined by the three amphibole groups in the Lizard peridotites (A-C) correspond closely to the range of Cr<sub>2</sub>O<sub>3</sub> and TiO<sub>2</sub> contents observed for the different amphibole 'types' in the Zabargad Island peridotites (Agrinier *et al.*, 1993).

Textural (Chapter 4), geochemical evidence and comparison with the literature (see above) suggests that the origin of three different amphibole compositional groups

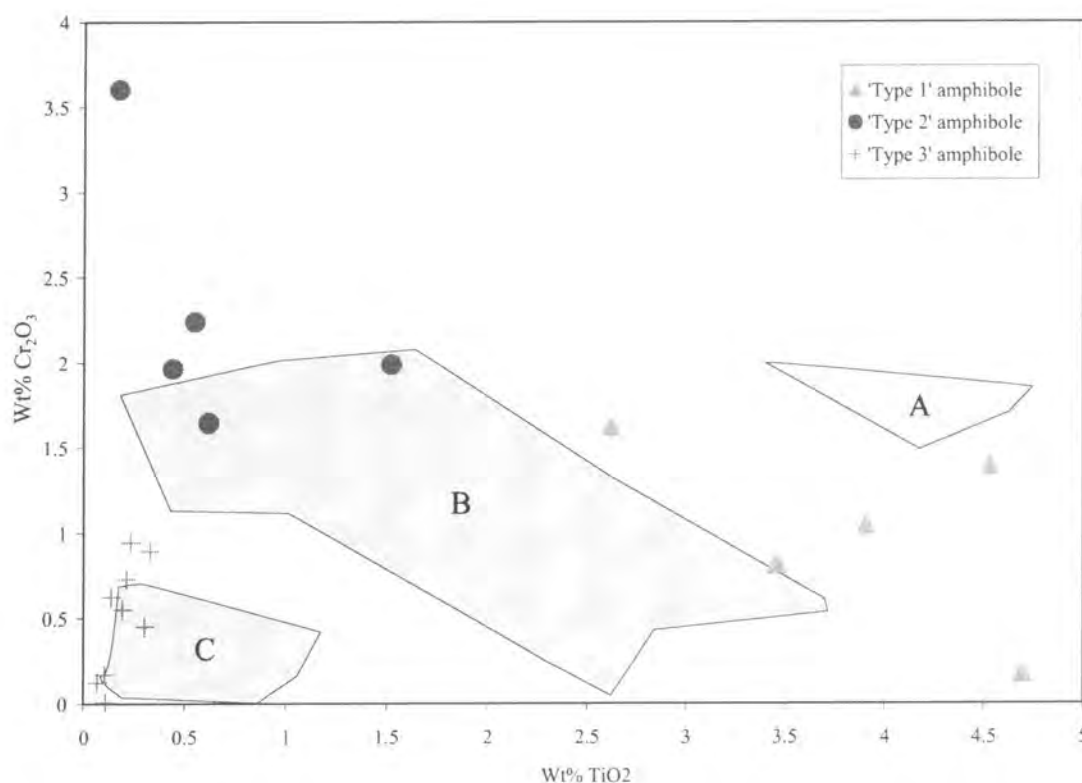


**Figure 5.37.** Plot of wt% Cr<sub>2</sub>O<sub>3</sub> versus wt% TiO<sub>2</sub> of amphiboles from rocks of the Lizard Ophiolite Complex, including - (A) brown amphiboles in mylonitic plagioclase-bearing peridotite, (B) pale brown-green coloured amphiboles in mylonitic amphibole-bearing peridotite, cumulate rocks, gabbroic veins and feldspathic band and (C) secondary colourless amphiboles in peridotite (Hydrous shear-zones) and Traboe cumulate rocks. The amphiboles from the Lizard Ophiolite Complex are compared with compositional fields defined for amphiboles from peridotites of Zabargad Island (Agrinier *et al.*, 1993).

(brown amphibole, green amphibole and colourless hornblende) in the Lizard peridotites are related to different melt + fluid- and/or fluid-rock interaction events and the thermal evolution during the tectonic evolution of the Lizard Ophiolite Complex.

The composition of the amphiboles within each group and comparison with data presented in the literature can be used to constrain the thermal conditions during these events and demonstrates that these events occurred at progressively lower temperatures. The Ti-rich pargasite-kaersutite amphiboles of mylonitic plagioclase-bearing peridotite represent the earliest amphibole group in the Lizard peridotites and recent experimental work (Niidua and Green *submitted min & Pet*) establishes that between 18-25Kb the maximum temperature stability limit of pargasite is 1075°C. In addition, and Agrinier *et al.* (1993) suggest that 'type 1' Ti-pargasite from Zabargad Island formed at temperatures around (900-1000°C).

The 'type 2' Cr-pargasite amphiboles from Zabargad Island are believed to have formed at temperatures around 700-800°C (Agrinier *et al.*, 1993). It is suggested that the pale coloured edenitic to pargasitic hornblende, typical of the mylonitic amphibole-bearing peridotite and feldspathic bands, and the early amphiboles of ultramafic Traboe cumulates, mafic Traboe cumulates and gabbroic veins developed at similar temperatures, on the basis of similarities in composition with the 'type 2' Cr-pargasites from Zabargad Island. The composition and stability of olivine, chlorite and colourless tremolite and tremolitic hornblende to magnesio-hornblende in hydrous shear-zones within the Lizard peridotites is suggestive of temperatures around 500-800°C on the basis of similarities with amphiboles of similar composition in chlorite-bearing peridotite mylonites from the Voltri Massif, NW Italy (Hoogerduijn Strating *et al.*, 1993).

Pyroxene thermobarometry, presented later in this chapter, provides further P-T constraints to substantiate temperatures suggested above. In the following chapter (Chapter 6), whole rock geochemical properties of the Lizard peridotites and associated rocks are presented and additional evidence for melt + fluid and/or fluid-rock is discussed.

### 5.6.3. Amphibole chemistry – Landewednack amphibolites

Landewednack amphibolites show variations in composition. These amphibole-types include brown and green-coloured amphibole and colourless hornblende, which were identified on the basis of microstructural evidence (Chapter 4). The analyses of amphiboles taken from the Landewednack amphibolites are then compared with those taken from amphibolites in ophiolites described in the literature. A comparison of the analyses from the Lizard with the published data will aid the interpretation of the metamorphic conditions responsible for any variations observed in the Landewednack amphibolites. Representative analyses of amphibole for all the Landewednack amphibolites are presented in Appendix D.

#### 5.6.3.a. Results

The principal compositional variations in amphibole are summarised below. Representative mineral analyses are given in Table 5.7. The full electron probe data set is presented in Appendix D.

	K (apfu)	Ti (apfu)
Brown-amphibole	0.012-0.07	0.07-0.28
Green amphibole	0.0001-0.16	0.041-0.14
Colourless hornblende	0.008	0.032

**Table 5.7.** Summary of the compositions of amphiboles in the Landewednack amphibolites

Brown amphiboles are characteristic of the earliest metamorphic assemblage in the Landewednack amphibolites (Section 4.4.1.d), and the composition of these amphiboles and relict brown amphibole cores within later green amphiboles ranges from pargasitic hornblende, ferroan pargasitic hornblende, edenitic hornblende, edenite, magnesio-hornblende types (according to the IMA amphiboles classification of Leake, 1978)(Figure 5.38). The green amphiboles that characterise a second metamorphic assemblage in these amphibolites (Sections 4.4.1.b and 4.4.1.d), occur as rims around relict pyroxene and brown amphiboles of the earliest metamorphic assemblage, range from ferroan pargasitic hornblende, edenitic hornblende, ferro- edenitic hornblende and



magnesio-hornblende to ferro-hornblende types. A third metamorphic assemblage is identified in the amphibolites (Sections 4.4.1.b and 4.4.1.d) and is distinguished by the presence of colourless hornblendes. Analysis of colourless hornblendes in a single sample (CAC 143) shows that they are actinolite in composition. Ti contents range from 0.032 to 0.48 and K contents range from 0.0001-0.16.

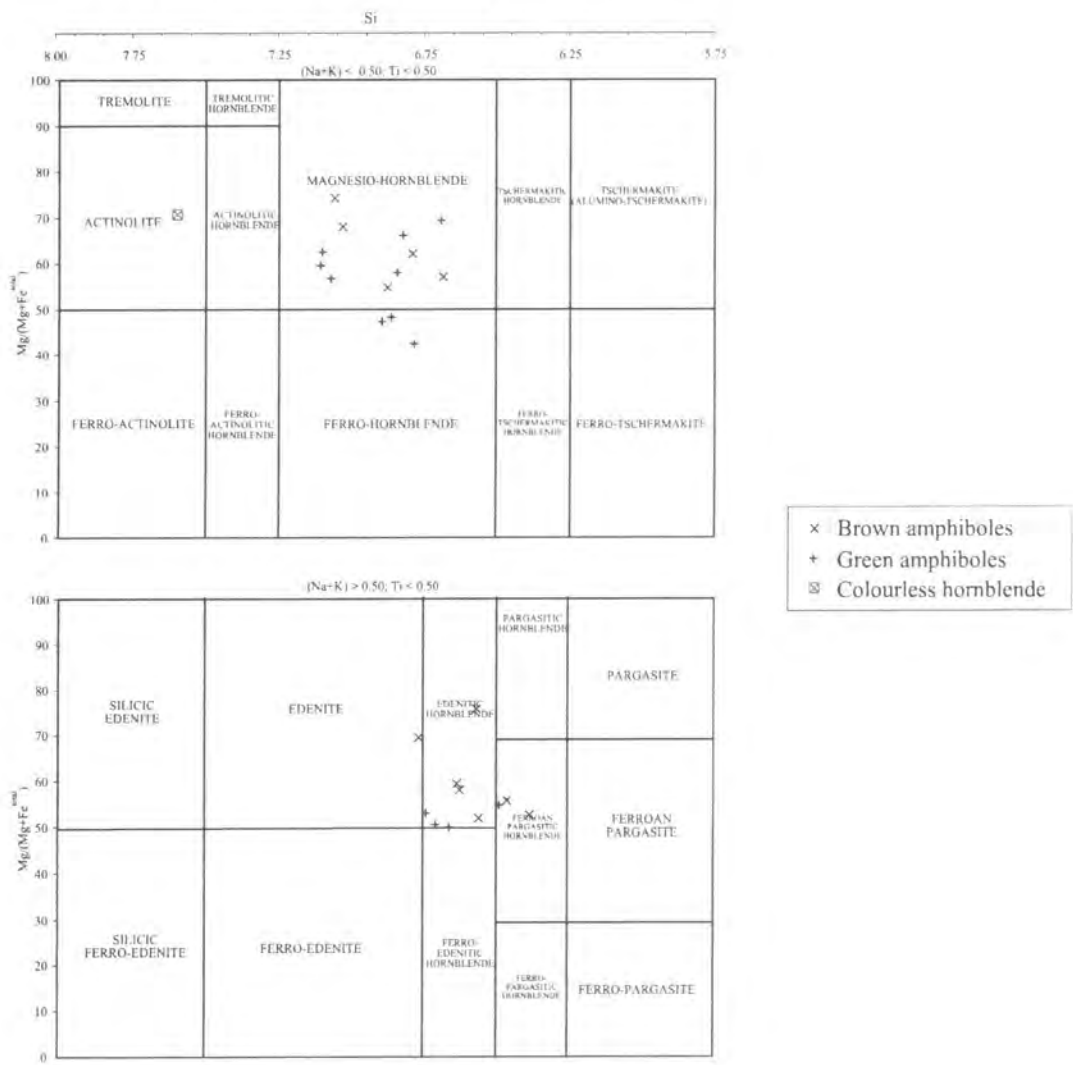


**Figure 5.38.** Classification of calcic amphiboles according to the IMA scheme (Leake, 1978). Brown and green coloured amphiboles and colourless hornblende for the three different metamorphic assemblages of the Landewednack amphibolites from the Lizard Ophiolite Complex are shown.  $Fe = Fe_{total}$ .

5.6.3.b. Interpretation and discussion

The compositional range defined by the brown and green amphiboles and colourless hornblende from the Landewednack amphibolites overlaps the range displayed by

amphibolites associated with the Troodos ophiolite (Spray and Roddick, 1981; Malpas *et al.*, 1992) and Oman ophiolite (Searle and Malpas, 1982). The brown and green coloured amphiboles from the Lizard amphibolites define different trends on a plot of K versus Ti (Figure 5.39), with the green amphibole showing a limited range of Ti contents and wide range of K contents in contrast to brown amphibole, which have more variable Ti contents and limited K contents.

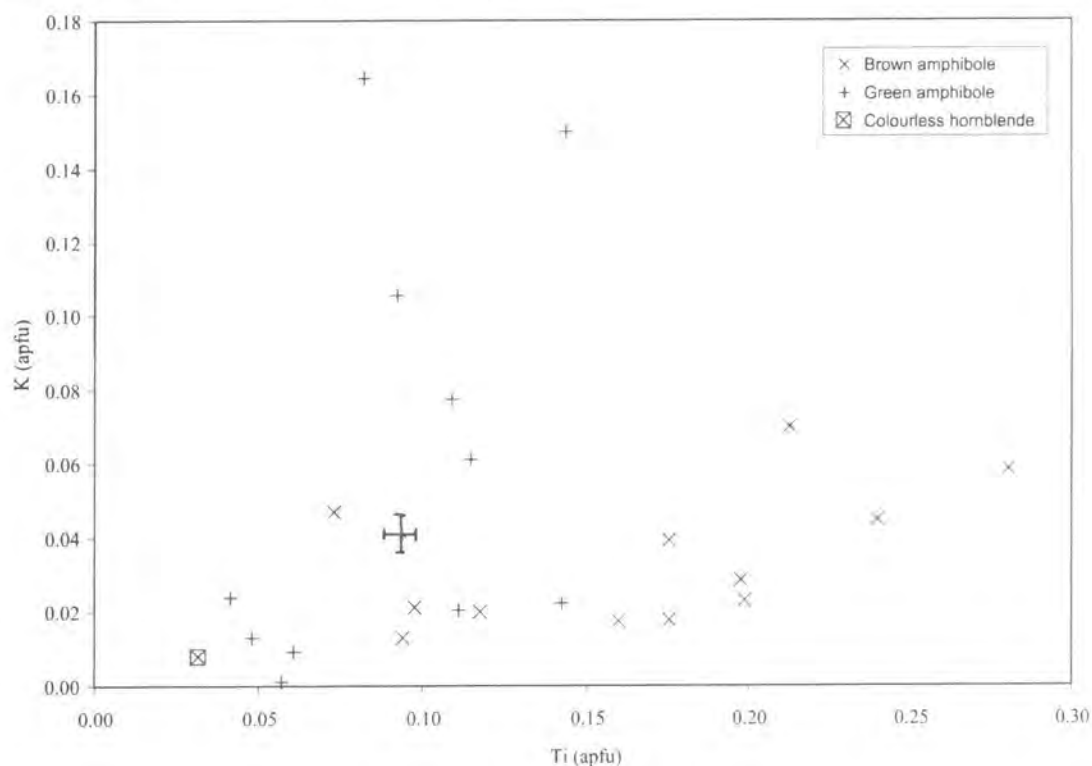


**Figure 5.39.** Plot of K versus Ti (apfu, atoms per formula unit) of brown and green coloured amphiboles and colourless hornblende for the three different metamorphic assemblages of the Landwednack amphibolites from the Lizard Ophiolite Complex are shown.

It is suggested that these different compositional trends and the different metamorphic mineral assemblages, including amphibole colour in the amphibolites, are related to contrasting metamorphic conditions e.g. temperature, pressure and/or variations in the composition metamorphic fluids. The composition of brown amphiboles in the Lizard amphibolites overlaps the range defined by pale brown/green amphiboles in the mylonitic amphibole-bearing peridotites, feldspathic bands, ultramafic Traboe cumulates, mafic Traboe cumulates and gabbroic veins (Figure 5.36). This suggests that the development of the amphibole-bearing assemblages in all of these rocks may be related to the same tectono-thermal event, as already proposed on the basis of textural evidence in the previous chapter (Chapter 4). The compositions of

colourless hornblende within a shear-zone in the amphibolites overlap the range defined by colourless hornblende hosting hydrous shear-zones in the Lizard peridotites, and secondary hornblende in the ultramafic Traboe cumulates and mafic Traboe cumulates (Figure 5.36). This similarity in composition also supports the conclusion based on field (Chapter 3) and microstructural (Chapter 4) evidence, that the shear-zones and secondary green to colourless hornblende in the Lizard peridotites, ultramafic Traboe cumulates, mafic Traboe cumulates and amphibolites are analogous.

On the basis of the geochemical properties of amphiboles in the Landwednack amphibolites, it is suggested that the transition from an amphibolite assemblage characterised by brown amphibole to green amphibole (via relict brown amphibole cores with green rims) and, finally, colourless hornblende is related to different tectono-thermal events. It is suggested that these different tectono-thermal events are associated with a decrease in temperature and a change in the composition of metamorphic fluids. This hypothesis contrasts with the findings of Green (1964b), who proposed that the metamorphism of the Lizard amphibolites is prograde rather than retrograde, and that brown amphibole-bearing assemblages post-date a green amphibole-bearing assemblage. However, Green (1964c) also notes that, in many specimens with a brown amphibole-bearing assemblage, there is evidence for incipient retrogression of brown amphibole to a blue-green amphibole, which supports the findings presented above. Further constraints for temperature and pressure conditions during metamorphism in the Lizard amphibolites are provided by thermobarometry later in this chapter.

### 5.6.3. Amphibole chemistry – summary

- Three different amphibole types were defined in the mylonitic peridotites and associated ultramafic and mafic rocks on the basis of microstructural observations and these were brown-amphibole, green amphibole and colourless hornblende (Chapter 4); and this is confirmed by variations in mineral composition.
- It is suggested that the three different amphibole types are related to different melt + fluid- and/or fluid-rock interaction events during the evolution of the peridotites and associated ultramafic and mafic rocks and that these events occurred at progressively lower temperatures.

- Three different amphibole types have also been defined in the Landewednack amphibolite and these were brown amphibole, green amphibole and colourless hornblende (Chapter 4); and this is also confirmed by variations in mineral composition. The green amphibole and colourless hornblende are similar in composition to amphiboles in the Lizard peridotites and associated ultramafic and mafic rocks.
- It is proposed that the different amphibole types (i.e. metamorphic mineral assemblages) in the Landewednack amphibolites were developed during different tectono-thermal events, which appear to have been associated with a decrease in temperature and a change in the composition of metamorphic fluids.

---

## 5.7. Plagioclase chemistry

---

Plagioclase is a relatively minor phase in the Lizard peridotites, as it is only observed in the plagioclase lherzolites, the transitional assemblage peridotites and the mylonitic plagioclase-bearing peridotites. However, the Traboe cumulate rocks associated with the peridotites often contain a high proportion of plagioclase. Therefore it is important to analyse these grains. The Landewednack amphibolites also contain abundant plagioclase. The chemistry of plagioclase in these rocks may reflect primary compositions, including igneous fractionation trends, in addition to compositions modified through metamorphism. The purpose of this sub-Section is to present analyses of plagioclase in the peridotites, associated cumulate rocks and the Landewednack amphibolites in order to determine the nature of their compositions, then identify and evaluate any significant compositional variations.

### 5.7.1. Plagioclase chemistry – results

The following discussion summaries the principal variations in plagioclase composition. In the following sub-Section, interpretations and discussions of this data and comparison with data presented in the literature are provided. Representative mineral analyses are given in Table 5.8. The full electron probe data set is presented in Appendix D.

	%An
Mylonitic plagioclase-bearing peridotite	68-74
Ultramafic Traboe cumulate	77
Mafic Traboe cumulate	45-79
Gabbroic vein	50-55
Troctolite	61
Mafic dyke	23-31
Landewednack amphibolite (brown amphibole assemblage)	52-71
Landewednack amphibolite (green amphibole assemblage)	31-55
Landewednack amphibolite (colourless hornblende assemblage)	10-24

**Table 5.8.** Summary of the compositions of plagioclases found in the ultramafic and mafic rocks from the Lizard Ophiolite Complex.

The An content of plagioclases ranges from An10 to An79 (Table 5.8). The highest values are found in the mafic Traboe cumulates and the lowest values in the colourless hornblende-bearing assemblage of the Landewednack amphibolites. The largest range of An contents are shown by plagioclases found in the mafic Traboe cumulates (An45-79).

### 5.7.2. Plagioclase chemistry – interpretation and discussion

In Figure 5.40, the range of plagioclase compositions for the mylonitic plagioclase-bearing peridotites is compared with plagioclase compositions of plagioclase-bearing peridotites from ophiolites presented in the literature. The development of plagioclase in plagioclase peridotites from ophiolites (Figure 5.40) is interpreted by Bonatti *et al.*, (1986), Hoogerduijn Strating *et al.*, (1993) and Rampone *et al.*, (1993) to be related to subsolidus reactions involving the breakdown of spinel and pyroxene and re-equilibration, which accompanies the spinel- to plagioclase-facies transition of peridotite.

The similarity between the composition of the plagioclase in the mylonitic plagioclase-bearing peridotites from the Lizard and the examples from the literature suggests that the origin of the plagioclase in the Lizard rocks may be attributed to metamorphic re-equilibration in response to the spinel- to plagioclase-facies transition. However, the possibility that the plagioclase is also derived from melt-rock interactions

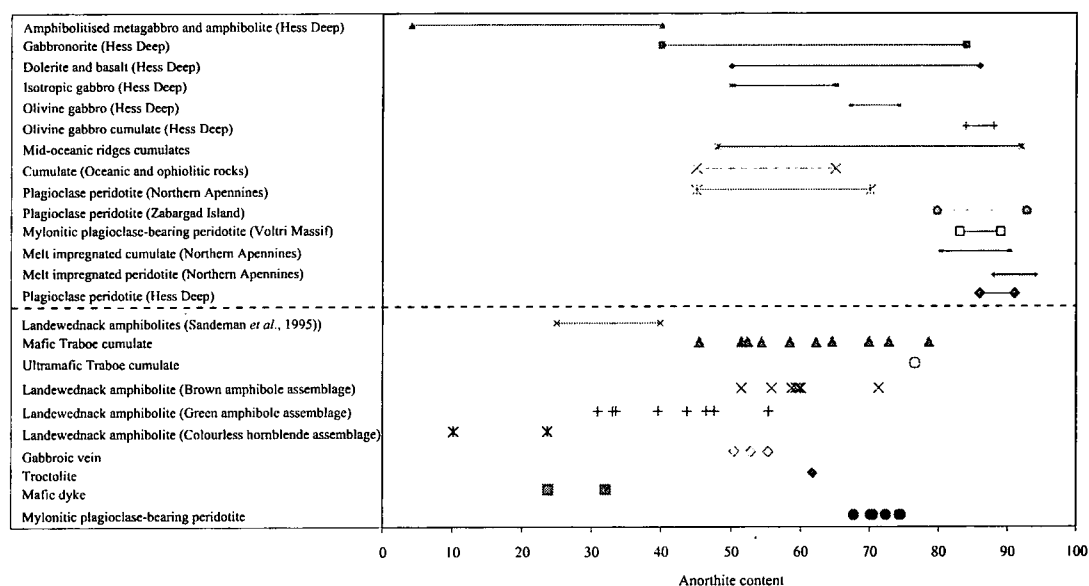


**Figure 5.40.** Diagram showing the anorthite content (%An) of plagioclase for rocks from the Lizard Ophiolite Complex (including data from Sandeman *et al.*, 1995 for Landwednack amphibolites) compared with ultramafic and mafic rocks from oceanic environments and ophiolites, including examples from Hess Deep (Girardeau and Francheteau, 1993; Hekinian *et al.*, 1993), Northern Apennine ophiolites (Rampone *et al.*, 1993; Rampone *et al.*, 1997), Voltri Massif (Hoogerduijn Strating *et al.*, 1993), Zabargad Island (Bonatti *et al.*, 1986), Oceanic and ophiolitic environments (Hebert *et al.*, 1989 and references therein), Mid-ocean ridge environments (Beard, 1986).

must also be considered, especially when variations in the composition of the other constituent phases (olivine, pyroxene and spinel) suggests that melt-rock interaction may be involved in addition to reactions accompanying the spinel to plagioclase-facies transition. Plagioclase-bearing peridotites and cumulates that represent the product of melt impregnation, from the Hess Deep (An 86 and 91) (Girardeau and Francheteau, 1993) and Northern Apennines (An80-94)(Rampone *et al.*, 1997), have higher anorthite contents than the mylonitic plagioclase-bearing peridotites from the Lizard. The presence of amphibole- and plagioclase-bearing veinlets (Chapter 4) in the mylonitic peridotite, and plagioclase veinlets in the coarse-grained lherzolites (Davies, 1984) also suggests that melt impregnation has occurred in the Lizard peridotites. If melt-interaction is responsible for the composition of the plagioclase in the Lizard peridotites, the reason for the An contents being lower than those presented for melt impregnated ultramafic rocks from Hess Deep and the Northern Apennines could be a consequence of differences in the composition of the infiltrating melt and the host rock. In conclusion, it is proposed that the composition of plagioclase in the mylonitic plagioclase-bearing peridotite from the Lizard may be related to reactions



accompanying the spinel to plagioclase-facies re-equilibration of the peridotite and melt-rock interaction.

The mafic Traboe cumulates from the Lizard exhibit a considerable range of plagioclase compositions (An<sub>45-79</sub>), which would be expected as a result of crystal fractionation processes. The variations in plagioclase composition in these cumulates is less likely to be a result of metamorphism, because plagioclase would be relatively stable at the pressure and temperature conditions which are calculated (Section 5.8) for deformation and metamorphism in these rocks.

The different mineral assemblages found in the Landewednack amphibolites, which are defined by the presence of brown amphibole, green amphibole and colourless hornblende respectively, plot as three distinct compositional groups on a diagram (Figure 5.40) displaying the anorthite content of plagioclase.

The range of anorthite contents of plagioclases in Landewednack amphibolites with a brown amphibole-bearing assemblage is similar to the range in the mafic Traboe cumulates, which possess both brown and green amphibole-bearing assemblages, and falls within the range defined by cumulate rocks from oceanic environments and ophiolites (Figure 5.40). Plagioclase compositions in Landewednack amphibolites with a green amphibole-bearing assemblage overlap the range of compositions obtained in a study of the same unit of amphibolites from the Lizard by Sandeman *et al.*, (1995). These amphibolites and those associated with colourless hornblende-bearing shear-zones have plagioclase compositions that overlap the range displayed by amphibolitised metagabbro and amphibolite (An<sub>4-40</sub>) from the Hess Deep (Hekinian *et al.*, 1993).

The variations in the compositions of plagioclases between the different metamorphic mineral assemblages of the Landewednack amphibolites, which all have a similar bulk whole rock composition (Chapter 6), do not appear to be primary in origin. This is because the anorthite contents of the Landewednack amphibolites are lower than the range observed for primary plagioclase compositions in mafic igneous rocks (see above) from ophiolites and oceanic environments. Alternatively it is proposed that the decrease in anorthite content of plagioclase from brown amphibole-bearing amphibolites via green amphibole-bearing amphibolites to colourless hornblende-bearing amphibolites is related to metamorphic processes (Plyusina, 1982; Blundy and Holland, 1990). The changes in the anorthite composition of plagioclase are related to equilibrium exchange reactions with co-existing calcic amphiboles, with plagioclase

becoming less calcic and amphibole more calcic at lower temperatures and pressures during metamorphism (Plyusina, 1982). It has already been suggested on the basis of amphibole compositions, that changes in the mineral assemblage in the amphibolite occurred in response to a decrease in temperature during different tectono-thermal events (Section 5.6.3.b). The temperature and pressure conditions of metamorphism in the Landewednack amphibolites are investigated later in this chapter with reference to the application of plagioclase-amphibole thermobarometry.

#### **5.7.4. Plagioclase chemistry – summary**

- It is suggested that the occurrence of plagioclase in the mylonitic plagioclase-bearing peridotites from the Lizard Ophiolite Complex may be controlled by reactions accompanying involving the breakdown of Al-rich spinel and pyroxenes during the spinel to plagioclase-facies re-equilibration of the peridotite. Variations in the composition of the plagioclase may be related to differences in the composition of spinel and/or pyroxene. The plagioclase may also been derived from melt-rock interactions.
- The large range (An<sub>45-79</sub>) compositions of plagioclases in the mafic Traboe cumulates are probably related to crystal fractionation processes.
- The compositional variations of plagioclases in the Landewednack amphibolites are directly correlated with the metamorphic mineral assemblage, based on the type of amphibole. It is suggested that the decrease in An content of plagioclase in the different metamorphic mineral assemblages may be related decreasing conditions of T and P during metamorphism, because plagioclase becomes less calcic at lower T and P as a consequence of equilibrium exchange reactions with co-existing calcic amphiboles.

---

### **5.8. Temperature and pressure evolution and conditions during deformation**

---

In the previous chapter (Chapter 4), microstructures of the Lizard peridotites and associated rocks, including ultramafic and mafic Traboe cumulates, have shown variations consistent with changes in the conditions of P and T during deformation. This evidence includes the results of a study of olivine petrofabrics for the peridotites,

which provides constraints for the temperature conditions during deformation. In the previous Sections, compositional variations of the constituent minerals in the Lizard peridotites and associated rocks e.g. decreasing  $\text{Al}_2\text{O}_3$  and CaO of orthopyroxene, decreasing  $\text{Al}_2\text{O}_3$  and increasing CaO of clinopyroxene, increasing Cr# and decreasing Mg# of spinel have been interpreted in terms of changes in the conditions of P and T during deformation and metamorphism. Similarly, it has been suggested that changes in the P and T conditions of metamorphism may be responsible for the low  $\text{Al}_2\text{O}_3$  contents and high CaO contents of clinopyroxene, and decreasing %An of plagioclases found in the Landwednack amphibolites. In the following sub-Sections published mineral thermometers and barometers are applied to the rocks of the Lizard Ophiolite Complex in order to substantiate the hypotheses that have already been proposed. This study will also provide additional new constraints, on the conditions of P and T during the deformation and metamorphism associated with the evolution of the Lizard Ophiolite Complex.

#### 5.8.1. Pyroxene thermobarometry

A variety of methods, based on mineral compositions, are used to determine the temperature and pressure values of equilibration of the Lizard peridotites and associated ultramafic and mafic rocks. The methods of determining these equilibration conditions are based on both experimental CMS (CaO–MgO– $\text{SiO}_2$ ) and CMAS (CaO–MgO– $\text{Al}_2\text{O}_3$ – $\text{SiO}_2$ ) systems, in addition to natural systems.

The thermometer of Wells (1977) is based on the exchange of Ca and Mg between clinopyroxene and orthopyroxene. The partitioning of Al and Cr in orthopyroxene (Witt-Eickchen and Seck, 1991) is not applicable to plagioclase-bearing assemblages, hence can only be applied to spinel lherzolites or relict spinel-facies orthopyroxene porphyroclasts in plagioclase-bearing assemblages. The Brey and Kohler (1990) thermometer is based on the partitioning of Na between orthopyroxene and clinopyroxene. The thermometer of Brey *et al.*, (1990) is also applied, and this is based on the partitioning of Fe, Mg, Ca and Na between orthopyroxene and clinopyroxene. Al and Cr solubility in pyroxene is utilised by the thermobarometer of Mercier (1980) for spinel facies peridotites. The  $\text{Al}^{\text{total}}$  content of amphibole is strongly dependent on pressure. Thus, the barometers of Johnson & Rutherford (1989) and Schmidt (1992) have been applied to amphibole compositions in the mylonitic

peridotites, feldspathic bands, ultramafic and mafic cumulates and gabbroic veins to provide estimates of pressure. The Mercier *et al.* (1984) barometer, based on Ca partitioning between co-existing orthopyroxene and clinopyroxene yielded unrealistic values for the Lizard peridotites (i.e. extremely high or low pressure and negative pressures). Processes other than temperature and pressure controlled equilibration may therefore affect the Ca concentration in the pyroxenes. The Kohler and Brey (1990) barometer based on Ca exchange between olivine and clinopyroxene also yielded unrealistic values, and is therefore not used. The erroneous results of the Mercier *et al.* (1984) and Kohler and Brey (1990) barometers highlight the fact that there can be problems when applying thermometers and barometers to natural rock systems.

One of main assumptions associated with the application of thermometers and barometers is that the chemical composition of the constituent minerals reflects equilibration at transient pressures and temperatures (Hoogerduijn Strating *et al.*, 1993). The results obtained from these techniques when applied to natural systems also depend on many other factors, including (1) analytical error, (2) secondary alteration of the constituent mineral phases, (3) the activity of other elements e.g. Na, Cr and  $\text{Fe}^{3+}$ , (4) non-ideal solution behaviour of the constituent phases, (5) deviations of the ideal cation ordering on sites of coexisting mineral phases, (6) grain size, (7) cooling rate, (8) the presence of fluids, and (9) the influence of deformation on the diffusion kinetics (Witt-Eickschen and Seck, 1991; Hoogerduijn Strating *et al.*, 1993). In particular, in preceding Sections describing and interpreting the compositions of the mineral phases in the Lizard peridotites and associated rocks, it has been demonstrated that the mineral compositions in these rocks have been modified by melt-rock interaction in addition to temperature and pressure controlled equilibration. The compositional changes resulting from the melt-rock interaction processes are therefore likely to influence the results of geothermometric and geobarometric calculations presented below. The closure temperature of cation-exchange reactions, on which the thermometers and barometers are based, are influenced by these and other factors and therefore the validity of these methods is questioned.

A comprehensive discussion of the principles pertinent to the thermometers and barometers utilised on the Lizard rocks and the effects of the factors influencing the results is beyond the scope of this study. With consideration of the problems associated with the use of thermometers and barometers, the results of thermometric and

barometric calculations cannot be considered as precise values. Additional constraints, particularly for pressure estimates, are obtained from associated mineral assemblages.

Four pyroxene thermometers and a single pyroxene thermobarometer have been selected from the methods presented in the literature (see Table 5.9) and applied to pyroxenes from the Lizard peridotites and associated ultramafic and mafic rocks. Pyroxenes with minimal exsolution lamellae were selected and, where present, a defocused beam analysis was used. The Witt-Eickschen and Seck (1991) thermometer has been applied to plagioclase-free assemblages and, in plagioclase-bearing assemblages, it is only applied to relict, coarse-grained, orthopyroxene porphyroclasts which are interpreted to have originally equilibrated at higher-pressure conditions. Additional pressure estimates for the mylonitic peridotites and associated ultramafic

Author(s)	Estimate	Mineral(s)	Method
Wells (1977)	Thermometer	Clinopyroxene-orthopyroxene pair	Mg-Ca exchange
Brey and Kohler (1990)	Thermometer	Clinopyroxene-orthopyroxene pair	Na partitioning
Brey <i>et al.</i> , (1990)	Thermometer	Clinopyroxene-orthopyroxene pair	Fe, Mg, Ca and Na partitioning
Witt-Eickschen and Seck (1991)	Thermometer	Orthopyroxene	Cr and Al partitioning
Mercier (1980)	Thermobarometer	Single pyroxene	Al and Cr solubility
Johnson and Rutherford (1989)	Barometer	Amphibole	Al <sup>total</sup> content
Schmidt (1992)	Barometer	Amphibole	Al <sup>total</sup> content
Spear (1980)	Thermometer	Amphibole-plagioclase pair	Na and Ca partitioning
Plyusina (1982)	Thermobarometer	Amphibole-plagioclase pair	An content of plagioclase and Al <sup>total</sup> content of amphibole
Blundy and Holland (1990)	Thermobarometer	Amphibole-plagioclase pair	An content of plagioclase and Al <sup>total</sup> content of amphibole

**Table 5.9.** Summary of methods used by the thermometers, barometers and thermobarometers for P-T estimates of equilibration of the Lizard peridotites, associated rocks and Landwednack amphibolites.

and mafic rocks are provided by the amphibole barometers of Johnson & Rutherford (1989) and Schmidt (1992) (Table 5.9). See Appendix C for the equations used for the P & T calculations.

### 5.8.1.a. Results

The results for all the thermometers used for each particular sample are presented on a graph to facilitate comparison of the different methods (Figure 5.41). The data presented for a thermometer in each sample represents an average value for all the clinopyroxene-orthopyroxene pairs, or single orthopyroxene compositions. Error bars for each result refer to the errors recommended by the authors. For each particular sample the average values, based on different thermometers, usually fall within a range of 110°C and are generally within error of different methods. However, the Brey *et al.* (1990) thermometer often yields results which are, in some examples, between 150-200°C lower than the other thermometers. Hence the results of this thermometer are omitted when they fall outside the error defined by the other methods.

The average values, obtained by the various thermometers, for pyroxene porphyroclasts in the spinel lherzolites yield temperatures that range between 1021 and 1197°C and thus appear to represent the crystallisation conditions of the earliest, pre-tectonic, peridotite mineral assemblage in the Lizard. Porphyroclasts in plagioclase lherzolites give temperatures between 1063-1121°C. In peridotite assemblages transitional between plagioclase lherzolites and mylonitic plagioclase-bearing peridotites, temperatures range between 1049 and 1164°C. The <sup>temperatures yielded by</sup> porphyroclasts in the plagioclase-bearing assemblages are therefore slightly lower than those in the spinel lherzolite. Although the temperatures in the plagioclase-bearing rocks are interpreted to reflect the relict, pre-tectonic and spinel-facies equilibration of the porphyroclasts, there has been incipient equilibration to lower temperature. Temperatures yielded by relict orthopyroxene porphyroclasts in mylonitic plagioclase-bearing peridotites support this observation. They are lower, ranging between 926 and 1080°C. Neoblasts in the mylonitic plagioclase-bearing peridotites provide lower temperatures between 919 and 1035°C. A similar range is observed in neoblasts in mylonitic amphibole-bearing peridotites, namely 965 to 1074°C.

Fine-grained pyroxene neoblasts in a feldspathic band (CAC 73) within mylonitic amphibole-bearing peridotite provide a temperature of 947°C, which is in error of results for the mylonitic peridotites. A similar range of temperatures, between 972 and 1061°C, is observed in ultramafic Traboe cumulates and these results



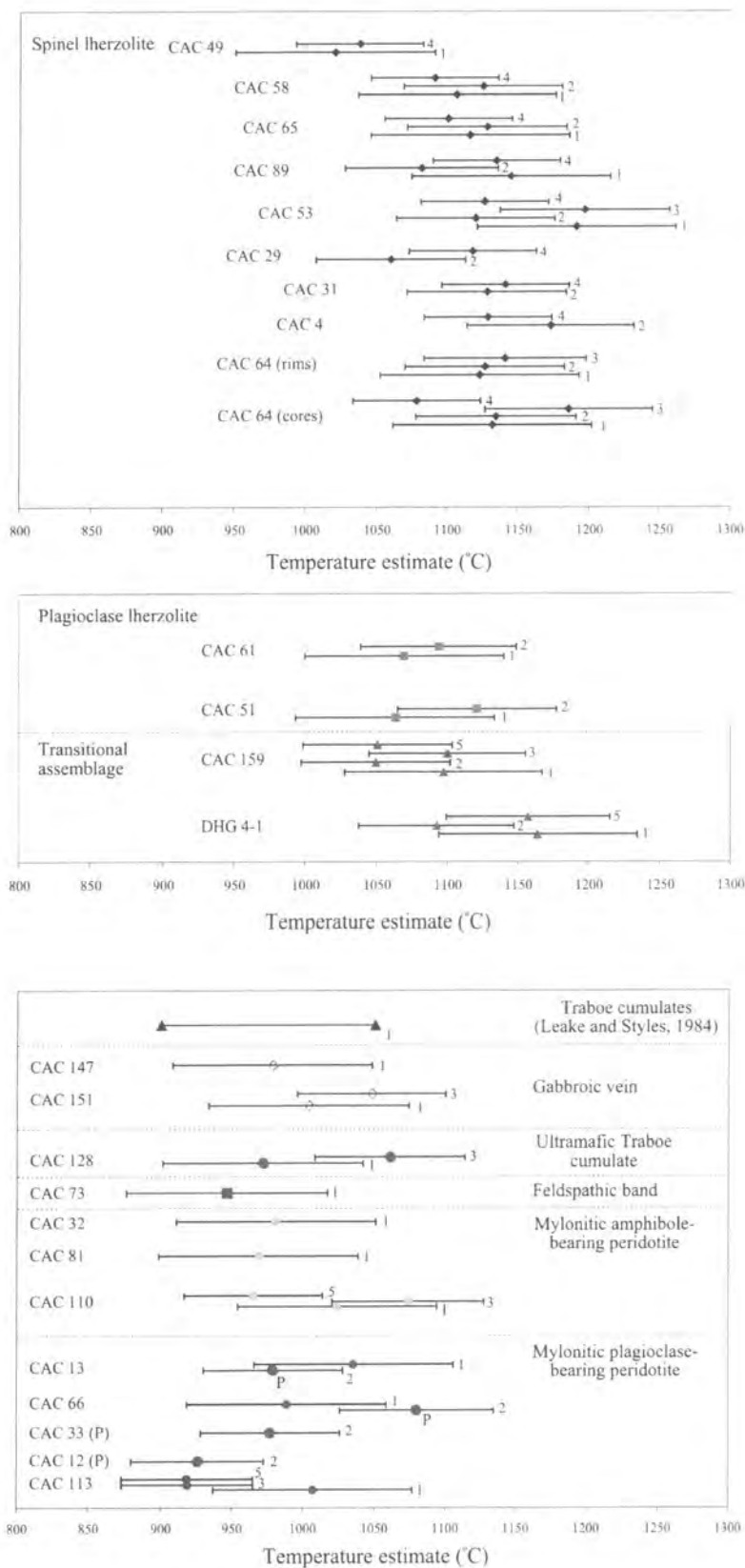


**Figure 5.41.** Diagram showing the temperature estimates based on pyroxene thermometry for the Lizard peridotites and associated rocks. Sample numbers are displayed and the thermometers applied include: (1) Wells (1977), (2) Witt-Eickschen and Seck (1991), (3) Brey and Kohler (1990), (4) Mercier (1980), (5) Brey *et al.*, (1990). Error bars are based on errors recommended by the authors.

are within error of the temperature range of 900-1050°C obtained by thermometry for layered ultramafic and mafic Traboe cumulates from the Traboe cumulate complex (Floyd *et al.*, 1993). Gabbroic veins yield a temperature range between 979 and 1048°C, which falls within the range given for the mylonitic peridotites and cumulate rocks.

Pressure estimates based on the Mercier (1980) thermobarometer are only applicable to the spinel facies peridotites, and the pressure values obtained for the spinel lherzolites range between 13.6 and 19.3 Kb (Figure 5.42). Pressure estimates for the mylonitic plagioclase-bearing peridotites and mylonitic amphibole-bearing

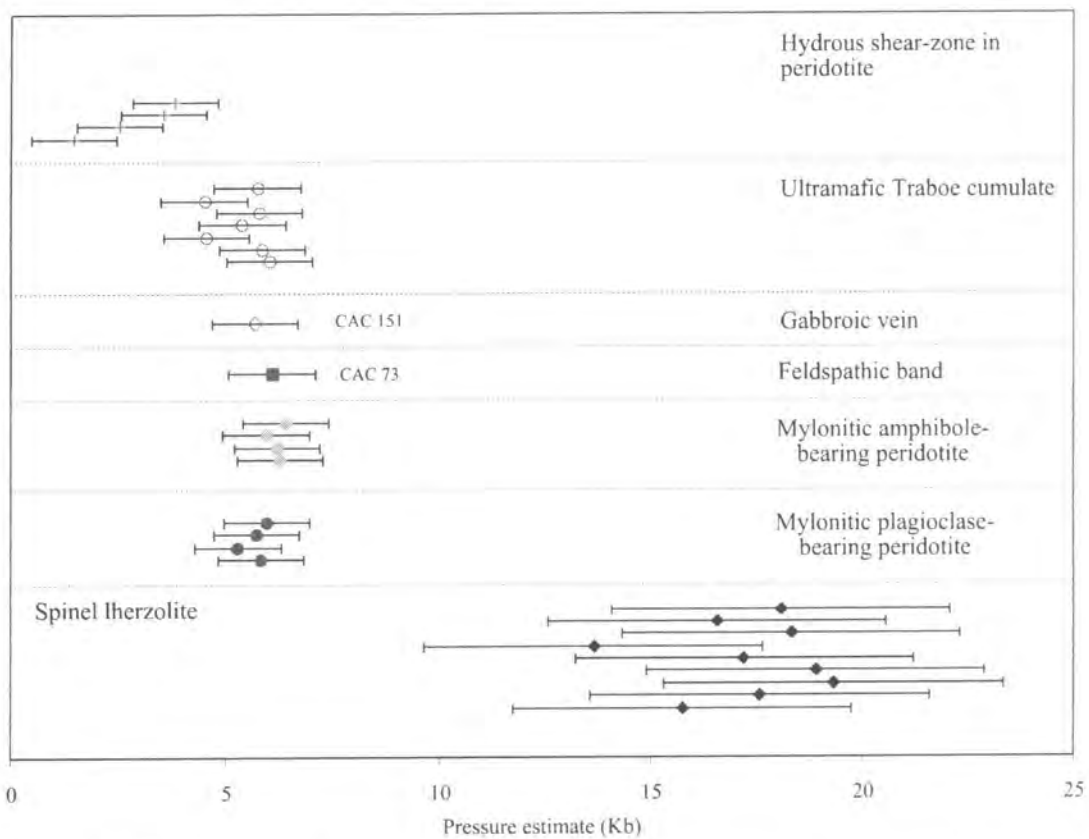


**Figure 5.42.** Diagram showing the pressure estimates based on a pyroxene barometer (Mercier, 1984) and an average value based on amphibole barometers (Johnson and Rutherford, 1989; Schmidt, 1992) for the Lizard peridotites and associated rocks. Error bars are based on errors recommended by the authors.

peridotites are provided by the amphibole barometers of Johnson & Rutherford (1989) and Schmidt (1992). The application of these barometers yields a pressure estimate of 5.3 Kb for the mylonitic plagioclase-bearing peridotite and between 6.2 and 6.4 Kb for the mylonitic amphibole-bearing peridotite. A feldspathic band (CAC 73) provides a

pressure estimate of 6 Kb. The ultramafic Traboe cumulates yield pressure estimates between 4.5 and 6 Kb and a gabbroic vein (CAC 151) gives a value of 5.7 Kb. These results are within error of the pressure estimates provided by the mylonitic peridotites, and the values are compatible with the presence of plagioclase in equilibrium with the other constituent mineral phases which suggests pressures <7.5 Kb. Amphiboles within hydrous shear-zones in the Lizard peridotites yield pressure estimates that are notably lower than the mylonitic peridotites, with values ranging between 1.5 and 3.9 Kb.

### 5.8.1.b. Interpretation and discussion

The results demonstrate a decrease in equilibration temperature from spinel lherzolite ( $1109^{\circ}\text{C} \pm 88$ ) to mylonitic plagioclase-bearing peridotite ( $977^{\circ}\text{C} \pm 58$ ) and mylonitic

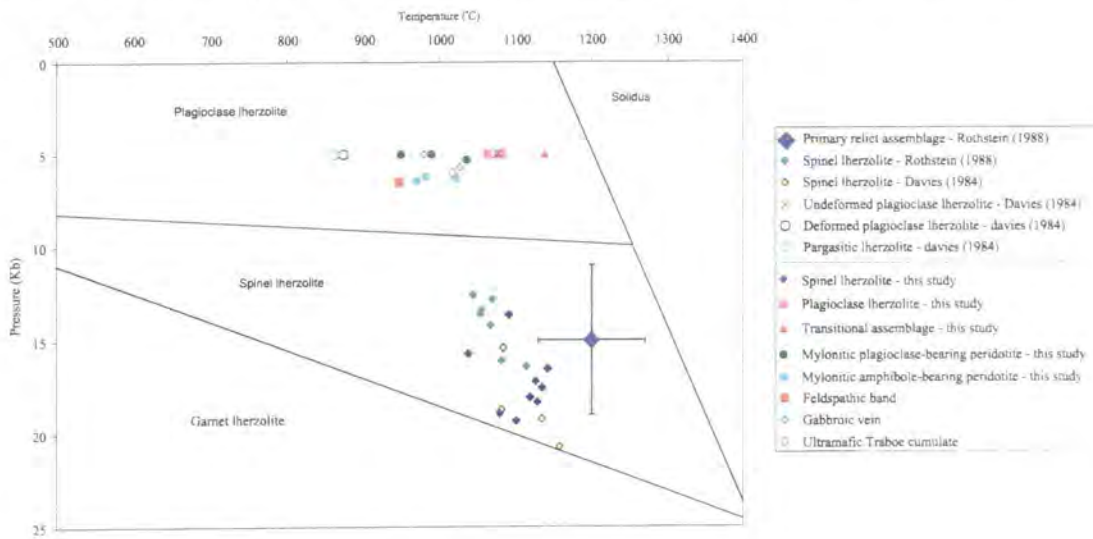


**Figure 5.43.** Diagram showing P-T trajectory of the Lizard peridotites and associated rocks (arrow). The diagram includes P-T estimates for the Lizard peridotites taken from Davies (1984) and Rothstein (1988). The P-T fields of the garnet, spinel and plagioclase lherzolite and the lherzolite solidus are after Davies (1984) and references therein.

amphibole-bearing peridotite ( $1020^{\circ}\text{C} \pm 54$ ), via plagioclase lherzolite ( $1092^{\circ}\text{C} \pm 29$ ) and transitional assemblage peridotite ( $1106^{\circ}\text{C} \pm 58$ ). These results support the discussion earlier in this chapter concerning pyroxene and spinel compositions. It was suggested that decreasing  $\text{Al}_2\text{O}_3$  and CaO of orthopyroxene, decreasing  $\text{Al}_2\text{O}_3$  and increasing CaO of clinopyroxene, increasing Cr# and decreasing Mg# of spinel may be related to decreasing P and T during deformation and metamorphism. The results also

broadly support deformation temperatures proposed on the basis of activated slip systems in olivine (Section 4.3.7.b).

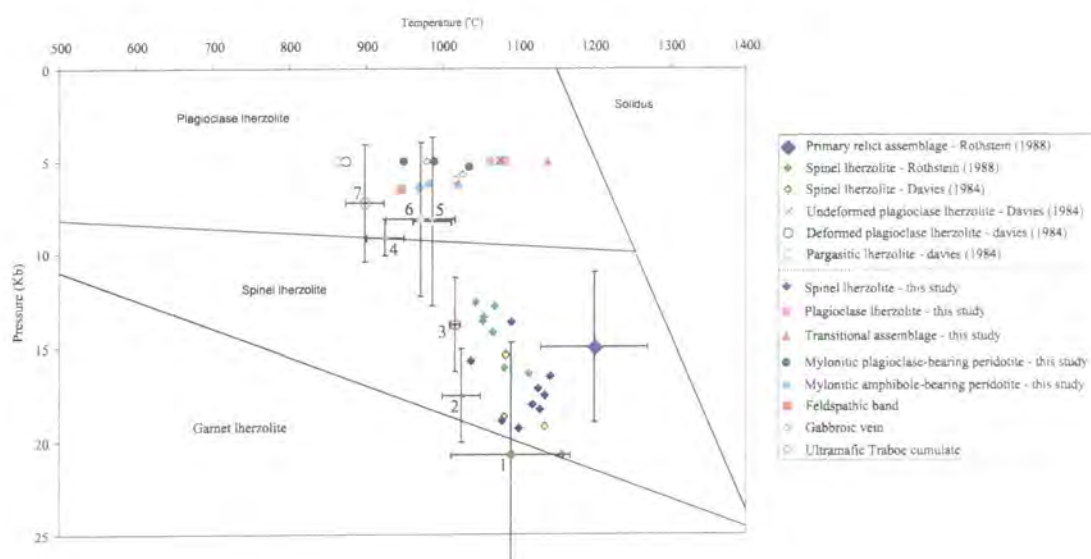
The results from this study, and previous studies on the Lizard peridotites by Davies (1983) and Rothstein (1988), are presented schematically on Figure 5.43. This diagram depicts the P-T trajectory of the Lizard peridotites during a history from initial upper mantle equilibration through re-equilibration at declining conditions of P and T in association with deformation. Estimates of pressure applied to the mylonitic peridotites are based on amphibole barometers. However, amphibole is not always present in these mylonitic peridotites and in particular in the plagioclase lherzolite and transitional peridotite, therefore a pressure value of 5 Kb is estimated for these rocks by comparison with values obtained by Davies (1983) for similar rocks from the Lizard. Temperature values for the Lizard peridotites are based on the average value of the different thermometers.

Figure 5.43 demonstrates that the results of this study are within the range of values presented by Davies (1983) and Rothstein (1988). Rothstein (1988) proposed that, at  $1200^{\circ} \pm 70^{\circ}\text{C}$  and  $15 \pm 4$  Kb, a large part of the Lizard peridotite contained extensive primary textural elements in an undeformed state. These primary textures are believed to have developed from an original equilibration within the upper mantle (Rothstein, 1988). Pyroxene in deformed spinel lherzolites yielded a mean temperature of  $1085^{\circ} \pm 70^{\circ}\text{C}$  and  $14.5 \pm 4$  Kb (Rothstein, 1988), which the author proposed to reflect sub-solidus re-equilibration of the pyroxenes with declining temperatures in association with the development of deformation fabrics. The P-T conditions demonstrate that these deformation processes were initiated in the spinel-facies of the upper mantle (Rothstein, 1988).

The temperature and pressure values yielded by spinel lherzolites in the course of this study are therefore compatible with this spinel-facies sub-solidus re-equilibration of the Lizard peridotite, although some values (Figure 5.43) approach the primary equilibration temperatures proposed by Rothstein (1988). However, the results from this study reveal that the process of sub-solidus re-equilibration, in association with the development of mylonitic fabrics, continued to lower temperature ( $<1074^{\circ}\text{C}$ ), and pressure ( $<7.5$  Kb) conditions than those discussed by Rothstein (1988). The results presented by Davies (1983) are also consistent with this observation. Davies (1983) demonstrated that pyroxenes in the spinel lherzolite equilibrated at conditions in

the region of 1100°C and 19 Kb, in the plagioclase lherzolite at 1076°C and 5 Kb, the mylonitic plagioclase-bearing peridotite at 874 °C and 5 Kb and in mylonitic amphibole-bearing peridotite the lowest P-T values are observed, 862°C and 5 Kb. It is therefore apparent that the re-equilibration of the Lizard peridotites spans a wide range of temperatures and pressures, which correspond to the spinel and plagioclase lherzolite facies.

The lowest P and T values are obtained in the mylonitic plagioclase-bearing peridotite and mylonitic amphibole-bearing peridotite, which are the most recrystallised and deformed of the Lizard peridotites. A similar P-T trajectory (Figure 5.44) has been obtained for the Voltri Massif peridotites (Hoogerduijn Strating *et al.*, 1993) and



**Figure 5.44.** Diagram showing P-T trajectory of the Lizard peridotites and associated rocks (arrow). The diagram includes P-T estimates for the Lizard peridotites taken from Davies (1984) and Rothstein (1988). The P-T fields of the garnet, spinel and plagioclase lherzolite and the lherzolite solidus are after Davies (1984) and references therein. Also included are P-T estimates for peridotites from various ophiolites, including: (1) granular spinel lherzolite, Voltri Massif (Hoogerduijn Strating *et al.*, 1993), (2) spinel lherzolite, External Ligurides (Rampone *et al.*, 1995), (3) spinel-bearing tectonites, Voltri Massif (Hoogerduijn Strating *et al.*, 1993), (4) plagioclase lherzolite, External Ligurides (Rampone *et al.*, 1995), (5) plagioclase-bearing peridotite mylonites, Voltri Massif (Hoogerduijn Strating *et al.*, 1993), (6) plagioclase-bearing tectonites, Voltri Massif (Hoogerduijn Strating *et al.*, 1993), (7) hornblende-bearing peridotite mylonites, Voltri Massif (Hoogerduijn Strating *et al.*, 1993).

External Liguride peridotites (Rampone *et al.*, 1995). However, spinel facies equilibration of the External Liguride peridotites occurred at lower temperatures (<1100°C) than the Lizard peridotites and Voltri Massif peridotites (Hoogerduijn

Strating *et al.*, 1993; Rampone *et al.*, 1995). These two examples from the literature are interpreted by the authors to represent fragments of subcontinental mantle emplaced at shallow levels by tectonic denudation mechanisms, during the early stages of rifting of the Jurassic Ligurian Piemontese basin (Rampone *et al.*, 1995). The P-T estimates yielded by the spinel lherzolites from the Lizard are also within error of estimates from peridotites that preserve fabrics developed during an asthenospheric uprise at mid-ocean spreading centres (Nicolas, 1986).

It is interesting to note that the temperatures and pressures of pyroxene re-equilibration in the feldspathic band (947°C and 6.5 Kb), ultramafic Traboe cumulates (1016°C and 6 Kb), Traboe cumulates (900-1050°C)(Floyd *et al.*, 1993) and gabbroic veins (979-1016°C and 5-6 Kb) are within error of the range defined by the mylonitic peridotites (919-1074°C and 5.3-6.4 Kb) from the Lizard. These results, in addition to the fact that these rocks are often interbanded/layered with the mylonitic peridotites and have identical fabric orientations (Chapter 3), suggest that the processes of deformation and re-equilibration of these rocks and the mylonitic peridotites were contemporaneous. The temperatures of re-equilibration yielded by the ultramafic Traboe cumulates (including Traboe cumulate complex, Floyd *et al.*, 1993) from the Lizard are similar to ultramafic rocks and cumulates from the Hess Deep, which re-equilibrated at temperatures within the range of 980-1100°C during re-crystallisation and associated melt-impregnation (Hekinian *et al.*, 1993). This re-equilibration occurred in response to tectonic processes associated with the emplacement of mantle in an intra-rift ridge environment (Hekinian *et al.*, 1993).

P-T conditions of 7-11 Kb, 750-850°C have been calculated for ultramafic and metabasic rocks immediately above and below the dynamothermal aureole contact of the Bay of Islands ophiolite complex (McCaig, 1983). Ultramafic rocks, which are found as basal mylonites of the White Hills peridotite (St. Anthony complex, Newfoundland), yield two-pyroxene temperatures of 900 to 950°C, and temperatures of 860°C have been calculated for 2-pyroxene amphibolites below the peridotites (Jamieson, 1980). Basal, mylonitic peridotites from the Oman ophiolite have pyroxene re-equilibration temperatures which are slightly higher, in the region of 1000°C (Boudier *et al.*, 1988). The temperatures yielded by ultramafic and metabasic rocks from examples of dynamothermal aureoles and basal peridotite mylonites from various ophiolite complexes (see above) are generally lower than those observed in mylonitic



peridotites and cumulates (900-1074°C) from the Lizard, and distinctly lower than in the coarse grained lherzolites (1063-1197°C). This suggests that the deformation associated with the Lizard peridotites, Traboe cumulates and gabbroic veins was not related to the development of a dynamothermal aureole. Alternatively, the deformation of the Lizard peridotites and associated rocks may be related to exhumation of mantle to shallow levels by tectonic denudation processes, similar to the mechanisms proposed for the Voltri Massif (Hoogerduijn Strating *et al.*, 1993) and External Ligurides peridotites (Rampone *et al.*, 1995). However, the association of deformed mantle peridotites, containing relict textures developed within the spinel lherzolite facies with lower crustal cumulate rocks of oceanic character, suggests a more complex tectonothermal evolution for the Lizard Ophiolite Complex. The presence of ultramafic and mafic Traboe cumulates in contact with the mantle peridotites, which possess similar mylonitic fabric orientations to the peridotites, suggests that deformation took place in an oceanic environment, or at least in a pre-oceanic rift environment. Furthermore, the relatively high temperatures in the ultramafic and mafic cumulates are inconsistent with prograde metamorphism of colder rocks in a dynamothermal aureole. However, they are compatible with the mylonitisation and break-up of hot, relatively young, lower oceanic crust (Floyd *et al.*, 1993; Hekinian *et al.*, 1993). It is therefore proposed on the basis of this and evidence discussed elsewhere (Chapters 3, 4 and 6) that a shear-zone contact located at or near to the Moho may be responsible for the exhumation of the Lizard peridotites from the spinel lherzolite to plagioclase lherzolite facies, and that the cumulates could represent the hanging-wall of this detachment. Further, more detailed, discussions of tectonic models to account for the ca.30 km exhumation of the Lizard peridotite are presented in Chapter 7.

The lowest pressure estimates, between 1.5 and 3.9 Kb, are calculated for hydrous shear-zones which cross-cut the fabric in the Lizard peridotites and associated rocks. This supports the field (Chapter 3) and microstructural (Chapter 4) evidence, that these structures are developed late in the evolution of the Lizard, during the thrusting of mantle over the Landewednack amphibolites. In the following section, estimates of pressure and temperature conditions during the metamorphism of these Landewednack amphibolites are presented.

### 5.8.2. Amphibole-plagioclase thermobarometry - Amphibolites

Estimates of conditions P and T of metamorphism in the amphibolitised mafic Traboe cumulates and Landewednack amphibolites are provided by amphibole barometers, and thermometers and thermobarometers applied to amphibole-plagioclase pairs (Table 5.1). The amphibole barometers of Johnson & Rutherford (1989) and Schmidt (1992) are based on the fact that the  $Al^{total}$  content of amphibole is strongly dependent on pressure. Blundy and Holland (1990) propose a amphibole barometer which is based on the  $Al^{iv}$  content of amphibole, stating that the barometer of Johnson & Rutherford (1989), which is based on the  $Al^{total}$  content of amphibole, does not yield temperature-dependent pressures. The thermometer of Blundy and Holland (1990) is based on the  $Al^{total}$  content of amphibole coexisting with plagioclase. The thermometer developed by Spear (1980) is based on the temperature dependent partitioning of Na and Ca between amphibole and plagioclase. Plyusina (1982) developed an empirical graphical thermobarometer, which utilises the anorthite content of plagioclase and the total alumina content of co-existing amphibole.

#### 5.8.2.a. Results

Temperature estimates of metamorphism of the amphibolitised mafic Traboe cumulates and Landewednack amphibolites based on three different methods (Spear, 1980; Plyusina, 1982; Blundy and Holland, 1990) are presented in Figure 5.45. The temperature estimates shown in Figure 5.45 represent the average values for numerous amphibole-plagioclase pairs, and errors are based on errors in the calculations as suggested by the respective authors. The thermometers of Spear (1980) and Plyusina (1982) yield temperatures, which are consistently within a range of 50°C. The Blundy and Holland (1990) thermometer consistently yields higher temperatures (ca. 160°C) than the Spear (1980) and Plyusina (1982) calibrations, so these results will be excluded from the following discussion. Landewednack amphibolites with a green amphibole-bearing assemblage yield temperatures that range between 525 and 638°C, and those with a brown amphibole-bearing assemblage yield a slightly higher temperature range, between 550 and 698°C. Amphibolitised mafic Traboe cumulates,

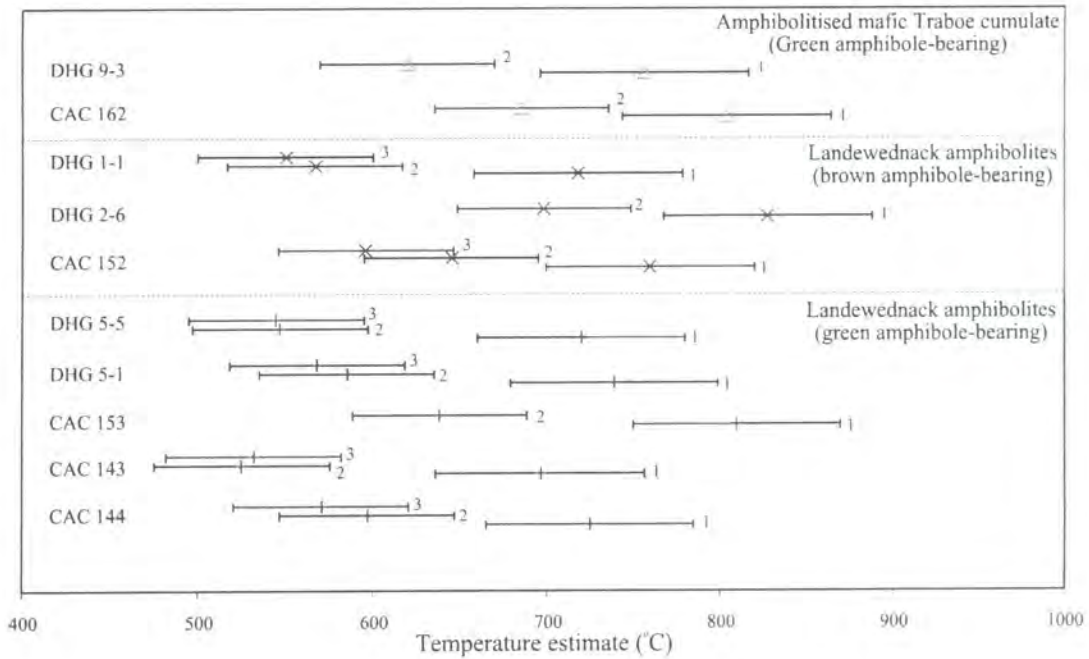


**Figure 5.45.** Diagram showing the temperature estimates based on plagioclase-amphibole thermometers for the amphibolitised mafic Traboe cumulate and Landwednack amphibolites. Sample numbers are displayed and the thermometers applied include: (1) Blundy and Holland (1990), (2) Spear (1980), (3) Plyusina (1982). Error bars are based on errors recommended by the authors.

with a green amphibole-bearing assemblage yield metamorphic temperatures between 618 and 683°C, which are slightly higher than those obtained in the Landwednack amphibolites.

Pressure estimates provided by the barometers of Plyusina (1982), Johnson & Rutherford (1989), Blundy and Holland (1990) and Schmidt (1992) generally produce a similar range of results (Figure 5.46). Landwednack amphibolites with a green amphibole-bearing assemblage produce pressure estimates that range between 2.6 and 6.4 Kb. Estimates of pressure yielded by Landwednack amphibolites with a brown amphibole-bearing assemblage fall within this range, with values between 2.2 and 5.9 Kb. Amphibolitised mafic Traboe cumulates with a green amphibole-bearing assemblage yield similar results, with pressure estimates between 3 and 5.6 Kb. It is interesting to note that the pressure estimates obtained for the hydrous shear-zones in the peridotites (1.5-3.9 Kb) (Figure 5.42) overlap the range defined by the green-amphibole-bearing Landwednack amphibolites (2.6-6.4 Kb). The amphibolites show distinctly lower pressure values than the mylonitic peridotites, and ultramafic Traboe

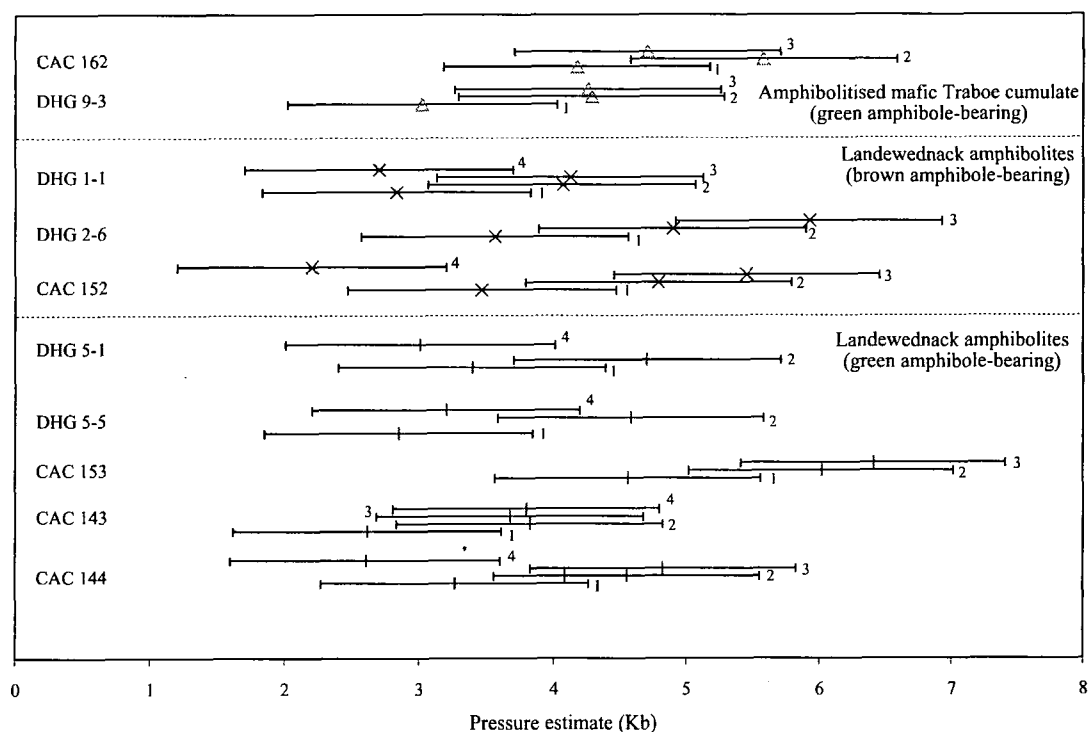


**Figure 5.46.** Diagram showing the pressure estimates based on plagioclase-amphibole barometers for the amphibolitized mafic Traboe cumulate and Landwednack amphibolites. Sample numbers are displayed and the thermometers applied include: (1) Johnson and Rutherford (1989), (2) Spear (1980), (3) Blundy and Holland (1990), (4) Plyusina (1982). Error bars are based on errors recommended by the authors.

cumulates with a brown-amphibole bearing metamorphic mineral assemblage.

### 5.8.2.b. Interpretation and discussion

Average P and T values of the amphibolites are plotted with the P and T estimates for the peridotites and associated rocks on Figure 5.47. This diagram illustrates that the maximum temperature and pressure conditions metamorphism are markedly lower than the conditions for the mylonitic peridotites, feldspathic band, ultramafic Traboe cumulates and gabbroic veins. This diagram also demonstrates that the Landwednack amphibolites with the green amphibole-bearing assemblage show the lowest P and T values. These results are within error of values presented by Sandeman *et al.*, (1995), which yield maximum temperatures of ca. 600°C and pressures of 3-4 Kb for the green amphibole-bearing assemblage of the Landwednack amphibolites. In Chapter 4, it was proposed on the basis of microstructural evidence, that the brown amphibole-bearing

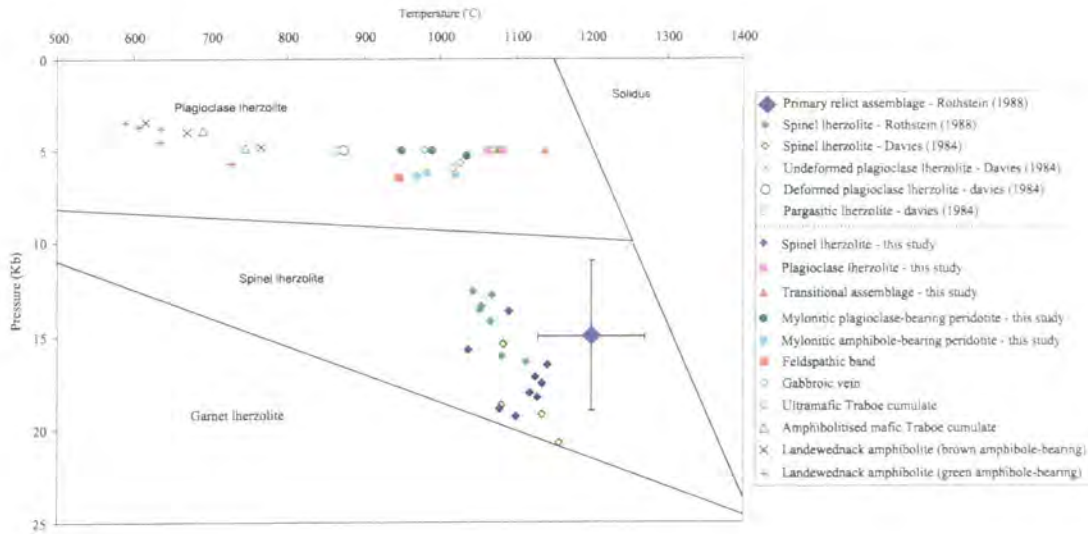


**Figure 5.47.** Diagram showing P-T estimates of the amphibolitized mafic Traboe cumulate and Landwednack amphibolites compared with the Lizard peridotites and associated rocks (arrow shows trajectory). The diagram includes P-T estimates for the Lizard peridotites taken from Davies (1984) and Rothstein (1988). The P-T fields of garnet, spinel and plagioclase Iherzolite and the Iherzolite solidus are after Davies (1984) and references therein.

assemblage in the Landwednack amphibolites represents the product of early high-temperature metamorphism of basaltic and gabbroic rocks. The temperatures yielded by the brown amphibole-bearing assemblage (611–762°C) are slightly higher than those of the green amphibole-bearing assemblage. However, these temperatures are too low to be consistent with high temperature metamorphism, in contrast to the high metamorphic temperatures (978–1026°C) yielded by pyroxene compositions in the ultramafic Traboe cumulates and gabbroic veins with the brown amphibole-bearing assemblage. These results suggest that the brown amphibole-bearing assemblage of the Landwednack amphibolites was indeed developed during a different metamorphic event, at lower temperature, than that recorded by the Traboe cumulates and gabbroic veins. Alternatively, there has been re-equilibration of the brown amphibole to lower temperature compositions during the later retrograde metamorphism, responsible for the development of a green amphibole-bearing assemblage. This second hypothesis is supported by the extensive development of green amphibole rims around the relict brown amphiboles in the Landwednack amphibolites.

Field and microstructural evidence suggest that the metamorphism of the Landwednack amphibolites took place during Top-to-the-NW thrusting, and emplacement of an overriding mantle unit (Chapter 3). Temperatures in the region of



700-860°C and pressures of 2-5 Kb have been calculated for amphibolites within metamorphic aureole immediately below peridotites from the St. Anthony complex, Newfoundland (Jamieson, 1979). Amphibolites beneath the Semail ophiolite in Oman yielded a temperature range of 670-750°C (Searle and Malpas, 1980). Malpas (1979) calculated temperatures of 720-850°C for amphibolites from the dynamothermal aureole of the Bay of Islands ophiolite complex, Newfoundland. McCaig (1983) calculated P-T conditions of 7-11 Kb, 750-850°C for rocks on both sides of the thrust plane of the same ophiolite.

The metamorphic conditions calculated for dynamothermal aureoles associated with other examples of ophiolites (see above) are therefore slightly different to the conditions in the Landwednack amphibolites (green amphibole-bearing assemblage) of the Lizard ophiolite complex. Although the pressure estimates (3-5.6 Kb) are comparable with these examples, the temperatures (525-638°C) are lower than the range observed in dynamothermal aureoles from other ophiolites complexes. This difference in metamorphic conditions in the dynamothermal aureole of the Lizard Ophiolite Complex can be explained by the nature of the thrust contact itself (Chapter 3).

In the examples of other ophiolite complexes, the thrust contact between the overriding mantle sheet and underlying dynamothermal aureole is characterised by the presence of peridotite mylonites in the mantle unit, which form an integral part of the aureole assemblage (Malpas, 1979). The peridotite mylonites and associated fabrics are developed within a zone, which may be up to 500 metres in thickness (Suhr and Cawood, 1993), above the thrust contact. In the examples of ophiolites with a dynamothermal aureole, there is a gradual transition downwards from coarser-grained peridotites, with moderately developed fabrics, to mylonitic peridotites with strongly developed fabrics that parallel those developed in the rocks in the dynamothermal aureole. Amphibole-bearing peridotite mylonites have been described in the lowermost (<20m) regions of these zones above the dynamothermal aureole (Jamieson, 1979; McCaig, 1980; Suhr and Cawood, 1993). Metamorphic temperatures in the range 750-1000°C have been calculated for these peridotite mylonites (see Section 5.8.1.b).

The thrust contact between peridotites and amphibolites of the dynamothermal aureole of the Lizard Ophiolite Complex shows several differences with other ophiolites. Field evidence (Chapter 3) has demonstrated that, although mylonites are



found within the peridotite immediately above the thrust contact with the Landewednack amphibolites, they are of limited extent and certainly not 500 metres in thickness. The basal mylonites in peridotites (hydrous shear-zones) from the Lizard are characterised by a mineral assemblage composed of colourless hornblende and chlorite, in contrast to the assemblage composed of recrystallised orthopyroxene, clinopyroxene and olivine +/- Ti-pargasite observed in other ophiolites (Malpas, 1979; Girardeau, 1982; Suhr and Cawood, 1993). This evidence demonstrates that the mylonite zones within the peridotites above the amphibolites in the Lizard Ophiolite Complex developed at lower metamorphic temperatures than peridotite mylonites from other ophiolites. This evidence is therefore in accord with the fact that the Landewednack amphibolites yield metamorphic temperatures lower than those of amphibolites of dynamothermal aureoles from other ophiolites (see above). Further discussion with additional constraints, regarding the tectonothermal evolution of these aureole rocks and the peridotite mylonites, including the tectonic models, is presented in Chapter 7.

### 5.8.3. Thermobarometry - summary

- The P-T estimates presented in the preceding section support the evidence for metamorphic re-equilibration at conditions of lower P and T as suggested by compositional trends of minerals in the peridotites, the associated ultramafic and mafic rocks and the Landewednack amphibolites.
- The early equilibration of the spinel lherzolite took place in the region of  $1200^{\circ}\text{C} \pm 70$  and  $15 \pm 4$  Kb. Later deformation and re-equilibration of the peridotites was initiated in the spinel facies stability field in the region of  $1000\text{--}1200^{\circ}\text{C}$  and 13.6–19.3Kb. Continued deformation and re-equilibration resulted in the development of mylonitic peridotites, which re-equilibrated at conditions of lower T ( $919\text{--}1074^{\circ}\text{C}$ ) and P (5–6Kb).
- The ultramafic Traboe cumulate were deformed and metamorphosed at conditions of high T ( $900\text{--}1050^{\circ}\text{C}$ ) and P (4.5–6Kb). It is suggested that this may have happened during the deformation and high-temperature metamorphism accompanying the break-up of hot lower oceanic crust.
- The metamorphic evolution of the Landewednack amphibolites took place at conditions of lower T ( $525\text{--}639^{\circ}\text{C}$ ) and P (2.6–6.4Kb). Hydrous shear-zones in the

amphibolites and peridotites developed at similar pressures (1.5-3.9Kb). It is proposed that the metamorphic evolution of the Landwednack amphibolites is related to the obduction of the Lizard Ophiolite Complex.

---

## 5.9. Mineral chemistry and thermobarometry: summary and discussion

---

Throughout this chapter the compositional trends observed in the different mineral phases, from the various rocks of the Lizard, have been interpreted as being the product of several geological processes. These processes include:

- Metamorphic re-equilibration
- Melt-rock interaction
- Igneous fractionation trends

In this final discussion, the evidence presented in the previous sections of this chapter is evaluated and summarised. The aim of this is to integrate and clarify the discussions that have been presented in order to explain the compositional variations of the different mineral phases. In addition, the P-T constraints provided by mineral thermometers and barometers are summarised and integrated with the processes listed above. In Chapter 7, tectonic and magmatic models are evaluated in order to account for the evidence presented and processes proposed in this Chapter.

### 5.9.1. Metamorphic re-equilibration

The Lizard peridotites have shown clear variations in the compositions of orthopyroxene, clinopyroxene and spinel, which are associated with a decrease in the overall grain-size from spinel lherzolite to mylonitic peridotites. These compositional changes include a decrease in the  $\text{Al}_2\text{O}_3$  content of orthopyroxene and clinopyroxene, a decrease of CaO in orthopyroxene and an increase of CaO in clinopyroxene. Spinel show an increase in Cr# and a decrease in Mg#, from spinel lherzolites to mylonitic peridotites. Similar compositional variations in orthopyroxene, clinopyroxene, and spinel are observed in peridotites from Zabargad Island (Bonatti *et al.*, 1986), the Voltri Massif (Hoogerduijn Strating *et al.*, 1993) and External Ligurides peridotites (Rampone *et al.*, 1993). Grain-size reduction of the host peridotite and the appearance of plagioclase also accompany the compositional variations of minerals in these

peridotites. These correlations are also found in the Lizard peridotites. The compositional changes in orthopyroxene, clinopyroxene, and spinel in the Lizard peridotites and the published examples, are related to changing conditions of T (and P) during syn-tectonic recrystallisation. To be more precise, these compositional changes are a consequence of subsolidus reactions that accompany the spinel- to plagioclase-facies transition in these mantle peridotites (Piccardo *et al.*, 1990; Hoogerduijn Strating *et al.*, 1993; Rampone *et al.*, 1993, 1995). The composition variations in the minerals in the Lizard peridotites are therefore the outcome of the tectonothermal evolution of the mantle, which involved significant exhumation, from the spinel-facies to the plagioclase-facies stability field. Microstructural evidence (Chapter 4) demonstrates that deformation, grain-size reduction and recrystallisation, leading to the development of mylonitic peridotites accompanied this evolution. However, it should be noted that processes other than metamorphic re-equilibration have modified the composition of the mineral phases in the Lizard peridotites, and these processes are discussed in the following sections. Compositional changes in the Traboe cumulate rocks, mafic rocks and feldspathic bands may also be a consequence of re-equilibration. In particular, changes in the anorthite content of plagioclase and the composition of amphibole in the Landwednack amphibolites are related to metamorphic re-equilibration.

### 5.9.2. Melt-rock interaction

The transition from spinel lherzolite to mylonitic peridotite is accompanied by a decrease in the forsterite content of olivine. This compositional change is inconsistent with partial melting trends involving higher degrees of melting, which would result in an increase in the forsterite content of olivine and it is also inconsistent with metamorphic re-equilibration, which would have no effect on the forsterite content. Alternatively this compositional trend may be a consequence of melt-rock interaction. This hypothesis is supported by similar compositional changes reported in the literature, for peridotites from ophiolitic and oceanic environments. Further evidence for melt-rock interaction in the Lizard peridotites is provided by increases in the Ti content of orthopyroxene, clinopyroxene and spinel. Although a Cr# value increase and a Mg# value decrease in spinel has been associated with metamorphic re-equilibration (see above), this compositional change is also consistent with melt-rock interaction. The presence of minor (<5%) Ti-pargasite and kaersutite amphibole in the mylonitic

plagioclase-bearing peridotite is also consistent with melt-rock interaction, as amphiboles of identical composition are documented in peridotites from ophiolitic environments which have been impregnated by melt. Finally, the most conclusive evidence for melt-rock interaction in the Lizard peridotites is changes in the whole rock composition. These whole rock compositional changes are discussed in detail in Chapter 6.

### **5.9.3. Igneous fractionation trends**

Both the ultramafic Traboe cumulates and the mafic Traboe cumulates display variations in the composition of the constituent mineral phases which are consistent with igneous fractionation. Olivines in the layered cumulates show a range of forsterite contents, which extends well beyond the range defined by the Lizard peridotites. In both orthopyroxenes and clinopyroxenes from the ultramafic Traboe cumulates and the mafic Traboe cumulates, a large range of Mg# is observed, which is consistent with igneous fractionation. Spinel grains in the ultramafic Traboe cumulates show a range of Mg#, which are associated with low Cr#. The spinels in these cumulates also show an increase in  $\text{Fe}^{3+}$ , which is correlated with decreasing Cr#. These variations are very different from the compositional trends observed in the peridotites, which are interpreted to reflect metamorphic re-equilibration and melt-rock interactions. Instead, it is suggested that the variations in mineral composition observed in these cumulates reflects igneous fractionation processes.

### **5.9.4. P-T evolution**

P-T constraints provided by mineral thermometers and barometers support the evidence of metamorphic re-equilibration suggested by compositional trends of minerals in the peridotites. The results demonstrate that a complex tectonothermal evolution is recorded by the composition of minerals in the peridotites, and these results support the conclusions founded on the basis of field (Chapter 3) and microstructural evidence (Chapter 4). These P-T constraints support the findings of Rothstein (1988), which revealed that the Lizard peridotites preserve evidence for textures that were developed in spinel lherzolites during an early equilibration of the mantle in an undeformed state in the region of  $1200^{\circ}\text{C} \pm 70$  and  $15\text{Kb} \pm 4$ . However, the majority of the peridotites

are extensively deformed, and P-T estimates show that this relates to subsequent deformation which was initiated in the spinel facies stability field in the region of 1000-1200°C and 13.6-19.3Kb. This deformation resulted in the development of mylonitic peridotites, which re-equilibrated at conditions of lower T and P, with P-T estimates suggesting temperature conditions between 919-1074°C and pressures between 5-6Kb. The results demonstrate that the cumulates also equilibrated under similar conditions, between 900-1050°C and 4.5-6Kb in the lower crust.

These P-T conditions are inconsistent with the P-T evolution observed in peridotites which are developed immediately above a dynamothermal aureole during emplacement of ophiolites. The results demonstrate that the Lizard peridotites have undergone tectonic exhumation of ca. 30km from the spinel to plagioclase facies. As an alternative to deformation associated with obduction and the development of a dynamothermal aureole, the deformation and P-T evolution of the Lizard peridotites may be related to exhumation of mantle to shallow levels by tectonic denudation processes, similar to the mechanisms proposed for the Voltri Massif (Hoogerduijn Strating *et al.*, 1993) and External Ligurides peridotites (Rampone *et al.*, 1995).

These processes would result in strain localisation within the mantle and the development of shear-zones characterised by the presence of peridotite mylonites. Furthermore, the equilibration conditions suggested by the Traboe cumulate rocks are consistent with high-temperature deformation and break-up of hot, lower oceanic crust, and not with prograde metamorphism of colder rocks (Floyd *et al.*, 1993). This suggests that the deformation of these cumulates, is associated with the evolution of the peridotites. However, these cumulates are not derived from the spinel facies stability field, and would not have undergone significant exhumation, therefore they may represent the hanging-wall of the proposed detachment zone, which was possibly developed close to the Moho.

In contrast to the peridotites and cumulates, the Landewednack amphibolites preserved evidence for a metamorphic evolution at lower grade. Maximum metamorphic temperatures of 525-638°C, and pressures of 2.6-6.4Kb have been calculated for the green amphibole-bearing assemblage, in amphibolites in the footwall of thrust contacts on the east coast of the Lizard (Chapter 3). The hanging-wall of these thrust contacts is composed of variably deformed peridotites, and includes the development of hydrous shear zones within the peridotites. These shear zones form the

actual contact between the amphibolite and peridotite, and are composed of colourless hornblende and chlorite. Barometric calculations suggest that these shear-zones were developed at pressures of 1.5-3.9Kb, similar to the estimates obtained for the Landewednack amphibolites. This thrust contact is interpreted to have developed during the obduction of the Lizard Ophiolite Complex, the mantle being decoupled from its substrate and emplaced over the amphibolites during top-to-the-NW thrusting (Jones, 1997). The deformation and metamorphism of the Landewednack amphibolites represents the development of a dynamothermal aureole that accompanied the emplacement of the mantle unit. Comparison of the field characteristics of this thrust contact and the P-T evolution of the Landewednack amphibolites, with examples of dynamothermal aureole of other ophiolites, reveals that there are significant differences. The metamorphic temperatures attained in the dynamothermal aureoles of other ophiolites are significantly higher than calculated for the Landewednack amphibolites. In addition, high-temperature (750-1000°C) peridotite mylonites which are characteristic of the overriding mantle sheet of other ophiolites, are not observed at the Lizard. This evidence suggests that the mantle of the overriding sheet of the Lizard was relatively cold during obduction, in comparison to the mantle of other ophiolites, and hence the metamorphic conditions in the dynamothermal aureole were correspondingly lower. Further discussion regarding the tectonothermal and magmatic history of the Lizard peridotites and Landewednack amphibolites with additional geochemical constraints are presented in Chapter 7.



**CHAPTER 6**  
**ISOTOPIC, MAJOR, TRACE AND RARE EARTH ELEMENT**  
**CHARACTERISATION OF THE ROCKS FROM THE LIZARD OPHIOLITE**  
**COMPLEX**

---

**6.1. Introduction**

---

It has already been established in the previous chapter (Chapter 5) that the Lizard peridotites display variations in mineral chemistry, which can be correlated with changes in microstructure from relatively, undeformed spinel and plagioclase lherzolites to mylonitic peridotites. These changes in mineral chemistry are associated with re-equilibration of the mineral assemblage to conditions of lower T and P, in addition to metasomatism in response to melt/fluid – rock interaction. Therefore analyses of major, trace and rare earth elements of the Lizard peridotites are presented in order to constrain the chemical evolution of the Lizard peridotites. In particular, evidence for metasomatism is investigated and the probable source of melt/fluid responsible is evaluated with reference to metasomatised peridotites from ophiolitic environments described in the literature. One of the overall aims of the investigation of the geochemical characteristics of the Lizard peridotites is to constrain the geodynamic environment in which the peridotites formed.

In this study, feldspathic bands, ultramafic and mafic Traboe cumulates, gabbroic veins, Landewednack amphibolites, Porthoustock amphibolites, mafic dykes from the Lizard Ophiolite Complex have been also been analysed. The analyses of these rocks include major and trace element analyses, rare earth element analyses as well as isotopic analyses. These analyses are used in an attempt to characterise the types of magma forming during the evolution of the Lizard Ophiolite Complex and to determine whether these are compatible with the oceanic environment proposed on the basis of geological observations of the previous chapters (Chapters 3, 4 & 5). The characterisation of geochemical properties of these rocks and the igneous processes responsible for any variations is made by comparison with similar rocks from oceanic and ophiolitic environments described in the literature.

Analyses of Ordovician basement rocks, including amphibolite layers within the Old Lizard Head Series (OLHS), deformed mafic sheets that cross-cut the OLHS and

the Lizard Head sill are also provided in order to characterise the magma types and provide geochemical constraints on the tectonic origin of the Ordovician basement unit (Chapter 3).

---

## **6.2. Major and trace elements**

---

Major and trace element analyses of selected samples were performed using the Philips PW 1500 spectrometer located in the Department of Geological Sciences at the University of Durham. Full details of sample selection, sample preparation, the analytical procedure, analytical errors and representative analyses are presented in Appendices A and D. All major element analyses are reported as anhydrous in wt% and trace elements are in ppm.

Analyses presented in this section include analyses of ultramafic and mafic rocks taken from the field outcrops, Traboe cumulate complex borehole cores and the Predannack borehole core (Institute of Geological Sciences borehole reports, 1978, 1979; Leake and Styles, 1984; M.T. Styles *pers comm*, 1997) and analyses provided D.H.Green (*pers comm.*, 1997). Additional analyses for the Lizard peridotites and Landewednack amphibolites are taken from Shepherd (1986).

### **6.2.1. Serpentinisation**

In order to successfully interpret the major and trace element compositions of the Lizard peridotites, it is important to establish whether or not serpentinisation modified the original compositions of these rocks. Several samples of serpentinised spinel lherzolite which show >90 % serpentinisation were analysed and are compared with the composition of the relatively fresh (<30 % serpentinisation) spinel and plagioclase lherzolites from the Lizard (Figure 6.1). Major elements are plotted against  $\text{TiO}_2$ , which is assumed to be immobile during serpentinisation. If the serpentinised samples fall on the same trend as the fresher lherzolites on a plot, it can be assumed that serpentinisation has not modified the abundance of that particular element. However, if the serpentinised samples deviate from the trend defined by the fresher lherzolites it can be assumed that this reflects addition or removal of the element being investigated as a consequence of serpentinisation. Figure 6.1 demonstrates that the serpentinised

herzolites are enriched in  $\text{Fe}_2\text{O}_3$ ,  $\text{Na}_2\text{O}$ ,  $\text{K}_2\text{O}$  and  $\text{SiO}_2$  and depleted in  $\text{CaO}$  and to some extent  $\text{MgO}$ , relative to the comparatively fresh spinel and plagioclase herzolite.  $\text{Al}_2\text{O}_3$  and  $\text{MnO}$  show little variation relative to the comparatively fresh herzolites. The decrease in  $\text{CaO}$  is thought to be related the breakdown of clinopyroxene during serpentinisation. The  $\text{CaO}$  increase in one of the samples is related to the presence of calcite veins.  $\text{Na}_2\text{O}$  and  $\text{K}_2\text{O}$  are well known mobile elements and it is suggested that

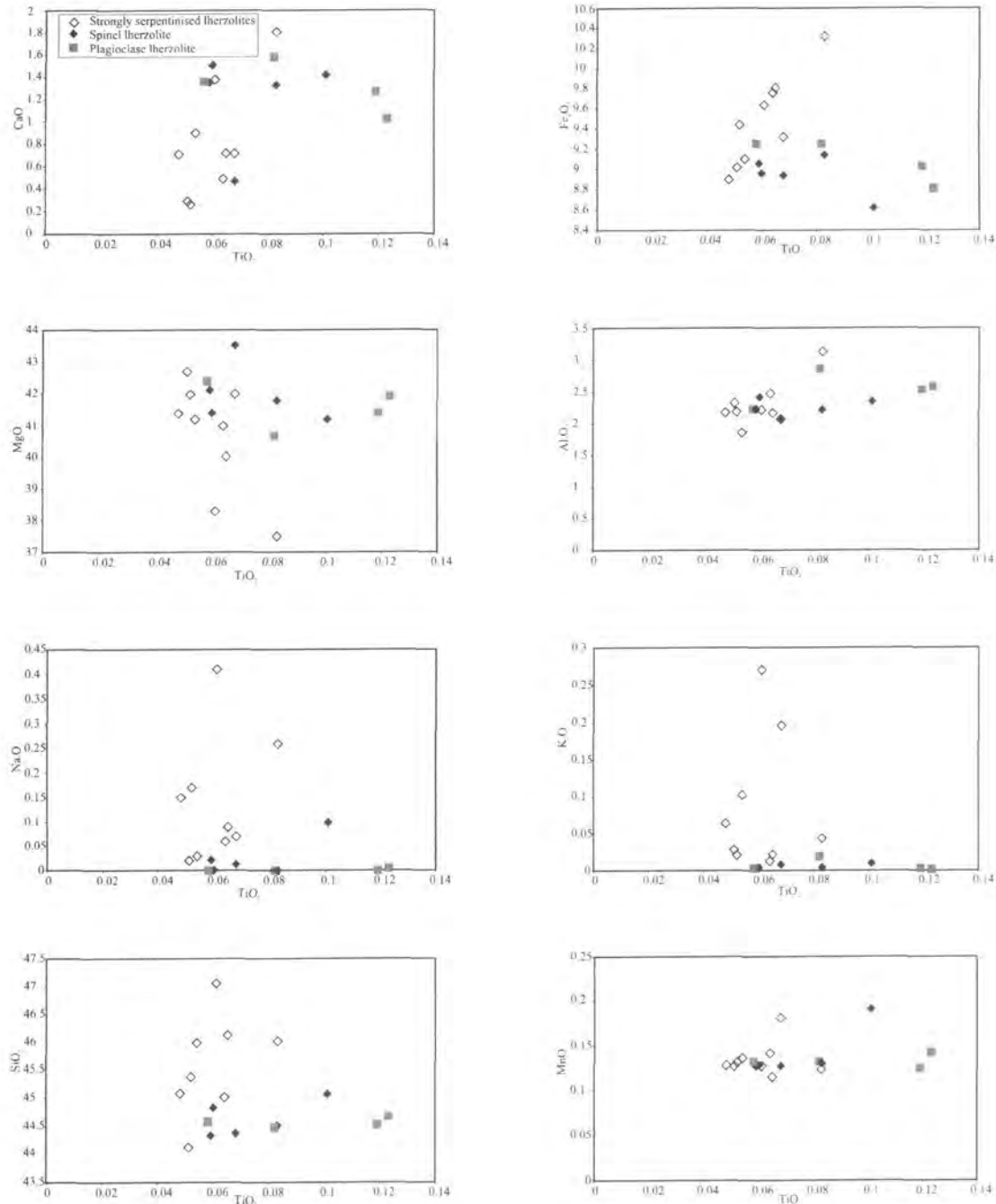


**Figure 6.1.** Graphs illustrating the variation of major elements with  $\text{TiO}_2$  (in wt%) for strongly (>90 % serpentinisation) serpentinised herzolites and relatively fresh (<30% serpentinisation) spinel and plagioclase herzolites.

the fluids present during serpentinisation were enriched in these elements. This evidence suggests that serpentinisation can indeed modify the primary composition of the peridotites as a result of the mobilisation of major elements. Therefore in this study, only the 'freshest' peridotite samples (<30 % alteration) have been used in order to reduce the possibility of misrepresentation of Fe<sub>2</sub>O<sub>3</sub>, Na<sub>2</sub>O, K<sub>2</sub>O, SiO<sub>2</sub>, CaO and MgO.

### **6.2.2. Lizard peridotites - results**

The volatile-free compositions of the Lizard peridotites show some well-defined trends. Abundances of MgO in the peridotites are negatively correlated with CaO, Na<sub>2</sub>O, Al<sub>2</sub>O<sub>3</sub>, TiO<sub>2</sub>, Sc and Zr contents. Ni contents are positively correlated with MgO concentrations, and Cr and V abundances show no correlation with MgO content (Figures 6.2.a-i). In addition, the different peridotite types (subdivided on the basis of field (Chapter 3) and microstructural (Chapter 4) evidence), which define these chemical trends, show systematic variations in major and trace element abundances that can be correlated with changes in microstructure. Spinel lherzolites display the highest MgO contents (41.2-43.5 wt%) and the plagioclase lherzolites (40.7-42.4 wt%) show values that overlap the range defined by the spinel lherzolites (Figure 6.2.a-i). However, the MgO concentrations decrease from the lherzolites to the mylonitic plagioclase-bearing peridotites (35.5-39.8 wt%) and mylonitic amphibole-bearing peridotites (36.5-39.5 wt%) via the peridotites with a transitional assemblage (40.3-40.4 wt%). A pyroxenite layer in spinel lherzolite shows the lowest MgO abundances (29.5 wt%).

Figure 6.2.a demonstrates that spinel lherzolite shows the lowest CaO abundances (0.47-1.51 wt%) and plagioclase lherzolites (1.0-1.6 wt%) display a range similar to the spinel lherzolites. Lherzolites by definition must contain 1-1.25 wt% CaO minimum for 5% clinopyroxene (M.T.Styles, *pers comm.*, 1999); therefore the low Ca content observed in these rocks is probably due to Ca loss due to serpentinisation. CaO contents increase from the lherzolites to the transitional assemblage peridotites (2.2-2.3 wt%) and the mylonitic plagioclase-bearing peridotite (2.0-3.4 wt%) and mylonitic amphibole-bearing peridotite (2.2-3.4 wt%). The highest CaO contents are observed in a pyroxenite layer in spinel lherzolite (10.1 wt%).

Na<sub>2</sub>O abundances are low (<0.6 wt%) in the Lizard peridotites (Figure 6.2.b). However, there is a trend of increasing Na<sub>2</sub>O from the spinel lherzolite (0-0.1 wt%) and

plagioclase lherzolite (0-0.005 wt%) via the transitional assemblage (0.06-0.11 wt%) to the mylonitic plagioclase-bearing peridotite (0.06-0.49 wt%) and the highest range is shown by the mylonitic amphibole-bearing peridotite (0.17-0.61 wt%). A pyroxenite layer in spinel lherzolite shows Na<sub>2</sub>O contents (0.18 wt%) within the range values shown by the transitional and mylonitic peridotites.

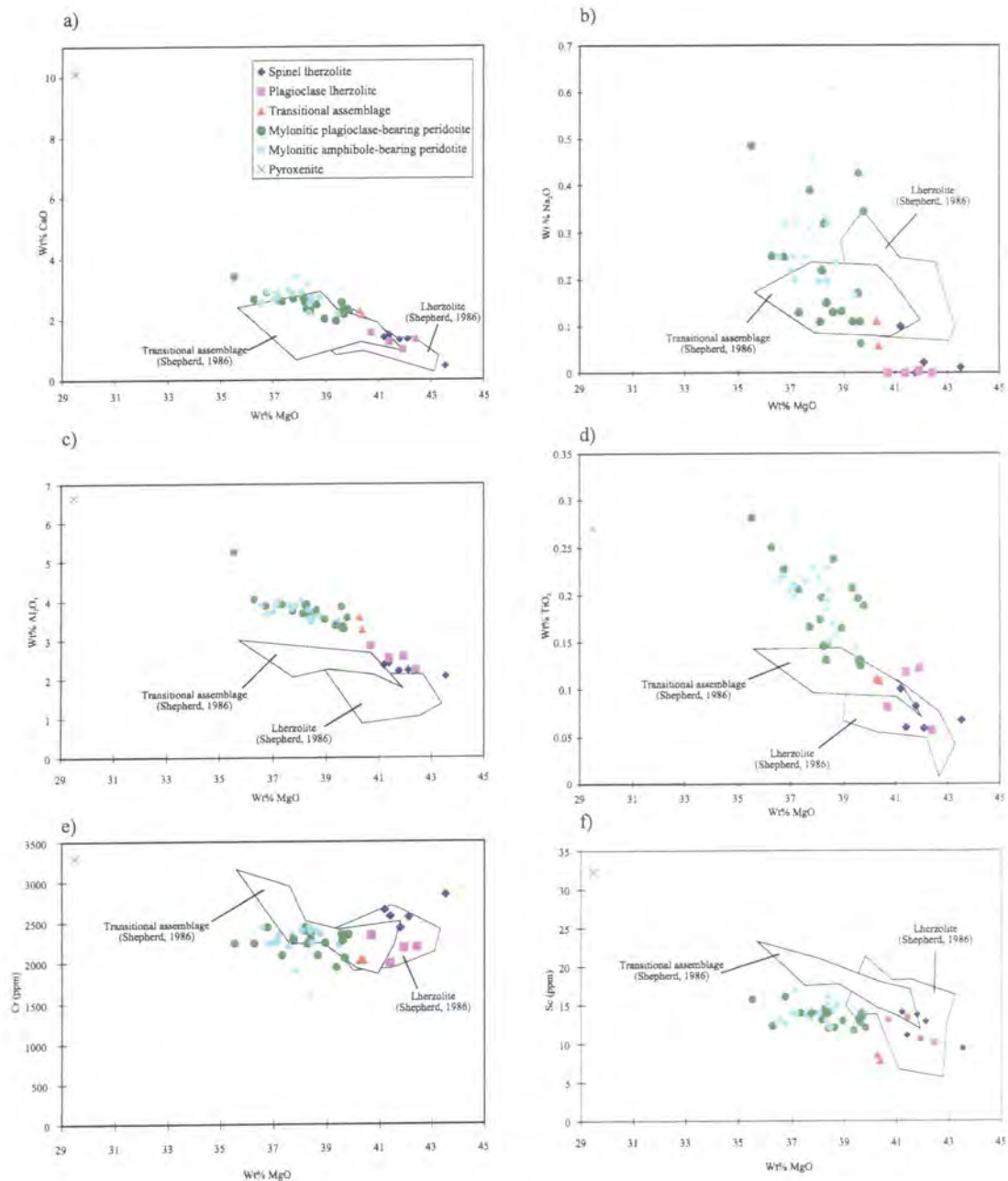


**Figure 6.2.a-f.** Whole rock abundances of wt% MgO versus (a) wt% CaO, (b) wt% Na<sub>2</sub>O, (c) wt% Al<sub>2</sub>O<sub>3</sub>, (d) wt% TiO<sub>2</sub>, (e) Cr (ppm) and (f) Sc (ppm) contents for the Lizard peridotites.

Spinel lherzolite displays the lowest Al<sub>2</sub>O<sub>3</sub> abundances (2.1-2.4 wt%), and these increase progressively from the plagioclase lherzolite (2.2-2.9 wt%), via the transitional

assemblage peridotite (3.3-3.6 wt%) to the mylonitic plagioclase-bearing peridotite (3.4-5.3 wt%) and mylonitic amphibole-bearing peridotite (3.5-4.0 wt%) (Figure 6.2.c). A pyroxenite layer in spinel lherzolite has the highest  $\text{Al}_2\text{O}_3$  abundance (6.7 wt%).

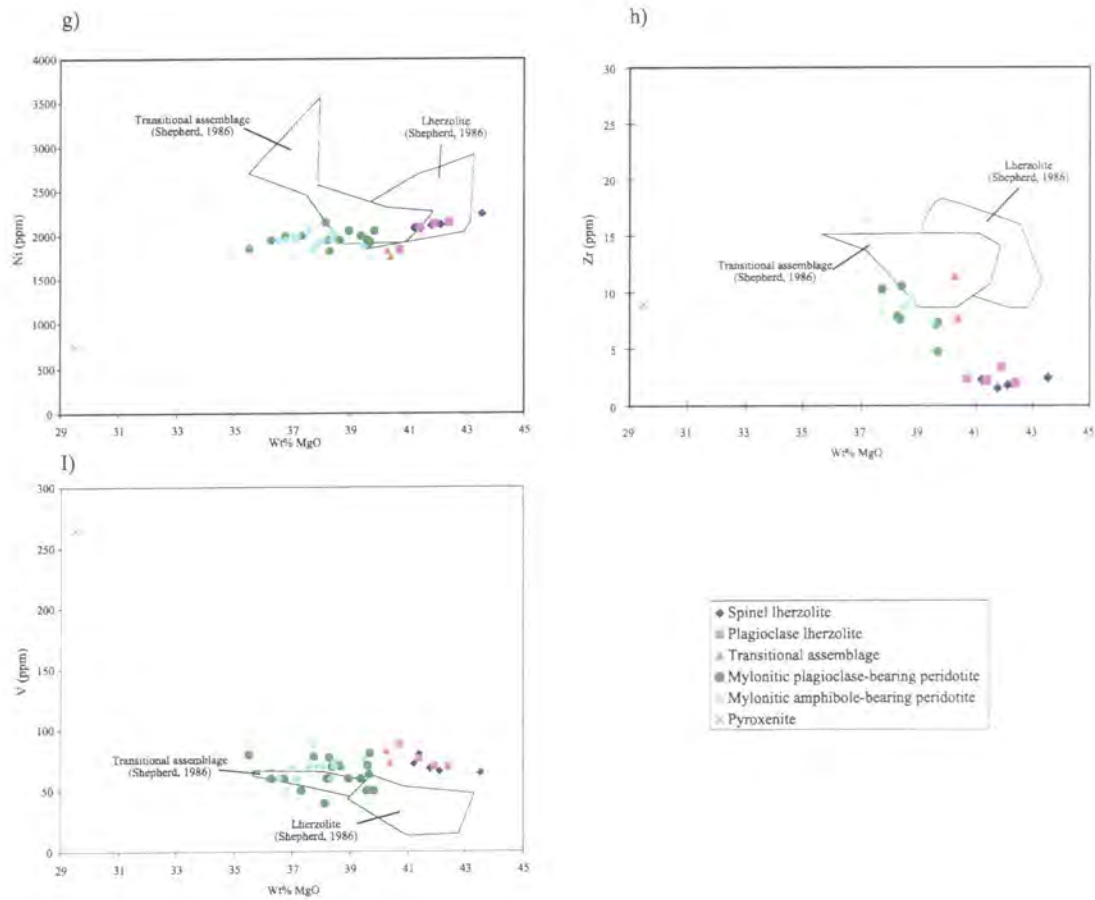


**Figure 6.2.g-i.** Whole rock abundances of wt% MgO versus (g) Ni (ppm), (h) Zr (ppm) and (i) V (ppm) contents for the Lizard peridotites.

The spinel lherzolite also shows the lowest range of  $\text{TiO}_2$  concentrations (0.06-0.1 wt%) and the plagioclase lherzolite (0.06-0.12 wt%) and transitional assemblage peridotite (0.11 wt%) fall within this range (Figure 6.2.d). The highest  $\text{TiO}_2$  contents are observed in the mylonitic plagioclase-bearing peridotite (0.13-0.28 wt%) and mylonitic amphibole-bearing peridotite (0.14-0.28 wt%), which is most likely related to the amphibole content of these samples. A pyroxenite layer in spinel lherzolite has  $\text{TiO}_2$  contents (0.27 wt%) that fall within the range defined by the mylonitic peridotites.

Spinel lherzolite (2433-2854 ppm) and a pyroxenite layer within spinel lherzolite (3298 ppm) display the highest Cr abundances (Figure 6.2.e). Plagioclase lherzolite (2004-2340 ppm), the transitional assemblage (2038-2044 ppm), the mylonitic plagioclase-bearing peridotite (1950-2450 ppm) and the mylonitic



amphibole-bearing peridotite (1600-2450 ppm) possess overlapping ranges of Cr values.

Sc abundances show an increase from spinel lherzolite (10-14 ppm) and plagioclase lherzolite (10-14 ppm) to mylonitic plagioclase-bearing peridotite (12-16 ppm) and mylonitic amphibole-bearing peridotite (12-17 ppm)(Figure 6.2.f). The transitional assemblage peridotites show Sc contents which are lower (8-9 ppm) than the trend defined by the other peridotite-types. The highest Sc concentration (32 ppm) is observed in a pyroxenite layer within spinel lherzolite. Increases in the Sc content of these samples are related to an increase in the clinopyroxene content.

The highest Ni concentration is shown by spinel lherzolite (2083-2242 ppm), and this decreases from the plagioclase lherzolite (1839-2146 ppm) to mylonitic plagioclase-bearing peridotite (1820-2150 ppm), mylonitic amphibole-bearing peridotite (1735-2050 ppm) and the transitional assemblage (1758-1824 ppm)(Figure 6.2.g). The lowest Ni contents as displayed by a pyroxenite layer (748 ppm) within spinel lherzolite. Variations in the Ni content are related to variations in the olivine content of these samples.

Spinel lherzolite (1.6-2.5 ppm) and plagioclase lherzolite (2.0-3.4 ppm) show the lowest Zr abundances (Figure 6.2.h). In contrast, the transitional assemblage (7.7-11.0 ppm), the mylonitic plagioclase-bearing peridotite (4.8-10.5 ppm), the mylonitic amphibole-bearing peridotite (7.3-16.5 ppm) and a pyroxenite layer (8.9 ppm) within spinel lherzolite show higher Zr contents.

Figure 6.2.i. demonstrates that the concentration of V in spinel lherzolite (64-80 ppm), plagioclase lherzolite (69-88 ppm), transitional assemblage (74-83 ppm), mylonitic plagioclase-bearing peridotite (40-80 ppm) mylonitic amphibole-bearing peridotite (50-94 ppm) are similar. The highest abundance of V is observed in a pyroxenite layer (265 ppm) within spinel lherzolite.

Analyses of lherzolites and transitional assemblage peridotites of the Lizard Ophiolite Complex taken from Shepherd (1986) are generally consistent with the data presented above (Figures 6.2.a-i). The transitional assemblage peridotites show lower MgO and higher CaO, Na<sub>2</sub>O, Al<sub>2</sub>O<sub>3</sub>, TiO<sub>2</sub>, Sc and V than the lherzolites. The lherzolites have slightly higher Ni than the transitional assemblage peridotites. The Sc and Na<sub>2</sub>O contents of the lherzolite and transitional assemblage peridotite taken from Shepherd (1986) are higher than those observed in the lherzolites and transitional

assemblage peridotites analysed during the course of this study. These differences are probably related to differences in the analytical procedure.

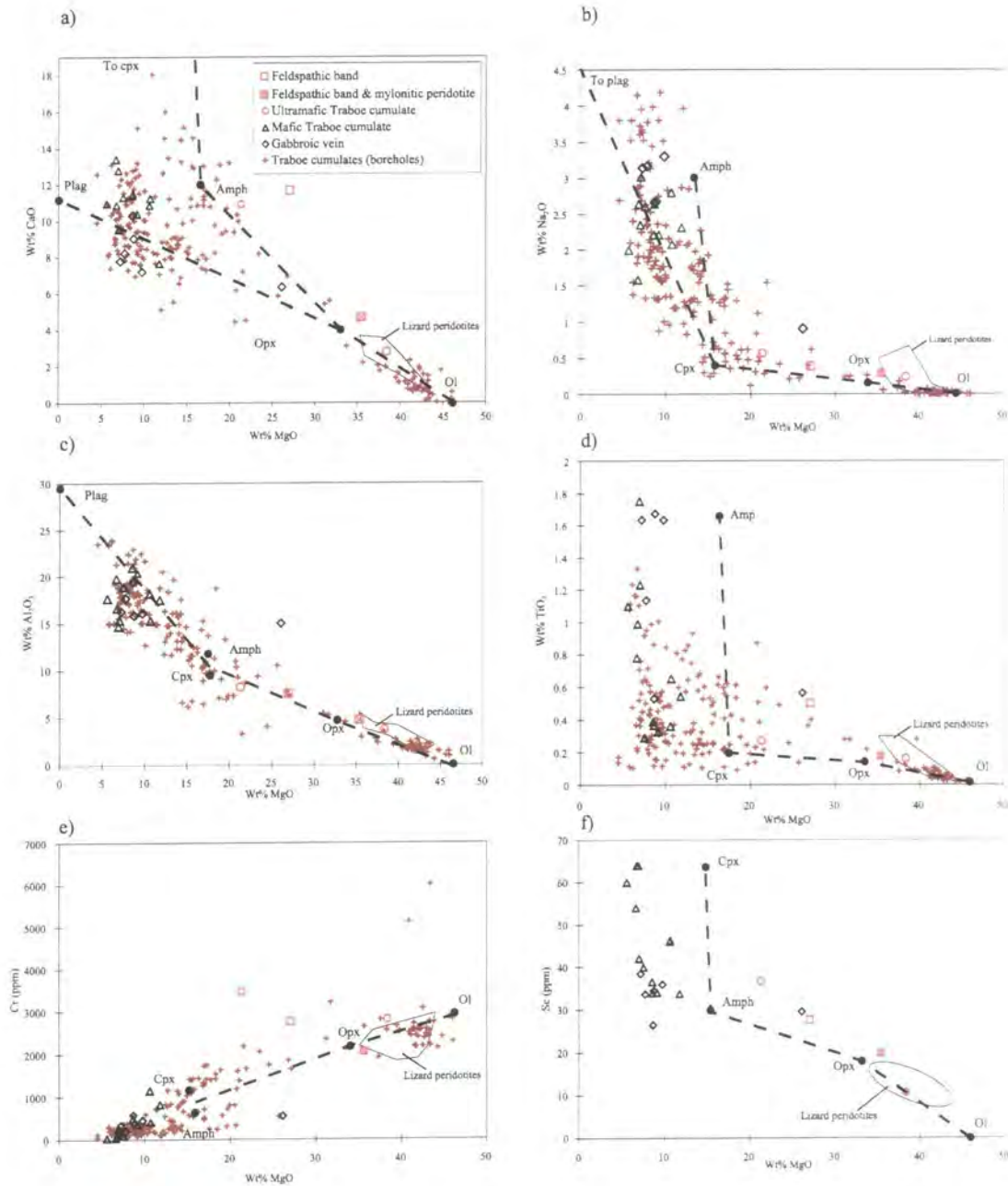


**Figure 6.3.a-f.** Whole rock abundances of wt% MgO versus (a) wt% CaO, (b) wt% Na<sub>2</sub>O, (c) wt% Al<sub>2</sub>O<sub>3</sub>, (d) wt% TiO<sub>2</sub>, (e) Cr (ppm) and (f) Sc (ppm) contents for feldspathic bands, ultramafic and mafic Traboe cumulates and gabbroic veins. Data for ultramafic and mafic Traboe cumulates from Traboe borehole core (Leake and Styles, 1984) is also shown. The range of compositions defined by the Lizard peridotites is included for comparison. Mineral fractionation control lines are shown: ol – olivine, opx – orthopyroxene, cpx – clinopyroxene, amph – amphibole and plag – plagioclase.

### 6.2.3. Rocks associated with the Lizard peridotites - results

In general, the chemical trends exhibited by these rocks are comparable to the trends demonstrated by the Lizard peridotites, for example MgO abundances are negatively correlated with CaO, Na<sub>2</sub>O, Al<sub>2</sub>O<sub>3</sub>, TiO<sub>2</sub>, Sc and V. In contrast, Ni and Cr contents are positively correlated with MgO abundances (Figure 6.3.a-i). Mineral fractionation control lines shown on Figure 6.3.a-i clearly demonstrate that the whole rock elements in these rocks are controlled by modal variation in the main minerals.

A feldspathic band shows lower MgO abundances (27 wt%) than the Lizard peridotites and a specimen containing both mylonitic amphibole-bearing peridotite

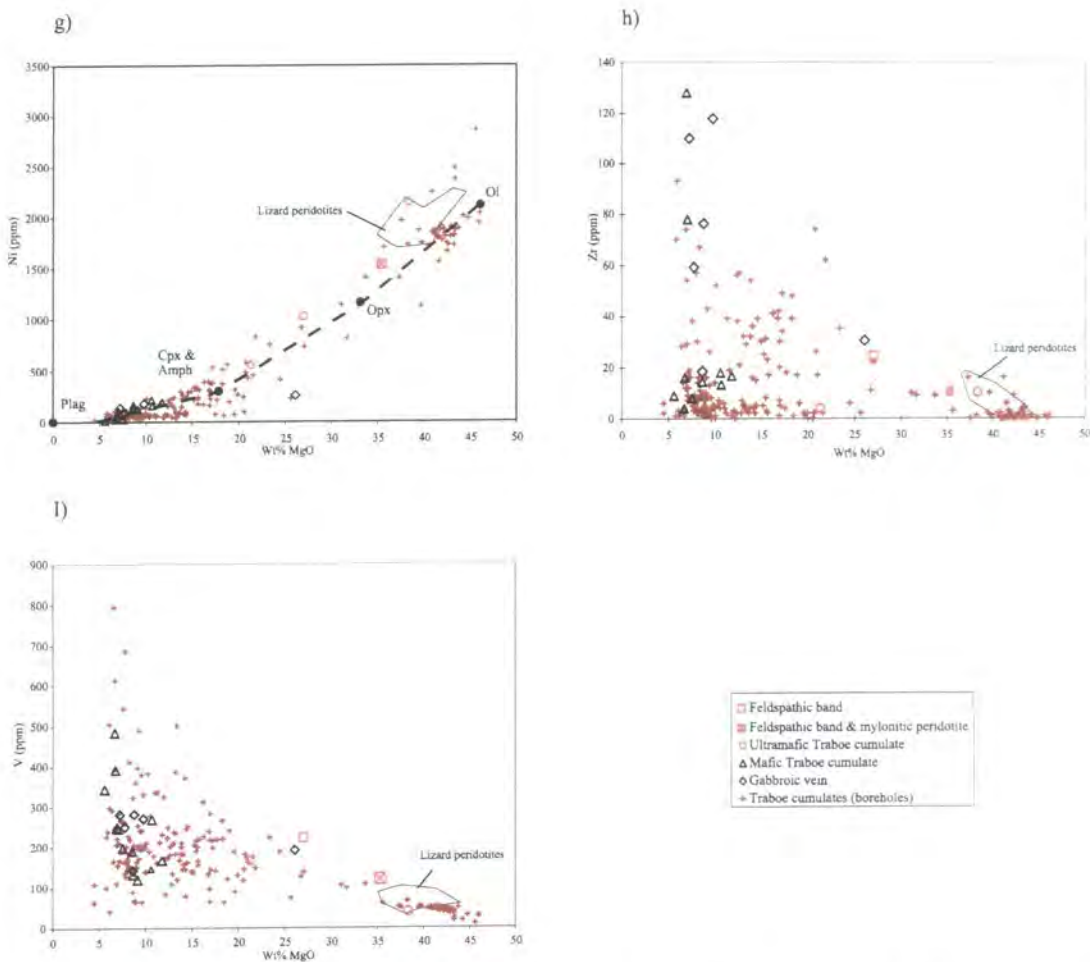


**Figure 6.3.g-i.** Whole rock abundances of wt% MgO versus (g) Ni (ppm), (h) Zr (ppm) and (i) V (ppm) contents for feldspathic bands, ultramafic and mafic Traboe cumulates and gabbroic veins. Data for ultramafic and mafic Traboe cumulates from Traboe borehole core (Leake and Styles, 1984) is also shown. The range of compositions defined by the Lizard peridotites is included for comparison.

and feldspathic bands (35.4 wt%) shows MgO contents similar to the mylonitic peridotites (Figure 6.2.a-i). Ultramafic Traboe cumulates show variable MgO abundances (21.3 and 38.3 wt% respectively). Mafic Traboe cumulates (5.6-11.8 wt%) and gabbroic veins (7.21-26.1 wt%) have much lower MgO concentrations than the Lizard peridotites. Analyses of borehole core drilled through the Traboe cumulate complex taken from Leake and Styles (1984) show that these ultramafic and mafic Traboe cumulates possess a wide range of MgO contents (4.5-46.0 wt%).

Figure 6.3.a. demonstrates that a feldspathic band has higher CaO abundances (11.7 wt%) than the Lizard peridotites and a specimen containing both mylonitic amphibole-bearing peridotite and feldspathic bands (4.7 wt%) shows CaO contents slightly higher than the mylonitic peridotites. Two specimens of ultramafic Traboe cumulates show different CaO contents (10.9 and 2.8 wt% respectively). Mafic Traboe cumulates (7.7-13.4 wt%) and gabbroic veins (6.3 and 10.3 wt%) display a similar range of CaO concentrations. The CaO abundance of ultramafic and mafic Traboe cumulates (0-18 wt%) from the Traboe cumulate complex borehole core (Leake and Styles, 1984) define a large compositional range due to a large range of clinopyroxene and amphibole contents.

A specimen of a feldspathic band and a specimen containing both mylonitic amphibole-bearing peridotite and feldspathic bands have Na<sub>2</sub>O contents (0.39 and 0.29 wt% respectively) similar to those of the mylonitic peridotites (Figure 6.2.b). Comparable Na<sub>2</sub>O abundances are observed in the ultramafic Traboe cumulates (0.56 and 0.24 wt%). The mafic Traboe cumulates display a restricted range of Na<sub>2</sub>O abundances (1.58-3.0 wt%) which is higher than the range defined by the Lizard peridotites. Gabbroic veins also possess relatively high Na<sub>2</sub>O contents (0.9-3.3 wt%). Ultramafic and mafic Traboe cumulates from the Traboe cumulate complex borehole cores (Leake and Styles, 1984) define the largest range of Na<sub>2</sub>O abundances (0-4.2 wt%) and this overlaps the range defined by the Lizard peridotites. Variations in amphibole content of these rocks control the whole rock Na<sub>2</sub>O content.

The Al<sub>2</sub>O<sub>3</sub> contents of a feldspathic band and a specimen containing both mylonitic amphibole-bearing peridotite and feldspathic bands (7.5 and 4.7 wt% respectively) are higher than the range defined by the Lizard peridotites (Figure 6.3.c). Two specimens of ultramafic Traboe cumulate possess Al<sub>2</sub>O<sub>3</sub> abundances both higher and similar to the Lizard peridotites (8.2 and 3.7 wt% respectively). Al<sub>2</sub>O<sub>3</sub> abundances in mafic Traboe cumulates (14.7-21 wt%) are considerably higher than those observed

in the Lizard peridotites. The  $\text{Al}_2\text{O}_3$  contents of gabbroic veins (15-19.4 wt%) are similar to those in the mafic Traboe cumulates. The ultramafic and mafic Traboe cumulates from the Traboe cumulate complex borehole core (Leake and Styles, 1984) define a wide range of  $\text{Al}_2\text{O}_3$  abundances (0.56-23.9 wt%). The  $\text{Al}_2\text{O}_3$  contents of the ultramafic Traboe cumulates from these borehole core samples are lower than observed in the mylonitic plagioclase-bearing peridotite and mylonitic amphibole-bearing peridotite, yet similar to the lherzolites. Higher whole rock  $\text{Al}_2\text{O}_3$  contents are consistent with an increased proportion of plagioclase.

A feldspathic band has higher  $\text{TiO}_2$  contents (0.5 wt%) than Lizard peridotites and a specimen containing both mylonitic amphibole-bearing peridotite and feldspathic bands (0.17 wt%) (Figure 6.3.d). Ultramafic Traboe cumulates show  $\text{TiO}_2$  abundances (0.16-0.27 wt%) that fall within the range defined by the Lizard peridotites. The  $\text{TiO}_2$  concentration of the mafic Traboe cumulates (0.29-1.75 wt%) is higher than in the ultramafic Traboe cumulates and the Lizard peridotites. Among the highest  $\text{TiO}_2$  contents (0.53-1.67 wt%) are displayed by the gabbroic veins. (0.02-1.33 wt%). Ultramafic and mafic Traboe cumulates from the Traboe cumulate complex borehole core (Leake and Styles, 1984) define a large range of  $\text{TiO}_2$  contents that overlap the ranges defined by the Lizard peridotites and gabbroic veins. The  $\text{TiO}_2$  contents of the ultramafic Traboe cumulates from these borehole core samples are lower than observed in the mylonitic plagioclase-bearing peridotite and mylonitic amphibole-bearing peridotite. Higher whole rock  $\text{TiO}_2$  concentrations suggest a greater proportion of Ti-rich amphibole.

The Cr concentration of a feldspathic band and a specimen containing both mylonitic amphibole-bearing peridotite and feldspathic bands (2753 and 2042 ppm respectively) are similar to the range defined by the Lizard peridotites (Figure 6.3.e). The Cr concentration of the ultramafic Traboe cumulates (2803 and 3468 ppm) is higher than the range defined by the Lizard peridotites. Mafic Traboe cumulates have much lower Cr abundances (27.4-1150 ppm) than the ultramafic Traboe cumulates. The gabbroic veins possess a relatively restricted range of Cr contents (207-544 ppm). Ultramafic and mafic Traboe cumulates from the Traboe cumulate complex borehole core (Leake and Styles, 1984) show a massive range of Cr abundances (38-6010 ppm), which overlap the range defined by the Lizard peridotites.

The Sc concentration of a feldspathic band and a specimen containing both mylonitic amphibole-bearing peridotite and feldspathic bands (27.5 and 20.1 ppm

respectively) are higher than the range defined by the Lizard peridotites (Figure 6.3.f). The ultramafic Traboe cumulate samples contain variable Sc abundances (10.5 and 36.6 ppm). Mafic Traboe cumulates possess (33.7-64.0 ppm) a range of Sc contents which are higher than observed in the ultramafic Traboe cumulates and the Lizard peridotites. In contrast, the gabbroic veins show a narrower range of Sc contents (26.4-38.4 ppm).

A feldspathic band and a specimen containing both mylonitic amphibole-bearing peridotite and feldspathic bands show lower Ni abundances (1032 and 1535 ppm) than the Lizard peridotites (Figure 6.3.g). Ultramafic Traboe cumulates have Ni contents (558 and 2150 ppm) which overlap the range defined by the Lizard peridotites. However, the mafic Traboe cumulates (17.5-216 ppm) possess much lower Ni contents than the Lizard peridotites. Gabbroic veins have a Ni content (93-262 ppm) similar to the mafic Traboe cumulates. The largest range of Ni abundances is found in ultramafic and mafic Traboe cumulates (19-2865 ppm) from the Traboe cumulate complex borehole core (Leake and Styles, 1984). The modal variation of olivine in these rocks controls the whole rock Ni content.

A feldspathic band has a higher Zr concentration (24 ppm) than a specimen containing both mylonitic amphibole-bearing peridotite and feldspathic bands (10 ppm)(Figure 6.3.h). Ultramafic Traboe cumulates show Zr contents (4 and 10 ppm) similar to those of the Lizard peridotites. The largest range of Zr concentrations (2-128 ppm) is found in the mafic Traboe cumulates, and the gabbroic veins (19-118) show a similar range of Zr contents.

A feldspathic band and a specimen containing both mylonitic amphibole-bearing peridotite and feldspathic bands have higher V contents (222 and 120 ppm) than the Lizard peridotites (Figure 6.3.i). Ultramafic Traboe cumulates show variable V contents (40 and 166 ppm). A wide range of V abundance is displayed (120-484 ppm) by mafic Traboe cumulates. In contrast, the gabbroic veins (191-282 ppm) display a relatively restricted range of V concentrations. The largest range of V contents is shown by ultramafic and mafic Traboe cumulates (10-794 ppm) from the Traboe cumulate complex borehole core (Leake and Styles, 1984).



#### **6.2.4. Lizard peridotites and associated rocks – Interpretation and discussion**

The results of a whole rock major and trace element analyses of the Lizard peridotites demonstrates several important chemical trends. The MgO content in the rocks is negatively correlated with CaO, Na<sub>2</sub>O, Al<sub>2</sub>O<sub>3</sub>, TiO<sub>2</sub>, Sc and Zr, whilst Ni is positively correlated with MgO (consistent with Ni being hosted by olivine). Cr and V concentrations show no correlation with MgO abundance. Spinel lherzolites and plagioclase lherzolites plot at the high-MgO end of these correlations, whilst the mylonitic plagioclase-bearing peridotite and mylonitic amphibole-bearing peridotite plot at the low-MgO end. Transitional assemblage peridotites are intermediate between the spinel and plagioclase lherzolites and the mylonitic peridotites.

In Figure 6.4, the major element compositions of relatively fresh (<30% serpentinisation) plagioclase lherzolite, transitional assemblage and mylonitic peridotites are normalised to the 'average' spinel lherzolite composition, which is assumed to represent the protolith peridotite composition prior to deformation. This plot clearly demonstrates that the transitional assemblage and mylonitic peridotites are enriched in CaO, Al<sub>2</sub>O<sub>3</sub>, Na<sub>2</sub>O, K<sub>2</sub>O, TiO<sub>2</sub> and MnO relative to the spinel lherzolite protolith. Plagioclase lherzolites generally have a composition similar to the spinel lherzolite. However, they are relatively enriched in P<sub>2</sub>O<sub>5</sub>. A similar diagram (Figure 6.5) shows the trace element composition of plagioclase lherzolite, the transitional assemblage and the mylonitic peridotites normalised to the 'average' spinel lherzolite composition. In this plot, the enrichment and depletion of these peridotites relative to the spinel lherzolite protolith composition is less obvious. The most significant differences are the enrichment of Zr, Y, Sr, Rb and Co in the transitional assemblage and mylonitic peridotites relative to spinel lherzolite. It is suggested that the differences between the composition of the spinel lherzolite and the plagioclase lherzolite, the transitional assemblage and the mylonitic peridotites are not related to serpentinisation or secondary alteration, because only 'fresh' samples were used. The compositional variations are therefore inferred to be related to differences in the petrogenesis of these rocks e.g. melt-rock interaction, and this is discussed later in this Section.

The compositional trends demonstrated by the Lizard peridotites are similar to those defined by peridotites from the Yugoslavian central Dinaric ophiolite belt (Lugovic *et al.*, 1991) and External Ligurides in Italy (Rampone *et al.*, 1995)(Figures

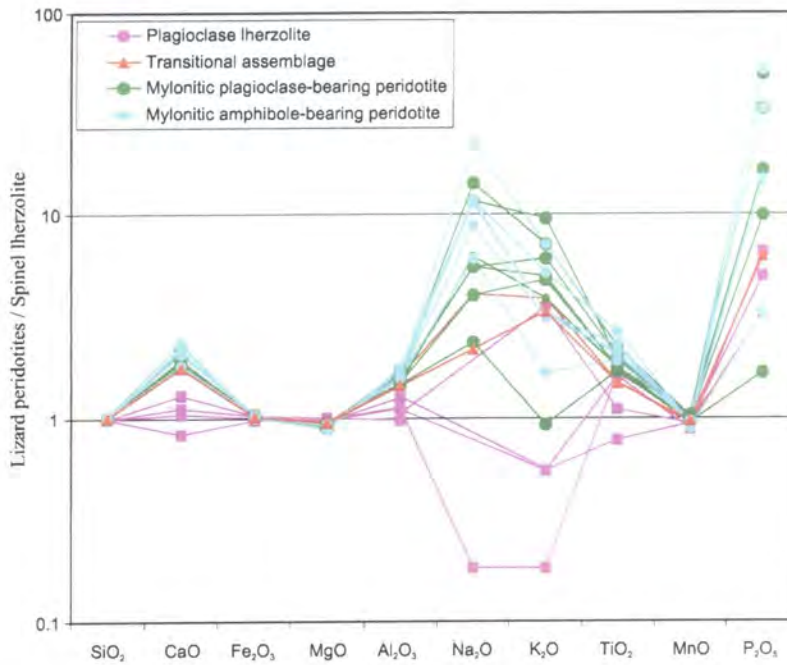


**Figure 6.4.** Whole rock, major element abundances of plagioclase ilherzolite, transitional peridotite and mylonitic peridotites normalised to the composition of spinel ilherzolite (= 1) from the Lizard Ophiolite Complex. Positive peaks (>1) represent enrichment of an element relative to spinel ilherzolite, and negative peaks (<1) indicate relative depletion.

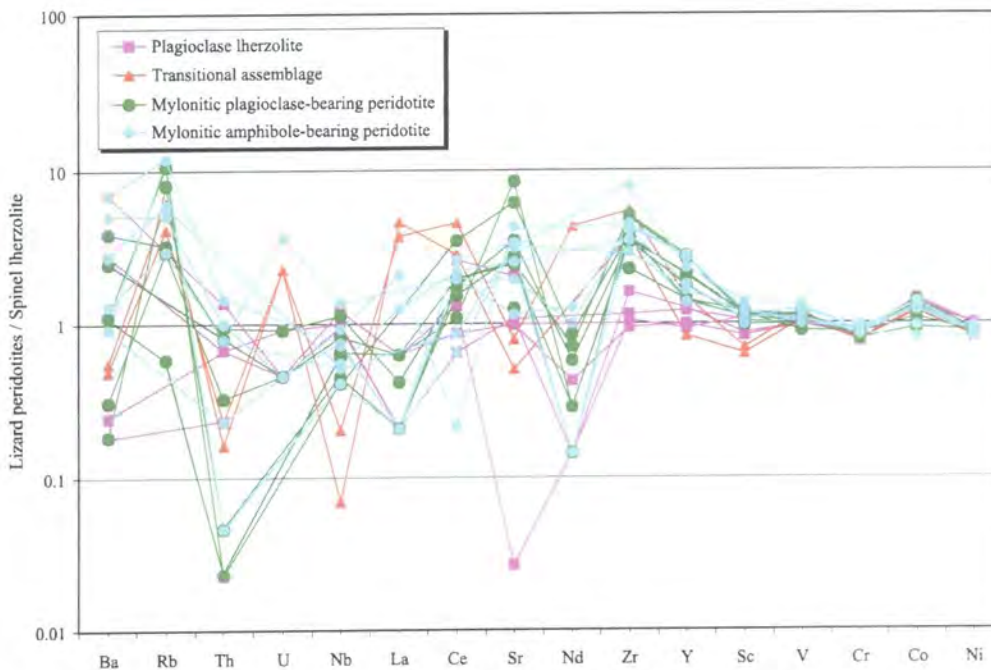


**Figure 6.5.** Whole rock, trace element abundances of plagioclase ilherzolite, transitional peridotite and mylonitic peridotites normalised to the composition of spinel ilherzolite (= 1) from the Lizard Ophiolite Complex. Incompatible elements (Ba-Y) are plotted in order of incompatibility increasing from left to right and compatible elements (Sc-Ni) are plotted at the right hand side of the plot. Positive peaks (>1) represent enrichment of an element relative to spinel ilherzolite, and negative peaks (<1) indicate relative depletion.

6.6.a-g). The trends defined by the Lizard peridotites overlap the primitive mantle estimates of Ringwood (1975), Jagoutz *et al.* (1979) and Hoffman (1988), that plot at the low-MgO end of the correlations (Figure 6.6.a-g). Peridotites from the Internal

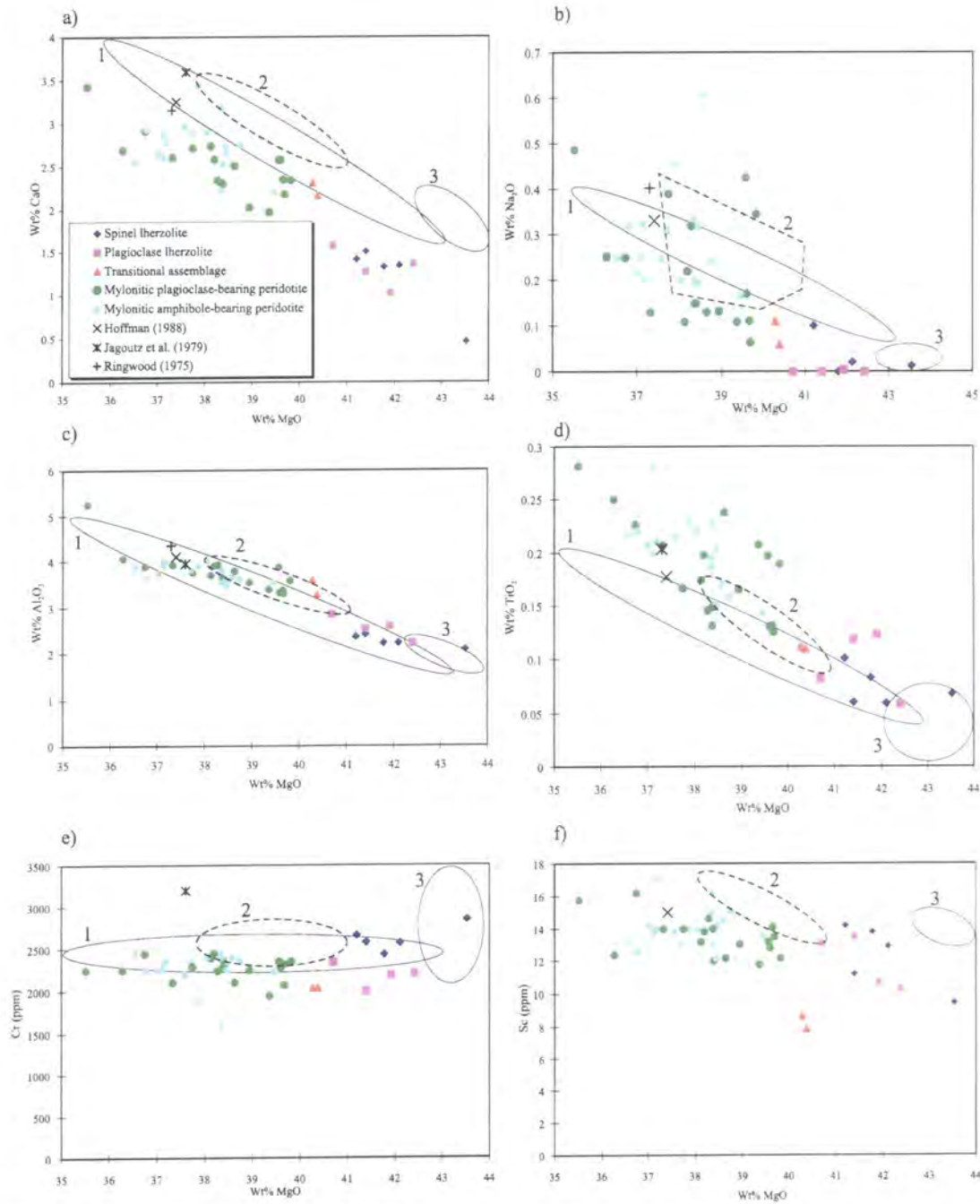


**Figure 6.6.a-f.** Whole rock abundances of wt% MgO versus (a) wt% CaO, (b) wt% Na<sub>2</sub>O, (c) wt% Al<sub>2</sub>O<sub>3</sub>, (d) wt% TiO<sub>2</sub>, (e) Cr (ppm) and (f) Sc (ppm) contents for the Lizard peridotites compared with estimates for primitive mantle composition of Ringwood (1975), Jagoutz *et al.* (1979) and Hoffman (1988). Also included for comparison are: (1) peridotites from the Yugoslavian central Dinaric ophiolite belt (Lugovic *et al.*, 1991), (2) peridotites from External Ligurides ophiolites, Italy (Rampone *et al.*, 1995) and (3) depleted peridotites from the Internal Ligurides ophiolites, Italy (Rampone, 1992).

Ligurides, Italy (Rampone, 1992) are more depleted than the Lizard peridotites, showing higher MgO, and lower CaO, Na<sub>2</sub>O, Al<sub>2</sub>O<sub>3</sub> and TiO<sub>2</sub> contents (Figure 6.6.a-g). In the mantle peridotites described in the literature, there are no observed changes in major and trace element chemistry, which can be correlated with changes in microstructure, e.g., increasing CaO and Al<sub>2</sub>O<sub>3</sub> contents from coarse-grained peridotites to mylonitic peridotites. Significantly, coarse-grained spinel lherzolites and plagioclase (or amphibole)-bearing deformed and mylonitic peridotites from Zabargad Island (Bonatti *et al.*, 1986) and the Voltri Massif (Hoogerduijn Strating *et al.*, 1993) all have a similar bulk composition. Therefore the compositional trends defined by the Lizard peridotites, which include a decrease in MgO and Ni contents, and an increase in CaO, Na<sub>2</sub>O, Al<sub>2</sub>O<sub>3</sub>, TiO<sub>2</sub>, Sc and Zr from the coarse-grained spinel and plagioclase lherzolites to the mylonitic peridotites, are unusual.

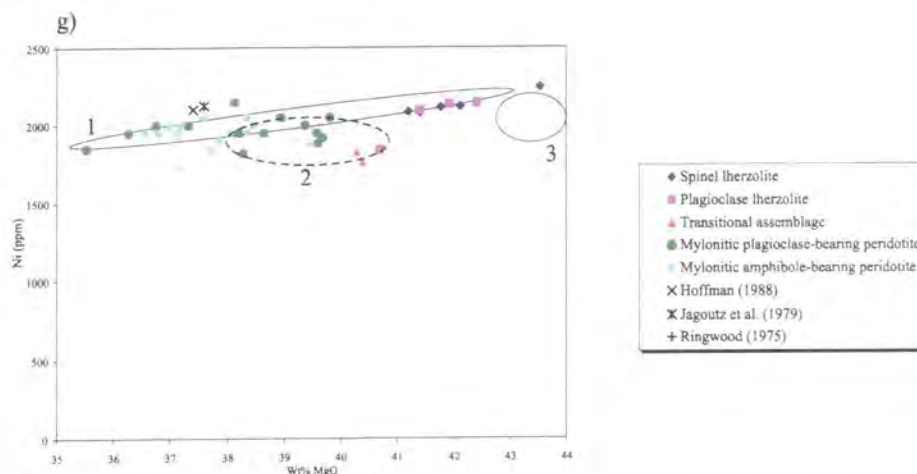


**Figure 6.6.g.** Whole rock abundances of wt% MgO versus (g) Ni (ppm) contents for the Lizard peridotites compared with estimates for primitive mantle composition of Ringwood (1975), Jagoutz *et al.* (1979) and Hoffman (1988). Also included for comparison are: (1) peridotites from the Yugoslavian central Dinaric ophiolite belt (Lugovic *et al.*, 1991), (2) peridotites from External Ligurides ophiolites, Italy (Rampone *et al.*, 1995) and (3) depleted peridotites from the Internal Ligurides ophiolites, Italy (Rampone, 1992).

A plot of Cr/Al versus Ni/Al (Figure 6.7)(Roberts and Neary, 1993) compares the composition of the Lizard peridotites with peridotites from several ophiolites (Roberts and Neary, 1993). This diagram is used because it provides an indication of the degree of depletion of the peridotites, i.e., the trend from low Cr/Al, Ni/Al ratios to high Cr/Al, Ni/Al ratios in peridotites reflects an increase in the degree of depletion (Roberts and Neary, 1993). This diagram clearly demonstrates that the Lizard peridotites have lower Cr/Al and Ni/Al ratios than peridotites from the Semail and Vourinos ophiolites. The Lizard peridotites have Cr/Al, Ni/Al ratios closer to those of



the Apennine peridotites (External Ligurides), and are therefore relatively 'fertile' and have undergone limited partial melting. This diagram also shows that the transitional assemblage, mylonitic plagioclase-bearing peridotite and mylonitic amphibole-

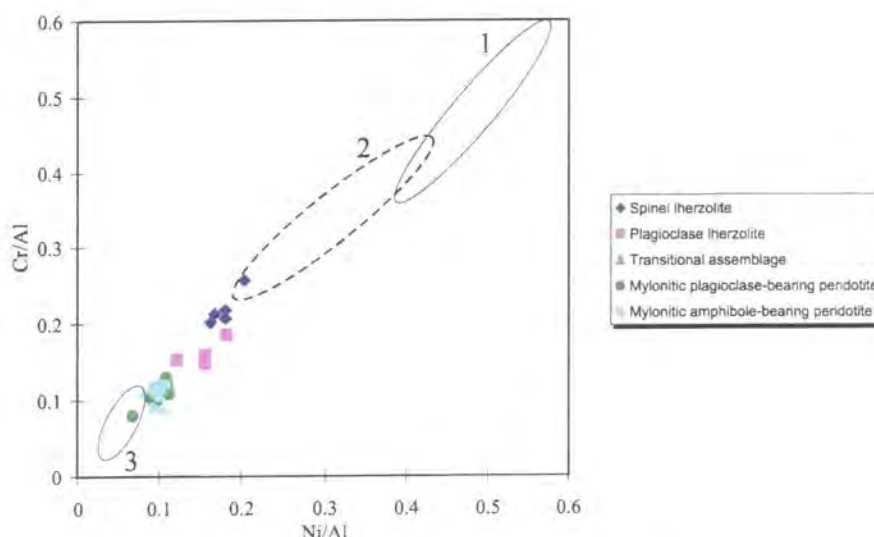


**Figure 6.7.** Cr/Al versus Ni/Al diagram for peridotites from the Lizard Ophiolite Complex compared with a series of ophiolitic peridotites, including: (1) Vourinos ophiolite, Greece, (2) Semail ophiolite, Oman and (3) Apennine ophiolites (External Ligurides), Italy. The trend from low Cr/Al, Ni/Al ratios to high Cr/Al, Ni/Al ratios indicate increasing depletion. Data sources: this study and Roberts and Neary (1993).

bearing peridotite, has lower Cr/Al, Ni/Al ratios than the spinel and plagioclase lherzolites from the Lizard Ophiolite Complex.

The process of deformation and recrystallisation of the Lizard peridotites cannot itself account for changes in composition from the spinel and plagioclase lherzolites to the mylonitic peridotites. Alternatively it is possible that during deformation the transitional assemblage peridotite, mylonitic plagioclase-bearing peridotite and mylonitic amphibole-bearing peridotite were enriched in certain major and trace elements. A process that causes the geochemical enrichment of a rock is metasomatism (Menzies and Hawkesworth (1987) and references therein), in which the interaction between a rock, and a melt or hydrous fluid results in a change of the bulk composition. Harte *et al.* (1987) demonstrate that metasomatism involving melt-rock interaction results in the bulk addition of Fe, Ti, Al, Cr, K, S, Zr, Nb, Ta, Hf and H<sub>2</sub>O to peridotites. The increase of TiO<sub>2</sub> in the transitional assemblage and mylonitic peridotites relative to the coarse-grained lherzolites suggests that the metasomatism may have been related to the infiltration of a melt. Eggler (1987) suggests that Ti is

relatively insoluble in H<sub>2</sub>O- and CO<sub>2</sub>-rich fluids and hence a magmatic component, rather than a fluid alone, is likely to be important. The presence of amphibole, a hydrous phase, in the mylonitic peridotites shows that a hydrous melt may have been responsible for the metasomatism of the peridotites. The composition of a feldspathic band and a specimen containing both mylonitic amphibole-bearing peridotite and feldspathic bands, suggests that these bands may represent the residual product of the hydrous melt responsible for melt/fluid-rock interaction of the peridotites. The feldspathic band plots on a linear trend with the peridotites and lie at the extreme low-MgO end of this trend. Spray (1982) obtained similar results after analysing an identical rock from the Lizard and proposed that these bands represent crystal segregations from picritic fluids. Amphibole-bearing peridotites, which form the wall-rock immediately adjacent (<20 cm) to amphibole pyroxenite veins from the Lherz massif, show similar chemical variations to the Lizard peridotites (Bodinier *et al.*, 1990). These peridotites show a trend of increasing Fe, Mn, Ti, Al, Ca and Na, and decreasing Mg and Ni towards the vein contact. However, the Lizard peridotites show evidence for uniform metasomatism in mylonitic peridotites on a scale of several kilometres, and therefore differs substantially from the centimetre scale metasomatism described for the Lherz Massif (Bodinier *et al.*, 1990). Further discussion regarding the melt/fluid-rock interaction and resultant metasomatism of the Lizard peridotites is presented in Section 6.3, with reference to the rare earth composition of these rocks.

The ultramafic and mafic Traboe cumulates analysed during the course of this study have a composition consistent with the larger number of analysis of ultramafic and mafic Traboe cumulates from the Traboe cumulate complex borehole core (Leake and Styles, 1984). The Traboe cumulates define linear chemical trends and the mafic Traboe cumulates analysed during this study plot at the low-MgO end of the compositional field defined by the borehole core analyses (Leake and Styles, 1984). It is also apparent that the ultramafic Traboe cumulates from the Traboe cumulate complex borehole core have higher MgO contents, and lower CaO, Na<sub>2</sub>O, Al<sub>2</sub>O<sub>3</sub>, TiO<sub>2</sub> and Zr abundances, than the mylonitic peridotites. This contradicts the findings of Green (1964a,b), which suggests that the ultramafic rocks in the Traboe region represent highly serpentinised mylonitic peridotites. These bulk rock analyses clearly demonstrate that the ultramafic rocks in the Traboe region have a different chemistry, consistent with these rocks being ultramafic cumulates. The large range of MgO, CaO,



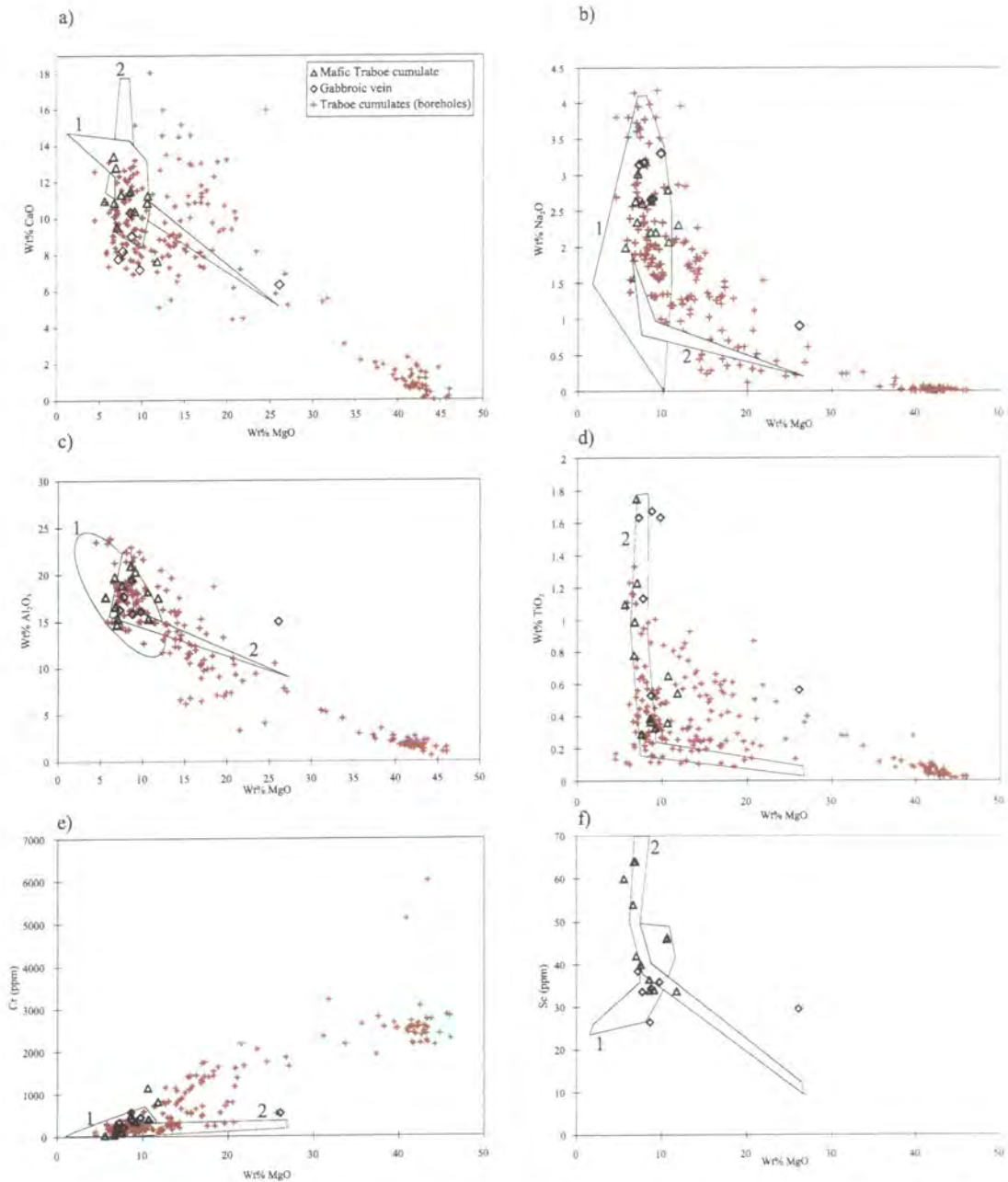


**Figure 6.8.a-f.** Whole rock abundances of wt% MgO versus (a) wt% CaO, (b) wt% Na<sub>2</sub>O, (c) wt% Al<sub>2</sub>O<sub>3</sub>, (d) wt% TiO<sub>2</sub>, (e) Cr (ppm) and (f) Sc (ppm) contents for the mafic Traboe cumulates, gabbroic veins and samples of ultramafic and mafic Traboe cumulates from Traboe borehole core (Leake and Styles, 1984) compared with gabbroic rocks from ophiolites: (1) gabbros from the Bridge River accretionary complex, SW British Columbia (Church *et al.*, 1995) and (2) layered gabbro cumulates from the Brooks Range ophiolite, Alaska (Harris, 1995).

Al<sub>2</sub>O<sub>3</sub>, Na<sub>2</sub>O and TiO<sub>2</sub> contents in the ultramafic Traboe cumulates are believed to be due to fractional crystallisation and magmatic differentiation of a similar magma source, because these processes could produce the wide range of compositions observed in these cumulates.

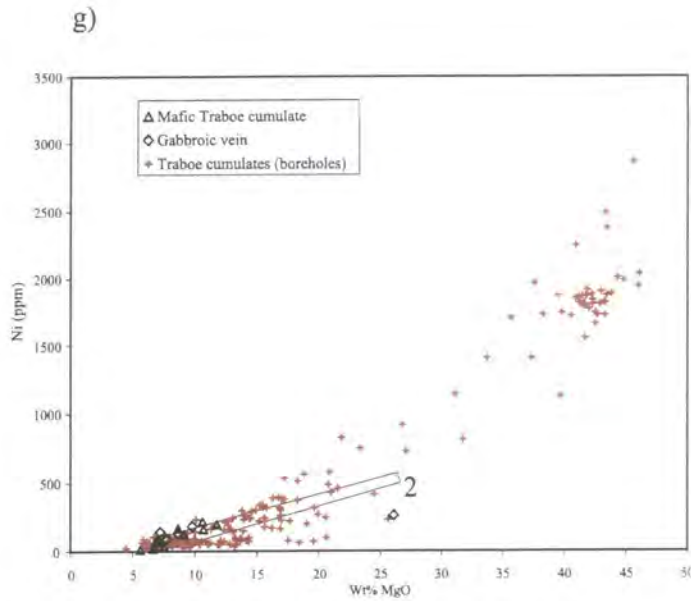


**Figure 6.8.g.** Whole rock abundances of wt% MgO versus (g) Ni (ppm) contents for the mafic Traboe cumulates, gabbroic veins and samples of ultramafic and mafic Traboe cumulates from Traboe borehole core (Leake and Styles, 1984) compared with (2) layered gabbro cumulates from the Brooks Range ophiolite, Alaska (Harris, 1995).

Figures 6.8.a-g. show that the mafic Traboe cumulates, including those from the Traboe cumulate complex borehole core, are compositionally similar to layered gabbro cumulates from the Brooks Range ophiolite, Alaska (Harris, 1995) and gabbroic rocks from the Bridge River accretionary complex, SW British Columbia (Church *et al.*, 1995). This supports the field, microstructural and mineral composition evidence (Chapters 3,4 & 5), which suggests that these mafic and ultramafic Traboe cumulates represent a highly deformed cumulate complex.

The whole-rock composition of gabbroic veins from the Lizard is very similar to gabbroic veins that cross-cut peridotites in the mantle sequence of the Jormua ophiolite, Finland (Peltonen *et al.*, 1998). These rocks also have a whole rock major and trace element composition which is identical to the mafic Traboe cumulates and ophiolitic gabbros (see above). The gabbroic veins may share the same magma source as the mafic Traboe cumulates.

### 6.2.5. Amphibolites and mafic dykes

In the previous section, the major and trace element chemistry of mafic Traboe cumulates and gabbroic veins associated with the Lizard peridotites have been discussed. In this section, the chemistry of mafic rocks that are not directly associated

with the Lizard peridotites is presented and includes Landewednack amphibolites and mafic dykes. Data for the Porthoustock amphibolites obtained from Shepherd (1986) are also included for comparison. Only a few plots are included in this section, and these are for elements that show clear differences between the Landewednack amphibolites and the mafic Traboe cumulates.

### 6.2.5.a. Results

These amphibolites and mafic rocks show several compositional trends, which can be used to distinguish them from the Traboe cumulates associated with the Lizard peridotites. Figure 6.9.a-b. demonstrates that the Landewednack amphibolites have a relatively restricted range of MgO contents (5.1-15.2 wt%), which fall at the low-end of the range defined by the Traboe cumulates (see Figure 6.3.a-i). The data for Landewednack amphibolites presented by Shepherd (1986) is consistent with this observation. The MgO contents of the Porthoustock amphibolites (Shepherd, 1986) overlap the range displayed by the Landewednack amphibolites. Mafic dykes show the largest range of MgO contents (8.5-22.9 wt%).

Landewednack amphibolites can be distinguished chemically from the mafic Traboe cumulates on the basis of whole rock  $\text{TiO}_2$  abundances, which are much higher

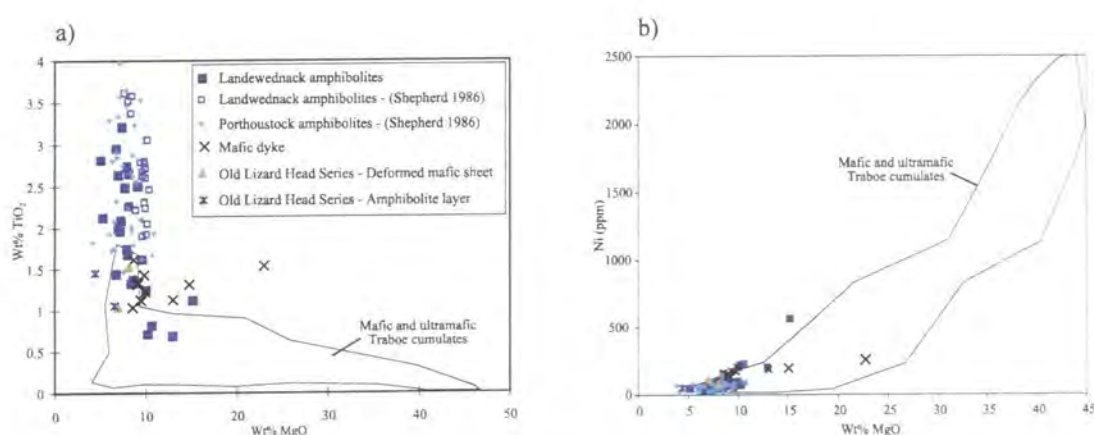


**Figure 6.9.** Whole rock abundances of  $\text{wt}\% \text{MgO}$  versus (a)  $\text{wt}\% \text{TiO}_2$  (b) Ni (ppm) for Landewednack amphibolites, Porthoustock amphibolites and mafic dykes from the Lizard Ophiolite Complex, including data from Shepherd (1986). Also included are deformed mafic sheets and amphibolite layers from the Old Lizard Head Series. The range of composition defined by the mafic and ultramafic Traboe cumulates are included from comparison (Leake and Styles, 1984).



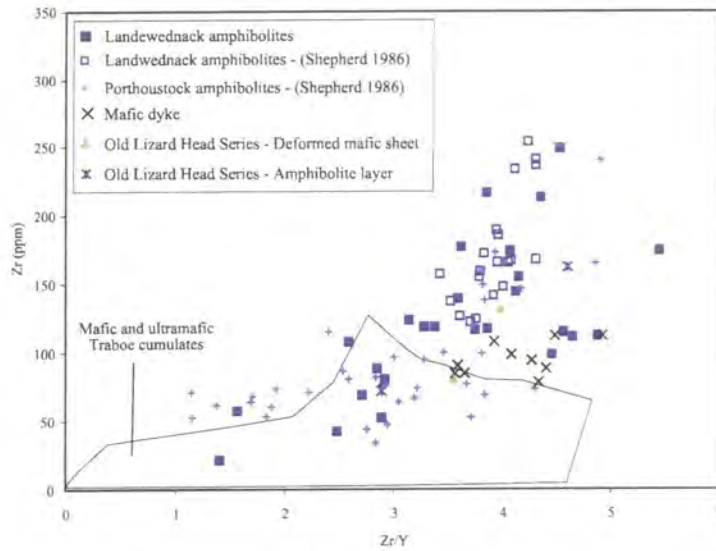


**Figure 6.10.** Whole rock abundances of Zr (ppm) versus Zr/Y ratio for Landwednack amphibolites, Porthoustock amphibolites and mafic dykes from the Lizard Ophiolite Complex, including data from Shepherd (1986). Also included are deformed mafic sheets and amphibolite layers from the Old Lizard Head Series. The range of composition defined by the mafic and ultramafic Traboe cumulates are included from comparison (Leake and Styles, 1984).

in the Landwednack amphibolites (0.7-3.2 wt%)(Figure 6.9.a). The data presented by Shepherd (1986) establishes that the Porthoustock amphibolites also possess high  $\text{TiO}_2$  contents. Mafic dykes show a restricted range of  $\text{TiO}_2$  abundances (1.0-1.6 wt%), which fall at the low-end of the range defined by the Landwednack amphibolites.

The Landwednack amphibolites, with the exception of a single sample, show low Ni contents (30-232 ppm) which fall at the low-end of the range defined by the Traboe cumulates (Figure 6.9.b). The Porthoustock amphibolites define a more restricted compositional range (17-107 ppm) (Shepherd, 1986). The mafic dykes have relatively high Ni abundances (132-270 ppm) which overlap the high-end of the range defined by the Landwednack amphibolites.

A plot (Figure 6.10) of Zr content versus Zr/Y ratio also distinguishes the Landwednack amphibolites from the mafic Traboe cumulates. The Landwednack amphibolites show a large range of Zr contents (21-249 ppm), far greater than the range observed in the Traboe cumulates. Comparable Zr contents (47-173 ppm) are characteristic of the Porthoustock amphibolites (Shepherd, 1986). The mafic dykes define a slightly different compositional trend from the amphibolites, which is characterised by lower Zr contents (78-112 ppm) at higher Zr/Y ratios (3.55-4.92).

### **6.2.5.b. Interpretation and discussion**

The analyses of major and trace elements in the Landewednack amphibolites, shows that these rocks have higher concentrations of 'immobile' elements ( $\text{TiO}_2$  and Zr) and a restricted range of Ni contents, in contrast to the mafic Traboe cumulates which have a greater range of composition, including more primitive chemical compositions. These chemical data therefore show that the amphibolitised mafic Traboe cumulates are not the metamorphic equivalent of the Landewednack amphibolites, a hypothesis proposed by Green (1964b). These results suggest that the Landewednack amphibolites are not cumulate in origin, and that a volcanic origin is more likely. However, the low Ti and Zr contents in some specimens indicate that gabbro bodies are also present in the Landewednack amphibolites. The compositional ranges defined by the Porthoustock amphibolites (Shepherd, 1986) overlaps the Landewednack amphibolites, and is suggests that some samples of the Porthoustock amphibolites are volcanic in origin. The majority of samples of the Porthoustock amphibolite have low Zr contents, which suggests that these samples have gabbroic protoliths. In summary, the Landewednack and Porthoustock amphibolites are derived from both basaltic and gabbroic protoliths, although the majority of Landewednack amphibolites appear to be volcanic in origin and the majority of the Porthoustock amphibolites appear to be gabbroic in origin.

On the basis of the chemical data presented so far, it is not possible to confirm whether or not the Traboe cumulates are derived from the same parental magmas as the Landewednack amphibolites and mafic dykes. Rare-earth element chemistry and isotopic compositions of these rocks are presented in later sections in order to establish the chemical relationships between these different rocks and the palaeotectonic setting that they formed in.

### **6.2.6. Ordovician basement**

Analyses of amphibolite layers in the Old Lizard Head Series (OLHS) and deformed mafic sheets that cross-cut the OLHS are presented in this section and compared with the composition of mafic rocks from the Lizard Ophiolite Complex.

#### **6.2.6.a. Results**

Amphibolite layers in the OLHS (4.4 and 6.6 wt%) have MgO abundances which overlap the range defined by the Landewednack amphibolites, and deformed mafic sheets that cross-cut the OLHS have similar MgO contents (6.9 and 8.0 wt%) (Figure 6.9.a-b).

Amphibolite layers in the OLHS have TiO<sub>2</sub> abundances (1.1 and 1.5 wt%) that fall at the low-end of the range defined by the Landewednack amphibolites (Figure 6.9.a). The deformed mafic sheets that cross-cut the OLHS have similar TiO<sub>2</sub> contents (1.0 and 1.5 wt%) to the amphibolite layers in the OLHS.

Amphibolite layers in the OLHS possess low Ni contents (24 and 57 ppm) and deformed mafic sheets that cross-cut the OLHS have higher Ni contents (92 and 121 ppm) (Figure 6.9.b).

The amphibolite layers in the OLHS also possess high Zr contents (71 and 162 ppm), and similar values (80 and 131 ppm) are observed in the deformed mafic sheets that cross-cut the OLHS (Figure 6.10).

#### **6.2.6.b. Interpretation and discussion**

Overall the MgO, TiO<sub>2</sub>, Ni and Zr contents of these rocks cannot be used reliably to distinguish them from the mafic rocks of the Lizard Ophiolite Complex. In a later section (Section 6.3) the rare earth element chemistry provides the basis for a more satisfactory method of examining the geochemical properties of these rocks.

#### **6.2.7. Summary**

The analyses of major and trace elements of rocks from the Lizard Ophiolite Complex and Ordovician basement rocks provide several important geochemical constraints on the processes involved in the evolution of these rocks and the nature of the tectonic environment in which they formed:

- Major and trace element composition of the Lizard peridotites display systematic changes which support the subdivision based on field and microstructural evidence. These changes include an increase in CaO, Na<sub>2</sub>O, Al<sub>2</sub>O<sub>3</sub>, TiO<sub>2</sub>, Sc and Zr



abundances and a decrease in MgO contents from the spinel lherzolites to the mylonitic plagioclase-bearing peridotite and mylonitic amphibole-bearing peridotite.

- Changes in the major and trace element composition of the Lizard peridotites are interpreted to result from metasomatism in response to fluid-rich melt - rock interaction during deformation.
- Ultramafic Traboe cumulates display a much wider compositional range than the Lizard peridotites, which is consistent with the interpretation that these rocks are layered cumulates associated with mafic Traboe cumulates and represent the upper mantle/lower crust section of the Lizard Ophiolite Complex.
- Mafic Traboe cumulates and gabbroic veins show major and trace element characteristics comparable with those of gabbroic rocks from oceanic and ophiolitic environments.
- Landewednack amphibolites display major and trace element geochemical properties that distinguish them from the mafic Traboe cumulates. The results demonstrate that these amphibolites have compositions that suggests they are derived from basaltic and gabbroic protoliths.
- Mafic dykes and the Porthoustock amphibolites have compositions similar to those of the Landewednack amphibolites, but the majority of Porthoustock amphibolite samples are derived from a gabbro protolith.
- Mafic rocks from the Ordovician basement unit display compositions characteristic of basaltic rocks and are indistinguishable from the mafic rocks of the Lizard Ophiolite Complex.

---

### **6.3. Rare Earth Elements**

---

Rare earth element analyses of selected samples were performed with the Elan 6000 ICP-MS spectrometer located in the Department of Geological Sciences at the University of Durham. Full details of sample selection, sample preparation, the analytical procedure, analytical errors and representative analyses are presented in Appendices A and D.

Analyses presented in this section also include samples of ultramafic and mafic rocks taken from the field outcrops, Traboe cumulate complex borehole cores and the

Predannack borehole core (Institute of Geological Sciences borehole reports, 1978, 1979; Leake and Styles, 1984; M.T. Styles, *pers comm*, 1997).

### 6.3.1. Lizard peridotites - results

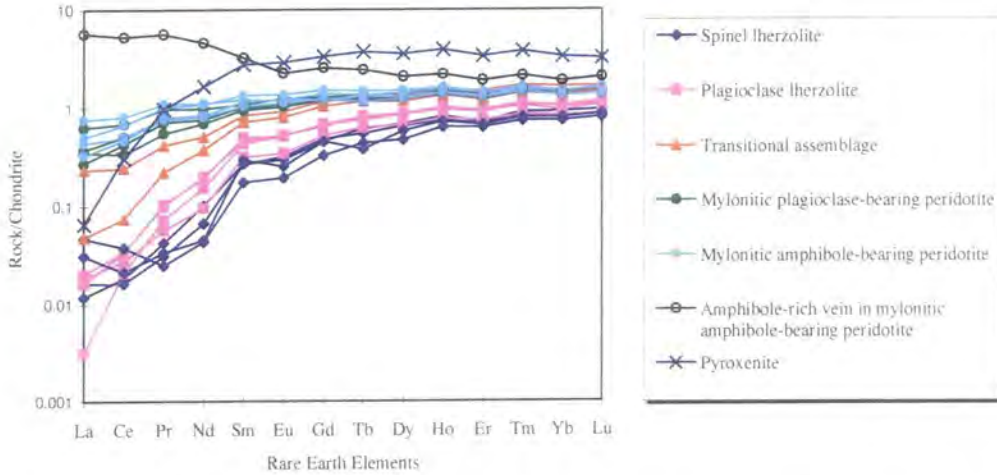


**Figure 6.11.** Chondrite normalised (Nakamura, 1974) rare earth element (REE) patterns for peridotites from the Lizard Ophiolite Complex.

In the following discussion the REE contents of the peridotites have been normalised to chondrite abundances using the normalising values of Nakamura (1974).

The spinel lherzolites and plagioclase lherzolites have nearly identical REE compositions, characterised by extreme depletion of LREE relative to chondrite (LREE close to detection limits), a positive slope from Sm to Lu and  $(Ce/Yb)_N$  ratios of (average = 0.029 and 0.03 respectively)(Figure 6.11). The two transitional assemblage peridotites analysed possess REE contents which are intermediate between the plagioclase lherzolites and mylonitic peridotites, and have  $(Ce/Yb)_N$  ratios of (0.05 and 0.15). The REE compositions of the mylonitic plagioclase bearing-peridotite and mylonitic amphibole-bearing peridotites are identical showing HREE contents ( $1 \times$  chondrite), which are nearly flat between Gd and Lu. They are only slightly depleted in LREE, with average  $(Ce/Yb)_N$  ratios of (average = 0.35) for the mylonitic plagioclase bearing-peridotite and (average = 0.44) for mylonitic amphibole-bearing peridotites. An amphibole-rich vein in a sample of mylonitic amphibole-bearing peridotite shows a marked LREE-enriched composition from La to Eu, with a  $(Ce/Yb)_N$  ratio of 2.8. This composition suggests that the LREE are predominantly hosted by the amphibole in these rocks.

A pyroxenite layer, hosted by spinel lherzolite, also shows a REE profile similar to that of the spinel lherzolites and is characterised by extreme LREE depletion giving a  $(Ce/Yb)_N$  ratio (0.09). However, the pyroxenite layer has a higher HREE abundance than the mylonitic peridotites. The pyroxenite layer is predominantly composed of clinopyroxene, and it is proposed that this mineral hosts a high-proportion of the HREE in the peridotites in order to account for the relatively high HREE content, which is known from mineral separate studies e.g. Frey (1969).

### 6.3.2. Rocks associated with the Lizard peridotites - results

Samples with a E prefix were analysed at NIGL (BGS, Keyworth) (M.T. Styles, *pers. comm.*, 1997).

A variety of REE patterns are displayed by the different rocks associated with the Lizard peridotites, and these generally show higher REE relative to chondrite

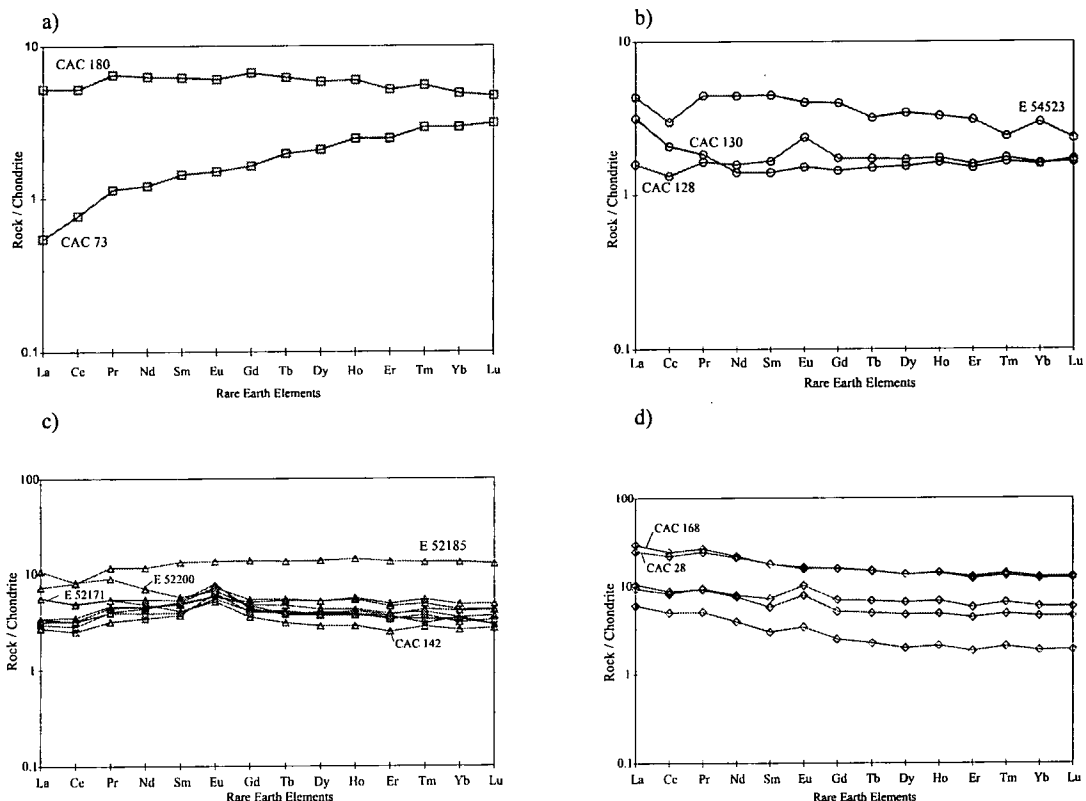


**Figure 6.12.** Chondrite normalised (Nakamura, 1974) rare earth element (REE) patterns of various rocks associated with the Lizard peridotites: (a) Feldspathic bands, (b) Ultramafic Traboe cumulates, (c) Mafic Traboe cumulates and (d) Gabbroic veins.

(Figure 6.12.a-d). The REE patterns of the ultramafic Traboe cumulates are different from the patterns characteristic of the Lizard peridotites and in particular they do not display the strong LREE depletion observed in the spinel lherzolites and plagioclase lherzolites from the Lizard. A feldspathic band (CAC 180) has a REE pattern which shows a positive slope from La to Pr, and a slight decrease in REE abundances from Pr to Lu, with a peak of 7\* chondrite at Gd (Figure 6.12.a). A sample of mylonitic amphibole-bearing peridotite containing feldspathic bands (CAC 73) possesses a different REE pattern from the feldspathic band (CAC 180). The pattern displayed by CAC 73 shows a strong increase from LREE to HREE, and is also very different to the REE patterns of the mylonitic amphibole-bearing peridotite, having higher HREE abundances.

The ultramafic Traboe cumulates display variable REE patterns and abundances (Figure 6.12.b). Sample CAC 130 shows a negative slope from La to Nd, a nearly flat REE pattern at 1.5\* chondrite from Nd to Lu and a minor positive Eu anomaly. Sample CAC 128 shows a different REE pattern, with similar REE abundances at 1.6\* chondrite from La to Lu. However, there is a marked positive Eu anomaly and a negative Ce anomaly. Sample E54523 also shows a very different REE pattern from samples CAC 130 and CAC 128. LREE increase in abundance from La to Nd with a negative anomaly displayed by Ce and there is a general decrease in REE from Sm to Lu. Tb and Eu display minor negative anomalies.

The mafic Traboe cumulates have higher REE contents than the Lizard peridotites, with Lu ranging between 2.7 and 12.6\* chondrite (Figure 6.12.c). With the exception of sample E52185, all of the samples show a strong positive Eu anomaly. The REE pattern of sample E52185 bears a strong similarity to the REE patterns of the Landwednack amphibolites (Section 6). This includes a positive slope from La to Sm and a fairly flat REE pattern between Sm and Lu at 14\* chondrite. The other mafic Traboe cumulates can be sub-divided into two groups on the basis of their REE patterns. Samples CAC 142 and E52200 display a negative slope from La to Lu, with  $[La]_N$  varying from 5.6 to 10.6 and a minor negative Ce anomaly that could be due to alteration. E52171 displays a slightly different REE pattern, with the REE showing a flat pattern between La and Sm, with  $[La]_N$  of 5.6. A second group is characterised by a REE pattern showing a slight increase from La to Sm and a decrease from Gd to Lu, with  $[La]_N$  varying between 2.7 and 3.5. A few of this second group of samples show a minor negative Ce anomaly.

The gabbroic veins can be subdivided into two groups on the basis of their REE patterns (Figure 6.12.d). Two samples, CAC 28 and 168, have higher  $[La]_N$ , of 25 and 29 respectively. These samples show an decrease in REE from La to Lu, and a minor negative Ce anomaly. A second group is characterised by a clear positive Eu anomaly and an decrease in REE from La to Lu, with  $[La]_N$  varying between 6 to 10.3. The REE pattern of this second group is similar to the REE patterns of two samples of mafic Traboe cumulate (CAC 142 and E52200).

MORB normalised (Pearce, 1980) geochemical patterns can also be used to distinguish between the mafic Traboe cumulates and the gabbroic veins (Figure 6.13.a-b). The mafic Traboe cumulates show enrichment of Sr, K, Rb and Ba relative to MORB and this is probably related to alteration (Figure 6.13.a). The other elements are depleted relative to MORB, particularly in Ta and Nb. The gabbroic veins are also enriched in Sr, K, Rb and Ba relative to MORB (Figure 6.13.b). There are no clear negative Ta and Nb anomalies. However, there is a strong negative Th anomaly, which distinguishes these rocks from the mafic Traboe cumulates.

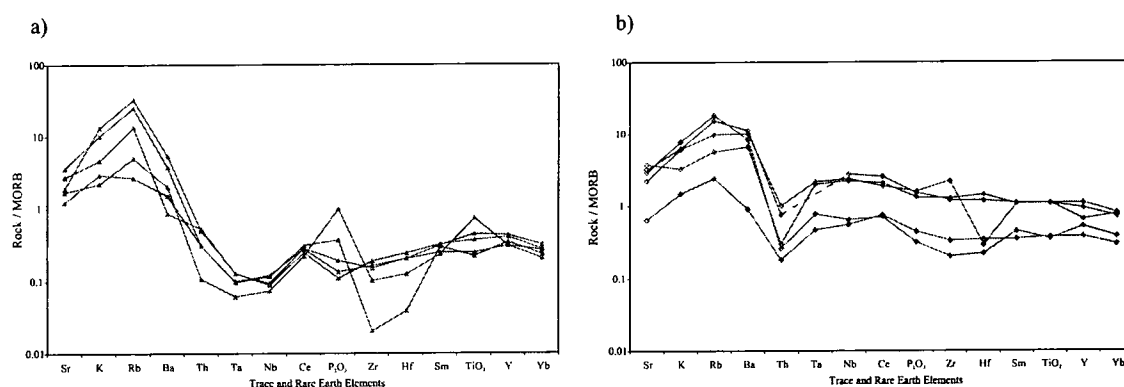


**Figure 6.13.** MORB normalised (Pearce, 1980) trace and rare earth element patterns for: (a) Mafic Traboe cumulates and (b) Gabbroic veins, associated with peridotites from the Lizard Ophiolite Complex.

### 6.3.3. Lizard peridotites and associated rocks – Interpretation and discussion

The spinel lherzolites and plagioclase lherzolites from the Lizard show extreme depletion of LREE relative to chondrite. Strongly LREE-depleted patterns are observed for spinel lherzolites from Errio-Tobbio lherzolites, NW Italy (Ottenello *et al.*, 1979), spinel lherzolites from the Central Dinaric ophiolite belt, Yugoslavia (Lugovic *et al.*, 1991) and Internal Ligurides (Northern Apennine) peridotites (Ottenello *et al.* 1984)

(Figure 6.14). Davies (1984) demonstrated that the very low abundances of LREE in association with relatively high HREE of the spinel lherzolites from the Lizard cannot be reproduced by batch melting models. However, these LREE-depleted compositions could be produced by fractional melting or incremental melting of very small melt increments (Lugovic *et al.*, 1991; Rampone *et al.*, 1991).

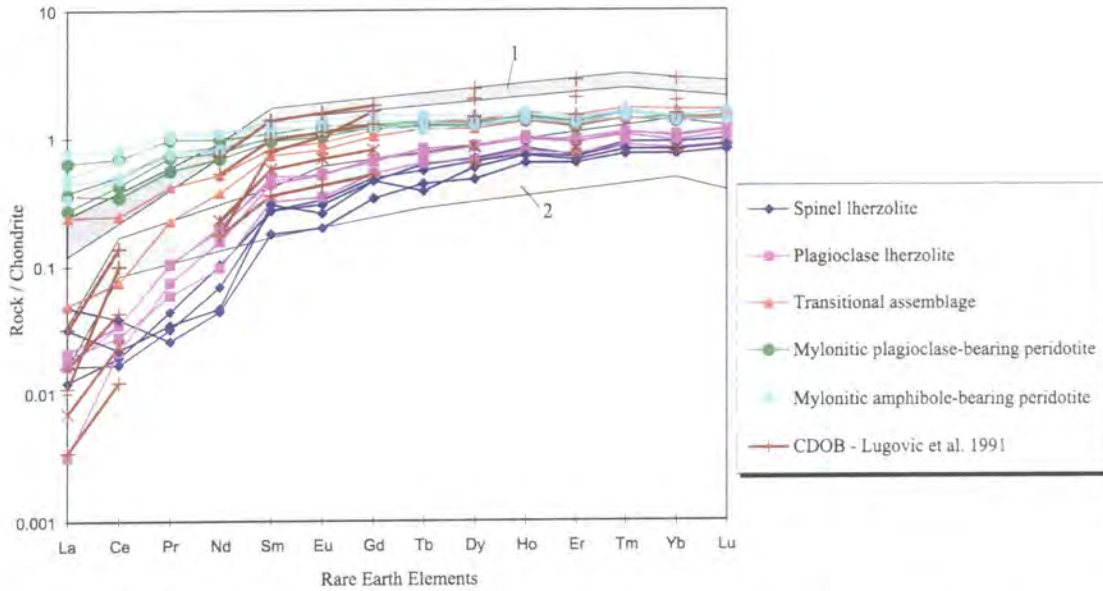


**Figure 6.14.** Chondrite normalised (Nakamura, 1974) rare earth element (REE) patterns for peridotites from the Lizard Ophiolite Complex compared lherzolites from the Central Dinaric Ophiolite Belt (Lugovic *et al.*, 1991), (1) spinel lherzolites from Errio-Tobbio lherzolites, NW Italy (Ottenello *et al.*, 1979), and (2) peridotites from the Internal Ligurides (Northern Apennine) (Ottenello *et al.*, 1984).

The mylonitic plagioclase-bearing peridotite and mylonitic amphibole-bearing peridotite and, to a lesser extent the transitional assemblage, show clear evidence for LREE enrichment relative to the spinel and plagioclase lherzolites. The LREE enrichment is illustrated by Figure 6.14, which demonstrates a progressive increase in LREE from spinel lherzolite to mylonitic plagioclase-bearing peridotite and mylonitic amphibole-bearing peridotite via plagioclase lherzolite and transitional assemblage peridotite. The enrichment of LREE in the Lizard peridotites, parallels an increase in the abundance of CaO, Na<sub>2</sub>O, Al<sub>2</sub>O<sub>3</sub>, TiO<sub>2</sub>, Sc and Zr (see Section 6.2), and this is illustrated by a plot of Al<sub>2</sub>O<sub>3</sub> wt% versus Sm (ppm)(Figure 6.15). It has already been suggested in Section 6.2.4. that melt/fluid-rock interaction is responsible for the resultant metasomatism of the mylonitic peridotites.

The enrichment of LREE in the mylonitic peridotites relative to the spinel and plagioclase lherzolites is therefore consistent with interaction with a LREE-enriched



melt. Small-scale LREE enrichment of peridotites adjacent to veins is well documented in the literature and includes mantle xenoliths from the Rhenish Massif (Witt and Seck, 1989), peridotites from the Lherz Massif (McPherson *et al.*, 1996), and mantle xenoliths from Romania (Chalot-Prat and Boullier, 1997). The major, trace and rare earth element enriched mylonitic peridotites from the Lizard are exposed over of

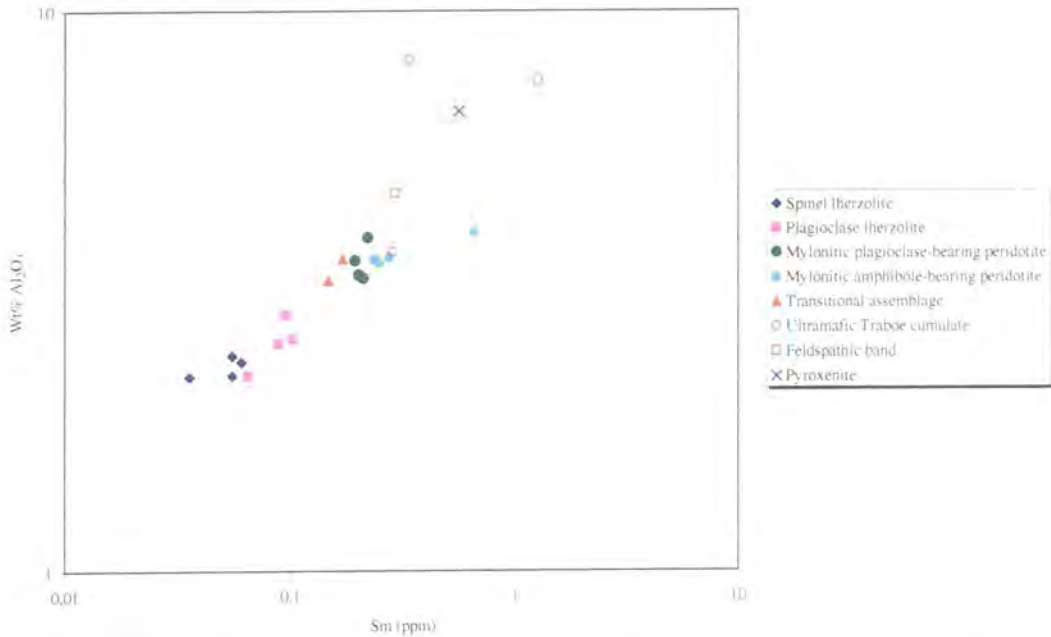


**Figure 6.15.** Plot of wt%  $\text{Al}_2\text{O}_3$  versus Sm (ppm) for peridotites, ultramafic Traboe cumulates and feldspathic bands from the Lizard Ophiolite Complex.

several kilometres (Chapter 3), and therefore the scale of melt-rock interaction of the Lizard peridotites differs substantially from the examples of small scale metasomatism adjacent to veins discussed above. However, km-scale pervasive melt percolation is invoked to explain metasomatism of peridotites from the Ronda Massif, Spain (Van der Wal and Bodinier, 1996). If a fluid/melt were to pass over a long distance through mantle peridotites it will eventually lose its LREE-enriched characteristics through equilibration with the peridotite (Witt and Seck, 1989)(Figure 6.16). Therefore, a process which avoids progressive modification of the composition of an infiltrating melt through equilibrium with the wall-rock must account for the consistent LREE enrichment of the mylonitic peridotite from the Lizard. The development of a reaction zone, which moves through the rock, is a possible mechanism of avoiding melt-rock interaction involving a melt with an evolving composition. Such a process would

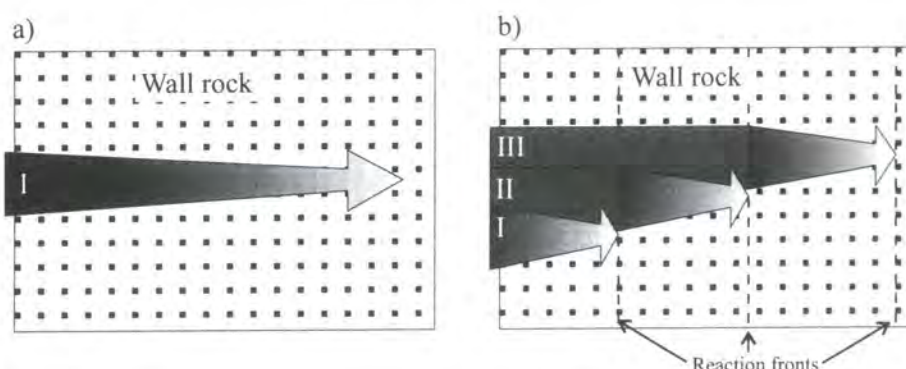


**Figure 6.16.** Cartoon illustrating two different melt-rock interaction processes: (a) Single melt batch (I) becomes progressively equilibrated with the wall rock and results in heterogeneous metasomatism of the wall rock (see text), (b) The development of reaction fronts and the infiltration of several batches of melt (I-III) produces homogeneous metasomatism of the wall rock (see text).

involve a melt which reacts with the rock until equilibrium is reached and subsequent batches of melt would pass through this zone unmodified until they reach the reaction front (McPherson *et al.*, 1996)(Figure 6.16). The shearing and grain-size reduction associated with formation of the mylonitic peridotites would facilitate the movement of melts through the rock.

The ultramafic Traboe cumulates and feldspathic bands are also included in Figure 6.15. A feldspathic band (CAC 180) shows the highest Sm concentration, which is probably related to the high content of clinopyroxene and amphibole in this sample (Chapter 4).

The REE patterns of the ultramafic Traboe cumulates are more variable than those observed in the mylonitic peridotites, and include LREE enriched patterns. In particular, sample CAC 128 shows a clear positive Eu anomaly and CAC 130 shows a minor positive Eu anomaly. The anomalies are typical features of plagioclase accumulation in cumulates (Beniot *et al.*, 1996). Several of the ultramafic Traboe cumulates display a negative Ce anomaly, which is not observed in the Lizard peridotites, and is probably due to secondary alteration. The varied REE patterns of these ultramafic cumulates is consistent with their variable mineralogy (Chapter 4). The high REE content of clinopyroxene and amphibole in particular means that they have a strong influence on the whole rock REE pattern.

The mafic Traboe cumulates were subdivided on the basis of REE patterns and include LREE-enriched and LREE-depleted samples, comparable with gabbros from ophiolitic environments (Beniot *et al.*, 1996; Kelemen *et al.*, 1997). These mafic cumulates all show a clear positive Eu anomaly and this is a feature of plagioclase

accumulation. Several of the mafic Traboe cumulates also show the slight negative Ce anomaly observed in the ultramafic Traboe cumulates. The Ce anomaly may be related to secondary alteration. The shape of the REE pattern in the LREE-depleted mafic Traboe cumulates is probably controlled by accumulation of clinopyroxene (now altered to amphibole). The LREE-enriched mafic Traboe cumulates appear to have a REE pattern controlled by plagioclase, which is usually LREE-enriched relative to clinopyroxene (Beniot *et al.*, 1996).

The gabbroic veins all show LREE enriched patterns. These rocks are subdivided into two groups on the basis of REE patterns. One group of samples (CAC 28 and 168) displays higher overall REE abundances and lacks a Eu anomaly. A second group is characterised by a strong positive Eu anomaly, a feature of plagioclase accumulation. All of the samples show minor negative Ce anomalies, similar to the anomalies observed in the ultramafic and mafic Traboe cumulates. These Ce anomalies may be related to secondary alteration.

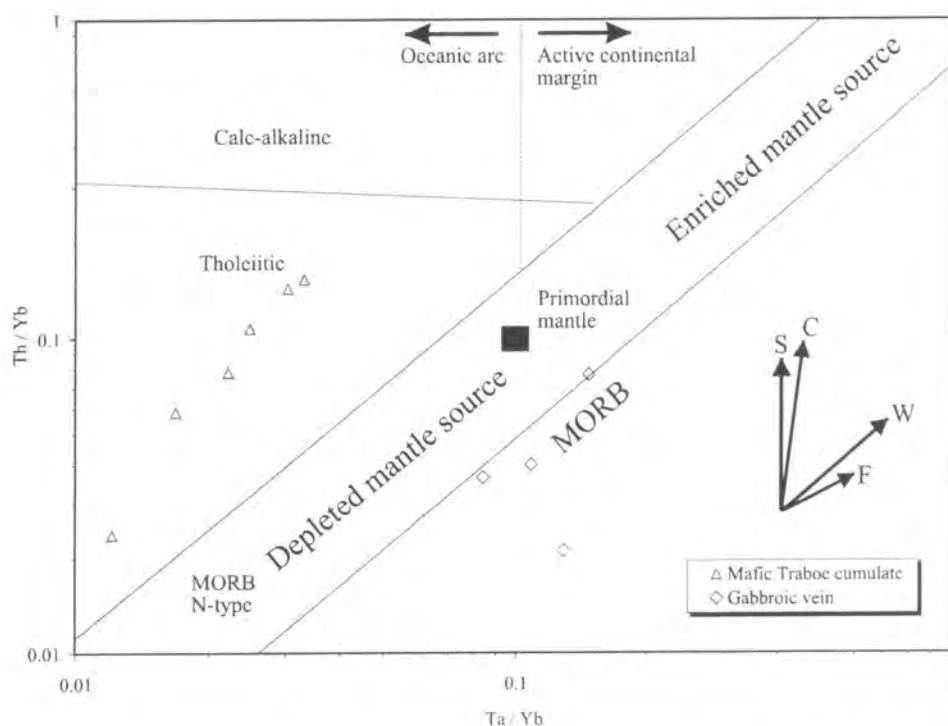


**Figure 6.17.** Th/Yb versus Ta/Yb discrimination diagram (Pearce, 1983) showing mafic Traboe cumulates and gabbroic veins from the Lizard Ophiolite Complex. The graph demonstrates that these different groups of rocks possess different ratios. Vectors shown indicate the influence of subduction components (S), within-plate enrichment (W), crustal contamination (C) and fractional crystallisation. (F)

A plot of Th/Yb ratio versus Ta/Yb ratio (Figure 6.17) demonstrates that the mafic Traboe cumulates define a linear trend within the tholeiitic compositional field, and this trend is probably related to source variations, including crustal contamination, and may also be influenced by different degrees of fractional crystallisation. However, the gabbroic mantle dykes do not plot on this trend, and are characterised by higher Ta/Yb ratios, therefore it is proposed that they are derived from distinct magma sources. The gabbroic veins possess Th/Yb ratio versus Ta/Yb ratios that are similar to MORB and the Landewednack amphibolites and mafic dykes (Section 6.3.4.b). The composition of both the mafic Traboe cumulates and gabbroic mantle dykes is consistent with depleted mantle sources.

#### **6.3.4. Amphibolites and mafic dykes**

Analyses of Landewednack amphibolites, Porthoustock amphibolites and mafic dykes from the Lizard Ophiolite Complex are presented in Appendix D. One of the main aims of this Section is to determine whether or not the Landewednack amphibolites share similar geochemical characteristics with the mafic Traboe cumulates and Porthoustock amphibolites. In addition the compositions of the amphibolites and mafic dykes are compared with data taken from the literature for volcanic and plutonic rocks from ophiolites, in order to verify the tectonic environment in which the Lizard Ophiolite Complex formed.

##### **6.3.4.a. Results**

Chondrite-normalised abundances of REE for the Landewednack amphibolites are presented in Figure 6.18. This diagram demonstrates that the amphibolites can be subdivided into three general groups on the basis of REE patterns. The majority of samples (A) show a pattern defined by a sharp increase in LREE from La ( $[La]_N = 8.9 - 28$ ) to Pr ( $[Pr]_N = 14-38$ ), then a small decrease in REE abundance to Lu ( $[Lu]_N = 8.5 - 21.5$ ) (Figure 6.18). A few samples show small negative Eu anomalies. A second group (B) is characterised by a increase in LREE from La ( $[La]_N = 7$  and  $11.5$ ) to Sm ( $[Sm]_N = 12.8$  and  $18$ ), then nearly flat REE patterns to Lu ( $[Lu]_N = 13$  and  $15$ ) (Figure 6.18). The third group (C) displays lower REE abundances and is characterised by a slight increase of LREE from La ( $[La]_N = 5.8$  and  $6.3$ ) to Pr ( $[Pr]_N = 7$  and  $7.9$ ), then a



slight decrease to Lu ( $[Lu]_N = 5.5$  and  $5.8$ ) (Figure 6.18). This group is also distinguished by the presence of a small positive Eu anomaly.

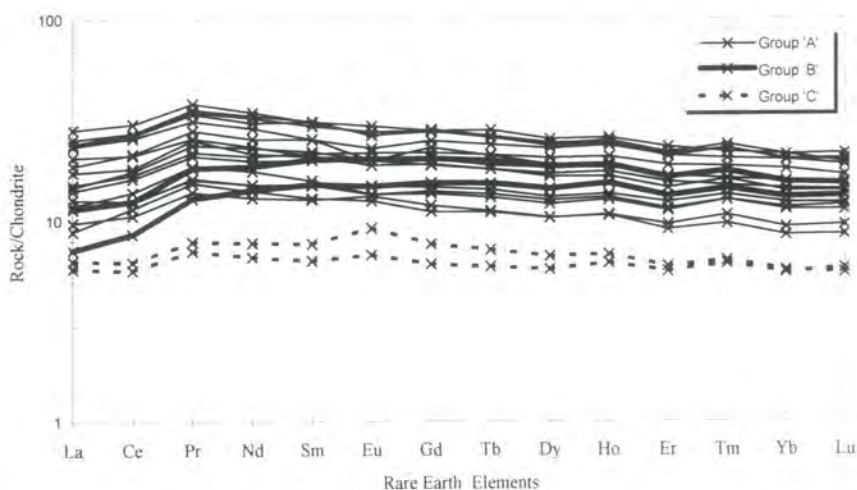


**Figure 6.18.** Chondrite normalised (Nakamura, 1974) rare earth element (REE) patterns for Landewednack amphibolites from the Lizard Ophiolite Complex. The amphibolites have been subdivided into three groups (A-C) on the basis of different REE patterns.

The Porthoustock amphibolites display slightly higher REE contents than the Landewednack amphibolites. The LREE abundance increases from La ( $[La]_N = 41 - 56$ ) to Pr ( $[Pr]_N = 51 - 66$ ), then shows a small decrease in REE to Lu ( $[Lu]_N = 18 - 27$ ) (Figure 6.19a). The REE pattern of the Porthoustock amphibolites is also distinguished from the Landewednack amphibolites by the presence of a clear negative Eu anomaly.

Mafic dykes from the Lizard Ophiolite Complex have chondrite normalised REE patterns that strongly resemble the REE patterns of the majority of the Landewednack amphibolites (group A). The LREE abundances increase from La ( $[La]_N = 7.5 - 19$ ) to Pr ( $[Pr]_N = 13.4 - 23.3$ ), then decrease to Lu ( $[Lu]_N = 8.3 - 12$ ) (Figure 6.19b). A few samples show a slight positive Eu anomaly.

A plot of the amphibolites and mafic rocks normalised to values of average MORB (Pearce, 1983) is used with the elements divided into two groups based on their relative mobility in aqueous fluids. Sr, K, Rb and Ba are mobile and plot on the left side of the graph, whilst the remaining elements are immobile. These immobile elements are not considered to be greatly changed by fractional crystallisation or variable degrees of partial melting and may therefore be used to discuss source characteristics (Pearce, 1983). The MORB-normalised REE abundances of the

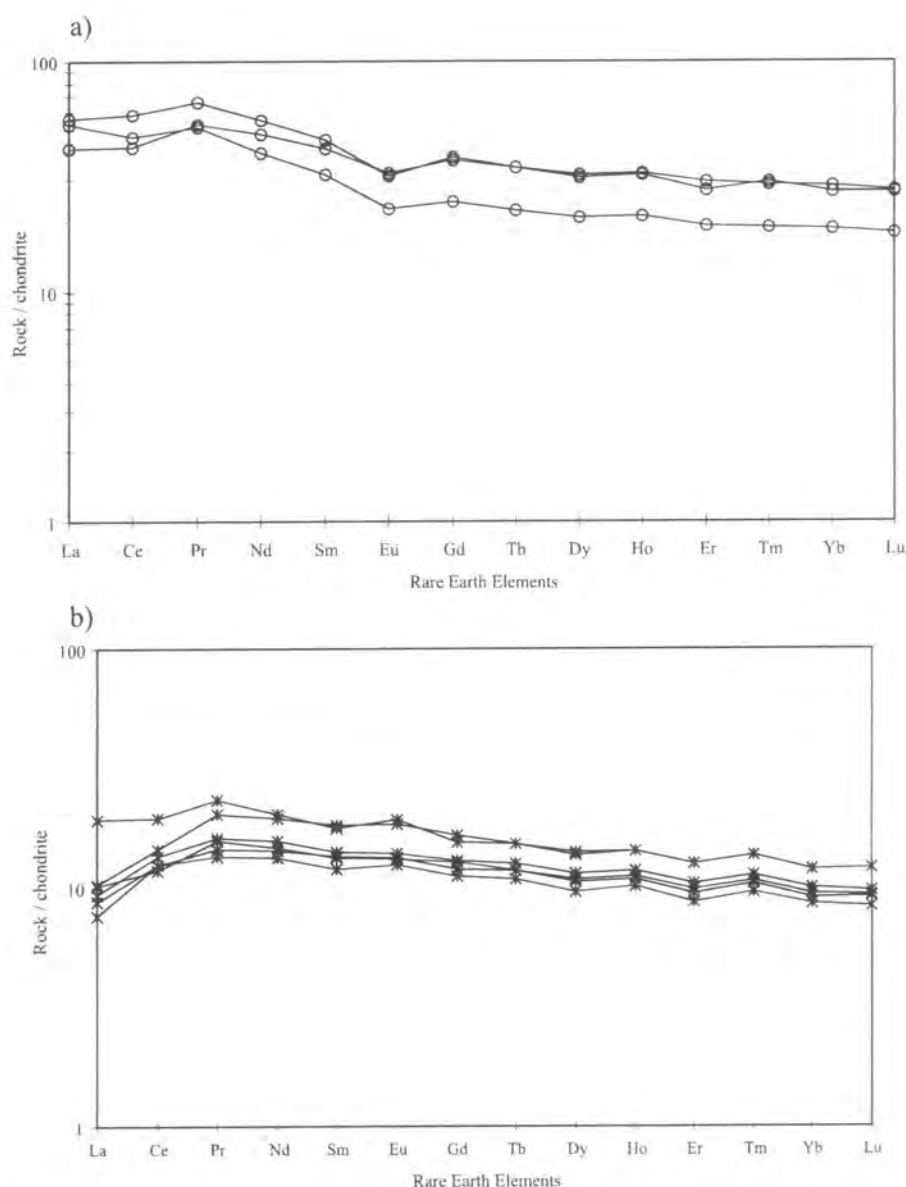


**Figure 6.19.** Chondrite normalised (Nakamura, 1974) rare earth element (REE) patterns for: **(a)** Porthoustock amphibolites and **(b)** Mafic dykes from the Lizard Ophiolite Complex.

Landwednack amphibolites generally show enrichment of the mobile elements, Sr, K, Rb and Ba, relative to MORB (Figure 6.20a). However, some of the amphibolites show a marked negative Th anomaly, whilst others show a negative Th-Ta-Nb anomaly. These different patterns cannot be correlated with the different groups defined on the basis of chondrite-normalised REE patterns.

The MORB normalised REE pattern of the Porthoustock amphibolite can be used to distinguish these rocks from the Landwednack amphibolites. The Porthoustock amphibolites do not show a large negative Th anomaly or a Th-Ta-Nb anomaly



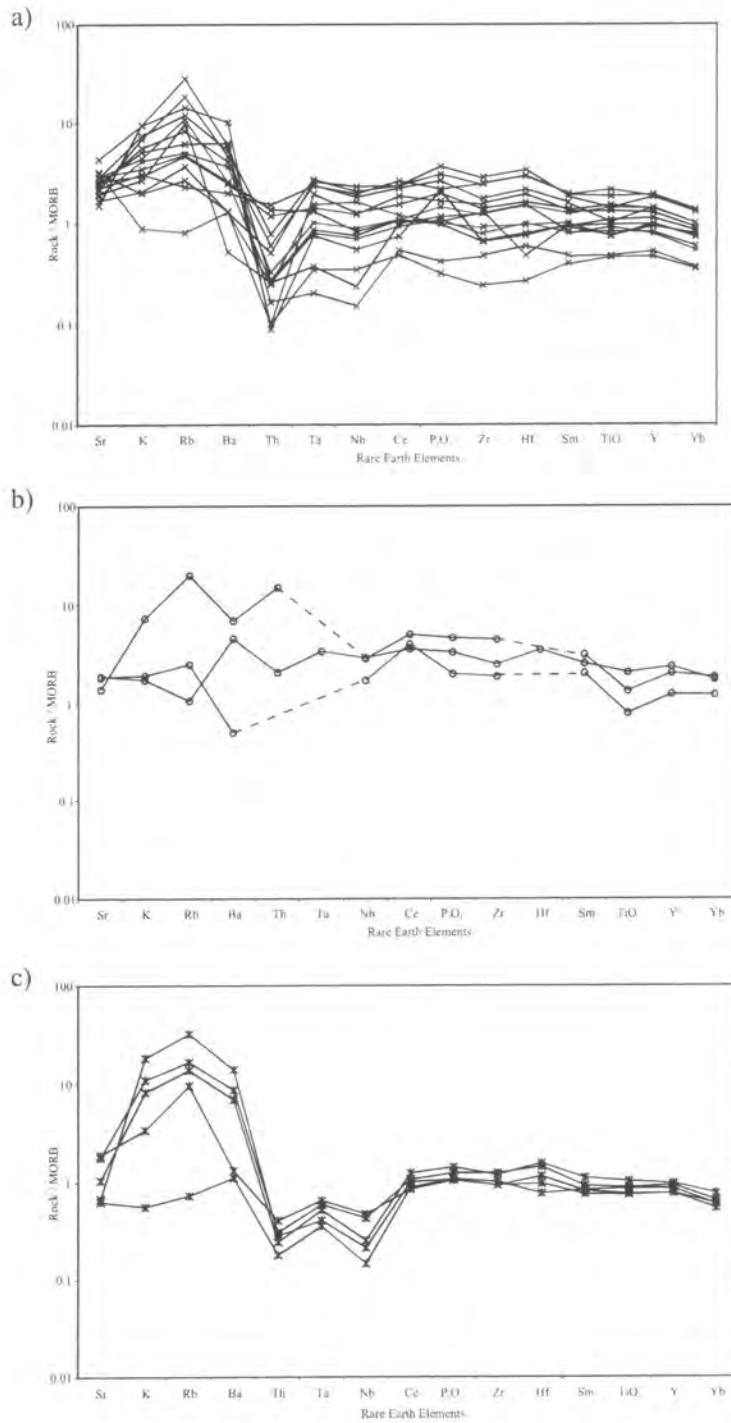


**Figure 6.20.** MORB normalised (Pearce, 1980) trace and rare earth element patterns for: **(a)** Landewednack amphibolites and **(b)** Porthoustock amphibolites and **(c)** Mafic dykes from the Lizard Ophiolite Complex.

(Figure 6.20b). The Porthoustock amphibolites display variable Sr, K, Rb and Ba contents.

Mafic dykes display a MORB-normalised REE pattern (Figure 6.20c) which is very similar to that of the Landewednack amphibolites. The mafic dykes are strongly

enriched in K, Rb and Ba relative to MORB, and show a clear negative Th-Ta-Nb anomaly, comparable with some of the Landewednack amphibolites.

#### **6.3.4.b. Interpretation and discussion**

The chondrite-normalised patterns defined by the Landewednack amphibolites and mafic dykes fall in the range defined for MORB (Schilling *et al.*, 1983) (Figure 6.21a-c). The group B Landewednack amphibolites, characterised by unfractionated HREE and depleted LREE are similar to the REE patterns of typical T-MORB (Schilling *et al.*, 1983) and suggest a mantle source depleted in LREE (Figure 6.21a). The majority of the Landewednack amphibolites have a different REE pattern (Group A) i.e. decreasing values from Pr to Lu and mafic dykes from the Lizard define a similar pattern to these (Figure 6.21a and c). The LREE depleted pattern defined by these rocks overlaps the REE pattern of lavas and dykes from the Oman ophiolite (Kelemen *et al.*, 1997) and mafic dykes from the Central Dinaric ophiolite belt, Yugoslavia (Lugovic *et al.*, 1991)(Figure 21a and c). Overall the general shapes of the patterns for the Landewednack amphibolites (Group B) and mafic dykes are similar to those of MORB or back-arc basins. The group C Landewednack amphibolites show lower REE abundances and resemble the patterns defined by the mafic Traboe cumulates (see Figure 6.12c). These samples were collected from just below thrust-contacts on the east coast of the Lizard where mafic Traboe cumulates also occur. The unusual REE patterns in these rocks suggests that the samples analysed may represent rocks composed of tectonically interleaved Landewednack amphibolite and mafic Traboe cumulate. This would explain the similarities between the compositions of these rocks and the mafic Traboe cumulates.

The MORB-normalised REE patterns of the Landewednack amphibolites and mafic dykes show enrichment of Sr, K, Rb and Ba and it is proposed that this enrichment is related to secondary alteration during amphibolite-facies metamorphism. The clear negative Th anomaly in the group A Landewednack amphibolites may be related to loss of a small melt fraction during metamorphism.

The LREE-enriched chondrite-normalised patterns displayed by the Porthoustock amphibolites suggest that these rocks are derived from a different magma source than that of the Landewednack amphibolites and mafic dykes which are LREE-

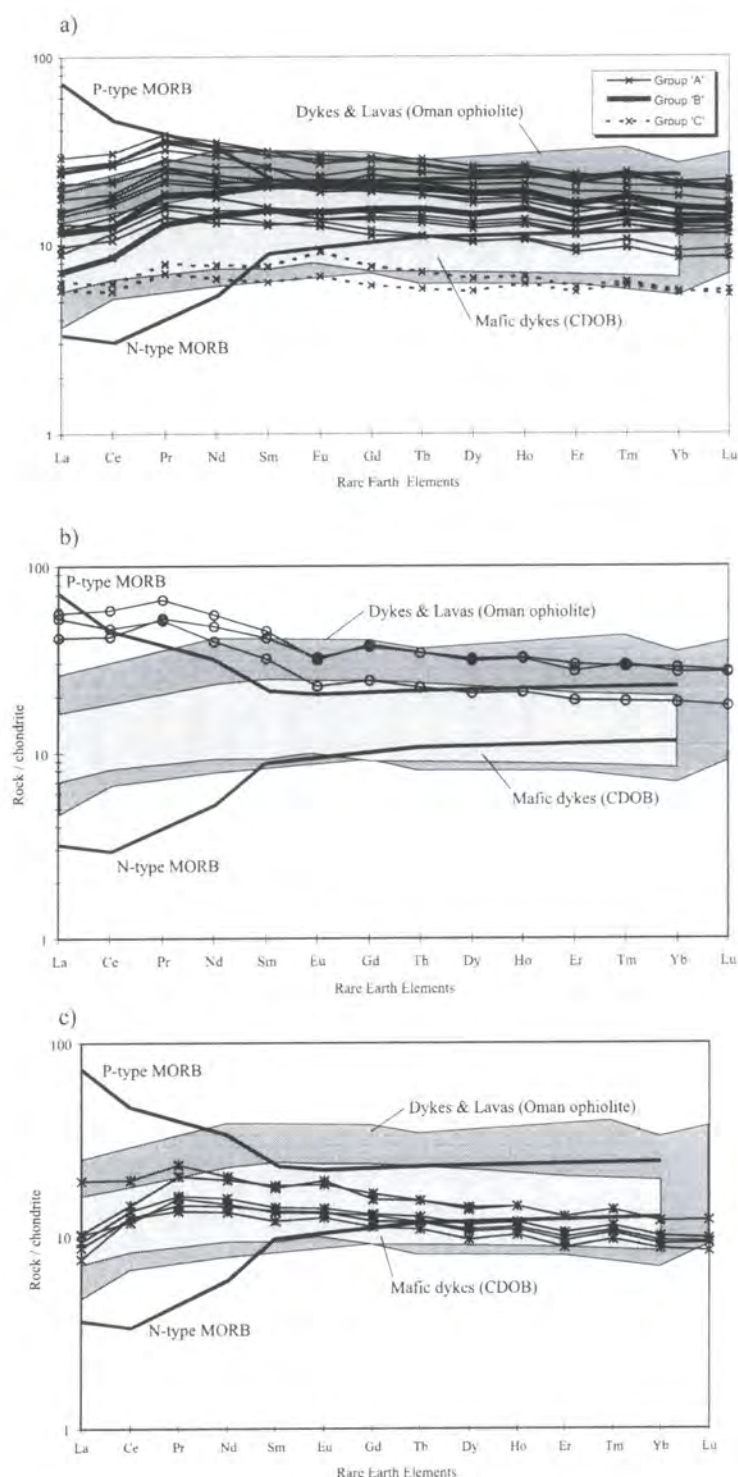


**Figure 6.21a-c.** Chondrite normalised (Nakamura, 1974) rare earth element (REE) patterns for: (a) Landewednack amphibolites, (b) Porthoustock amphibolites and (c) Mafic dykes from the Lizard Ophiolite Complex compared with the REE patterns defined from mafic rocks from oceanic environments and ophiolites: MORB (Schilling *et al.*, 1983), mafic dykes from the Central Dinaric Ophiolite Belt, Yugoslavia (Lugovic *et al.*, 1991) and dykes and lavas from the Oman ophiolite (Kelemen *et al.*, 1997).

depleted. The REE pattern of the Porthoustock amphibolites suggests that the source may have been more enriched in REE than the source of the Landewednack

amphibolites and mafic dykes. This pattern is more typical of a subduction-related or island arc origin (Styles, 1992), because rocks formed in these environments are invariably LREE-enriched due to contamination involving slab-derived fluids, in contrast to the MORB-like Landewednack amphibolites and the mafic dykes. The

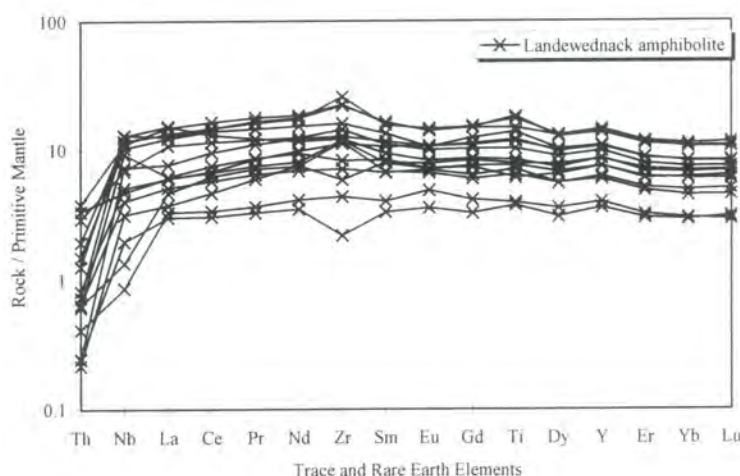


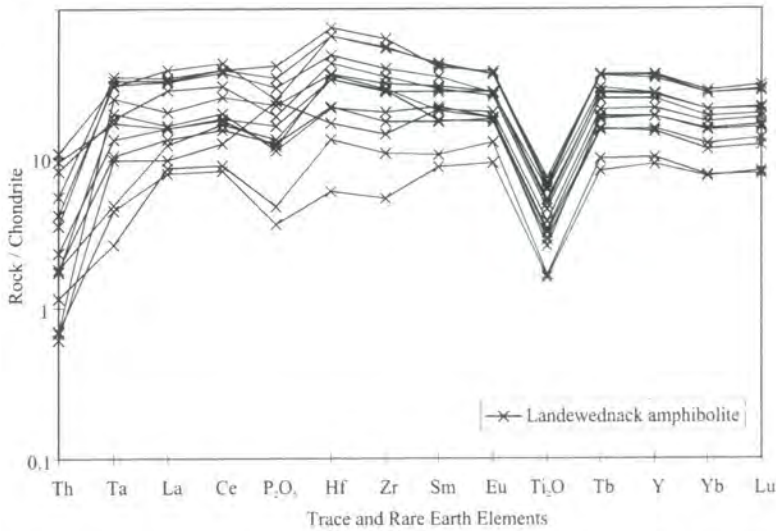
**Figure 6.22.** Primitive mantle (Hoffman, 1988) normalised trace and rare earth element pattern of Landewednack amphibolites from the Lizard Ophiolite Complex. The absence of a negative Ta anomaly suggests the amphibolites do not have island-arc – suprasubduction-zone affinities.

negative Eu anomaly displayed by the Porthoustock amphibolites suggests that Eu was preferably partitioned into plagioclase during fractionation (Wilson, 1989). Davies (1984) presented REE data for an early dyke suite, which showed LREE-enriched characteristics similar to those of the Porthoustock amphibolites. These dykes are exposed within the sheeted dyke complex within the Crousa gabbro, immediately south of the Porthoustock amphibolites. These data therefore support the conclusions of Bromley (1979), Vearncombe (1980) and Gibbons & Thompson (1991), who suggested that the Porthoustock amphibolites may represent the deformed equivalent of a gabbro-sheeted dyke complex. The samples of Porthoustock amphibolite analysed may therefore represent the deformed equivalent of the early REE-enriched dyke suite.

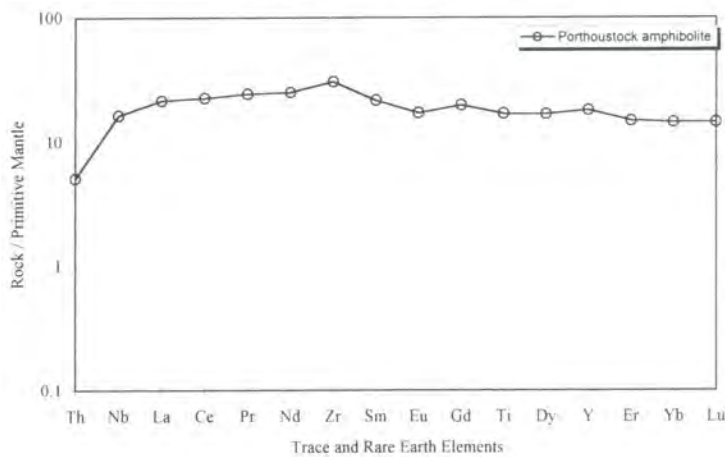
The Landewednack amphibolites do not display a negative Nb anomaly on a plot of REE normalised to primitive mantle values of Hoffman (1988) (Figure 6.22) or a negative Ta anomaly on REE patterns normalised to the chondrite values of Elthon (1991) (Figure 6.23) and this confirms the non-arc, MORB like characteristics of these rocks. The Porthoustock amphibolites, which showed LREE enriched patterns on a chondrite normalised plot do not display a Nb or Ta anomaly on either Figure 6.24 or



Figure 6.25, and this suggests that they do not have a island-arc – suprasubduction-zone geochemical characteristics.



**Figure 6.23.** Chondrite (Elthon, 1991) normalised trace and rare earth element pattern of Landewednack amphibolites from the Lizard Ophiolite Complex. The absence of a negative Ta anomaly suggests the amphibolites do not have island-arc – suprasubduction-zone affinities.



**Figure 6.24.** Primitive mantle (Hoffman, 1988) normalised trace and rare earth element pattern of Porthoustock amphibolite from the Lizard Ophiolite Complex. The absence of a negative Ta anomaly suggests the amphibolites do not have island-arc – suprasubduction-zone affinities.

The Landewednack amphibolites and mafic dykes predominantly plot in the ‘ocean floor basalt’ field of a Ti-Zr-Y discriminant diagram (Pearce and Cann, 1973), which is typical of basalt from mid-ocean ridge (MORB) and back-arc basins environments (Figure 6.26). The elements (Ti-Zr-Y) used in this diagram are considered to be the least susceptible to secondary alteration and therefore these are considered to represent protolith compositions. The Porthoustock amphibolites also possess MORB chemistry. The oceanic affinity of the Landewednack amphibolites

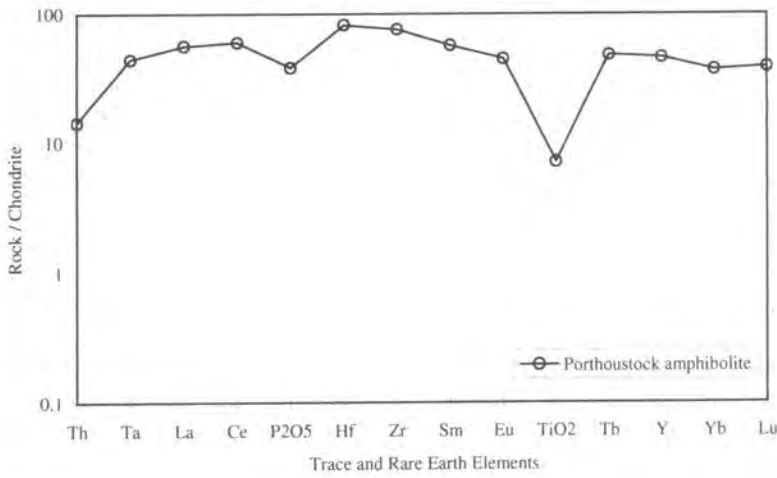


**Figure 6.25.** Chondrite (Elthon, 1991) normalised trace and rare earth element pattern of Porthoustock amphibolite from the Lizard Ophiolite Complex. The absence of a negative Ta anomaly suggests the amphibolites do not have island-arc – suprasubduction-zone affinities.

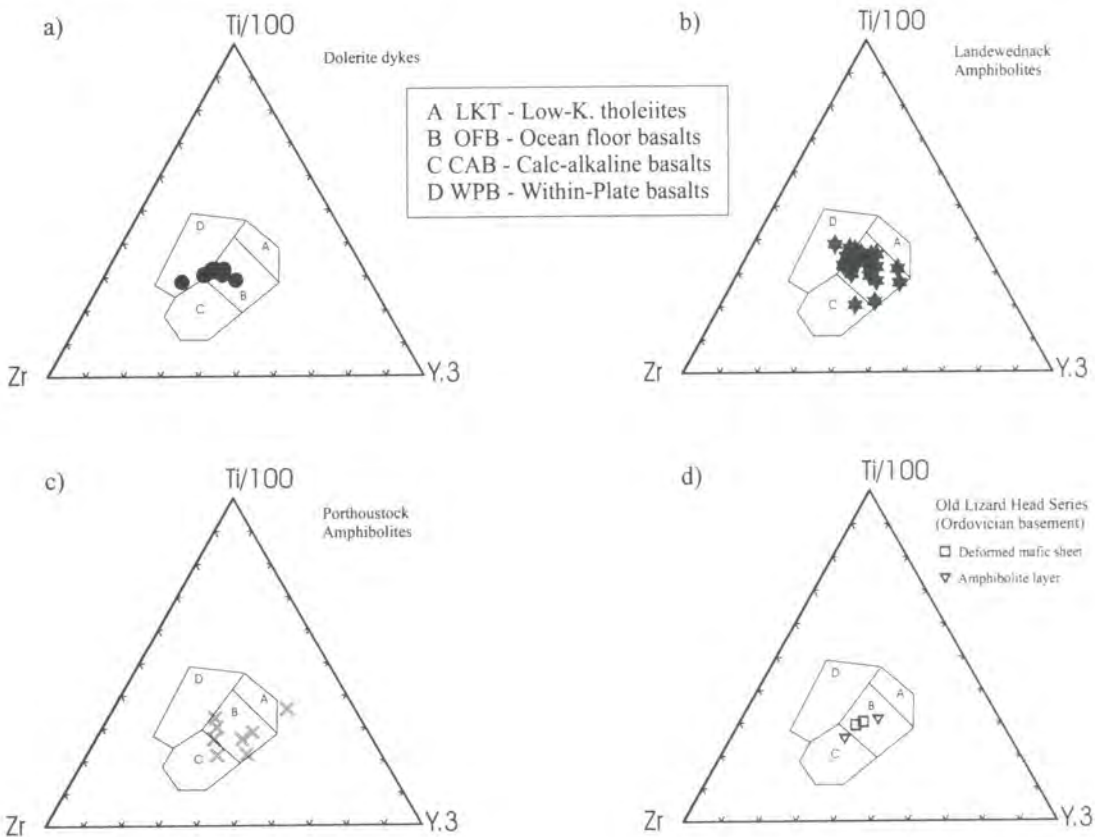


**Figure 6.26.** Ti-Zr-Y discriminant diagram (Pearce and Cann, 1973), which demonstrates the ‘oceanic character’ of: (a) mafic dykes, (b) Landewednack amphibolites and (c) Porthoustock amphibolites from the Lizard Ophiolite Complex. Deformed mafic sheets and amphibolite layers (d) from the Old Lizard Head Series are also shown.



supports the ophiolite nature of the Lizard Ophiolite Complex and these rocks are believed to have originally been tholeiitic basalts, and represent relict oceanic crust. Mafic rocks from many of the better-known ophiolites, including Bay of Islands (Casey *et al.*, 1985) and Oman (Searle and Malpas, 1982) have a MORB-like chemical composition which is similar to the Landewednack amphibolites.

In order to investigate whether the different mafic rocks from the Lizard Ophiolite Complex are derived from similar magma sources, they have been plotted on a Th/Yb versus Ta/Yb discrimination diagram (Pearce, 1983)(Figure 6.27). This diagram demonstrates that the Landewednack amphibolites, Porthoustock amphibolites and mafic dykes from the Lizard have similar Th/Yb and Ta/Yb ratios. These Th/Yb versus Ta/Yb discrimination diagram demonstrate that these different rocks are derived from a depleted mantle source, and they are similar in composition to MORB. It is important to note that these ratios overlap the range defined by the gabbroic veins associated with the Lizard peridotites. The range of Th/Yb and Ta/Yb ratios defined by the mafic Traboe cumulates is distinct from the range defined by the Landewednack

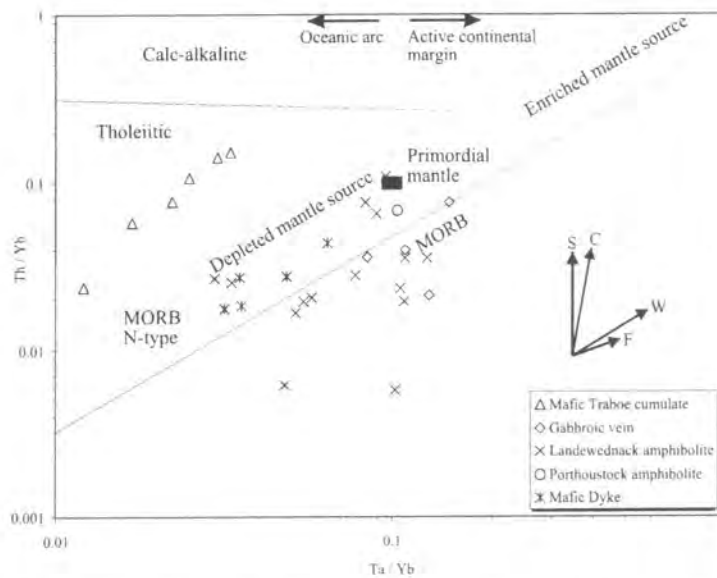


**Figure 6.27.** Th/Yb versus Ta/Yb discrimination diagram (Pearce, 1983) showing Landewednack amphibolites, Porthoustock amphibolites and mafic dykes from Lizard Ophiolite Complex. Mafic Traboe cumulates and gabbroic veins from the Lizard Ophiolite Complex are included for comparison. The graph demonstrates that the mafic Traboe cumulates possess higher Th/Yb ratios and lower Ta/Yb ratios than the other rocks. Vectors shown indicate the influence of subduction components (S), within-plate enrichment (W), crustal contamination (C) and fractional crystallisation (F)

amphibolites, and this is strong evidence against the mafic Traboe cumulates being the metamorphic equivalent of the Landwednack amphibolites, a hypothesis previously proposed by Green (1964b). This diagram suggests that the Landwednack amphibolites, Porthoustock amphibolites, mafic dykes and gabbroic veins are derived from the same magma source or at least a source of similar composition.

### **6.3.5. Ordovician basement**

The purpose of this section is to present analyses of REE for amphibolite layers within the Old Lizard Head Series (OLHS), deformed mafic sheets that cross-cut the OLHS, and the Lizard Head sill and compare this data with the data for Devonian mafic rocks from the Lizard Ophiolite Complex. These rocks represent a slice of basement and it is therefore important to characterise the nature of the magma sources of these rocks and provide geochemical constraints regarding the tectonic environment in which these rocks were developed. The results are also compared with analyses of the Man of War gneiss (MOWG) taken from Sandeman *et al.* (1997), which also comprise this Ordovician basement unit.

#### **6.3.5.a. Results**

The REE content of rocks from the OLHS have been normalised to chondrite and plotted on Figure 6.28, in order to allow comparison with the Lizard Ophiolite Complex. The mafic rocks from the OLHS define two different REE patterns. Amphibolite layers within the OLHS and interlayered with meta-sediments have strongly LREE enriched patterns, with the REE abundance decreasing from La ( $[La]_N = 39.7$  and  $54$ ) to Lu ( $[Lu]_N = 11.3$  and  $15$ ). These rocks also display small negative Eu and Ce anomalies. The deformed mafic sheet, which cross-cuts the OLHS meta-sediments, displays REE patterns very similar to those of the mafic dykes from the Lizard Ophiolite Complex. These REE patterns are characterised by a sharp increase in LREE abundance from La ( $[La]_N = 11.6 - 16$ ) to Pr ( $[Pr]_N = 14.6 - 21.9$ ), then a decrease in REE to Lu ( $[Lu]_N = 8.4 - 12.6$ ). A sample taken from the Lizard Head Sill shows a large decrease in REE abundance from La ( $[La]_N = 87$ ) to Er ( $[Er]_N = 6.4$ ), then weak REE enrichment to Lu ( $[Lu]_N = 8.3$ ). The REE patterns of samples of the Man of War Gneiss are identical to that of the Lizard Head Sill.

The deformed mafic sheets that cross-cut the OLHS display a MORB normalised REE pattern which is nearly identical to that of the mafic dykes (Figure 6.20c) of the Devonian Lizard Ophiolite Complex.

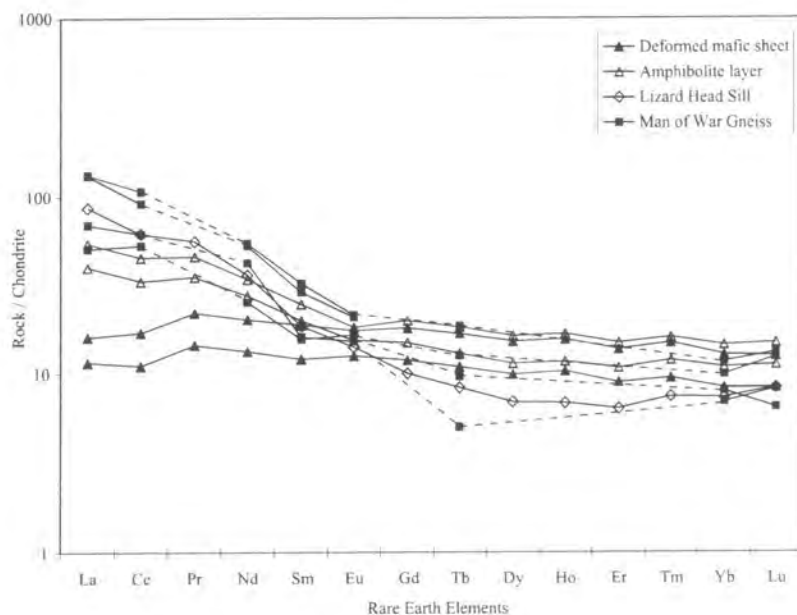


**Figure 6.28.** Chondrite normalised (Nakamura, 1974) rare earth element (REE) patterns for deformed mafic sheets that cross-cut the Old Lizard Head Series (OLHS), amphibolite layers within the OLHS, the Lizard Head Sill and the Man of War Gneiss (MOWG) from the Ordovician basement.

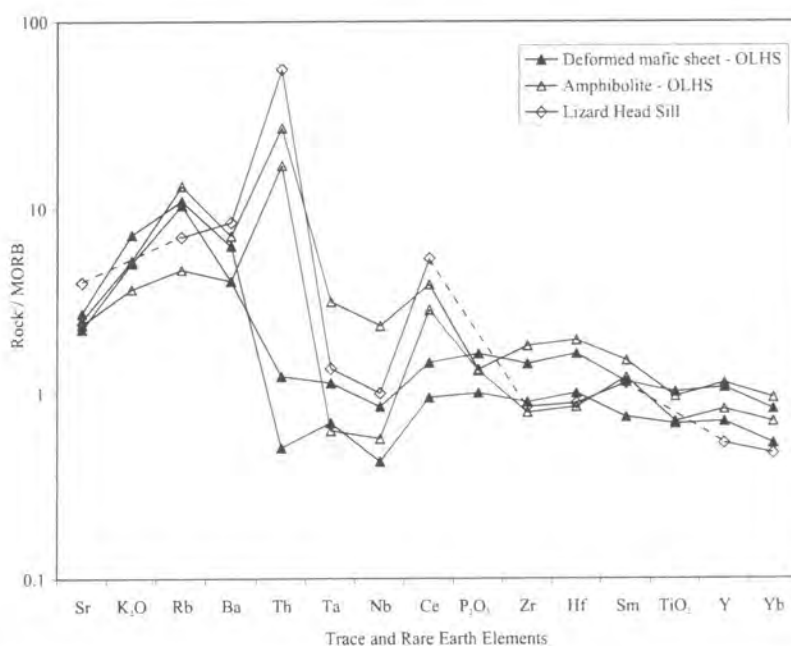


**Figure 6.29.** MORB normalised (Pearce, 1983) trace and rare earth element (REE) patterns for deformed mafic sheets that cross-cut the Old Lizard Head Series (OLHS), amphibolite layers within the OLHS, the Lizard Head Sill from the Ordovician basement.

Amphibolite layers within the OLHS show a MORB normalised REE pattern which is completely different to the other amphibolites and mafic rocks from the Lizard Ophiolite Complex, including the deformed mafic sheets (Figure 6.29). The REE pattern is characterised by a large positive Th anomaly, which contrasts with the negative Th anomaly observed in the Landewednack amphibolites. These rocks also show a clear positive Ce anomaly. The REE pattern of the Lizard Head Sill is remarkably similar to these amphibolite layers.

#### **6.3.5.b. Interpretation and discussion**

The deformed mafic sheets that cross-cut the Ordovician OLHS series display both chondrite and MORB normalised patterns which are nearly identical to the mafic dykes from the Lizard Ophiolite Complex. This suggests that the deformed mafic sheets may be part of the same suite as these dykes.

Amphibolite layers in the Ordovician OLHS display chondrite-normalised REE patterns, which are very different to that of the Devonian mafic rocks of the Lizard Ophiolite Complex. The strongly LREE-enriched patterns are very similar to the REE pattern basalts of island arc origin derived from a LREE-enriched mantle source (Wilson, 1989). The MORB-normalised REE patterns of these rocks, which include enrichment of Sr, K, Rb, Ba, Th, and P, are also consistent with an island arc origin for these rocks, as the enrichment of these elements suggest the involvement of a subduction-zone fluid. Whereas Sr, K, Rb and Ba are likely to be transported in an aqueous fluid, Th and P are more likely to be transported in a partial melt (Wilson, 1989). The Ta and Nb trough for these rocks could suggest that these elements were retained in a titaniferous phase e.g. ilmenite or titanite in the subducted rock (Saunders *et al.*, 1980), although, a Ta-Nb trough is also a characteristic feature of crustal contamination of basalt (Pearce, 1983).

The granitic Lizard Head Sill displays chondrite normalised and MORB normalised REE patterns which are very similar to the amphibolite layers in the OLHS. It is also interesting to note that the chondrite-normalised REE pattern of the Man of War Gneiss (MOWG) is identical to that of the Lizard Head Sill. This similarity in REE composition between the Lizard Head Sill and the MOWG suggests that both were derived from the same source, alternatively the Lizard Head Sill could be derived

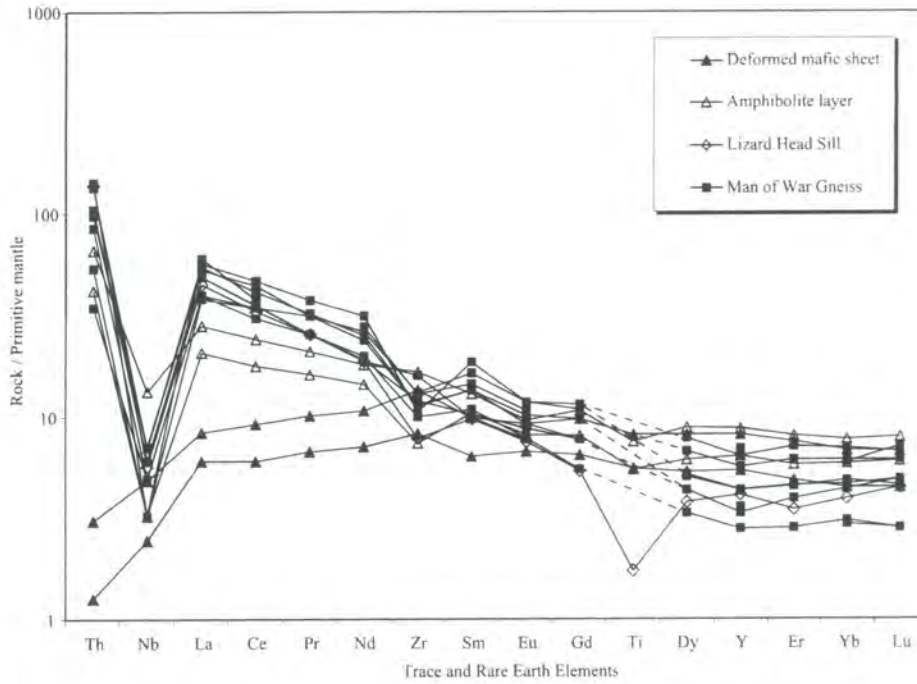


**Figure 6.30.** Primitive mantle normalised (Hoffman, 1988) trace and rare earth element (REE) patterns for deformed mafic sheets that cross-cut the Old Lizard Head Series (OLHS), amphibolite layers within the OLHS, the Lizard Head Sill and the Man of War Gneiss (MOWG) from the Ordovician basement. Note the clear negative Nb anomaly for all the rocks except the deformed mafic sheets, this is a characteristic feature of mafic rocks from island-arc – suprasubduction-zone environments.

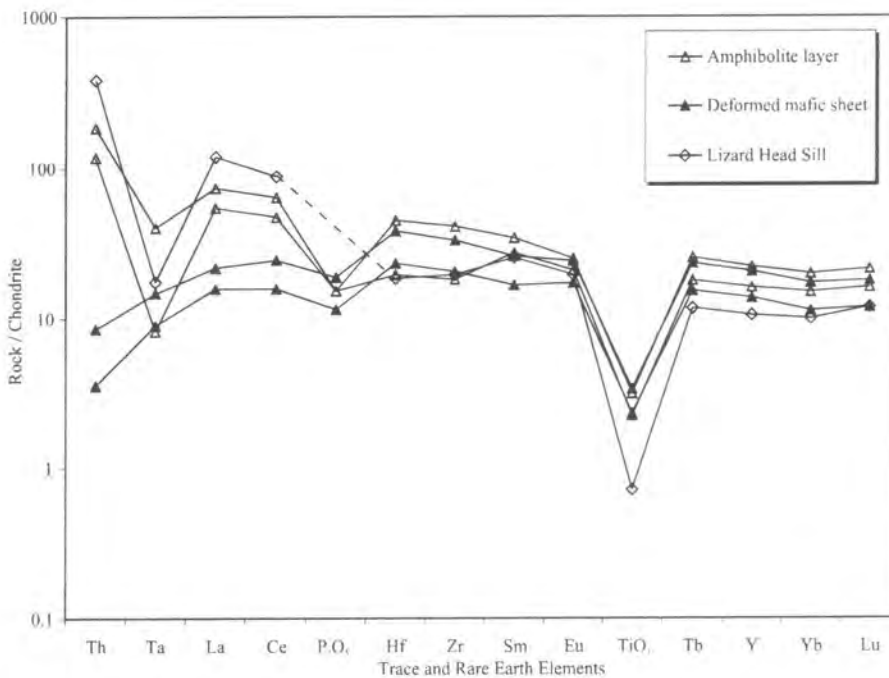


**Figure 6.31.** Chondrite normalised (Elthon, 1991) trace and rare earth element (REE) patterns for deformed mafic sheets that cross-cut the Old Lizard Head Series (OLHS), amphibolite layers within the OLHS and the Lizard Head Sill from the Ordovician basement. Note the clear negative Ta anomaly for all the rocks except the deformed mafic sheets; this is a characteristic feature of mafic rocks from island-arc – suprasubduction-zone environments.

by melting of the MOWG. This supports the observation of Flett (1946) who interpreted the Lizard Head sill as an offshoot of the MOWG. This interpretation was recently questioned by Sandeman *et al.* (1997), who suggested on the basis of normative composition and major element composition, that the Lizard Head Sill was chemically similar to the MOWG but probably unrelated.

A plot of trace element-normalised to the primitive mantle values of Hoffman (1988)(Figure 6.30) demonstrates that the amphibolite layers in the OLHS, Lizard Head Sill and MOWG have identical REE patterns. These patterns are characterised by strong enrichment of Th, the depletion of Nb, and minor depletion of Zr. This diagram presents strong evidence that these three different rock suites are derived from the same or a similar magma source. A negative Nb anomaly relative to Th and La may represent an island-arc – suprasubduction-zone geochemical signature (Jenner *et al.*, 1991). Elthon (1991) has demonstrated that Ta depletion in lavas and dolerites from the Bay of Islands ophiolite is a characteristic of magmas erupted above a subduction zone. A plot

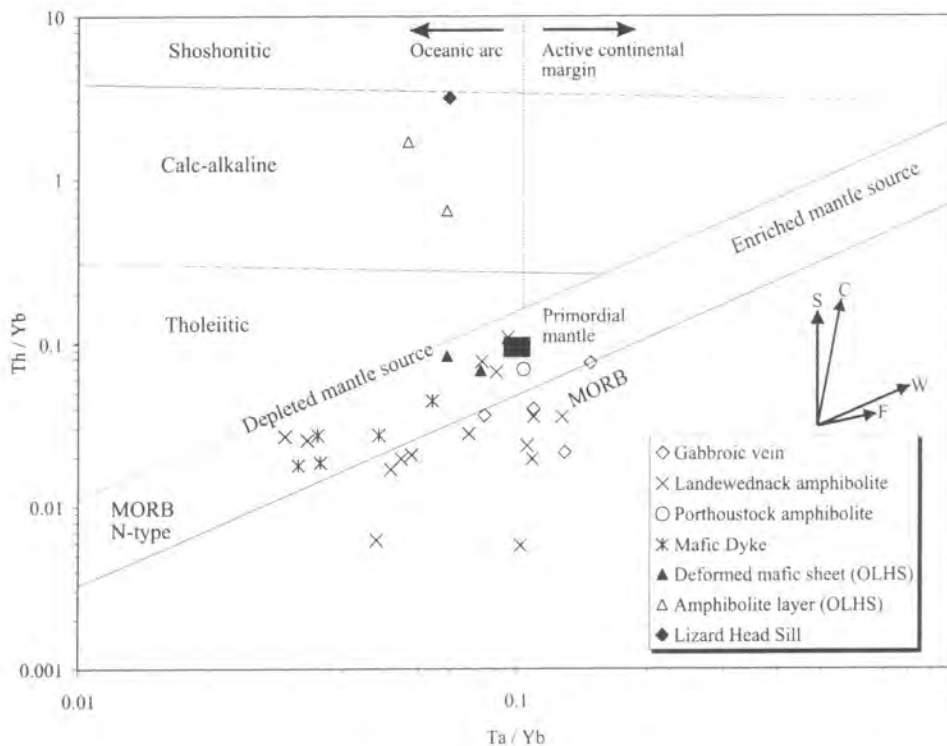


**Figure 6.32.** Th/Yb versus Ta/Yb discrimination diagram (Pearce, 1983) showing deformed mafic sheets that cross-cut the Old Lizard Head Series (OLHS), amphibolite layers within the OLHS and the Lizard Head Sill. Note the similarity between the ratios of the deformed mafic sheets and the Landewednack amphibolites, Porthoustock amphibolites, mafic dykes and gabbroic veins from Lizard Ophiolite Complex. Vectors shown indicate the influence of subduction components (S), within-plate enrichment (W), crustal contamination (C) and fractional crystallisation.(F)



of the REE of the rocks from the Ordovician basement rocks normalised to the chondrite values of Elthon (1991)(Figure 6.31) displays a strong negative Ta anomaly for the patterns of the amphibolite layers in the OLHS and the Lizard Head sill and therefore confirms the subduction zone geochemical characteristics of these rocks.

Deformed mafic sheets that cross-cut OLHS rocks plot in the 'ocean floor basalt' field of the Ti-Zr-Y discriminant diagram (Pearce and Cann, 1973) and amphibolite layers in the OLHS plot both in the 'calc-alkaline basalt' and 'ocean floor basalt' fields (Figure 6.26).

The Th/Yb and Ta/Yb ratios of the deformed mafic sheets that cross-cut the OLHS overlap the range defined by the Landewednack amphibolites, Porthoustock amphibolites and mafic dykes from the Lizard Ophiolite Complex (Figure 6.32). These results suggest that the deformed mafic sheets may be derived from the same magma source, or at least a source of similar composition. This Th/Yb versus Ta/Yb discrimination diagram (Pearce, 1983) suggests that the deformed mafic sheets are derived from a depleted mantle source and this is similar to the composition of MORB. The amphibolite layers within the OLHS and the Lizard Head sill have much higher Th/Yb ratios (1.4 – 6.8) than the deformed mafic sheets (Th/Yb = 0.056-0.09). The Th/Yb ratios (1.1 – 9.4) of the MOWG (Sandeman *et al.*, 1997) are comparable with the range defined by the amphibolites layers within the OLHS and the Lizard Head sill. The similarity in these Th/Yb and Ta/Yb ratios suggests that the amphibolites layers within the OLHS, the Lizard Head sill and the MOWG are derived from the same magma source or a source of similar composition, distinct from the source of the cross-cutting deformed mafic sheet. This Th/Yb versus Ta/Yb discrimination diagram (Pearce, 1983) demonstrates that the amphibolites layers within the OLHS and the Lizard Head sill plot within the calc-alkaline oceanic arc domain, in contrast to the MORB-like compositions of the deformed mafic sheets, Landewednack amphibolites, Porthoustock amphibolites and mafic dykes. The higher Th/Yb ratios in the amphibolites layers within the OLHS, Lizard Head sill and MOWG are believed to reflect the influence of subduction-zone fluids enriched in Th during the petrogenesis of these rocks or crustal contamination (Pearce, 1983).

### **6.3.6. Summary**

Trace element characteristics of rocks from the Lizard ophiolite Complex provide important new constraints regarding the genesis and tectonic evolution of this ophiolite. New REE analyses of rocks from the Ordovician basement unit has provided important clues with regard to the origin of this suite of rocks. The most salient results of the REE characteristics of rocks from the Lizard Ophiolite Complex and Ordovician basement unit are summaries below:

- Mylonitic plagioclase-bearing peridotite and mylonitic amphibole-bearing peridotite are enriched in LREE relative to spinel and plagioclase ilherzolites. The LREE enrichment is consistent with metasomatism involving a LREE enriched volatile-rich melt.
- The presence of a km-scale reaction front involving discrete batches of infiltrating melt must be invoked as a possible mechanism to account for the km-scale, uniform LREE enrichment of the mylonitic peridotites.
- The trace element characteristics of mafic Traboe cumulates and gabbroic veins are different. A Th/Yb versus Ta/Yb discrimination diagram reveals that these rocks have different Th/Yb and Ta/Yb ratios and demonstrates that they do not plot on mutual crustal contamination or fractional crystallisation trends. This data also demonstrates that the gabbroic veins are unlikely to be the metamorphic equivalent of the mafic Traboe cumulates.
- Landewednack amphibolites and mafic dykes from the Lizard ophiolite Complex display MORB-like trace element compositions. In contrast the Porthoustock amphibolites show LREE enriched REE patterns, which is suggestive of an island-arc or subduction zone genesis.
- The REE patterns of the Porthoustock amphibolites are similar to an early dyke suite identified by Davies (1984) and therefore support models that suggest that these rocks are the deformed equivalents of this early dyke suite, which comprises a sheeted dyke complex.
- Landewednack amphibolites, Porthoustock amphibolites, mafic dykes and gabbroic veins show similar, MORB-like Th/Yb ratio and Ta/Yb ratios suggesting derivation from a similar magma source.

- Deformed mafic sheets that cross-cut the Old Lizard Head Series (OLHS) show REE characteristics that are very similar to the mafic dykes of the Lizard Ophiolite Complex, suggesting that they may be derived from the same or a similar magma source.
- Amphibolite layers with the OLHS and the Lizard Head sill display strongly LREE enriched patterns, and negative Nb and Ta anomalies, which are geochemical signatures of genesis in an island-arc or subduction zone environment. A Th/Yb versus Ta/Yb diagram strongly supports the involvement of subduction zone fluids or crustal contamination in the petrogenesis of amphibolite layers with the OLHS and the Lizard Head sill. The Man of War gneiss displays very similar, island-arc or subduction zone geochemical characteristics, suggesting that these different rocks are derived from the same or a similar magma source.

---

#### **6.4. Isotopic evidence – results and interpretation**

---

$^{143}\text{Nd}/^{144}\text{Nd}$  and  $^{87}\text{Sr}/^{86}\text{Sr}$  isotopic ratios for the ultramafic and mafic Traboe cumulates, Landewednack amphibolites, Porthoustock amphibolites, mafic dykes, Crousa gabbro and Kennack Gneiss from the Lizard Ophiolite Complex and the Man of War gneiss and Lizard Head sill from the Ordovician basement were provided by Mike Styles (*pers. comm.*, 1997). Analyses of these samples were performed at the NERC Isotope Geosciences Laboratory (British Geological Survey, Keyworth).

The initial ratio ( $T = 375$ )  $^{143}\text{Nd}/^{144}\text{Nd}$  is based on the age of the Crousa gabbro calculated from a combined mineral and whole rock Sm-Nd isochron (Davies, 1984).

##### **6.4.1. Lizard Ophiolite Complex – results and interpretation**

The initial ( $T=375$  Ma)  $^{143}\text{Nd}/^{144}\text{Nd}$  ratios of various ultramafic, mafic and granitic rocks are plotted on Figure 6.33 for comparison. This diagram demonstrates that the  $^{143}\text{Nd}/^{144}\text{Nd}$  ratios of the Crousa gabbro (0.51252 - 0.51269), mafic dykes (0.51266 and 0.51269) and Landewednack amphibolites (0.51255 – 0.51266) overlap. The similarity in the range of  $^{143}\text{Nd}/^{144}\text{Nd}$  ratios for these rocks is consistent with the REE chemistry of the Landewednack amphibolites and mafic dykes, which suggest that they are derived from the same source. The diagram demonstrates that the Porthoustock

amphibolites possess an overlapping range of  $^{143}\text{Nd}/^{144}\text{Nd}$  ratios (0.51253 and 0.51256) and are consistent with the REE chemistry which suggested that these rocks have a similar magma source to that of the Landewednack amphibolites. The mafic Traboe cumulates display a wide range of  $^{143}\text{Nd}/^{144}\text{Nd}$  ratios (0.51211 – 0.51252), which are

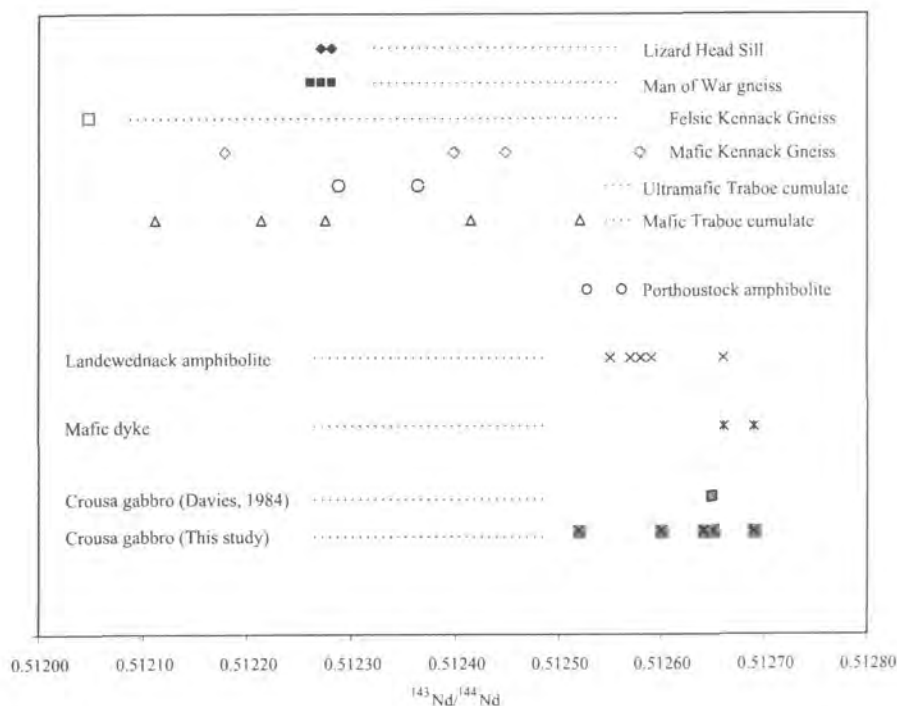


**Figure 6.33.** Diagram displaying the initial ( $T=375$  Ma)  $^{143}\text{Nd}/^{144}\text{Nd}$  ratio of the Crousa gabbro, mafic dykes, Landewednack amphibolite, Porthoustock amphibolite, ultramafic and mafic Traboe cumulates and Kennack Gneiss from the Lizard Ophiolite Complex. The  $^{143}\text{Nd}/^{144}\text{Nd}$  ratio obtained for the Crousa gabbro by Davies (1984) is included for comparison. The  $^{143}\text{Nd}/^{144}\text{Nd}$  ratio for the Man of War gneiss and the Lizard Head sill from the Ordovician basement rocks are also included.

much lower than the range defined by the Landewednack amphibolites. The highest  $^{143}\text{Nd}/^{144}\text{Nd}$  ratio = 0.51252 is for a deformed dyke intersected by the Traboe boreholes, this has a chondrite normalised REE pattern, which is very similar to the REE patterns of the Landewednack amphibolite and mafic dykes and is therefore likely to belong to the same suite as the mafic dykes. The ultramafic Traboe cumulates possess  $^{143}\text{Nd}/^{144}\text{Nd}$  ratios (0.51229 – 0.51236) that fall in the range defined by the mafic Traboe cumulates. These data demonstrate that the ultramafic and mafic Traboe cumulates are derived from the same source, and that this is different from the source of the Landewednack amphibolites, mafic dykes and Crousa gabbro. The large range of  $^{143}\text{Nd}/^{144}\text{Nd}$  ratios displayed by the mafic Traboe cumulates is probably related to

mixing of different batches of magma during the formation of the Lizard cumulate complex.

The mafic component of the Kennack Gneiss displays a large range of  $^{143}\text{Nd}/^{144}\text{Nd}$  ratios (0.51218 – 0.51258) with the highest values overlapping the range defined by the Landwednack amphibolites and Crousa gabbro. The lowest  $^{143}\text{Nd}/^{144}\text{Nd}$  ratio (0.51205) is defined by the felsic component of the Kennack Gneiss. These results clearly demonstrate that the Kennack Gneiss is not necessarily the product of anatexis of the Landwednack amphibolites alone, as proposed in several previous studies (Sanders, 1955; Kirby, 1979; Vearncombe, 1980; and Malpas & Langdon, 1987). The data suggests that the Kennack Gneiss is likely to be the product of mixing of a felsic magma derived from melting of a source exotic to the Lizard and a mafic magma, which may include a component similar to the Landwednack amphibolite (M.T.Styles *pers comm.* 1998).

A plot of  $\epsilon\text{Nd}$  versus  $\epsilon\text{Sr}$  (Figure 6.34) demonstrates that the Landwednack amphibolites and Crousa gabbro display a wide range of  $\epsilon\text{Sr}$  values (-1 – 16 and -17 – 25 respectively). These values define a linear trend which lies along the seawater

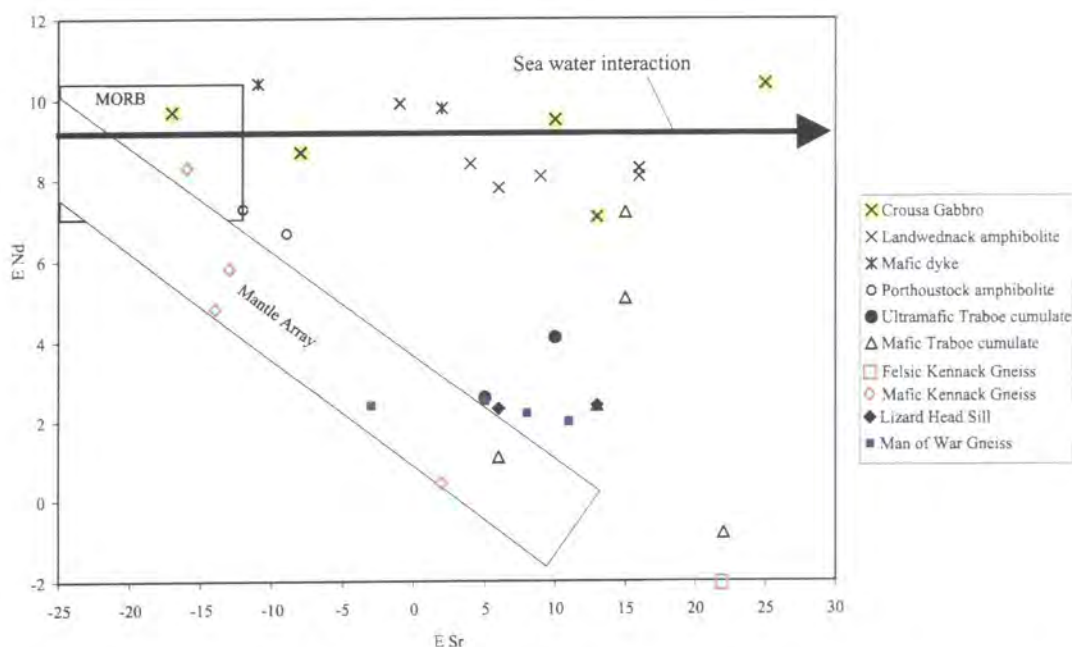


**Figure 6.34.** Plots showing  $\epsilon\text{Nd}$  versus  $\epsilon\text{Sr}$  for Crousa gabbro, Landwednack amphibolite, mafic dykes, Porthoustock amphibolite, ultramafic and mafic Traboe cumulates and Kennack Gneiss from the Lizard Ophiolite Complex. The Lizard Head Sill and Man of War Gneiss from the Ordovician basement unit are included for comparison. The sea water contamination trend is based on the data of McCulloch *et al.*, (1981). Compositional fields for MORB and the Mantle Array are taken from Wilson (1989) and references therein.

interaction trend calculated by McCulloch *et al.*, (1981). This large scatter of  $\epsilon\text{Sr}$  values in these rocks is therefore thought to be due to seawater interaction during hydrothermal alteration of these oceanic crustal rocks (Beniot *et al.*, 1996). The increase  $\epsilon\text{Sr}$  may also be related to fluid interaction during amphibolite facies metamorphism. The increase in  $\epsilon\text{Sr}$  has shifted these rocks to the right of the mantle array. The positive  $\epsilon\text{Nd}$  values of these rocks imply a depleted mantle source and lie within the range of most volcanic and plutonic ophiolitic rocks (Richard and Allegre, 1980). These  $\epsilon\text{Nd}$  values are also similar to the range defined by MORB. This suggests that the mantle source of Landewednack amphibolites, mafic dykes, Crousa gabbro and Porthoustock amphibolites is similar in composition to the mantle source of MORB.

The ultramafic Traboe cumulates and mafic Traboe cumulates define a more restricted range of  $\epsilon\text{Sr}$  values (5 – 22), which may reflect more limited hydrothermal alteration, serpentinisation or metamorphism (Figure 6.34). The range of  $\epsilon\text{Nd}$  for the ultramafic and mafic Traboe cumulates approach negative values, which suggests involvement of both depleted and enriched mantle sources.

The felsic component of the Kennack Gneiss displays the lowest  $\epsilon\text{Nd}$  (-2.1) and a high  $\epsilon\text{Sr}$  value (22), which suggests derivation from an enriched source. The mafic component of the Kennack Gneiss shows a large range of  $\epsilon\text{Nd}$  (0.4 - 8.3) and  $\epsilon\text{Sr}$  (2 - -16), which defines a linear trend between the range defined by MORB and the felsic component of the Kennack Gneiss. These data suggest that the mafic component of the Kennack Gneiss was derived from mixing of at least two magma sources. One source has a Nd isotopic composition equivalent to MORB and another source has the Nd isotopic composition of the felsic component of the Kennack Gneiss. The Nd isotopic composition of the Landewednack amphibolites falls within the range defined by MORB, which suggests that a melted component of the Landewednack amphibolites may represent one of the sources of the mafic Kennack Gneiss. The Nd isotopic composition of the felsic component of the Kennack Gneiss approaches the Nd isotopic composition of Palaeozoic metasedimentary rocks to the north of the Lizard Ophiolite Complex, including samples of the Mylor series, Portscatho Formation, Porthtowan Formation and Meadfoot Group ( $\epsilon\text{Nd}$  = -5.2 - -11.5)(Darbyshire & Shepherd, 1994). These Palaeozoic metasedimentary rocks structurally underlie the Lizard Ophiolite Complex and, therefore the felsic component of the Kennack gneiss may be derived



from melting of this unit during obduction. Further work is required to substantiate this possibility.

#### **6.4.2. Ordovician basement – results and interpretation**

A limited range of  $^{143}\text{Nd}/^{144}\text{Nd}$  ratios, which overlap, characterise the MOWG (0.51226 – 0.51228) and the Lizard Head sill (0.51227 – 0.51228)(Figure 6.33). This isotopic data strongly supports the REE chemistry of these rocks, which suggests that they are derived from the same source and that this source is enriched relative to the source of MORB.

#### **6.4.3. Summary**

The isotopic composition of rocks from the Lizard Ophiolite Complex and the Ordovician basement unit confirms several of the conclusions that have been proposed on the basis of major, trace and rare earth element chemistry:

- Landewednack amphibolites, mafic dykes, Crousa gabbro and Porthoustock amphibolites from the Lizard Ophiolite Complex show a similar range of initial  $^{143}\text{Nd}/^{144}\text{Nd}$  ratios and this confirms that these rocks are derived from a source of the same or similar Nd isotopic composition. The initial  $^{143}\text{Nd}/^{144}\text{Nd}$  ratios of these rocks overlap the range defined by MORB, confirming the MORB-like REE characteristics of these rocks.
- Ultramafic and mafic Traboe cumulates display a wide range of initial  $^{143}\text{Nd}/^{144}\text{Nd}$  ratios that do not overlap with the Landewednack amphibolites. This suggests that these rocks are derived from a heterogeneous or different source, and the wide range of values may suggest mixing of sources of variable compositions.
- The isotopic composition of the felsic component of the Kennack Gneiss is distinct from any rocks of the Lizard Ophiolite Complex and suggests derivation from an enriched source. The mafic component of the Kennack Gneiss displays a wide range of Nd isotopic compositions. The data is consistent with mixing between a magma source equivalent to the felsic Kennack Gneiss and another source compositionally equivalent to MORB or the Landewednack amphibolites. This data

clearly demonstrates that the Kennack Gneiss is not derived from anatexis of the Landwednack amphibolites alone.

- A wide range of  $\epsilon\text{Sr}$  displayed by the Landwednack amphibolites, mafic dykes and Crousa gabbros is suggestive of extensive hydrothermal alteration involving seawater and/or fluid interaction during amphibolite facies metamorphism.
- The Lizard Head sill and MOWG possess a restricted and overlapping range of initial  $^{143}\text{Nd}/^{144}\text{Nd}$  ratios. This confirms REE characteristics that suggest that these rocks are derived from the same source or a source of similar REE composition.

---

## **6.5. Whole rock geochemistry – summary and discussion**

---

The preceding sections have demonstrated that the various rocks of the Lizard Ophiolite Complex and Ordovician basement exhibit several important geochemical characteristics. These geochemical characteristics provide important clues to the nature of the chemical evolution of these rocks and the tectonic environment in which they formed. In the following section the most significant geochemical properties of the different rocks from the Lizard Ophiolite Complex and the Ordovician basement rocks are summarised.

### **6.5.1. Lizard peridotites**

- Spinel lherzolites, which represent the least deformed assemblage of the Lizard peridotites, have major and trace element compositions comparable with spinel lherzolites from several ophiolite complexes. The spinel lherzolites from the Lizard display extreme depletion of LREE, which suggests very low degrees of melting.
- The mylonitic plagioclase-bearing peridotite, mylonitic amphibole-bearing peridotite and transitional assemblage peridotites show higher CaO, Na<sub>2</sub>O, TiO<sub>2</sub>, Sc and Zr abundances, LREE enrichment and lower MgO contents than the spinel lherzolites and plagioclase lherzolites.

- Changes in the major, trace and rare earth element from the spinel lherzolite to mylonitic peridotites are interpreted as the result of metasomatism in response to volatile-rich melt-rock interaction during deformation.
- The km-scale, uniform major, trace and LREE enrichment of the mylonitic peridotites suggests the presence of a km-scale reaction front involving discrete batches of infiltrating melt rather than a single batch of percolating melt.

#### **6.5.2. Ultramafic and mafic Traboe cumulates**

- Ultramafic Traboe cumulates have a major, trace and rare earth element composition that distinguishes them from the Lizard peridotites and is consistent with these rocks being ultramafic cumulates.
- Mafic Traboe cumulates display a wide range of major and trace element compositions transitional with the ultramafic Traboe cumulates and it is proposed that igneous fractionation processes may be responsible for these variations.
- The REE patterns of the mafic Traboe cumulates include a clear positive Eu anomaly, which is a feature of plagioclase accumulation. The REE patterns of these rocks are comparable with gabbroic rocks from various ophiolite complexes.
- The Th/Yb and Ta/Yb ratios of the mafic Traboe cumulates are different from the other mafic rocks of the Lizard Ophiolite Complex and do not plot on a mutual fractional crystallisation or crustal contamination trend, suggesting that these cumulates are derived from a different magma source during an early crust forming event.
- Ultramafic and mafic Traboe cumulates possess similar Nd isotopic compositions, which are in turn distinct from the Landewednack amphibolites. Variations in the isotopic composition of these rocks suggest mixing of parental magmas with different isotopic composition.

### **6.5.3. Gabbroic veins**

- The Th/Yb and Ta/Yb ratios of gabbroic veins are distinct from the mafic Traboe cumulates, yet similar to the Landewednack amphibolites. This suggests that these gabbroic rocks are derived from a magma source that is different to the source of the mafic Traboe cumulates and similar in composition to the source of the Landewednack amphibolites.

### **6.5.4. Landewednack amphibolites and mafic dykes**

- Major and trace element geochemical properties of the Landewednack amphibolites, including higher TiO<sub>2</sub> and Zr abundances, distinguish them from the mafic Traboe cumulates.
- The major, trace and rare earth element compositions of the Landewednack amphibolites and mafic dykes are similar to typical T-MORB.
- The Nd isotopic composition of the Landewednack amphibolites, mafic dykes and Crousa gabbro are similar, suggesting that these rocks are derived from the same source or a source of similar Nd isotopic composition. A large range of  $\epsilon$ Sr displayed by these rocks suggests extensive hydrothermal alteration involving sea-water and/or fluid interaction during amphibolite facies metamorphism.

### **6.5.5. Porthoustock amphibolites**

- The Porthoustock amphibolites display LREE-enriched patterns that distinguish them from the Landewednack amphibolites. The REE patterns are similar to the early dyke suite identified by Davies (1984) and support the hypothesis that these rocks are the deformed equivalent of this early dyke suite that comprises a sheeted dyke complex. In contrast, the Th/Yb and Ta/Yb ratios of these amphibolites and the Landewednack amphibolites are similar, suggesting derivation from a magma source of similar composition.

- The Nd isotopic composition of the Porthoustock amphibolites also suggests that they are derived from a magma source of similar composition to the source of the Landewednack amphibolites.

#### **6.5.5. Ordovician basement**

- Deformed mafic sheets that cross-cut the Old Lizard Head Series (OLHS) show REE characteristics that are very similar to the mafic dykes of the Lizard Ophiolite Complex, and suggests that they may be derived from the same or a similar magma source.
- Amphibolite layers with the OLHS and the Lizard Head sill show geochemical signatures of that are characteristic of genesis in an island-arc or subduction zone environment. The Man of War gneiss displays very similar, island-arc or subduction zone geochemical characteristics, suggesting that these different rocks are derived from the same or a similar magma source.
- The Lizard Head sill and MOWG possess overlapping range of Nd isotopic ratios, suggesting that these rocks are derived from the same source, or at least sources of similar isotopic compositions.

## CHAPTER SEVEN

### SYNTHESIS, DISCUSSION AND CONCLUSIONS

#### 7.1. Introduction

This chapter contains a summary and discussion of the main findings of this study. The chapter is sub-divided into four sections:

- 1 A tectonic model for the evolution of the Lizard Ophiolite Complex based on the findings of this study.
- 2 Review of the regional tectonic implications of this model.
- 3 The implications for the early evolution of mantle rocks in ophiolite complexes.
- 4 A consideration of the role of the structural geology of the mantle during lithospheric deformation.

#### 7.2. Summary of the tectonic evolution of the Lizard Ophiolite Complex

The tectono-magmatic model presented in this study involves Devonian rocks of the Lizard Ophiolite Complex in five tectonic events, three of which occurred during the early to late Devonian. An earlier episode relates to a fragment of Ordovician basement that became tectonically incorporated within the basal structural unit of the Lizard Ophiolite Complex. Late Carboniferous to Triassic extensional faulting resulted in dismemberment of the post-obduction geometry of the Lizard Ophiolite complex (Power *et al.*, 1996):

- An early sequence of intrusive and deformation events during evolution of a basement unit that includes rocks with island arc - supra-subduction zone geochemical characteristics formed during the earliest Ordovician (~499-488Ma).
- Exhumation of mantle and development of high-temperature sub-vertical fabrics in mantle peridotites and associated cumulates in response to the construction of early oceanic lithosphere during the early Devonian (~397Ma).
- Later magmatism and extensional tectonics associated with intrusion of gabbro and basaltic dykes in an oceanic regime. Cross-cutting, deformed mafic sheets with similar geochemical characteristics to these basaltic dykes occur within the



Ordovician basement unit. If these deformed mafic sheets belong to the same intrusive suite as the basaltic dykes associated with the Lizard Ophiolite Complex, it is possible that the Ordovician rocks may have been close in proximity to developing oceanic crust, and thus spatially linked to the Devonian ophiolitic rocks prior to emplacement.

- Top-to-the-NW thrusting and contemporaneous magmatism during the tectonic emplacement of the Lizard Ophiolite Complex during the Middle to Late Devonian (~390-366Ma). This included incorporation of the Ordovician basement within the basal part of the Lizard Ophiolite Complex. Reactivation of thrust-related contacts resulted in the development of serpentine-filled faults, and is possibly related to late stage collapse of the of the nappe pile (Jones, 1997).
- Fault block rotation associated with displacements along high angle brittle extensional faults, during the late Carboniferous to Triassic, is probably responsible for the apparently extensional nature of the top-to-the-NW, emplacement-related thrusts.

### 7.2.1. Early evolution of Ordovician basement

The earliest deformation event is recorded in Ordovician basement rocks exposed on the SW part of the Lizard Peninsula. New geochronological data (Section 3.2) has demonstrated that the Old Lizard Head Series (OLHS) are at least early Ordovician (~488-499Ma) and it is therefore proposed that this unit is genetically related to the Man of War Gneiss (MOWG). The MOWG has recently been dated as early Ordovician (499 ±8/-3 Ma) (Sandeman *et al.*, 1997). Previous studies have proposed that the metasedimentary and metavolcanic rocks of the OLHS represented deformed and metamorphosed seafloor sediments and ocean floor basalts that formed part of the Devonian upper ocean crust sequence of the Lizard Ophiolite Complex (e.g. Styles, 1992). In the past, the Landewednack amphibolites have been interpreted as metamorphosed ocean floor basalts that were transitional with the OLHS (e.g. Bromley, 1979). The new geochronological data demonstrates that the OLHS (and MOWG) are unrelated to the Landewednack amphibolites and other Devonian rocks of the Lizard Ophiolite Complex.

Amphibolite layers within the OLHS display geochemical characteristics typical of magmas erupted above an island-arc – suprasubduction-zone (Section 6.3). The Lizard Head Sill, which cross-cuts the OLHS, also displays island-arc or subduction zone geochemical characteristics (Section 6.3). Sandeman *et al.* (1997) recently demonstrated that the MOWG also possess geochemical variations characteristic of granitoids formed in supra-subduction zone environments.

On the basis of the new and existing geochronological (Chapter 3) and geochemical evidence (Chapter 6), it is proposed that the OLHS and MOWG represent a fragment of Ordovician arc-type crust. The regional geological implications of this basement unit will be discussed later (Section 7.2). The earliest fabrics preserved in the OLHS and MOWG are generally steep and these are cross-cut by the Lizard Head Sill and therefore developed during an Ordovician deformation event. There is insufficient structural evidence to determine the tectonic processes responsible for this deformation episode. Jones (1997) proposed that these early steep fabrics were developed during the emplacement of the Lizard Ophiolite Complex in the Devonian. Jones (1997) also suggested that early steep fabrics of similar orientation in the Landewednack amphibolites were contemporaneous with those in the OLHS. These interpretations can now be rejected in light of the new geochronological evidence.

Tectonic models for the later emplacement of Devonian rocks of the Lizard Ophiolite Complex as a structural unit overlying the Ordovician basement rocks will be discussed in Section 7.2.4.

### **7.2.2. Early mantle exhumation and development of oceanic crust**

The earliest deformation event in the Devonian rocks of the Lizard Ophiolite Complex is preserved in the Lizard peridotites, ultramafic and mafic Traboe cumulates and gabbroic veins (Sections 3.3 & 3.4). The Lizard peridotites include relatively undeformed coarse-grained lherzolites through to highly deformed mylonitic peridotites. Evidence demonstrating that the different peridotite-types are genetically related includes:

- Sub-vertical foliations and down-dip mineral lineations are observed in exposures of both end-member peridotite-types (Section 3.3),

- The presence in some areas of gradational contacts between coarse-grained lherzolite and mylonitic peridotite (Section 3.3),
- Microstructures of the peridotite suggest that the mylonitic peridotites are the deformed equivalent of the coarse-grained lherzolites (Section 4.3),
- The chemical composition of relict orthopyroxene and clinopyroxene porphyroclasts in mylonitic peridotites is similar to porphyroclasts in the coarse-grained lherzolites (Section 5.3 & 5.4).
- Systematic changes in bulk chemical composition from the coarse-grained lherzolites to mylonitic peridotites (Section 6.2 and 6.3).

Microstructural evidence (Section 4.3) reveals that the coarse-grained peridotites can be sub-divided into spinel lherzolite and plagioclase lherzolite. The mylonitic peridotites are also sub-divided into a mylonitic plagioclase-bearing peridotite and mylonitic amphibole-bearing peridotite. A microstructural evolution from spinel lherzolite to mylonitic amphibole-bearing peridotite, via plagioclase lherzolite, a transitional assemblage peridotite and mylonitic plagioclase-bearing peridotite has been established. A process of increasing deformation, dynamic recrystallisation and grain size reduction constitutes the microstructural evolution. The presence of plagioclase replacing aluminous spinel in the more deformed peridotites indicates that there has been a sub-solidus transition in response to a progressive decrease in pressure during deformation (Section 4.3). Olivine petrofabrics indicate that deformation of the coarse-grain lherzolites occurred at relatively high temperature ( $T > 1000^{\circ}\text{C}$ ) and, in the mylonitic peridotites, that the deformation continued to lower temperatures ( $700\text{--}1000^{\circ}\text{C}$ ) (Section 4.3). Development of pargasitic hornblende in the mylonitic amphibole-bearing peridotite is related to the breakdown of clinopyroxene. This suggests that hydrous melt/fluids were present during deformation and caused a metasomatic interaction (Section 4.3).

Compositional variations in orthopyroxene, clinopyroxene and spinel support microstructural evidence for a decrease in P and T conditions during deformation of the peridotites (Sections 5.4, 5.5 & 5.6). In addition, mineral thermometers and barometers also demonstrate that the peridotites have re-equilibrated at progressively lower conditions of P and T during deformation (Section 5.9). The P-T estimates suggest that there has been ca. 30km exhumation of the Lizard peridotites during deformation. The P-T trajectory of the peridotites follows a non-adiabatic subsolidus cooling gradient

(i.e. temperatures decrease with decreasing pressure). This P-T trajectory would suggest that there has been very limited partial melting during exhumation. Variations in the composition of the constituent minerals in transitional assemblage peridotites and mylonitic peridotites are also suggestive of melt-rock interaction processes (Chapter 5). The most conclusive evidence for melt-rock interaction is the changes in the bulk composition of the peridotites (Chapter 6). Transitional assemblage peridotites and mylonitic peridotites are enriched in certain major and trace elements, particularly alkalis, Ti, Ca, Al and, more importantly, LREE elements, relative to the spinel and plagioclase lherzolites. The uniform enrichment of these elements suggests the presence of a km-scale reaction front involving discrete batches of infiltrating melt during deformation.

Green (1964a) proposed that the structural and chemical evolution of the Lizard peridotites was related to the intrusion of a peridotite diapir into continental crust. Several pieces of evidence appear to support Green's (*op cit.*) model:

- Steep fabrics in the peridotites,
- The presence in the Lizard peninsula of a region of mylonitic peridotite broadly surrounding a central area of coarse-grained peridotites,
- The evidence of a microstructural evolution from a coarse-grained peridotite protolith to mylonitic peridotites,
- Re-equilibration of the mineral assemblage in the deformed peridotite to conditions of lower P and T.

Green (*op cit.*) strengthened his diapir model by proposing the presence of a dynamothermal aureole adjacent to the mylonitic peridotites. He contended that the deformed mafic rocks adjacent to the peridotites were a higher-grade metamorphic equivalent to the Landewednack amphibolites. This interpretation is consistent with the field evidence in some areas, but geochemical data presented in the present study confirms the earlier suggestion of Leake & Styles (1984) which demonstrates that the 'aureole rocks' of Green (*op cit.*), now referred to as ultramafic and mafic Traboe cumulates, display a much wider range of bulk compositions than the Landewednack amphibolites (Chapter 6). This demonstrates that the ultramafic and mafic Traboe cumulates are *not* the metamorphosed equivalent of the Landewednack amphibolites. The bulk composition and the composition of the constituent mineral phases (Chapter 5) establish that the Traboe rocks are highly deformed and metamorphosed ultramafic

and mafic cumulates. The Traboe cumulate complex (Leake & Styles, 1984) is tectonically interleaved with mylonitic peridotites. P-T estimates (Chapter 5) suggest that these cumulates re-equilibrated at similar conditions to the mylonitic peridotites. This data is consistent with the similar fabric orientations in the mylonitic peridotites and the cumulates. Although many authors have criticised Green's (*op cit.*) interpretation of the evolution of the Lizard peridotites, few have proposed an alternative model to account for the evidence for an early tectonic evolution of the peridotites and associated cumulates. The majority of studies have instead focused on the ophiolitic aspect of the Lizard. Styles & Kirby (1980) demonstrated that the Lizard peridotites have a sheet-like form and that its present day form is not diapiric. They proposed that it could represent the sliced-off top of a sub-oceanic diapir that rose to the upper levels of oceanic mantle beneath a ridge or transform region. Clark *et al.* (1998) recently showed that the deformation of the mafic Traboe cumulates and the development of the early steep fabrics in these rocks occurred during the Early Devonian or earlier (~397Ma) (Section 3.4).

Considering the evidence presented above, a model is favoured whereby the deformation of the peridotites was initiated in the upper mantle at a depth of ca. 30 km. Development of peridotite mylonite shear zones accommodated the tectonic exhumation and the formation of plagioclase-bearing assemblages record the re-equilibration of the peridotite to conditions of lower P (and T). Deformation near the base of oceanic crust is inferred from the similarity of fabric orientations and estimates of P and T for the high-grade metamorphism of both the Traboe cumulates and the mylonitic peridotites. The relatively fertile major and trace element composition of the coarse-grained lherzolitic peridotites from the Lizard suggests that they have undergone limited partial melting and could therefore represent fragments of subcontinental lithospheric mantle, possibly exhumed in an incipient oceanic rift. However, spinel compositions in the spinel lherzolites suggest the possibility that they are derived from an 'oceanic margin' geodynamic setting. The whole rock and spinel compositions, combined with a lack of evidence for the former presence of a significant oceanic crustal sequence, argue against the Lizard Ophiolite Complex representing an extensive ocean with spreading ridges. However, the compositions of the metamorphosed mafic rocks associated with the Lizard peridotites (Chapter 6) are similar to MORB from slow-spreading ridges. The Lizard Ophiolite Complex shows many differences in detail to several of the better known ophiolites, for example Troodos, Oman and the Bay of

Islands (e.g. Coleman, 1977). It has, however, many features comparable with ophiolite complexes in the Northern Apennines and Liguria (NW Italy)(e.g. Drury *et al.*, 1990) and Zabargad Island (northern Red Sea)(e.g. Piccardo *et al.*, 1988). These include:

- 1) Exhumation of mantle due to tectonic denudation;
- 2) P-T estimates demonstrating exhumation involving a non-adiabatic (sub-solidus) gradient;
- 3) Limited "wet" partial melting;
- 4) Development of a lherzolite-type mantle sequence with a discontinuous, relatively thin crustal sequence.

Various tectonic models have been proposed to explain the bulk extension of continental lithosphere and, the resultant exhumation of fairly fertile mantle during the incipient oceanic rifting. In the literature, two main models have been put forward (see Bolliot *et al.*, 1988; Piccardo *et al.*, 1990; Hoogerduijn Strating *et al.*, 1993; and references therein):

- 1) Symmetric pure shear deformation of the upper mantle (e.g. McKenzie, 1978; Figure 7.1), which can also involve asthenospheric vertical diapirism (e.g. Boudier & Nicolas, 1985; and references therein; Nicolas *et al.*, 1994).
- 2) Tectonic denudation of the upper mantle by asymmetric simple shear (e.g. Wernicke, 1985; Figure 7.2).

Evidence in favour of either of these two (end-member) alternatives is derived from:

- 1) The investigation of structures and geometries recorded in deep seismic sections (e.g. Serpa & de Voogd, 1987; Serpa *et al.*, 1988; Reston, 1990);
- 2) The systematic comparison of model calculations with measured surface response in terms of vertical movements, heat-flow, gravity anomalies, and magmatism (see Hoogerduijn Strating *et al.*, 1993; and references therein).

According to the former model (e.g. Figure 7.1), exhumation of peridotites in both fast- and slow-spreading continental and oceanic rifts is normally thought to occur in mantle diapirs in response to symmetric, pure shear extension (e.g. Nicolas, 1986; Nicolas *et al.*, 1994). Recently a two-stage model has been proposed for rift development (Nicolas *et al.*, 1994). The first stage of rifting of a structurally and thermally homogeneous lithosphere is thought to require *both* an initial plume heating of the base of the



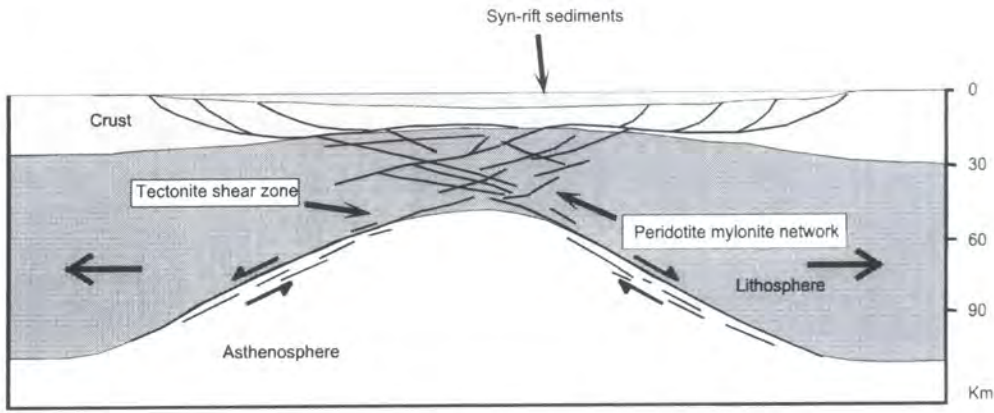


**Figure 7.1.** Symmetric “pure-shear” (e.g. Mackenzie, 1978) model for the tectonic exhumation and deformation of mantle during rifting. Taken from Visser *et al.* (1995).

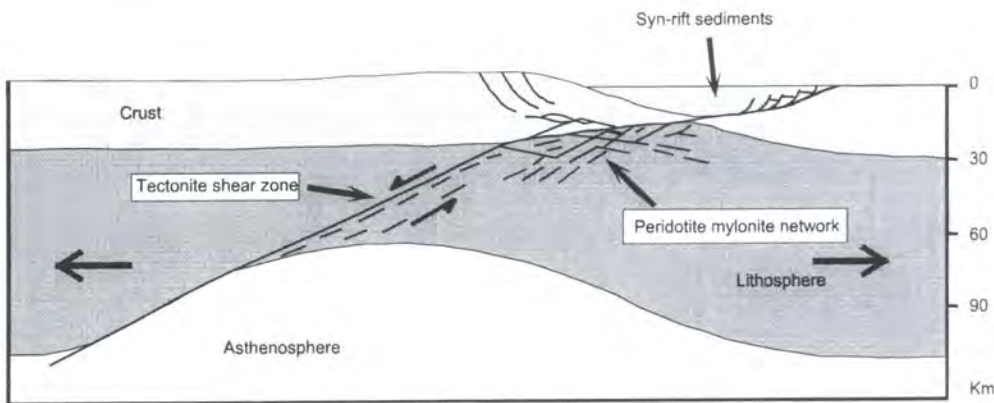


**Figure 7.2.** Asymmetric “simple-shear” (e.g. Wernicke, 1985) detachment model for the tectonic exhumation and deformation of mantle during rifting. Taken from Visser *et al.* (1995).

lithosphere and that a tensile stress is applied to the lithosphere (Nicolas *et al.*, 1994). This stage is characterised by lithospheric rupture and conforms to the Mackenzie (1978) symmetric pure-shear extension model, but with the additional requirement of weakening of the base of the lithosphere as a consequence of thermal thinning in response to an upwelling mantle diapir. It is emphasised that a tensile stress must be applied to the lithosphere because the pressure exerted by a rising mantle diapir is negligible (Nicolas *et al.*, 1994). After creation of a weakness zone in the lithosphere, a second stage follows a 10–15 Ma period of thermal relaxation. This second stage involves large extension by homogeneous stretching of the lithosphere, which is controlled by tectonic stretching of the lithosphere. Heat transport in diapirs is thought to be controlled by convective flow only, therefore implying an adiabatic system (e.g. Hoogerduijn Strating, 1993; and references therein). Temperature paths in the region of  $0.6^{\circ}\text{C}/\text{km}$  have been proposed for the exhumation of convecting asthenospheric mantle

as it rises passively beneath extending lithosphere deforming by bulk pure shear (Nicolas, 1986; Hoogerduijn Strating *et al.*, 1993; *and references therein*). This type of super-solidus adiabatic gradient is typical for oceanic basins with well-developed (symmetric) spreading ridges (e.g. Forsyth, 1977). It has recently been demonstrated by P-T estimates for peridotites from the Erro-Tobbio Massif (NW Italy) that exhumation of these peridotites involved a distinctly non-adiabatic gradient between 2 and 5°C/km and it was proposed that this seems inconsistent with mantle diapirism (Hoogerduijn Strating *et al.*, 1993). The latter, alternative model (e.g. Figure 7.2), explaining the inferred subsolidus exhumation of the Erro-Tobbio peridotites is provided by considering the thermal response of continental lithosphere on simple shear extension (Hoogerduijn Strating *et al.*, 1993; *and references therein*). Several model studies, considering this factor (Buck *et al.*, 1988; Ruppel *et al.*, 1988; Latin & White, 1990) have established that mantle rocks exhumed in the footwall of an inclined lithospheric detachment accommodating simple shear extension are cooled significantly, as a result of continuous contact with colder hanging-wall rocks (Hoogerduijn Strating, 1990). In contrast, mantle rocks exhumed in a rift dominated by pure shear symmetric extension will show near adiabatic decompression and extensive low-pressure partial melting (Hoogerduijn Strating, 1990; *and references therein*). On the basis of these observations, Hoogerduijn Strating *et al.* (1993) suggested that the non-adiabatic subsolidus uplift path of the Erro-Tobbio peridotites is most consistent with tectonic denudation during incipient rifting dominated by slightly to strongly asymmetric extension. A similar tectonic evolution has been suggested for peridotites in several other ophiolite complexes (e.g. Kizildag, Josephine and Troodos ophiolites; Dilek & Eddy, 1992), lherzolites exposed in modern, asymmetric oceanic rifts (e.g. Zabargad Island; Piccardo *et al.*, 1988; Voggenreiter *et al.*, 1988), the early evolution of many continental margins of slow-spreading oceans and marginal or back-arc basins (Bolliot *et al.*, 1987; Kastens *et al.*, 1988; LePichon & Barbier, 1988; Mutter *et al.*, 1989; Dilek & Eddy, 1992).

Based upon the above observations and similarities to the ophiolite complexes from Liguria (Hoogerduijn Strating *et al.*, 1993) it is suggested that prior to the intrusion of the Crousa gabbro and later mafic dykes (i.e. later oceanic crust development), the exhumation and deformation of the Lizard peridotites may also be consistent with asymmetric extension in the early stages of oceanic rifting. Evidence

supporting this hypothesis includes P-T estimates (Chapter 5) that suggest non-adiabatic (sub-solidus) ( $\sim 5^{\circ}\text{C}/\text{km}$ ) exhumation of the Lizard peridotites and the rather fertile nature of the spinel lherzolite i.e. prior to re-fertilisation during later deformation and syn-tectonic melt infiltration resulting in the development of mylonitic peridotites.

Following the model suggested above, the mylonitic peridotites of the Lizard Ophiolite Complex are thought to represent the footwall of a major mantle shear zone and the deformed and metamorphosed ultramafic and mafic Traboe cumulates represent the hangingwall near to the base of an oceanic crust sequence (Figure 7.3). It is suggested that the ultramafic and mafic cumulates represent the hangingwall of the proposed shear-zone on the basis that these rocks cannot have originated at the depths ( $\sim 30\text{ km}$ ) from which the Lizard peridotites originated. This is because the mineral assemblages (e.g. plagioclase and Cr-rich spinel), that comprise the cumulate rocks would be unstable at this depth. Later, emplacement-related deformation and brittle faulting make it difficult, if not impossible, to deduce the original geometry of these shear zones. Therefore the present-day distribution of the mylonitic peridotites cannot be completely resolved in terms of a tectonic model. All that is known is that the foliations in the mylonitic peridotites and overlying Traboe cumulates strike NW-SE, dip steeply NE and mineral lineations plunge down-dip. This suggests that extension and rifting was NE-SW directed, which is consistent with the orientation of the later mafic dyke suite and gabbro mylonite shear zones associated with the Crousa gabbro

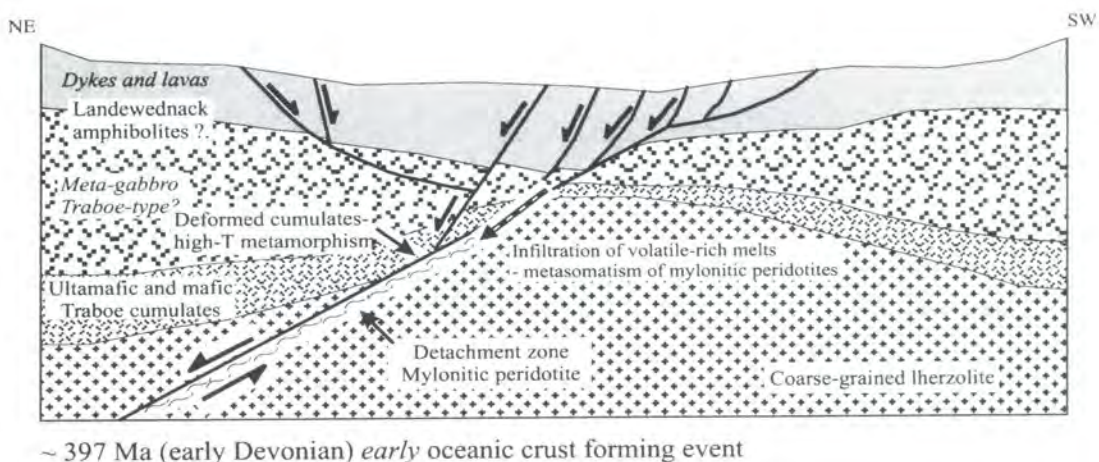


**Figure 7.3.** Schematic diagram showing a possible interpretation of the early evolution of the Lizard Ophiolite Complex associated with rifting and development of early oceanic crust. Mylonitic peridotites are developed in a detachment zone (mantle shear zone) during exhumation of mantle and cumulates are disrupted, deformed and highly metamorphosed ( $900\text{--}1050^{\circ}\text{C}$ ) in the hangingwall.



(Chapter 3). It has also been established that during exhumation, the mylonitic peridotites were chemically enriched in response to melt-rock interaction involving volatile-rich melt. Early steep fabrics preserved in the Landewednack amphibolites may have also developed during oceanic rifting and may thus represent deformation and associated high-temperature metamorphism higher in the oceanic crust sequence. The steep fabrics preserved in the Lizard peridotites and relict fabrics in the Landewednack amphibolites are inconsistent with the low- to moderately-dipping extensional shear-zones depicted in Figure 7.3. This implies that there has been re-orientation of the dip of the fabrics preserved in the peridotites. A possible mechanism to account for these steep fabrics is rotation of fault blocks during extensional faulting. However, it seems that this rotation must have taken place prior to the later magmatism associated with the Crousa gabbro, because the gabbro sheets and vertical mafic dykes associated with this magmatism chill against peridotites with a sub-vertical fabric. Extensional faulting associated with this later magmatism can also be invoked to have caused the observed fabric rotation.

Further discussion regarding the implications for the early mantle evolution of the Lizard Ophiolite Complex and other ophiolite complexes is presented in Section 7.3.

### **7.2.3. Later magmatism and extensional tectonics**

Intrusion of the Crousa gabbro, associated gabbro dykes and later mafic dykes clearly post-dates the deformation of the Lizard peridotites. Isotopic data (Chapter 6) demonstrates that the Crousa gabbro and mafic dykes were probably derived from a magma source similar to the source of the Landewednack amphibolites. Thus, there appears to have been a later phase of magmatism and construction of oceanic crust following a period of mantle exhumation, oceanic rifting and early oceanic crust formation (see Section 7.2.2)(Figure 7.4). Gibbons & Thompson (1991) and Roberts *et al.* (1993) have suggested that extensional shear zones represented by mylonite zones including the Porthoustock amphibolites (Section 3.4.3.b) and gabbro mylonite zones in the Crousa gabbro body (Section 3.4.3.a) indicate that this period of magmatism was dominated by ductile extension of the oceanic crust. Roberts *et al.* (1993) drew comparisons with examples of modern oceanic crust and proposed that accommodation of extension by displacement along faults and ductile shear zones was a feature typical

of magma-starved, slow spreading ridges. Shear zones in the Crousa gabbro strike NW-SE, dip towards the NE and show a top-to-the-NE displacement, whereas the fabric in the Porthoustock amphibolites strikes NW-SE, predominantly dip SW and shear-sense indicators suggest at top-to-the-SW displacement.

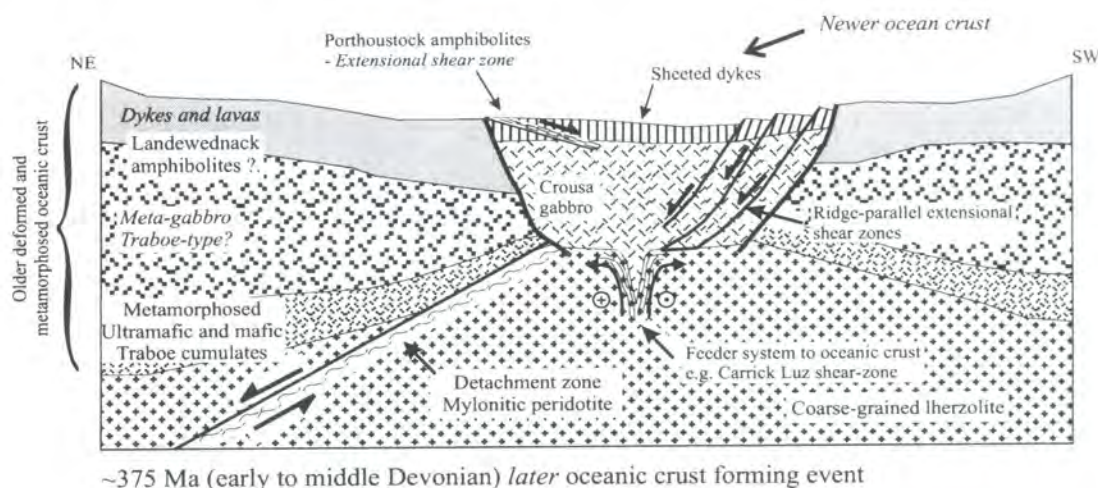


**Figure 7.4.** Schematic diagram depicting the later magmatism and extensional tectonics. Showing the intrusion of the Crousa gabbro and extensional shear zones, including the Porthoustock amphibolites. The Carrick Luz shear-zone is depicted as a feeder system to the overlying Crousa Gabbro (ocean crust) (after Andrews & Jolly, *in press*), see discussion in text.

It has recently been suggested that the Carrick Luz shear-zone (Andrews & Jolly, *in press*; Chapter 3) represents part of a feeder system to the developing overlying crust (Figure 7.4). The dextral shear-zone is a steep 150 m wide band of gabbro mylonite within coarse-grained spinel lherzolite. On the basis of a 11° clockwise rotation of the trend of the main generation of mafic dykes in the overlying oceanic crust to the shear-zone, Andrews & Jolly (*in press*) propose that development of the oceanic crust occurred above an oblique spreading centre. Figure 7.4 that shows this shear-zone may represent the feeder zone to the overlying crust, but the possibility that the pre-existing mantle shear-zone could also represent a feeder zone cannot be excluded, although there is currently no field evidence to support this hypothesis.

It is therefore apparent that during this later evolution of the oceanic crust sequence of the Lizard Ophiolite Complex, tectonic processes rather than magmatism dominated extension. This observation is consistent with the tectonic model proposed for the earlier evolution of the upper mantle and lower crust sequence of the Lizard (Section 7.2.2). It is also evident that the NE-SW directed extension inferred from the

mylonitic fabrics in the Lizard peridotites and Traboe cumulates continued during the later evolution of this oceanic crust sequence.

#### 7.2.4. Emplacement of the Lizard Ophiolite Complex

Emplacement or obduction of the Lizard Ophiolite Complex was responsible for the juxtaposition of several different lithological units, which are the Lizard peridotites, Landwednack amphibolites and Ordovician basement. This included top-to-the-NW thrusting of mantle peridotites over Landwednack amphibolites (Figure 7.5), which represent deformed and metamorphosed oceanic crust. This is in keeping with the

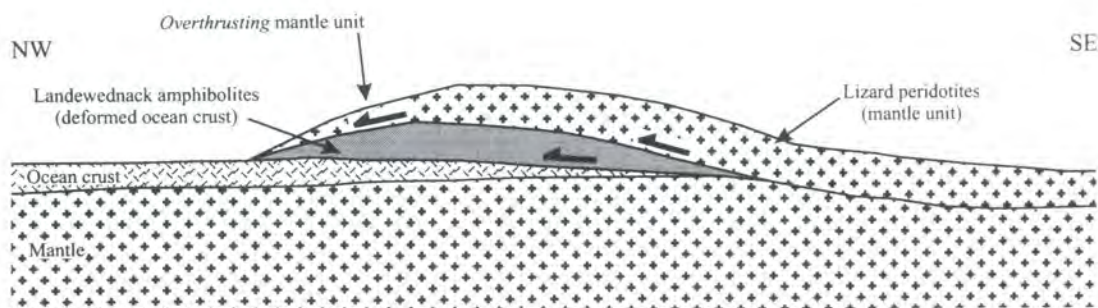


**Figure 7.5.** Sketch illustrating the overthrusting of the mantle unit over Landwednack amphibolites.

obduction-related structural evolution of several well-known ophiolites, for example Bay of Islands (Suhr & Cawood, 1993) and Oman (Searle & Malpas, 1980). The fact that mantle peridotites structurally overlie deformed oceanic crust demonstrates that the detachment surface that forms the contact between these units extended down at least to the upper mantle. Although the basal part of the Lizard Ophiolite Complex and emplacement-related structures are in many ways comparable with other ophiolite complexes, there are several unusual features observed in the Lizard which distinguish it from the basal sequence of 'typical' ophiolite complexes (e.g. Williams & Smyth, 1973):

- 1) The basal part of the peridotite unit is not composed of high-temperature mylonitic peridotites.



- 2) The absence of an inverted metamorphic zonation in amphibolites below the peridotite unit from amphibolite- and granulite-facies rocks at the top to sub-greenschist facies at the base.
- 3) The extensive magmatism during emplacement, involving the intrusion of a mixed suite of felsic and mafic magmas along the detachment surface.
- 4) The re-activation of thrust contacts involving the development of apparently extensional, serpentine-filled fault zones.
- 5) The present day kinematics of the thrust contact between the overlying peridotite and underlying amphibolite suggesting apparently extensional displacements.

Several lines of evidence suggest that the final phase of overthrusting of the Lizard Ophiolite Complex occurred at lower temperature ( $< 638^{\circ}\text{C}$ ) than other examples of ophiolite complexes (see above). This evidence includes estimates of the conditions of P & T during metamorphism of the Landwednack amphibolites (Chapter 5) and a lack of high-temperature peridotite mylonites at the base of the peridotite unit. Instead deformation in the basal part of the peridotite unit was accommodated by the development of hydrous shear zones composed of amphibole and chlorite (Chapters 3 & 4)(compare Figure 1.4 with Figures 3.46, 3.48 & 3.50). These shear zones cross-cut the earlier steep fabrics in the peridotite and are parallel to both the thrust contact and fabrics developed in the underlying amphibolites. Shear-sense indicators within these shear zones are consistent with top-to-the-NW displacement of the peridotite unit over the Landwednack amphibolites. During emplacement, low-angle fabrics were developed in the Landwednack amphibolites. These fabrics cross-cut earlier steeper fabrics related to construction of the oceanic crust sequence (Section 7.2.2). Amphibolites with a steep fabric are characterised by a high-temperature metamorphic mineral assemblage composed of brown amphibole + plagioclase (Chapter 4). In areas where the amphibolites have low-angle fabrics, the mineral assemblage is characterised by the presence of a retrograde metamorphic assemblage composed of green amphibole + plagioclase (Chapter 4). A third retrograde metamorphic assemblage occurs in narrow shear zones and is distinguished by the presence of colourless hornblende (Chapter 4). It is proposed that the latter two retrograde metamorphic mineral assemblages were developed during metamorphism associated with the emplacement of the Lizard Ophiolite Complex. Similar metamorphic assemblages are developed in the

mafic Traboe cumulates and gabbroic veins. Emplacement-related fabrics are also observed in the rocks of the Ordovician basement. These fabrics were developed during thrusting of Devonian rocks of the Lizard Ophiolite Complex over the basement (Chapter 3).

SHRIMP dating of the felsic component of the Kennack Gneiss, part of a syn-tectonic magmatic suite intruded during emplacement of the Lizard Ophiolite Complex, has constrained emplacement to an age of ca. 390-384 Ma (Chapter 3). Additional age determinations provided by SHRIMP dating (Chapter 3), provide dates ranging between ca. 392-374 Ma for the metamorphism of Landewednack amphibolites and a gabbroic vein. With consideration of analytical errors this indicates that the thermal event(s) associated with emplacement of the Lizard Ophiolite Complex span a minimum of 18 Ma and a maximum of 47 Ma. This data is consistent with the span of age ranges for the emplacement of other ophiolites, for example the Semail ophiolite in Oman (Searle & Malpas, 1980) and the Bay of Islands ophiolite in Newfoundland (Cawood & Suhr, 1992).

Several conclusions can be drawn from the evidence presented above and in the preceding chapters. Emplacement of the Lizard Ophiolite Complex took place as an intra-oceanic thrusting event (Figure 7.5; Chapter 3; Chapter 6). The mantle unit was relatively cool during emplacement and peridotite mylonites were not developed at its base. This meant that an inverted metamorphic zonation was not developed in the underlying amphibolites. It is suggested that some residual heat was present in the mantle unit and was responsible for the amphibolite-grade metamorphism of the Landewednack amphibolites, an event distinct from the earlier deformation and high-temperature (900-1050°C) metamorphism of the Traboe cumulates. This phase of relatively cool emplacement should not be confused with the later, cold emplacement of the Lizard Ophiolite Complex over Meneage melange sediments and volcanic rocks (Barnes & Andrews, 1984), i.e., the event discussed above occurred earlier and in an intra-oceanic setting.

The origin of the Kennack Gneiss is poorly constrained. Isotopic evidence (Chapter 6; Darbyshire & Shepherd, 1994) suggests that the felsic component may possibly be derived from melting of Palaeozoic metasedimentary rocks under-thrust beneath the Lizard Ophiolite Complex and similar to those exposed to the north of the Lizard Ophiolite Complex. The mafic component of the Kennack Gneiss has

geochemical properties similar to arc-derived magmas (Floyd *et al.*, 1993). It is therefore possible that emplacement of the Lizard Ophiolite Complex actually involved underthrusting of oceanic crust beneath mantle in a subduction zone and that the Kennack Gneiss is the product of melting of subducted mafic rocks. It is proposed that the Lizard Ophiolite Complex was emplaced as a series of thrust sheets, with the peridotites forming the highest structural unit above a unit of deformed and metamorphosed oceanic crust while, Ordovician basement forms the lowest structural unit.

Reactivation of the thrust contact between the peridotite and Landewednack amphibolite involved the development of apparently extensional, serpentine-filled fault zones. The serpentine-filled faults could have formed during reactivation of thrust contacts in response to late stage foreland-directed collapse of the nappe pile (Jones, 1997)(Figure 7.6). This model would explain why the majority of the serpentine-filled fault zones are more steeply dipping than the original thrust contacts (Chapter 3). It is suggested that overthrusting of the mantle unit provided the necessary load for gravity-driven, vertical tectonic thinning. The development of serpentine-filled faults demonstrates that reactivation is a significant feature in the structural evolution of the Lizard Ophiolite Complex. These findings have important implications for the development of basal serpentinite zones of other ophiolite complexes, for example the Semail ophiolite, Oman (Searle & Malpas, 1980), which may have also developed during re-activation of earlier, higher-temperature thrust contacts.

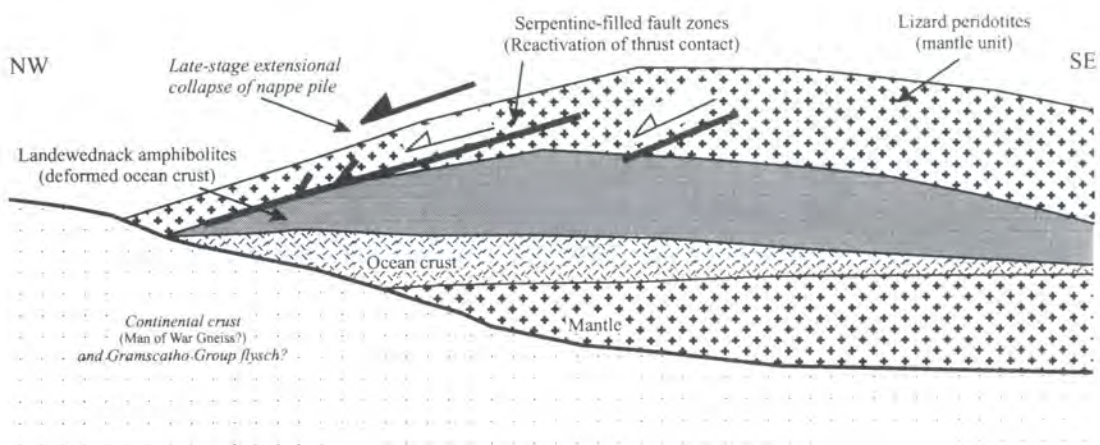


**Figure 7.6.** Late -stage extensional collapse of the nappe pile, facilitated by reactivation of earlier thrust contacts (cf. Jones, 1997) is proposed to account for the development of serpentine-filled faults.

On the east coast of the Lizard, thrust contacts between the overlying peridotite and underlying Landewednack amphibolites strike NE-SW and dip at a low-angle towards the NW. Shear sense indicators within shear zones in the basal part of the peridotites and in the amphibolites indicate a top-to-the-NW apparently extensional displacement (Chapter 3). It is suggested that the present day geometry of these contacts may be related to post-emplacement fault-block rotation facilitated by displacement along later steep brittle faults (Figure 7.7) or related to the extensional collapse phase (Figure 7.6) and reactivation of the emplacement-related thrusts.

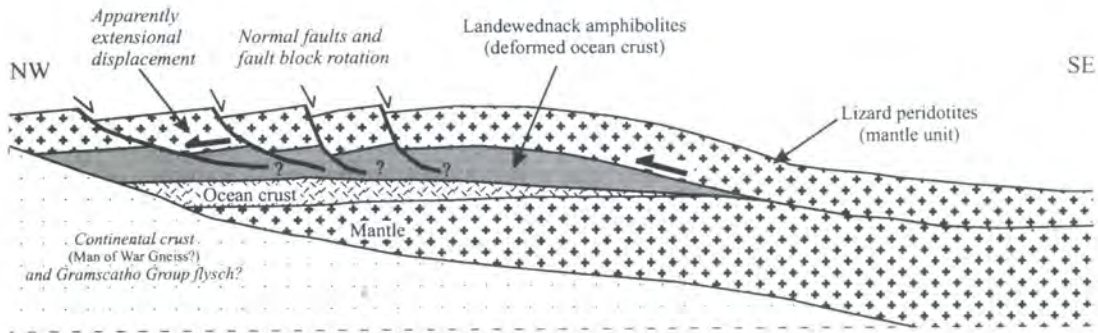


**Figure 7.7.** A sketch, which demonstrates that later post-emplacement faulting and rotation of the thrust contact within rotated fault blocks may explain the present day geometry and apparently extensional displacements along thrust contacts between peridotite and amphibolite on the east coast of the Lizard peninsula.

### 7.3 Regional tectonic implications of evolution of the Lizard Ophiolite Complex

#### 7.3.1. Ordovician evolution of NW Europe

Sandeman *et al.* (1997) demonstrated that the early Ordovician age of the MOWG is significantly older than any other in situ igneous or meta-igneous rocks in SW England. The association of the MOWG and the OLHS which both exhibit arc-like geochemical characteristics has important implications for the pre-Hercynian geological history of NW Europe (Sandeman *et al.*, 1997). Several other complexes in the northern and western European Variscides, which incorporate granitic rocks, pelitic metasediments, ophiolitic units, oceanic island volcanics, calc-alkaline volcanics and high P-T metabasites, yield U-Pb ages in the range ca. 480-510 Ma (Sandeman *et al.*, 1997).



These complexes include: the Morais complex of northern Portugal (Dallmeyer & Tucker, 1993); the Malpica-Tuy allochthon in NW Spain (Santos Zalduegui *et al.*, 1995); the Sudeten Batholith of SW Poland (Oliver *et al.*, 1993); and the Góry Sowie Massif of SW Poland (Kröner & Hegner, 1998). A similarity in ages of these complexes and their geological similarity are evidence for the existence of an active magmatic arc in the Cambrian and Ordovician times (Kröner & Hegner, 1998). This arc would have extended between the English Channel to the SW Sudetes of Poland. Sandeman *et al.* (1997) consider that during the Ordovician, eastern Avalonia was probably separated from northern Gondwana by the Rheic ocean basin.

### **7.3.2. Devonian tectonic evolution of SW England**

The tectonic models (Sections 7.2.2, 7.2.3. & 7.2.4) proposed for the tectonic evolution of the Devonian rocks of the Lizard Ophiolite Complex are broadly compatible with the tectonic model for the evolution of south Cornwall presented by Holder & Leveridge (1986a) (Chapter 2; Figure 2.3). The Holder & Leveridge (*op cit.*) model predicts the presence of an ocean basin in the Gedinian - Siegenian (i.e. Early Devonian). Direct comparisons have been made between the association between the Lizard Ophiolite Complex, Carrick Nappe flysch, Dodman Phyllites and the Eddystone gneisses (Normannian Nappe) in SW England with the Giessen/Selke Nappe, Northern Phyllite zone and the Mid-German Crystalline Rise of the Harz and eastern Rhineland in Germany (Holder & Leveridge, 1986b). Similarities between these two regions of the Rheohercynian zone led Holder & Leveridge (1986a) to propose the existence of an extensive along-strike oceanic basin in the north European Variscides, rather than the localised short-lived basin suggested previously by Badham (1982). It has been suggested that the crustal thinning necessary to produce the Gramscatho basin and oceanic crust represented by the Lizard Ophiolite Complex may have arisen as a local pull-apart associated with dextral strike-slip faulting (Badham, 1982). The localised nature of the rocks of the Lizard Ophiolite Complex is compatible with this model and, more significantly with the NW-SE trend of the sheeted dyke complex which implies NE-SW directed extension, which is consistent with an E-W dextral shear (Sanderson, 1984). Furthermore, isotopic evidence presented by Davies (1984) demonstrates that the magmatic evolution of the Lizard Ophiolite Complex is analogous to that of the

early stages of rifting of the Red Sea, which represents a relatively small intracontinental basin. Barnes & Andrews (1986) reviewed previously published field and geochemical data on the Lizard Ophiolite Complex and Meneage Formation and, following Badham (1982) suggested that the findings were consistent with the Lizard Ophiolite Complex being developed in a pull-apart basin associated with an E-W trending intracontinental dextral transform fault zone. Barnes & Andrews (1986) suggested similarities between the development of the Lizard Ophiolite Complex and the Caymen Ridge (Wadge & Burke, 1983; Mann *et al.*, 1983), rifting of the Baja California and Salton Sea basin associated with San Andreas fault system (Cromwell & Sylvester, 1979). The suggestion that the E-W trending Start-Perranporth line (SPL) in S.Devon and Cornwall marked a major basement fault during the Devonian (Holdsworth, 1989) has provided further support for the model of Badham (1982). The SPL basement fault zone appears to have been a major E-W continental dextral megashear that formed the northern boundary for a series of pull-apart basins (Holdsworth, *op cit.*). Further evidence for the NE-SW directed extension during development of the later crust sequence of the Lizard Ophiolite Complex is demonstrated by a series of NW-SE orientated extensional shear zones that dip towards the NE in the Crousa gabbro. These shear zones have been interpreted to represent ridge-parallel faults that controlled lithospheric extension during construction of the later oceanic crust sequence (Roberts *et al.*, 1993). Following Badham (*op cit.*), Sanderson (*op cit.*), Barnes & Andrews (*op cit.*) and Holdsworth (*op cit.*), it is suggested that the Lizard Ophiolite Complex and the Gramscatho flysch basin formed in a dextral pull-apart basin (Figure 7.8) during the early Devonian. Several lines of evidence support this hypothesis: (1) In Section 7.2.1 it is suggested that the deformation and exhumation of Lizard peridotites may be consistent with asymmetric extension in the early stages of oceanic rifting. Asymmetric extension in a pull-apart basin is not an atypical feature of extending crustal lithosphere. For example it has been demonstrated by COCORP deep seismic reflection profiles that the Death Valley pull-apart basin in southeastern California shows an asymmetrical architecture (Serpa *et al.*, 1988) and the exhumation of Errio-Tobbio peridotites of NW Italy is believed to have been accommodated km- to 100-m-scale extensional shear zones in the mantle by asymmetric extension associated with 'passive' rifting in a pull-apart domain such as the Piemonte-Ligurian ocean (Hoogerduijn Strating, 1990). (2) The rather fertile chemistry of the Lizard peridotites (Chapter 6) is similar to sub-continental mantle, this



and the limited crust sequence of the ophiolite and the localised nature of the Lizard Ophiolite Complex are compatible with a pull-apart model. (3) A NE-SW extension direction is inferred from the fabrics in the mylonitic peridotites and deformed Traboe cumulates that strike NW-SE and dip steeply NE, in addition to the NW-SE orientation of mafic dykes of the sheeted dyke complex and extensional shear zones in the Crousa gabbro (see above). This extension direction is consistent with development of a pull-apart basin associated with E-W trending intracontinental dextral fault zone; i.e. the SPL (see above).

In light of the findings of Holdsworth (*op cit.*) and the evidence presented in this thesis (see above) the former existence of an extensive along-strike basin in the north European Variscides during the Early Devonian (Holder & Leveridge, 1986a) is rejected. Alternatively it is suggested that the Giessen/Selke Nappe, Northern Phyllite zone and the Mid-German Crystalline Rise of the Harz and eastern Rhineland in

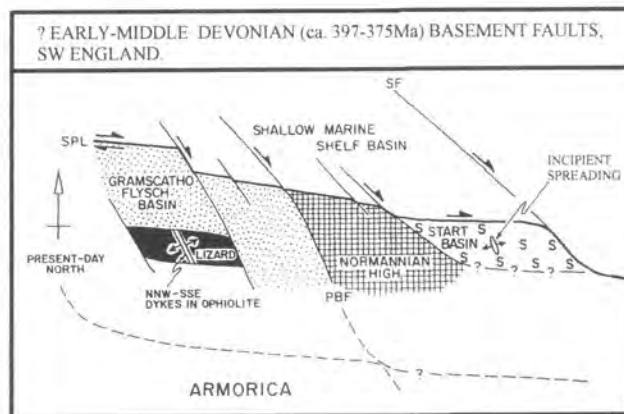


**Figure 7.8.** Speculative sketch map showing the suggested fault and basin configuration in pre-Devonian basement ca. 397-375 Ma. SPL, Start-Perranporth line fault; PBF, Plymouth Bay fault; SF, Sticklepeth fault. Adapted after Holdsworth (1989).

Germany (Holder & Leveridge, 1986b), the Gramscatho flysch and Lizard Ophiolite Complex (Normannian Nappe) and possibly the Start Complex (Holdsworth, *op cit.*) formed in a series of separate dextral pull-apart basins along the Rhenohercynian zone.

Closure of the ocean basin, top-to-the-NW thrusting and obduction of oceanic crust was initiated in the Emsian (i.e. late-Early Devonian), and Holder & Leveridge (*op cit.*) suggested that complete closure of the ocean basin had occurred by the Fammenian (i.e. Late Devonian), which is compatible with the span of U-Pb ages presented in Chapter 3. Holder & Leveridge (*op cit.*) proposed that closure of the ocean

basin was probably associated with a southward dipping subduction zone below a Normannian Nappe. This model is supported by the arc-like geochemical characteristics of the Kennack Gneiss, which was intruded during emplacement of the Lizard Ophiolite Complex and the felsic component of this mixed felsic and mafic suite may have been derived from melting of rocks in the under-thrust Gramscatho Group flysch (Figure 7.9). The source of the mafic component is not known. A major omission in the Holder & Leveridge (*op cit.*) model is the lack of the inclusion of a

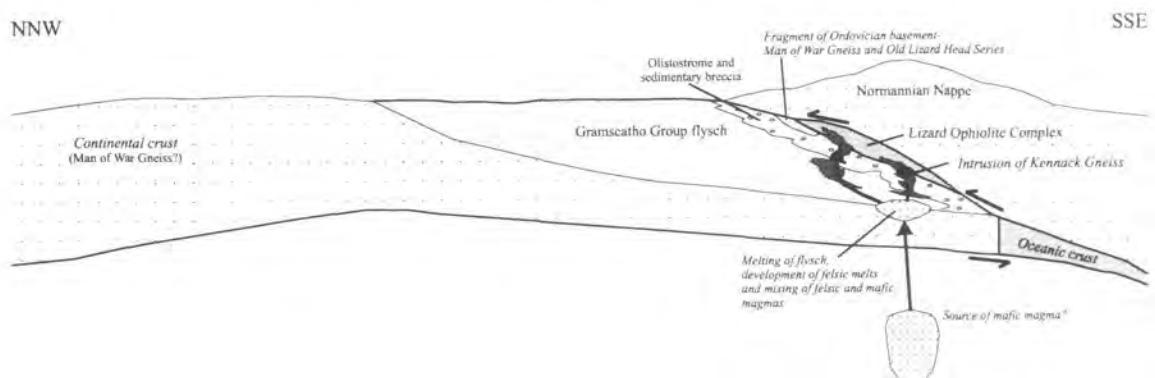


**Figure 7.9.** A model for the closure of a Devonian ocean basin accommodated by a southerly dipping subduction zone. Kennack Gneiss intrusions along the thrust contact below the Lizard Ophiolite Complex are inferred to be derived from melting of the 'underthrust' Gramscatho Group flysch forming felsic magmas and mixing with mafic magmas from an unknown source. Adapted after Holder & Leveridge (1986a).

fragment of Ordovician basement at the base of the Lizard Nappe, but the Ordovician age of these rocks was not known at the time the model was presented.

#### 7.4. Implications for the early evolution of mantle rocks in ophiolite complexes

The implications of early evolution of the mantle section in ophiolite sequences have been overlooked in many studies. It has often been assumed that the fabrics in peridotites were developed during the ascent of a mantle diapir beneath a mid-ocean ridge. Although mantle diapirism may be responsible for the evolution of mantle in some ophiolite complexes, it is not the only possible process. The combined structural and geochemical approach adopted in this present study demonstrates that the early evolution of the Lizard peridotites is consistent with tectonic exhumation by asymmetric extension during the development of an oceanic rift (Section 7.2.2). This tectonic model highlights the importance of a wide-range of deformation processes that

operate in the upper mantle and the effects of syn-tectonic melt-fluid infiltration. In the following sections the implications of these processes are discussed.

#### 7.4.1. Mantle fabrics in ophiolite complexes

Until recently, early pre-emplacement related fabrics in mantle section of ophiolites were interpreted in terms of asthenospheric flow beneath mid-oceanic ridges (e.g. Ceuleneer *et al.*, 1988). Following a detailed study of fabrics in the mantle section of

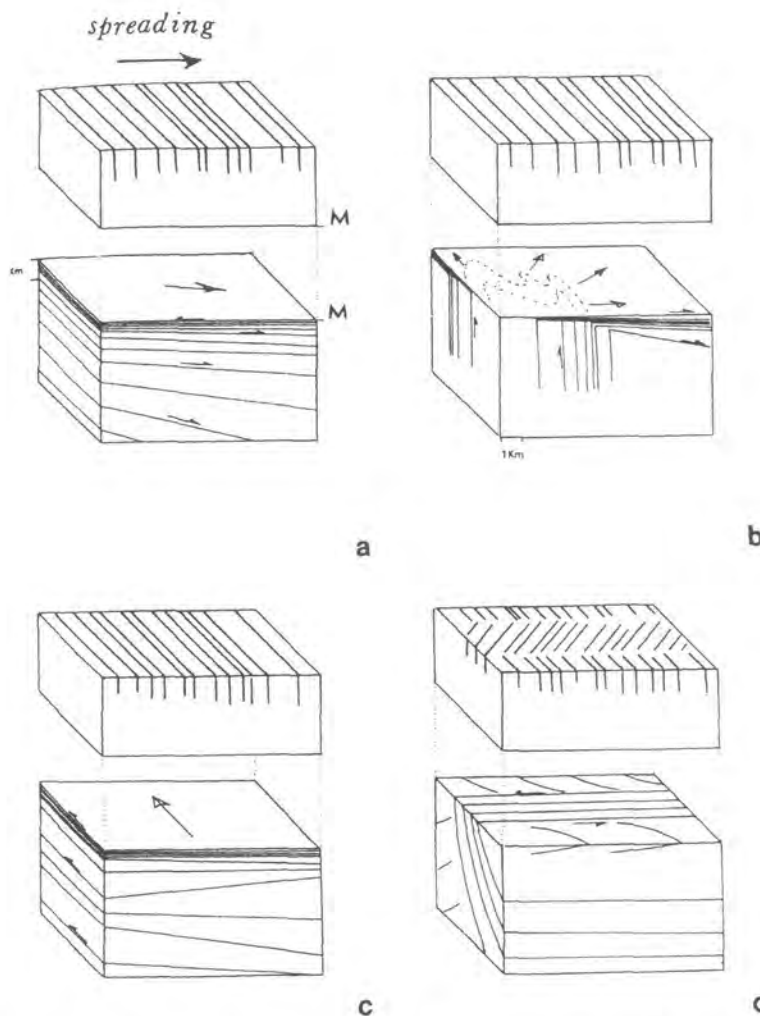


**Figure 7.10.** Sketch of the four asthenospheric flow patterns below spreading centres, based on recognition of such patterns in the Oman mantle peridotites. Upper boxes: Crustal reference plane (sheeted dykes and Moho discontinuity). Lower boxes: Asthenospheric flow planes and lines. *M* – Moho. (a) Homogeneous flow at right angles to ridge axis, (b) Vertical flow lines, down-dip flow planes and curved flow plane trajectories, (c) Flow line parallel to ridge axis, (d) Flow planes strongly dipping and striking normal to the ridge axis. Subhorizontal flow lines indicate strike-slip (from Ceuleneer *et al.*, 1988).

the Oman ophiolite, Ceuleneer *et al.* (1988) documented four well-contrasted asthenospheric flow patterns (Figure 7.10). These included: a) homogeneous flow away from a ridge axis, b) flow in asthenospheric diapirs, c) channeling of mantle flow along a ridge axis, and, d) asthenospheric flow in a broad mantle shear zone. The only flow pattern that bears any similarity with the steep fabrics observed in the Lizard peridotites is that associated with diapirs, but the swing of the fabric from vertical to sub-horizontal a few hundred metres below the cumulates is not observed in the Lizard. In all of these flow pattern models deformation fabrics are restricted to the mantle section and are not observed in the overlying cumulates. In the Lizard Ophiolite Complex, deformation fabrics in the mylonitic peridotites and overlying Traboe cumulates are parallel and interpreted as contemporaneous (Section 7.2.2). As a consequence, it was proposed in Section 7.2.2. that these fabrics were developed during tectonic exhumation of the mantle in response to the early stages of oceanic rifting in a pull-apart basin and that deformation of the Traboe cumulates occurred in the hangingwall of a mantle shear zone. The development of a pull-apart basin is often associated with very rapid, focused zones of extension and this could adequately accommodate the ca. 30km exhumation of the Lizard peridotites. This interpretation is based, in part, on a tectonic model proposed for the evolution of Liguria ophiolite complexes (Hoogerduijn Strating, 1991), with which the peridotites of the Lizard Ophiolite Complex share many similarities. Thus, the Moho is defined not only by an igneous compositional change from mantle peridotites to ultramafic and mafic cumulates, but more significantly by a major detachment surface. Rheological consequences of this detachment surface are discussed in Section 7.4.3. Therefore mantle fabrics and the microstructural characteristics of peridotites from ophiolite complexes around the world should be studied in detail as they provide important clues as to the structural evolution of mantle in oceanic lithosphere. In particular, these fabrics in ophiolites that have previously been interpreted to represent asthenospheric flow beneath mid-ocean ridges require re-examination. Piccardo *et al.* (1993) recently proposed that the Zabargad Island (Red Sea) peridotites were tectonically exhumed in a lithosphere-scale dipping extensional detachment zone during the early rifting stage of the northern sector of the Red Sea. The microstructural and chemical evolution of the Lizard peridotites is remarkably similar to that of the Zabargad Island peridotites and provides further support for the tectonic model proposed for the early evolution of mantle section of the Lizard Ophiolite Complex.

#### 7.4.2. Implications of syn-tectonic melt infiltration

Mylonitic peridotites from the Lizard Ophiolite Complex are chemically enriched in LREE and certain major and trace elements relative to the less deformed coarse-grained lherzolites. In Chapter 6, it was suggested that a km-scale reaction front involving discrete batches of infiltrating melt during deformation was responsible for this enrichment. Development of amphibole grains in the mylonitic peridotites suggests that the infiltrating melt was volatile-rich. The source of the melt is not known, but it may have been derived from the lower oceanic crustal rocks (Traboe cumulates) that formed the hangingwall of the shear zones responsible for the tectonic exhumation of the peridotites. Melts could have gained access to the mantle via shear zones represented by the mylonitic peridotites. Alternatively, the melts could have been generated at deeper (asthenospheric) levels during initiation of rifting and infiltrated mantle shear zones during extension of the overlying lithosphere. Regardless of whether the volatile-rich melts are derived from lower oceanic crustal rocks, or from the mantle (asthenospheric), it is clear that the melts have preferentially infiltrated and metasomatised the mylonitic peridotites that formed the mantle shear zone. A process of pervasive melt flow through porous peridotite is favoured rather than melt flow through fractures. When a melt flows through fractures, the reaction surface between melt and host peridotite is limited and therefore metasomatism is also spatially limited (Van der Wal & Bodinier, 1996). If pervasive melt flow through porous peridotite occurred the reactional surface is nearly unlimited and hence km-scale metasomatism of the peridotite is possible (Van der Wal & Bodinier, 1996). Km-scale pervasive porous melt flow has been proposed by Van der Wal & Bodinier (1996) to account for structural and geochemical features of the Ronda massif in southern Spain.

Structural and geochemical evidence from the Lizard suggests that porous flow of volatile-rich melt in the mantle was preferentially focused along actively deforming shear zones. Several different explanations are presented for this process and are based on the recent findings of Kelemen & Dick (1995). Kelemen & Dick (*op cit.*) investigated evidence for focused melt flow in mantle shear zones exposed in the Josephine peridotite in SW Oregon. Models include the hypothesis of Stevenson (1986), who proposed that weaker material in the mantle might be created by the presence of heterogeneous melt distribution and areas rich in melt would deform more

rapidly than surrounding peridotite. As a consequence, a pressure gradient would be created in which melt would flow into the weak zones (shear zones), maintaining and enhancing the initial rheological contrast (Kelemen & Dick, *op cit.*). Presence of anisotropic permeability in rocks with a strong crystal shape fabric and/or strong lattice preferred orientation may also favour focused melt flow along shear zones (Kelemen & Dick, *op cit.*). Focused flow of melt may also enhance localised deformation and the development of shear zones, i.e. there is a positive feedback mechanism involving 'melt-lubrication' of shear zones. In Section 6.3.3, it was suggested that the presence of a reaction front could account for the km-scale uniform metasomatism of the mylonitic peridotites in the Lizard Ophiolite Complex. Alternatively, 'clogging' of the intergranular porosity of the peridotite by crystallisation of the syn-tectonic melts during cooling associated with exhumation of the mantle could lead to defocusing of intergranular melt flow and migration of flow into adjacent 'un-clogged' regions of intergranular porosity.

One of the difficulties in an investigation syn-tectonic melt infiltration is determining whether the recrystallised nature of mantle shear zones facilitated melt infiltration, or whether the initial development of a shear zone is the result of deformation enhanced by melt flow, i.e. which came first? (Kelemen & Dick, *op cit.*). In the Lizard Ophiolite Complex, deformed peridotites which show no geochemical evidence for melt infiltration are observed (e.g. spinel and plagioclase lherzolites) and it is only the highly deformed mylonitic peridotites that show significant metasomatism as a result of melt infiltration. This indicates that the mylonitic peridotites probably formed in response to the development of focused flow networks in deforming peridotites that led to continued localisation of strain, increased recrystallisation and metasomatism i.e. shear zones formed first.

The presence of melts in deforming peridotites can lead to significant rheological weakening. For example, in the mylonitic amphibole-bearing peridotite from the Lizard Ophiolite Complex, the replacement of pyroxene by amphibole, a weaker phase, is suggestive of reaction softening (Karato *et al.*, 1986). This reaction is thought to be associated with interaction with volatile-rich melts. The influx of chemically active volatile-rich melts, synchronous with deformation is thought to have result in the breakdown of the *load-bearing framework*, in which the bulk rheology is controlled by a strong, interlocking network of silicate phases dominated by olivine (Handy, 1990). Breakdown of the *load-bearing framework* leads to the development of



localised *interconnected weak layers* (or shear zones), which now control the bulk strength of the fault rock and as a consequence, the rheological behaviour of the shear zone (Handy, 1990). Thus, the mylonitic peridotites from the Lizard Ophiolite Complex appear to represent areas of mantle rock that were significantly weakened during deformation as a consequence of transformation of the mineral phases in response to the influx of volatile-rich melts.

Melt 'lubricated' shear zones may therefore significantly weaken the upper mantle beneath rift zones and incipient ocean basins, relative to regions of deforming upper mantle where there is no influx of chemically active volatile-rich melt. Where developed, melt 'lubricated' shear zones would represent major structural discontinuities, which control the rheological behaviour of the upper mantle.

Further discussion of the rheological implications of syn-tectonic melt infiltration is presented below (Section 7.4.3).

#### **7.4.3. Rheological implications and strength of the mantle**

Jaroslow *et al.* (1996) predicted that zones of weakness in oceanic lithosphere may promote the existence of long-lived faults in the upper mantle at slow-spreading ridges and that this could facilitate tectonic exhumation of lower crust/upper mantle to higher structural levels by extension along low-angle detachment faults. Field and microstructural observations and geochemical analyses of deformed peridotites from the Lizard Ophiolite Complex suggest evidence to support the existence of similar detachment faults. Evidence from the Lizard shows that a detachment fault may have existed at the base of developing oceanic crust (i.e. the Moho) and that this fault is represented by mylonitic peridotites and high-temperature deformation of ultramafic and mafic Traboe cumulates. Shear localisation in the upper mantle is regarded by several authors (e.g. Kirby, 1985; Rutter and Brodie, 1988; Jaroslow *et al.*, 1996) to represent a possible weakening mechanism and may therefore 'eliminate' a significant part of the strength profile i.e. a localised reduction in the strength of the mantle. Thus trans-lithospheric failure and continental breakup can be facilitated at stresses much lower than expected, even than those predicted for wet dislocation creep at constant microstructure (Visser *et al.*, 1995). In the previous section (Section 7.4.2), it was proposed that the presence of melt 'lubricated' shear zones could provide localised zones of weakness in the mantle as a consequence of reaction softening processes. The

presence of a fluid during deformation can also result in weakening of rocks deforming by diffusion creep by increasing the bulk and grain boundary diffusion coefficients (Karato *et al.*, 1986). Another processes that may significantly weaken mantle shear zones can include the operative deformation mechanism. For instance, Rutter & Brodie (1988) and Jaroslow *et al.* (1996) demonstrated with reference to experimental work that shear zones characterised by intense grain size reduction, and therefore the operation of grain size sensitive diffusion creep processes, will be significantly weaker than those in which deformation was accommodated by brittle processes or grain size insensitive dislocation creep (Figure 7.11). On the basis of flow law data, Rutter & Brodie (*op cit.*) also showed that the most dramatic weakening is at *lower* temperatures, because the diffusion creep field expands with decreasing temperatures due to the smaller activation energy for diffusion creep relative to dislocation creep (Chapter 1: Figure 1.6). In summary, the four dominant weakening mechanisms recognised in mantle rocks at a microstructural scale are:

- Grain size reduction leading to the operation of diffusion creep.
- Infiltration of melt in deforming shear zones.
- Reaction softening caused by mineralogical phase changes (possibly in response to the interaction of volatile-rich melts).
- Fluid flux facilitating intragranular and intergranular deformation mechanisms.

Of these weakening mechanisms, reaction softening appears to have been the most important in weakening of the Lizard peridotites during deformation.

It is inferred that shear zone localisation and significant weakening of the mantle during the rifting associated with the tectonic exhumation of the Lizard peridotites was primarily related to syn-tectonic volatile-rich melt infiltration and the resultant progressive transformation to hydrated weaker phases e.g. amphibole. In other studies of mantle shear zones, a change in the dominant deformation has been invoked as the primary control for strain localisation and resultant weakening of the mantle (e.g. Vissers *et al.*, 1995; Jaroslow *et al.*, 1996). In recent studies of mantle rocks from SW Cyprus influx of chemically active hydrous fluids during deformation has been proposed to lead to long term weakening (Bailey, 1997; Jones *et al.*, 1997), but in general little emphasis has been placed on the role of melt infiltration as a mechanism of weakening. Therefore this study highlights an alternative process that has important

implications for the rheology of upper mantle during continental breakup and oceanic rifting and therefore merits further investigation.

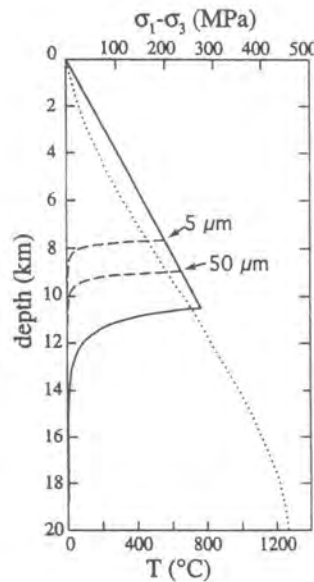


**Figure 7.11.** Schematic mechanical strength vs depth profile of the oceanic lithosphere. The dotted curve represents an inferred geotherm for 1-Ma lithosphere at a slow-spreading ridge. The upper line represents the brittle strength based on Byerlee's law for frictional sliding and the lower curve represents the ductile strength of the mantle assuming an olivine composition. The solid curve is for deformation accommodated by dislocation creep (from Jaroslow *et al.*, 1996).

## 7.5. Structural geology of the upper mantle

The present study and the studies discussed in the previous section (e.g. Kirby, 1985; Rutter and Brodie, 1988; Vissers *et al.*, 1995; Jaroslow *et al.*, 1996) highlight the rheological significance of localised deformation in the upper mantle during continental rifting and the early stages of oceanic rifting. Structural studies of orogenic peridotite massifs and ophiolites such as these supports the increasing acceptance that shear zones in the lithospheric upper mantle to some extent accommodate large-scale displacements associated with crustal extension and continental breakup. In addition to field based studies, deep seismic studies beneath extensional domains reveal the presence of deep reflectors beneath the seismic Moho, but it cannot be confirmed if these actually represent shear zones (e.g. Serpa & de Voogd, 1987; Serpa *et al.*, 1988; Reston, 1990).

The studies discussed above suggest that the mantle could play a major role in lithosphere deformation, because of its greater strength and the fact that it makes up a large part of the lithospheric plate. The weaker crust could then deform passively along with the mantle; i.e. the crust and mantle should deform coherently as part of the plate, a process known as vertically coherent deformation (VCD) (Silver & Chan, 1988; 1991). In a recent review, Silver (1996) shows that mantle fabric patterns, as revealed by seismic anisotropy from beneath continents derived from shear-wave splitting data suggest that mantle deformation is coherent and contemporaneous with deformation of the crust. The results also demonstrated that there is no clear evidence for a significant (~100 km thick) subcontinental decoupling zone, suggesting that the continental lithosphere is coupled to general mantle circulation. This study demonstrates that deformation is not limited to the crust, but it is a phenomenon that pervasively deforms the entire continental lithosphere, which is most consistent with the VCD model (Silver, *op cit.*). The mantle deformation described by Silver (*op cit.*) primarily relates to orogeny and is therefore very different to the mantle deformation fabrics described in the present study, which are not orogenic. The fabrics described in the present study are related to extensional tectonics and exhumation of the mantle, but the principles regarding the coherence of lithospheric deformation during orogenic deformation are believed to apply during lithospheric extension.

The findings of Silver (1996) further reinforces the importance of the investigation of structural geology of the mantle, since mantle deformation is not just a process limited to the study of ophiolites, but one that plays a major role in lithospheric deformation in general.

---

#### 7.4.4. Final conclusions

---

- Field, geochronological, microstructural and geochemical studies have demonstrated that rocks exposed on the Lizard peninsula include Ordovician basement and Devonian rocks of the Lizard Ophiolite Complex. Evidence for three tectono-magmatic events during Early to Late Devonian times has been identified in the rocks of the Lizard Ophiolite Complex.
- A basement, and structurally lowermost unit, comprising granitic (MOWG) and layered meta-sedimentary and meta-basic (OLHS) rocks of earliest Ordovician age (~499-488Ma) is interpreted as fragments of arc-type crust developed in an active magmatic arc during closure of an ocean basin (Rheic ocean?).

- Tectonic exhumation of mantle along extensional lithosphere-scale mantle shear zones in the Early Devonian or earlier (~397 Ma) may be responsible for the early tectonic evolution of the mantle section of the Lizard Ophiolite Complex. It is proposed that this may have occurred during asymmetric extension associated with continental breakup and oceanic rifting. During exhumation, the high-T and high-P mineral assemblage (~1200°C & 15Kb) of the Lizard peridotites progressively re-equilibrated to conditions of lower T and P (~919-1074°C & 5-6Kb). High temperature (~900-1050°C) deformation of ultramafic and mafic Traboe cumulates is consistent with deformation and metamorphism of early formed oceanic crust in the hangingwall of the inferred shear zone, which may have been located at the base of the crustal sequence close to the Moho.
- The later evolution of a second generation of oceanic crust sequence shown by gabbro and mafic dyke intrusion in the early to middle Devonian (~ 375 Ma) primarily involved magmatism, but NE-SW directed extension of the oceanic crust may have been predominantly accommodated by low-angle ductile shear zones, suggestive of a magma-starved slow-spreading ridge environment.
- Emplacement of the Lizard Ophiolite Complex took place during the Middle to Late Devonian (~390-366Ma). Top-to-the-NW thrusting facilitated decoupling of the mantle and emplacement over deformed and metamorphosed oceanic crust. During emplacement, widespread magmatism involved the intrusion of a mixed suite of felsic and mafic magmas that may well have been focused along the detachment surface. The geochemical characteristics of this suite of intrusive rocks suggests that initial emplacement of the Lizard Ophiolite Complex may have taken place in a subduction zone environment. Extensive, apparently extensional re-activation of thrust contacts involved the development serpentine-filled fault zones.
- It is proposed that infiltration of volatile-rich melts during the early mantle deformation and exhumation along extensional shear zones could have led to significant localisation of strain and weakening of the upper mantle. The main evidence supporting this hypothesis being mylonitic peridotites that demonstrate confirmation of chemical enrichment as a result of melt impregnation. Weakening may have occurred by replacement of strong mineral phases e.g. pyroxene by weaker phases e.g. amphibole i.e. reaction softening, characterised by the development of mylonitic amphibole-bearing peridotites. It is concluded that this and other weakening processes may also be responsible for the development and enhancement of mantle shear zones in other ophiolite complexes and present-day oceanic lithosphere during oceanic rifting.

## REFERENCES

- Agrinier, P., Mevel, C., Bosch, D. and Javoy, M.,** 1993. Metasomatic hydrous fluids in amphibole peridotites from Zabargad Island (Red Sea). *Earth and Planetary Science Letters*, **120**, 187-205.
- Alabaster, T., Pearce, J.A. and Malpas, J.,** 1982. The volcanic stratigraphy and petrogenesis of the Oman ophiolite complex, *Contributions to Mineralogy and Petrology*, **81**, 168-183.
- Alexander, A.C. and Shail, R.K.,** 1996. Late- to post-Variscan structures on the coast between Penzance and Pentewan, south Cornwall. *Proceedings of the Ussher Society*, **9**, 72-78.
- Andrews, J.R. and Jolly, R.J.H.** (in press). Asymmetric pattern of sub-moho gabbro dyke emplacement at an oblique spreading centre in the Lizard Ophiolite Complex, UK.
- Badham, J.P.N.,** 1982. Strike-slip orogens-an explanation for the Hercynides. *Journal of the Geological Society, London*, **139**, 493-504.
- Badham, J.P.N. and Kirby, G.A.,** 1976. Ophiolites and the generation of ocean crust: data from the Lizard Complex, Cornwall. *Bull. Soc. Geol. France*, **4**, 855-858.
- Bailey, W.R.,** 1997. The Structural Evolution of a microplate suture zone, SW Cyprus. Unpublished Ph.D. Thesis, University of Durham.
- Barber, D.J.,** 1985. Regimes of plastic deformation – processes and microstructures: an overview. In: Wenk, H.,-R. (ed), *Preferred orientation in deformed metals and rocks: an introduction to modern texture analysis*. Academic Press, New York.
- Barnes, R.P.,** 1984. Possible Lizard-derived material in the underlying Meneage Formation. *Journal of the Geological Society, London*, **141**, 79-85.
- Barnes, R.P. and Andrews, J.R.,** 1984. Hot or Cold emplacement of the Lizard Complex?. *Journal of the Geological Society, London*, **141**, 37-39.
- Barnes, R.P. and Andrews, J.R.,** 1986. Upper Palaeozoic ophiolite generation and obduction in south Cornwall. *Journal of the Geological Society, London*, **143**, 117-124.
- Basaltic Volcanism Study Project,** 1981. *Basaltic volcanism on the terrestrial planets*. New York: Pergamon Press, 1286 pp.
- Beard, J.S.,** 1986. Characteristic mineralogy of arc-related cumulate gabbros: Implications for the tectonic setting of gabbroic plutons and for andesite genesis. *Geology*, **14**, 848-851.



- Beniot, M., Polve, M. and Ceuleneer, G.,** 1996. Trace element and isotopic characterization of mafic cumulates in a fossil mantle diapir (Oman ophiolite). *Chemical Geology*, **134**, 199-214.
- Benn, K. and Laurent, R.,** 1987. Intrusive suite documented in the Troodos ophiolite plutonic complex, Cyprus. *Geology*, **15**, 821-824.
- Berthé, D., Choukroune, P. and Jegouzo, P.,** 1979. Orthogneiss, mylonite and non-coaxial deformation of granites: the example of the South Armorican Shear-zone. *Journal of Structural Geology*, **1**, 31-42.
- Bird, P.,** 1978. Initiation of intracontinental subduction in the Himalaya. *Journal of Geophysical Research*, **83**, 4975-4987.
- Blundy, J.D. and Holland, T.J.B.,** 1990. Calcic amphibole equilibria and a new amphibole-plagioclase geothermometer. *Contributions to Mineralogy and Petrology*, **104**, 208-224.
- Bolliot, G., Recq, M., Winterer, E.L. Meyer, A.W., Applegate, J., Baltuck, M., Bergen, J.A., Comas, M.C., Davies, T.A., Dunham, K., Evans, C.A., Girardeau, J., Goldberg, G., Haggerty, J., Janas, L.F., Johnson, J.A., Kasahara, J., Loreau, J.P., Luna-Sierra, E., Moullade, M., Ogg, J., Sarti, M., Thurow, J. and Williamson, M.,** 1987. Tectonic denudation of the upper mantle along passive margins: a model based on drilling results (ODP leg 103, western Galica margin, Spain). *Tectonophysics*, **132**, 335-342.
- Bodinier, J.L., Vasseur, G., Vernieres, J., Dupuy, C. and Fabries, J.,** 1990. Mechanisms of mantle metasomatism: Geochemical evidence from the Lherz Orogenic Peridotite. *Journal of Petrology*, **31**, 597-628.
- Bonatti, E. and Hamlyn, P.R.,** 1981. Oceanic ultramafic rocks. In: Emiliani, C. (ed.), *The Sea*, **7**, 241-283. J. Wiley and Sons, New York.
- Bonatti, E., Ottonello, G. and Hamlyn, P.R.,** 1986. Peridotites from the Island of Zabargad (St. John), Red Sea: Petrology and geochemistry. *Journal of Geophysical Research*, **91**, 599-631.
- Bonatti, E. and Michael, P.J.,** 1989. Mantle peridotites from continental rifts to ocean basins to subduction zones. *Earth and Planetary Science Letters*, **91**, 297-311.
- Bonney, T.G.,** 1883. The Hornblendic and other Schists of the Lizard District, with some additional Notes on the Serpentine. *Quarterly Journal of the Geological Society*, **xxxix**, 1-24.
- Bonney, T.G.,** 1887. Origin of certain Banded Gneisses. [Letter]. *Geological Magazine*, **iv**, 573-574.
- Bouchez, J.L., Lister, G.S. and Nicolas, A.,** 1983. Fabric Asymmetry and Shear Sense in Movement Zones. *Geologische Rundschau*, **72**, 401-419.

- Boudier, F. and Coleman, R.G.,** 1981. Cross section through the peridotite in the Semail Ophiolite, Southeastern Oman Mountains. *Journal of Geophysical Research*, **86**, 2573-2592.
- Boudier, F., Nicolas, A. and Bouchez, J.L.,** 1982. Kinematics of oceanic thrusting and subduction from basal sections of ophiolites. *Nature*, **296**, 825-828.
- Boudier, F. and Nicolas, A.,** 1985. Harzburgite and lherzolite subtypes in ophiolitic and oceanic environments. *Earth and Planetary Science Letters*, **76**, 84-92.
- Boudier, F., Ceuleneer, G. and Nicolas, A.,** 1988. Shear zones, thrusts and related magmatism in the Oman ophiolite: Initiation of thrusting on an oceanic ridge. *Tectonophysics*, **151**, 275-296.
- Boudier, F. and Nicolas, A.,** 1995. Nature of the Moho Transition Zone in the Oman Ophiolite. *Journal of Petrology*, **36**, 777-796.
- Boullier, A.M. and Guegen, Y.,** 1975. SP Mylonites: Origin of some Mylonites by superplastic flow. *Contributions to Mineralogy and Petrology*, **50**, 93-104.
- Boullier, A.M. and Nicolas, A.,** 1975. Classification of textures and fabrics of peridotite xenoliths from South African Kimberlites. In: Ahrens (ed.), *Physics and Chemistry of the Earth*, **9**, 97-105. Oxford: Pergamon.
- Brey, G.P., Kohler, T. and Nickel, K.G.,** 1990. Geothermobarometry in four-phase lherzolites I. Experimental results from 10 to 60 Kb. *Journal of Petrology*, **31**, 1313-1352.
- Brey, G.P. and Kohler, T.,** 1990. Geothermobarometry in four-phase lherzolites II. New thermobarometers and a practical assessment of existing thermobarometers. *Journal of Petrology*, **31**, 1353-1378.
- Bromley, A.V.,** 1973. The sequence of emplacement of basic dykes in the Lizard Complex, South Cornwall (abstract). *Proceedings of the Ussher Society*, **2**, 508.
- Bromley, A.V.,** 1975. Is the Lizard Complex, South Cornwall, a fragment of Hercynian ocean crust?. *The Lizard*, **5**, 2-11.
- Bromley, A.V.,** 1979. Ophiolitic origin of the Lizard Complex. *Cambourne School of Mines Journal*, **79**, 25-38.
- Buck, W.R., Martinez, F., Steckler, M.S. and Cochran, J.R.,** 1988. Thermal consequences of lithospheric extension: pure and simple. *Tectonics*, **7**, 213-234.
- Burret, C. and Griffiths, J.** 1977. A case for a mid-European ocean. In: *La Chaîne Varisque D'Europe Moyenne et Occidentale*. Colloque interne CNRS, Rennes, **243**, 313-328.
- Carter, N.L. and Ave Lallemant, H.G.** 1970. High temperature flow of dunite and peridotite. *Geological Society of America Bulletin*, **81**, 2181-2202.

- Casey, J.F., Elthon, D.L., Siroky, F.X., Karson, J.A. and Sullivan, J., 1985.** Geochemical and geological evidence bearing on the origin of the Bay of Islands and Coastal Complex Ophiolites of western Newfoundland. *Tectonophysics*, **116**, 1-40.
- Cawood, P.A. and Suhr, G., 1992.** Generation and obduction of ophiolites: Constraints from the Bay of Islands Complex, western Newfoundland. *Tectonics*, **11**, 884-897.
- Ceuleneer, G., Nicolas, A. and Boudier, F., 1988.** Mantle flow patterns at an oceanic spreading centre: The Oman peridotites record. *Tectonophysics*, **151**, 1-26.
- Chalot-Prat, F. and Boullier, A-M., 1997.** Metasomatism in the subcontinental mantle beneath the Eastern Carpathians (Romania): new evidence from trace element geochemistry. *Contributions to Mineralogy and Petrology*, **129**, 284-307.
- Chen, Y., Clark, A.H., Farrar, E., Wasteneys, H.A.H.P., Hodgson, M.J. and Bromley, A.V., 1993.** Diachronous and independent histories of plutonism and mineralisation in the Cornubian Batholith, southwest England. *Journal of the Geological Society, London*, **150**, 1183-1191.
- Church, W.R. and Stevens, R.K., 1971.** Early Palaeozoic ophiolite complexes of the Newfoundland Appalachians as mantle-oceanic crust sequences. *Geophysical Research*, **76**, 1460-1466.
- Church, B.N., Dostal, J., Owen, J.V. and Pettipas, A.R., 1995.** Late Paleozoic gabbroic rocks of the Bridge River accretionary complex, southwestern British Columbia: geology and geochemistry. *Geologische Rundschau*, **84**, 710-719.
- Claoue-Long, J.C., Compston, W., Roberts, J. and Fanning, C.M., 1995.** Two Carboniferous ages: A comparison of SHRIMP zircon dating with conventional zircon ages and  $^{40}\text{Ar}/^{39}\text{Ar}$  analysis. In: *Geochronology, Timescales and Global Stratigraphic Correlation*. Society for Sedimentary Geology Special Publication, **54**, 3-21.
- Clark, A.H., Sandeman, H.A., Liu, C., Scott, D.J., Farrar, E., Archibald, D.A., Bromley, A.V., Jones, K.A. and Warr, L.N. 1998a.** An emerging geochronological record of the construction and emplacement of the Lizard ophiolite, SW Cornwall (extended abstract). *Ussher Society Annual Conference*, Bideford, 4-6 Jan., 1998, Programme and Abstracts, 6-7.
- Clark, A.H., Scott, D.J., Sandeman, H.A., Bromley, A.V. and Farrar, E., 1998b.** Siegenian generation of the Lizard ophiolite: U-Pb zircon age data for plagiogranite, Porthkerris, Cornwall. *Journal of the Geological Society, London*, **155**, 595-598.
- Cocks, L.R.M. and Fortey, R.A., 1982.** Faunal evidence for oceanic separations in the Palaeozoic of Britain. *Journal of the Geological Society, London*, **139**, 465-478.
- Coleman, R.G., 1971.** Petrologic and geophysical nature of serpentinites, *Geological Society of America Bulletin*, **82**, 897-918.
- Coleman, R.G., 1977.** *Ophiolites*. Berlin: Springer-Verlag, pp229.

- Compston, W., Williams, I.S. and Meyer, C., 1984.** U-Pb geochronology of zircons from lunar breccia 73217 using a sensitive high mass-resolution ion microprobe. In: Boynton, W.V. *et al.* (eds.), *Proceeding of the fourteenth lunar and planetary science conference, part 2, Journal of Geophysical Research*, **89B**, 525-534.
- Crowell, J.C. and Sylvester, A.G., 1979.** *Tectonics of the Junction between the San Andreas Fault System and the Salton Trough, southeastern California*. Department Geological Sciences, University of California, Santa Barbara, CA 93106, 193pp.
- Culpan, N., 1993.** A study of chromian spinels from the Lizard Ophiolite, Cornwall, England. MSc Mining Geology, Camborne Schools of Mines. September 1993.
- Dallmeyer, R.D. and Tucker, R.D., 1993.** U-Pb zircon age for the Lagoa augen gneiss, Morais complex, Portugal: tectonic implications. *Journal of the Geological Society, London*, **150**, 405-410.
- Darbyshire, D.P.F. and Shepherd, T.J., 1994.** Nd and Sr isotopic constraints on the origin of the Cornubian batholith, SW England, *Journal of the Geological Society of London*, **151**, 795-802.
- Davies, G.R., 1983.** *The isotopic evolution of the British lithosphere*, Unpublished Ph.D. Thesis, Open University.
- Davies, G.R., 1984.** Isotopic evolution of the Lizard Complex, *Journal of the Geological Society of London*, **141**, 3-14.
- Dick, H.J.B., 1977.** Partial melting in the Josephine Peridotite I: The effect on mineral composition and its consequences for geobarometry and geothermometry. *American Journal of Science*, **277**, 801-832.
- Dick, H.J.B. and Bullen, T., 1984.** Chromian spinel as a petrogenetic indicator in abyssal and alpine-type peridotites and spatially associated lavas, *Contributions to Mineralogy and Petrology*, **86**, 54-76.
- Dilek, Y. and Eddy, C.A., 1992.** The Troodos (Cyprus) and Kizildag (S. Turkey) Ophiolites as Structural Models for Slow-Spreading Ridge Segments. *The Journal of Geology*, **100**, 305-322.
- Dodson, M.H., 1961.** Isotopic ages from the Lizard peninsula, South Cornwall. *Proceedings of the Geological Society of London*, **1591**, 133-136.
- Doody, J.J. and Brooks, M., 1986.** Seismic refraction investigation of the structural setting of the Lizard and Start Complexes, SW England. *Journal of the Geological Society, London*, **143**, 135-139.
- Droop, G.T.R., 1987.** A general equation for estimating  $\text{Fe}^{3+}$  concentrations in ferromagnesian silicates and oxides from microprobe analyses, using stoichiometric criteria. *Mineralogical Magazine*, **51**, 431-435.

- Drury, M.R., Hoogerduijn Strating, E.H., and Vissers, R.L.M.,** 1990. Shear zone structures and microstructures in mantle peridotites from the Voltri Massif, Ligurian Alps, N.W. Italy. *Geologie en Mijnbouw*, **69**, 3-17.
- Drury, M.R. and Urai, J.L.** 1990. Deformation-related recrystallization processes. *Tectonophysics*, **172**, 235-253.
- Dupuy, C., Mevel, C., Bodinier, J.-L. and Savoyant, L.,** 1991. Zabargad peridotite: Evidence for multistage metasomatism during Red Sea rifting. *Geology*, **19**, 722-725.
- Edwards, S.J. and Malpas, J.,** 1995. Multiple origins for mantle harzburgites: examples from the Lewis Hills, Bay of Islands ophiolite, Newfoundland. *Canadian Journal of Earth Sciences*, **32**, 1046-1057.
- Edwards, S.J. and Malpas, J.,** 1996. Melt-peridotite interactions in shallow mantle at the East Pacific Rise: Evidence from ODP Site 895 (Hess Deep). *Mineralogical Magazine*, **60**, 191-206.
- Eggler, D.H.,** 1987. Solubility of major and trace elements in mantle metasomatic fluids. Experimental constraints. In: *Mantle Metasomatism*, Menzies, M.A. and Hawkesworth, C.J. (eds.), Academic Press, London, 21-39.
- Elthon, D.,** 1991. Geochemical evidence for formation of the Bay of Islands ophiolite above a subduction zone. *Nature*, **354**, 140-143.
- Etheridge, M.A., Cox, S.F., Wall, V.J. and Vernon, R.H.,** 1984. High fluid pressures during regional metamorphism and deformation: Implications for mass transport and deformation mechanisms. *Journal of Geophysical Research*, **89**, 4344-4358.
- Fabries, J., Bodinier, J.-L., Dupuy, C., Lorand, J.-P. and Benkerrou, C.,** 1989. Evidence for modal metasomatism in the orogenic spinel lherzolite body from Caussou (northeastern Pyrenees, France). *Journal of Petrology*, **30**, 199-228.
- Fabries, J., Lorand, J.-P., Bodinier, J.-L. and Dupuy, C.,** 1991. Evolution of the upper mantle beneath the Pyrenees: Evidence from orogenic spinel lherzolite massifs. In: Menzies, M.A., Dupuy, C. and Nicolas, A. (eds.), *Orogenic Lherzolites and Mantle Processes*, Journal of Petrology Special Lherzolites Issue, 211-227.
- Fergusson, C.L. and Cawood, P.A.,** 1995. Structural history of the metamorphic sole of the Bay of Islands Complex, western Newfoundland. *Canadian Journal of Earth Sciences*, **32**, 533-544.
- FitzGerald, J.D., Etheridge, M.A. and Vernon, R.H.** 1983. Dynamic recrystallisation in a naturally recrystallized albite. *Textures Microstruct.*, **5**, 219-237.
- Flett, J.S.,** 1946. *The geology of the Lizard and Meneage* (Sheet 359). Memoir of the Geological Survey of Great Britain, 2nd edition, HMSO, London.
- Flett, J.S. and Hill, J.B.,** 1912. *The geology of the Lizard and Meneage*. Memoir of the Geological Survey of Great Britain, 1st edition, HMSO, London.

- Floyd, P.A.**, 1984. Geochemical characteristics and comparison of the basic rocks of the Lizard Complex and the basaltic lavas within the Hercynian troughs of SW England. *Journal of the Geological Society, London*, **141**, 61-70.
- Floyd, P.A., Lees, G.J. and Parker, A.** 1976. A preliminary geochemical twist to the Lizard's new tale. *Proceedings of the Ussher Society*, **4**, 414-423.
- Floyd, P.A., Exley, C.S. and Styles, M.T.**, 1993. *Igneous Rocks of South-West England*. Geological Conservation Review Series. Chapman and Hall, London.
- Forsyth, D.W.**, 1977. The evolution of the upper mantle beneath mid-ocean ridges. *Tectonophysics*, **38**, 89-118.
- Fowler, C.M.R.**, 1993. *The Solid Earth, An Introduction to Global Geophysics*. Cambridge University Press, 472pp.
- Fox, H.J.**, 1888. On the gneissic rocks off the Lizard, with notes on the specimens by Teall, J.J.H. *Quarterly Journal of the Geological Society of London*, **44**, 309-317.
- Fox, H.J. and Teall, J.J.H.**, 1889. On the junction of hornblende schist and serpentine in the Ogo Dour district. *Royal Geological Society of Cornwall Transactions*, **11**, p.213.
- Freeman, J.**, 1996. Mantle-melt and mantle-fluid interactions in suprasubduction zones from the Troodos Massif, Cyprus. Unpublished Ph.D. Thesis, University of Durham.
- Frey, F.A.**, 1969. Rare earth abundances in a high-temperature peridotite intrusion, *Geochimica et Cosmochimica Acta*, **33**, 1429-1447.
- Gass, I.G.**, 1968. Is the Troodos massif of Cyprus a fragment of Mesozoic oceanic floor?, *Nature*, **220**, 39-42.
- Gass, I.G.**, 1980. The Troodos Massif: Its role in the unravelling of the ophiolite problem and its significance in the understanding of constructive margin processes. In: Panayiotou, A. (ed.), *Ophiolites: Proceedings of the International Symposium, Cyprus, 1979*. Geological Survey Department, Nicosia, 25-35.
- Gibbons, W. and Thompson, L.** 1991. Ophiolitic mylonites in the Lizard complex: Ductile extension in the lower oceanic crust. *Geology*, **19**, 1009-1012.
- Girardeau, J.**, 1982. Tectonic structures related to thrusting of ophiolitic complexes: the White Hills Peridotite, Newfoundland. *Canadian Journal of Earth Sciences*, **19**, 709-722.
- Gillespie, M.R., Styles, M.T., Henney, P.J., Wetton, P.D., Sullivan, M.A. and Perez-Alvarez, M.S.**, 1994. A new approach to map production and petrogenetic interpretation using petrological databases: an example from the Huntly-Knock intrusions of Aberdeenshire. *British Geological Survey Technical Report, Mineralogy and Petrology Series No. WG/94/14*.



- Gillespie, M.R. and Styles, M.T.,** 1998. BGS rock classification scheme, Volume 1, Classification of igneous rocks. *British Geological Survey Research Report*, RR/97/02.
- Girardeau, J. and Nicolas, A.,** 1981. The structure of two ophiolite massifs, Bay of Islands, Newfoundland: a model for the oceanic crust and upper mantle. *Tectonophysics*, **77**, 1-34.
- Girardeau, J. and Mercier, J.-C.C.,** 1988. Petrology and texture of the ultramafic rocks of the Xigaze ophiolite (Tibet): constraints for the mantle structure beneath slow-spreading ridges. *Tectonophysics*, **147**, 33-58.
- Girardeau, J. and Francheteau, J.,** 1993. Plagioclase-wehrlites and peridotites on the East Pacific Rise (Hess Deep) and the Mid-Atlantic Ridge (DSDP Site 334): evidence for magma percolation in the oceanic upper mantle. *Earth and Planetary Science Letters*, **115**, 137-149.
- Green, D.H.,** 1964a. The petrogenesis of the high temperature peridotite intrusion in the Lizard area, Cornwall. *Journal of Petrology*, **5**, 134-188.
- Green, D.H.,** 1964b. The metamorphic aureole of the peridotite at the Lizard, Cornwall. *Journal of Geology*, **5**, 134-188.
- Green, D.H.,** 1964c. A re-study and re-interpretation of the geology of the Lizard Peninsula, Cornwall. In: Hosking, K.F.G. and Shrimpton, G.J., *Present views on some aspects of the geology of Cornwall and Devon*, Royal Geological Society of Cornwall, 87-114.
- Hacker, B.R.,** 1990. Simulation of the metamorphic and deformational history of the metamorphic sole of the Oman ophiolite. *Journal of Geophysical Research*, **95**, 4895-4907.
- Hacker, B.R.,** 1991. The role of deformation in the formation of metamorphic gradients: Ridge subduction beneath the Oman ophiolite. *Tectonics*, **10**, 455-473.
- Halliday, A.N. and Mitchell, J.G.,** 1976. Structural, K-Ar and  $^{40}\text{Ar}/^{39}\text{Ar}$  age studies of adularia K-feldspars from the Lizard Complex, England. *Earth and Planetary Science Letters*, **29**, 227-237.
- Handy, M.R.,** 1989. Deformation regimes and the rheological evolution of fault zones in the lithosphere: the effects of pressure, temperature, grain size and time. *Tectonophysics*, **163**, 119-152.
- Handy, M.R.,** 1990. The solid-state flow of polyminerallic rocks. *Journal of Geophysical Research*, **95**, 8647-8661.
- Handy, M.R.,** 1994. Flow laws for rocks containing two non-linear viscous phases: a phenomenological approach. *Journal of Structural Geology*, **16**, 287-301.
- Hanmer, S. and Passchier, C.W.,** 1991. Shear sense indicators: a review. Geological survey of Canada, Paper 90-17, 1-71.

- Harris, R.A.**, 1995. Geochemistry and tectonomagmatic affinity of the Misheguk massif, Brooks Range ophiolite, Alaska. *Lithos*, **35**, 1-25.
- Harte, B.**, 1977. Rock nomenclature with particular relation to deformation and recrystallisation textures in olivine-bearing xenoliths. *Journal of Geology*, **85**, 279-288.
- Harte, B., Winterburn, P.A. and Gurney, J.J.**, 1987. Metasomatic and enrichment phenomena in garnet peridotite facies mantle xenoliths from the Matsoku Kimberlite pipe, Lesotho. In: *Mantle Metasomatism*, Menzies, M.A. and Hawkesworth, C.J. (eds.), Academic Press, London, 21-39.
- Hebert, R., Bideau, D. and Hekinian, R.**, 1983. Ultramafic and mafic rocks from the Garret transform fault near 13°30'S on the East Pacific Rise: Igneous petrology. *Earth and Planetary Science Letters*, **65**, 107-125.
- Hebert, R., Serri, G. and Hekinian, R.**, 1989. Mineral chemistry of ultramafic tectonites and ultramafic to gabbroic cumulates from the major oceanic basins and Northern Apennine ophiolites (Italy) – A comparison. *Chemical Geology*, **77**, 183-207.
- Hebert, R. and Laurent, R.**, 1989. Mineral chemistry of ultramafic and mafic plutonic rocks of the Appalachian ophiolites, Quebec, Canada. *Chemical Geology*, **77**, 265-285.
- Hekinian, R., Bideau, D., Francheteau, J., Cheminee, J.-L., Armlio, R., Lonsdale, P. and Blum, N.**, 1993. Petrology of the East Pacific Rise crust and upper mantle exposed in Hess Deep (Eastern Equatorial Pacific). *Journal of Geophysical Research*, **98**, 8069-8094.
- Hofmann, A.W.**, 1988. Chemical differentiation of the Earth: the relationship between mantle, continental crust, and oceanic crust. *Earth and Planetary Science Letters*, **90**, 297-314.
- Holder, M.T. and Leveridge, B.E.**, 1986a. A model for the tectonic evolution of south Cornwall. *Journal of the Geological Society of London*, **143**, 125-134.
- Holder, M.T. and Leveridge, B.E.**, 1986b. Correlation of the Rhenohercynian Variscides. *Journal of the Geological Society of London*, **143**, 141-147.
- Holdsworth, R.E.**, 1989. Short Paper: The Start-Perranporth line: a Devonian terrane boundary in the Varsican orogen of SW England?. *Journal of the Geological Society of London*, **146**, 419-421.
- Holdsworth, R.E., Bailey, W.R., Imber, J., Butler, C.A. and Lloyd, G.**, 1997. The structural role played by fluids during reactivation of mid-crustal and upper mantle fault zones. Extended abstract, *Geofluids 2 '97; Second International Conference on Fluid Evolution, Migration and Interaction in Sedimentary Basins and Orogenic Belts*.
- Hoogerduijn Strating, E.H.**, 1991. The evolution of the Piemonte-Ligurian ocean: a structural study of ophiolite complexes in Liguria (NW Italy). Ph.D. Thesis, University of Utrecht, *Geologica Ultraiectina*, **74**, 145pp.

- Hoogerduijn Strating, E.H., Piccardo, G.B., Rampone, E., Scambelluri, M., Vissers, R.L.M., Drury, M.R. and Van der Wal, D.,** 1990. The structure and petrology of the Erro-Tobbio peridotite (Voltri Massif, Ligurian Alps): a two days excursion with emphasis on processes in the upper mantle, *Ophioliti*, **15**, 119-184.
- Hoogerduijn Strating, E.H., Rampone, E., Piccardo, G.B., Drury, M.R., Vissers, R.L.M.,** 1993. Subsolidus emplacement of mantle peridotites during incipient oceanic rifting and opening of the Mesozoic Tethys Voltri Massif, NW Italy, *Journal of Petrology*, **34**, Part 5, 901-927.
- Hopkinson, L. and Roberts, S.,** 1995. Ridge axis deformation and coeval melt migration within layer 3 gabbros: evidence from the Lizard complex U.K., *Contributions to Mineralogy and Petrology*, **121**, 126-138.
- Hopkinson, L. and Roberts, S.,** 1996. Fluid evolution during tectonic exhumation of oceanic crust at a slow-spreading paleoridge axis: evidence from the Lizard ophiolite U.K., *Earth and Planetary Science Letters*, **141**, 125-136.
- Institute of Geological Sciences (IGS),** 1978. Boreholes 1977, *Institute of Geological Sciences*.
- Institute of Geological Sciences (IGS),** 1979. Boreholes 1978, *Institute of Geological Sciences*.
- Jacques, A.L. and Green, D.H.,** 1980. Anhydrous melting of peridotite at 0-15 kb pressure and the genesis of tholeiitic basalts. *Contributions to Mineralogy and Petrology*, **73**, 287-310.
- Jagoutz, E., Palme, H., Baddenhausen, H., Blum, K., Cendales, M., Dreibus, G., Spettel, B., Lorenz, V. and Wanke, H.,** 1979. The abundance of major, minor and trace elements in the earth's mantle derived from ultramafic nodules. Proceedings of the 10th Lunar and Planetary Science Conference, *Geochimica et Cosmochimica Acta*, **2**, (Supplement II), 2031-2050.
- Jamieson, R.A.,** 1980. Formation of metamorphic aureoles beneath ophiolites – Evidence from the St. Anthony complex, Newfoundland. *Geology*, **8**, 150-154.
- Jamieson, R.A.,** 1981. Metamorphism during ophiolite emplacement – The petrology of the St. Anthony complex. *Journal of Petrology*, **22**, 397-449.
- Jamieson, R.A.,** 1986. P-T paths from high temperature shear zones beneath ophiolites. *Journal of Metamorphic Geology*, **4**, 3-22.
- Jaroslów, G.E., Hirth, G. and Dick, H.J.B.,** 1996. Abyssal peridotite mylonites: implications for grain-size sensitive flow and strain localization in the oceanic lithosphere. *Tectonophysics*, **256**, 17-37.
- Jin, D., Karato, S.-I. and Obata, M.,** 1998. Mechanisms of shear localization in the continental lithosphere: inference from the deformation microstructures of peridotites from the Ivrea zone, northwestern Italy. *Journal of Structural Geology*, **20**, 195-209.

- Johnson, M.C. and Rutherford, M.A., 1989.** Experimental calibration of the aluminium-in-hornblende geobarometer with application to Long-Valley Caldera (California) volcanic rocks. *Geology*, **17**, 837-841.
- Jones, K.A., 1994.** The most southerly point thrust – an example of ductile thrusting in the Lizard Complex, SW Cornwall. *Proceedings of the Ussher Society*, **8**, 254-261.
- Jones, K.A., 1997.** Deformation and emplacement of the Lizard Ophiolite Complex, SW England, based on evidence from the Basal Unit, *Journal of the Geological Society of London*, **154**, 871-885.
- Karato, S., Paterson, M.S. and Fitzgerald, J.D., 1986.** Rheology of synthetic olivine aggregates: Influence of grain size and water. *Journal of Geophysical Research*, **91**, 8151-8176.
- Kastens, K., Mascle, J. et al., 1988.** ODP Leg 107 in the Tyrrhenian Sea: insights into passive margin and back arc evolution. *Geological Society of America Bulletin*, **100**, 1140-1156.
- Kelemen, P.B., Shimizu, N., Sallers, V.J.M., 1995.** Extraction of mid-Ocean ridge basalt from the upwelling mantle by focused flow of melt in Dunite conduits. *Nature*, **375**, 747-753.
- Kelemen, P.B. and Dick, H.J.B., 1995.** Focused melt flow and localized deformation in the upper mantle: Juxtaposition of replacive dunite and ductile shear zones in the Josephine peridotite, SW Oregon, *Journal of Geophysical Research*, **100**, No.B1, 423-438.
- Kelemen, P.B., Koga, K. and Shimizu, N., 1997.** Geochemistry of gabbro sills in the crust-mantle transition zone of the Oman ophiolite: implications for the origin of the oceanic lower crust. *Earth and Planetary Science Letters*, **146**, 475-488.
- Kirby, G.A., 1979.** The Lizard Complex as an ophiolite. *Nature*, **282**, 58-61.
- Kirby, G.A., 1984.** The petrology and geochemistry of dykes of the Lizard Ophiolite Complex, Cornwall. *Journal of the Geological Society, London*, **141**, 53-59.
- Kirby, S.H., (1985).** Rock mechanics observations pertinent to the rheology of the continental lithosphere and the localisation of strain along shear zones. *Tectonophysics*, **119**, 1-27.
- Kohler, T.P. and Brey, G.P., 1990.** Calcium exchange between olivine and clinopyroxene calibrated as a geothermobarometer for natural peridotites from 2 to 60 Kb with applications. *Geochimica et Cosmochimica acta*, **54**, 2375-2388.
- Kornprobst, J. and Tabit, A., 1988.** Plagioclase-bearing ultramafic tectonites from the Galicia margin (Leg 103, Site 637): comparison of their origin and evolution with low pressure ultramafic bodies in western Europe. *Proceedings of the Ocean Drilling Project Scientific Research*, **103**, 253-263.

- Knipe, R.J.**, 1989. Deformation mechanisms – recognition from natural tectonites. *Journal of Structural Geology*, **11**, 127-146.
- Kröner, A. and Hegner, E.**, 1998. Geochemistry, single zircon ages and Sm-Nd systematics of granitoid rocks from the Gory Sowie (Owl Mts), Polish west Sudetes: evidence for early Palaeozoic arc-related plutonism. *Journal of the Geological Society, London*, **155**, 711-724.
- Kurat, G., Palme, H., Embey-Isztin, A., Touret, J., Ntaflos, T., Spettel, B., Brandstatter, F., Palme, C., Dreibus, G. and Prinz, M.**, 1993. Petrology and geochemistry of peridotites and associated vein rocks of Zabargad Island, Red Sea, Egypt. *Mineralogy and Petrology*, **48**, 309-341.
- Latin, D. and White, N.**, 1990. Generating melt during lithospheric extension: Pure shear vs. simple shear. *Geology*, **18**, 327-331.
- Le Maitre, R.W., Bateman, P., Dudek, A., Keller, J., Lamyre, J., Le Bas, M.J., Sabine, P.A., Schmid, R., Sorensen, H., Streckeisen, A., Woolley, A.R. and Zanettin, B.**, 1989. (eds.) A classification of Igneous rocks and glossary of terms, Recommendations of the International Union of Geological Sciences Subcommittee on the Systematics of Igneous Rocks. Blackwell Scientific Publications
- Le Pichon, X. and Barbier, F.**, 1987. Passive margin formation by low-angle faulting within the upper crust: the northern Bay of Biscay margin. *Tectonics*, **6**, 133-150.
- Leake, B.E.**, 1978. Nomenclature of amphiboles, *The Canadian Mineralogist*, **16**, 501-516.
- Leake, R.C. and Styles, M.T.**, 1984. Borehole sections through the Traboe hornblende schists, a cumulate complex overlying the Lizard peridotite, , *Journal of the Geological Society of London*, **141**, 41-52.
- Leveridge, B.E., Holder, M.T. and Day, G.A.**, 1984. Thrust nappe tectonics in the Devonian of south Cornwall and the western English Channel. In: Hutton, D.H.W. and Sanderson, D.J. (eds.), *Variscan tectonics of the North Atlantic region*, Special Publication of the Geological Society, London, **14**, 103-112.
- Leveridge, B.E., Holder, M.T. and Goode, A.J.J.**, 1990. *Geology of the Country around Falmouth*. Memoir for 1:50 000 Geological Sheet 352 (England and Wales), British Geological Survey.
- Lindsley, D.H.**, 1983. Pyroxene thermometry. *American Mineralogist*, **68**, 477-493.
- Lugovic, B., Altherr, R., Raczek, I., Hoffman, A.W. and Majer, V.**, 1991. Geochemistry of peridotites and mafic igneous rocks from the Central Dinaric Ophiolite Belt, Yugoslavia. *Contributions to Mineralogy and Petrology*, **106**, 201-216.
- Malpas, J.**, 1979. The dynamothermal aureole of the Bay of Islands ophiolite suite. *Canadian Journal of Earth Sciences*, **16**, 2086-2101.

- Malpas, J., Stevens, R.K. and Strong, D.F., 1973.** Amphibolite associated with Newfoundland ophiolite: Its classification and tectonic significance. *Geology*, **1**, 45-47.
- Malpas, J., and Langdon, G.S., 1987.** The Kennack Gneiss of the Lizard Complex, Cornwall, England: partial melts produced during ophiolite emplacement. *Canadian Journal of Earth Sciences*, **24**, 1966-1974.
- Malpas, J., Xenophontos, C. and Williams, D., 1992.** The Ayia Varvara Formation of SW Cyprus: a product of complex collisional tectonics. *Tectonophysics*, **212**, 193-211.
- Maltman, A.J., 1978.** Serpentinite textures in Anglesey, North Wales, United Kingdom. *Geological Society of America Bulletin*, **89**, 972-980.
- Mann, P., Hempton, M.R., Bradley, D.C. and Burke, K. 1983.** Development of pull-apart basins. *Journal of Geology*, **91**, 529-54.
- McCaig, A.M., 1983.** P-T conditions during emplacement of the Bay of Islands ophiolite complex. *Earth and Planetary Science Letters*, **63**, 459-473.
- McCulloch, M.T., Gregory, R.T., Wasserburg, J. and Taylor, H.P., 1981.** Sm-Nd, Rb-Sr, and  $^{18}\text{O}/^{16}\text{O}$  isotopic systematics in an oceanic crustal section: evidence from the Semail ophiolite. *Journal of Geophysical Research*, **86**, 2721-2736.
- McKenzie, D., 1978.** Some remarks on the development of sedimentary basins. *Earth and Planetary Science Letters*, **40**, 25-32.
- McKerrow, W.S. and Zeigler, A.M., 1972.** Palaeozoic oceans. *Nature*, **240**, 92-94.
- McPherson, E., Thirlwall, M.F., Parkinson, I.J., Menzies, M.A., Bodinier, J.L., Woodland, A., Bussod, G., 1996.** Geochemistry of metasomatism adjacent to amphibole-bearing veins in the Lherz peridotite Massif. *Chemical Geology*, **134**, No.1-3, pp.135-157.
- Menzies, M.A. and Hawkesworth, C.J., 1987.** (eds.) Mantle Metasomatism. Academic Press, (London).
- Menzies, M.A. and Dupuy, C. 1991.** Orogenic massifs: protolith, process and provenance. *Journal of Petrology*, Special Lherzolite Issue, 1-16.
- Mercier, J.C., 1976.** Single pyroxene geothermometry and geobarometry. *American Mineralogist*, **61**, 603-615.
- Mercier, J.C., 1980.** Single pyroxene thermobarometry. *Tectonophysics*, **70**, 1-37.
- Mercier, J.C., 1985.** Olivine and Pyroxenes, in: Preferred orientation in deformed rocks: An introduction to modern texture analysis. Academic Press, inc. 407-430.
- Mercier, J.C., and Nicolas, A., 1975.** Textures and fabrics of upper mantle peridotites as illustrated by xenoliths from basalts, *Journal of Petrology*, **16**, 454-96.



- Mercier, J.C., Benoit, V. and Girardeau, J., 1984.** Equilibrium state of diopside-bearing harzburgites from ophiolites: geobarometric and geodynamic implications. *Contributions to Mineralogy and Petrology*, **85**, 391-403.
- Mercier, J.C., Glucklich, M. and Dupuy, C., 1993.** In search of a primitive upper mantle. *Chemical Geology*, **85**, 391-403.
- Miller, J.A. and Green, D.H., 1961a.** Preliminary age determinations in the Lizard area. *Nature (London)*, **191**, 159-160.
- Miller, J.A. and Green, D.H., 1961b.** Age determinations of rocks in the Lizard (Cornwall) area. *Nature (London)*, **192**, 1175-1176.
- Moore, E.M., 1969.** Petrology and structure of the Vourinos Ophiolite Complex, Northern Greece. *Geological Society of America Special Paper*, **118**, pp74.
- Mukherji, A., 1992.** The occurrence of chromites within the Ultramafic rocks of the Lizard Ophiolite, Cornwall, England. MSc Mining Geology, Camborne School of Mines. October 1992.
- Mutter, J.C., Larson, R.L. and Northwest Australian Study Group, 1989.** Extension of the Exmouth Plateau, offshore northwestern Australia: Deep seismic reflection/refraction evidence for simple and pure shear mechanisms. *Geology*, **17**, 15-18.
- Nakamura, N., 1974.** Determination of REE, Ba, Fe, Mg, Na and K in carbonaceous and ordinary chondrites. *Geochimica et Cosmochimica Acta*, **38**, 757-73.
- Nicolas, A., 1986.** Structure and petrology of peridotites: Clues to their geodynamic environment. *Reviews of Geophysics*, **24**, 875-895.
- Nicolas, A., 1989.** Structures of ophiolites and dynamics of oceanic lithosphere, Kluwer Academic Publishers, Netherlands, pp367.
- Nicolas, A., Bouchez, J.L., Boudier, F. and Mercier, J.C., 1971.** Textures, structures and fabrics due to solid state flow in some European lherzolites. *Tectonophysics*, **12**, 55-86.
- Nicolas, A. and Poirier, J.P., 1976.** *Crystalline Plasticity and Solid State Flow in Metamorphic Rocks*. J. Wiley and Sons, pp144.
- Nicolas, A., Boudier, F. and Bouchez, J.L., 1980.** Interpretation of peridotite structures from ophiolitic and oceanic environments. *American Journal of Science*, **280**, 192-210.
- Nicolas, A. and Christensen, N.I., 1987.** Formation of anisotropy in upper mantle peridotites: a review. In: Fuchs, K. (ed.), *The composition, structure and dynamics of the lithosphere-asthenosphere system*, American Geophysical Union Memoir, 111-123.

- Nicolas, A., Achauer, U. and Daignieres, M., 1994. Rift initiation by lithospheric rupture. *Earth and Planetary Science Letters*, **123**, 281-298.
- Nutman, A.P., Green, D.H., Cook, C.A. and Styles, M.T., (in prep.). U-Pb zircon and monazite age constraints on tectonothermal events in the Lizard Complex, Cornwall, England.
- Nicolas, A., Ceuleener, G., Boudier, F. and Misseri, M. 1988. Structural mapping in the Oman ophiolites: mantle diapirism along an oceanic ridge. *Tectonophysics*, **151**, 27-56.
- Oliver, G.J.H., Corfu, F. and Krogh, T.E., 1993. U-Pb ages from SW Poland: evidence for a Caledonian suture zone between Baltica and Gondwana. *Journal of the Geological Society, London*, **150**, 355-369.
- Ottenello, G., Piccardo, G.B., Ernst, W.G., 1979. Petrogenesis of some Ligurian peridotites - II. Rare Earth Element chemistry. *Geochimica et Cosmochimica Acta*, **43**, 1273-1284.
- Ottenello, G., Piccardo, G.B., Joron, J.L., 1984. Rare earth and 3d transition element geochemistry of peridotitic rocks: II. Ligurian peridotites and associated basalts. *Journal of Petrology*, **25**, 379-393.
- Ozawa, K., 1994. Melting and melt segregation in the mantle wedge above a subduction zone: Evidence from the chromite-bearing peridotites of the Miyamori ophiolite complex, northeastern Japan. *Journal of Petrology*, **35**, 647-678.
- Passchier, C.W. and Simpson, C., 1986. Porphyroclast systems as kinematic indicators. *Journal of Structural Geology*, **8**, 831-843.
- Passchier, C.W. and Trouw, R.A.J., 1996. *Microtectonics*, Berlin, New York, Springer.
- Pearce, J.A., 1980. Geochemical evidence for genesis and eruptive setting of lavas from Tethyan ophiolites. In: Panayiotou, A. (ed.), *Proceedings of the International Symposium, Cyprus, 1979*. Geological Survey Department, Nicosia, 261-272.
- Pearce, J.A., 1983. Role of the subcontinental lithosphere in magma genesis at active continental margins. In: Hawkesworth, C.J. and Norry, M.J. (eds.), *Continental basalts and mantle xenoliths*. Shiva, Cheshire, U.K., 230-249.
- Pearce, J.A. and Cann, J.R., 1973. Tectonic setting of basic volcanic rocks determined using trace element analysis. *Earth and Planetary Science Letters*, **19**, 290-300.
- Pearce, J.A., Alabaster, T., Shelton, A.W. and Searle, M.P., 1981. The Oman ophiolite as a Cretaceous arc-basin complex: evidence and implications. *Philosophical Transactions of the Royal Society of London*, **A300**, 299-317.

- Pearce, J.A., Lippard, S.J. and Roberts, S., 1984.** Characteristics and tectonic significance of supra-subduction zone ophiolites. In: Kokelaar, B.P. & Howells, M.F. (eds.), *Marginal Basin Geology*. Geological Society of London Special Publication, **16**, 77-94.
- Peltonen, P., Kontinen, A. Huhma, H., 1998.** Petrogenesis of the Mantle sequence of the Jormua Ophiolite (Finland): Melt migration in the upper mantle during Palaeoproterozoic continental break-up. *Journal of Petrology*, **39**, 297-329.
- Peters, T.J., Nicolas, A. and Coleman, R.G., 1991.** *Ophiolites genesis and evolution of the oceanic lithosphere*. Dordrecht: Kluwer Academic, 903pp.
- Piccardo, G.B., Messiga, B. and Vannucci, R., 1988.** The Zabargad peridotite-pyroxenite association: petrological constraints on its evolution. *Tectonophysics*, **150**, 135-162.
- Piccardo, G.B., Rampone, E., Vannucci, R., 1990.** Upper mantle evolution during continental rifting and ocean formation: evidences from peridotite bodies of the Western Alpine – Northern Apennine system. *Mem. Soc. Geol. France*, **156**, 323-333.
- Piccardo, G.B., Rampone, E., Vannucci, R., Shimizu, N., Ottolini, L. and Bottazzi, P., 1993.** Mantle processes in the sub-continental lithosphere: the case study of the rifted spinelherzolites from Zabargad (Red Sea). *European Journal of Mineralogy*, **5**, 1039-1056.
- Pike, J.E. and Schwarzman, E.C., 1977.** Classification of textures in ultramafic xenoliths. *Journal of Geology*, **85**, 49-61.
- Plyusina, L.P., 1982.** Geothermometry and geobarometry of plagioclase-hornblende bearing assemblages. *Contributions to Mineralogy and Petrology*, **80**, 140-146.
- Potts, P.J., 1987.** *A handbook of silicate rock analysis*. Blackie, London.
- Potts, P.J., Tindle, A.G. and Webb, P.C., 1992.** Geochemical reference material compositions. Whittles Publishing, London.
- Power, M.R., Alexander, A.C., Shail, R.K. and Scott, P.W., 1996.** A re-interpretation of the internal structure of the Lizard Complex. *Proceedings of the Ussher Society*, **9**, 63-97.
- Power, M.R., Alexander, A.C., Shail, R.K. and Scott, P.W., 1997.** Alteration and mineralisation within the Lizard Complex peridotite, south Cornwall: constraints on the timing of serpentinisation. *Proceedings of the Ussher Society*, **10**, 63-97.
- Rampone, E., Bottazzi, P. and Ottolini, L., 1991.** Complementary Ti and Zr anomalies in orthopyroxene and clinopyroxene from mantle peridotites. *Nature*, **354**, 518-521.
- Rampone, E., 1992.** Studio petrologico e geochimico delle peridotiti dell' Appennino settentrionale. Ph.D. thesis. Univ Genova, Italy.

- Rampone, E., Piccardo, G.B., Vannucci, R., Bottazzi, P. and Ottolini, L., 1993.** Subsolidus reactions monitored by trace element partitioning: the spinel- to plagioclase-facies transition in mantle peridotites. *Contributions to Mineralogy and Petrology*, **115**, 1-17.
- Rampone, E., Hofmann, A.W., Piccardo, G.B., Vannucci, R., Bottazzi, P., Ottolini, L., 1995.** Petrology, Mineral and Isotope Geochemistry of the External Liguride Peridotites (Northern Apennines, Italy). *Journal of Petrology*, **36**, 81-105.
- Rampone, E., Piccardo, G.B., Vannucci, R. and Bottazzi, P., 1997.** Chemistry and origin of trapped melts in ophiolitic peridotites. *Geochimica et Cosmochimica Acta*, **61**, 4557-4569.
- Ramsay, J.G. and Graham, R.H., 1970.** Strain variations in shear belts. *Canadian Journal of Earth Science*, **7**, 786-813.
- Rathey, P.R. and Sanderson, D.J., 1984.** The structure of SW Cornwall and its bearing on the emplacement of the Lizard Complex. *Journal of the Geological Society, London*, **141**, 87-95.
- Reston, T.J., 1990.** Mantle shear zones and the evolution of the North Sea Basin. *Geology*, **18**, 272-275.
- Richard, P. and Allegre, C.J., 1980.** Neodymium and strontium isotope study of ophiolite and orogenic lherzolite petrogenesis. *Earth and Planetary Science Letters*, **47**, 65-74.
- Ringwood, A.E., 1966.** The chemical composition and origin of the earth. In: Hurley, P., (ed.), *Advances in Earth Science*, MIT Press, Cambridge, Mass., 287-356.
- Ringwood, A.E., 1975.** *Composition and Petrology of the Earth's Mantle*. New York: McGraw-Hill, 618pp.
- Rivalenti, G., Vannucci, R., Rampone, E., Mazzucchelli, M., Piccardo, G.B., Piccirillo, E.M., Bottazzi, P. and Ottolini, L., 1996** Peridotite clinopyroxene chemistry reflects mantle processes rather than continental versus oceanic settings. *Earth and Planetary Science Letters*, **139**, 423-437.
- Roberts, S., Andrews, J.R., Bull, J.M. and Sanderson, D.J., 1993.** Slow-spreading ridge-axis tectonics: evidence from the Lizard complex, UK. *Earth and Planetary Science Letters*, **116**, 101-112.
- Roberts, S. and Neary, C., 1993.** Petrogenesis of ophiolitic chromite. In: Prichard, H.M., Alabaster, T., Harris, N.B.W. and Neary, C.R. (eds.), *Magmatic Processes and Plate Tectonics*, Geological Society Special Publication, **76**, 257-272.
- Roddick, J.C. and van Breemen, O., 1994.** U-Pb zircon dating: a comparison of ion microprobe and single grain conventional analyses. In: *Radiogenic age and isotopic studies*, Report 8, Geological Survey of Canada Current Research, 1994-F, 1-9.

- Rollin, K.E.**, 1986. Geophysical surveys on the Lizard Complex, Cornwall. *Journal of the Geological Society, London*, **143**, 437-446.
- Rothstein, A.T.V.**, 1977. The distribution and origin of primary textures in the Lizard Peridotite, Cornwall. *Proceedings of the Geologists Association*, **88**, 93-105.
- Rothstein, A.T.V.**, 1981. The primary crescumulates of the Lizard peridotite, Cornwall. *Geological Magazine*, **118**, 491-500.
- Rothstein, A.T.V.**, 1988. An analysis of the textures within the primary assemblage peridotite, the Lizard, Cornwall. *Proceedings of the Geologists Association*, **99**, 181-92.
- Rothstein, A.T.V.**, 1994. Directional features within an assemblage of primary textures preserved in a kilometre section of the upper mantle peridotite, from the Lizard, Cornwall. *Proceedings of the Ussher Society*, **8**, 248-253.
- Rothstein, A.T.V.**, 1998. Relic primary features of the spinel-bearing dunites of the primary assemblage peridotite, the Lizard, Cornwall. *Proceedings of the Ussher Society*, **11**, 56-78.
- Ruppel, C., Royden, L. and Hodges, K.V.**, 1988. Thermal modelling of extensional tectonics: application to pressure-temperature-time histories of metamorphic rocks. *Tectonics*, **7**, 947-957.
- Rutter, E.H.** 1983. Pressure solution in nature, theory and experiment. *Journal of the Geological Society, London*, **140**, 725-740.
- Rutter, E.H. and Brodie, K.H.**, 1988. The role of tectonic grain size reduction in the rheological stratification of the lithosphere. *Geologische Rundschau*, **77**, 295-308.
- Sandeman, H.A.**, 1988. A field, petrographical and geochemical investigation of the Kennack Gneiss, Lizard Peninsula, South-West England. Msc. Thesis, Memorial University of Newfoundland, Canada.
- Sandeman, H.A., Chen, Y., Clark, A.H. and Farrar, E.**, 1995. Constraints on the P-T conditions and age of emplacement of the Lizard ophiolite, Cornwall: amphibole-plagioclase thermobarometry and  $^{40}\text{Ar}/^{39}\text{Ar}$  geochronology of basal amphibolites. *Canadian Journal of Earth Sciences*, **32**, 261-272.
- Sandeman, H.A., Clark, A.H., Styles, M.T., Scott, D.J., Malpas, J.G. and Farrar, E.**, 1997. Geochemistry and U-Pb and  $^{40}\text{Ar}/^{39}\text{Ar}$  geochronology of the Man of War Gneiss, Lizard Complex, SW England: pre-Hercynian arc-type crust with a Sudeten-Iberian connection. *Journal of the Geological Society, London*, **154**, 403-417.
- Sanders, L.D.**, 1955. Structural observations on the S.E. Lizard. *Geological Magazine*, **92**, 231-240.

- Sanderson, D.J.**, 1984. Structural variation across the northern margin of the Variscides in NW Europe. In: Hutton, D.H.W. & Sanderson, D.J. (eds) *Variscan Tectonics of the North Atlantic Region*. Special Publication of the Geological Society, London, **14**, 149-165.
- Santos Zalduegui, J.F., Scharer, U. and Gil Ibarguchi, J.L.**, 1995. Isotope constraints on the age and origin of magmatism and metamorphism in the Malpica-Tuy allochthon, Galicia, NW Spain. *Chemical Geology*, **121**, 91-103.
- Seager, A.F., Fitch, F.J. and Miller, J.A.**, 1975. Dating post-metamorphic hydrothermal mineralization in the Lizard complex, Cornwall. *Geological Magazine*, **112**, 519-522.
- Seager, A.F., Fitch, F.J. and Miller, J.A.**, 1978. Dating of adularia and the relationship of hydrothermal events in the Lizard complex, Cornwall. *Geological Magazine*, **115**, 211-214.
- Selfridge, G.C.**, 1935. An X-ray and optical investigation of the serpentine minerals. *American Mineralogist*, **21**, 463-503.
- Serpa, L. and de Voogd, B.**, 1987. Deep seismic reflection evidence for the role of extension in the evolution of continental crust: *Royal Astronomical Society Geophysical Journal*, **89**, 55-60.
- Serpa, L., de Voogd, B., Wright, L., Willemin, J., Oliver, J., Hauser, E. and Troxel, B.**, 1988. Structure of the central Death Valley pull-apart basin and vicinity from COCORP profiles in the southern Great Basin. *Geological Society of America Bulletin*, **100**, 1437-1450.
- Seyler, M. and Bonatti, E.**, 1994. Na, Al<sup>iv</sup> and Al<sup>vi</sup> in clinopyroxenes of subcontinental and suboceanic ridge peridotites: A clue to the different melting processes in the mantle?. *Earth and Planetary Science Letters*, **122**, 281-289.
- Schilling, J.-G., Zajac, M., Evans, R., Johnston, W., White, J.D., Devine, J.D. and Kingsley, R.**, 1983. Petrologic and geochemical variations along the Mid-Atlantic Ridge from 27°N to 73°N. *American Journal of Science*, **283**, 510-586.
- Schmidt, M.W.**, 1992. Amphibole composition in tonalite as a function of pressure – An experimental calibration of the Al-in-hornblende barometer. *Contributions to Mineralogy and Petrology*, **110**, 304-310.
- Schmid, S.M.**, 1994. Textures of geological materials: computer model predictions versus experimental interpretations based on rock deformation experiments and field studies. In: *Textures of geological materials*, Bunge, H.J., Siegesmund, S., Skrotzki, W. and Weber, K., (eds), DEM Informationsges, Oberursel, pp.279-301.
- Searle, M.P., Lippard, S.J., Smewing, J.D. and Rex, D.C.**, 1980. Volcanic rocks beneath the Semial Ophiolite nappe in the northern Oman mountains and their significance in the Mesozoic evolution of Tethys. *Journal of the Geological Society, London*, **137**, 589-604.



- Searle, M.P. and Malpas, J.,** 1980. Structure and metamorphism of rocks beneath the Semail ophiolite of Oman, and their significance in ophiolite obduction. *Transactions of the Royal Society of Edinburgh*, **71**, 213-228.
- Searle, M.P. and Malpas, J.,** 1982. Obduction processes in ancient, modern and future ophiolites. In: Gass, I.G., Lippard, S.J. and Shelton, A.W. (eds.), *Ophiolites and oceanic lithosphere*, Geological Society of London, Special Publication **13**, 303-319.
- Shepherd, A.,** 1986. The geochemistry and evolution of the Lizard Complex, Cornwall. Unpublished Ph.D. Thesis, University of Nottingham.
- Silver, P. and Chan, W.W.,** 1988. Implications for continental structure and evolution from seismic anisotropy. *Nature*, **355**, 34-39.
- Silver, P. and Chan, W.W.,** 1988. Shear-wave splitting and subcontinental mantle deformation. *Journal of Geophysical Research*, **96**, 429-454.
- Silver, P.,** 1996. Seismic anisotropy beneath the continents: Probing the depths of geology. *Annual Review of Earth and Planetary Science*, **24**, 385-432.
- Smewing, J.D., Christensen, N.I., Bartholomew, I.D. and Browning, P.,** 1984. The structure of the oceanic upper mantle and lower crust as deduced from the northern section of the Oman ophiolite. In: Gass, I.G., Lippard, S.J. and Shelton, A.W. (eds.), *Ophiolites and oceanic lithosphere*, Geological Society of London, Special Publication, **13**, 41-54.
- Somervail, A.,** 1884. The serpentine of the Lizard. *Geological Magazine*, **vi**, p.96.
- Spear, F.S.,** 1980. NaSi  $\leftrightarrow$  CaAl exchange equilibrium between plagioclase and amphibole: An empirical model. *Contributions to Mineralogy and Petrology*, **72**, 33-41.
- Spray, J.G.,** 1982. Mafic segregations in ophiolite mantle sequences. *Nature*, **299**, 524-528.
- Spray, J.G. and Roddick, J.C.,** 1981. Evidence for Upper Cretaceous transform fault metamorphism in West Cyprus. *Earth and Planetary Science Letters*, **55**, 273-291.
- Steiger, R.H. and Jager, E.,** 1977. Subcommittee on geochronology: Convention on the use of decay constants in geo- and cosmochemistry. *Earth and Planetary Science Letters*, **36**, 359-362.
- Stevenson, D.J.,** 1986. On the role of surface tension in the migration of melts and fluids. *Geophysical Research Letters*, **13**, 1149-1152.
- Streckeisen, A.,** 1973. Plutonic Rocks. Classification and nomenclature recommended by the IUGS Subcommittee on the systematics of igneous rocks. *Geotimes*, **18** (10), 267-280.

- Styles, M.T.**, 1992. The Lizard Ophiolite Complex. *OUGS Journal*, **13.2**, Symposium Edition 1992.
- Styles, M.T., and Kirby, G.A.**, 1980. New Investigations of the Lizard complex, Cornwall, England and a discussion of an ophiolite model. *Ophiolites: Proceedings of the International Symposium, Cyprus, 1979*. Geological Survey Department, Nicosia, 512-26.
- Styles, M.T. and Rundle, C.C.**, 1984. The Rb-Sr isochron age of the Kennack Gneiss and its bearing on the age of the Lizard Complex, Cornwall. *Journal of the Geological Society, London*, **141**, 15-19.
- Suhr, G.**, 1991. Structural and magmatic history of upper mantle peridotites in the Bay of Islands Complex, Newfoundland. Ph.D. Thesis, St. John's, Newfoundland, Memorial University.
- Suhr, G.**, 1993. Evaluation of upper mantle microstructures in the Table Mountain Massif, Bay of Islands Ophiolite. *Journal of Structural Geology*, **15**, 1273-1292.
- Suhr, G., and Cawood, P.A.**, 1993. Structural history of ophiolite obduction, Bay of Islands, Newfoundland. *Geological Society of America Bulletin*, **105**, 399-410.
- Suhr, G. and Robinson, P.T.**, 1994. Origin of mineral chemical stratification in the mantle section of the Table Mountain Massif (Bay of Islands Ophiolite, Newfoundland, Canada). *Lithos*, **31**, 81-102.
- Thayer, T.P.**, 1960. Some critical differences between alpine-types and stratiform peridotite-gabbro complexes. Internat. Geol. Congr. 21<sup>st</sup>, Copenhagen, Proc., Pt. 13, pp247-259.
- Thayer, T.P.**, 1969. Peridotite-gabbro complexes as keys to petrology of mid-ocean ridges. *Geological Society of America Bulletin*, **80**, 1511-1522.
- Tilley, C.E.**, 1937. Anthophyllite-cordierite granulites of the Lizard. *Geological Magazine*, **74**, 300-309.
- Van der Wal, D. and Bodinier, J.-L.**, 1996. Origin of the recrystallisation front in the Ronda peridotite by km-scale pervasive porous melt flow, *Contributions to Mineralogy and Petrology*, **112**, 387-405.
- Varfalvy, V., Hebert, R. and Bedard, J.H.**, 1996. Interactions between melt and upper-mantle peridotites in the North Arm Mountain Massif, Bay of Islands Ophiolite, Newfoundland, Canada: Implications for the genesis of boninitic and related magmas. *Chemical Geology*, **129**, 71-90.
- Vearncombe, J.R.**, 1980. The Lizard ophiolite and two phases of suboceanic deformation. In: Panayiotou, A. (ed.), *Proceedings of the International Symposium, Cyprus, 1979*. Geological Survey Department, Nicosia, 527-537.

- Vissers, R.L.M., Drury, M.R., Hoogerduijn Strating, E.H. and van der Wal, D.,** 1991. Shear zones in the upper mantle: a case study in an Alpine lherzolite massif. *Geology*, 990-993.
- Vissers, R.L.M., Drury, M.R., Hoogerduijn Strating, E.H., Spiers, C.J. and van der Wal, D.,** 1995. Mantle shear zones and their effect on the lithosphere strength during continental breakup. *Tectonophysics*, **249**, 155-171.
- Voggenrieter, W., Hotzl, H. and Mechie, J.,** 1988. Low-angle detachment origin for the Red Sea rift system?. *Tectonophysics*, **150**, 51-75.
- Wadge, G. and Burke, K.,** 1983. Neogene Caribbean plate rotation and associated Central American tectonic evolution. *Tectonics*, **2**, 633-643.
- Ware, N.G.,** 1991. Combined Energy-Dispersive-Wavelength-Dispersive Quantitative Electron Microprobe Analysis. *X-Ray Spectroscopy*, **20**, 73-79.
- Wells, P.R.A.,** 1977. Pyroxene thermometry in simple and complex systems. *Contributions to Mineralogy and Petrology*, **62**, 129-39.
- Wernicke, B.,** 1985. Uniform sense normal simple shear of the continental lithosphere. *Canadian Journal of Earth Sciences*, **22**, 108-125.
- Wheeler, J.,** 1987. The significance of grain-scale stresses in the kinetics of metamorphism. *Contributions to Mineralogy and Petrology*, **17**, 397-404.
- White, S.H., Burrows, S.E., Carreras, J., Shaw, N.D. and Humphreys, F.J.,** 1980. On mylonites in ductile shear zones, *Journal of Structural Geology*, **1**, 175-187.
- White, J.C. and Mawer, C.K.,** 1988. Dynamic recrystallization and associated exsolution in perthites – evidence of deep crustal thrusting. *Journal of Geophysical Research*, **93**, 325-337.
- Whittaker, E.J. and Zussman, J.,** 1956. The characterization of the serpentine minerals by X-ray diffraction, *Mineralogical Magazine*, **31**, 107-126.
- Wilkinson, J.J. and Knight, R.R.W.,** 1989. Palynological evidence from the Porthleven area, south Cornwall: implications for Devonian stratigraphy and Hercynian structural evolution. *Journal of the Geological Society, London*, **146**, 739-742.
- Willet, S.D. and Beaumont, C.,** 1994. Subduction of Asian lithospheric mantle beneath Tibet inferred from models of continental collision. *Nature*, **369**, 642-645.
- Williams, H.,** 1973. Bay of Islands map-area, Newfoundland. *Canadian Geological Survey Paper*, **72-34**, pp7.
- Williams, H. and Smyth, W.R.,** 1973. Metamorphic aureoles beneath ophiolite suites and alpine peridotites: tectonic implications with west Newfoundland examples. *American Journal of Science*, **273**, 594-621.

**Williams, P.F., Goodwin, L.B. and Ralser, S., 1994.** Ductile Deformation Processes. In: Hancock, P.L., (ed.) *Continental Deformation*, Pergamon Press, Oxford, 1-27.

**Williams, I.S., Buick, I.S. and Cartwright, I., 1996.** An extended episode of early Mesoproterozoic metamorphic fluid flow in the Reynolds, central Australia. *Journal of Metamorphic Geology*, **14**, 29-47.

**Wilson, M., 1989.** Igneous Petrogenesis, A Global Tectonic Approach. HarperCollins Academic, pp466.

**Wilson, A.C. and Taylor, R.T., 1976.** Stratigraphy and sedimentation of west Cornwall. *Transactions of the Royal Geological Society of Cornwall*, **20**, 246-259.

**Wintsch, R.P. and Dunning, J., 1985.** The effect of dislocation density of aqueous solubility of quartz and some geological implications. *Journal of Geophysical Research*, **90**, 3649-3657.

**Witt, G. and Seck, H.A., 1989.** Origin of amphibole in recrystallized and porphyroclastic mantle xenoliths from the Rhenish Massif: implications for the nature of mantle metasomatism. *Earth and Planetary Science Letters*, **91**, 327-340.

**Witt-Eikschén, G., and Seck, H.A., 1991.** Solubility of Ca and Al in orthopyroxene from Spinel peridotite: an improved version of an empirical geothermometer. *Contributions to Mineralogy and Petrology*, **106**, 431-39.

**Woodland, A.B., Kornprobst, J., Bodinier, L.-L., McPherson, E. and Menzies, M.A., 1996.** Metasomatism interactions in the lithospheric mantle: petrological evidence from the Lherz massif, French Pyrennes. In: Menzies, M.A. *et al.* (eds.), *Melt Processes and Exhumation of garnet, spinel and plagioclase facies mantle*. Chemical Geology, **134**, 83-112.

**Zeigler, P.A., 1982.** *Geological atlas of western and central Europe*. Amsterdam, Elsevier.

**Zhou, M., Robinson, P.T., Malpas, J. and Zijin, Li., 1996.** Podiform chromites in the Loubusa ophiolite (southern Tibet): Implications for melt-rock interaction in the upper mantle. *Journal of Petrology*, **37**, 3-21.

**Paterson, M.S., 1969.** The ductility of rocks. In: A.S.Argon (ed) *Physics of Strength and Plasticity*. MIT Press, Cambridge, Mass., 377-392.

**Turner, F.J. and Weiss, L.E., 1963.** Structural analysis of metamorphic tectonites. McGraw-Hill, New York. pp 545.

**Jones, R.R., Holdsworth, R.E. and Bailey, W., 1997.** Lateral extrusion in transpression zones: the importance of boundary conditions. *Journal of Structural Geology*, **19**, 1201-1217.

---

**APPENDICES**

---

---

**APPENDIX A: ANALYTICAL TECHNIQUES**

---

The procedures presented in A.1-A.3 are taken from Freeman (1996), but data presented was obtained during the course of the present study.

**A.1 Sample Preparation**

All the samples analysed in this study were prepared in the same way. Prior to sample preparation the samples were sorted into batches of similar lithological type. The samples were then processed in these batches, starting with the most chemically depleted lithology first e.g. peridotite, in order to minimise cross-sample contamination.

Before samples were crushed, they were brushed clean under running water and then dried using a high-pressure air hose.

Samples were crushed in a Pulverisette jaw crusher. Before crushing began the machine was stripped and thoroughly cleaned to avoid any contamination from previous users. The crusher was also carefully cleaned between each sample using a wire brush and absolute alcohol. A dust extractor helped to reduce the build up of dust within the machine, which speeded up the cleaning process.

Samples were then milled in a agate ball mill for 30 minutes. The mill was cleaned using sharp sand before use, between each sample batch and at the end of the day's work. Between each sample the mill was cleaned under running water with a nylon brush and dried using a high-pressure air hose.

**A.2 X-Ray Fluorescence Analysis**

All samples were analysed for major and selected trace elements by XRF at the University of Durham. Major elements were analysed on fusion discs and trace elements on pressed pellets.

Before the fusion discs were prepared, the loss on ignition (LOI) for each sample was determined. Firstly, the powder was dried at 105°C to remove any surface water. Then a known amount of powder was heated at 900°C in porcelain crucibles for two hours to derive the LOI. Fusion discs were prepared by thoroughly mixing  $0.45\text{g} \pm 0.001\text{g}$  of the LOI powder with  $2.25 \pm 0.001\text{g}$  of dried lithium metaborate/lithium tetraborate flux (Spectroflux 100B) using a pestle and mortar. Effective mixing ensures good totals when the samples are analysed. The powder was then placed in a platinum crucible and heated in a furnace at 1050°C for 25 minutes. After removing the sample from the furnace, the molten mixture was homogenised by 'swirling' the crucible. The melt was then poured into moulds on a hot plate and quenched with a metal plunger. After the discs had cooled they were labelled, bagged and stored in a desiccator. Care was taken not to touch the analytical surface to avoid Na contamination.

Pressed pellets were made by mixing approximately 10g of sample with 8 to 10 drops of Mowiol binder in a beaker using a glass rod. The amount of Mowiol used varied according to the properties of each sample and had to be judged from experience. The mix was pressed at 10 bars for approximately 30 seconds. The pellets were labelled then dried overnight at 110°C.

Fusion discs and pellets were analysed on a Philips PW 1500 spectrometer with a Rhodium tube. The machine was calibrated using international standards. Only standards with compositions close to those expected from the unknowns were used so that high concentration standards did not skew the calibration line at low levels. As a precaution, in-house peridotite standard samples were run prior to the unknowns to check the calibration. During the analyses, a drift monitor was analysed every 6 samples. If the variation of the repeat analyses of the monitor had exceeded 1% for the major elements or 10% for the trace elements (Potts, 1987) the analytical run would have been stopped and the XRF re-calibrated. In practice the drift of the machine was very small as indicated by the precision values presented below.

### **A.2.1. XRF Error control**

Two main elements of error control were studied during the XRF analyses;



- a) how accurate the calibration was in relation to the accepted values for the international standards,
- b) the instrumental precision.

Accuracy: the accuracy of the calibration can be judged by comparing the values obtained for the analyses of international standards with the published accepted values. Because there are relatively few low level international standards with elemental abundances similar to the unknowns the international standards which were run as a check of accuracy were the same as those used in the calibration. This means that the accuracy of the technique will be slightly over-estimated. The results of the analyses of the international standards are summarised in Table A.1.

	PCC-1 (n=4)			DTS-1 (n=3)			NIM-D (n=2)			W-2 (n=0)		
<b>Discs</b>	CAC	Accept	RSD	CAC	Accept	RSD	CAC	Accept	RSD	CAC	Accept	RSD
SiO <sub>2</sub>	43.47	43.86	1.2	40.27	40.42	1.1	38.68	38.96	1.2	-	-	-
Al <sub>2</sub> O <sub>3</sub>	0.67	0.71	7.3	0.22	0.19	13.7	0.24	0.3	5.9	-	-	-
Fe <sub>2</sub> O <sub>3</sub>	8.62	8.68	2.8	8.68	8.69	3.0	16.99	17	0.1	-	-	-
MgO	45.17	45.71	2.1	50.03	49.64	0.6	44.01	43.51	0.6	-	-	-
CaO	0.57	0.55	3.7	0.13	0.17	12.1	0.3	0.28	0.0	-	-	-
TiO <sub>2</sub>	0.01	0.014	25.2	0.01	0.005	46.6	0.02	0.02	0.0	-	-	-
MnO	0.12	0.125	3.4	0.13	0.12	3.8	0.23	0.22	1.8	-	-	-
<b>Pellets</b>	PCC-1 (n=4)			DTS-1 (n=3)			NIM-D (n=2)			W-2 (n=6)		
Zn	43.6	42	6.4	47.5	48	5.7	90.2	90	3.1	79.1	77	3.9
Cu	9.1	10	4.1	7.7	7.5	18.2	11.9	10	71.0	105.7	103	4.4
Ni	2386	2400	2.3	2400.	2350	0.9	2150	2040	4.8	64.5	70	4.9
Co	109.4	110	5.1	137.5	139	4.0	220.6	208	1.8	43.1	44	7.2
Cr	2696	2730	1.6	3932.	3920	2.0	2998	2870	0.9	91.7	93	3.7
V	33.2	30	4.5	10.5	12	7.3	36.3	40	1.8	261.8	262	0.7
Sc	7.2	8.5	15.4	3.3	3.5	42.9	5.3	-	-	32.2	35	7.5

**Table A.1.** Summary of international standard analysis for major elements analysed on fusion discs and trace elements on pressed pellets, n= number of repeat analysis, CAC = analyses made during this study, accept = accepted values for the international standards from Potts *et al.* (1992), RSD = relative standard deviation. Oxide data in wt%, elements in ppm.

**Instrumental precision:** the instrumental precision was determined by making repeat analysis of the same disc/pellet during the analytical run. The standard deviation of the analyses obtained is a measure of how reliably the XRF repeats each measurement (i.e. how well the crystals return to the same positions etc.). The results are summarised in Table A.2.

Disc				Pellet	
	Instrument Precision CAC 180B	Instrument Precision CAC 159	Instrument Precision CAC 169		Instrument Precision CAC 130
SiO <sub>2</sub>	0.19	0.08	0.317	Zn	2.33
Al <sub>2</sub> O <sub>3</sub>	0.06	0.06	0.775	Cu	0.49
Fe <sub>2</sub> O <sub>3</sub>	0.02	0.43	0.138	Ni	32.46
MgO	0.39	0.46	1.981	Co	0.35
CaO	0.02	0.02	0.194	Cr	11.31
TiO <sub>2</sub>	0.00	0.00	0.276	V	1.06
MnO	0.00	0.00	0.532	Sc	1.56
Ni	12.07	46.97			
Cr	107.63	59.33			
V	3.61	3.34			

**Table A.2.** Summary of relative standard deviations for instrumental precision; all values in %.

### **A.3. ICP-MS Analysis**

Sc, Ti, V, Cr, Mn, Co, Ni, Cu, Zn, Ga, Rb, Sr, Y, Zr, Nb, Cs, Ba, La, Ce, Pr, Nd, Sm, Eu, Gd, Tb, Dy, Ho, Er, Tm, Yb, Lu, Hf, Ta, Pb, Th and U were analysed by inductively coupled plasma mass spectrometry on a Perkin Elmer Sciex 6000 at the University of Durham. Samples were prepared as follows.

All the equipment was scrupulously cleaned before the samples were dissolved. Funnels, volumetric flasks etc. were leached overnight with 5% nitric acid. The Teflon vials were cleaned by heating overnight with approximately 2 ml of Analar™ nitric acid. This process was repeated 3 times before the vials were used for

	X-108		W2		BCR-1	
Sc	<b>33.44±2.12</b>	33.86	<b>34.68±2.57</b>	35.39	<b>33.25±0.59</b>	32.6
V	<b>215.55±3.1</b>	218.34	<b>263.94±2.7</b>	264.14	<b>418±9.2</b>	407
Cr	<b>471.03±18.4</b>	466.83	<b>96.34±9.8</b>	99.5	<b>11.07±0.664</b>	16
MnO	<b>0.15±0.006</b>	0.15	<b>0.17±0.004</b>	0.17	<b>0.19±0.006</b>	0.18
Co	<b>38.12±0.573</b>	38.32	<b>44.91±0.537</b>	45.47	<b>37.48±0.549</b>	37
Ni	<b>122.92±5.7</b>	116.67	<b>79.33±13.1</b>	97.53	<b>9.20±1.218</b>	13
Cu	<b>82.41±1.68</b>	85.63	<b>102.25±1.78</b>	105.74	<b>24.57±1.092</b>	19
Zn	<b>132.16±139.2</b>	66.12	<b>79.53±11.8</b>	77.27	<b>124.01±21.6</b>	129.5
Ga	<b>9.28±0.053</b>	9.33	<b>17.39±0.25</b>	17.53	<b>21.79±0.221</b>	22
Rb	<b>12.42±0.215</b>	13.03	<b>19.80±0.353</b>	20.36	<b>47.51±0.441</b>	47.2
Sr	<b>87.50±1.48</b>	85.47	<b>198.38±1.463</b>	193.31	<b>337.3±4.15</b>	330
Y	<b>4.31±0.045</b>	4.26	<b>22.72±0.320</b>	21.36	<b>37.94±0.325</b>	38
Zr	<b>24.16±0.250</b>	25.13	<b>92.72±</b>	92.87	<b>190.7±1.7</b>	195
Nb	<b>0.53±0.013</b>	0.56	<b>7.68±0.073</b>	7.76	<b>12.99±0.055</b>	13.5
Ba	<b>35.56±0.453</b>	35.44	<b>172.64±2.1</b>	167.08	<b>682.5±14.4</b>	681
La	<b>0.87±0.040</b>	0.93	<b>10.37±0.099</b>	10.61	<b>25.29±0.281</b>	24.9
Ce	<b>1.63±0.018</b>	1.73	<b>22.55±0.231</b>	23.03	<b>53.06±0.681</b>	53.7
Pr	<b>0.27±0.008</b>	0.25	<b>3.01±0.035</b>	2.94	<b>7.01±0.071</b>	6.8
Nd	<b>1.27±0.021</b>	1.14	<b>13.36±0.222</b>	13.22	<b>29.97±0.174</b>	28.8
Sm	<b>0.34±0.016</b>	0.38	<b>3.29±0.033</b>	3.36	<b>6.71±0.045</b>	6.59
Eu	<b>0.12±0.002</b>	0.12	<b>1.07±0.007</b>	1.12	<b>1.97±0.023</b>	1.95
Gd	<b>0.45±0.017</b>	0.44	<b>3.73±0.070</b>	3.63	<b>6.87±0.137</b>	6.68
Tb	<b>0.08±0.002</b>	0.08	<b>0.62±0.002</b>	0.62	<b>1.08±0.010</b>	1.05
Dy	<b>0.57±0.014</b>	0.59	<b>3.77±0.026</b>	3.71	<b>6.36±0.050</b>	6.34
Ho	<b>0.14±0.003</b>	0.12	<b>0.77±0.006</b>	0.74	<b>1.29±0.010</b>	1.26
Er	<b>0.45±0.009</b>	0.48	<b>2.16±0.018</b>	2.23	<b>3.57±0.026</b>	3.63
Tm	<b>0.09±0.003</b>	0.09	<b>0.35±0.003</b>	0.34	<b>0.57±0.004</b>	0.56
Yb	<b>0.62±0.014</b>	0.68	<b>2.04±0.015</b>	2.03	<b>3.39±0.024</b>	3.38
Lu	<b>0.11±0.002</b>	0.11	<b>0.32±0.003</b>	0.33	<b>0.53±0.004</b>	0.51
Hf	<b>0.66±0.011</b>	0.69	<b>2.47±0.015</b>	2.49	<b>4.96±0.047</b>	4.95
Ta	<b>0.09±0.083</b>	0.052	<b>0.52±0.028</b>	0.54	<b>0.83±0.046</b>	0.81
Th	<b>0.13±0.003</b>	0.13	<b>2.17±0.021</b>	2.04	<b>6.07±0.034</b>	5.98

**Table A.3.** Comparison of accepted standard values for international standards (Potts *et al.*, 1992) and in-house standards (normal type), and values obtained during this study (bold type). Quoted standard deviations obtained from five separate measurements in 5 different analytical sessions. All values in ppm. Except MnO wt%.

the first time, and then once between each batch of samples. The samples were prepared in batches of 30, each batch included three blanks and one or two repeat samples.

Samples of  $0.1 \pm 0.001$  g were digested with 1 ml of Aristar™ nitric acid and 4 ml of Aristar™ hydrofluoric acid for 48 hours. The product was evaporated almost to dryness and then taken up in 1 ml of Aristar™ nitric acid and again evaporated to near dryness. A further 1 ml of Aristar™ nitric acid was added the product again evaporated to near dryness. The samples were redissolved with 2.5 ml Aristar™ nitric acid and approximately 15 ml of deionised water, and then boiled for 30 minutes. The cooled solutions were spiked with 1.25 ml of a 2 ppm Bi, Re and Rh internal standard spike solution and made up accurately to 50 ml.

The samples were further diluted 1:10 with 5% nitric before running on the ICP-MS. The ICP-MS was configured to make 2 replicate analyses per sample with dwell times of 20 ms for all elements except Rb, Sr, Nb, Y, Zr and the REE when dwell times of 40 ms were used, and 50 scans were made across the mass range per replicate. Calibration lines were constructed from analyses of international standards and in-house peridotite samples. The standard values and the values obtained during the analytical runs are compared in Table A.3.

### A.3.1. ICP-MS detection limits

Because the machine had to operate close to the detection limit in order to obtain reliable data for the unknowns, it was important to have good blank data. Therefore three blanks per batch of samples were made. Satisfactory results were obtained using Aristar™ hydrofluoric acid and Romil™ Ultrapurity nitric acid. Despite careful laboratory work, differences were still found between blanks made for each sample batch. Because the unknown concentrations were so low, the blank correction for each sample was made using the relevant blank from the sample batch, rather than calculating a bulk average blank. The detection limit was taken as 3 times the standard deviation of the blank, and typical values for several blanks are presented in Table A.4.

	Blank A	Blank B	Blank C		Blank A	Blank B	Blank C
Sc	0.225	0.836	1.539	Ce	0.004	0.004	0.004
V	0.030	0.018	0.208	Pr	0.002	0.001	0.003
Cr	0.502	3.240	1.510	Nd	0.003	0.004	0.005
Mn	0.000	0.000	0.000	Sm	0.005	0.010	0.011
Co	0.024	0.040	0.029	Eu	0.000	0.003	0.001
Ni	0.149	0.000	0.806	Gd	0.007	0.021	0.008
Cu	0.065	0.015	0.039	Tb	0.000	0.001	0.001
Zn	68.184	0.000	7.174	Dy	0.002	0.002	0.004
Ga	0.003	0.059	0.016	Ho	0.000	0.001	0.001
Rb	0.008	0.010	0.018	Er	0.002	0.004	0.006
Sr	0.007	0.012	0.011	Tm	0.000	0.001	0.000
Y	0.001	0.018	0.008	Yb	0.001	0.000	0.003
Zr	0.011	0.033	0.003	Lu	0.000	0.000	0.000
Nb	0.001	0.004	0.003	Hf	0.003	0.004	0.009
Ba	0.036	0.177	0.052	Ta	0.002	0.004	0.001
La	0.000	0.002	0.006	Th	0.000	0.000	0.002

**Table A.4.** Summary of detection limits at 3\*s.d. of the blank for three different blank samples. Values in ppm.

### A.3.2. ICP-MS precision

Trying to estimate the precision of the technique for such low level analyses is difficult. Standard instrumental precision for the ICP-MS, measured by making repeat measurements of a sample throughout an analytical run, is high. The standard deviation and relative standard deviation of two standards, which were run 5 times during a single analytical session are shown in Table A.5. As the Table shows many elements have a precision of better than 1% and most are better than 7%. Sc, Zn and Ta appear to have the worst instrumental precision, up to 20.9%.

	BHV01	X-108		BHV01	X-108
Sc	7.1	4.2	Ce	0.8	1.8
V	1.0	1.0	Pr	0.8	1.1
Cr	0.7	1.0	Nd	0.8	3.1
Mn	0.7	1.0	Sm	1.2	3.0
Co	0.6	1.2	Eu	0.6	3.1
Ni	1.2	1.5	Gd	1.7	4.3
Cu	0.8	1.5	Tb	0.6	1.3
Zn	0.9	20.4	Dy	0.6	3.3
Ga	1.4	0.8	Ho	0.4	1.6
Rb	0.7	1.3	Er	0.7	2.5
Sr	0.8	1.2	Tm	1.2	1.1
Y	1.1	0.9	Yb	1.5	2.0
Zr	0.7	1.4	Lu	0.9	1.0
Nb	0.6	1.5	Hf	1.2	1.9
Ba	0.8	0.8	Ta	5.2	20.9
La	1.3	2.8	Th	0.6	1.5

**Table A.5.** Summary of the relative standard deviations for the elements in standards BHV01 and X-108 based on 7 and 5 replicate analysis respectively in a single analytical session.

However, these values are the best possible estimate of the precision because other factors can introduce significant errors into the data. Two of the most significant factors are likely to be:

- differences in inter-run calibration lines – the samples were run over several days on the ICP-MS so a different calibration line had to be constructed for each days analyses. Because the unknowns were at such low concentrations, small differences in the slope of the calibration lines between runs produces significant differences in the calculated concentrations.
- sampling inhomogeneity – this is a possible cause of error especially for elements concentrated in minor phases (e.g. Zr) and is exacerbated by the small sample size used in ICP-MS analysis (0.1g).

These factors will result in the ‘method precision’ being worse than the instrumental precision.



	X-108	W2	BHV01	AGV1	Average
Sc	5.75	9.46	6.86	16.33	9.60
V	2.78	2.28	0.72	1.41	1.80
Cr	1.07	8.08	9.94	37.08	14.04
Mn	3.36	1.46	0.36	3.63	2.20
Co	1.30	1.58	0.99	2.12	1.50
Ni	1.20	16.61	19.98	4.08	10.47
Cu	1.20	1.65	0.57	2.19	1.40
Zn	67.06	14.84	13.45	16.86	28.05
Ga	1.35	1.56	0.87	1.63	1.35
Rb	1.51	1.60	1.33	0.40	1.21
Sr	1.55	0.62	1.40	0.95	1.13
Y	1.68	1.21	0.50	0.99	1.09
Zr	1.53	0.39	1.03	0.45	0.85
Nb	0.78	0.72	0.82	1.00	0.83
Ba	2.14	0.86	1.09	0.22	1.08
La	4.95	0.94	1.00	0.28	1.79
Ce	0.70	0.71	0.77	0.73	0.73
Pr	1.26	1.06	0.73	1.00	1.01
Nd	2.06	1.69	0.59	0.63	1.24
Sm	3.05	1.16	0.50	1.45	1.54
Eu	1.28	1.19	0.80	1.33	1.15
Gd	5.28	1.21	1.11	0.59	2.05
Tb	2.75	1.28	1.23	0.43	1.42
Dy	1.51	1.32	0.39	0.67	0.97
Ho	1.73	0.54	0.77	1.07	1.03
Er	1.82	1.91	0.39	1.61	1.43
Tm	2.36	1.15	1.12	1.60	1.56
Yb	2.35	1.03	2.11	1.21	1.67
Lu	1.71	1.48	0.95	1.36	1.37
Hf	3.75	1.01	1.14	1.06	1.74
Ta	80.81	5.31	3.22	4.37	23.43
Th	1.52	0.92	1.07	0.38	0.97

**Table A.6.** Summary of relative standard deviations calculated for analyses of standard samples made at the beginning of each days analytical run: the same solution of each standard was used for each analysis.

	CAC 159 (n=2)	CAC 135 (n=2)	CAC 49 (n=4)	CAC 81 (n=2)	Average
Sc	2.9	10.7	31.4	24.8	17.5
V	1.2	1.2	5.4	6.9	3.7
Cr	0.4	0.3	5.4	7.5	3.4
MnO	1.8	0.6	4.7	12.7	4.9
Co	1.3	0.8	3.3	5.3	2.6
Ni	1.1	0.2	1.3	2.7	1.3
Cu	0.4	0.1	3.0	1.3	1.2
Zn	163.9	10.6	14.4	17.0	51.5
Ga	0.6	0.2	6.0	11.8	4.6
Rb	1.9	0.6	7.8	7.2	4.4
Sr	4.4	1.0	22.9	16.7	11.3
Y	1.6	0.0	20.5	17.5	9.9
Zr	6.9	1.3	129.6	9.3	36.8
Nb	7.8	2.3	38.2	2.4	12.7
Ba	2.8	1.1	61.8	44.5	27.5
La	5.3	2.2		13.4	7.0
Ce	13.7	1.8		15.7	10.4
Pr	6.7	1.9	93.4	14.5	29.1
Nd	1.2	0.7	12.1	16.4	7.6
Sm	0.5	0.5	28.2	5.4	8.6
Eu	3.8	1.0	18.2	10.0	8.2
Gd	2.2	1.0	23.7	14.3	10.3
Tb	1.4	0.1	21.8	19.3	10.6
Dy	1.3	0.6	15.0	11.7	7.1
Ho	0.6	1.7	17.3	13.9	8.4
Er	2.5	0.2	16.2	18.4	9.3
Tm	0.6	0.5	17.4	18.9	9.3
Yb	0.5	0.6	17.1	12.8	7.7
Lu	3.9	2.2	16.1	11.9	8.5
Hf	4.9	4.3	29.6	11.5	12.6
Ta	19.4	5.4	26.5	27.3	19.7
Th	74.9	8.5	60.6	27.8	42.9

**Table A.7.** Summary of relative standard deviations of duplicate analyses, n = number of analyses.

The errors introduced by differences in calibration line gradients and machine efficiencies during each daily run can be estimated from replicate analyses made of the

calibration standards at the beginning of each days analyses. The relative standard deviation data calculated for four days analyses of the calibration standards are summarised in Table A.6.

As Table A.6. shows, the precision is generally worse when the between run variation is taken into account. However, the majority of elements still have an average precision of better than 2%, although Zn and Ta are poorer at 28% and 23%. The REE precision is considerably better than obtained by Freeman (1996), who obtained values ranging between 6.3% and 64.8% for various REE elements.

To try to estimate the extent to which sampling inhomogeneity affects the precision, duplicate solutions were made for several samples. The results of these duplicate analyses are given in Table A.7.

As the table shows, the precision values are slightly worse for most elements once the effects of sampling inhomogeneity have been taken into account and, in particular, considerably worse for Zn, Zr and Th. Notably, the duplicate analysis of CAC 49 are particularly poor, and may be because this is a peridotite sample, depleted in trace elements and REE.

	S.D.		S.D.
Sc	1.661	Ce	0.004
V	1.009	Pr	0.010
Cr	256.868	Nd	0.027
MnO	0.001	Sm	0.025
Co	0.737	Eu	0.008
Ni	-	Gd	0.061
Cu	0.063	Tb	0.007
Zn	-	Dy	0.046
Ga	0.073	Ho	0.010
Rb	0.016	Er	0.061
Sr	0.150	Tm	0.011
Y	0.146	Yb	0.050
Zr	0.257	Lu	0.004
Nb	0.008	Hf	0.019
Ba	0.362	Ta	0.043
La	0.006	Th	0.006

**Table A.8.** Summary of the estimated standard deviation values for the ICP-MS analyses.

	CAC 116	CAC 135	CAC 144	CAC 165	CAC 166	CAC 172
Zr (ICP-MS)	16.2264	18.2268	30.453	28.3519	28.3789	72.7499
Zr (XRF)	107.9	42.3	213	138.9	114.9	123.3

**Table A.9.** Comparison of Zr data provided by ICP-MS and XRF for the same sample. Note that values are distinctly lower when analysed by ICP-MS. Values in ppm.

Table A.9 demonstrates the effects of incomplete dissolution of minor phases (e.g. zircon) in amphibolite samples. Values for Zr, which is hosted by zircon, are distinctly lower in analyses made by ICP-MS in comparison with analyses made by XRF. This phenomena is related to the incomplete dissolution of zirconium during the sample preparation stage. Thus, values for Zr obtained by ICP-MS are not reported in this study, alternatively values obtained by XRF are used.

Sample CAC 152	Hf	Zr
ICP-MS (standard preparation)	2.5101	70.6498
ICP-MS (fusion-disc preparation)	5.008	221.3988
XRF	-	216.8

**Table A.10.** Comparison of Hf data provided by ICP-MS analysis of a sample prepared using the standard procedure (see above) compared with the same sample prepared using a fused disc. Values in ppm.

Solubility problems also seem to effect the element Hf (Table A.10), which is also hosted by zircon and does not dissolve properly during the standard ICP-MS preparation procedure (see above). However, in a sample that was prepared using a fused-disc (see Section A.2) and then analysed by ICP-MS, the Hf values are higher and this suggests that this procedure eliminates the solubility problem associated with zirconium. This is confirmed by the fact that the Zr value obtained by ICP-MS using a fused-disc is similar to the value obtained by XRF (Table A.10). Unfortunately only a few samples were prepared using the fused-disc method, therefore an alternative method of obtaining valid Hf data must be used. Thus, the Hf data presented has been re-calculated on the basis of that the real Hf and Zr values differ from the measured Hf and Zr by insoluble zircon, which typically has a Zr/Hf ratio of 34. Therefore the difference in Zr between XRF and ICP-MS ( $\Delta Zr$ ) has been used to correct Hf by the expression:

$$\text{Hf (real)} = \text{Hf (measured)} + \Delta\text{Zr}/34$$

All re-calculated values for Hf shown in Appendix D are quoted in italics.

The above discussion illustrates the difficulties inherent in trying to obtain reliable low level determinations of the trace elements in depleted peridotites. As a best estimate of the precision obtained during this study, the average relative standard deviations values calculated in Tables A.6 and A.7 were themselves averaged, and then converted to ppm by multiplying by an averaged lherzolite value. The results obtained are presented in Table A.8 and are the basis upon which errors can be calculated.

#### **A.4. Electron Probe Micro-Analysis**

Major element analysis of representative mineral phases was performed at the British Geological Survey, Keyworth, by energy-dispersive spectrometry (EDS) using a Cambridge Instruments Microscan 5 electron microprobe (accelerating voltages 15kV, specimen current 5 nA, with counting times of 60 seconds). Additional analyses to obtain better data for minor elements were conducted at BGS by wavelength-dispersive spectrometry (WDS) using a Cameca SX50 electron microprobe (accelerating voltages 15 kV, specimen current 5 nA, counting time 60 seconds). Analyses were also conducted at the Research School of Earth Sciences, the Australian National University, Canberra, by EDS using a fully automated Cameca Camebax electron microprobe using the methods of Ware (1991) (accelerating voltage 15 kV, Beam current 4-6 nA, counting time 80 seconds). Additional data, which is presented for several of the mineral phases in the following sections, includes analyses provided by M.T.Styles (British Geological Survey) and D.H.Green, M.Cmiral and W.Lus (Research School of Earth Sciences, the Australian National University, Canberra).

The calibration was checked periodically during the analyses of the unknowns on the different machines by analysing in-house standards.

The majority of specimens probed showed evidence of alteration of the mineral phases under investigation, for example alteration of olivine to serpentine minerals. Therefore samples showing the least alteration were selected and analyses were taken from grains showing the least alteration, or where this was not possible, at a distance from the alteration. Several analyses (>5) of different grains in a single sample were collected in order identify the altered grains, and discard them in order to reduce the

possibility of including them in the final representative composition. The representative composition of each mineral phase under investigation, in each particular sample, is therefore an average value based on the analyses of several grains. For pyroxenes and spinels, analysis of the core and rims of grains were taken to demonstrate any core to rim compositional variation. In some rocks, both relict porphyroclasts and neoblasts of pyroxene were present, therefore analyses of both grains were taken. When exsolution lamellae were observed in pyroxenes, a defocused beam was used to obtain a homogenous composition for these grains.

Microprobe analysis cannot detect the two oxidation states of iron,  $\text{Fe}^{2+}$  and  $\text{Fe}^{3+}$  separately, therefore the  $\text{Fe}^{2+}/\text{Fe}^{3+}$  ratios in the minerals analysed have to be estimated by computation after the analysis has been performed. All methods of computation of the  $\text{Fe}^{2+}/\text{Fe}^{3+}$  ratios have their limitations and assumptions, however, the method of Droop (1987) has been applied. This method is well established in the literature and produces favourable results. With this method, the number of  $\text{Fe}^{3+}$  ions per  $X$  oxygens in the mineral formula,  $F$ , is given by formula (A).

$$(A) \quad F = 2X(1-T/S)$$

Where  $T$  is the ideal number of cations per formula unit, and  $S$  is the observed cation per  $X$  oxygens calculated assuming all iron to be  $\text{Fe}^{2+}$  (Droop, 1987). This formula has been applied to the microprobe analysis obtained for spinels, pyroxenes and amphiboles. The resulting  $\text{Fe}^{2+}/\text{Fe}^{3+}$  ratios calculated for spinels were consistent, however, the results for the pyroxenes and amphiboles in particular were unrealistic and included negative values. Therefore, only the data presented for spinel analysis includes recalculated  $\text{Fe}^{2+}/\text{Fe}^{3+}$  ratios. Examination of the data presented in the literature shows that the pyroxenes in rocks from the Lizard contain negligible  $\text{Fe}^{3+}$  ratios and this is also the case for the majority of the amphibole analysis. It is therefore assumed that the data presented for the pyroxenes and amphiboles is satisfactory, even with the omission of the recalculation of  $\text{Fe}^{2+}/\text{Fe}^{3+}$  ratios, for the reasons presented above. All of the iron in olivine can be assumed to be  $\text{Fe}^{2+}$ , therefore no re-calculation was required.

Formula for olivine, pyroxene, spinel, amphibole and plagioclase analyses were calculated using 4, 6, 32, 23 and 8 oxygens respectively.

The graphs in Chapter 5 are annotated with  $2\sigma$  error bars. For several mineral parameters (e.g. Cr# in spinel), the errors are smaller in size than the points on the graph. In these cases, the error bars have been omitted for clarity, and the error can be assumed to be less than the size of the points on the graph. Errors are based on errors produced by the Zaf calculations of the electron microprobe software.



### **A.5 Sensitive High Mass-Resolution Ion Micro-Probe (SHRIMP) Analysis**

The following analytical methods are taken from Nutman *et al.* (*in prep*).

#### **A.5.1. Analytical methods and results**

Following coarse crushing, sample chips were hand picked and then standard heavy liquid and isodynamic techniques were used to produce zircon and monazite concentrates. These were then hand-picked using a binocular microscope, to produce a varied assortment of least metamict and damaged grains for analysis. Assessment grains and choice sites for analysis was based on transmitted and reflected light microscopy and cathode luminescence imaging.

U-Th-Pb isotopic ratios and concentrates were determined in zircon separates using SHRIMPs I and II and were referenced to the Australian National University standard zircon SL13 (572 Ma;  $^{206}\text{Pb}/^{238}\text{U} = 0.0928$ ). Further details of the zircon analytical procedure and data assessment are given Compston *et al.* (1984), Roddick & van Breemen (1994) and Claoue-Long *et al.* (1995).

Monazite analyses were undertaken following the method outlined by Williams *et al.* (1996), using monazites from Thompson mine, Canada as a standard. Several isotope dilution thermal ionisation analyses of these have average U content of 2100 ppm and a mean  $^{207}\text{Pb}/^{206}\text{Pb}$  age of  $1767 \pm 0.3$  Ma, but with slight dispersion of  $^{206}\text{Pb}/^{238}\text{U}$  ages, giving both slightly positive to negative discordant points (C.Roddick, written communication, 1995). A  $^{206}\text{Pb}/^{238}\text{U}$  age of 1767 Ma is used for the Thompson monazite standard. As discussed by Williams *et al.* (1996), the  $^{204}\text{Pb}$ -corrected  $^{207}\text{Pb}/^{206}\text{Pb}$  ages obtained by SHRIMP on Thompson monazites are slightly too young relative to the isotope dilution data. This is best accounted for by an isobaric interference under the  $^{204}\text{Pb}$  peak, at count rates of 0.5 to 1.5 counts per second. The problem is compounded by high background counts (measured at mass  $\sim 204.1$ ). As pointed-out by Williams *et al.* (1996), correction of mass 204 counts of some monazite unknowns using an amount assessed from the Thompson standard leads to the  $^{204}\text{Pb}$  values less than the background counts. This demonstrates that this interference is variable, depending on the chemistry of the monazite suite in question. Fortunately in the case of the unknown monazites reported in this paper, this problem is of no

consequence because their young age has meant that  $^{206}\text{Pb}/^{238}\text{U}$  ratios, after correction for small amounts of common Pb by the  $^{207}\text{Pb}$  method (Compston *et al.*, 1984) has been used in the age calculation. Summary data is given in Table A.9.

Quoted errors on isotopic ratios take into account fluctuations in ion count rates above that expected from counting statistics alone (e.g. Williams *et al.* 1996). Errors are purely based on counting statistics (e.g. Page & Laing, 1992) give a false impression of precision, and hence ease of resolution of geological events. This is particularly the case in very high Th and U monazites and zircons, where the counting statistics component of error can be subordinate to that due to intra analysis fluctuation in ion counting rates. In addition,  $^{206}\text{Pb}/^{238}\text{U}$  ratios have an extra error component (typically 1.5 to 2.0%) from calibration of the measurement using the standard zircon SL13.

Sample	Lithology	Metamorphism	Igneous	Zircon inheritance
96/510	Landewednack Amphibolite	392 ±5 Ma (z)		
96/517	Felsic Kennack Gneiss		384 ±16 Ma (z) 390 ±16 Ma (m)	500-600,>1700 Ma
96/530	Gabbroic vein	385 ±7 Ma (z)		
96/543	Landewednack Amphibolite	374 ±15 Ma (z)		
96/546	Pelite layer	~390 Ma (z)	~425 Ma (z)	450-600,~750,>1100Ma
97/719	Granite – Lizard Head Sill		499 ±7 Ma	
97/712	Granite – Lizard Head Sill		488 ±9 Ma	
97/713	Felsic Kennack Gneiss		390 Ma	500 Ma and Palaeoproterozoic
97/714	Felsic Kennack Gneiss		390 Ma	500 Ma and Palaeoproterozoic
97/716	Granite sheet		360 Ma	

**Table A.11.** Summary of studied samples, including sample lithology and calculated ages.

Most ages presented in this paper are weighted means ( $2\sigma$ ; with analyses with the largest analytical error receiving the lowest weighting) derived from  $^{206}\text{Pb}/^{238}\text{U}$  ratios of

analyses from the isotopically least-disturbed sites (those having close to concordant U/Pb ages, with lowest non-radiogenic components of Pb) in grains which form optical microscopy and cathode luminescence (CL) imagery were ascertained to belong to single populations. The decay constants and present-day  $^{238}\text{Pb}/^{235}\text{U}$  value given by Steiger and Jager (1977) were used to calculate the ages. Tera-Wasserburg  $^{207}\text{Pb}/^{206}\text{U}$  vs.  $^{238}\text{Pb}/^{206}\text{U}$  plots for the zircon and monazites analysed during the course of this study are presented on Figure A.1.

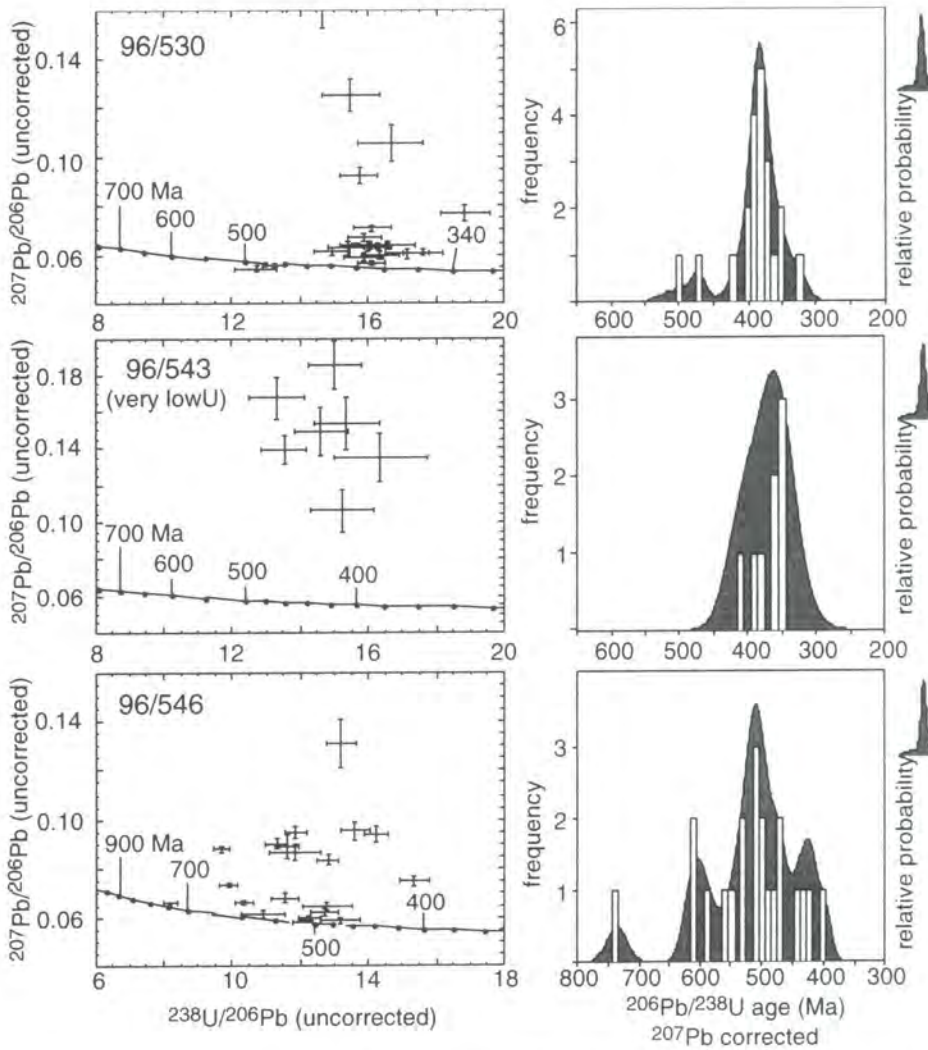


**Figure A.1.a.** Tera-Wasserburg  $^{207}\text{Pb}/^{206}\text{U}$  vs.  $^{238}\text{Pb}/^{206}\text{U}$  plots for 96/530 (Gabbroic vein) zircon, 96/543 (Landwednack amphibolite) zircon and 96/546 (Pelite layer in Landwednack amphibolite) zircons. Errors on plots are depicted at the  $1\sigma$  level.

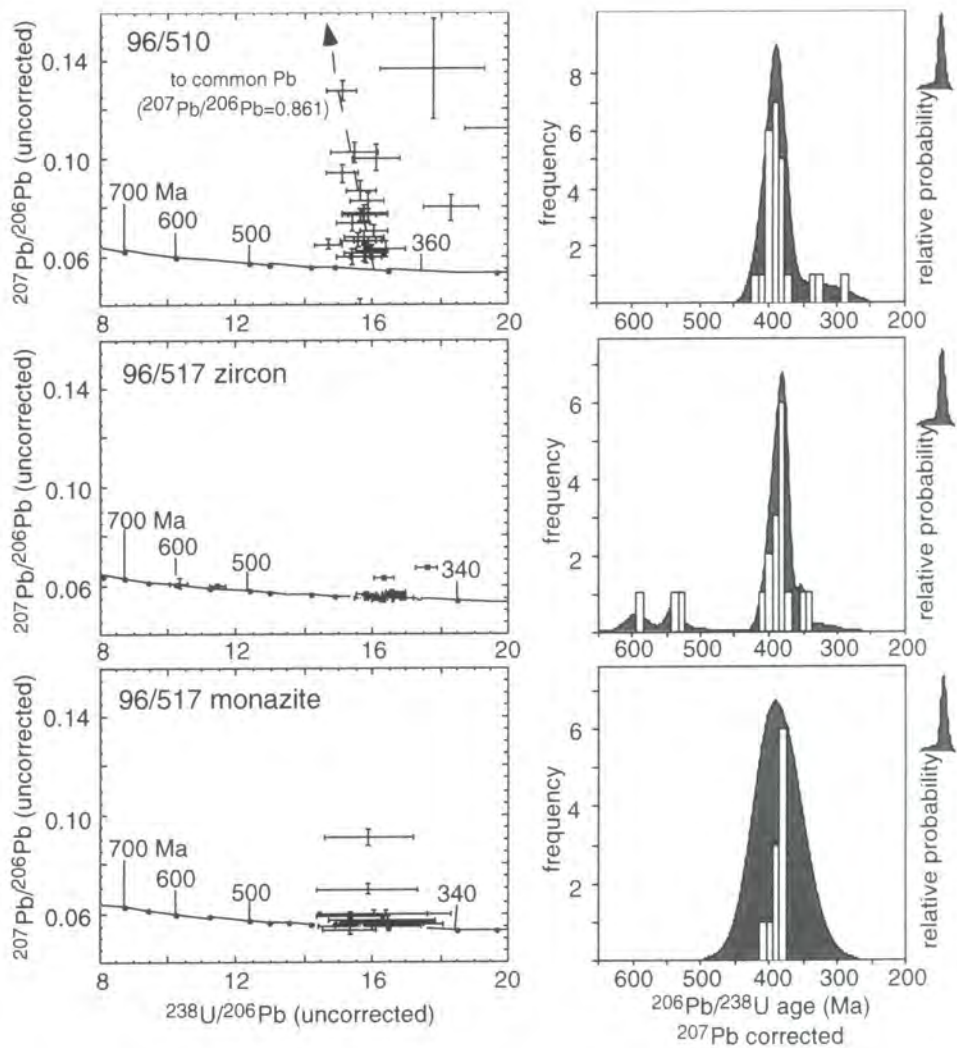


**Figure A.1.b.** Tera-Wasserburg  $^{207}\text{Pb}/^{206}\text{Pb}$  vs.  $^{238}\text{Pb}/^{206}\text{Pb}$  plots for 96/510 (Landewednack amphibolite) zircon, 96/517 (Felsic Kennack Gneiss) zircon and 96/517 (Felsic Kennack Gneiss) monazite. Errors on plots are depicted at the  $1\sigma$  level.

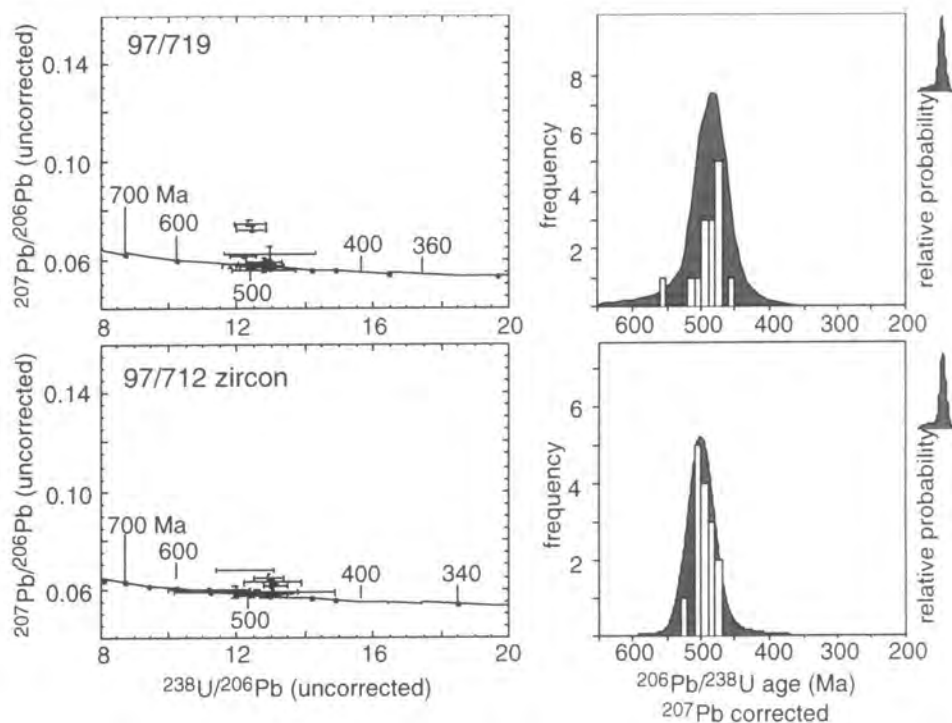


**Figure A.1.c.** Tera-Wasserburg  $^{207}\text{Pb}/^{206}\text{U}$  vs.  $^{238}\text{Pb}/^{206}\text{U}$  plots for 97/719 (Lizard Head Sill-deformed) zircon, 97/712 (Lizard Head Sill) zircon. Errors on plots are depicted at the  $1\sigma$  level.

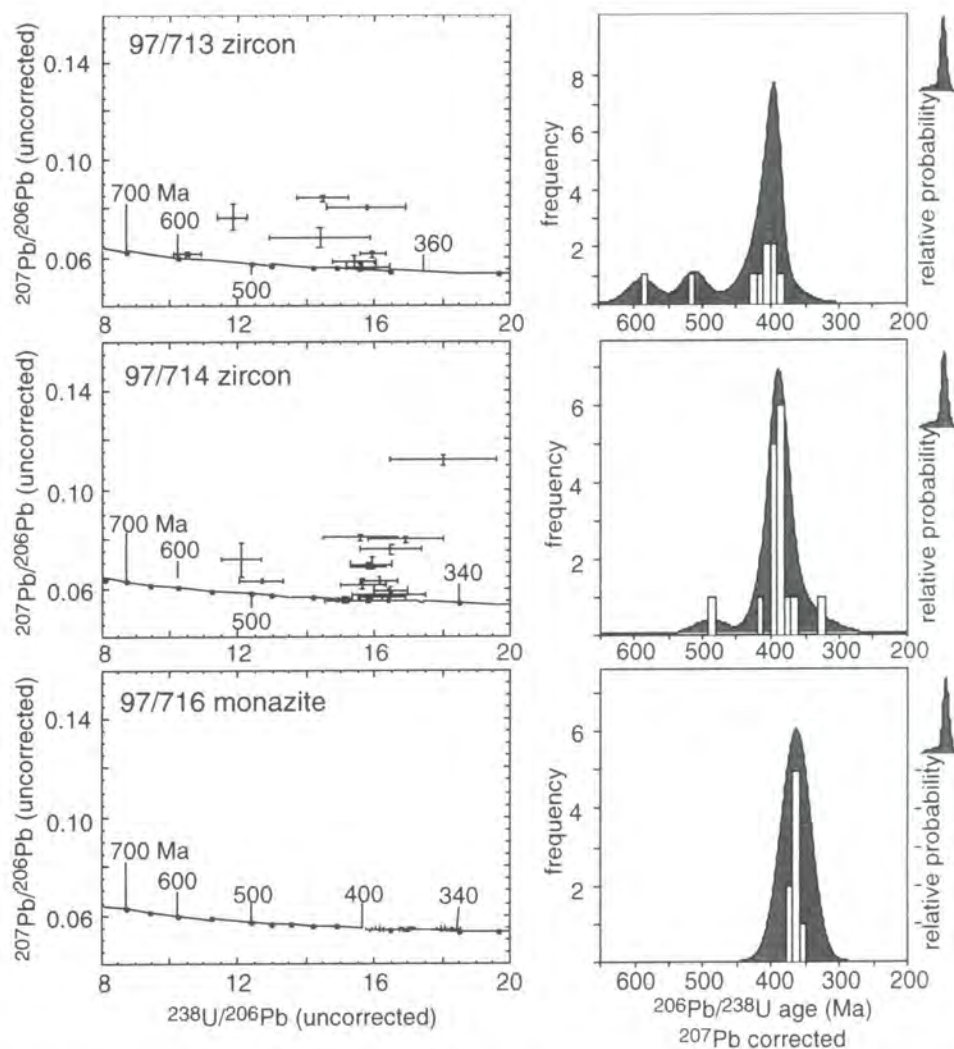


**Figure A.1.d.** Tera-Wasserburg  $^{207}\text{Pb}/^{206}\text{U}$  vs.  $^{238}\text{Pb}/^{206}\text{U}$  plots for 97/713 (Felsic Kennack Gneiss) zircon, 97/714 (Felsic Kennack Gneiss) zircon and 97/716 (Granite sheet) monazite. Errors on plots are depicted at the  $1\sigma$  level.



---

## APPENDIX B: GEOGRAPHICAL INFORMATION SYSTEM (GIS)

---

### **B.1 INTRODUCTION**

This section describes the approach of using Geographical Information Systems (GIS) as part of this work to complement detailed field and petrological studies of the ultramafic rocks of the Lizard Complex. The primary aim of this method is to produce petrogenetic maps of the ultramafic rocks of the Lizard Complex and to observe if the information can reveal large-scale patterns of variation in mineralogical and textural features in the ultramafic rocks. In the previous publications on the Lizard, two authors Flett (1946) and Green (1964a), have produced detailed maps which have sub-divided the peridotites. The map of Flett (1946) is based on the secondary alteration characteristics of the peridotites, and Green (1964a) produced a map based on both the primary petrographic features of the peridotites and deformation characteristics. Several authors (Bromley 1979; Kirby 1979, Leake & Styles 1984) have proposed that the Lizard peridotites comprise both harzburgites and lherzolites, and suggest that in certain areas harzburgite is predominant. Therefore, one of the aims of this study is to use the GIS technique to provide a rigorous method of clarifying the observations of the previous publications, in addition to revealing new petrographic features.

GIS was used in this study as it provides a relatively rapid and qualitative method of displaying, querying and analysing information stored in a database, in a map format. The database consists of petrographic information obtained from thin-sections of samples collected from the Lizard Complex. Over the Years a large number of thin sections have been prepared from outcrop and core material of the Lizard Complex. The most important collection include those of the BGS, collected principally by JS Flett and MT Styles, those of the Sedgewick Museum collection at Cambridge University, collected by DH Green and further sections prepared in the course of the present study.

The purpose of the GIS approach is to produce new lithological and petrogenetic information on the Lizard Complex from petrographic data obtained from all available thin sections. This approach is based on the methodology described in BGS report WG/94/14 14 (Gillespie et al. 1994) on the Huntly-Knock intrusions of

Aberdeenshire. The following outlines of the objectives and methodology utilised in the GIS approach are based on and taken from Gillespie et al. 1994). The results of the study on Lizard rocks are described and the implications for petrogenesis and deformation are discussed.

## **B.2 OBJECTIVES**

In summary the principal objectives are:

- 1) to collate, from diverse sources, all the thin sections for ultramafic rocks available from the Lizard Complex, and to identify all those that are relevant to this study;
- 2) to utilise the new approach to geological mapping and petrogenetic interpretation designed and tested by BGS report WG/94/14 (Gillespie et al. 1994). This involves a standardised description of the petrogenetic features, which have been recorded on a computer spreadsheet and computer-generated maps of selected petrographic features from these data have been produced using GIS software;
- 3) to identify possible refinements and changes to the BGS 1:50,000 litho-structural map of the Lizard Complex on the basis of information generated in (2), and from other information, where appropriate;
- 4) to utilise this information in an investigation into the origin and emplacement of the Lizard Complex.

## **B.3 METHODOLOGY**

The general approach adopted in this study is based on the methods utilised in BGS BGS report WG/94/14 (Gillespie et al. 1994). This procedure involves: selecting thin sections for petrographic description; designing and producing a *pro forma* sheet and accompanying Procedure Notes; performing petrographic descriptions of all selected thin sections; transferring petrographic data from the *pro forma* sheet onto a computer

database; constructing maps using the ArcView (v.3) GIS software from data selected from the database. These procedures are described below.

### **B.3.1 Thin section selection**

The process of selecting thin sections for petrographic description started by viewing BGS excel spreadsheet database of all BGS-registered thin sections from the area covered by Sheet 359. This process was supplemented by viewing the “hard copy” catalogue of thin sections from the area covered by Sheet 359. In addition a copy of the catalogue of samples collected by D.H.Green was obtained from the Earth Sciences Department at Cambridge University. The list of thin sections created was then refined by only selecting ultramafic rocks, because the principle aim of this investigation is to study the ultramafic rocks. In some examples the catalogues did not provide an accurate geographic location for a particular thin section, these examples were omitted, as they are useless in a GIS study. From this point the database was further reduced by briefly examining all the thin sections using an optical microscope and removing all those that were clearly non-ultramafic or those with >90% secondary alteration. In many examples two or more thin sections have identical grid reference locations and, where these have identical mineralogical and textural features, only one was retained in the dataset.

The final total of 296 thin sections represents virtually all of the presently available thin sections of ultramafic rock from the Lizard complex that have a unique grid reference or accurate geographic location.

Of the 296 thin sections described in this study, 97 were from samples collected by JS Flett, 2 were from samples collected by DCK, 2 were from samples collected by JEM, 3 were from samples collected by M, 51 were from samples collected by DH Green, 70 were from samples collected by MT Styles and 71 were from samples collected by the author.

### B.3.2. The pro forma sheet

The *pro forma* (Figure B.1) sheet used in this study was entitled 'Petrographic description - mafic and ultramafic rocks', the *pro forma* sheet is a modification of the *pro forma* sheet used in Gillespie et al. (1994). The principle purpose of the sheet is to ensure a simple, standardised and consistent approach to recording petrographic information from ultramafic rocks (Gillespie et al. 1994). The *pro forma* approach allows petrographic features to be recorded relatively rapidly, and directs the one to select and record features, which are relevant to a particular study. The majority of the *pro forma* sheet is designed so that information is recorded in tick-boxes, this serves to maximise the speed and ease of description of the information recorded. The form is divided into several segments which deal with different petrographic features, namely hand specimen characteristics, primary mineralogy, secondary mineralogy, modal volumes of the primary and secondary phases, estimated modal volumes of the primary phases (based on an assessment of residual primary phases and secondary alteration), grainsize, primary textures, physical alteration, chemical alteration and spinel - colour and texture. An advantage of this technique is that the form can be easily adapted to take into account other features. Data recorded can be transferred easily onto a computer database from which maps of different features, or combinations of features can be displayed, queried and analysed using GIS software. The principle aim of this method is to provide a flexible system for identifying meaningful patterns within large databases to improve mapping of lithologies, to establish variations in primary and secondary mineralogy, to identify variations in primary textures and physical alteration and to identify (or confirm the presence of) large-scale features such as faults or ductile shear zones.

The petrographic features included on the *pro forma* were chosen after reviewing the approach described in Gillespie et al. (1994) and on the basis of a preliminary study of a sub-set of sections, to identify aspects of petrography which have potential significance in determining lithological variations and interpreting aspects of the petrogenesis.

A set of 'Procedure Notes' accompanies the *pro forma* sheet and describes in detail how the petrographic information should be evaluated and recorded in each

**Petrographic description - mafic and ultramafic rocks**

Petrographer  BGS sample code  Other sample code

**HAND SPECIMEN**  
 none ☐ Colour   
 Grainsize   
 Fabric

More than one Pro-forma for this thin section ☐

**MINERALOGY**

Primary minerals - residual	Modal volume (%)	Secondary minerals	Modal volume (%)	Estimated primary modal volume (%)	Grainsize				
					< 10µm VFG	10 - 250 FG	250 - 2000 MG	> 16000 CG	Pheno/ Porph
OPX	<input type="text"/>	SERP	<input type="text"/>	<input type="text"/>	<input type="text"/>	<input type="text"/>	<input type="text"/>	<input type="text"/>	<input type="text"/>
CPX	<input type="text"/>	BAST	<input type="text"/>	<input type="text"/>	<input type="text"/>	<input type="text"/>	<input type="text"/>	<input type="text"/>	<input type="text"/>
AMPH	<input type="text"/>	CHLOR	<input type="text"/>	<input type="text"/>	<input type="text"/>	<input type="text"/>	<input type="text"/>	<input type="text"/>	<input type="text"/>
OLIV	<input type="text"/>	TALC	<input type="text"/>	<input type="text"/>	<input type="text"/>	<input type="text"/>	<input type="text"/>	<input type="text"/>	<input type="text"/>
PLAG	<input type="text"/>	CARB	<input type="text"/>	<input type="text"/>	<input type="text"/>	<input type="text"/>	<input type="text"/>	<input type="text"/>	<input type="text"/>
SPINEL	<input type="text"/>	SAP	<input type="text"/>	<input type="text"/>	<input type="text"/>	<input type="text"/>	<input type="text"/>	<input type="text"/>	<input type="text"/>
	<input type="text"/>	SAUSS	<input type="text"/>	<input type="text"/>	<input type="text"/>	<input type="text"/>	<input type="text"/>	<input type="text"/>	<input type="text"/>
		CL-AMPH	<input type="text"/>	<input type="text"/>	<input type="text"/>	<input type="text"/>	<input type="text"/>	<input type="text"/>	<input type="text"/>
		PY-AMPH	<input type="text"/>	<input type="text"/>	<input type="text"/>	<input type="text"/>	<input type="text"/>	<input type="text"/>	<input type="text"/>
		PB-AMPH	<input type="text"/>	<input type="text"/>	<input type="text"/>	<input type="text"/>	<input type="text"/>	<input type="text"/>	<input type="text"/>
		DB-AMPH	<input type="text"/>	<input type="text"/>	<input type="text"/>	<input type="text"/>	<input type="text"/>	<input type="text"/>	<input type="text"/>
		GR-AMPH	<input type="text"/>	<input type="text"/>	<input type="text"/>	<input type="text"/>	<input type="text"/>	<input type="text"/>	<input type="text"/>

**Primary textures**

Foliation - weak	<input type="text"/>	OPX cleavage - straight	<input type="text"/>
strong	<input type="text"/>	bent	<input type="text"/>
Exsolution - lamellae	<input type="text"/>	recrystallised	<input type="text"/>
blebs	<input type="text"/>		
Polkilitic / Ophitic	<input type="text"/>		
Interstitial pyroxene	<input type="text"/>		
Layering	<input type="text"/>		

**Physical alteration**

Primary (Porphyroclastic)	<input type="text"/>
Granular	<input type="text"/>
Recrystallised	<input type="text"/>
Schistose - mylonitic	<input type="text"/>
Recrystallisation of SERP	<input type="text"/>
Recrystallised olivine	<input type="text"/>

**Chemical alteration**

	Modal volume (%)
Serpentinisation	<input type="text"/>
CPX to AMPH	<input type="text"/>
OPX to AMPH	<input type="text"/>
Fresh PLAG	<input type="text"/>
AMPH to CHLOR	<input type="text"/>

**SPINEL - COLOURS & TEXTURES**

Black	<input type="text"/>
Brown	<input type="text"/>
Green	<input type="text"/>
Equant	<input type="text"/>
Skeletal	<input type="text"/>

**Interstitial**

SPINEL to CHLOR / rim	<input type="text"/>
SPINEL to MAG rim	<input type="text"/>
SPINEL to PLAG rim	<input type="text"/>

Comments  None ☐

Rock name

Primary  Present

**Figure B.1.** The *pro forma* sheet used to record petrographic features of the Lizard rocks.

section of the *pro forma*. The Procedure Notes are based on and modified after those of Gillespie et al. (1994).

### **B.3.3. Transferring petrographic data from *pro forma* sheets onto an Excel database**

An additional set of Procedure Notes entitled “Transferring petrographic data from *pro forma* sheets onto an Excel database” was prepared. These Procedure Notes are modified after Gillespie et al. (1994) and maximise consistency in the process of transferring petrographic data from the *pro forma* sheets onto an Excel database. The Procedure Notes describe how data recorded on a *pro forma* sheet should be transferred onto an Excel database for the purpose of data manipulation and map generation using GIS software. Numeric data, such as the modal volume of each primary phase, were transferred directly, whereas data recorded in tick-boxes were converted to a numeric scheme before being entered on the database. The database has the National Grid Reference and petrographic data for the 296 thin sections recorded in 69 columns. The database has to be saved in dBASE III, dBASE IV, a tab-delimited or comma-delimited text file before export to GIS software.

### **B.3.4 Working with GIS - summary**

#### ***Digitizing***

In order to view the petrographic database in a map-format as base map is required. The base maps were prepared by digitizing features on 1:10 000 scale Ordnance Survey topographic map sheets SW 72 SW; SW 72 SE; SW 82 SW; SW 61 NE; SW 71 NW; SW 71 NE; SW 61 SE; SW 71 SW which cover the Lizard area shown in the 1:50 000 scale geological map sheet 359. The features selected for digitizing were the MLWS coastline and 1km spaced gridlines, other features such as roads and topographic contours were omitted because it was decided they were not necessary. The features on each of the 1:10 000 map sheets were digitized separately using a digitizing table and Arc/Info software. Each of the 1:10 000 map sheets were digitized accurately and referenced to National Grid Reference co-ordinates. The eight separate digitized maps were then ‘joined’ using Arc/Info software to provide a complete map coverage of the Lizard area, showing the coastline and 1km gridlines. This map provides the basis for the GIS display, query and analysis.



***Displaying, querying and analyzing the data using Arcview (v.3)***

Arcview (v.3) is a GIS software package, which is relatively simple to use, and most functions can be performed using pull-down menus. All the tasks required for GIS work are contained within this program, therefore one is not required to transfer data between sub-programs manually as one has to with Arc/Info (used to digitize the maps).

When using Arcview, work is usually compiled as a Project. A Project allows one to organise the different Arcview components, these consist of Views, Tables, Layouts, Charts and Scripts. A view is an interactive map that allows the user to display, explore, query and analyse geographic data efficiently, by defining the geographic data that will be used and how it will be displayed. A View comprised of several Themes, which represent a distinct set of geographic features in a particular geographic data source.

In this GIS based study the project created is referred to as the 'Lizard Project'. The Lizard Project consists of a View component, titled Lizard View, which is composed of several Themes. The Themes used are the coastline and 1km grid squares which were digitized and also a Theme which shows the main lithological contacts, which is based on the 1:50 000 geological map Sheet 359.

The petrographic data stored in an Excel database is used to create a Table in Arcview. The Table can be viewed to allow the user to check its contents, or data can be added or deleted. The Table of petrographic data contains X-Y coordinates in the form of National Grid References, therefore data may be accessed and displayed as a particular Theme on the Lizard View. For example, a Theme showing the location of all the thin sections in the Table may be displayed as points on a View. These points can be defined to represent any particular component of the petrographic database stored in the Table. These points can all be given a user defined colour, shape or size, for instance, if one selects 'primary rock name' from the Table, a Theme may be created showing all 'dunites' as a red circle, 'lherzolites' with a blue square, and 'harzburgites' with a green triangle etc. Therefore the resulting View would show a coastline map of the Lizard, the 1km grid-squares, the main lithological contacts and a series of coloured symbols which represent the location of all the thin sections and define their primary rock type. Other symbol types are also utilised in the Lizard Project, for example area proportional symbols are used to represent the average

grainsize of minerals in a thin section. This allows one to produce a map composed of circles, where the size of the circle is proportional to the average grainsize of the rock sample at each particular locality.

The properties of the data displayed on the resulting maps (Views) map also be changed using a 'query builder', for example, one may decide to display only the samples which have <55% serpentinisation. This function allows one to query several petrographic features together. One may therefore create a map showing the location of thin sections defined by their primary rock name, whilst omitting those with <55% serpentinisation and/or those with a recrystallised texture.

Views can be created which show several layers of petrographic information (Themes) superimposed on one another and a 'basemap' of the coastline, 1km grid lines and the main lithological contacts. Thus allowing one to produce a series of spatially co-registered maps showing a variety of lithological, mineralogical and petrological information. The maps (Views) can be examined at any scale in Arcview and hard copy maps can be created.

## APPENDIX C: Thermometry and barometry equations

### C.1 Wells (1977) pyroxene thermometer

$$T(^{\circ}\text{K}) = \frac{7341}{3.355 + 2.44 X_{\text{Fe}}^{\text{opx}} - \ln K}$$

Where

$$X_{\text{Fe}}^{\text{opx}} = \frac{\text{Fe}^{2+}}{\text{Fe}^{2+} + \text{Mg}^{2+}}$$

### C.2. Brey and Kohler (1990) pyroxene thermometer

$$T(^{\circ}\text{K}) = \frac{35000 + 61.5 \times P}{\sqrt[2]{\ln \frac{\text{Na}^{\text{opx}}}{\text{Na}^{\text{cpx}}} + 19.8}}$$

Where  $P$  is the pressure in Kb.

### C.3. Brey *et al.* (1990) pyroxene thermometer

$$T(^{\circ}\text{K}) = \frac{(23644 + (24.9 + (126.3 \times \left\{ \frac{\text{Fe(T)}^{\text{cpx}}}{\text{Fe(T)}^{\text{cpx}} + \text{Mg}^{\text{cpx}}} \right\}))) * P}{13.38 + Kd * + 11.59 \times \left\{ \frac{\text{Fe(T)}^{\text{opx}}}{\text{Fe(T)}^{\text{opx}} + \text{Mg}^{\text{opx}}} \right\}}$$

Where  $Kd^*$  is:  $\sqrt[2]{\ln \left[ \frac{1 - \text{Ca}^{\text{opx}} *}{1 - \text{Ca}^{\text{cpx}} *} \right]}$

$\text{Ca}^{\text{opx}} *$  and  $\text{Ca}^{\text{cpx}} *$  are the  $\frac{\text{Ca}^{\text{opx}}}{1 - \text{Na}^{\text{opx}}}$  and  $\frac{\text{Ca}^{\text{cpx}}}{1 - \text{Na}^{\text{cpx}}}$  respectively.

#### **C.4 Witt-Eickschen and Seck (1991) pyroxene thermometer**

$$T(^{\circ}\text{C})_{Cr-Al-opx} = 636.54 + 2088.21 \times x_{Al}^{M1} + 14527.32 \times x_{Cr}^{M1}$$

Where:  $x_{Al}^{M1}$  = the Al on the M1-site of orthopyroxene,

$x_{Cr}^{M1}$  = the Cr on the M1-site of orthopyroxene.

#### **C.5. Mercier (1980) pyroxene barometer**

$$P(\text{Kb}) = \frac{351.32 \times \ln XKw - 706.14 \times \ln XKa + 299.13}{D}$$

$$\text{Where: } Xkw = \frac{6 \times W}{1 - 2 \times W}$$

$$Xka = \frac{\frac{A}{1 - A}}{[1 - 2.87 \times FCr]^2}$$

$$W = \frac{Ca^{opx}}{Fe^{2+opx} + Fe^{3+opx} + Mn^{opx} + Mg^{opx} + Ca^{opx}}$$

$$A = \frac{Al^{opx} - Na^{opx}}{2}$$

$$FCr = \frac{Cr^{opx}}{Al^{opx} + Cr^{opx} - Na^{opx}}$$

$$D = \ln XKa \times \ln XKw - 8.6751 \times \ln XKw + 2.2595 \times XKa + 24.568$$

#### **C.6 Johnson and Rutherford (1989) amphibole barometer**

$$P(\text{Kb}) = (4.23 \times (Al^{iv} + Al^{vi}) - 3.46)$$

### **C.7 Schmidt (1992)**

$$P(\text{Kb}) = -3.01 + (4.76 \times (\text{Al}^{\text{iv}} + \text{Al}^{\text{vi}}))$$

### **C.8 Spear (1980) amphibole-plagioclase thermometer**

$$T(^{\circ}\text{K}) = \frac{-8600}{\ln Kd - 8.04}$$

$$\text{Where: } Kd = \frac{\text{An}^{\text{plag}}}{\text{Ab}^{\text{plag}}} \times \frac{\text{Na}^{\text{amph}}}{\text{Ca}^{\text{amph}}}$$

### **C.9 Blundy and Holland (1990) amphibole-plagioclase thermobarometer**

$$P(\text{Kb}) = 7.29 \times \text{Al}_{\text{amph}}^{\text{iv}} - 4.63$$

$$T(^{\circ}\text{K}) = \frac{0.677 \times P - 48.98 + Y}{-0.0429 - 0.008314 \times \ln K}$$

$$\text{Where: } Y = 8.06 + 25.1 \times \sqrt[2]{1 - \text{Ab}^{\text{plag}}} \text{ only if } \text{Ab}^{\text{plag}} < 0.5,$$

$$K = \frac{\text{Si}^{\text{amph}} - 4}{8 - \text{Si}^{\text{amph}}} \times \text{Ab}^{\text{plag}}$$

---

## APPENDIX D: GEOCHEMICAL DATA

---

This appendix contains a listing of the electron microprobe and whole rock XRF and ICP-MS geochemical data used in this thesis. The following abbreviations are used in the data tables:

P core	Porphyroclast core
P rim	Porphyroclast rim
Neoblas	Neoblast
Neo core	Neoblast core
Neo rim	Neoblast rim
Clust	Pyroxene cluster

Analyses of samples with prefix 'E' were provided by M.T.Styles (BGS).

Samples with a prefix 'ANU' or 'DHG' are samples from Professor David Green's collection and were analysed by the author whilst at the Research School of Earth Sciences, ANU, Canberra.

The data in this appendix is quoted in wt% oxide for the major elements and in ppm for the trace elements.

Samples marked with an 'x' were analysed by energy-dispersive spectrometry (EDS). Samples *not* marked with an 'x' were analysed by wavelength-dispersive spectrometry (WDS).



	SiO2	Al2O3	Cr2O3	FeO	Fe2O3	MnO	MgO	CaO	NiO	Total	Si	Al	Cr	Fe2+	Fe3+	Mn	Mg	Ca	Ni	Total	Mg#
★	CAC 49	41.873	0.123	0.103	8.874	0.324	0.130	49.405	0.030	101.097	1.014	0.003	0.002	0.180	0.006	0.003	1.784	0.001	0.000	3.000	90.845
★	CAC 4	44.651	0.300	0.085	7.819	0.115	43.595	0.058	0.325	99.110	1.089	0.009	0.002	0.159	0.002	0.002	1.585	0.006	0.006	2.937	90.859
★	CAC 53	41.225	0.185	0.115	8.796	0.927	0.115	48.493	0.058	100.168	1.011	0.005	0.002	0.180	0.017	0.002	1.772	0.002	0.000	3.000	90.763
★	CAC 89	41.534	0.110	0.034	9.524	0.052	48.596	0.076	0.340	100.188	1.016	0.003	0.001	0.195	0.001	0.001	1.772	0.002	0.000	2.999	90.096
★	CAC 39	40.706	0.042	0.062	9.324	0.440	49.014	0.036	0.432	100.274	0.996	0.001	0.001	0.191	0.008	0.004	1.787	0.001	0.007	3.000	90.357
★	CAC 31	40.856	0.136	0.056	8.743	0.290	49.598	0.030	0.397	100.441	0.995	0.004	0.001	0.178	0.005	0.004	1.801	0.001	0.008	3.000	91.001
★	CAC 64	41.998			9.710	0.140	49.893	0.013		102.151	1.006			0.195		0.003	1.782	0.000		2.986	90.151
★	CAC 58	41.843	0.030	0.083	8.579	1.407	0.198	49.558	0.043	102.103	1.006	0.001	0.001	0.172	0.025	0.004	1.776	0.001	0.000	3.000	91.148
★	CAC 65	41.603	0.090	0.068	9.038		0.193	48.875	0.010	100.118	1.017	0.003	0.001	0.185		0.004	1.781	0.000		2.998	90.601
★	CAC 74	41.673			9.760		0.144	48.891	0.004	100.904	1.011			0.198		0.003	1.768	0.000		2.980	89.931
★	CAC 61	41.558	0.098	0.120	9.129	0.779	0.150	48.855	0.058	101.001	1.011	0.003	0.002	0.186	0.014	0.003	1.771	0.002	0.000	3.000	90.513
★	CAC 51	41.710	0.118	0.048	9.010	0.636	0.140	49.138	0.038	101.124	1.011	0.003	0.001	0.183	0.012	0.003	1.776	0.001	0.000	3.000	90.671
★	amu 5-8	40.730			10.058	0.429	0.081	49.093		100.391	0.996			0.206	0.008	0.001	1.790			3.000	89.691
★	CAC 159	41.099			10.582	0.151	49.066	0.026	0.354	101.278	0.999			0.215		0.003	1.777	0.001		2.994	89.205
★	amu 4-1	41.209			10.432		48.838			100.479	1.009			0.214			1.783			2.990	89.300
★	CAC 115	41.734			11.056	0.158	48.660	0.013	0.404	102.024	1.008			0.223		0.004	1.751	0.000		2.985	88.701
★	CAC 130	41.278			10.806	0.133	48.475	0.010	0.379	101.081	1.005			0.220		0.003	1.759	0.000		2.987	88.900
★	CAC 128	39.341			20.188	0.273	40.501	0.227	0.127	100.657	1.005			0.431	0.007	0.006	1.543	0.006		2.992	78.145
★	troct L1	39.012			17.831	0.169	42.315	0.089		99.767	0.997			0.381		0.004	1.612			3.000	80.880
★	amu 6-9	41.394			10.514		45.860	0.056		97.824	1.037			0.218			1.708	0.001		2.963	88.687
★	CAC 73	41.450	0.088	0.070	10.376	0.624	0.178	48.353	0.060	101.412	1.008	0.002	0.001	0.211	0.011	0.004	1.753	0.002	0.000	3.000	89.254
★	CAC 8	42.761	0.157	0.067	9.363	0.179	48.140	0.106	0.331	101.237	1.029	0.004	0.001	0.189		0.004	1.728	0.003	0.006	2.969	90.162
★	CAC 13	41.493	0.033	0.037	10.048	0.124	0.197	48.170	0.067	100.469	1.016	0.001	0.001	0.206	0.002	0.004	1.757	0.002	0.000	3.000	89.229
★	CAC 14	41.585	0.048	0.078	10.098	0.469	0.243	48.585	0.045	101.419	1.010	0.001	0.001	0.205	0.009	0.005	1.758	0.001	0.000	3.000	89.558
★	CAC 12	40.640	0.072	0.080	8.780	0.931	0.140	48.950	0.016	100.281	0.994	0.002	0.002	0.180	0.017	0.003	1.784	0.000	0.008	3.000	90.857
★	CAC 67	41.845			10.761		0.140	49.021	0.015	102.178	1.007			0.217		0.003	1.758	0.000		2.985	89.030
★	CAC 75	41.638			10.819		0.151	49.146	0.002	102.098	1.003			0.218		0.003	1.765	0.000		2.990	89.004
★	CAC 66	41.533	0.073	0.083	9.356	1.071	0.120	48.913	0.070	101.517	1.006	0.002	0.002	0.189	0.020	0.002	1.766	0.002	0.000	3.000	90.312
★	CAC 27	40.533	0.100	0.023	10.301	0.382	0.188	48.275	0.033	100.226	0.996	0.003	0.000	0.212	0.007	0.004	1.768	0.001	0.004	3.000	89.309
★	CAC 33	40.710	0.089	0.064	9.226	0.440	0.129	48.099	0.030	100.338	0.995	0.003	0.001	0.189	0.008	0.003	1.789	0.001	0.008	3.000	90.464
★	CAC 113	41.798			10.474	0.167	48.814	0.023	0.398	101.674	1.010			0.212		0.003	1.758	0.001	0.008	2.990	89.256
★	CAC 96	40.813			10.196	0.288	49.084	0.087		100.470	0.997			0.208	0.005		1.788	0.001		3.000	89.561
★	CAC 80	42.197	0.053	0.110	10.500	0.343	48.937	0.067		102.433	1.014	0.002	0.002	0.211		0.007	1.752	0.002		2.996	89.251
★	CAC 32	42.133	0.110	0.043	10.452	0.170	49.040	0.053		102.343	1.013	0.003	0.001	0.210	0.002	0.004	1.759	0.001	0.000	3.000	89.324
★	CAC 68	41.553	0.070	0.097	10.180	0.133	48.397	0.027		100.667	1.015	0.002	0.002	0.208		0.003	1.762	0.001		3.000	89.443
★	CAC 82	41.660	0.113	0.045	9.828	0.636	0.175	48.815	0.043	101.521	1.010	0.003	0.001	0.199	0.012	0.003	1.764	0.001	0.000	3.000	89.855
★	CAC 81	41.865	0.080	0.143	8.980	1.239	0.148	49.375	0.040	102.197	1.007	0.002	0.003	0.181	0.022	0.003	1.770	0.001	0.000	3.000	90.742
★	CAC 15	40.243	0.065	0.063	9.147	1.104	0.148	48.623	0.045	100.091	0.988	0.002	0.001	0.188	0.020	0.003	1.780	0.001	0.008	3.000	90.454
★	CAC 110	41.414			11.071		0.162	48.598	0.007	101.621	1.004			0.225		0.003	1.756	0.000		2.988	88.666
★	E52175	41.664	0.000	0.022	8.639		0.062	49.401	0.000	100.260	1.012	0.000	0.000	0.176		0.001	1.789	0.000	0.008	2.989	91.066
★	E52193	41.023		0.047	10.959	0.209	47.527	0.026	0.463	100.222	1.009	0.000	0.001	0.223		0.003	1.742	0.001	0.009	2.991	88.637
★	E52180	40.956	0.070	0.068	10.439	0.141	47.279	0.034	0.170	99.130	1.014	0.001	0.001	0.216		0.003	1.745	0.001	0.003	2.986	88.981
★	E52199	41.520	0.841	0.110	9.890	0.178	47.345	0.069	0.287	99.579	1.020	0.005	0.001	0.203		0.004	1.735	0.002	0.006	2.979	89.508
★	E52198	41.284			9.216	0.131	48.091	0.016		98.709	1.019	0.000	0.000	0.190		0.001	1.769	0.000	0.000	2.980	90.293
★	E52195	40.878			9.432		47.417			97.727	1.020	0.000	0.000	0.197		0.000	1.763	0.000	0.000	2.980	89.959
★	E52210	39.480			20.983	0.451	40.000			100.914	1.009	0.000	0.000	0.448		0.010	1.524	0.000	0.000	2.991	77.265

Table D.1 Olivine analyses

	SiO <sub>2</sub>	TiO <sub>2</sub>	Al <sub>2</sub> O <sub>3</sub>	Cr <sub>2</sub> O <sub>3</sub>	Fe <sub>2</sub> O <sub>3</sub>	FeO	MgO	MnO	CaO	Na <sub>2</sub> O	Total	Si	Ti	Al	Cr	Fe <sup>3+</sup>	Fe <sup>2+</sup>	Mg	Mn	Ca	Total	Mg#
CAC 64																						
core	55.978	0.105	4.150	0.909	0.000	6.245	32.181	0.144	1.639	0.047	101.397	1.912	0.003	0.167	0.025	0.000	0.179	1.638	0.004	0.060	3.991	90.172
rim	55.944	0.100	4.076	0.886	0.000	6.465	32.376	0.141	1.562	0.026	101.575	1.910	0.003	0.164	0.024	0.000	0.184	1.647	0.004	0.057	3.995	89.935
CAC 53																						
core	54.353	0.100	5.246	0.693	0.239	5.887	31.269	0.140	1.699	0.108	99.480	1.889	0.003	0.215	0.019	0.006	0.171	1.620	0.004	0.063	3.991	90.133
rim	54.135	0.085	4.845	0.615	2.116	4.646	31.740	0.065	1.550	0.145	99.400	1.879	0.002	0.198	0.017	0.055	0.135	1.643	0.002	0.058	3.989	89.632
CAC 89																						
core	55.504	0.129	3.463	0.801	0.444	5.904	31.805	0.068	1.719	0.129	99.575	1.927	0.003	0.142	0.022	0.012	0.172	1.646	0.002	0.064	3.989	89.988
CAC 65																						
core	55.394	0.067	4.679	0.770	0.358	5.216	31.758	0.166	1.981	0.196	100.222	1.906	0.002	0.190	0.021	0.009	0.150	1.629	0.005	0.073	3.985	91.088
CAC 58																						
core	55.206	0.096	5.141	0.709	1.085	5.308	31.623	0.149	1.700	0.236	100.800	1.891	0.003	0.208	0.019	0.028	0.152	1.615	0.004	0.062	3.983	89.966
neoblas	55.850	0.110	4.270	0.540	1.755	4.851	32.635	0.130	1.180	0.210	100.850	1.906	0.003	0.171	0.015	0.045	0.138	1.660	0.004	0.043	3.984	90.051
CAC 29																						
core	52.980	0.170	5.650	0.470	1.799	4.821	31.370	0.190	1.390	0.130	98.970	1.854	0.004	0.233	0.013	0.047	0.141	1.636	0.006	0.052	3.987	89.673
rim	53.800	0.200	4.530	0.530	1.505	4.786	31.770	0.180	1.770	0.100	99.171	1.879	0.005	0.186	0.015	0.040	0.140	1.654	0.005	0.066	3.989	90.219
CAC 49																						
P core	54.976	0.104	5.384	0.886	1.400	4.866	32.037	0.099	1.603	0.156	101.060	1.877	0.003	0.217	0.024	0.036	0.139	1.631	0.003	0.059	3.988	90.307
P rim	55.190	0.090	5.210	0.750	5.620	31.560	32.040	0.020	2.140	0.080	100.460	1.899	0.003	0.211	0.021		0.162	1.619	0.001	0.079	3.994	90.926
neoblas	55.830	0.020	4.330	0.480	6.220	32.420	32.420	0.030	1.040	0.000	100.320	1.925	0.000	0.176	0.013		0.179	1.666	0.001	0.039	3.999	90.314
CAC 4																						
core	53.400	0.140	4.420	0.950	1.495	4.344	31.490	0.120	2.150	0.090	98.600	1.876	0.004	0.183	0.026	0.040	0.128	1.649	0.004	0.081	3.989	90.796
rim	53.320	0.130	4.200	0.960	1.527	4.026	30.780	0.160	3.160	0.130	98.393	1.881	0.003	0.175	0.027	0.041	0.119	1.618	0.005	0.119	3.987	91.040
CAC 31																						
P core	53.840	0.090	4.850	0.760	1.653	4.402	32.020	0.170	1.610	0.120	99.516	1.871	0.002	0.199	0.021	0.043	0.128	1.659	0.005	0.060	3.988	90.646
P rim	53.750	0.150	4.970	0.760	1.475	4.463	32.040	0.080	1.560	0.110	99.358	1.869	0.004	0.204	0.021	0.039	0.130	1.661	0.002	0.058	3.988	90.795
neoblas	53.650	0.040	4.700	0.630	2.527	3.766	31.770	0.190	2.310	0.120	99.703	1.865	0.001	0.193	0.017	0.066	0.110	1.647	0.006	0.086	3.990	90.363
2553	53.328	0.062	5.843	0.678	6.284	30.724	30.724		1.891		98.811	1.871	0.002	0.242	0.019			1.607		0.071	3.996	89.707
2558	54.773	0.000	4.390	0.813	6.438	31.298	31.298		2.290		100.000	1.902		0.180	0.022		0.187	1.620		0.085	3.997	89.655
CAC 74																						
P core	55.655	0.103	3.931	0.849	0.000	6.408	32.422	0.154	0.839	0.020	100.379	1.918	0.003	0.160	0.023	0.000	0.185	1.665	0.005	0.031	3.989	90.016
P rim	55.846	0.107	3.516	0.806	0.000	6.738	32.354	0.150	0.829	0.055	100.398	1.926	0.003	0.143	0.022	0.000	0.194	1.664	0.004	0.031	3.991	89.544
CAC 51																						
core	55.918	0.132	4.014	0.790	0.033	6.072	32.184	0.166	1.492	0.076	100.560	1.921	0.004	0.163	0.022	0.001	0.175	1.649	0.005	0.055	3.993	90.386
rim	57.230	0.130	2.370	0.660	1.786	4.823	33.650	0.150	0.880	0.220	101.220	1.945	0.003	0.095	0.018	0.046	0.137	1.704	0.004	0.032	3.984	90.317
neoblas	57.620	0.230	2.400	0.580	6.990	6.990	33.480	0.030	1.030	0.130	102.340	1.949	0.006	0.096	0.015		0.198	1.688	0.001	0.038	3.991	89.524
CAC 61																						
P core	55.445	0.135	4.920	0.785		6.630	31.425	0.050	1.250	0.090	100.450	1.912	0.003	0.200	0.021		0.191	1.616	0.002	0.046	3.992	89.433
P rim	55.490	0.130	2.840	0.730	1.733	5.130	32.820	0.255	1.195	0.130	100.130	1.917	0.003	0.116	0.020	0.045	0.148	1.690	0.007	0.044	3.991	89.739
neoblas	56.669	0.203	2.591	0.693	0.538	6.061	32.600	0.226	1.394	0.170	100.780	1.945	0.005	0.105	0.019	0.014	0.174	1.668	0.007	0.051	3.988	89.880
DHG 5-8																						
core	55.177	0.121	3.112	0.799	0.784	5.934	32.302	0.107	1.935		100.271	1.913	0.002	0.127	0.022	0.020	0.172	1.670	0.002	0.072	4.000	89.662
rim	55.716	0.113	2.412	0.743	0.490	6.308	32.971	0.000	1.281	0.000	100.034	1.931	0.003	0.099	0.020	0.013	0.183	1.704	0.000	0.048	4.000	89.698
CAC 159																						
core	55.266	0.174	3.972	0.683	0.156	6.848	31.900	0.156	1.637	0.035	100.826	1.906	0.005	0.162	0.019	0.004	0.198	1.639	0.005	0.061	3.999	89.038
rim	56.427	0.195	2.661	0.676	0.000	6.800	32.521	0.156	1.100	0.031	100.565	1.944	0.005	0.108	0.019	0.000	0.196	1.670	0.005	0.041	3.989	89.496
DHG 4-1																						
P core	54.918	0.141	4.078	0.782		8.008	31.904		1.330		101.162	1.907	0.004	0.167	0.021		0.203	1.651		0.049	4.002	89.069
P rim	55.659	0.186	2.568	0.645	7.148	33.356	33.356		0.678		100.239	1.929	0.005	0.105	0.018		0.204	1.724		0.025	4.010	89.405
neoblast	55.332	0.189	2.117	0.458	0.806	6.449	33.456		0.798		99.604	1.929	0.005	0.087	0.013	0.021	0.188	1.740		0.030	4.012	89.261

Table D.2 Orthopyroxene analyses

	SiO <sub>2</sub>	TiO <sub>2</sub>	Al <sub>2</sub> O <sub>3</sub>	Cr <sub>2</sub> O <sub>3</sub>	Fe <sub>2</sub> O <sub>3</sub>	MgO	MnO	CaO	Na <sub>2</sub> O	Total	Si	Ti	Al	Cr	Fe <sub>3</sub> <sup>+</sup>	Fe <sub>2</sub> <sup>+</sup>	Mg	Mn	Ca	Total	Mg#
★	DHG 4-18	55.484	0.238	2.321	0.509	1.108	6.956	0.096	1.345	100.509	1.925	0.006	0.095	0.014	0.029	0.202	1.678	0.001	0.050	4.000	87.914
	CAC 115	55.236	0.141	4.681	0.643	0.000	7.015	0.131	1.253	100.900	1.900	0.004	0.190	0.018	0.000	0.202	1.628	0.004	0.046	3.994	88.962
	CAC 130																				
	P core	56.203	0.099	3.503	0.272	0.000	7.527	0.179	0.414	100.785	1.932	0.002	0.142	0.008	0.000	0.216	1.669	0.005	0.015	3.991	88.527
	P rim	56.640	0.094	3.122	0.316	0.000	7.305	0.193	0.445	100.664	1.947	0.002	0.127	0.009	0.000	0.210	1.667	0.006	0.016	3.984	88.809
	neoblast	57.402	0.071	1.449	0.216	0.000	7.189	0.195	0.428	100.794	1.970	0.002	0.059	0.006	0.000	0.206	1.731	0.006	0.016	3.996	89.354
	CAC 128	55.853	0.124	1.359	0.182	0.313	12.997	29.447	0.723	101.963	1.955	0.003	0.056	0.005	0.008	0.381	1.536	0.010	0.027	4.000	79.796
★	DHG 6-9	56.231	0.082	1.651	0.197	-0.058	8.962	0.131	0.650	100.067	1.964	0.001	0.068	0.005		0.261	1.669		0.024	3.993	86.495
★	CAC 73																				
	P core	56.110	0.110	3.970	0.360	1.505	6.111	0.090	0.605	101.280	1.914	0.003	0.160	0.010	0.039	0.175	1.658	0.003	0.022	3.982	88.609
	neo(mafic)	57.713	0.200	1.398	0.153	0.582	6.816	0.283	0.633	100.985	1.976	0.005	0.056	0.004	0.015	0.195	1.707	0.008	0.023	3.989	89.042
	neo(ULM)	57.385	0.085	1.673	0.307	1.419	6.198	0.125	0.583	100.847	1.963	0.002	0.068	0.008	0.037	0.177	1.709	0.004	0.021	3.989	88.878
	CAC 67																				
	P core	56.268	0.202	3.096	0.325	0.507	6.859	0.148	0.656	101.391	1.924	0.005	0.125	0.009	0.013	0.196	1.696	0.004	0.024	3.999	89.015
	P rim	56.548	0.180	2.717	0.393	0.510	7.058	0.182	0.512	101.638	1.930	0.004	0.109	0.011	0.013	0.201	1.705	0.005	0.019	3.999	88.835
	neoblast	56.460	0.193	1.875	0.359	0.756	6.602	0.159	0.752	100.719	1.944	0.005	0.076	0.010	0.020	0.190	1.720	0.005	0.028	4.000	89.120
	CAC 75																				
	P core	55.480	0.221	4.590	0.628	0.015	6.877	0.155	1.631	101.471	1.899	0.006	0.185	0.017	0.000	0.197	1.624	0.005	0.060	3.996	89.171
	P rim	56.759	0.200	2.906	0.617	0.087	7.336	0.175	0.762	101.938	1.933	0.005	0.117	0.017	0.002	0.209	1.679	0.005	0.028	3.994	88.818
	neoblast	57.252	0.235	1.961	0.492	0.000	7.331	0.140	0.741	101.670	1.953	0.006	0.079	0.013	0.000	0.209	1.703	0.004	0.027	3.996	89.059
	CAC 113																				
	P core	55.343	0.153	4.717	0.617	0.000	7.100	0.146	0.775	100.505	1.908	0.004	0.192	0.017	0.000	0.205	1.625	0.004	0.028	3.985	88.816
	P rim	57.035	0.206	2.465	0.491	0.000	7.185	0.152	0.859	100.958	1.957	0.005	0.100	0.013	0.000	0.206	1.663	0.004	0.032	3.983	88.962
	neoblast	56.003	0.139	1.901	0.316	0.000	4.704	0.146	1.110	97.169	1.945	0.004	0.495	0.008	0.000	0.136	1.153	0.004	0.042	3.812	89.449
★	CAC 66																				
	P core	55.103	0.147	4.657	0.647	1.984	4.861	0.157	1.177	100.567	1.890	0.004	0.188	0.018	0.051	0.139	1.644	0.005	0.043	3.982	89.608
	P rim	57.080	0.227	2.787	0.700	0.756	6.070	0.220	0.903	102.067	1.933	0.006	0.111	0.019	0.019	0.172	1.687	0.006	0.033	3.987	89.826
	neoblast	56.970	0.285	1.840	0.380	0.976	5.698	0.238	0.688	100.300	1.957	0.007	0.075	0.010	0.025	0.164	1.719	0.007	0.025	3.989	90.098
	CAC 13																				
	P core	55.322	0.250	4.510	0.412	1.655	5.595	0.160	0.618	100.896	1.893	0.006	0.182	0.011	0.043	0.160	1.663	0.005	0.023	3.985	89.130
	P rim	55.597	0.210	4.723	0.437	1.368	5.769	0.283	0.520	101.420	1.893	0.005	0.189	0.012	0.035	0.164	1.663	0.008	0.019	3.989	89.300
	neoblast	58.054	0.158	1.596	0.288	0.496	6.770	0.148	0.632	101.632	1.972	0.004	0.064	0.008	0.013	0.192	1.711	0.004	0.023	3.992	89.299
★	CAC 14																				
	P core	57.135	0.200	2.555	0.545	0.309	6.802	0.205	0.580	101.570	1.946	0.005	0.103	0.015	0.008	0.194	1.702	0.006	0.021	3.999	89.416
	neoblast	58.227	0.208	1.278	0.252	0.594	6.404	0.222	0.635	101.467	1.979	0.005	0.051	0.007	0.015	0.182	1.722	0.006	0.023	3.991	89.725
★	CAC 8																				
	P core	56.660	0.200	1.880	0.330	1.227	5.606	0.100	0.650	100.853	1.940	0.005	0.076	0.009	0.032	0.160	1.742	0.003	0.024	3.990	90.067
	P rim	54.700	0.530	2.900	0.650	0.767	4.879	0.130	7.620	100.527	1.913	0.014	0.120	0.018	0.020	0.143	1.470	0.004	0.286	3.986	90.022
	neo core	56.490	0.190	1.610	0.340	2.929	4.205	0.230	0.620	101.483	1.924	0.005	0.065	0.009	0.075	0.120	1.766	0.007	0.023	3.993	90.064
	elast	56.840	0.150	1.770	0.390	0.649	6.166	0.260	0.630	100.775	1.950	0.004	0.072	0.011	0.017	0.177	1.731	0.008	0.023	3.991	89.939
★	CAC 12																				
	P core	54.710	0.250	3.240	0.400	1.940	4.985	0.190	0.610	99.524	1.901	0.007	0.133	0.011	0.051	0.145	1.714	0.006	0.023	3.989	89.759
	P rim	56.280	0.200	1.580	0.360	1.157	5.309	0.240	0.600	99.726	1.948	0.005	0.064	0.010	0.030	0.154	1.747	0.007	0.022	3.987	90.481
	neo rim	56.000	0.160	1.450	0.300	1.684	5.004	0.140	0.690	99.419	1.944	0.004	0.059	0.008	0.044	0.145	1.755	0.004	0.026	3.989	90.264
	elast	56.240	0.300	1.190	0.270	1.924	4.868	0.120	0.680	99.833	1.945	0.008	0.049	0.007	0.050	0.141	1.756	0.004	0.025	3.985	90.195
★	CAC 33																				
	P core	55.620	0.210	2.150	0.510	0.994	5.446	0.120	0.640	99.230	1.935	0.005	0.088	0.014	0.026	0.158	1.734	0.004	0.024	3.988	90.384
	P rim	55.230	0.210	2.900	0.640	2.504	4.657	0.190	0.650	100.631	1.900	0.005	0.118	0.017	0.065	0.134	1.719	0.006	0.024	3.988	89.634
	neo core	55.610	0.220	2.370	0.660	1.048	6.067	0.090	0.690	99.995	1.926	0.006	0.097	0.018	0.027	0.176	1.713	0.003	0.026	3.991	89.407
	neo rim	54.890	0.210	2.640	0.620	1.832	5.382	0.090	0.880	99.513	1.911	0.005	0.108	0.017	0.048	0.157	1.708	0.003	0.033	3.990	89.302
	neo rim	55.810	0.290	1.870	0.440	1.698	5.582	0.140	0.780	100.200	1.930	0.008	0.076	0.012	0.044	0.161	1.727	0.004	0.029	3.991	89.361

Table D.2 Orthopyroxene analyses

	SiO <sub>2</sub>	TiO <sub>2</sub>	Al <sub>2</sub> O <sub>3</sub>	Cr <sub>2</sub> O <sub>3</sub>	Fe <sub>2</sub> O <sub>3</sub>	FeO	MgO	MnO	CaO	Na <sub>2</sub> O	Total	Si	Ti	Al	Cr	Fe <sup>3+</sup>	Fe <sup>2+</sup>	Mg	Mn	Ca	Total	Mg#
CAC 27																						
P core	55.110	0.280	2.390	0.520	1.443	5.661	32.850	0.190	0.810	0.090	99.345	1.921	0.007	0.098	0.014	0.038	0.165	1.707	0.006	0.030	3.987	89.377
P rim	55.670	0.320	2.010	0.400	1.810	5.451	33.410	0.240	0.710	0.110	100.131	1.926	0.008	0.082	0.011	0.047	0.158	1.723	0.007	0.026	3.988	89.375
neoblast	56.060	0.200	1.370	0.170	1.649	5.526	33.670	0.260	0.550	0.110	99.565	1.947	0.005	0.056	0.005	0.043	0.161	1.744	0.008	0.020	3.989	89.542
CAC 96																						
P core	54.640	0.236	3.553	0.622	1.823	5.671	32.605	0.124	1.146	0.192	100.614	1.891	0.006	0.145	0.017	0.047	0.164	1.682	0.002	0.042	3.997	88.825
neoblast	56.148	0.267	1.846	0.375	0.758	6.489	33.620	0.092	0.733		100.328	1.940	0.007	0.075	0.010	0.020	0.188	1.732	0.001	0.027	4.000	89.313
DHG 4-6	56.116	0.263	1.572	0.253	0.700	6.851	33.429	0.138	0.679		100.002	1.948	0.007	0.064	0.007	0.018	0.199	1.730	0.001	0.025	4.000	88.845
DHG 6-1																						
P core	54.651	0.163	4.394	0.589	1.131	6.153	32.399	0.102	1.226		100.809	1.884	0.004	0.179	0.016	0.029	0.177	1.665	0.001	0.045	4.000	88.954
neoblast	56.035	0.173	1.702	0.330	1.450	6.236	33.581	0.133	0.761		100.400	1.938	0.004	0.069	0.009	0.038	0.180	1.732	0.002	0.028	4.000	88.813
CAC 82	57.477	0.082	2.055	0.247	0.925	6.041	33.767	0.158	0.553	0.127	101.017	1.960	0.002	0.083	0.007	0.024	0.172	1.717	0.005	0.020	3.989	89.750
CAC 81	58.117	0.085	2.045	0.375	0.775	6.187	34.025	0.123	0.667	0.175	102.233	1.960	0.002	0.081	0.010	0.020	0.175	1.711	0.004	0.024	3.987	89.804
CAC 80	58.346	0.120	1.986	0.368	1.038	5.924	34.072	0.236	0.702	0.206	102.524	1.961	0.003	0.079	0.010	0.026	0.167	1.708	0.007	0.025	3.985	89.856
CAC 32	57.992	0.118	1.518	0.253	1.475	5.660	34.227	0.228	0.577	0.138	101.665	1.965	0.003	0.061	0.007	0.038	0.160	1.729	0.007	0.021	3.989	89.725
CAC 68	57.351	0.102	1.942	0.300	0.726	6.519	33.561	0.149	0.599	0.116	101.000	1.961	0.003	0.078	0.008	0.019	0.186	1.710	0.004	0.022	3.991	89.292
CAC 110	57.032	0.089	1.955	0.378	0.149	7.308	33.357	0.178	0.685	0.026	101.157	1.955	0.002	0.079	0.010	0.004	0.209	1.704	0.005	0.025	3.996	88.884
CAC 15																						
neo core	55.250	0.050	2.110	0.310	2.176	4.842	33.310	0.220	0.710	0.110	99.088	1.927	0.001	0.087	0.009	0.057	0.141	1.732	0.006	0.027	3.987	89.725
neo rim	52.490	0.060	1.840	0.270	6.088	1.122	33.650	0.140	0.580	0.130	96.370	1.879	0.002	0.078	0.008	0.164	0.034	1.796	0.004	0.022	3.985	90.088
CAC 151	52.873	0.334	1.342	0.139	0.661	20.730	22.863	0.442	1.204	0.012	100.601	1.951	0.009	0.058	0.004	0.019	0.639	1.257	0.014	0.048	4.000	65.640
CAC 147	52.729	0.254	0.582	0.069	0.011	24.611	18.609	0.632	2.981	0.036	100.515	1.989	0.007	0.026	0.002	0.000	0.777	1.047	0.020	0.120	3.991	57.393
DHG6-13																						
opx core	50.870	0.156	0.856	0.102	2.606	26.062	18.512	0.439	1.103		100.706	1.940	0.003	0.038	0.001	0.075	0.831	1.053	0.014	0.045	4.000	53.738
opx rim	50.431	0.135	1.067		3.081	25.485	18.186	0.447	1.428	0.156	100.414	1.930	0.004	0.048	0.000	0.089	0.815	1.037	0.014	0.059	3.996	53.429
47037	52.175	0.169	0.785	0.095	1.318	21.695	21.745	0.557	1.081	0.043	99.662	1.959	0.005	0.035	0.003	0.037	0.681	1.217	0.018	0.043	3.998	62.885
47036	51.540	0.267	1.001	0.059	1.382	23.005	20.523	0.565	1.259	0.034	99.634	1.950	0.008	0.045	0.001	0.039	0.728	1.157	0.018	0.051	3.998	60.129
DHG6-4	51.438	0.165	0.787		2.436	23.399	20.357	0.366	1.246		100.195	1.943	0.005	0.035	0.000	0.069	0.739	1.146	0.012	0.050	4.000	58.642
E52190	54.053	0.139	2.362	0.099		16.464	26.445	0.353	0.557	0.301	100.771	1.942	0.004	0.100	0.003		0.495	1.416	0.011	0.021	3.992	74.104
E52179	53.024	0.079	3.040	0.070		15.914	26.028	0.362	0.684	0.377	99.578	1.927	0.002	0.130	0.002		0.484	1.410	0.011	0.027	3.992	74.446
E52199	55.812	0.082	2.873	0.358		6.811	33.113	0.159	0.944	0.149	100.302	1.928	0.001	0.117	0.010		0.197	1.706	0.005	0.035	3.998	89.654
E52184	54.885	0.086	1.824	0.203		12.855	28.531	0.284	0.389	0.295	99.352	1.965	0.002	0.077	0.006		0.386	1.521	0.009	0.015	3.981	79.754
E52187	53.664	0.138	1.206	0.178		20.912	23.892	0.493	0.615	0.305	101.402	1.959	0.004	0.052	0.005		0.639	1.300	0.015	0.024	3.998	67.046
E52175	57.084	0.014	0.629	0.157		6.331	33.867	0.137	0.180	0.057	98.456	1.995	0.000	0.026	0.004		0.185	1.764	0.004	0.007	3.985	90.509
E52180	56.538	0.024	1.115	0.129		7.176	34.300	0.290	0.264	0.112	99.949	1.959	0.000	0.046	0.004		0.208	1.772	0.009	0.010	4.007	89.495
E52198	57.315	0.068	0.632	0.104		6.585	33.950	0.139	0.136	0.175	99.104	1.994	0.001	0.026	0.003		0.192	1.761	0.004	0.005	3.985	90.189
E52193	54.684	0.037	0.629	0.192		7.419	35.809	0.141	0.700	0.142	99.754	1.916	0.000	0.026	0.004		0.217	1.870	0.004	0.026	4.063	89.586
E52187	51.905	0.121	0.678	0.189		27.393	18.811	0.570	1.008	0.345	101.019	1.969	0.003	0.030	0.003		0.869	1.064	0.018	0.041	3.998	55.038
E52190	52.692	0.170	0.820	0.106		22.854	21.691	0.543	0.664	0.332	99.872	1.974	0.005	0.036	0.002		0.716	1.212	0.017	0.027	3.989	62.845
E52185	50.843	0.115	0.774	0.074		30.204	15.964	0.829	0.884	0.374	100.058	1.977	0.003	0.035	0.001		0.982	0.925	0.027	0.037	3.987	48.508
E52203	54.463	0.008	1.100	0.014		19.929	19.231	0.572	1.172	0.548	97.037	2.062	0.000	0.049	0.000		0.631	1.085	0.018	0.048	3.893	63.237

Table D.2 Orthopyroxene analyses

	SiO <sub>2</sub>	TiO <sub>2</sub>	Al <sub>2</sub> O <sub>3</sub>	Cr <sub>2</sub> O <sub>3</sub>	Fe <sub>2</sub> O <sub>3</sub>	MgO	MnO	CaO	Na <sub>2</sub> O	Total	Si	Ti	Al	Cr	Fe <sup>3+</sup>	Fe <sup>2+</sup>	Mg	Mn	Ca	Total	Mg#
CAC 64																					
Core	52.621	0.251	4.721	1.424	0.115	2.708	0.109	22.424	0.432	101.295	1.888	0.007	0.200	0.041	0.003	0.081	0.882	0.003	0.862	3.997	91.304
Rim	52.501	0.259	5.207	1.413	0.000	3.004	0.087	21.406	0.459	101.269	1.881	0.007	0.220	0.040	0.000	0.090	0.904	0.003	0.822	3.998	90.969
Neoblast	52.272	0.248	4.317	1.102	0.636	16.634	0.091	23.097	0.290	100.740	1.887	0.007	0.184	0.032	0.017	0.063	0.895	0.003	0.894	4.000	91.842
CAC 53																					
core	50.436	0.210	6.281	1.121	2.987	17.173	0.111	20.186	0.594	99.025	1.833	0.006	0.269	0.032	0.082	0.013	0.931	0.003	0.786	3.956	90.767
rim	50.810	0.420	6.980	1.250	0.973	15.880	0.160	21.450	0.540	100.300	1.835	0.012	0.297	0.036	0.027	0.066	0.855	0.005	0.830	3.961	90.248
CAC 89	51.066	0.184	5.750	1.176	2.031	16.934	0.114	21.396	0.251	100.075	1.847	0.005	0.245	0.034	0.055	0.049	0.913	0.004	0.829	3.980	89.780
CAC 65	51.791	0.247	6.114	1.320	1.089	16.417	0.084	21.509	0.624	100.814	1.859	0.007	0.259	0.037	0.029	0.057	0.878	0.003	0.827	3.956	90.994
CAC 58																					
core	51.611	0.229	6.677	1.196	2.216	15.931	0.127	21.956	0.806	101.314	1.842	0.006	0.281	0.034	0.060	0.030	0.848	0.004	0.839	3.943	90.479
neobl	51.950	0.210	5.770	1.015	1.929	15.910	0.175	22.485	0.735	100.900	1.864	0.006	0.244	0.029	0.052	0.031	0.851	0.006	0.865	3.946	91.133
CAC 49																					
core	51.562	0.293	6.117	1.110	1.252	15.965	0.068	23.123	0.445	101.155	1.849	0.008	0.258	0.031	0.034	0.043	0.854	0.002	0.889	3.968	91.789
neoblast	52.340	0.370	5.470	1.190	0.796	16.170	0.220	22.880	0.560	101.230	1.873	0.010	0.231	0.034	0.021	0.046	0.863	0.006	0.877	3.961	92.778
CAC 20																					
core	52.071	0.466	4.185	1.129	2.115	17.066	0.085	22.313	0.484	101.043	1.872	0.013	0.177	0.032	0.057	0.034	0.915	0.003	0.859	3.961	90.935
rim	52.219	0.397	3.120	1.119	1.404	16.060	0.081	20.769	0.440	99.213	1.903	0.011	0.134	0.032	0.039	0.049	0.981	0.003	0.811	3.963	91.819
2553	51.398	0.350	7.033	0.998	3.088	15.043		22.970		100.878	1.850	0.009	0.298	0.028		0.093	0.807		0.886	3.973	89.675
2558	50.803	0.290	5.767	1.187	3.017	15.830		22.627		99.520	1.859	0.008	0.249	0.034		0.092	0.863		0.887	3.992	90.342
CAC 31																					
core	49.563	0.307	6.063	1.207	2.865	17.783	0.130	19.677	0.347	98.624	1.817	0.008	0.262	0.035	0.079	0.021	0.972	0.004	0.773	3.970	90.675
rim	50.370	0.260	5.900	1.200	1.853	16.210	0.110	21.630	0.480	99.216	1.841	0.007	0.254	0.035	0.051	0.037	0.883	0.003	0.847	3.959	90.965
neoblast	50.078	0.230	6.112	1.206	2.194	16.490	0.078	21.444	0.418	99.236	1.830	0.006	0.263	0.035	0.060	0.030	0.898	0.002	0.840	3.965	90.851
CAC 29-n	52.065	0.630	3.155	0.715	0.949	16.650	0.055	23.380	0.360	99.255	1.905	0.017	0.136	0.021	0.026	0.040	0.908	0.002	0.916	3.971	93.245
CAC 61																					
P core	51.348	0.368	6.658	1.000	1.020	17.278	0.095	20.270	0.383	101.045	1.839	0.010	0.281	0.028	0.027	0.085	0.922	0.003	0.778	3.973	89.162
neoblast	52.075	0.455	4.845	1.240	1.601	16.558	0.083	22.423	0.473	101.323	1.867	0.012	0.205	0.035	0.043	0.054	0.885	0.003	0.861	3.965	90.076
CAC 51	52.064	0.378	5.234	1.316	0.477	16.596	0.090	21.936	0.420	100.752	1.874	0.010	0.222	0.038	0.013	0.073	0.890	0.003	0.846	3.969	91.203
DHG-5.8	51.241	0.211	4.457	1.234	1.347	17.299		22.192		100.143	1.863	0.006	0.191	0.035	0.037	0.066	0.938	0.000	0.864	4.000	90.139
CAC 159	51.174	0.475	4.988	1.098	1.049	16.489	0.070	21.521	0.428	99.895	1.865	0.013	0.214	0.032	0.029	0.079	0.896	0.002	0.841	4.000	89.238
DHG-4.1																					
porph C	50.151	0.454	7.025	0.997	0.734	17.320		19.860	0.254	99.888	1.821	0.012	0.301	0.029	0.020	0.094	0.937		0.773	3.987	89.160
porph R	50.053	0.764	6.244	1.148	2.275	15.224		23.336	0.514	100.890	1.815	0.021	0.267	0.033	0.062	0.040	0.823		0.907	3.968	88.924
neoblast	51.893	0.623	3.566	1.213	1.460	16.906		22.546	0.378	100.602	1.882	0.017	0.152	0.035	0.040	0.061	0.914		0.876	3.978	90.044
CAC 44																					
core	49.918	0.500	7.000	0.820	3.006	15.068	0.163	22.820	0.660	100.494	1.809	0.014	0.299	0.021	0.082	0.016	0.814	0.005	0.886	3.948	89.221
rim	50.576	0.550	5.230	0.936	2.324	15.294	0.106	22.908	0.650	99.617	1.850	0.015	0.225	0.027	0.064	0.032	0.834	0.003	0.898	3.949	89.690
neoblast	52.228	0.545	3.347	1.017	1.998	16.578	0.088	23.035	0.500	100.632	1.890	0.015	0.143	0.029	0.054	0.039	0.895	0.003	0.893	3.961	90.524
DHG-4.18	51.239	0.395	4.947	0.823	1.602	17.441		20.315	0.386	99.863	1.863	0.011	0.212	0.024	0.044	0.083	0.945	0.000	0.791	3.973	88.207
CAC 99	51.043	0.218	4.834	1.205	1.521	16.917		22.253	0.216	100.270	1.856	0.006	0.207	0.035	0.042	0.063	0.917	0.000	0.867	3.992	89.781
CAC 130	54.613	0.143	1.363	0.353	0.055	17.467	0.089	24.183	0.187	100.592	1.970	0.004	0.058	0.010	0.002	0.065	0.940	0.003	0.935	3.997	93.436
CAC 128	53.759	0.272	1.742	0.281	0.492	16.585	0.148	22.859	0.267	100.672	1.954	0.007	0.075	0.008	0.014	0.130	0.899	0.005	0.890	4.000	86.243
DHG-6.9	53.734	0.148	1.914	0.498	0.601	17.153		23.960	0.186	100.444	1.946	0.004	0.082	0.014	0.016	0.068	0.926	0.000	0.930	3.987	91.635
CAC 73																					
neobl(felsic)	54.654	0.288	1.764	0.312	1.934	17.704	0.110	24.146	0.272	101.594	1.946	0.008	0.074	0.009	0.052	0.026	0.940	0.003	0.921	3.979	92.391
DHG-6.7	50.510	1.216	4.360	0.348	2.514	15.037	0.099	21.158	0.654	100.421	1.856	0.034	0.189	0.008	0.070	0.139	0.824	0.001	0.833	3.953	79.794
DHG-L1	51.358	1.047	3.252	0.669	1.429	15.757		21.977	0.339	100.363	1.883	0.029	0.141	0.019	0.039	0.141	0.861	0.000	0.864	3.976	82.837
CAC 113	51.885	0.668	4.758	0.999	0.016	15.381	0.072	22.251	0.607	99.787	1.893	0.018	0.205	0.029	0.000	0.096	0.836	0.002	0.870	3.993	89.656
CAC 66	52.466	0.776	4.528	1.004	1.116	16.018	0.064	23.152	0.640	101.420	1.880	0.021	0.191	0.028	0.030	0.057	0.856	0.002	0.889	3.954	90.759
CAC 12	51.245	0.765	3.310	0.680	3.127	17.220	0.140	21.945	0.570	99.233	1.875	0.021	0.143	0.020	0.086	0.007	0.939	0.004	0.860	3.956	90.975

Table D.3 Clinopyroxene analyses

	SiO <sub>2</sub>	TiO <sub>2</sub>	Al <sub>2</sub> O <sub>3</sub>	Cr <sub>2</sub> O <sub>3</sub>	Fe <sub>2</sub> O <sub>3</sub>	FeO	MgO	MnO	CaO	Na <sub>2</sub> O	Total	Si	Ti	Al	Cr	Fe <sup>3+</sup>	Fe <sup>2+</sup>	Mg	Mn	Ca	Total	Mg#
CAC 33																						
core	51.435	0.793	3.540	1.050	1.729	1.351	16.190	0.115	22.795	0.530	99.528	1.883	0.022	0.153	0.030	0.048	0.041	0.883	0.004	0.894	3.938	90.848
rim	51.487	0.803	3.257	0.823	1.661	1.332	16.097	0.107	23.123	0.497	99.186	1.891	0.022	0.141	0.024	0.046	0.041	0.881	0.003	0.910	3.960	91.032
neoblast	50.570	1.180	4.150	1.100	1.767	1.620	15.960	0.130	22.490	0.530	99.497	1.856	0.033	0.180	0.032	0.049	0.050	0.873	0.004	0.884	3.961	89.861
CAC 8	52.555	0.655	2.840	0.765	2.783	0.325	17.110	0.090	22.750	0.665	100.539	1.898	0.018	0.121	0.022	0.076	0.010	0.921	0.003	0.880	3.948	91.509
CAC 13	53.918	0.708	2.802	0.713	0.349	2.524	18.093	0.113	21.158	0.598	100.892	1.931	0.019	0.119	0.020	0.009	0.009	0.966	0.003	0.813	3.957	91.898
CAC 96	51.490	0.883	3.438	0.833	2.069	1.302	16.343	0.000	23.314	0.444	100.115	1.877	0.024	0.148	0.024	0.057	0.040	0.888	0.000	0.911	3.969	90.207
DHG-6-1	52.414	0.558	4.212	1.103	0.912	3.276	19.230	0.000	18.581	0.392	100.678	1.881	0.015	0.178	0.031	0.025	0.098	1.029	0.000	0.715	3.973	89.324
DHG-4-6	51.339	0.934	3.599	0.801	1.682	1.847	16.134	0.088	23.268	0.391	99.994	1.876	0.026	0.155	0.023	0.046	0.056	0.879	0.000	0.911	3.972	89.339
CAC 67	52.759	0.610	-3.201	0.722	1.095	2.206	16.745	0.088	22.617	0.533	100.574	SiO <sub>2</sub>	0.017	0.137	0.021	0.030	0.067	0.903	0.003	0.877	4.000	93.119
CAC 110	53.706	0.233	2.653	0.609	0.072	2.895	17.009	0.083	22.552	0.409	100.189	1.946	0.006	0.114	0.018	0.002	0.088	0.919	0.003	0.874	3.997	91.121
CAC 81	54.313	0.047	2.740	0.683	1.576	1.189	17.063	0.127	23.820	0.443	101.677	1.934	0.001	0.115	0.019	0.042	0.035	0.906	0.004	0.909	3.967	92.100
CAC 32	54.853	0.125	2.085	0.683	1.963	0.838	17.450	0.133	23.945	0.423	102.038	1.945	0.003	0.087	0.019	0.052	0.025	0.922	0.004	0.910	3.968	92.274
CAC 151	51.816	0.609	2.375	0.167	0.351	8.450	14.228	0.193	20.639	0.364	99.191	1.940	0.017	0.105	0.005	0.010	0.265	0.794	0.006	0.828	3.996	74.300
CAC 147	52.577	0.348	1.151	0.121	0.149	10.915	13.274	0.367	20.900	0.221	100.022	1.974	0.010	0.051	0.004	0.004	0.343	0.743	0.012	0.841	3.996	68.166
DHG-6-13																						
core	50.745	0.419	1.821	0.129	3.004	9.118	12.699	0.157	21.851	0.246	100.189	1.913	0.012	0.081	0.001	0.085	0.288	0.714	0.005	0.883	3.982	65.688
rim	51.204	0.320	1.845	0.098	2.229	9.530	12.813	0.093	21.384	0.354	99.870	1.931	0.009	0.082	0.001	0.063	0.301	0.720	0.002	0.864	3.973	66.441
47037	52.318	0.240	1.218	0.201	0.303	8.559	14.837	0.269	20.289	0.321	98.554	1.971	0.007	0.054	0.006	0.009	0.270	0.833	0.009	0.819	3.976	74.971
47036	51.788	0.450	2.153	0.091		10.562	14.242	0.313	18.877	0.325	98.762	1.954	0.013	0.096	0.002		0.333	0.801	0.010	0.763	3.972	70.626
90703	53.013	0.320	1.773	0.112	0.645	6.173	16.220	0.180	20.933	0.342	99.711	1.954	0.009	0.077	0.003	0.018	0.190	0.891	0.006	0.827	3.975	81.068
47033	51.862	0.160	1.760	0.055	1.749	8.476	12.609	0.507	22.298	0.459	99.935	1.948	0.005	0.078	0.000	0.049	0.266	0.706	0.016	0.897	3.967	69.102
47040	51.980	0.825	3.080	0.113	0.884	5.933	16.148	0.187	19.605	0.572	99.327	1.918	0.023	0.134	0.003	0.025	0.183	0.888	0.006	0.775	3.955	81.047
DHG-6-5	53.162	0.141	1.365	0.145	1.216	4.272	16.337	0.083	23.145	0.198	100.082	1.953	0.003	0.059	0.005	0.034	0.131	0.895	0.000	0.911	3.991	84.436
DHG-6-4	51.496	0.252	1.287	0.164	2.226	8.690	13.423	0.123	22.039	0.266	99.948	1.937	0.007	0.057	0.004	0.063	0.274	0.753	0.003	0.888	3.987	69.106
CAC 153	52.985	0.108	1.203	0.033	1.023	7.805	13.026	0.334	23.705	0.371	100.593	1.969	0.003	0.053	0.001	0.029	0.243	0.722	0.011	0.944	4.000	72.689
DHG-1-1	52.519	0.193	1.105	0.085	2.918	6.157	13.055	0.206	24.358	0.441	101.037	1.948	0.003	0.048	0.000	0.081	0.191	0.722	0.006	0.968	3.968	72.588
DHG-5-5	52.462	0.111	0.858		3.247	6.250	12.668	0.488	24.148	0.535	100.766	1.954	0.001	0.038	0.000	0.091	0.195	0.703	0.015	0.964	3.961	71.117
90878	52.203		0.375			6.550	13.573	0.120	24.630		99.070	1.969	0.000	0.017	0.000	0.046	0.207	0.763	0.004	0.995	4.000	75.133
90885	52.185	0.000	1.674	0.010	2.557	5.680	14.404	0.292	23.260	0.204	100.266	1.935	0.000	0.073	0.000	0.071	0.176	0.796	0.009	0.924	3.985	76.288
DHG-2-6	51.407	0.182	1.405	0.010	3.006	8.920	11.788	0.172	23.490	0.316	100.694	1.933	0.005	0.062	0.000	0.085	0.280	0.661	0.004	0.946	3.977	64.381
90880	52.785	0.105	1.020	0.010	0.816	8.526	13.280	0.230	24.025		100.797	1.963	0.003	0.045	0.000	0.023	0.265	0.736	0.007	0.957	4.000	71.882
90881	52.287	0.127	1.450	0.010	0.359	8.830	13.530	0.263	22.963		99.819	1.959	0.004	0.064	0.000	0.010	0.277	0.756	0.008	0.922	4.000	72.489
90882	52.005	0.210	0.892	0.010	0.509	9.318	12.585	0.342	22.943	0.190	99.004	1.974	0.006	0.040	0.000	0.015	0.296	0.712	0.011	0.933	3.986	69.648
90884	52.303	0.140	0.693	0.010	0.950	6.538	14.137	0.137	24.033		98.942	1.967	0.004	0.031	0.000	0.027	0.206	0.793	0.004	0.969	4.000	77.316
90890	52.567	0.267	1.460	0.010	1.443	7.178	13.400	0.230	23.507	0.330	100.391	1.953	0.007	0.064	0.000	0.040	0.223	0.742	0.007	0.936	3.974	73.808
E52179	50.955	0.482	4.357	0.256		4.869	14.584	0.132	22.835	0.538	99.007	1.892	0.013	0.191	0.008		0.151	0.807	0.004	0.909	3.975	84.218
E52199	52.403	0.174	4.831	0.909		2.383	16.067	0.112	22.890	0.543	99.007	1.896	0.005	0.206	0.026		0.072	0.867	0.003	0.887	3.961	92.316
E52210	51.796	0.364	3.432	0.383		4.988	15.773	0.218	23.580	0.320	100.834	1.898	0.009	0.148	0.011		0.153	0.862	0.003	0.926	4.010	84.930
E52204	52.680	0.233	2.574	0.298		3.635	16.318	0.121	23.171	0.277	99.307	1.937	0.006	0.112	0.009		0.112	0.894	0.003	0.913	3.986	88.878
E52187	52.011	0.307	1.765	0.224		10.387	13.328	0.136	21.951	0.467	100.573	1.944	0.009	0.078	0.007		0.325	0.743	0.004	0.879	3.988	69.579
E52190	52.403	0.623	2.581	0.189		6.624	14.816	0.049	21.119	0.551	98.955	1.948	0.017	0.113	0.006		0.206	0.821	0.002	0.841	3.954	79.949
E52185	51.033	0.289	1.915	0.079		12.498	11.462	0.318	21.513	0.549	99.657	1.946	0.008	0.086	0.001		0.399	0.652	0.010	0.879	3.981	62.050
E52203	50.421	0.615	3.849	0.153		9.694	12.809	0.123	20.952	0.702	99.318	1.900	0.017	0.171	0.005		0.106	0.720	0.004	0.846	3.969	70.190
E52205	51.664	0.348	2.572			10.204	12.834	0.346	21.602	0.490	99.318	1.938	0.010	0.114	0.000		0.320	0.718	0.011	0.868	3.978	69.155
E54523	53.530	0.113	0.914	0.081		3.040	16.114	0.140	25.602	0.155	99.689	1.968	0.003	0.040	0.001		0.093	0.883	0.004	1.009	4.002	90.428
E54520	49.712	0.484	5.397	0.165		7.464	13.471	0.118	22.176	0.630	99.617	1.856	0.014	0.237	0.005		0.233	0.750	0.004	0.887	3.986	76.291

Table D.3 Clinopyroxene analyses



	SiO <sub>2</sub>	TiO <sub>2</sub>	Al <sub>2</sub> O <sub>3</sub>	V <sub>2</sub> O <sub>3</sub>	Cr <sub>2</sub> O <sub>3</sub>	Fe <sub>2</sub> O <sub>3</sub>	MgO	MnO	ZnO	Total	Si	Ti	Al	V	Cr	Fe <sup>3+</sup>	Fe <sup>2+</sup>	Mg	Mn	Total	Mg#	Cr#
CAC 64																						
C	0.009	0.090	40.953	0.107	25.070	3.664	14.278	0.127	0.248	100.318	0.002	0.015	10.855	0.019	4.458	0.620	2.686	5.287	0.024	24.007	66.316	29.113
R	0.015	0.085	42.691	0.096	24.367	2.694	13.699	0.127	0.212	100.334	0.003	0.014	11.199	0.017	4.288	0.451	2.350	5.424	0.024	24.005	68.020	27.693
CAC 31																						
Bc	0.036	0.084	51.729	0.075	16.235	1.158	11.913	0.002	0.119	99.799	0.007	0.014	13.020	0.013	2.741	0.186	2.128	5.872	0.000	23.999	73.403	17.393
Br	0.020	0.076	52.030	0.079	15.976	0.984	11.858	0.013	0.165	99.671	0.004	0.012	13.093	0.014	2.697	0.158	2.118	5.879	0.002	24.003	73.518	17.082
CAC 29																						
Bc	0.254	0.214	33.078	0.347	31.125	3.890	19.305	0.074	0.170	100.113	0.061	0.038	9.240	0.066	5.861	0.697	3.839	4.122	0.015	23.969	51.774	38.844
Br	0.013	0.108	33.435	0.223	31.832	3.106	19.929	0.044	0.201	100.240	0.003	0.019	9.554	0.042	5.998	0.557	3.966	4.018	0.009	24.002	50.327	39.093
Ge	0.011	0.054	54.150	0.162	12.182	2.271	13.427	0.053	0.187	100.201	0.002	0.009	13.528	0.028	2.055	0.362	2.390	5.590	0.010	24.003	70.048	13.184
Gr	0.022	0.037	52.830	0.124	13.690	1.814	14.635	0.072	0.182	100.157	0.005	0.006	13.330	0.021	2.329	0.294	2.629	5.530	0.009	24.002	67.056	14.888
CAC 4	0.208	0.143	37.315		27.800	3.015	13.072	0.155		96.690	0.049	0.025	10.294		5.145	0.531	2.559	5.228	0.031	23.862	67.140	33.324
CAC 20																						
brown-c	0.150	0.430	42.285		24.850	2.632	12.682	0.150		99.814	0.033	0.072	11.077		4.367	0.440	2.357	5.512	0.028	23.888	70.045	28.277
brown-r	0.200	0.377	42.937		23.477	2.918	12.717	0.203		99.752	0.044	0.063	11.228		4.118	0.487	2.360	5.598	0.038	23.937	70.345	26.837
CAC 44																						
brown-c	0.285	0.530	27.895		36.835	4.692	19.233	0.340		100.850	0.069	0.096	7.923		7.019	0.851	3.877	3.967	0.069	23.871	50.574	46.974
brown-r	0.325	0.480	28.385		36.130	4.311	18.630	0.345		99.597	0.079	0.088	8.115		6.929	0.787	3.780	3.974	0.071	23.823	51.256	46.060
CAC 49	0.173	0.110	51.685		16.513	3.676	9.887	0.200		100.783	0.037	0.017	12.899		2.764	0.386	1.751	5.852	0.036	23.941	76.970	17.647
CAC 65	0.073	0.244	40.386		25.546	4.759	12.808	0.272		99.472	0.017	0.043	10.616		4.721	0.831	2.485	5.138	0.054	23.902	67.402	30.781
CAC 53	0.100	0.183	51.897		15.487	3.633	8.991	0.213		99.241	0.023	0.030	13.060		2.614	0.584	1.606	5.963	0.039	23.918	78.788	16.680
CAC 89	0.045	0.305	28.875		35.605	5.911	16.601	0.330		99.707	0.011	0.055	8.190		6.810	1.076	3.357	4.318	0.069	23.887	56.261	45.401
CAC 58	0.059	0.275	34.630		30.575	5.333	14.706	0.301		99.590	0.014	0.049	9.401		5.768	0.953	2.922	4.727	0.061	23.894	61.801	38.024
KE20																						
CAC 74																						
C	0.006	0.255	29.434	0.196	34.943	3.704	18.666	0.206	0.538	99.454	0.002	0.047	8.423	0.038	6.729	0.677	3.801	4.164	0.043	24.019	52.279	44.404
R	0.021	0.131	31.243	0.169	33.619	2.945	16.739	0.152	0.502	98.187	0.005	0.024	8.909	0.033	6.432	0.537	3.388	4.568	0.031	24.016	57.416	41.929
DHG-5.8		0.420	29.812		34.744	5.378	17.752	0.220		100.807	0.000	0.075	8.389		6.567	0.951	3.490	4.443	0.015	23.931	56.005	43.908
CAC 61	0.263	0.380	31.820		32.460	7.067	14.704	0.380		100.301	0.062	0.068	8.820		8.820	1.253	2.897	4.663	0.076	23.860	61.554	40.663
CAC 51	0.163	0.587	28.047		38.553	4.346	16.026	0.373		100.082	0.039	0.106	7.950		7.357	0.789	3.232	4.298	0.078	23.848	57.076	48.063
CAC 159																						
C	0.003	0.742	27.437	0.280	33.554	7.362	19.072	0.200	0.169	100.358	0.001	0.136	7.858	0.055	6.464	1.348	3.886	4.180	0.041	24.000	51.824	45.152
R	0.007	0.513	29.656	0.283	34.576	3.509	18.234	0.150	0.298	99.209	0.002	0.093	8.470	0.055	6.633	0.641	3.698	4.330	0.031	24.006	53.941	43.925
CAC 128																						
C	0.077	0.242	33.396	0.344	28.590	4.242	23.635	0.267	0.490	99.969	0.018	0.045	9.492	0.067	5.522	0.784	4.818	3.116	0.055	24.004	39.279	36.940
R	0.009	0.265	32.829	0.342	29.541	3.944	23.842	0.263	0.396	99.980	0.002	0.049	9.386	0.067	5.699	0.729	4.862	3.089	0.054	24.008	38.852	37.885
CAC 130																						
Core	0.002	0.046	49.730	0.077	16.409	0.623	14.563	0.076	0.405	97.933	0.001	0.008	12.953	0.013	2.883	0.105	2.700	5.272	0.014	24.015	66.135	18.227
Rim	0.016	0.075	50.602	0.070	15.638	0.326	14.388	0.094	0.415	97.808	0.004	0.013	13.140	0.012	2.735	0.054	2.656	5.316	0.018	24.014	66.682	17.231
CAC 39																						
Gc	0.434	0.075	54.263	0.163	9.891	2.083	20.003	0.096	0.456	100.864	0.097	0.012	13.789	0.028	1.694	0.339	3.614	4.304	0.018	23.966	54.360	10.940
Gr	0.010	0.046	51.949	0.173	12.896	1.014	22.413	0.095	0.391	100.620	0.002	0.008	13.502	0.031	2.258	0.167	4.148	3.813	0.018	24.011	47.896	14.325
CAC 151	0.003	49.034	0.025	0.519	0.113	0.000	45.339	0.393	0.051	97.629	0.001	0.268	0.008	0.116	0.025	0.000	10.557	0.163	0.509	21.657	1.517	75.116
CAC 115	1.586	0.203	33.305	0.185	27.025	7.230	17.866	0.264	0.739	100.592	0.366	0.036	9.193	0.035	5.007	1.274	3.503	4.253	0.052	23.846	54.839	35.243
CAC 73																						
Green	0.140	0.055	63.670		3.245	3.722	8.101	0.090		99.293	0.029	0.009	15.355		0.526	0.568	1.374	6.182	0.015	24.057	81.819	3.310
Brown	0.140	0.108	42.225		24.490	4.751	13.682	0.295		100.221	0.033	0.018	11.276		4.418	0.803	2.571	4.909	0.058	24.087	65.626	28.152
CAC 48	SiO <sub>2</sub>	TiO <sub>2</sub>	Al <sub>2</sub> O <sub>3</sub>	V <sub>2</sub> O <sub>3</sub>	Cr <sub>2</sub> O <sub>3</sub>	Fe <sub>2</sub> O <sub>3</sub>	MgO	MnO	ZnO	Total												
br - C	0.010	0.326	34.745	0.135	30.723	3.614	13.784	0.005	0.084	98.817	0.002	0.057	9.570		5.677	0.636	2.694	5.362	0.001	23.999	66.558	37.233
br - R	0.014	0.316	34.949	0.128	30.402	3.727	14.127	0.007	0.121	99.000	0.003	0.055	9.618		5.613	0.655	2.759	5.295	0.001	23.999	65.745	36.852

Table D.4 Spinel analyses

	SiO2	TiO2	Al2O3	V2O3	C2O3	Fe2O3	FeO	MgO	MnO	ZnO	Total	Si	Ti	Al	V	Cr	Fe3+	Fe2+	Mg	Mn	Total	Mg#	C#
CAC 37																							
br - C	0.018	0.291	31.899	0.188	31.752	4.954	16.637	13.221	0.037	0.133	99.130	0.004	0.052	8.993		6.005	0.892	3.328	4.715	0.008	23.998	58.619	40.040
br - R	0.007	0.321	29.810	0.196	33.647	5.055	17.751	12.347	0.006	0.274	99.415	0.002	0.059	8.513		6.446	0.922	3.597	4.460	0.001	23.999	55.355	43.091
L1		0.308																				58.900	35.600
L2		0.245																				55.500	35.600
L3		0.144																				65.500	35.200
KE15																						57.020	34.500
KE10																						69.040	35.500
KE14																						69.600	28.500
A25		0.272																				72.600	29.500
A26		0.243																				75.900	28.400
A27		0.287																				74.900	29.400
CAC 113																							
Green C	0.016	0.125	45.711	0.129	19.160	5.408	11.637	18.101	0.027	0.220	100.534	0.003	0.020	11.735	0.023	3.300	0.886	2.120	5.877	0.003	24.004	73.490	21.949
Green R	0.025	0.058	47.175	0.117	18.935	2.116	11.992	17.423	0.202	0.139	98.182	0.005	0.010	12.288	0.021	3.309	0.352	2.216	5.739	0.038	24.001	72.143	21.216
Green C	0.020	0.316	29.256	0.238	32.158	6.317	18.732	11.384	0.201	0.146	98.767	0.005	0.058	8.420	0.047	6.243	1.167	3.840	4.150	0.042	23.998	51.939	42.633
CAC 67																							
C-Br	0.015	0.376	29.415	0.276	33.506	5.325	20.396	10.696	0.177	0.197	100.378	0.004	0.069	8.406	0.054	6.424	0.972	4.137	3.865	0.037	24.001	48.303	43.323
C-Gr	0.009	0.216	45.208	0.175	19.735	3.583	15.409	15.523	0.108	0.326	100.289	0.002	0.036	11.811	0.032	3.467	0.598	2.862	5.129	0.021	24.009	64.186	22.694
R-Gr	3.854	0.076	40.665	0.165	20.817	4.251	12.524	15.624	0.169	0.257	98.439	0.868	0.013	10.683	0.030	3.669	0.713	2.335	5.191	0.032	23.574	68.972	25.733
CAC 75																							
C	0.004	0.280	32.587	0.280	32.140	4.437	18.424	12.367	0.186	0.153	100.858	0.001	0.050	9.034	0.053	6.023	0.788	3.645	4.341	0.037	24.000	54.358	40.008
R	0.013	0.113	36.830	0.168	29.075	2.707	16.932	13.491	0.139	0.178	99.645	0.003	0.020	10.044	0.031	5.396	0.478	3.313	4.659	0.028	24.003	58.443	35.033
CAC 27																							
Be	0.022	0.738	27.532	0.422	32.400	7.139	23.318	8.880	0.109	0.206	100.765	0.006	0.137	7.982	0.083	6.327	1.328	4.816	3.256	0.023	23.996	40.338	44.317
Br	0.021	0.308	30.754	0.363	32.634	4.119	21.741	9.899	0.118	0.227	100.185	0.005	0.057	8.771	0.071	6.278	0.759	4.425	3.568	0.024	23.999	44.638	41.827
Ge	0.035	0.078	50.507	0.190	13.275	5.051	14.593	16.632	0.039	0.241	100.639	0.007	0.013	12.804	0.033	2.296	0.823	2.652	5.328	0.007	24.001	66.768	15.251
Gr	0.057	0.065	50.507	0.227	15.257	2.907	14.616	16.567	0.083	0.305	100.591	0.012	0.011	12.809	0.040	2.634	0.471	2.650	5.313	0.015	24.002	66.722	17.036
CAC 8																							
brown-c	0.130	0.170	39.465		26.960	3.070	14.797	14.740	0.130		99.462	0.030	0.029	10.592		4.854	0.526	2.818	5.004	0.025	23.879	63.973	31.426
brown-r	0.190	0.195	37.340		29.525	2.551	15.610	14.285	0.090		99.785	0.044	0.034	10.115		5.365	0.441	3.000	4.895	0.018	23.911	61.996	34.660
CAC 12																							
brown-c	0.195	0.440	37.690		26.630	4.561	13.486	15.260	0.230		98.492	0.045	0.076	10.232		4.850	0.791	2.598	5.240	0.045	23.877	66.855	32.157
brown-r	0.210	0.160	36.810		27.940	5.777	12.771	15.380	0.260		99.309	0.048	0.028	9.938		5.060	0.996	2.447	5.252	0.050	23.818	68.221	33.740
CAC 33	0.480	0.510	24.330		35.475	8.761	19.316	10.230	0.200		99.302	0.119	0.095	7.131		6.975	1.640	4.017	3.792	0.042	23.811	48.561	49.448
CAC 96																							
core		0.508	30.371		31.336	8.459	20.249	11.603			102.526	0.000	0.090	8.460		5.855	1.504	4.002	4.088	0.000	24.000	50.532	40.904
rim		0.580	26.954		35.879	7.554	20.855	10.962			102.784	0.000	0.105	7.621		6.806	1.364	4.184	3.920	0.000	24.000	48.373	47.174
DHG-6-1		0.458	27.142		34.351	8.548	23.193	9.576			103.268	0.000	0.084	7.849		6.659	1.445	4.356	3.500	0.000	23.885	44.551	45.917
DHG-4-6		0.896	24.578		34.463	9.894	21.982	9.543	0.216		101.571	0.000	0.166	7.149		6.727	1.838	4.539	3.511	0.023	23.953	43.614	48.480
CAC 66	0.140	0.415	32.500		32.510	7.245	14.290	13.695	0.100		100.896	0.034	0.074	8.913		6.030	1.278	2.802	4.755	0.019	23.905	62.920	40.354
CAC 13	0.343	0.595	30.720		33.447	3.277	19.978	10.950	0.417		99.727	0.082	0.213	8.558		6.351	0.592	4.010	3.852	0.084	23.658	48.997	42.600
CAC 14	0.495	0.438	31.498		32.120	5.654	18.189	11.348	0.375		100.116	0.121	0.078	8.702		6.155	1.029	3.677	3.977	0.076	23.816	51.959	41.429
CAC 15	0.143	0.123	32.583		30.283	6.641	13.253	13.253	0.143		98.012	0.034	0.022	9.158		5.710	1.192	2.960	4.712	0.029	23.816	61.418	38.405
CAC 82	0.087	0.097	40.637		26.810	4.620	13.886	14.567	0.220		100.923	0.020	0.016	10.779		4.771	0.783	2.614	4.885	0.042	23.910	65.138	30.680
CAC 81	0.120	0.100	32.270		33.180	8.240	13.255	13.770	0.200		101.135	0.029	0.018	8.843		6.099	1.442	2.578	4.770	0.038	23.817	64.920	40.819
CAC 80	0.163	0.230	32.850		35.823	4.421	16.438	12.043	0.177		102.146	0.038	0.041	8.989		6.577	0.773	3.193	4.167	0.035	23.812	56.615	42.253
CAC 32	0.190	0.250	29.865		34.925	7.502	16.664	11.580	0.345		101.321	0.045	0.045	8.369		6.569	1.343	3.314	4.105	0.069	23.859	55.331	43.974
CAC 68	0.243	0.177	34.437		28.170	6.905	17.500	11.797	0.337		99.565	0.058	0.031	9.604		5.268	1.230	3.463	4.159	0.068	23.880	54.570	35.424

### Table D.4 Spinel analyses

	SiO2	TiO2	Al2O3	V2O3	Cr2O3	Fe2O3	FeO	MgO	MnO	ZnO	Total	Si	Ti	Al	V	Cr	Fe3+	Fe2+	Mg	Mn	Total	Mg#	Cr#
CAC 110																							
Core	0.008	0.202	30.319	0.186	33.683	4.429	18.695	11.682	0.125	0.370	99.698	0.002	0.037	8.622	0.036	6.439	0.804	3.778	4.202	0.026	24.011	52.659	42.715
Rim	0.039	0.160	31.717	0.165	34.110	2.802	18.467	11.964	0.229	0.224	99.877	0.009	0.029	8.937	0.032	6.448	0.504	3.692	4.263	0.046	24.000	53.589	41.911
E52175	0.269	0.038	24.077		43.853	3.305	18.654	10.181	0.248		100.625	0.066	0.007	6.957		8.507	0.611	3.829	3.721	0.052	23.750	49.288	55.011
E52184	0.370	0.088	41.893		22.882	4.410	17.112	13.413	0.230		100.396	0.083	0.015	11.099		4.105	0.755	3.257	4.481	0.044	23.839	57.907	26.998
E52193	0.330	0.012	47.341		19.550	2.125	15.462	14.967	0.254		100.043	0.072	0.002	12.224		3.411	0.352	2.843	4.888	0.048	23.838	63.230	21.815
E52180	0.310	0.177	46.436		20.435	2.112	13.871	16.116	0.124		99.582	0.068	0.017	12.028		3.554	0.350	2.551	5.280	0.019	23.867	67.422	22.810
E52187	0.149	0.057	46.331		21.963	1.436	11.937	17.130	0.055		99.057	0.033	0.009	11.980		3.810	0.237	2.190	5.603	0.010	23.872	71.896	24.128
E52199	0.268	0.115	52.075		15.532	1.462	12.246	17.950	0.133		99.781	0.057	0.012	13.060		2.626	0.235	2.185	5.695	0.024	23.894	72.269	16.739
E52210	0.314	0.082	51.246		6.397	9.243	20.394	12.223	0.233		100.131	0.069	0.010	13.313		1.115	1.536	3.766	4.016	0.043	23.868	51.603	7.726
E52204	1.458	0.160	46.137		11.027	7.990	20.613	12.366	0.404		100.155	0.325	0.027	12.138		1.946	1.342	3.848	4.115	0.076	23.818	51.676	13.818

Table D.4 Spinel analyses

	SiO <sub>2</sub>	TiO <sub>2</sub>	Al <sub>2</sub> O <sub>3</sub>	Cr <sub>2</sub> O <sub>3</sub>	MgO	CaO	MnO	FeO	Na <sub>2</sub> O	K <sub>2</sub> O	Total	Si	Ti	Al	Cr	Mg	Ca	Mn	Fe <sup>2+</sup>	Na	K	Total	Mg#
CAC 67	43.236	3.814	12.150	1.826	16.874	11.786	0.057	5.420	2.820	0.098	100.203	6.176	0.410	2.045	0.206	3.593	1.803	0.007	0.648	0.781	0.018	15.668	84.727
CAC 13	41.385	4.195	11.145	1.560	18.930	10.305	0.090	5.990	1.570	0.050	95.075	6.081	0.462	1.929	0.181	4.168	1.616	0.012	0.743	0.444	0.009	15.624	84.878
CAC 14	43.365	3.480	12.390	1.963	17.428	11.818	0.095	5.118	1.695	0.048	97.255	6.204	0.375	2.089	0.222	3.717	1.811	0.012	0.612	0.470	0.008	15.500	85.857
CAC 8	42.740	4.680	12.230	1.820	16.290	12.090	0.040	4.330	3.400	0.030	97.830	6.120	0.504	2.064	0.206	3.477	1.855	0.005	0.518	0.944	0.027	15.727	83.024
CAC 12	42.020	4.550	11.710	1.840	16.150	12.050	0.120	4.100	3.320	0.090	96.010	6.133	0.499	2.014	0.212	3.514	1.884	0.015	0.500	0.939	0.017	15.733	87.534
CAC 33	42.295	3.830	12.065	1.820	16.355	12.020	0.105	4.415	3.065	0.365	96.375	6.152	0.419	2.068	0.209	3.547	1.873	0.013	0.537	0.864	0.068	15.756	86.848
CAC 27																							
Core	41.753	4.640	12.195	1.745	16.213	12.010	0.133	5.090	2.105	0.110	96.045	6.087	0.509	2.095	0.201	3.524	1.876	0.016	0.621	0.595	0.020	15.563	85.025
Rim	42.335	4.535	11.985	1.800	16.470	12.365	0.030	4.550	1.525	0.085	95.765	6.161	0.496	2.056	0.207	3.573	1.928	0.004	0.554	0.430	0.016	15.435	86.582
CAC 110	44.000	1.832	12.748	1.951	17.453	12.019	0.049	4.826	2.720	0.032	99.767	6.277	0.197	2.143	0.238	3.711	1.837	0.006	0.576	0.752	0.006	15.696	86.571
CAC 72	44.067	1.466	11.808	1.169	17.992	10.734	0.053	4.659	2.461	0.242	94.700	6.536	0.032	2.064	0.130	3.971	1.707	0.007	0.454	0.708	0.046	15.066	89.750
CAC 82	46.861	0.686	12.226	1.453	18.446	12.244	0.121	3.773	2.183	0.080	97.943	6.571	0.072	2.020	0.161	3.855	1.840	0.014	0.442	0.593	0.014	15.567	89.706
CAC 81	45.310	0.933	13.163	1.958	17.790	12.473	0.173	4.500	3.012	0.112	99.198	6.325	0.084	2.233	0.182	3.744	1.873	0.013	0.506	0.874	0.015	15.821	88.094
CAC 80	45.363	1.655	12.792	2.023	17.673	12.792	0.067	4.125	2.053	0.133	98.588	6.384	0.179	2.160	0.210	3.621	1.939	0.010	0.476	0.562	0.005	15.525	88.372
CAC 32	44.820	1.442	12.768	1.945	17.417	12.442	0.125	4.500	3.072	0.098	98.522	6.332	0.153	2.126	0.217	3.668	1.884	0.015	0.531	0.841	0.018	15.711	87.344
CAC 68	45.969	1.037	11.989	1.208	17.846	12.544	0.092	4.571	2.163	0.140	97.440	6.520	0.110	2.005	0.136	3.773	1.906	0.011	0.543	0.596	0.026	15.611	87.429
CAC 15																							
Core	44.318	0.593	11.527	1.378	18.462	11.757	0.132	4.587	2.298	0.090	95.243	6.452	0.065	1.978	0.159	4.007	1.834	0.016	0.538	0.649	0.017	15.748	87.768
Rim	44.530	0.700	11.470	1.533	18.308	12.045	0.043	4.423	2.310	0.080	95.543	6.460	0.076	1.961	0.176	3.959	1.872	0.005	0.537	0.650	0.015	15.727	88.066
DHG-6-9	43.683	1.553	11.890	1.496	18.150	10.686	0.227	5.977	2.338	0.578	96.397	6.334	0.172	2.019	0.170	3.940	1.639	0.006	0.739	0.652	0.108	15.780	84.209
CAC 130	45.107	1.200	12.116	1.690	17.581	12.130	0.053	4.069	2.579	0.217	98.858	6.455	0.129	2.043	0.191	3.750	1.860	0.006	0.487	0.715	0.040	15.659	88.505
CAC 128	43.905	2.550	12.396	1.297	15.965	12.053	0.098	6.537	2.604	0.278	99.811	6.309	0.276	2.099	0.147	3.420	1.856	0.012	0.786	0.725	0.051	15.647	81.321
CAC 73	45.589	1.471	12.598	1.149	17.841	12.499	0.116	4.224	2.161	0.053	97.656	6.442	0.156	2.098	0.128	3.758	1.908	0.014	0.499	0.592	0.009	15.583	88.274
CAC 115	53.293	0.317	4.989	0.602	23.249	11.432	0.063	2.891	0.966	0.021	100.009	7.339	0.033	0.814	0.066	4.779	1.686	0.007	0.333	0.258	0.004	15.312	93.479
CAC 74	54.851	0.227	4.453	0.561	21.953	12.615	0.030	2.517	0.842	0.019	100.301	7.517	0.024	0.722	0.061	4.484	1.853	0.006	0.289	0.224	0.003	15.448	91.531
CAC 75	50.280	0.433	8.184	0.446	22.387	11.622	0.064	3.692	1.156	0.012	100.465	6.954	0.045	1.334	0.049	4.615	1.722	0.007	0.427	0.310	0.002	15.448	91.531
CAC 113	48.987	0.136	10.441	0.150	19.651	11.985	0.099	3.849	1.779	0.009	99.236	6.872	0.014	1.725	0.016	4.109	1.801	0.012	0.451	0.484	0.002	15.476	90.101
DHG-6-1	51.890	0.273	5.440	0.465	23.096	11.780	0.065	3.541	0.824	0.049	97.079	7.240	0.023	0.890	0.030	4.809	1.759	0.000	0.414	0.222	0.002	15.389	92.077
CAC 27	46.200	0.223	11.798	0.070	19.512	11.632	0.065	4.095	1.750	0.040	95.367	6.620	0.024	1.993	0.008	4.168	1.786	0.008	0.491	0.486	0.007	15.602	89.467
CAC 29	51.687	0.227	6.160	0.407	21.353	12.293	0.080	3.541	0.824	0.049	97.079	7.240	0.023	0.890	0.030	4.809	1.759	0.000	0.414	0.222	0.002	15.389	92.077
90703	44.649	2.855	11.627	0.489	14.830	11.042	0.113	10.272	2.308	0.365	98.579	6.424	0.309	1.972	0.056	3.181	1.702	0.014	1.236	0.644	0.067	15.336	92.800
CAC 151	42.099	3.662	12.345	0.609	13.710	9.176	0.092	10.664	1.542	2.293	98.296	6.263	0.411	2.171	0.072	3.051	1.449	0.012	1.331	0.442	0.446	15.575	69.628
DHG-6-5	44.462	1.800	11.955	0.651	15.607	12.210	0.092	7.404	1.869	0.440	96.399	6.465	0.197	2.049	0.075	3.383	1.902	0.000	0.900	0.527	0.082	15.580	78.983
DHG-6-4	44.215	2.226	10.239	0.380	12.014	11.964	0.085	14.238	1.500	0.890	97.686	6.558	0.249	1.793	0.045	2.656	1.902	0.003	1.768	0.433	0.169	15.575	60.032
90899	43.685	2.675	13.855		15.230	11.330		9.020	2.375	0.085	98.255	6.255	0.288	2.338	0.000	3.251	1.738	0.000	1.080	0.660	0.016	15.626	75.065
90901	42.915	2.628	10.655	0.090	11.468	11.445	0.243	14.743	1.888	0.133	96.140	6.471	0.298	1.894	0.011	2.578	1.849	0.031	1.859	0.552	0.025	15.567	58.099
DHG-9-3	45.426	1.072	9.130		10.414	11.111	0.190	19.084	1.188	0.094	97.710	6.812	0.121	1.614	0.000	2.328	1.785	0.024	2.395	0.346	0.018	15.442	49.289
47033	45.019	0.464	10.386	0.030	10.133	11.207	0.479	19.398	1.327	0.386	98.807	6.708	0.052	1.823	0.000	2.251	1.789	0.060	2.417	0.383	0.073	15.577	48.224
CAC 162	44.377	0.527	10.728	0.011	8.651	11.122	0.336	20.814	1.228	0.134	99.917	6.701	0.060	1.910	0.001	1.947	1.800	0.043	2.629	0.360	0.026	15.475	42.552
DHG-9-3	45.264	1.043	9.255		10.071	11.506	0.220	19.103	1.416	0.120	97.998	6.785	0.118	1.637	0.000	2.249	1.848	0.028	2.396	0.412	0.023	15.496	48.424
47040																						#DIV/0!	
brown	43.645	4.273	12.095	0.188	15.023	10.573	0.158	10.325	2.763	0.388	99.450	6.244	0.460	2.039	0.021	3.205	1.620	0.019	1.236	0.766	0.071	15.684	72.173
colours	42.278	0.113	16.740		13.075	11.113	0.220	12.665	2.965	0.170	99.338	6.100	0.012	2.842	0.000	2.809	1.718	0.027	1.530	0.828	0.031	15.897	64.744
DHG-2-6	43.898	1.759	9.911	0.120	10.663	12.241	0.126	17.891	2.006	0.150	98.643	6.552	0.198	1.744	0.003	2.373	1.958	0.013	2.233	0.581	0.029	15.682	51.510
DHG-1-1	45.977	0.656	8.921		11.705	12.444	0.162	17.019	1.554	0.249	98.685	6.799	0.073	1.555	0.000	2.580	1.972	0.020	2.105	0.445	0.047	15.590	55.070
90880	44.180	2.180	11.543	0.105	11.088	12.390	0.153	15.903	1.868	0.240	99.593	6.457	0.240	1.988	0.012	2.416	1.940	0.019	1.944	0.529	0.045	15.597	55.414
90881	44.750	1.794	10.372		11.936	11.936	0.218	15.800	1.540	0.122	98.424	6.594	0.199	1.801	0.000	2.622	1.884	0.027	1.947	0.440	0.023	15.538	57.386
90882	42.397	2.475			10.330	11.280	0.230	16.775	2.228	0.305	97.367	6.380	0.280	2.031	0.000	2.318	1.819	0.029	2.111	0.650	0.059	15.678	52.329
90884	45.104	1.432	9.704		12.862	12.142	0.123	13.794	1.274	0.093	96.462	6.709	0.160	1.701	0.000	2.852	1.935	0.016	1.716	0.367	0.018	15.473	62.436
90890	44.503	1.567	10.377		11.797	12.190	0.200	14.523	1.793	0.093	96.983	6.629	0.176	1.822	0.000	2.619	1.945	0.017	1.809	0.518	0.018	15.553	59.144
90892	45.220	0.860	12.39																				

	SiO <sub>2</sub>	TiO <sub>2</sub>	Al <sub>2</sub> O <sub>3</sub>	Cr <sub>2</sub> O <sub>3</sub>	MgO	CaO	MnO	FeO	Na <sub>2</sub> O	K <sub>2</sub> O	Total	Si	Ti	Al	Cr	Mg	Ca	Mn	Fe <sup>2+</sup>	Na	K	Total	Mg#
★ 90893	49.044	0.910	8.851	0.162	15.787	12.167	0.110	9.580	1.284	0.115	97.810	6.994	0.098	1.488	0.018	3.356	1.859	0.013	1.142	0.355	0.021	15.344	74.604
★ 90894	46.795	1.615	9.857	0.140	14.548	11.517	0.113	11.580	1.732	0.213	98.000	6.758	0.175	1.678	0.016	3.132	1.782	0.014	1.399	0.491	0.039	15.484	69.131
★ CAC 152	44.409	1.900	9.730	0.059	12.237	10.463	0.263	15.940	2.239	0.368	99.642	6.617	0.213	1.708	0.007	2.617	1.671	0.033	1.986	0.647	0.070	15.652	57.777
★ CAC 143	48.330	1.080	8.720	0.109	14.793	11.309	0.199	12.187	1.192	0.108	100.136	6.965	0.117	1.482	0.012	3.178	1.746	0.024	1.469	0.333	0.020	15.329	68.393
★ DHG-5-5	44.826	0.723	8.831		11.099	12.241	0.406	17.803	1.296	0.858	98.084	6.736	0.082	1.564	0.000	2.486	1.971	0.052	2.238	0.378	0.165	15.671	52.628
★ DHG-8-1	45.116	0.958	8.516		9.802	12.029	0.248	19.294	1.342	0.401	97.707	6.821	0.109	1.517	0.000	2.209	1.948	0.032	2.440	0.393	0.077	15.547	47.520
★ DHG-5-1	44.537	0.821	9.677		10.552	12.024	0.259	19.121	1.427	0.557	98.975	6.653	0.092	1.703	0.000	2.350	1.925	0.033	2.389	0.413	0.106	15.663	49.588
★ 90878	46.433	0.585	8.848		12.578	12.238	0.135	14.438	1.068		96.318	7.040	0.057	1.372	0.000	2.920	1.957	0.012	1.726	0.265	0.000	15.350	62.860
★ 90882	47.280	0.370	6.835		11.865	15.235	0.125	14.205	1.140	0.125	97.185	7.044	0.041	1.200	0.000	2.655	2.432	0.016	1.770	0.329	0.024	15.491	59.822
★ 90883	45.223	0.553	11.870		14.597	11.453	0.135	11.280	1.700	0.050	96.520	6.603	0.061	2.043	0.000	3.177	1.792	0.017	1.377	0.481	0.009	15.560	69.759
★ 90885	46.680	0.422	7.842		11.962	12.250	0.145	16.058	0.808	0.085	96.208	7.009	0.048	1.388	0.000	2.677	1.971	0.015	2.017	0.235	0.013	15.373	57.026
★ 90887	44.900	0.977	8.957		12.363	11.760	0.220	15.740	1.130	0.107	96.153	6.765	0.111	1.591	0.000	2.777	1.898	0.028	1.983	0.330	0.020	15.504	58.336
★ 90888	46.318	1.045	10.008	0.110	13.920	12.230	0.128	12.470	1.428	0.328	97.940	6.742	0.114	1.717	0.013	3.021	1.907	0.016	1.518	0.403	0.061	15.511	66.554
★ CAC 153	43.172	1.269	11.193	0.046	10.918	11.976	0.270	16.247	1.648	0.782	99.535	6.485	0.144	1.982	0.006	2.444	1.928	0.034	2.041	0.480	0.150	15.677	54.490
★ CAC 144	44.529	1.259	9.404		10.437	11.303	0.301	18.421	1.810	0.115	99.649	6.703	0.142	1.670	0.003	2.341	1.823	0.039	2.320	0.529	0.022	15.554	50.230
★ CAC 143	53.776	0.295	4.016	0.062	17.101	10.831	0.230	12.460	0.501	0.045	101.479	7.568	0.032	0.669	0.007	3.587	1.633	0.028	1.467	0.137	0.008	15.110	70.973
★ E52175	46.591	0.218	11.513	1.800	18.957	11.925	0.091	3.212	2.332	0.156	96.922	6.604	0.023	1.923	0.202	4.006	1.811	0.011	0.381	0.641	0.028	15.645	91.319
★ E52179	50.356	0.569	7.134	0.352	17.882	12.400	0.167	6.461	1.131	0.075	96.527	7.175	0.062	1.211	0.040	3.796	1.896	0.020	0.772	0.315	0.014	15.301	83.097
★ E52187	48.239	0.972	9.079	0.238	17.385	11.925	0.162	6.866	1.490	0.261	96.589	6.913	0.105	1.537	0.027	3.715	1.832	0.016	0.822	0.415	0.048	15.431	81.884
★ E52199	51.625	0.189	6.524	0.655	20.306	12.812	0.048	2.752	0.843	0.049	95.914	7.279	0.020	1.084	0.073	4.268	1.936	0.001	0.325	0.230	0.009	15.242	92.933
★ E52210	52.742	0.193	5.164	0.260	19.384	12.734	0.167	5.978	0.680		96.988	7.433	0.016	0.858	0.006	4.073	1.923	0.012	0.705	0.186	0.000	15.211	85.246
★ E52204	51.193	0.310	6.231	0.618	18.564	13.074	0.170	5.771	0.991	0.020	97.042	7.251	0.033	1.040	0.069	3.941	1.984	0.020	0.684	0.272	0.004	15.299	85.218
★ E52198	49.775	0.268	7.894	0.673	20.099	12.216	0.039	2.844	1.473	0.103	95.373	7.082	0.029	1.323	0.076	4.264	1.862	0.005	0.339	0.406	0.016	15.401	92.645
★ E54520	49.824	0.358	7.105	0.109	16.661	13.077	0.039	8.720	0.798	0.041	96.732	7.169	0.039	1.205	0.012	3.574	2.016	0.005	1.049	0.223	0.008	15.299	77.303
★ E54523	50.791	0.207	6.494	0.090	18.498	13.130	0.132	5.844	0.875	0.081	96.094	7.256	0.022	1.095	0.005	3.939	2.010	0.016	0.699	0.243	0.015	15.300	84.934
★ E52205	49.785	0.855	5.380		14.125	11.270	0.293	14.915	1.203	0.130	97.858	7.274	0.094	0.927	0.000	3.076	1.765	0.036	1.823	0.341	0.006	15.342	62.788
★ E52203	48.953	1.056	6.572	0.216	12.982	12.468	0.206	13.886	0.877	0.083	97.299	7.182	0.117	1.136	0.025	2.839	1.960	0.026	1.704	0.249	0.016	15.253	62.498
★ E52185	48.616	0.818	5.570	0.041	12.536	11.120	0.186	16.391	1.168	0.092	96.525	7.260	0.092	0.981	0.003	2.791	1.780	0.024	2.048	0.339	0.018	15.334	57.677
★ E52184	45.580	1.138	11.865	0.400	16.850	11.950	0.103	5.873	1.971	0.327	96.058	6.578	0.124	2.019	0.046	3.625	1.848	0.013	0.709	0.552	0.060	15.572	83.634
★ E52180	49.231	0.609	9.766	0.340	19.646	12.127	0.131	3.443	1.413	0.144	96.929	6.911	0.064	1.616	0.038	4.111	1.824	0.016	0.404	0.385	0.026	15.403	91.048
★ E52170	46.195	0.283	10.992	0.096	11.159	11.770	0.147	9.800	0.118		96.972	6.965	0.032	1.954	0.011	2.508	0.286	0.019	1.237	0.034	0.000	15.037	66.977
★ E52171	48.460	0.905	6.578	0.088	13.145	11.116	0.337	15.982	1.097	0.068	97.775	7.132	0.100	1.140	0.010	2.884	1.753	0.042	1.968	0.313	0.013	15.355	59.441

Table D.5 Amphibole analyses

Table D.6 Plagioclase analyses

	SiO <sub>2</sub>	Al <sub>2</sub> O <sub>3</sub>	CaO	FeO	SiO <sub>2</sub>	BaO	Na <sub>2</sub> O	K <sub>2</sub> O	Rb <sub>2</sub> O	Total	Si	Al	Ca	Fe <sup>2+</sup>	Sr	Ba	Na	K	Total	Ab no.	An no.
DHG-4-6	49.281	32.271	15.426	0.235			2.915			100.069	2.251	1.738	0.755	0.007			0.258	0.000	5.009	25.485	74.515
CAC 96	49.774	31.891	15.129	0.105			3.188			100.068	2.271	1.715	0.740	0.003			0.282	0.000	5.012	27.595	72.405
CAC 67	50.478	30.462	14.282	0.052		0.012	3.352	0.028	0.001	98.696	2.328	1.656	0.706	0.002		0.000	0.319	0.002	4.994	29.786	70.214
CAC 113	51.757	29.911	13.603	0.140		0.019	3.589	0.074	0.003	99.103	2.371	1.615	0.668	0.005	0.001	0.000	0.319	0.004	4.983	32.320	67.680
CAC 66	49.867	32.020	15.523	0.180			2.950	0.023		100.333	2.262	1.712	0.755	0.007			0.260	0.001	4.997	25.591	74.409
CAC 13	44.170	24.970	12.750	3.130			2.950	0.090		97.340	2.129	1.418	0.658	0.126			0.276	0.006	4.613	29.513	70.487
DHG-6-7	60.696	24.832	6.468	0.184			7.896	0.070		100.145	2.694	1.302	0.310	0.005			0.678	0.002	4.990	68.657	31.343
XH985	62.570	23.722	4.476	0.130			8.204	0.310		99.370	2.778	1.241	0.213	0.004			0.706	0.011	4.953	76.834	23.166
DHG-4-1	52.633	29.560	12.726	0.302			4.451	0.052		99.725	2.394	1.585	0.620	0.011			0.393	0.001	5.005	38.749	61.251
47040	55.931	28.946	9.273	0.423			5.486	0.043		100.102	2.501	1.525	0.401	0.016			0.425	0.002	4.962	51.688	48.312
90703	53.800	29.693	10.753	0.200			4.890	0.318		99.653	2.435	1.584	0.521	0.008			0.429	0.018	4.995	45.138	54.862
47036	54.902	29.637	10.502	0.453			5.288	0.130		100.912	2.447	1.556	0.501	0.017			0.457	0.007	4.986	47.667	52.333
47037	52.490	29.375	11.255	0.125			6.235	0.050		100.310	2.411	1.567	0.346	0.005			0.547	0.003	5.079	50.061	49.939
CAC 162	52.490	29.343	12.825	0.237	0.070	0.008	4.311	0.028	0.003	99.316	2.399	1.581	0.628	0.009	0.002	0.000	0.382	0.002	5.002	37.793	62.207
DHG-9-3	54.264	28.468	10.813	1.052			5.025	2.151		101.773	2.454	1.518	0.525	0.033			0.440	0.020	4.991	45.588	54.412
CAC 144	59.693	25.513	7.877	0.206	0.076	0.007	6.664	0.090	0.000	100.126	2.658	1.339	0.376	0.008	0.002	0.000	0.575	0.005	4.963	60.498	39.502
DHG-5-1	56.221	23.203	8.424	3.498			6.125	0.220		99.758	2.572	1.243	0.417	0.146			0.538	0.013	5.078	56.333	43.667
DHG-1-1	60.281	25.251	6.915	0.317			7.781	0.069		100.614	2.673	1.319	0.328	0.012			0.669	0.002	5.003	67.063	32.937
DHG-5-5	60.685	24.419	6.321	0.402			7.857	0.272		99.956	2.706	1.283	0.302	0.015			0.679	0.015	5.000	69.226	30.774
DHG-8-1	59.890	25.269	7.014	0.315			7.706	0.069		100.263	2.666	1.326	0.335	0.012			0.665	0.002	5.005	66.532	33.468
90878	54.205	30.500	11.335				5.045			101.130	2.418	1.603	0.542				0.436		4.999	44.603	55.397
90887	55.435	28.692	9.643	0.000			6.156	0.074		100.000	2.492	1.520	0.465				0.537	0.004	5.018	53.600	46.400
90888	56.208	27.953	9.661	0.260			5.870	0.055		100.000	2.524	1.480	0.465	0.010			0.511	0.003	4.993	52.371	47.629
DHG-2-6	53.236	29.746	12.546	0.224			4.662	0.056		100.469	2.403	1.583	0.607	0.008			0.408	0.001	5.009	40.191	59.809
90880	53.352	30.257	11.378	0.062			4.955			100.000	2.408	1.610	0.550	0.002			0.434		5.004	44.076	55.924
90881	52.011	31.691	11.725	0.141			4.439			100.000	2.350	1.688	0.568	0.005			0.389		5.000	40.655	59.345
90883	49.160	33.596	14.022	0.104			3.111			100.000	2.237	1.801	0.684	0.004			0.274		5.000	28.646	71.354
90884	52.837	31.187	12.287	0.160			4.523	0.060		100.903	2.369	1.648	0.590	0.002			0.393	0.001	5.004	39.981	60.019
90893	53.491	29.947	11.879	0.074			4.614	0.000		100.000	2.415	1.594	0.575	0.003			0.404		4.990	41.278	58.722
90894	55.330	28.518	10.551				5.473	0.059		100.000	2.489	1.512	0.509				0.477	0.003	4.990	48.417	51.583
CAC 143	63.053	22.998	4.904	0.145		0.030	8.774	0.108	0.000	100.069	2.790	1.200	0.233	0.005	0.002	0.001	0.753	0.006	4.989	76.374	23.626
90890	66.430	21.900	2.030	0.110			9.950			100.420	2.896	1.125	0.095	0.004			0.841		4.962	89.868	10.132
E52179	49.320	31.162	15.424	0.200			2.627	0.026		98.758	2.277	1.697	0.764	0.008			0.235	0.002	4.981	23.494	76.506
E52184	55.951	27.369	10.711	0.165			5.392	0.033		99.621	2.523	1.455	0.518	0.006			0.471	0.002	4.975	47.671	52.329
E52187	54.143	28.704	11.947	0.234			4.719	0.046		99.792	2.447	1.531	0.580	0.009			0.413	0.003	4.982	41.591	58.409
E52190	56.519	27.482	10.561	0.210			5.504	0.095		100.371	2.533	1.452	0.507	0.004			0.478	0.005	4.980	48.552	51.448
E52185	50.101	30.735	14.640	0.343			3.034	0.050		98.903	2.306	1.668	0.722	0.013			0.271	0.002	4.982	27.267	72.733
E52205	52.075	29.978	13.333	0.340			4.050			99.775	2.375	1.611	0.651	0.003			0.216	0.004	4.999	35.474	64.526
E52203	48.367	31.211	15.808	0.270			2.391	0.089		98.135	2.253	1.714	0.790	0.011			0.216	0.004	4.987	21.449	78.551
47033	56.210	27.670	8.860	0.240			5.870	0.100		98.950	2.544	1.476	0.430	0.009			0.515	0.006	4.979	54.523	45.477
90899	50.556	31.622	14.249	0.153			3.386	0.030		100.000	2.302	1.697	0.695	0.006			0.299	0.002	5.000	30.071	69.929
90901	53.275	30.555	11.655	0.170			4.910			100.520	2.302	1.697	0.695	0.006			0.299	0.002	5.000	30.071	69.929



	CAC 65	CAC 53	CAC 49	CAC 89	CAC 38	CAC 51	CAC 69	CAC 61	CAC 70	CAC 66	CAC 96	CAC 67	CAC 82	CAC 80	CAC 68	CAC 128	CAC 130	CAC 73	CAC 81	CAC 44	CAC 100	CAC 26	CAC 159
XRF data																							
SiO <sub>2</sub>	44.37	44.82	45.06	44.51	44.33	44.58	44.53	44.47	44.67	45.26	44.17	45.25	45.32	44.8	45.68	47.22	44.77	44.57	46.45	49.7	45.09	45.18	
CaO	0.47	1.51	1.42	1.33	1.35	1.36	1.27	1.58	1.023	2.18	2.58	2.34	2.89	2.2	2.62	10.92	2.78	4.67	10.12	8.57	2.31	2.16	
Fe <sub>2</sub> O <sub>3</sub>	8.94	8.96	8.62	9.14	9.06	9.25	9.03	9.25	8.81	9.1	9.17	9.32	9.01	9.29	9.2	9.82	9.24	8.85	6	5.24	9.22	9.17	
MgO	43.53	41.4	41.2	41.78	42.11	42.41	41.4	40.7	41.92	39.68	39.6	38.28	37.72	39.46	37.13	21.31	38.34	35.38	29.48	10.67	40.28	40.38	
Al <sub>2</sub> O <sub>3</sub>	2.09	2.42	2.36	2.22	2.23	2.23	2.54	2.86	2.59	3.3	3.32	3.93	3.83	3.53	4.01	8.22	3.71	4.73	6.65	21.66	3.6	3.29	
Na <sub>2</sub> O	0.013	0.001	0.099	0	0.022	0	0	0	0.005	0.064	0.17	0.319	0.308	0.165	0.323	0.563	0.241	0.282	0.175	3.683	0.111	0.06	
K <sub>2</sub> O	0.008	0.004	0.01	0.004	0.001	0.003	0.003	0.019	0.001	0.005	0.021	0.052	0.018	0.009	0.028	0.074	0.029	0.02	0.021	0.205	0.021	0.02	
TiO <sub>2</sub>	0.068	0.06	0.101	0.083	0.059	0.058	0.119	0.082	0.123	0.126	0.131	0.146	0.169	0.143	0.199	0.269	0.159	0.174	0.271	0.085	0.112	0.11	
MnO	0.127	0.128	0.191	0.13	0.127	0.132	0.124	0.132	0.142	0.134	0.133	0.139	0.125	0.135	0.132	0.154	0.135	0.13	0.141	0.072	0.133	0.14	
P <sub>2</sub> O <sub>5</sub>	0.001	0	0.001	0.001	0	0.003	0.004	0	0	0.001	0	0.006	0.002	0.001	0.031	0.006	0.006	0.001	0.001	0.007	0.002	0.00	
TOTAL	99.61	99.31	99.05	99.21	99.29	100.3	99.01	99.08	99.27	99.85	99.3	99.78	99.38	99.72	99.35	98.57	99.42	98.91	99.31	99.9	100.879	100.51	
LOI	12.05	12.29	12.34	10.98	11.08	11.24	12.24	11.66	13.12	11.17	8.87	9.77	10.35	10.69	10.74	2.55	7.18	8.84	11.99	4.04	9.39	9.36	
Zr	2.5	2.3	2.3	1.6	1.8	2	2.2	2.4	3.4	4.8	7.1	7.9	8.4	7.3	16.5	4	10.1	10.3	6.1	8.9	0	11.4	7.65
Pb	19.1	6.9	21	6.8	10.2	11.6	7.4	7.2	33.8	9.6	6.9	21.6	7.2	8.9	9.2	-	14.8	8.9	16.4	12.5	12.4	4.9	6.5
Zn	47	45.3	283.8	47.3	45.3	48.4	41.5	42	364.4	42.8	43.7	123.1	42	42.6	47.7	53.6	64.9	37.4	71.1	27.3	36.9	45.4	39.2
Cu	26.9	15.6	8.6	17.6	16.2	6.1	13.7	10.6	7.8	31.1	26.6	13.2	10.6	43	76.3	88.9	15.3	143.1	20.3	29.3	27.3	39.7	
Ni	2242.4	2078.7	2083.3	2113.4	2121.6	2146.2	2092.7	1839.4	2132.7	1920.6	1883.4	1820.5	1839.4	1878.4	1735.3	557.6	2149.5	153.3	2022	748.4	369.2	1824.1	1757.8
Co	108.2	69.1	63.6	78.7	68.1	112.3	108.3	95.6	102.8	71.8	97.6	102.8	95.6	99.9	62.4	79.4	99.1	53.3	74.2	33.9	29.8	95.7	92.2
Cr	2853.9	2580.9	2670.2	2433.4	2569.4	2206.8	2003.3	2339.4	2188.8	2068.3	2284.7	2241.7	2339.4	2228.3	2263.6	3468.2	2802.9	2042.4	3257.8	3298.3	71.5	2043.6	2038.2
V	64.5	79.8	71.8	68.7	66	69.4	76.2	88	70.4	80.4	70.6	77.7	88	76.2	93.7	166.2	39.7	120.3	84.5	264.8	6.4	82.8	71.6
Ba	0	3.8	0	1.3	3	0.3	11.2	4.5	0.4	4	0.5	6.3	4.5	11.2	8.2	7	-	5	2.1	0.6	6	0.9	0.8
Sc	9.5	11.2	14.2	13.8	12.9	10.3	13.5	13.1	10.7	13.5	12.8	14.6	13.1	13.5	17.1	36.6	10.5	20.1	14.5	32.3	10.9	8.7	7.9
ICP-MS data																							
Ga	1.997	1.977	1.977	1.951	1.923	1.811	2.207	2.563	2.164		2.891	3.217		2.886	3.756	7.035	3.355	3.892	2.680	4.157	12.447	2.909	2.517
Rb	0.306	0.248	0.349	0.188	0.188	0.297	0.324	0.918	0.279		0.794	2.290		0.306	1.779	2.212	1.557	0.857	2.480	2.639	2.967	0.276	0.484
Sr	3.090	5.382	2.576	2.428	2.494	2.223	2.494	2.223	2.635		29.127	23.392		10.821	14.630	90.002	17.847	14.853	10.109	4.434	412.216	3.960	4.126
Y	1.810	1.666	1.403	1.716	1.738	1.738	2.197	2.305	2.241		3.058	3.353		3.308	4.998	3.926	3.826	5.708	3.129	8.848	3.261	2.759	
Nb	0.002	0.004	0.009	0.009	-	0.005	0.002	0.002	0.003		0.008	0.053		0.063	0.210	0.273	0.023	0.016	0.046	0.000	0.007	0.052	0.017
Cs	1.954	1.642	2.266	1.373	1.183	1.183	1.323	1.623	1.212		1.067	3.318		0.530	2.385	2.485	3.137	3.145	6.455	12.843	19.718	1.304	2.977
Ba	0.535	0.822	0.662	0.385	0.718	0.718	0.648	1.552	0.322		1.443	4.573		3.839	12.182	14.119	10.708	2.927	2.254	0.610	9.497	0.813	0.872
La	0.005	0.010	0.015	0.004	0.004	0.006	0.001	0.007	0.005		0.088	0.203		0.244	1.818	0.506	1.018	0.173	0.140	0.021	0.318	0.076	0.015
Ce	0.014	0.019	0.033	0.016	0.024	0.024	0.018	0.030	0.029		0.373	0.597		0.707	4.547	1.152	1.801	0.661	0.437	0.269	0.779	0.212	0.064
Pr	0.004	0.004	0.003	0.005	0.005	0.006	0.008	0.011	0.012		0.080	0.109		0.123	0.630	0.184	0.207	0.127	0.085	0.110	0.110	0.047	0.025
Nd	0.042	0.029	0.027	0.064	0.064	0.061	0.097	0.128	0.121		0.481	0.621		0.706	2.892	0.994	0.887	0.762	0.512	1.050	0.516	0.324	0.239
Sm	0.055	0.061	0.036	0.055	0.055	0.065	0.089	0.095	0.102		0.211	0.220		0.248	0.658	0.337	0.284	0.291	0.212	0.562	0.096	0.171	0.147
Eu	0.023	0.020	0.020	0.015	0.025	0.025	0.027	0.040	0.041		0.087	0.097		0.092	0.173	0.183	0.117	0.116	0.087	0.224	0.314	0.072	0.062
Gd	0.129	0.127	0.092	0.136	0.136	0.145	0.190	0.179	0.190		0.326	0.355		0.330	0.704	0.479	0.398	0.452	0.342	0.918	0.105	0.320	0.289
Tb	0.031	0.019	0.022	0.028	0.028	0.032	0.038	0.041	0.041		0.062	0.067		0.066	0.121	0.086	0.075	0.098	0.057	0.186	0.015	0.068	0.059
Dy	0.237	0.201	0.164	0.226	0.232	0.232	0.298	0.299	0.299		0.433	0.458		0.443	0.712	0.585	0.527	0.717	0.424	1.218	0.086	0.468	0.400
Ho	0.058	0.051	0.045	0.053	0.053	0.055	0.068	0.072	0.068		0.094	0.103		0.100	0.153	0.122	0.114	0.174	0.097	0.273	0.016	0.110	0.094
Er	0.163	0.153	0.144	0.158	0.170	0.170	0.207	0.211	0.218		0.275	0.300		0.295	0.427	0.355	0.339	0.557	0.286	0.758	0.045	0.334	0.281
Tm	0.030	0.027	0.025	0.029	0.029	0.029	0.035	0.036	0.037		0.047	0.048		0.051	0.070	0.058	0.055	0.097	0.048	0.125	0.007	0.056	0.048
Yb	0.203	0.178	0.165	0.185	0.185	0.185	0.211	0.234	0.227		0.298	0.318		0.321	0.412	0.355	0.349	0.648	0.297	0.733	0.052	0.363	0.305
Lu	0.033	0.030	0.028	0.030	0.031	0.031	0.037	0.040	0.039		0.048	0.050		0.048	0.070	0.056	0.058	0.106	0.047	0.109	0.009	0.058	0.051
Hf	0.022	0.024	0.015	0.032	0.032	0.033	0.043	0.050	0.050		0.143	0.160		0.159	0.351	0.153	0.175	0.236	0.137	0.262	0.015	0.097	0.076
Ta	0.016	0.013	0.014	0.019	0.019	0.014	0.012	0.013	0.013		0.016	0.018		0.016	0.023	0.027	0.016	0.016	0.012	0.013	0.010	0.031	0.024
Th	0.001	0.001	0.001	0.001	0.001	0.002	0.000	0.001	0.001		0.001	0.017		0.005	0.183	0.030	0.025	0.004	0.001	0.001	0.007	0.002	0.002
U	0.001	-	-	0.001	0.001	0.001	0.000	0.002	0.022		0.001	0.006		0.009	0.046	0.012	0.019	0.006	0.001	0.001	0.003	0.001	0.001

Table D.7 Whole rock data

Nb. Samples marked by a '●' are highly altered, therefore the data was not used (i.e., high CO<sub>2</sub>X).

XRF data	CAC 180	CAC 1	CAC 2	CAC 3	CAC 4	CAC 5	CAC 6	CAC 7	CAC 8	CAC 9	CAC 10	CAC 11	CAC 12	CAC 13	CAC 14	CAC 16	CAC 17	CAC 19	CAC 20	CAC 21	CAC 126	CAC 162	CAC 163
SiO <sub>2</sub>	46.73	● 45.08	● 45.37	● 45.98	● 47.06	● 44.38	● 45.86	● 44.12	44.74	44.87	43.77	44.46	44.78	44.49	44.58	48.09	45.01	46.39	46.01	46.12	48.09	46.56	47.91
CaO	11.68	2.18	2.19	1.86	2.22	2.07	2.42	2.33	3.37	3.65	3.62	3.59	3.65	3.76	3.57	0.69	2.48	3.02	3.13	2.17	10.4	10.98	11.27
Fe <sub>2</sub> O <sub>3</sub>	5.97	8.9	9.44	9.1	9.64	9.32	9.6	9.02	9.2	9.43	9.35	9.28	9.23	9.38	9.26	9.5	9.76	9.78	10.32	9.81	6.69	14.76	10.6
MgO	27.03	41.38	41.99	41.19	38.29	42	36.67	42.71	39.66	38.59	38.75	38.45	38.39	37.75	38.38	36.07	41	38.65	37.5	40.04	9.14	5.59	10.68
Al <sub>2</sub> O <sub>3</sub>	7.54	0.71	0.26	0.9	1.38	0.72	3.98	0.29	2.35	2.53	2.75	2.74	2.3	2.72	2.31	4.99	0.49	1.42	1.81	0.72	20.34	17.62	15.29
Na <sub>2</sub> O	0.38	0.15	0.17	0.03	0.41	0.07	0.32	0.02	0.11	0.61	0.24	0.32	0.15	0.39	0.15	0.02	0.06	0.11	0.26	0.09	2.209	1.994	2.073
K <sub>2</sub> O	0.05	0.064	0.021	0.102	0.27	0.196	0.474	0.028	0.026	0.039	0.017	0.018	0.033	0.039	0.027	0.011	0.013	0.03	0.044	0.022	1.496	0.325	0.434
TiO <sub>2</sub>	0.30	0.048	0.052	0.054	0.061	0.068	0.074	0.051	0.132	0.171	0.159	0.152	0.149	0.167	0.132	0.012	0.064	0.128	0.083	0.065	0.326	1.098	0.653
MnO	0.12	0.128	0.131	0.136	0.127	0.181	0.105	0.127	0.135	0.135	0.133	0.136	0.143	0.144	0.146	0.149	0.141	0.163	0.123	0.115	0.104	0.236	0.168
P <sub>2</sub> O <sub>5</sub>	0.02	0.02	0.02	0.02	0.01	0	0.01	0.01	0.02	0.02	0.02	0.02	0.03	0.01	0.02	0.01	0	0.02	0	0.01	0.043	0.117	0.023
TOTAL	100.02	98.66	99.65	99.37	99.47	99.01	99.52	98.71	99.75	100.05	98.81	99.17	98.86	98.85	98.58	99.54	99.02	99.71	99.28	99.16	98.83	99.28	99.09
LOI	7.44	12.00	15.50	11.00	10.30	13.10	11.50	12.50	8.20	9.20	8.00	8.40	10.10	8.70	8.90	13.50	11.90	10.70	10.70	11.80	3.00	1.1	1.26
Zr	24.2	2.6	0.4	0.9	1.3	1.9	2.3	1	7.3	8.9	9.4	8.7	10.5	10.2	7.6	1.6	1.2	5.1	4.3	2.8	1.8	9	13.3
Pb	0.6	1.2	5.6	6.9	6.4	8.7	5.9	3.1	1.3	0.4	4.9	0.7	17.4	10.1	11.9	-	8.1	7.1	6.7	3.8	2.8	1.8	14.4
Zn	31.8	47.2	40.7	55.4	45.2	98.7	160.4	40.6	26.9	34.8	53.6	51.7	88.1	53.1	84.5	70.8	51.8	39.3	49.1	27.8	63.1	98.6	98.5
Cu	130.1	8.6	8.5	1.7	9.1	10.3	8.2	6.2	7.3	5.9	5.9	3.1	2.2	6.7	7.2	8.7	6.6	5.4	8	9.1	6.1	73.2	73.5
Ni	1032.1	2144	2173.5	2375.5	2083.9	2305.9	2149.3	2220.3	1947.2	1874.2	1841.8	1843.7	1881.1	1879.8	1930.2	2143.8	2171.9	2147	2073.7	2177.9	127.6	17.5	161.5
Co	56.9	87.3	114.6	116.6	87.1	110.6	65.8	92.1	109.3	105.6	94.6	107.4	85.2	96.3	94.7	59.1	56.7	87.8	76.5	104.5	39.6	48.8	54.1
Cr	2752.8	3790.3	2557.5	2568.4	2655.4	2103.7	2630.4	2787.8	2326.5	2393.6	2360.4	2317.9	2278.6	2296.4	2376.8	2167.8	2747.4	2737.4	2831.8	2356.5	352.2	27.4	407.5
V	222.2	56.8	58.9	62.9	53.4	45.5	66.7	56.8	63.4	73.4	69.8	73.4	70.5	78.2	69.9	61	72.3	65.9	72.7	53.4	119.8	343.7	288.9
Ba	1.1	0.5	-	0.8	1.2	1.4	3.6	0.6	1.8	-	1.5	-	0.3	-	0.3	0.3	0.5	0.3	-	0.4	86.9	29.2	22.2
Sc	27.5	17.6	6.1	14	7.5	10.9	12.6	11.1	14.1	14.5	15.1	12.2	12	14	14	10.1	13.2	8.2	8.7	11.3	34	60	46.3
ICP-MS data																							
Ga	5.331								2.657		3.189	3.056			2.993						14.898	17.990	13.006
Rb	1.986								2.112		1.805	0.857			1.669						49.506	9.854	5.266
Sr	54.677								13.994		10.084	9.477			8.625						421.513	201.400	146.010
Y	12.198								3.172		3.701	3.538			3.373						9.982	8.947	12.533
Nb	0.597								0.041		0.038	0.024			0.010						0.398	0.256	0.417
Cs	9.958								3.834		3.026	0.976			3.085						54.468	2.503	4.485
Ba	7.435								0.876		1.502	2.092			1.620						73.485	39.381	29.915
La	1.677								0.120		0.161	0.107			0.113						1.104	0.866	1.008
Ce	4.503								0.440		0.584	0.410			0.296						3.032	2.182	2.781
Pr	0.726								0.088		0.114	0.090			0.062						0.513	0.351	0.499
Nd	3.962								0.534		0.691	0.531			0.442						2.836	2.139	2.813
Sm	1.259								0.202		0.275	0.237			0.193						0.969	0.752	1.004
Eu	0.465								0.085		0.106	0.094			0.080						0.448	0.484	0.444
Gd	1.841								0.347		0.421	0.385			0.313						1.330	1.108	1.396
Tb	0.312								0.063		0.075	0.068			0.067						0.234	0.194	0.264
Dy	2.003								0.425		0.517	0.489			0.446						1.457	1.305	1.788
Ho	0.419								0.094		0.113	0.109			0.105						0.299	0.287	0.393
Er	1.168								0.282		0.327	0.321			0.304						0.873	0.839	1.100
Tm	0.183								0.049		0.054	0.053			0.053						0.131	0.139	0.176
Yb	1.076								0.299		0.329	0.327			0.317						0.773	0.893	1.049
Lu	0.160								0.048		0.054	0.055			0.051						0.124	0.142	0.166
Hf	0.673								0.146		0.181	0.166			0.140						0.097	0.298	0.480
Ta	0.055								0.015		0.020	0.013			0.013						0.017	0.011	0.018
Th	0.078								0.004		0.005	0.002			0.013						0.060	0.021	0.061
U	0.029								0.002		0.003	0.003			0.004						0.017	0.017	0.109

Table D.7 Whole rock data

	CAC 134	CAC 167	CAC 142	CAC 28	CAC 151	CAC 147	CAC 125	CAC 168	CAC 190	CAC 145	CAC 135	CAC 143	CAC 152	CAC 127	CAC 144	CAC 116	CAC 165	CAC 166	CAC 169	CAC 170	CAC 171	CAC 172	CAC 173
XRF data																							
SiO <sub>2</sub>	49.76	50.14	46.58	50.02	48.63	50.46	42.38	50.19	49.62		49.3	47.77	46.26	44.51	46.19	47.7	49.43	49.87	48.62	49.29	47.39	46.80	46.86
CaO	7.65	11.53	11.42	9.05	10.33	7.78	6.34	7.19	8.22		10.51	8.67	9.36	12.07	9.4	9.67	9.93	10.31	10.68	8.40	9.45	11.73	9.77
Fe <sub>2</sub> O <sub>3</sub>	7.1	5.62	8.18	11.14	7.52	11.41	7.01	11.44	11.85		7.39	10.89	14.51	9.27	15.61	15.59	12.15	10.09	9.70	8.64	11.37	12.51	13.14
MgO	11.79	8.63	8.56	8.76	8.65	7.21	26.09	9.75	7.74		10.19	12.94	7.94	15.21	7.38	5.22	7.14	6.78	8.68	9.97	9.61	8.11	8.10
Al <sub>2</sub> O <sub>3</sub>	17.51	19.58	20.95	15.84	19.41	16.26	14.99	16.06	17.66		16.95	15.21	14.08	15.14	13.06	14.2	15.57	18.09	17.74	17.77	16.52	15.70	15.48
Na <sub>2</sub> O	2.31	2.638	2.209	2.683	2.656	3.145	0.904	3.302	3.17		2.524	1.29	3.248	1.216	3.325	3.356	3.429	3.357	2.76	3.94	2.91	3.07	3.07
K <sub>2</sub> O	1.939	0.675	0.693	0.922	1.177	0.935	0.223	0.497	0.765		1.029	1.422	0.459	0.135	0.31	0.624	0.436	0.522	0.66	0.40	1.40	0.30	0.83
TiO <sub>2</sub>	0.543	0.365	0.387	1.673	0.529	1.634	0.563	1.634	1.134		0.712	0.69	2.747	1.122	3.211	2.128	1.963	1.447	1.37	1.25	1.62	2.27	2.65
MnO	0.11	0.088	0.122	0.178	0.1	0.229	0.147	0.23	0.234		0.119	0.174	0.21	0.162	0.234	0.249	0.209	0.169	0.16	0.14	0.21	0.22	0.25
P <sub>2</sub> O <sub>5</sub>	0.013	0.016	0.022	0.019	0.038	0.183	0.053	0.159	0.118		0.05	0.038	0.259	0.119	0.361	0.173	0.198	0.125	0.13	0.14	0.25	0.24	0.31
TOTAL	98.73	99.282	99.13	100.46	99.04	99.25	98.7	100.452	100.511		98.77	99.09	99.06	98.95	99.08	98.9	100.455	100.76	100.49	99.94	100.73	100.93	100.47
LOI	2.80	1.23	2.66	2.18	3.04	1.41	7.36	2.10	2.67	3.98	1.6	2.62	0.59	2.6	1.17	0.59	1.44	1.14	2.12	1.98	3.71	3.42	3.09
Zr	16.7	14.4	2.7	76.3	18.5	109.9	30.3	117.7	59.25	16.4	42.3	21.3	216.8	80.1	213	107.9	138.9	114.9	69.1	110.9	57.3	123.3	154.9
Pb	3.6	8.8	1.6	12.2	3.9	1.3	5.3	0.2	0.9	2.4	3.2	6.4	4.7	1.9	0.3	16.4	11.2	9.2	4	1.8	10.5	24.7	14.4
Zn	45.1	37.8	62.6	75.5	56.1	100.2	81	80.1	81.4	58.2	50.8	81.8	115.7	66.1	123.2	103.5	87	80.1	52.7	68.1	99.5	106.8	99.5
Cu	108	20	22.8	78.9	29.1	73.4	8.9	105.5	60	59.9	78.7	13.2	69.2	22.7	138.6	39.5	75.4	33.8	6.1	62.5	34.2	83.6	41.9
Ni	194.1	166.2	82	129.1	131.7	142.3	261.5	179.2	92.5	1243.5	221.8	202.1	60.8	562.9	42.4	50.9	73.8	70.3	115.6	216.6	85.7	108.4	50.2
Co	40.8	37.1	45.6	54.6	45	46.3	53.4	49.8	36.4	67.8	41.1	58.4	45.7	52.2	54.2	57.3	44.9	40.5	44.9	39.4	48.5	57.1	54.4
Cr	821.1	505.3	292.3	377.7	572.8	327.1	543.8	449.5	207.9	2121.6	664.8	606.5	198.7	728.3	64.2	83.7	257.4	283.8	600.5	498.2	236.3	300.2	75.6
V	167.2	132.3	190.1	281.9	141.9	281.2	191.4	271	249.9	69.8	164.3	261.3	401.6	219.4	431.2	344.2	325.3	277.5	266.4	160.3	274.2	373.1	373.5
Ba	98.9	35.1	80.8	189.5	161.2	206.6	10.4	109	114.3	2.4	88.9	92.5	31.7	23.3	20.2	57.7	48	62.3	58.5	9.8	171	26.3	67.5
Sc	33.7	33.9	36.5	34.4	26.4	38.4	29.5	35.9	33.6	12.6	33.4	40.3	49.2	32.3	52	52.5	44.1	42.6	48.1	27	43.8	49.7	49.8
ICP-MS data																							
Ga	13.189	14.287	14.759	16.961	15.101	18.905	9.610	16.541	17.851		13.372	13.070	21.598	15.425	20.116	18.633	18.331	17.637	16.496	14.201	15.546	18.136	18.583
Rb	64.099	26.403	31.004	19.695	36.803	31.074	4.850	11.325	12.267		36.929	57.095	4.628	1.641	7.233	9.981	9.340	9.683	21.628	19.306	28.673	5.369	16.623
Sr	224.400	322.869	397.413	272.374	351.870	388.460	77.445	451.418	294.342		253.800	181.015	267.374	382.460	201.639	223.303	307.949	342.689	346.637	235.463	518.100	376.390	285.886
Y	11.878	9.021	6.667	31.558	15.768	28.145	11.499	33.686	27.950		15.684	14.117	56.956	29.401	55.095	42.143	38.480	29.378	23.584	24.610	33.411	41.719	42.631
Nb	0.306	0.323	0.368	8.413	2.286	9.638	1.962	7.869	2.653		0.532	1.212	6.807	5.713	7.984	3.128	4.262	2.906	2.478	0.827	1.948	4.478	6.338
Cs	17.240	4.206	27.312	2.901	3.720	2.323	6.218	2.058	2.464		1.965	19.555	0.183	0.937	4.788	1.871	1.007	1.669	8.696	7.190	2.782	0.764	0.692
Ba	105.368	16.844	64.599	202.435	170.149	225.237	18.225	132.008	124.641		93.252	117.057	39.585	25.903	26.053	72.710	49.958	51.401	51.090	10.476	203.617	26.211	82.092
La	0.946	1.074	1.787	8.004	3.001	1.935	3.300	9.308	4.088		2.017	1.843	0.908	3.812	7.696	3.666	6.622	3.696	3.133	2.849	2.290	4.700	7.523
Ce	2.415	2.723	4.130	18.975	7.152	4.310	7.565	20.800	10.814		5.393	4.893	26.214	12.000	23.488	10.844	18.287	10.664	9.202	9.972	7.429	15.291	22.267
Pr	0.447	0.443	0.603	2.742	1.036	0.576	1.015	2.951	1.791		0.882	0.793	4.291	2.083	4.003	2.038	2.876	1.811	1.554	1.723	1.442	2.659	3.505
Nd	2.731	2.411	3.009	13.195	4.979	2.519	4.806	13.870	9.471		4.889	4.158	21.838	11.110	20.906	11.673	14.709	9.543	8.187	8.836	8.947	14.474	18.116
Sm	1.034	0.798	0.832	3.627	1.482	0.617	1.174	3.614	3.029		1.557	1.280	6.246	3.211	6.324	4.073	4.239	3.047	2.581	2.625	3.074	4.469	5.162
Eu	0.559	0.425	0.397	1.248	0.775	0.267	0.612	1.202	1.146		0.708	0.521	2.049	1.041	2.033	1.557	1.451	1.042	1.019	0.965	1.139	1.544	1.528
Gd	1.488	1.117	0.985	4.306	1.913	0.689	1.438	4.387	4.052		2.116	1.673	7.619	3.762	7.836	5.591	5.248	3.862	3.285	3.065	4.248	5.724	6.368
Tb	0.275	0.205	0.156	0.738	0.345	0.113	0.252	0.754	0.711		0.358	0.294	1.318	0.652	1.319	0.987	0.899	0.675	0.560	0.551	0.763	0.984	1.053
Dy	1.789	1.292	0.993	4.637	2.233	0.689	1.637	4.672	4.495		2.281	1.957	8.228	4.141	8.327	6.316	5.660	4.327	3.533	4.932	6.204	6.470	
Ho	0.373	0.267	0.202	0.984	0.474	0.149	0.344	1.021	0.946		0.475	0.430	1.742	0.887	1.718	1.319	1.159	0.915	0.742	0.750	1.070	1.296	1.349
Er	1.039	0.758	0.568	2.755	1.311	0.418	0.984	2.861	2.776		1.329	1.254	4.902	2.522	4.758	3.669	3.270	2.579	2.032	2.152	2.970	3.623	3.666
Tm	0.161	0.123	0.093	0.441	0.216	0.069	0.163	0.466	0.443		0.209	0.201	0.784	0.416	0.752	0.578	0.527	0.417	0.318	0.350	0.474	0.571	0.579
Yb	0.915	0.681	0.577	2.667	1.300	0.414	1.009	2.786	2.693		1.243	1.212	4.650	2.547	4.371	3.400	3.072	2.496	1.856	2.034	2.856	3.427	3.396
Lu	0.144	0.112	0.091	0.428	0.202	0.065	0.158	0.441	0.415		0.187	0.197	0.733	0.405	0.677	0.517	4.5257147	3.6720362	0.290	0.323	0.448	0.527	0.519
Hf	0.567	0.483	0.084	0.707	0.537	2.872	0.829	3.532	1.031		1.385	0.617	5.000	2.240	6.869	3.462	4.526	3.672	2.302	3.514	1.768	3.757	5.055
Ta	0.023	0.022	0.017	0.394	0.142		0.085	0.360	0.154		0.037	0.062	0.418	0.277	0.461	0.184	0.255	0.239</					

Table D.7 Whole rock data

	CAC174	CAC160	CAC30	CAC35	CAC120	CAC196	CAC197	CAC141	CAC183	CAC184	CAC185	CAC186	CAC18	MS1668
XRF data														
SiO2	46.28	48.01	49.63	44.35	48.77	42	48.82	68.56	50.59	54.89	51.28	50.57	46.35	
CaO	10.92	8.74	9.5	12.43	9.89	6.54	9.35	2.36	7.18	7.41	8.67	9.65	9.27	
Fe2O3	12.96	15.7	7.89	8.53	8.48	7.51	6.4	4.39	12.84	10.36	9.08	6.95	8.58	
MgO	6.69	4.77	9.48	14.73	9.1	22.94	12.99	2.35	6.57	4.4	8.09	6.98	13.06	
Al2O3	16.39	14.08	16.9	16.86	16.05	18.35	17.56	14.16	16.56	16.86	16.66	20.4	16.55	
Na2O	2.21	3.622	3.736	1.417	3.011	0.708	1.288	4.697	4.341	3.041	4.011	3.211	1.61	
K2O	1.11	0.261	0.513	0.084	1.646	1.24	2.742	1.614	0.55	0.785	0.76	1.085	1.965	
TiO2	2.96	3.113	1.121	1.31	1.315	1.536	1.131	0.835	1.059	1.454	1.521	1.037	1.719	
MnO	0.18	0.262	0.13	0.162	0.147	0.171	0.124	0.077	0.298	0.251	0.152	0.127	0.136	
P2O5	0.44	0.399	0.125	0.131	0.15	0.171	0.129	0.166	0.16	0.161	0.197	0.121	0.25	
TOTAL	100.12	98.96	99.03	100	98.57	101.177	100.534	99.19	100.148	99.612	100.421	100.131	99.99	
LOI	3.44	0.33	1.73	5.49	1.81	7.90	4.17	1.31	1.91	1.70	1.96	1.89	4.10	
Zr	248.9	297	84.6	90.4	112.2	107.55	84.3	189.3	71.45	162.3	131	80.3	145	
Pb	5.5	6	12.6	13.3	15.3	6.6	6.6	14.6	5.2	11	4.8	3.9	7.8	
Zn	86.9	147.4	55.6	56	70.8	56.1	43.5	47.8	139.5	182.2	92.8	61.9	61.2	
Cu	3.6	52	54.3	60.1	56.9	4.7	66.7	22.2	53.3	53	17.8	12.9	9.2	
Ni	58.5	26.1	190.7	189.2	165.8	270.6	188.8	16.9	24.1	56.9	92	121.3	174.2	
Co	50.6	46.5	40.7	39.6	40.5	34.9	34.2	11.5	40.7	31.9	35.1	29.3	45.5	
Cr	135.2	17.3	372.8	329.3	283.7	358.4	288.2	43.7	29.8	163.9	285.8	232.1	300.4	
V	529.6	378.8	196.7	170.9	185.8	229.4	175.9	65.7	336.5	262.6	241.3	171.1	276.1	
Ba	100.5	93.2	39.3	31.3	158.7	138.6	291.1	323.8	69.4	137.4	89.5	119.9	55.1	
Sc	58.5	42.7	28.1	22.8	28.4	24.5	24	13.9	44.1	30.3	30.5	25.3	39.3	
ICP-MS data														
Ga	20.451	22.341	14.006	12.216	14.145	10.020	14.455		15.154	20.153	15.945	14.562		15.810
Rb	23.912	2.138	19.378	1.457	33.279	27.607	64.813		9.254	26.532	20.751	21.967	26.100	14.098
Sr	336.469	226.607	227.230	75.762	215.558	125.675	80.956		285.893	298.819	270.152	328.336	378.000	479.300
Y	53.856	71.065	23.411	25.782	28.068	29.086	23.010		24.889	34.204	32.174	21.253		16.174
Nb	7.196	10.106	1.653	0.511	1.510	0.888	0.739		2.007	8.228	2.959	1.517		3.514
Cs	1.711	0.221	5.900	1.459	81.297	27.790	24.850		0.798	1.221	19.682	2.271		0.674
Ba	105.223	91.749	26.424	22.411	175.210	141.017	285.042		81.437	142.469	81.205	125.538	206.600	167.410
La	8.112	13.170	2.690	2.296	2.918	3.247	3.235		12.690	17.277	5.118	3.710	6.121	27.694
Ce	23.493	36.090	8.566	8.837	10.597	12.404	10.156		28.427	38.806	14.694	9.561	16.911	53.483
Pr	3.891	5.885	1.530	1.668	1.914	2.285	1.759		3.893	5.093	2.452	1.632	2.604	6.205
Nd	20.379	29.829	8.056	9.109	10.135	12.303	9.219		17.330	21.391	12.710	8.431	12.773	22.509
Sm	5.992	8.351	2.500	2.734	3.042	3.674	2.702		4.030	5.007	3.794	2.459	3.581	3.748
Eu	2.123	2.489	0.952	1.026	1.105	1.424	1.000		1.178	1.393	1.342	0.970	1.473	1.084
Gd	7.668	10.134	3.043	3.353	3.788	4.579	3.490		4.114	5.498	4.972	3.295	4.227	2.760
Tb	1.293	1.710	0.535	0.585	0.656	0.763	0.588		0.647	0.915	0.837	0.546	0.760	0.416
Dy	8.077	10.729	3.368	3.726	4.015	4.772	3.686		3.893	5.608	5.215	3.406	4.694	2.395
Hg	1.698	2.230	0.695	0.778	0.846	1.000	0.781		0.820	1.179	1.094	0.721	0.993	0.483
Er	4.677	6.144	1.955	2.107	2.340	2.822	2.203		2.410	3.345	3.104	2.009	2.822	1.436
Tm	0.747	0.989	0.314	0.345	0.380	0.449	0.352		0.391	0.532	0.491	0.312	0.449	0.248
Yb	4.421	5.948	1.845	2.016	2.216	2.616	2.069		2.416	3.209	2.803	1.841	2.604	1.628
Lu	0.690	0.919	0.293	0.317	0.343	0.410	0.315		0.385	0.507	0.428	0.284	0.410	0.283
Hf	7.777	8.500	1.674	2.246	1.022	1.548	1.097		1.641	3.022	0.641	0.715		2.112
Ta	0.485	0.615	0.118	0.064	0.107	0.093	0.073		0.113	0.568	0.205	0.125		0.246
Th	0.158	0.411	0.081	0.036	0.061	0.048	0.056		3.396	5.404	0.247	0.103		11.122
U	0.075	0.235	0.040	0.014	0.024	0.017	0.033		0.956	1.302	0.066	0.202		3.703

Table D.7 Whole rock data

Sample No.	CAC 1	CAC 2	CAC 3	CAC 4	CAC 5	CAC 6
Grid Ref.	73251647	73251647	73251647	73251647	73251647	73251647
Location	Kennack B/H 683*	Kennack B/H 879*	Kennack B/H 230*	Kennack B/H 3605*	Kennack B/H 465*	Kennack B/H 4703*
Lithology	Spinel lherz.	Spinel lherz.	Spinel lherz.	Spinel lherz.	Spinel lherz.	Spinel lherz.
Sample No.	CAC 7	CAC 8	CAC 9	CAC 10	CAC 11	CAC 12
Grid Ref.	73251647	69011634	69011634	69011634	69011634	72152200
Location	Kennack B/H 726*	Predannack B/H 142*	Predannack B/H 364*	Predannack B/H 5745*	Predannack B/H 8346*	Countybridge B/H 34*
Lithology	Spinel lherz.	Myl. Pl-bearing perid.	Myl. Amph-bearing perid.	Myl. Amph-bearing perid.	Myl. Amph-bearing perid.	Myl. Pl-bearing perid.
Sample No.	CAC 13	CAC 14	CAC 15	CAC 16	CAC 17	CAC 18
Grid Ref.	72152200	72152200	72152200	N/A	N/A	N/A
Location	Countybridge B/H 201*	Countybridge B/H 260*	Countybridge B/H 2646*	St Keverne B/H 68.5m	St Keverne B/H 89.6m	St Keverne B/H 89.6m
Lithology	Myl. Pl-bearing perid.	Myl. Pl-bearing perid.	Myl. Amph-bearing perid.	Spinel lherz.	Spinel lherz.	Gabbro Mylonite
Sample No.	CAC 19	CAC 20	CAC 21	CAC 22	CAC 23	CAC 24
Grid Ref.	N/A	N/A	N/A	71691251	72591469	72661473
Location	St Keverne B/H 94.6m	St Keverne B/H 97m	St Keverne B/H 111m	Pilla Cove	Kildown Point	Kildown Point
Lithology	Spinel lherz.	Spinel lherz.	Spinel lherz.	Landewednack amphibolite	Mafic Kennack Gneiss	Landewednack amphibolite
Sample No.	CAC 25	CAC 26	CAC 27	CAC 28	CAC 29	CAC 30
Grid Ref.	74321668	68511365	68201357	68241339	70861367	72761560
Location	300m E Green Saddle	Kynance Cove	Lawnick Pit	Lawnick Pit	150m SW Treveddon Gate	Carlson Cove
Lithology	Harzburgite	Transitional assemblage perid.	Myl. Pl-bearing perid.	Gabbroic vein	Spinel lherz.	Mafic Dyke
Sample No.	CAC 31	CAC 32	CAC 33	CAC 34	CAC 35	CAC 36
Grid Ref.	76731664	71202223	71202223	71202223	66861360	66611588
Location	Beagles Point	Trevasick Quarry	Trevasick Quarry	Trevasick Quarry	Polstone Point	Parc Bean Cove
Lithology	Spinel lherz.	Myl. Amph-bearing perid.	Myl. Pl-bearing perid.	Myl. Pl-bearing perid.	Mafic Dyke	Serpentinised myl. perid.
Sample No.	CAC 37	CAC 38	CAC 39	CAC 40	CAC 41	CAC 42
Grid Ref.	78531812	80412315	80372306	80122314	80032317	80022317
Location	Dolar Point	Pol Gwara	Middle Porthkerns Qy	350m W Porthallow	230m W Porthallow	234m W Porthallow
Lithology	Dunite	Amph-bearing perid.	Amph-bearing perid.	Dunite	Dunite	Dunite
Sample No.	CAC 43	CAC 44	CAC 45	CAC 46	CAC 47	CAC 48
Grid Ref.	79891568	72691568	73671656	74181664	74451662	74881670
Location	150m SE Porthallow	Point N of Carlson Cove	Kennack Sands	300m E of Kennack Sands	Green Saddle	Cove just E Compass Cove
Lithology	Dunite	Websterite vein	Dunite	Harzburgite	Dunite	Dunite
Sample No.	CAC 49	CAC 50	CAC 51	CAC 52	CAC 53	CAC 54
Grid Ref.	74921678	73431697	73341745	72921728	72541736	72421779
Location	200m S Poldowrian	Gwendreath Quarry	450m N Gwendreath Qy	300m NW Gwendreath farm	700m NW Gwendreath Farm	800m NW Gwendreath Farm
Lithology	Spinel lherz.	Spinel lherz.	Plag. lherz.	Plag. lherz.	Spinel lherz.	Dunite
Sample No.	CAC 55	CAC 56	CAC 57	CAC 58	CAC 59	CAC 60
Grid Ref.	72611770	73021757	73381719	72031834	71521894	70821894
Location	650m NW Gwendreath Farm	550m NNW Gwendreath Farm	300m NE Gwendreath Qy	500m NE Trewithno	900m N Trewithno	200m NE Trewithno
Lithology	Serpentinised lherz.	Dunite	Spinel lherz.	Spinel lherz.	Spinel lherz.	Spinel lherz.
Sample No.	CAC 61	CAC 62	CAC 63	CAC 64	CAC 65	CAC 66
Grid Ref.	71261956	70541809	76211740	76391685	72491777	73841883
Location	1300m NNE Trencoon	500m SSW Trencoon	120m S Mount Iarl	Downas Valley	750m NW Gwendreath Farm	650m W Trelin
Lithology	Plag. lherz.	Spinel lherz.	Spinel lherz.	Spinel lherz.	Spinel lherz.	Myl. Pl-bearing perid.

Table D.8 Sample list

Sample No.	CAC 67	CAC 68	CAC 69	CAC 70	CAC 71	CAC 72
Grid Ref	74061953	73981962	72341955	71791962	70241708	68321357
Location	800m NW Tolan	850m NW Tolan	700m SW Croft Pascoe Pool	Groonhilly Downs	250m S Trelease	200m NW Tor Balk (Kynace Cove)
Lithology	Myl. Pl-bearing perid.	Myl. Amph-bearing perid.	Plag. Iherz.	Plag. Iherz.	Spinel Iherz.	Myl. Amph-bearing perid.
Sample No.	CAC 73	CAC 74	CAC 75	CAC 76	CAC 77	CAC 78
Grid Ref	68051443	68971416	69131430	69141431	69061424	67641558
Location	125m S Kynace Farm	1000m NE Kynace Cove	1250m NE Kynace Cove	1255m NE Kynace Cove	1150m NE Kynace Cove	600m E Pol Cornick
Lithology	Myl. Amph-bearing perid.	Spinel Iherz.	Myl. Pl-bearing perid.	Myl. Pl-bearing perid.	Spinel Iherz.	Myl. Amph-bearing perid.
Sample No.	CAC 79	CAC 80	CAC 81	CAC 82	CAC 83	CAC 84
Grid Ref	68921786	69051815	67901824	66801713	67471627	75641667
Location	1000m SW Penhale	600m SE Penhale	1000m S Mullion	750m S Mullion Cove	500m E Predannack Wollas	Lankidden Cove
Lithology	Myl. Amph-bearing perid.	Myl. Amph-bearing perid.	Myl. Amph-bearing perid.	Myl. Amph-bearing perid.	Myl. Amph-bearing perid.	Harzburgite
Sample No.	CAC 85	CAC 86	CAC 87	CAC 88	CAC 89	CAC 90
Grid Ref	75641667	75641667	75641667	75641667	77071622	77791630
Location	Lankidden Cove	Lankidden Cove	Lankidden Cove	Lankidden Cove	Pen Boar	Coastguard lookout - Blackhead
Lithology	Dunite	Harzburgite	Dunite	Dunite	Spinel Iherz.	Plag. Iherz.
Sample No.	CAC 91	CAC 92	CAC 93	CAC 94	CAC 95	CAC 96
Grid Ref	69911953	71032042	69631838	69201909	69022000	67371352
Location	1000m N Penhale	1400m E Bodhym Hill	250m SW Penhale	400m NE Weaver	Clahar Carn	Rail Point
Lithology	Plag. Iherz.	Plag. Iherz.	Plag. Iherz.	Myl. Amph-bearing perid.	Plag. Iherz.	Myl. Pl-bearing perid.
Sample No.	CAC 97	CAC 98	CAC 99	CAC 100	CAC 101	CAC 102
Grid Ref	77831618	78181689	78691746	78321802	72811545	72841509
Location	Black Head	800m NNE Black Head	End of Chynalls Point	Perprean Cove	By Black Rock (Pollesco)	250m N Enys Head
Lithology	Dunite	Dunite	Pyroxenite vein	Troctolite	Myl. Amph-bearing perid.	Dunite
Sample No.	CAC 103	CAC 104	CAC 105	CAC 106	CAC 107	CAC 108
Grid Ref	72841520	72781530	72761515	72781557	68751870	68561883
Location	North of Enys Head	Cliff top N Enys Head	Cliff top, N Enys Head	S-Side Carleton Cove	By SE Quarry, Weaver	200m S, NW Quarry, Weaver
Lithology	Mafic Kemack Gneiss	Myl. Pl-bearing perid.	Spinel Iherz.	Hydrous shear-zone	Myl. Amph-bearing perid.	Myl. Pl-bearing perid.
Sample No.	CAC 109	CAC 110	CAC 111	CAC 112	CAC 113	CAC 114
Grid Ref	68131820	66731775	66531742	67141753	67021481	67021481
Location	300m SW Treprisson Farm	200m S Mullion Cove	Mullion Cliff	SE Mullion Cove	NE Pengersick	NE Pengersick
Lithology	Myl. Pl-bearing perid.	Myl. Amph-bearing perid.	Fault Rock	Myl. Amph-bearing perid.	Myl. Pl-bearing perid.	Myl. Pl-bearing perid.
Sample No.	CAC 115	CAC 116	CAC 117	CAC 118	CAC 119	CAC 120
Grid Ref	67021481	71701253	71441287	71431292	66831488	66841485
Location	NE Pengersick	Kilcobben Point	Entrance Balk Quarry	Balk Quarry	Vellan Head	Vellan Head
Lithology	Myl. Pl-bearing perid.	Landedrednack amphibolite	Fault Rock	Hydrous shear-zone	Fault rock	Mafic Dyke
Sample No.	CAC 121	CAC 122	CAC 123	CAC 124	CAC 125	CAC 126
Grid Ref	68901482	6891482	67061481	67501444	67021529	67031529
Location	Vellan Head	Vellan Head	NE Pengersick	100m N Gew Graze	Georges Cove	Georges Cove
Lithology	Mafic Dyke	Shear/fault rock	Myl. Pl-bearing perid.	Myl. Pl-bearing perid.	Gabbroic vein	Mafic Traboe cumulate
Sample No.	CAC 127	CAC 128	CAC 129	CAC 130	CAC 131	CAC 132
Grid Ref	68891563	66881563	66881563	73832041	73961963	72851571
Location	Potstone Point	Pol Cornick	Pol Cornick	Cope, 300m SE Traboe Cross	275m NW Fox Covert (W Trelan)	S-Side, Little Cove, Pollesco
Lithology	Landedrednack amphibolite	Ultramafic Traboe cumulate	Gabbroic vein	Ultramafic Traboe cumulate	Myl. Amph-bearing perid.	Weldstone vein

Table D.3 Sample list



Sample No.	CAC 133	CAC 134	CAC 135	CAC 136	CAC 137	CAC 138
Grid Ref.	72661472	72661472	72661472	72661472	72661472	72661471
Location	3m Above contact Kildown Point	12m South contact, Kildown Point	11m South contact, Kildown Point	Just above (<1m) contact, Kildown Pt	Main Contact zone, Kildown Point	80m SW contact, Kildown Point
Lithology	Myl. Amph-bearing perid.	Mafic Traboe cumulate	Landwednack amphibolite	Myl. Amph-bearing perid.	Hydrous shear-zone	Myl. Amph-bearing perid.
Sample No.	CAC 139	CAC 140	CAC 141	CAC 142	CAC 143	CAC 144
Grid Ref.	72171423	72171424	72171425	72171426	72171427	72181421
Location	Devils Frying pan	Devils Frying pan	Devils Frying pan	Devils Frying pan	Devils Frying pan	Devils Frying pan
Lithology	Myl. Amph-bearing perid.	Felsic Kennack Gneiss	Kennack Gneiss	Mafic Traboe cumulate	Landwednack amphibolite	Landwednack amphibolite
Sample No.	CAC 145	CAC 146	CAC 147	CAC 148	CAC 149	CAC 150
Grid Ref.	68241339	68241339	68241339	68241339	68171354	68111345
Location	Shore, S-Side Lawarnick Pit	Shore, S-Side Lawarnick Pit	S-Side Pit Lawarnick Pit	S-Side Pit Lawarnick Pit	Top Lawarnick Pit	NE Nantivet Rock
Lithology	Gabbroic vein	Gabbroic vein	Gabbroic vein	Gabbroic vein	Hydrous shear-zone	Gabbroic vein
Sample No.	CAC 151	CAC 152	CAC 153	CAC 154	CAC 155	CAC 156
Grid Ref.	68111346	65981684	66291715	71202223	66451587	67851435
Location	NE Nantivet Rock	150m S "Men-te-Heul", N Predannack Hd	N side Fault, Ryniau	Trevassick Quarry	150m W Parc Bean Cove	250m E Grew Graze
Lithology	Gabbroic vein	Landwednack amphibolite	Landwednack Amphibolite	Myl. Pl-bearing perid.	Mylonitised amphibolite	Gabbroic vein
Sample No.	CAC 157	CAC 158	CAC 159	CAC 160	CAC 161	CAC 162
Grid Ref.	67321388	69351276	68811312	80952202	80462311	80302308
Location	The Horse, Kynance Cliff	S end Pentreath Beach	100m W Kynance Cove Car Park	Cliffs 200m NE Porthoustock	N Porthkerris	Back of Porthkerris Quarry
Lithology	Myl. Pl-bearing perid.	Myl. Pl-bearing perid.	Transitional assemblage perid.	Porthoustock amphibolite	Leucogabbro	Mafic Traboe cumulate
Sample No.	CAC 163	CAC 164	CAC 165	CAC 166	CAC 167	CAC 168
Grid Ref.	80472300	79872316	66271718	66451723	66781836	66681803
Location	W end Qy Face, Porthkerris	E Porthallow	N side of Fault, Ryniau	100 m west, Predannack Manor, Ryniau	Cliff top, Between Mullion & Pollunian	Below Mullion Cove Hotel
Lithology	Mafic Traboe cumulate	Qtz bearing mylonite	Landwednack amphibolite	Landwednack amphibolite	Mafic Traboe cumulate	Gabbroic vein
Sample No.	CAC 169	CAC 170	CAC 171	CAC 172	CAC 173	CAC 174
Grid Ref.	66901872	66901872	69011634	69011634	69011634	69011634
Location	South End Pollunian Cove	South End Pollunian Cove	E52150 - Predannack BH - 296.62m	E52152 - Predannack BH - 301.46m	E53007 - Predannack BH - 309m	E53008 - Predannack BH - 316m
Lithology	Landwednack amphibolite	Landwednack amphibolite	Landwednack amphibolite	Landwednack amphibolite	Landwednack amphibolite	Landwednack amphibolite
Sample No.	CAC 175	CAC 176	CAC 177	CAC 178	CAC 179	CAC 180
Grid Ref.	75401665	75401665	71431292	71431292	68751322	67371345
Location	W-side Cove, 200m SE of Spermic Cove	W-side Cove, 200m SE of Spermic Cove	Contact zone - Balk Quarry	N-side of Quarry, by edge	100m W Kynance Cove Car Park	150m SE Rill Point
Lithology	Hydrous shear-zone	Gabbro Mylonite	Hydrous shear-zone	Hydrous shear-zone	Plag. lherz.	Feldspathic band
Sample No.	CAC 181	CAC 182	CAC 183	CAC 184	CAC 185	CAC 186
Grid Ref.	67371345	67371345	70131147	70111138	70101136	70041147
Location	150m SE Rill Point	150m SE Rill Point	Base of Cliff below MSP Café	3m East of Arch&Stack, Vellan Drang	20m South of Arch&Stack, Vellan Drang	Under Old Slipway, Polpeur Cove
Lithology	Feldspathic band	Feldspathic band	Ol.HS amphibolite	Ol.HS amphibolite	Deformed mafic sheet	Deformed mafic sheet
Sample No.	CAC 187	CAC 188	CAC 189	CAC 190	CAC 191	CAC 192
Grid Ref.	71541315	67051476	67041476	66881563	81092161	80552300
Location	Cove, N of Pam Voose Cove	Cliff Top E Pengersick	Cliff Top E Pengersick	Pol Cornick	Porthoustock Point	Porthkerris Quarry
Lithology	Flasser Gabbro	Myl. Pl-bearing perid.	Myl. Pl-bearing perid.	Landwednack amphibolite	Coarse-grained gabbro	Granite vein
Sample No.	CAC 193	CAC 194	CAC 195	CAC 196	CAC 197	MS 1668
Grid Ref.	78351860	68801502	69351265	72791590	72791590	69421151
Location	North Side of Coverack Cove	100m East of Lion Rock, Pentreath beach	South end of Pentreath Beach	Enys Head, North of Kildown Cove	Enys Head, North of Kildown Cove	Lizard Head
Lithology	Coarse-grained gabbro	Mafic Dyke	Landwednack amphibolite	Mafic dyke within Kennack Gneiss	Mafic dyke within Kennack Gneiss	Granite vein

Table D.8 Sample list

Sample No.	E 52170	E 52171	E 52175	E 52179	E 52180	E 52184
Grid Ref.	73612147	73612147	73612147	73612147	73612147	73612147
Location	Traboe BH1 20.7m	Traboe BH1 25.3m	Traboe BH1 39.9m	Traboe BH1 46.97m	Traboe BH1 49.70m	Traboe BH1 63.11m
Lithology	Mafic Traboe cumulate	Mafic Traboe cumulate	Ultramafic Traboe cumulate	Ultramafic Traboe cumulate	Mafic Traboe cumulate	Mafic Traboe cumulate

Sample No.	E 52185	E 52187	E 52190	E 52193	E 52198	E 52199
Grid Ref.	73612147	73612147	73612147	73612147	74082104	74082104
Location	Traboe BH1 64.0 m	Traboe BH1 72.0m	Traboe BH1 78.0m	Traboe BH1 99.4m	Traboe BH2 49.25m	Traboe BH2 60.5m
Lithology	Mafic Traboe cumulate	Ultramafic Traboe cumulate	Ultramafic Traboe cumulate	Ultramafic Traboe cumulate	Ultramafic Traboe cumulate	Ultramafic Traboe cumulate

Sample No.	E 52203	E 52205	E 52204	E 52210	E 54520	E 54523
Grid Ref.	73682152	73682152	73682152	73682152	73682152	73682152
Location	Traboe BH3 26.83m	Traboe BH3 43.9m	Traboe BH3 38.84m	Traboe BH3 72.31m	Traboe BH3 45.72m	Traboe BH3 69.49m
Lithology	Mafic Traboe cumulate	Mafic Traboe cumulate	Ultramafic Traboe cumulate	Ultramafic Traboe cumulate	Mafic Traboe cumulate	Mafic Traboe cumulate

Sample No.	anu 4-1	anu 4-18	anu 5-8	anu 6-9	troct L1	DHG 1-1
Grid Ref.	N/A	N/A	N/A	N/A	N/A	N/A
Location	Kynance Cove	Poltesco	Pen Voose Cove	Pol Cornick	Perprean Cove	Kilcobben Point
Lithology	Transitional assemblage perid.	Pyroxenite vein	Plag. Ilherz.	Ultramafic Traboe cumulate	Troctolite	Landedwack amphibolite

Sample No.	DHG 2-6	DHG 4-6	DHG 5-1	DHG 5-5	DHG 6-1	DHG 6-4
Grid Ref.	N/A	N/A	N/A	N/A	N/A	N/A
Location	Ryniau	Kynance Cove	Pen Olver	Pen Olver	Vellan Head	Pol Cornick
Lithology	Landedwack amphibolite	Myl. Pl-bearing perid.	Landedwack amphibolite	Landedwack amphibolite	Myl. Pl-bearing perid.	Gabbroic vein

Sample No.	DHG 6-5	DHG 6-7	DHG 6-13	DHG 8-1	2553	2558
Grid Ref.	N/A	N/A	N/A	N/A	N/A	N/A
Location	Pol Cornick	Pol Cornick	Parc Bean Cove	Penra Head	N/A	N/A
Lithology	Gabbroic vein	Mafic Dyke	Gabbroic vein	Portloustock amphibolite	Spinel Ilherz.	Spinel Ilherz.

Sample No.	47033	47036	47037	47040	90703	90878
Grid Ref.	N/A	N/A	N/A	N/A	N/A	N/A
Location	Georges Cove	Georges Cove	Georges Cove	Coverack	Pol Cornick	Nr. The Chair, Ryniau
Lithology	Gabbroic vein	Gabbroic vein	Gabbroic vein	Crousa gabbro	Gabbroic vein	Landedwack amphibolite

Sample No.	90880	90881	90882	90883	90884	90885
Grid Ref.	N/A	N/A	N/A	N/A	N/A	N/A
Location	Nr. The Chair, Ryniau	Nr. The Chair, Ryniau	Nr. The Chair, Ryniau	Nr. The Chair, Ryniau	Nr. The Chair, Ryniau	90m S Ryniau
Lithology	Landedwack amphibolite	Landedwack amphibolite	Landedwack amphibolite	Landedwack amphibolite	Landedwack amphibolite	Landedwack amphibolite

Sample No.	90887	90888	90890	90892	90893	90894
Grid Ref.	N/A	N/A	N/A	N/A	N/A	N/A
Location	90m S Ryniau	90m S Ryniau	The Chair, Nr. Ryniau	The Chair, Nr. Ryniau	The Chair, Nr. Ryniau	The Chair, Nr. Ryniau
Lithology	Landedwack amphibolite	Landedwack amphibolite	Landedwack amphibolite	Landedwack amphibolite	Landedwack amphibolite	Landedwack amphibolite

Sample No.	90899	90901	L1	L2	L3	KE15
Grid Ref.	N/A	N/A	75691668	75691668	75691668	N/A
Location	The Chair, Nr. Ryniau	S-side Ogo Dour Cove	Lankidden Cove	Lankidden Cove	Lankidden Cove	Kennack Sands
Lithology	Landedwack amphibolite	Landedwack amphibolite	Dunite	Dunite	Dunite	Dunite

Sample No.	KE10	KE14	KE20	A25	A26	A27
Grid Ref.	N/A	N/A	N/A	N/A	N/A	N/A
Location	Kennack Sands	Kennack Sands	Kennack Sands	Perprean Cove	Perprean Cove	Perprean Cove
Lithology	Dunite	Dunite	Spinel Ilherz.	Dunite	Dunite	Dunite

Table D.8 Sample list

## THE TECTONIC EVOLUTION OF PERIDOTITES IN THE LIZARD OPHIOLITE COMPLEX, SOUTH-WEST ENGLAND

C.A. COOK, R.E. HOLDSWORTH AND M.T. STYLES



Cook, C.A., Holdsworth, R.E. and Styles, M.T. 1988. The tectonic evolution of peridotites in the Lizard Ophiolite Complex, south-west England. *Geoscience in south-west England*, 8, 000-000.

The mantle peridotites of the Lizard Complex, south-west England, preserve direct and indirect evidence for several deformation episodes: 1) Extensional uplift of mantle prior to the formation of oceanic crust in an incipient ocean basin; 2) Their subsequent emplacement by thrusting in an intra-oceanic setting at the onset of obduction; 3) Extensional reactivation of the intra-oceanic thrust contacts in response to late stage collapse of a nappe pile (Jones, 1997).

An early fabric is characterised by a sub-vertical foliation and a steeply plunging mineral lineation. This fabric pre-dates the formation of oceanic crust as it is cross-cut by MORB-type gabbro intrusions and dykes. Among the least deformed peridotites are spinel- and plagioclase-lherzolites with a coarse to medium-grained porphyroclastic texture. With increasing deformation, these pass transitionally into mylonitic plagioclase-bearing peridotites and mylonitic amphibole-bearing peridotites which have a medium to fine-grained porphyroclastic textures. The presence of 'fertile' spinel lherzolite and the orientation of the peridotite fabric is not typical of emplacement of peridotites at an oceanic spreading centre. Alternatively it is proposed that systematic changes in microstructure, mineral chemistry and geothermometry of the different peridotite types are related to changing conditions of P and T during tectonically controlled uplift of mantle. Changes in the whole-rock compositions of the deformed peridotites are thought to be related to syn-tectonic metasomatism by hydrous melts. The subsolidus trajectory of the peridotites suggests deformation in the footwall of an extensional shear zone or in the margins of an upwelling mantle diapir.

C.A. Cook and R.E. Holdsworth, Reactivation Research Group, Department of Geological Sciences,  
University of Durham, Durham, DH1 3LE  
M.T. Styles, British Geological Survey, Keyworth, Nottingham, NG12 5GG

## INTRODUCTION

The Lizard Complex (Figure 1) forms the highest structural level exposed in the Variscan nappe stack of south-west England (Holder and Leveridge, 1986). The Lizard Complex has previously been interpreted as a peridotite diapir with a dynamothermal aureole overprinted on regionally metamorphosed amphibolites (Green, 1964). More recently, the Lizard Complex has been considered as a highly deformed and dismembered Devonian ophiolite assemblage (Bromley, 1979; Styles and Kirby, 1980). In the ophiolite models, the mantle section of the Lizard consists of variably deformed peridotites (Flett and Hill, 1912; Green, 1964; Rothstein, 1977, 1981, 1988, 1994; Davies, 1984). A detailed discussion of the ophiolite model and a summary of the different lithologies represented in the Lizard complex is presented in a review by Floyd *et al.* (1993).

The Lizard complex of high-grade metamorphic rocks is separated from the low-grade, Gramscatho group Devonian metasediments to the north by a high-angle extensional fault, related to reactivation of earlier thrust faults (Power *et al.*, 1996).

This paper describes fabrics which predate the main magmatic events related to the formation of oceanic crust. These fabrics are related to deformation of a high pressure and high-temperature spinel lherzolite protolith and its subsequent evolution to lower P and T assemblages during uplift of the mantle. Details are provided about the nature of fabrics related to this deformation and the subsequent changes in peridotite microstructure, mineral and whole-rock geochemistry. These

observations are consistent with other examples of deformed mantle, and provide important new constraints on the tectonic evolution of the Lizard peridotites.

## FIELD OBSERVATIONS

Field evidence suggests that the peridotites are one of the earliest rock types formed in the ophiolite part of the Lizard complex. Borehole evidence (Leake and Styles, 1984) suggests that the peridotites are the substrate on/in which the highly deformed ultramafic/mafic rocks of the Traboe cumulate complex were formed. Controversial contacts between peridotite and amphibolite in the Ogo Dour cove area, on the west coast, suggest that some amphibolites at this locality are intrusive into peridotite. The peridotites are clearly intruded by the Crousa gabbro, MORB-type basaltic dykes and the Kennack Gneiss (Figure 1 for locations).

In the field two main types of peridotite can be identified: coarse-grained lherzolites in low-strain areas, and mylonitic peridotites in high-strain zones. The coarse-grained lherzolites are exposed in the central, southern and eastern parts of the Lizard (Figure 1), whilst the mylonitic peridotites are predominant in the northern and western areas. In most areas, the different peridotite types are juxtaposed by later brittle faults, although gradational contacts are preserved near Kynance Cove (Figure 1).

In the field, coarse-grained lherzolites have a fabric defined by slightly stretched orthopyroxene porphyroclasts, spinel, olivine and recrystallised clinopyroxene. Pyroxene-rich



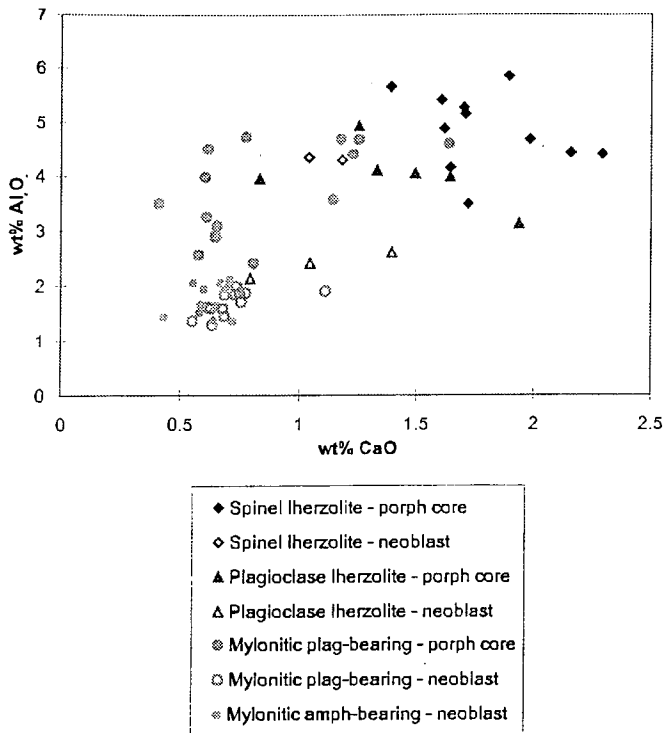


**Figure 3** = Plot of  $\text{Al}_2\text{O}_3$  vs  $\text{CaO}$  for orthopyroxenes from spinel lherzolite, plagioclase lherzolite, mylonitic plagioclase-bearing peridotite, and mylonitic amphibole-bearing peridotite. Major element analysis of orthopyroxenes were performed at the British Geological Survey, Keyworth, by Wavelength-dispersive spectrometry using a Cameca SX50 electron microprobe and at the Research School of Earth Sciences, the Australian National University, Canberra, by energy-dispersive spectrometry using a fully automated Cameca Camebax electron microprobe using the methods of Ware (1991).

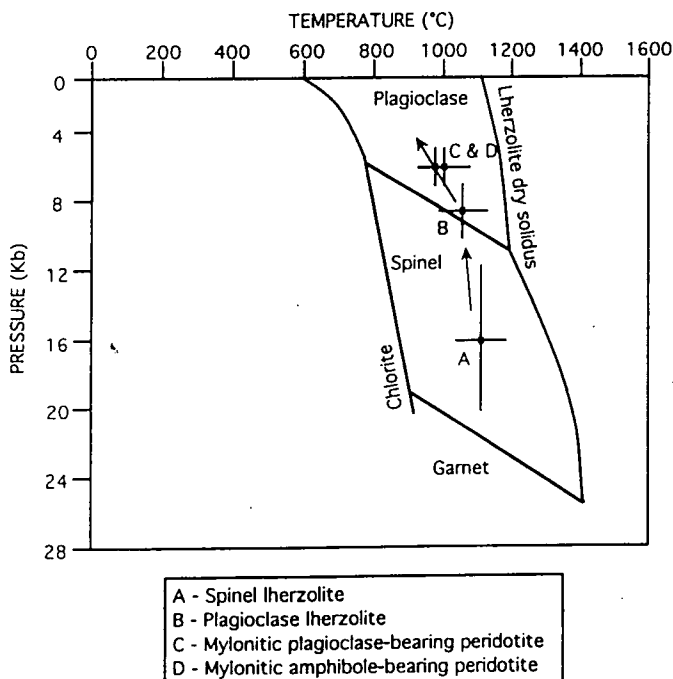


**Figure 4** = The inferred P-T path for the Lizard peridotites, based upon data obtained from the thermometer of Wells (1977) and Witt-Eikschén and Seck (1991), and data presented in Rothstein (1988) and Davies (1984).

consistent with the smaller number of analyses of mineral separates presented by Green (1964).

Cores of porphyroclasts in the coarse-grained spinel lherzolites have slightly higher  $\text{Al}_2\text{O}_3$  and  $\text{CaO}$  than the rims, which have compositions approaching those of the adjacent neoblasts. This suggests that during deformation the rims are reacting and approaching equilibrium with the fine-grained neoblasts (Hoogerduijn Strating *et al.*, 1993). A significant feature of this data is that the composition of orthopyroxene porphyroclasts in the mylonitic plagioclase-bearing peridotites is similar to porphyroclasts in the coarse-grained lherzolites. This suggests that the orthopyroxene porphyroclasts in the mylonitic peridotites are relicts from a coarse-grained lherzolite protolith.

These compositional changes are interpreted as reflecting changing conditions of temperature and pressure, synchronous with dynamic recrystallisation of the peridotites.

An inferred P-T trajectory for the evolution of the peridotites is presented in Fig.4, and the results confirm that the tectonic evolution of the peridotites is accompanied by a decrease in P and T. This P-T trajectory is based on estimates of pyroxene equilibration temperatures and the results are consistent with those of Rothstein (1988) and Davies (1984).

## WHOLE ROCK GEOCHEMISTRY

### Major and trace elements

Volatile free compositions of the different peridotite types are shown in Figure 5. These two graphs show that the mylonitic peridotites have compositions which are different from the spinel and plagioclase lherzolites as there is virtually no overlap for the composition fields for these and many other elements. In particular, the mylonitic peridotites have lower  $\text{MgO}$ , and higher  $\text{TiO}_2$  and  $\text{Al}_2\text{O}_3$  than the coarse-grained lherzolites.

### Rare Earth Elements

The chondrite normalised compositions for the Lizard peridotites analysed in this study (Figure 6) are comparable with the analyses from the Lizard published by Frey (1969), although there are subtle differences which may be due to different analytical techniques used.

The spinel lherzolites and plagioclase lherzolites have identical REE compositions, characterised by extreme depletion of LREE relative to chondrite (LREE close to detection limits) and they possess (Ce/Yb) normalised ratios of (average = 0.03). The REE compositions of the mylonitic plagioclase bearing-peridotite and mylonitic amphibole-bearing peridotites are identical, but contrast markedly with the spinel and plagioclase lherzolites. The mylonitic peridotites show similar HREE to the spinel and plagioclase lherzolites, but they are much less depleted in LREE, approaching chondritic values, and possess (Ce/Yb) normalised ratios of (average = 0.35) for the mylonitic plagioclase bearing-peridotite and (average = 0.44) for mylonitic amphibole-bearing peridotites.

## INTERPRETATION OF GEOCHEMICAL DATA

The geochemical compositions of the Lizard peridotites shown in Figures 5 and 6 reveal that peridotites vary in composition, between the coarse-grained lherzolites and the mylonitic peridotites. If the mylonitic peridotites were simply the products of deformation and re-equilibration of a coarse-grained lherzolite protolith, as suggested by field, microstructural and mineral compositions above, they would be expected to show a similar whole rock composition. The observed changes in geochemistry suggest, however, that during deformation, the mylonitic peridotites

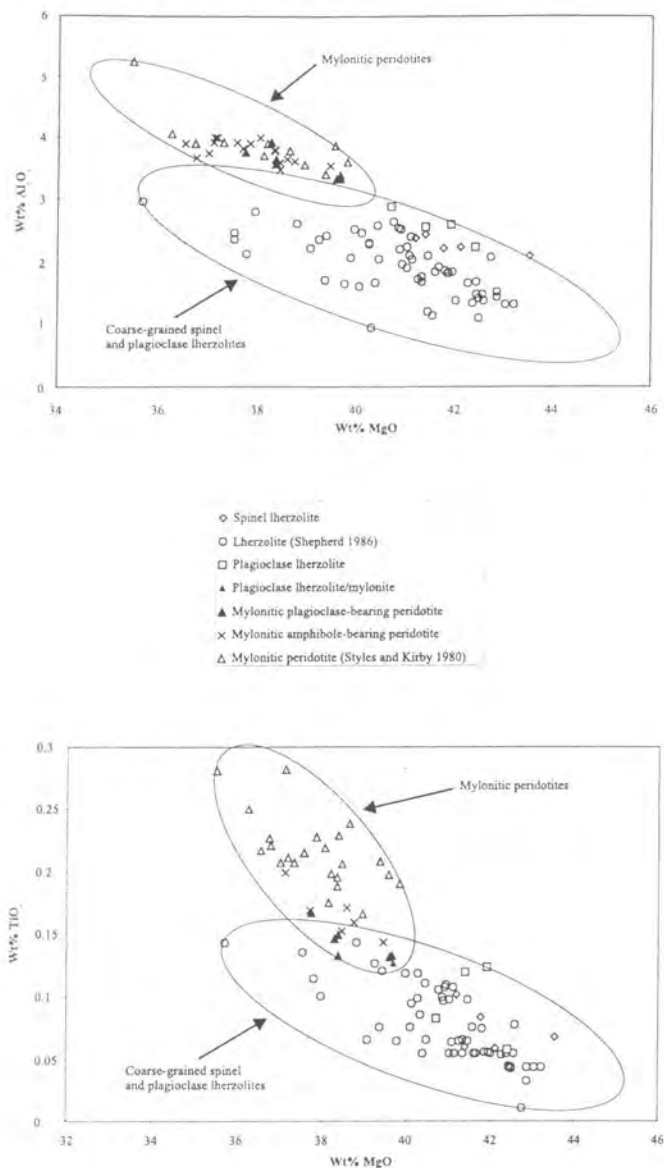


**Figure 5** = Plot of  $Al_2O_3$  and  $TiO_2$  against MgO for whole-rock samples of Lizard peridotite. Peridotite samples were analysed by XRF at the University of Durham. Includes data from Shepherd (1986), Styles and Kirby (1980) and D.H. Green (pers comm). All major element compositions are reported as volatile-free.

were enriched in major, trace and rare earth elements. A process that causes the geochemical enrichment of a rock is metasomatism, related to the interaction between a rock, and a melt and/or a hydrous fluid resulting in a change of the bulk composition. The increase of  $TiO_2$  in the whole-rock composition of the mylonitic peridotites relative to the coarse-grained lherzolites suggests that the metasomatism was related to the infiltration of a melt. Eggler (1987) suggests that Ti is relatively insoluble in  $H_2O$  and  $CO_2$  rich fluids and hence a magmatic component, rather than a fluid alone, is likely to be important. Using petrological, whole-rock REE and isotopic studies, Davies (1984) concluded that the composition of the mylonitic peridotites is related to a melt infiltration event. The presence of amphibole, a hydrous phase, in the mylonitic peridotites shows that hydrous fluids must also have been associated with the melt responsible for the metasomatism of the peridotites.

## DISCUSSION

The data presented in the preceding sections suggest that mylonitic plagioclase-bearing peridotites were formed by syn-

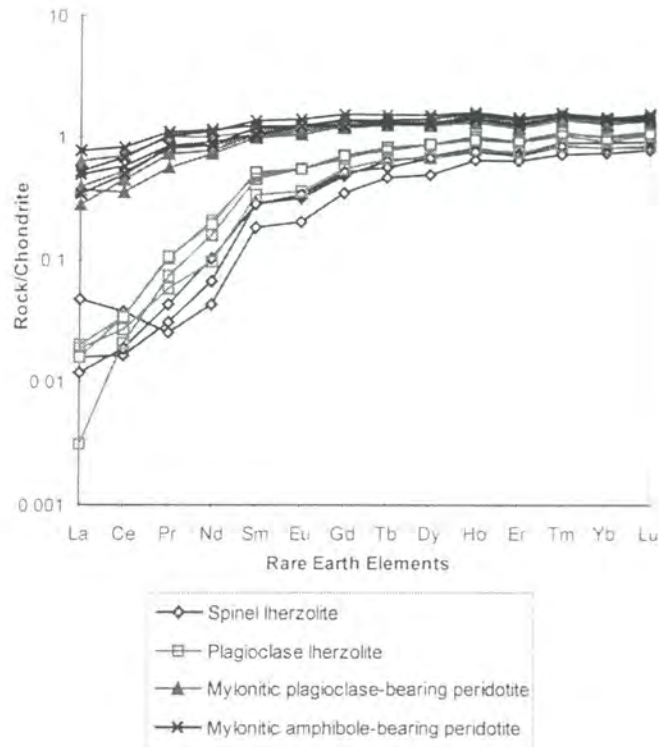
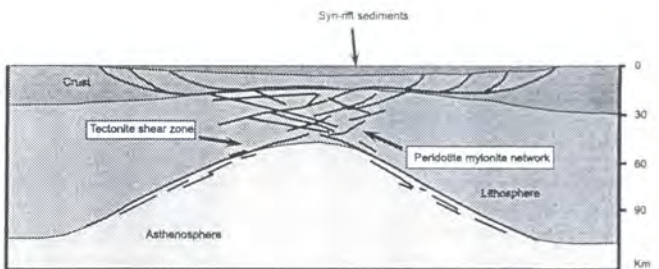
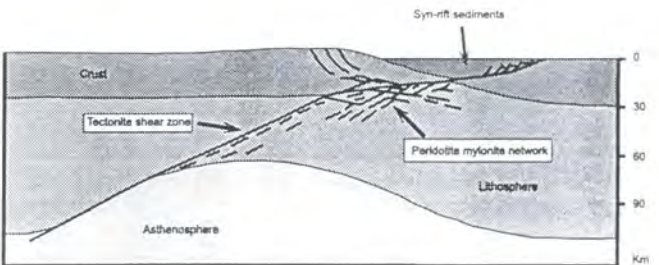


**Figure 6** = Chondrite-normalised REE compositions of the Lizard peridotites. Analysis by ICP-MS at the University of Durham. Normalising values of Nakamura (1974).



a) symmetric, diapirism



b) asymmetric, detachment

**Figure 7** = Possible interpretations of the tectonic environment responsible for the uplift and deformation of the Lizard peridotites. After Visser et al (1995).



tectonic metasomatism caused by the addition of a hydrous, fluid-rich melt during the recrystallisation and re-equilibration of a coarse-grained spinel/plagioclase lherzolite host during deformation in the upper mantle.

A subsequent interaction of a hydrous fluid with the mylonitic plagioclase-bearing peridotite resulted in pyroxene being replaced by pargasitic hornblende, thus producing mylonitic amphibole-bearing peridotite. This would account for both the presence of mylonitic amphibole bearing peridotite over 100's m of outcrop, and mm scale interbanded zones within mylonitic plagioclase-bearing peridotite. This is also compatible with the very similar bulk composition.

The evidence presented here suggests that the metasomatic event and later hydrous fluid interaction seem to have preferentially occurred in the high-strain zones now composed of mylonitic peridotite. Evidence from the Lizard and other examples of deformed mantle, such as Zabargad Island (Agrinier *et al.*, 1993) and the Josephine peridotite, south-west Oregon (Keleman and Dick, 1995), suggest that melt flow is preferentially focused along actively deforming ductile shear zones. What is not clear, however, is whether the recrystallised nature of the shear zones facilitates melt infiltration, or whether the shear zone is the result of deformation enhanced by fluid flow (Keleman and Dick, 1995).

In terms of a tectonic environment these processes could occur either in the deforming margins of a peridotite diapir as proposed by Green (1964), or during footwall uplift along an extensional detachment within the mantle (Figure 7). The present-day geographic distribution of the peridotite mylonites in the Lizard complex may be consistent with either model, however, the effects of later faulting and thrusting hamper interpretation of the original geometry of these shear-zones.

## CONCLUSIONS

The Lizard peridotites show a metamorphic evolution from a high-temperature and high-pressure spinel lherzolite protolith, via plagioclase lherzolite to mylonitic plagioclase-bearing peridotite during deformation related to the uplift of the mantle to conditions of lower P and T.

During uplift and deformation, hydrous melt flow was localised within the high-strain zones resulting in metasomatism forming mylonitic plagioclase-bearing peridotites. At a lower P/T an interaction with hydrous fluid resulted in the formation of mylonitic amphibole-bearing peridotite. These results highlight the importance of the relationship between deformation in mantle rocks and focused flow of melt and fluids. Although there are many differences in detail, this modern study supports the main findings of Green (1964) that the Lizard shows extensive evidence for the re-equilibration of lherzolitic peridotite under conditions of decreasing temperature and pressure.

## ACKNOWLEDGEMENTS

The authors thank Dr Julian Pearce and Prof. D.H.Green for discussions on aspects of the Lizard peridotites which have improved the text. Prof. D.H.Green and Martin Cimral of RSES, Australian National University provided electron microprobe data and Nick Ware assisted with microprobe analysis at ANU. Ron Hardy is thanked for help with sample preparation and XRF analyses at Durham, and Chris Ottley, for help with sample preparation and ICP-MS analyses at Durham. CAC gratefully acknowledges receipt of a PhD studentship grant from the British Geological Survey and a Durham Postgraduate Research Award. This paper is published with approval of the Director, British Geological Survey (NERC).

## REFERENCES

- BROMLEY, A.V. 1979. Ophiolitic origin of the Lizard Complex. *Cambourne School of Mines Journal*, **79**, 25-38.
- DAVIES, G.R. 1984. Isotopic evolution of the Lizard Complex, *Journal of the Geological Society of London*, **141**, 3-14.
- EGGLER, D.H. 1987. Solubility of major and trace elements in mantle metasomatic fluids. Experimental constraints. In: *Mantle Metasomatism*. Eds: MENZIES, M.A. and HAWKESWORTH, C.J., Academic Press, London, 21-39.
- FLETT, J.S. and HILL, J.B. 1912. The geology of the Lizard and Meneage, *Geological Survey of Great Britain*, Sheet Memoir 359, 2nd edition 1946 (revised).
- FLOYD, P.A., EXLEY, C.S. and STYLES, M.T. 1993. *Igneous Rocks of South-West England*. Geological Conservation Review Series. Chapman and Hall, London.
- FREY, F.A. 1969. Rare earth abundances in a high-temperature peridotite intrusion, *Geochimica et Cosmochimica Acta*, **33**, 1429-1447.
- GREEN, D.H. 1964. The petrogenesis of the high temperature peridotite intrusion in the Lizard area, Cornwall. *Journal of petrology*, **5**, 134-188.
- HOLDER, M.T. and LEVERIDGE, B.E. 1996. A model for the tectonic evolution of south Cornwall. *Journal of the Geological Society of London*, **143**, 125-134.
- HOOGERDIJN STRATING, E.H., RAMPONE, E., PICCARDO, G.B., DRURY, M.R., VISSERS, R.L.M. 1993. Subsolidus emplacement of mantle peridotites during incipient oceanic rifting and opening of the Mesozoic Tethys Voltri Massif, NW Italy, *Journal of Petrology*, **34**, Part 5, 901-927.
- JONES, K.A. 1997. Deformation and emplacement of the Lizard Ophiolite Complex, SW England, based on evidence from the Basal Unit, *Journal of the Geological Society of London*, **154**, 871-885.
- KELEMEN, P.B. and DICK, H.J.B. 1995. Focused melt flow and localized deformation in the upper mantle: juxtaposition of replacive dunite and ductile shear zones in the Josephine peridotite, SW Oregon, *Journal of Geophysical Research*, **100**, No.B1, 423-438.
- LEAKE, B.E. 1978. Nomenclature of amphiboles, *Canadian Mineralogist*, **16**, 501-516.
- LEAKE, R.C. and STYLES, M.T. 1984. Borehole sections through the Trestle hornblende schists, a cumulate complex overlying the Lizard Peridotite. *Journal of the Geological Society of London*, **141**, 41-52.
- MERCIER, J.-C.C., and NICOLAS, A., 1975. Textures and fabrics of upper mantle peridotites as illustrated by xenoliths from basalts, *Journal of Petrology*, **16**, 454-496.
- NAKAMURA, N. 1974. Determination of REE, Ba, Fe, Mg, Na and K in carbonaceous and ordinary chondrites. *Geochimica et Cosmochimica Acta*, **38**, 757-773.
- POWER, M.R., ALEXANDER, A.C., SHAIL, R.K. & SCOTT, P.W. 1996. A re-interpretation of the internal structure of the Lizard Complex. *Proceedings of the Ussher Society*, **9**, 63-97.
- ROTHSTEIN, A.T.V. 1977. The distribution and origin of primary textures in the Lizard Peridotite, Cornwall. *Proceedings of the Geologists Association*, **88**, 93-105.
- ROTHSTEIN, A.T.V. 1981. The primary cumulates of the Lizard peridotite, Cornwall. *Geological Magazine*, **118**, 491-500.
- ROTHSTEIN, A.T.V. 1988. An analysis of the textures within the primary assemblage peridotite, the Lizard, Cornwall. *Proceedings of the Geologists Association*, **99**, 181-92.



- ROTHSTEIN, A.T.V. 1994. Directional features within an assemblage of primary textures preserved in a kilometre section of the upper mantle peridotite, from the Lizard, Cornwall. *Proceedings of the Ussher Society*, **8**, 248-253.
- SHEPHERD, A. 1986. *The geochemistry and evolution of the Lizard Complex, Cornwall*. Unpublished Ph.D. Thesis, University of Nottingham.
- STYLES, M.T., and KIRBY, G.A. 1980. New Investigations of the Lizard complex, Cornwall, England and a discussion of an ophiolite model. *Proceedings of the International Ophiolite Symposium, Cyprus, 1979*. Geological Survey Department, Nicosia, 512-26.
- WARE, N.G. 1991. Combined Energy-Dispersive-Wavelength-Dispersive Quantitative Electron Microprobe Analysis. *X-Ray Spectroscopy*, **20**, 73-79.
- WELLS, P.R.A. 1977. Pyroxene thermometry in simple and complex systems. *Contributions to Mineralogy and Petrology*, **62**, 129-39.
- WITT-EIKSCHEN, G., and SECK, H.A. 1991. Solubility of Ca and Al in orthopyroxene from Spinel peridotite: an improved version of an empirical geothermometer. *Contributions to Mineralogy and Petrology*, **106**, 431-39.